

ASD-TR-61-628
PART II

408 925

CATALOGED BY UDU
AS AD No. 408925

STUDIES OF THE BRITTLE BEHAVIOR OF CERAMIC MATERIALS

TECHNICAL DOCUMENTARY REPORT No. ASD-TR-61-628, I

APRIL 1963

DIRECTORATE OF MATERIALS AND PROCESSES
AERONAUTICAL SYSTEMS DIVISION
AIR FORCE SYSTEMS COMMAND
WRIGHT-PATTERSON AIR FORCE BASE, OHIO

Project No. 7350, Task No. 735001

(Prepared under Contract No. AF 33(616)-7485
by Armour Research Foundation of Illinois Institute of Technology
Chicago, Illinois; Nicholas A. Weil, Author)

BEST
AVAILABLE COPY

ERRATUM TO REPORT NO. ASD-TOR-61-028, Part 2

"STUDIES OF BRITTLE BEHAVIOR OF CERAMIC MATERIALS"

There are four statements that should be deleted from the text of the report because they resulted from a misunderstanding on the part of the program manager responsible for the conduct of the program at the time. These statements are:

- Page 9: "Neither the precise composition, nor the density or specific grain size distribution for this material has been supplied by A. I., despite recurrent statements that such will be done. If such information is not received from A. I. in the near future, analysis of the material will be secured locally."
- Page 37: "For this series only the as-received Wesgo AL-99 was explored and the BeO was not tested at all, since only the medium volume size of specimen was supplied by A. I."
- (second par.)
- Page 41: "To reduce the details of presentation, again only the final Weibull plots are presented for this series; also, as stated, data for BeO could not be secured, since this material was supplied in only one volume."
- (second par.)
- Page 62: "First the specimens were not supplied according to specifications; neither the volumetric variation nor different grain sizes were rendered available to us for experimental work on BeO."
- (first par.)

It should also be stated that Atomics International (with authorization from the program manager) made the BeO samples available to the program in 1962 without charge and this assistance is gratefully acknowledged.

With regard to the statement on page 9, the burden of material characterization was with the program manager and the Atomics International personnel did not make any commitments or promises to provide density, grain size distribution, or any other material property. This was clearly understood in correspondence with A. I. The statement on page 62 should also be deleted for the same reason.

The statements on pages 37 and 41 should also be deleted since the BeO materials sizes and shapes were agreed upon, and it was understood that no attempt would be made to fabricate other sizes or shapes at A. I.

In summary, the statements on page 9, page 37, page 41, and page 62 are erroneous, and due to an unfortunate choice of words, leave an erroneous impression about the role of A. I. in this program. The BeO materials were provided to this program "gratis" by A. I., who, we believe, had no responsibility for characterization of the materials. We are sorry for this unfortunate error.

**BEST
AVAILABLE COPY**

NOTICES

ASTIA release to OTS not authorized.

The information furnished herewith is made available for study upon the understanding that the Government's proprietary interests in and relating thereto shall not be impaired. It is desired that the Staff Judge Advocate (RDJ), Aeronautical Systems Command, Post Office Box 1395, Baltimore 3, Maryland, be promptly notified of any apparent conflict between the Government's proprietary interests and those of others.

This document may not be reproduced or published in any form in whole or in part without prior approval of the Government. Since this is a progress report, the information herein is tentative and subject to changes, corrections and modifications.

Copies of ASD Technical Reports and Technical Notes should not be returned to the Aeronautical Systems Division unless return is required by security considerations, contractual obligations, or notice on a specific document.

FOREWORD

This report represents the Final Report on the continuation phase of Armour Research Foundation (ARF) Project No. 8203, funded under Contract No. AF33(616)-7465, and covering the work performed during the period December 1, 1961 to November 30, 1962. In view of the fact that this work represents a direct continuation of the first phase of this effort, reported on ASD-TR 61-628*, it has been decided to identify this report with the number ASD-TR 61-628 II, even though the first numeral was not designated with the postfix I.

This contract is supported by the Ceramics and Graphite Branch (ASRCMC), Metals and Ceramics Laboratory, Materials Central of the Aeronautical Systems Division, Air Force Systems Command (ASD of AFSC). With all sponsored research, but particularly with a program as large and diverse as this one, the success of the effort is strongly influenced by the guidance given it by the sponsoring agency. It is pleasing to acknowledge in this regard the frequent exchange of helpful information and suggestions advanced during the pursuit of this research program by J. B. Blandford, the technical monitor for this project, as well as by W. B. Ramke, Head, and the entire staff of the Ceramics and Graphite Branch of Materials Central, ASD, all of who took an abiding interest in the progress of this work.

* N. A. Weil, Ed., Studies of the Brittle Fracture of Ceramic Materials
ASD-TR 61-628 (April 1962).

ACKNOWLEDGEMENTS

Contributions to the work described in this report were made by the following persons:

Task 1	S. A. Bortz, R. F. Firestone, C. Hardison, H. Nagao, N. A. Weil
Task 2	B. W. Abbott, J. K. Anderson, R. M. Chaney, J. Cistaro, R. H. Cornish, J. W. Dally, J. Staulcup, R. J. Wolf
Task 3	J. Cistaro, I. M. Daniel, R. F. Firestone, C. Hardison, A. Juskeys, R. Miller, T. Niiro, J. Peri, E. Sevin, N. A. Weil
Task 4	J. R. Dvorak, P. R. V. Evans, Harry Konjevich, R. McGill
Task 5	part 1 P. L. DePirro, K. S. Mendelson, P. D. Southgate part 2 L. M. Atlas, J. W. Stuart
Task 6	J. Congleton, D. Hardie, R. N. Parkins, N. J. Petch
Task 7	E. Orowan
Task 8	I. B. Cutler, D. L. Johnson
Task 9	A. G. Pincus, J. W. Szymazek, A. Garufy, H. Lockwood, M. C. Houle, D. C. Lord, W. E. Rollins, L. M. Osika, J. E. Burke, W. B. Hillig, M. L. Kronberg, L. Navias, R. C. DeVries, C. A. Bruch
Task 10	R. B. Day, K. A. Olsen, R. J. Stokes
Task 11	G. T. Murray
Task 12	A. E. Gorum
Task 13	part 1 J. J. Corey, J. Cistaro, W. F. Riley part 2 E. L. McDowell, R. E. Welch
Task 14	P. R. V. Evans, J. Durek, R. Firestone, R. McGill
Task 15	part 1 L. M. Atlas, J. W. Stuart part 2 N. A. Weil

ABSTRACT

Factors influencing the fundamental behavior of brittle, non-metallic ceramics were investigated. Poly and single crystals of magnesium oxide beryllium oxide, and two grades of aluminum oxide were the principal materials used. Fifteen problem areas were probed in individual studies termed tasks:

- Task 1 - Effect of Structural Size: the "Zero Strength" studied the statistical fracture characteristics of the four oxides. The Weibull theory was found to descriptively characterize the cumulative distribution function of the fracture strengths and to adequately predict the variation of mean strength with specimen size.
- Test temperature, prior thermal history, surface finish, test atmosphere, and specimen finish were found to influence the Weibull zero strength, flow density exponent and scale parameters.
- Task 2 - The Effect of Strain Rate from 10^{-7} to 10^1 sec^{-1} at temperatures from 75° to 1800°F on the fracture stress in bending for the four oxides was experimentally determined. A technique for achieving uniaxial tension in a state of dynamic loading was developed.
- Task 3 - The Effect of Non-Uniform Stress Fields on the fracture characteristics of the brittle materials was studied. With the assumptions of the Weibull theory as a basis, extensive theoretical derivations for the risk the rupture of bend specimens were carried out to interpret experimental observations.
- Task 4 - The Effect of Microstructure on the fracture mechanisms of the polycrystalline oxides was studied under uniaxial compression in the temperature range 1000 - 1900°C . The fracture strength showed a marked dependence on temperature and grain size. A brittle-ductile fracture transition temperature was not observed.
- Task 5 - Internal Friction Measurements were made to determine the effect of anneal time and temperature, stress amplitude and dislocation density on dislocation damping. Attempts were made to explain experimental results in terms of the analytical models of Koehler, Granato-Lucke and Brailford. Damping studies made on polycrystalline aluminum oxide showed that at temperatures below 800°C , the relaxation process resembles that in alkali-free glass.
- Task 6 - Effect of Surface Energy on Brittle Fracture was studied using three techniques (1) crack propagation in plates containing pre-drilled cracks, (2) adsorption isotherm determinations and (3) zero-creep determinations at elevated temperatures.

- Task 7 - Fracture Mechanisms were investigated along two distinct lines: various-temperature studies on polycrystals and microscopic and X-ray studies on single crystals. The importance of kinking induced high stresses in crack nucleation was established. Crack initiation was also traced to the arrest of dislocation bonds by an obstacle band, and to the simultaneous widening of two conjugate dislocation bands where cracks are nucleated by stresses in finite tilt boundaries.
- Task 8 - The Effect of Impurities on Strength was investigated by examining the influence of carefully controlled additions of selected doping elements, Fe_2O_3 , ZrO_2 , SiO , TiO_2 and Cr_2O_3 .
- Task 9 - Static Fatigue: Delayed Fracture studied the corrosion processes which affect long-term strength. Fatigue theory was applied to low-temperature experimental data on mono and polycrystalline aluminum oxide. The observed bend strength of monocrystalline aluminum oxide was found quite sensitive to the prior thermal history.
- Task 10 - Effect of Thermal-Mechanical History on the Mechanical Properties of Magnesium Oxide included three investigations: (1) the effect of heat treatment on the aging of fresh dislocations; (2) the effect of heat treatment on microstructure and the resistance of the lattice to the movement of fresh dislocations and (3) the mobilization of grown-in dislocations by such means as heat treatment, fluctuating thermal stresses, and stressing at high temperatures.
- Task 11 - Surface Active Environments, as an embrittling effect on the mechanical properties of the mono and polycrystalline oxide were studied. Gaseous environments included hydrogen, nitrogen, air and water vapor.
- Task 12 - Dislocation Studies of the existence of plastic flow in the oxides followed two approaches: thin fiber electron transmission microscopic and plastic flow studies in bulk specimens.
- Task 13 - Crack Propagation studies were initiated to determine condition required for the catastrophic propagation of such cracks and available methods of arrest. An experimental technique for determining the stress fields about cracks was developed. A search and comprehensive review of existing steady-state and dynamic solutions for stress fields surrounding cracks in semi-infinite plates was made.
- Task 14 - Rheotropic Behavior was explored to determine the possibility of introducing room-temperature ductility into polycrystalline oxides by effects ascribable to elevated temperature deformation. The sintering characteristics of submicron magnesium oxide powders were studied.

Task 15 - Effect on Porosity and Grain Size on Strength and Elastic Modulus was studied analytically and experimentally. The literature is reviewed and the Hashin's analysis of the effect of elastic inclusion is extended to yield closed-form solutions for Young's modulus. These results are then simplified to yield definitive and simple expressions of uniform format for the effect of porosity on all the elastic constants.

PUBLICATION REVIEW

This report has been reviewed and is approved.

FOR THE COMMANDER:



W. G. Ramke
Chief, Ceramics and Graphite Branch
Metals and Ceramics Laboratory
Directorate of Materials and Processes

TABLE OF CONTENTS

	<u>Page</u>
I. <u>INTRODUCTION</u>	1
II. <u>MATERIALS</u>	6
1. Aluminum Oxide	6
2. Magnesium Oxide	7
3. Beryllium Oxide	8
III. <u>DISCUSSION</u>	10
<u>Task 1 - EFFECT OF STRUCTURAL SIZE: THE</u> <u>ZERO STRENGTH</u>	
ABSTRACT	10
1. Introduction	11
2. Experimental Techniques	12
A. Materials	12
B. Specimens	13
C. Testing Conditions	13
3. Theoretical Considerations	16
4. Experimental Results	22
A. Selection of Population Samples	22
B. Data Acquisition and Presentation	24
5. Evaluation and Discussion of Experimental Results	48
A. Effect of Parametric Variables on Strength	48
B. The Effect of Size on Strength	54
C. The Beryllium Oxide Test Series	62
6. Conclusion	70
7. References	73
<u>Task 2 - EFFECT OF STRAIN RATE</u>	
ABSTRACT	75
1. Introduction	76
2. Strain Rate Effects in Bending	77
A. Bending Fixtures	77
B. Elevated Temperature Furnace	80
C. Measurement of Failure Loads and Strain Rates	83
D. Specimens	85
3. Results	86
4. Discussion	100
A. Room Temperature Behavior	100
B. Behavior at 1000°F	102
C. Behavior at 1800°F	103
5. Preliminary Investigation of a Stress Wave Technique for Determining the Tensile Strength of Ceramic Materials	106

6. Summary	111
7. References	112

Task 3 - EFFECT OF NON-UNIFORM STRESS FIELDS

ABSTRACT	114
1. Introduction	115
2. Application of Weibull's Theory to Bending Specimens	117
A. Risk of Rupture	117
B. Relationship between Bending and Tensile Strengths	125
C. Conclusion	127
3. Analytical Determination of Material Parameters	129
A. Material Governed by Volumetric Flaw Distribution	129
B. Material Governed by Surface Flaw Distribution	132
4. Experimental Results	136
A. Columbia Resin CR-39	142
B. Wesgo Aluminum Oxide AL-995	155
C. Beryllium Oxide	160
D. Magnesium Oxide (ARF)	160
5. Conclusion	160
6. References	163

Task 4 - EFFECT OF MICROSTRUCTURE

ABSTRACT	164
1. Introduction	165
2. Materials	168
A. Polycrystalline Magnesium Oxide	168
B. Polycrystalline Aluminum Oxide	169
3. Apparatus and Testing Procedure	175
4. Results	178
A. Magnesium Oxide	178
B. Aluminum Oxide (Lucalox)	186
5. Discussion	194
6. Conclusion	199
7. References	201

Task 5 - INTERNAL FRICTION MEASUREMENTS

ABSTRACT	203
1. Introduction - Part One	204
2. Specimen Deformation	205
3. Dislocation Damping Above Room Temperature	210
4. Annealing of Dislocation Damping	214
A. Pinning by Vacancies	214
B. Analysis of Results	215
C. Anomalous Precipitation Kinetics	223
5. Point Defect Relaxation and Vacancy Diffusion	225
6. Damping Below Room Temperature	229
7. Theory of Dislocation Damping	233

8.	Theory of Amplitude Independent Damping	233
A.	The Brailsford Model	233
B.	Modification of Brailsford's Theory	235
C.	Application of Brailsford's Theory to Magnesium Oxide	240
D.	Effect of a Localized Charge Cloud	241
9.	Amplitude Dependent Damping	242
A.	Outline of The Granato-Lucke Theory of Dislocation Break-Away	242
B.	Analysis of Experimental Results on Amplitude Dependent Damping	246
10.	Conclusion	251
11.	Introduction - Part Two	254
12.	Experimental Methods	257
13.	Experimental Results	260
14.	Conclusion	268
15.	References	268

Task 6 - EFFECT OF SURFACE ENERGY

ABSTRACT	271
1. Introduction	272
2. The Fracture of Pre-Cracked Plates	273
A. Central Cracks	273
B. Crack Branching	282
C. Cantilever Loading of an Edge Crack	285
D. Discussion and Conclusion	285
3. Lowering of Surface Energy	290
A. Experimental Techniques	290
B. Discussion of Results	293
4. Surface Energy of Aluminum Oxide from the Stress Required to Prevent Surface Contraction	302
A. Results	303
B. Discussion	303
5. Contributing Personnel	306
6. References	307

Task 7 - FRACTURE MECHANISMS

ABSTRACT	308
1. Introduction	309
2. Work with Polycrystalline Specimens	312
A. Design of the High Temperature Testing Machine	312
B. Dogbone Specimens	322
C. Experimental Results	328
3. Experiments on Single Crystals of Magnesium Oxide	351
A. Preparation of Specimens	352
B. Features of Plastic Deformation in Magnesium Oxide Crystals	353

C.	Tension and Compression in the Kinks	365
D.	Crack Formation in Magnesium Oxide Crystals	371
E.	Discussion of Results	
4.	Appendix	398
5.	References	400

Task 8 - IMPURITY INFLUENCES

ABSTRACT	404
1. Introduction	405
2. Methods of Sample Preparation	406
3. Studies on Polycrystalline Magnesium Oxide	410
A. Effect of Annealing, Polishing and Temperature on Strength	410
B. Effect of Impurities on Strength of Room Temperature	416
C. Effect of Impurities on Strength at Elevated Temperatures	429
4. Studies on Polycrystalline Aluminum Oxide	429
A. Effect of Impurities on Strength at Elevated Temperatures	429
B. Statistical Analysis of Data	431
C. Effect of Titanium Oxide Additions on Strength of Aluminum Oxide at Room Temperature	438
D. Recrystallization Studies	440
5. Microhardness Studies	440
6. Sintering as a Function of Impurity Content	454
7. Preliminary Studies for the Preparation of High-Purity, Polycrystalline Oxides	460
8. Conclusion	460
9. References	466

Task 9 - STATIC FATIGUE· DELAYED FRACTURE

ABSTRACT	467
1. Introduction	468
2. Method of Approach	470
A. Dynamic and Static Testing	470
B. Atmospheres and Temperatures	471
3. Materials	471
A. Sapphire	471
B. Polycrystalline Aluminum Oxide	476
4. Experimental Equipment	477
A. Dynamic Bending	477
B. Static Bending	478
5. Experimental Results for Sapphire	480
A. Condition of Specimens	480
B. Effect of Thermal History	482
C. Base Level Strength of Sapphire	482
D. Constant Strain-Rate Tests on Sapphire	485
E. Delayed Failure Tests on Sapphire	491
F. Sapphire Fracture Surfaces	491

6.	Experimental Results for Polycrystalline Aluminum Oxide	494
A	Strength Versus Grain Size and Testing Rate	494
B.	Constant Strain-Rate on Lucalox	496
C	Delayed Failure Tests on Lucalox	502
7.	Discussion of Experimental Results	502
A	Fatigue Failure Theory	502
8.	Application of the Fatigue Theory to Low Temperature Tests on Al_2O_3	508
A.	Sapphire	508
B.	Polycrystalline Aluminum Oxide	511
9.	The High Temperature Fatiguing Characteristics of Al_2O_3	513
A.	Sapphire	513
B.	Polycrystalline Aluminum Oxide	514
10.	Conclusion	514
11	References	517

Task 10 - EFFECT OF THERMAL-MECHANICAL HISTORY

ABSTRACT	520
1. Introduction	521
2. Effect of Thermal History on the Mobility of 'Aged' Dislocations at Room Temperature	522
A Experimental Procedure	522
B. Mechanical Tests	523
C. Etch Pit Studies	527
D. Thin Film Studies	531
3. Effect of Thermal History of the Mobility of 'Fresh' Dislocations at Room Temperature	543
4 Some Attempts to Move 'Grown-In' Dislocations in Magnesium Oxide Single Crystals	546
A. By Heat Treatment	546
B By the Application of a Tensile Stress at Room Temperature	547
C. By the Application of a Fluctuating Stress at Room Temperature	549
D. By the Application of a Tensile Stress at High Temperatures	551
5. Conclusion	553
6. References	555

Task 11 - SURFACE ACTIVE ENVIRONMENTS

ABSTRACT	556
1. Introduction	557
2. Experimental Procedures	558
A Materials	558
B. Specimen Exposure	562
C Testing Procedure	563
3. Results	563
A. Magnesium Oxide Bicrystal Studies	563

B	Magnesium Oxide Single Crystal Studies	567
C	Aluminum Oxide Single Crystal Studies	570
D	Polycrystalline Aluminum Oxide Studies	576
4.	Discussion	577
A	Magnesium Oxide	577
B	Aluminum Oxide	578
5.	References	579

Task 12 - DISLOCATION STUDIES

ABSTRACT	581
1. Introduction	582
2. Experimental Procedures and Observations	583
A Electron Microscope Studies	583
B Plastic Flow Studies in Bulk Samples of Polycrystalline Magnesium Oxide	584
3. Conclusion	587
4. References	588

Task 13 - CRACK PROPAGATION

ABSTRACT	589
1 Introduction	590
2 Experimental Studies	591
3. Recommendations for Future Work	595
4 Static and Steady Dynamic Crack Solutions	597
5 Steady State Solutions from Static Solution	602
6. Transient Dynamic Crack Propagation	605
7 Conclusion	605
8. References	606

Task 14 - RHEOTROPIC BEHAVIOR

ABSTRACT	608
1. Introduction - Part One	609
2 Discussion	609
3 Introduction - Part Two	610
4 Materials	612
5 Experimental Procedure and Results	615
A Hot Pressing Experiments	615
B Cold Pressing and Sintering Experiments	620
6. References	632

Task 15 - EFFECT OF POROSITY

ABSTRACT	633
1 Introduction - Part One	634
2 Experimental Procedures	640
A Preparation of Aluminum Oxide Specimens	640
B. Strength Measurements	640
C Elastic Modulus	642
D Bulk Specific Gravity, Porosity	642

E	Internal Friction	643
F	Grain Size, Surface Area, and Grain Contact Area	644
3.	Experimental Results	644
4.	Introduction - Part Two	648
5.	Effect of Porosity on Elastic Constants	650
	A. The State-of-the-Art	650
	B. Analytical Studies	654
	C. Evaluation and Discussion	659
6.	Effect of Porosity on Strength of Elastic Substances	668
7.	Conclusion	678
8.	References	681

LIST OF ILLUSTRATIONS

<u>Figure</u>		<u>Page</u>
1-1	Dogbone Specimens Used for Tension and Bending	14
1-2	Flexure Test Specimen	15
1-3	Loading Fixture Used to Test Prismatic Bars in Pure Bending	15
1-4	Distribution Curve of Bending Strengths of Wesgo Al-995 in Air at 20°C	26
1-5	Distribution Curve of Bending Strengths, As-Received Wesgo Al-995 in Air at 1000°C	27
1-6	Distribution Curves of Bending Strengths, As-Received Lucalox	28
1-7	Distribution Curves of Bending Strengths As-Received ARF Magnesium Oxide	29
1-8	Graphical Determination of Weibull Parameters for Wesgo Aluminum Oxide in Air at 20°C	30
1-9	Graphical Determination of Weibull Parameters, As-Received Wesgo Al-995 in Air at 1000°C	31
1-10	Graphical Determination of Weibull Parameters, As-Received Wesgo Al-995 in Air at 1000°C	32
1-11	Graphical Determination of Weibull Parameters, Lucalox in Air at 1000°C	33
1-12	Graphical Determination of Weibull Parameters, ARF Magnesium Oxide in Air at 20°C	34
1-13	Graphical Determination of Weibull Parameters, ARF Magnesium Oxide in Air at 1000°C	35
1-14	Graphical Determination of Weibull Parameters, As-Received Wesgo Al-995 in Air at 20°C	38
1-15	Graphical Determination of Weibull Parameters, Lucalox in Air at 20°C	39
1-16	Graphical Determination of Weibull Parameters, ARF Magnesium Oxide in Air at 20°C	40
1-17	Distribution Curve, As-Received Wesgo Al-995 in Air at 1000°C	42
1-18	Distribution Curve Ground. Wesgo Al-995 in Air at 1000°C	43
1-19	Distribution Curve, Annealed Wesgo Al-995 in Air at 20°C	44
1-20	Distribution Curve, Large Lucalox Specimens in Air at 1000°C	45
1-21	Graphical Determination of Weibull Parameters, ARF Magnesium Oxide in Air at 1000°C	46
1-22	Comparison of Theory and Experiments for Size Effects in Wesgo Al-995 in Air at 20°C	59
1-23	Comparison of Theory and Experiments for Size Effects in Lucalox	60
1-24	Comparison of Theory and Experiments for Size Effects in ARF Magnesium Oxide	61

1-25	Cumulative Distribution Curves, Three Beryllium Oxide Specimen Groups of the Same Volume in Air at Room Temperature	63
1-26	Graphical Determination of Weibull Parameters, Three Beryllium Oxide Specimen Groups of the Same Volume in Air at Room Temperature	65
1-27	Combined Cumulative Distribution Curve, All Beryllium Oxide in Air at 20°C	66
1-28	Graphical Determination of Weibull Parameters, All Beryllium Oxide Specimens in Air at 20°C	67
1-29	Combined Cumulative Distribution Curve, Truncated Series of All Beryllium Oxide Specimens in Air at 20°C	68
1-30	Graphical Determination of Weibull Parameters, Truncated Series of All Beryllium Oxide Specimens in Air at 20°C	69
2-1	Bend Test Apparatus for Small Magnesium Oxide Specimens	78
2-2	Typical Bend Test Apparatus Positioned in Universal Machine for Intermediate Size Dogbone Specimen	79
2-3	Typical Bend Test Apparatus in Closed Furnace	81
2-4	Typical Bend Apparatus in Open Furnace	82
2-5	Temperature Gradient in Center Section of Glo-bar Furnace at 1800°F	84
2-6	Failure Stress Versus Strain Rate, Wesgo Al-995 at Room Temperature, Intermediate-size Specimen	89
2-7	Failure Stress Versus Strain Rate, Lucalox at Room Temperature, Intermediate-size Specimen	90
2-8	Failure Stress Versus Strain Rate, ARF Magnesium Oxide at Room Temperature, Intermediate-size Specimen	91
2-9	Failure Stress Versus Strain Rate, ARF Magnesium Oxide at Room Temperature, Small-size Specimen	92
2-10	Failure Stress Versus Strain Rate, Beryllium Oxide at Room Temperature, 1/4 in. x 1/4 in. x 4 in. Specimens	93
2-11	Failure Stress Versus Strain Rate, Wesgo Al-995 at 1000°F, Intermediate-size Specimen	94
2-12	Failure Stress Versus Strain Rate, Lucalox at 1000°F, Intermediate-size Specimen	95
2-13	Failure Stress Versus Strain Rate, Wesgo Al-995 at 1800°F, Intermediate-size Specimen	96
2-14	Failure Stress Versus Strain Rate, Lucalox at 1800°F, Intermediate-size Specimen	97
2-15	Failure Stress Versus Strain Rate, ARF Magnesium Oxide at 1800°F, Intermediate-size Specimen	98
2-16	Failure Stress Versus Strain Rate, Beryllium Oxide at 1800°F, 1/4 in. x 1/4 in. x 4 in. Specimen	99
2-17	Impact Strength of Al ₂ O ₃ and MgO	104

2-18	Stress Wave Reflection at a Free Boundary	107
2-19	Strain Gage Records of Pulse Propagation in a Polycrystalline Al_2O_3 Bar	110
3-1	Prismatic Beam Under Four-point Loading and Distribution of Extreme Fiber Stress	137
3-2	Schematic Diagram of Loading Fixture Used for Testing Prismatic Bars in Pure Bending	138
3-3	Isochromatic Fringe Pattern in a CR-39 Prismatic Specimen Under Four-point Loading	139
3-4	Comparison of Experimental Values with Theoretical Cumulative Distribution Curve of Best Fit	141
3-5	Cumulative Distribution Curves of Failure Stresses in Wesgo Al-995 Under Pure Bending	144
3-6	Probability Density Curve of Failure Stresses in Wesgo Al-995 Bending Specimens A and C	146
3-7	Variation of Two Extreme Values of m (taken from end slopes of curves) with Assumed Value of σ_u for Wesgo Al-995 at Room Temperature	148
3-8	Graphical Determination of Material Parameters for Wesgo Al-995 at Room Temperature	150
3-9	Cumulative Distribution Curves of Failure Stresses in Wesgo Al-995 Under Pure Bending at 1000°C	152
3-10	Variation of Average and Extreme Values of m (with assumed value of σ_u) for Wesgo Al-995 at 1000°C	153
3-11	Graphical Determination of Material Parameters for Wesgo Al-995 at 1000°C	154
3-12	Cumulative Distribution Curves of Failure Stresses in Beryllium Oxide Under Pure Bending at Room Temperature (3 types specimens plotted separately)	157
3-13	Cumulative Distribution Curve of Failure Stresses in Beryllium Oxide Under Pure Bending at Room Temperature (3 types of specimens combined)	158
3-14	Graphical Determination of Material Parameters for Beryllium Oxide at Room Temperature	159
4-1	As Hot-pressed Polycrystalline Magnesium Oxide	171
4-2	Polycrystalline Magnesium Oxide Hot-pressed and Annealed at 1900°C	171
4-3	Photomicrograph of Lucalox at 0.005 mm Grain Size	173
4-4	Photomicrograph of Lucalox Little Evidence of Porosity; Material Approximately of Theoretical Density	173
4-5	High Temperature Compression Testing Apparatus	176
4-6	Lucalox Rams, Discs and a Compression Test Specimen Used in the High Temperature Compression Testing Experiments	178

4-7	Variation of Fracture Strength with Temperature for Magnesium Oxide at Three Grain-size Levels	180
4-8	Petch-type Analysis for Magnesium Oxide in the Temperature Range 1000° - 1600°C	181
4-9	Autographic Records of Load-Strain Curves of Polycrystalline Magnesium Oxide at Various Test Temperatures	183
4-10	Intergranular Fracture in Polycrystalline Magnesium Oxide, Compression Tested at 1000°C	184
4-11	Intergranular and Transgranular Fractures in Magnesium Oxide, Compression Tested at 1000°C	184
4-12	Intergranular and Transgranular Fracture in Magnesium Oxide, Compression Tested at 1000°C	185
4-13	Intergranular Fracture and Some Evidence of Grain Change in Shape in Magnesium Oxide after Compression Testing at 1600°C	185
4-14	Polycrystalline Magnesium Oxide Compression Specimen Fractured at 1200°C	187
4-15	Polycrystalline Magnesium Oxide Compression Specimen Fractured at 1400°C	187
4-16	Polycrystalline Magnesium Oxide Compression Specimen Fractured at 1600°C	187
4-17	Variation of Fracture Strength with Temperature for Lucalox of Nearly Theoretical Density	188
4-18	Variation of Fracture Strength with Temperature for Lucalox Containing Porosity	189
4-19	Petch-type Analysis for Lucalox in the Temperature Range 1000° - 1900°C	190
4-20	Lucalox Specimens Before and After Testing in Compression at 1600°C	192
4-21	Lucalox Specimens Before and After Testing in Compression at 1700°C	192
4-22	Lucalox Specimens Before and After Testing in Compression at 1900°C	193
4-23	Cross Section of Lucalox Specimen Compression Tested at 1900°C Illustrating the Non-uniform Strain Pattern and the Zones of Maximum Shear Strain	193
4-24	Photomicrograph Showing the Extensive Porosity that Develops in Regions of Maximum Shear in Lucalox, Compression Tested at 1900°C	195
4-25	Photomicrograph of an Area Adjacent to the Platen-specimen	195
5-1	Apparatus for Deforming Bar Specimens and Measuring Creep Curves	206
5-2	Fabrication Sequence for Plastically Deformed Dumbell Specimens	209
5-3	Creep Curves on Three Specimens Deformed in Bending	211

5-4	Early Stages of Creep for Several Specimens	212
5-5	Temperature Dependence of Logarithmic Decre- ment for a Specimen Taken at Several Stages of Anneal	213
5-6	Annealing of Dislocation Damping in Specimen 1092	216
5-7	Annealing of Dislocation Damping in Specimen 1095	217
5-8	Method of Anneal Curve Synthesis	219
5-9	Composite Anneal Curve for Specimen 1092	220
5-10	Composite Anneal Curve for Specimen 1095	221
5-11	Anneal Curves for Several Specimens Converted to the Equivalent 500°C Curve	222
5-12	Relaxation Peak Near 200°C Taken at 43.2 Kilocycles Specimen 1026	226
5-13	Relaxation Peak Due to Chromium - Vacancy Pair Relaxation in Chromium-Doped Specimen 1272	228
5-14	Section of Low Temperature Apparatus	230
5-15	Low Temperature Apparatus (inverted for easy specimen mounting)	231
5-16	Schematic Drawing of a Dislocation	233
5-17	Plot of Amplitude Dependent Component of Damping	247
5-18	Derived Probability Distribution for Sum of Adjacent Loop Lengths Between Point Defect Pinning Locations	250
5-19	Damping Decrement Q^{-1} as a Function of Tempera- ture, Wesgo Al-995 and Morganite Measured in Air	261
5-20	Damping Decrement Q^{-1} as a Function of Tempera- ture, Wesgo Al-995 Annealed and Measured in Oxygen	262
5-21	Damping Decrement Q^{-1} as a Function of Tempera- ture, Wesgo Al-995 Annealed and Measured in Hydrogen	263
5-22	Arrhenius Plots, Steady State Creep Rates for Wesgo Al-995 Al_2O_3	264
6-1	Loading System Used to Obtain Uniaxial Tension of Thin Plates	274
6-2	Measurements on the Axiality of Loading Achieved Using the Device in Figure 6-1	275
6-3	Measured Values of σ_c^2 for Various Values of K Deduced Values of σ_c^2 for Various Values of K	277
6-4	Measured Values of σ_c^2 for Magnesium Oxide and Deduced Values of σ_c^2 for Various Values of K	278
6-5	Measured Values of σ_c^2 for Glass and Deduced Values of σ_c^2 for Various Values of K	279
6-6	Cleavage Crack in Magnesium Oxide Single Crystal Stopped by Running into Zone of Compressive Stresses	287
6-7	Electron Micrographs of Polycrystalline Magnesium Oxide Fracture Surfaces Illustrating Normal Etch- ing Features	289

6-8	Partitioned Adsorption Cell	291
6-9	Adsorption Curves for Carbon Dioxide on Ultra-Microid Aluminum Oxide at -78 and 19°C	294
6-10	Freundlich Plot for Adsorption of Carbon Dioxide on Ultra-Microid Aluminum Oxide at 19°C	296
6-11	Lowering of Surface Energy of Aluminum Oxide as a Result of Adsorption of Carbon Dioxide at Different Partial Pressures	297
6-12	Adsorption Curve for Water on Ultra-Microid Aluminum Oxide at Ambient Temperature	299
6-13	Langmuir Isotherm for Adsorption of Water on Ultra-Microid Aluminum Oxide at Ambient Temperature	300
6-14	Constant Stress Creep Curves for Aluminum Oxide at 1900°C	304
6-15	Creep Rate as Function of Stress for Aluminum Oxide at 1900°C	305
7-1	High-Temperature Vacuum Furnace for Use with 5000-lb Testing Machine	314
7-2	High Temperature Testing Facility	317
7-3	Upper Part of Testing Machine	318
7-4	Torque Assembly	320
7-5	Central Part of Inside of Testing Machine	321
7-6	Distribution of Tensile Stress Across the Side of a Square Shaft in Torsion $\sigma = \frac{KM}{A^3}$	324
7-7	Ratio of Maximum Stresses on Long Side (σ_B) Against Short Side (σ_A) for Rectangular Bars in Torsion	324
7-8	Maximum Stress in Rectangular Bar Under Torsion, as Function of Side-Length Ratio	326
7-9	Magnesium Oxide Dogbone Showing "Parting Line" and Stepped Fracture Surface	327
7-10	Types of Cracks Present in ARF Magnesium Oxide Dogbones	327
7-11	Distribution of Fracture Strengths of As-Received ARF Magnesium Oxide at Room Temperature	332
7-12	Fracture Origin	335
7-13	Distribution of Normal Stress at the Circumference of a Spherical Cavity	336
7-14	Change of Position of Fracture Surface with Temperature	340
7-15	Torque Versus Twist ARF Polycrystalline Magnesium Oxide 20°C and 400°C	343
7-16	Magnesium Oxide Fracture Surfaces at 1200°C	344
7-17	Relaxation Curve for ARF Magnesium Oxide at 1500°C in Torsion	347
7-18	M/M ₀ Versus t for Relaxation of ARF Magnesium Oxide at 1500°C	348

7-19	$\frac{M}{M_0}$. . . Versus ϕ for ARF Magnesium Oxide in the Range 900°C - 1500°C $A = 0.7\text{eV}$	350
7-20	Lateral Growth of Dislocation Bands During Two Stages of Compression, Each Followed by a Stage of Etching	355
7-21	Formation of a Kink at an Intersection of Two Conjugate Dislocation Bands	359
7-22	Lattice Rotation at Intersections of Conjugate Dislo- cation Bands	359
7-23	Possible Modes of Elimination of the Kink Non-accom- modation Stresses at an Intersection of Two Dislo- cation Bands	362
7-24	Twofold Lattice Rotation at an Intersection of Two Conjugate Dislocation Bands, and Crack Nucleation by Simultaneous Action of Two Dislocation Bands	364
7-25	Formation of a Kink Band Out of the Captured Por- tion of the Narrow Dislocation Band Under the Imposed Shear of the Broadening Band	367
7-26	Birefringent Kink Bands	368
7-27	Crack Formation Due to Sharp Variation in Shear Angle in Dislocation Bands	368
7-28	Crack Formation Resulting from Variation of Shear Angle in the Broadening Band	373
7-29	Crack Formation Resulting from Variation in Shear Strain	374
7-30	Crack Formation by the Arrest of Homogeneous Shear in Vertical Bands by Extensive Homogeneously Sheared Region	376
7-31	Dislocation Arrangements Showing Incomplete Kink Accommodation for the Arrested Bands of Figure 7-30	377
7-32	Crack Formation by the Simultaneous Broadening of Two Conjugate Dislocation Bands	380
7-33	Model of Crack Formation for the Compression Case of Figure 7-32 a and b	381
7-34	Spalling Fracture in a Compressed Crystal Result- ing from a Crack of the Kind Shown in Figure 7-32 a and .	381
7-35	Model of Crack Formation for the Tension Case of Figure 7-32 c	383
7-36	Crack Formation by Inhomogeneous Distribution of Shear	383
7-37	Analysis of Stresses Present in the Case of Crack Formation by the Mechanism Illustrated in Figure 7-29 a	392
7-38	Proposed Mechanism of Crack Formation in the Plane Strain Tension Experiment	397
7-39	Normal Stresses Arising in the Quadrangle of an Intersection, Which is Due to Lattice Rotation	399

8-1	Strength of Magnesium Oxide at Various Temperatures	415
8-2	Firing Schedule of Impure Magnesium Oxide Discs in Electrical Furnace. Average Firing Rate. 27°C per Hour	417
8-3	Room Temperature Strength of Magnesium Oxide as a Function of Ferric Oxide Impurity Level	418
8-4	Room Temperature Strength of Magnesium Oxide as a Function of Aluminum Oxide Impurity Level	419
8-5	Room Temperature Strength of Magnesium Oxide as a Function of Zirconium Oxide with Impurity Level	420
8-6	Room Temperature Strength of Magnesium Oxide as a Function of Chromic Oxide Impurity Level	421
8-7	Room Temperature Strength of Magnesium Oxide as a Function of Titanium Oxide Impurity Level	422
8-8	Room Temperature Strength of Magnesium Oxide as a Function of Strontium Oxide Impurity Level	423
8-9	Room Temperature Strength of Aluminum Oxide as a Function of Titanium Oxide Impurity Level	439
8-10	Schematic Diagram Showing Locations at Which Microhardness Measurements Made on Single Crystal Magnesium Oxide into Which Ferrous Oxide had been Diffused	450
8-11	Microhardness Number of Polycrystalline Magnesium Oxide as a Function of Impurity	453
8-12	Effect of 10,000 ppm Titanium Oxide on Sintering of Aluminum Oxide	459
9-1	Load Geometry for Sapphire	473
9-2	Optic Axis Orientations for Sapphire	475
9-3	Molybdenum High-Temperature Test Apparatus	479
9-4	Low-Temperature Autoclave Test Apparatus	479
9-5	Relative Wear Rates of Sapphire Rods of Various Orientations	481
9-6	Effect of Anneal Time at 1200°C on Bend Strength of Sapphire	483
9-7	Temperature-Atmosphere Effects on the Bend Strength of As-Received Sapphire	486
9-8	Temperature-Atmosphere Effects on the Bend Strength of Heat-Treated Sapphire	488
9-9	Comparison of Bend Strengths of As-Received and Annealed Sapphire	489
9-10	Bend Strength and Young's Modulus Versus Temperature for Annealed Sapphire	490
9-11	Static Fatigue Curve for Sapphire	493
9-12	Bend Strength and Density as a Function of Surface Grain Size for Lucalox Extruded Rods	495
9-13	Microstructure of Standard Lucalox Test Material	497

9-14	Effect of Surface Grain Size, Loading Rate and Temperature on the Bend Strength of Lucalox	498
9-15	Temperature-Atmosphere Effects on the Bend Strength of Standard Lucalox	499
9-16	Vacuum Bend Strength and Young's Modulus Versus Temperature for Lucalox	501
9-17	Hypothetical Changes in Flaw Geometry Due to Corrosion or Dissolution(9-25)	506
9-18	Schematic Fatigue Curve(9-25)	509
10-1	Effect of Heat Treatment on the Strength of Prestrained Crystals. Stress Deflection Curves Before and After One Hour Anneals	524
10-2	Effect of Heat Treatment on the Strength of Prestrained Crystals	525
10-3	Effect of Heat Treatment on Etch Pit Appearance Following a One Hour Anneal	528
10-4	Effect of Half-hour Anneal at 1000°C on Etch Pit Appearance	530
10-5	Electron Transmission Micrograph of a Simple Slip Band Consisting of Screw Dislocations Injected into a Thin Film of Magnesium Oxide. Note Debris Between Dislocations at C and D	532
10-6	Mechanism for the Generation of Debris Consisting of Positive and Negative Dislocation Dipoles in a Slip Plane	534
10-7	Electron Transmission Micrograph Showing Dislocation Distribution in a Bulk Magnesium Oxide Crystal Deformed at Room Temperature	537
10-8	Electron Transmission Micrograph Showing Dislocation Distribution in a Bulk Crystal Deformed at Room Temperature and Annealed at 650°C for Two Hours	538
10-9	Electron Transmission Micrograph Showing Dislocation Distribution in a Bulk Crystal Deformed at Room Temperature and Annealed at 920°C for Two Hours. Note Some of the Coarse Dipoles are Beginning to Break Up	539
10-10	Electron Transmission Micrograph Showing Dislocation Distribution in a Bulk Crystal Deformed at Room Temperature and Annealed at 1050°C for Two Hours	541
10-11	Electron Transmission Micrograph Showing Dislocation Distribution in a Bulk Crystal Deformed at Room Temperature and Annealed at 1250°C for Two Hours	542
10-12	Effect of Heat Treatment on the Lattice Resistance to the Motion of Fresh Dislocation	544
10-13	Slip Band Intersections Produced in Crystals Subjected to Half Cycle (tension-unload) Mechanical Stressing	550

10-14	Slip Band Intersections Produced in Crystals Subjected to Full Cycle (tension-compression) Mechanical Stressing	550
10-15	Tensile Stress Strain Curves for Chemically Polished Magnesium Oxide Crystals Deformed at 850°C	552
10-16	Effect of Heat Treatment on Yield Stress of Crystals Preannealed at 2000°C	554
11-1	Form of Magnesium Oxide Bicrystals Used in the Tests	559
11-2	Crystallographic Orientation for Sapphire Specimens	561
11-3	Schematic Arrangement of Bicrystal in Testing Jigs	564
11-4	Aluminum Oxide Crystal Surfaces Exposed to Steam Spray for 18 Hours, Specimen Held at 180°C	574
12-1	Bend Characteristics of 97 Per cent Dense Polycrystalline Magnesium Oxide	585
12-2	Tension Surface of Polycrystalline Magnesium Oxide Bend Specimen	586
13-1	Photoelastic Fringe Patterns Associated with a Running Crack in a CR-39 Beam	593
13-2	Arrangement of the Optical Elements in the Polariscope for the Studies with Transmitted Light	594
13-3	Schematic Arrangement of the Elements of the Polariscope to Permit Simultaneous Recording of Patterns from the Beam and Coating	596
13-4	Westergaard Crack Problems	599
13-5	Propagating Semi-infinite Crack	600
13-6	Propagating Internal Crack	600
13-7	Crack at Free Boundary	604
14-1	Schematic Outline of Extrusion Techniques Studied for Magnesium Oxide	611
14-2	Electron Micrograph, Vitro Magnesium Oxide Powder	616
14-3	Electron Micrograph, Mallinckrodt Magnesium Oxide Powder	616
14-4	Electron Micrograph, Fisher Magnesium Oxide Powder	616
14-5	Fisher Magnesium Oxide Powder + 1/2 w/o Lithium Fluoride Hot-pressed at 2350°F	618
14-6	Vitro Submicron Magnesium Oxide Powder + 1/2 w/o Lithium Fluoride Hot-pressed at 2350°F	618
14-7	Vitro Submicron Magnesium Powder Hot-pressed at 2350°F Without Any Additives	619
14-8	Compacting Pressure Versus Green Density, All Three Magnesium Oxide Powders	622

14-9	Fired Density Versus Green Density, Vitro Magnesium Oxide	624
14-10	Fired Density Versus Green Density, Mallinckrodt Magnesium Oxide	624
14-11	Fired Density Versus Green Density, Fisher Magnesium Oxide	624
14-12	Fired Density Versus Green Density, 1300°C Firing	625
14-13	Fired Density Versus Green Density, 1700°C Firing	625
14-14	Photomicrograph of Typical Area on Vitro Magnesium Oxide Specimen No. 28	628
14-15	Photomicrograph of Typical Area on Mallinckrodt Magnesium Oxide Specimen No. 109	629
14-16	Photomicrograph of Typical Area on Fisher Mag- nesium Oxide Specimen No. 150	630
15-1	Porosity Dependence of Elastic Modulus of Aluminum Oxide Ceramics	647
15-2	Analytical Prediction for Effect of Porosity and Poisson's Ratio Upon Young's Modulus	664
15-3	Analytical Prediction for Effect of Porosity and Poisson's Ratio Upon Shear Modulus	665
15-4	Analytical Prediction for Effect of Porosity and Poisson's Ratio Upon Bulk Modulus	666

LIST OF TABLES

<u>Table</u>	<u>Page</u>
I Summary, Research Tasks on Original Phase of Program	2
II Summary, Research Tasks on Continuation Phase of Program	4
1-I Summary, Weibull Material Constants for Bend Tests of Specimens in Air	36
1-II Summary, Material Constants from Bend Tests of Specimens in Air	47
2-I Summary, Results of Strain Rate Experiments at Room Temperature	87
2-II Summary, Results of Strain Rate Experiments at 1000°F	88
2-III Summary, Results of Strain Rate Experiments at 1800°F	88
2-IV Summary, Results of Linear Fit Strain Rate Parameters	101
3-I Experimental Results of Wesgo Al-995 at Room Temperature	143
3-II Experimental Results of Wesgo Al-995 at 1000°C	151
3-III Experimental Results of Beryllium Oxide at Room Temperature	156
3-IV Preliminary Results of Bend Tests on ARF Magnesium Oxide at Room Temperature	160
3-V Summary of Basic Weibull Material Parameters for Completed Test Series	161
4-I Grain Size of Magnesium Oxide Specimens	168
4-II Chemical Analysis of Hot-Pressed and Annealed Magnesium Oxide	170
4-III Grain Size and Density Data, Lucalox Specimens	172
4-IV Semi-quantitative Spectro-Chemical Analysis of Lucalox	174
4-V Values of the Parameters σ_0 and k for Magnesium Oxide Determined Using the Petch Equation	179
4-VI Values of the Parameters σ_0 and k for Lucalox Determined Using the Petch Equation	194
4-VII Variation in Shear Modulus with Temperature for Magnesium Oxide and Aluminum Oxide	198
5-I Bending Data on Single Crystal Specimens	208
6-I Surface Energies Calculated Assuming Ideal Griffith Crack Behavior	280
6-II Calculations for Effective Crack Radii	281
6-III Surface Energy Calculations for Various Assumptions of k in Berry's Theory	284
6-IV Surface Energy Values from Edge Cracks in Polycrystalline Specimens	286

7-I	Possible Methods for Improving the Strength of Refractory Materials	311
7-II	Test on Dogbones in Torsion at Room Temperature	329
7-III	Fracture Strengths of ARF Magnesium Oxide at Room Temperature	333
7-IV	Results of Experiments on Magnesium Oxide Dogbone Specimens at Elevated Temperatures	338
8-I	Comparative Spectrographical Analysis	408
8-II	The Effect of Annealing, Polishing and Temperature on Strength of High-Purity Polycrystalline Magnesium Oxide*	412
8-III	The Effects of Annealing on the Room Temperature Strength of Iron-doped, High-purity Polycrystalline Magnesium Oxide*	414
8-IV	Average Fired Density and Grain Size of Magnesium Oxide Specimens Doped with Impurities Before Sintering	424
8-V	Statistical Analyses for Population Identification of Undoped Magnesium Oxide Samples Fired with Different Doped Lots	426
8-VI	Results of Linear Regression Analyses of the Strengths of Doped and Undoped Polycrystalline Magnesium Oxide	427
8-VII	Summary of Modulus of Rupture Experiments on Doped Magnesium Oxide Specimens Tested at $660^{\circ} + 10^{\circ}\text{C}$ and at 1000°C in Air	430
8-VIII	Summary, Modulus of Rupture, Density and Grain Size of Doped Aluminum Oxide Tested in Air at 1050°C	432
8-IX	Statistical Analyses for Population Identification Comparing Doped Polycrystalline Aluminum Oxide Samples with Undoped Lots	434
8-X	Results of Linear Regression Analyses for Strength Data on Doped and Undoped Aluminum Oxide Tested at Various Temperatures	435
8-XI	Results of Linear Regression Analyses of Strength Data on Doped and Undoped Aluminum Oxide Tested at Various Temperatures	436
8-XII	Room Temperature Knoop Hardness and Modulus of Rupture for Doped and Undoped Polycrystalline Aluminum Oxide*	443
8-XIII	Room Temperature Knoop Hardness and Modulus of Rupture for Doped and Undoped Polycrystalline Magnesium Oxide	444
8-XIV	Microhardness Single Crystal Magnesium Oxide as a Function of Angle	446
8-XV	Effects of Polishing and Etching on the Microhardness of Single Crystal Magnesium Oxide	446
8-XVI	Microhardness Data on Magnesium Oxide	447

8-XVII	Knoop Microhardness Measurements as Function of Impurity Concentration in Polycrystalline Magnesium Oxide	452
8-XVIII	Geometry Relationships Used in Diffusion Sintering Models	455
8-XIX	Values of the Parameters Appearing in Equation 8-3 for Various Diffusion Models	457
8-XX	Density and Grain Size of Polycrystalline, High-purity Magnesium Oxide as Functions of Firing Time	461
9-I	Reported Room Temperature Bend Strength Data for Sapphire	476
9-II	Effect of Heat Treatment of Sapphire on Bend Strength at Room Temperature	483
9-III	Effect of Temperature and Basal Plane Orientation on Observed Bend Strength of Sapphire	484
9-IV	Static Fatigue Data on Sapphire	492
9-V	Static Fatigue Data on Standard Lucalox	503
9-VI	Low-Temperature Bend Strengths and Coefficients of Variations of Standard Lucalox Specimens	516
11-I	Magnesium Oxide Bicrystal Compression Tests at Room Temperature	565
11-II	Magnesium Oxide Bicrystal Compressive Tests at 900°C	566
11-III	Magnesium Oxide Bicrystal Compressive Tests at 900°C	566
11-IV	Outer Fiber Strain at Fracture on Magnesium Oxide Crystals Cleaves and Sprinkled with 250-Mesh Carborundum Powder	568
11-V	Elevated Temperature Aging of Magnesium Oxide Crystals, Bend Tests Conducted at Room Temperature	569
11-VI	Effect of Hydrogen and Nitrogen on the Room Temperature Bend Strength of Aluminum Oxide Single Crystals	570
11-VII	Effect of Moisture on Observed Bend Strength of Aluminum Oxide Single Crystals at Room Temperature	571
11-VIII	X-Ray Analysis of Steam-Sprayed Alpha-Aluminum Oxide Powder	575
11-IX	Effect of Moisture on Observed Bend Strength of Polycrystalline Aluminum Oxide (Morganite) at Room Temperature	576
14-I	Chemical Analysis of Magnesium Oxide Powders	614
14-II	Property Data	615
14-III	Density Data for Magnesium Oxide Compacts	617
14-IV	Regression Analysis	626
14-V	Grain Count Data for Specimens Fired at 1700°C	631

15-I	Procedures for Preparing Aluminum Oxide Ceramics	641
15-II	Properties of Aluminum Oxide Ceramics Prepared by Different Methods	645
15-III	Values of Constants for Elastic Moduli	662
15-IVa	Values of Normalized Bulk Modulus, $K^* = K^*/K_o$, as a Function of Porosity and Poisson's Ratio of Matrix	663
15-IVb	Values of Normalized Shear Modulus, $G^* = G^*/G_o$, as a Function of Porosity and Poisson's Ratio of Matrix	663
15-IVc	Values of Normalized Young's Modulus, $E^* = E^*/E_o$, as a Function of Porosity and Poisson's Ratio of Matrix	663
15-V	Compilation of Constants in Knudsen's Porosity-Grain Size-Strength Relationships	673
15-VI	Compilation of Values for Porosity Exponent, for Knudsen Strength Relationship	674

I. INTRODUCTION

The program is aimed at diverse and fundamental studies of the causes and mechanisms of fracture in inorganic, non-metallic ceramics, and the parameters influencing their strength and failure characteristics. The initial investigations were reported in ASD-TR-61-628.

Because of the wide-ranging research interests and large over-all effort involved, it was decided at the very outset of this program to divide the investigation into individual Tasks, each concerned with the investigation of a single well-defined effect bearing upon the brittle fracture of ceramic substances. Each Task was to be headed by a Principal Investigator responsible for its technical planning and the execution of work, with over-all program direction supplied by N. A. Weil, acting as Project Coordinator. About one-half of the original Tasks was subcontracted to leading academic and industrial research organizations, on topics where the Principal Investigator for the Task has established in outstanding reputation or achieved unique progress in the scientific field concerned.

The initial areas of investigation included 11 Tasks. A comprehensive breakdown of the original Tasks, is presented as Table I. As can be seen, five of the original Tasks were conducted at the Foundation, while six were subcontracted, in keeping the general philosophy of this program.

All of the original Tasks were continued during the extension phase of this work. However, because the technical effort was largely completed in Tasks 1, 4 and 9; only a modest additional effort, aimed primarily at filling in missing pieces of information or completing some partially finished experimental series, was spent on these tasks. Likewise, a lessened rate of activity was exerted on Tasks 2 and 3, as these tasks were gradually approaching their stated objectives. On the other hand, intensified effort was exerted on Task 5, whose objectives were now expanded to

Table I
SUMMARY, RESEARCH TASKS ON ORIGINAL PHASE OF PROGRAM

Task	Principal Investigator	Ceramic Oxide	Experimental Technique	Temperature	Environment	Specimen	Parameters Measured
1. Effect of Structural Size; 'The Zero Strength'	S. A. Bortz, Armour Research Foundation	Polycrystalline Al_2O_3 , MgO	Rupture	Room, Elevated	Neutral, Oxidizing, Saturated	Dogbone	Strength, Deformation, Fracture Source
2. Effect of Strain Rate	H. R. Nelson, Armour Research Foundation	Polycrystalline Al_2O_3 , Graphite	Rupture	Room, Elevated	Neutral, Oxidizing	Dogbone	Strength, Strain Rate, Fracture Surface
3. Effect of Non-Uniform Stress Fields	N. A. Weil, I. M. Daniel, Armour Research Foundation	Polycrystalline Al_2O_3 , CR-39, Graphite, Plexiglas	High-speed Photography Photoelasticity Rupture	Room	Air	Disc, Theta, Beam, Dogbone	Stress Gradient, Strength
4. Effect of Microstructure	P. R. V. Evans, Armour Research Foundation	Polycrystalline Al_2O_3 , MgO	Electron-Microscopy Crystallography Crushing	Room to 1000 °C	Air	Solid Cylinder	Grain Size, Strength, Deformation
5. Internal Friction and Lattice Defects	P. D. Southgate, Armour Research Foundation	Monocrystalline MgO	Rupture, Log. Decrement	to 800 °C	Vacuum	Cleaved Single-Crystal Beam	Internal Friction, Dislocation Pile-up, Crack Nucleation
6. Effect of Surface Energy	W. T. Petch, University of Durham	Polycrystalline Al_2O_3	Electron-Microscopy Crystallography Rupture	Room to near Melting	Air, Vacuum	Thin Plate, Rod, Single Crystal	Strength, Dislocation Density, Surface Energy
7. Fracture Mechanisms	E. Orowan, Massachusetts Institute of Technology	Monocrystalline MgO, KCl, NaCl	Birefringence Etch-pit X-ray Back Scatter Compression	Varied	Inert, Air, Vacuum	Single Crystal Compressive	Dislocation Glide Bands, Crack Nucleation, Strength
8. Impurity Influences	I. B. Cutler, University of Utah	Polycrystalline Al_2O_3 , MgO	Crystallography Etching	Room, Elevated		Disc, Beam	Grain Size, Impurities, Strength
9. Static Fatigue; Delayed Fracture	R. T. Charles, General Electric	Polycrystalline Al_2O_3 , Monocrystalline MgO	Crystallography Rupture	-19 °C to 1000 °C	Neutral, Oxidizing, Saturated	Thin Rod, Beam	Fracture Surface, Time, Strength, Yielding
10. Effect of Thermal Mechanical History	R. T. Stokes, Minneapolis-Honeywell	Monocrystalline MgO	Birefringence Etch-pit Crystallography	Room to 2000 °C	Air	Cleaved Single Crystal	Time, Strength, Dislocation Density
11. Surface Active Environments	A. T. Murray, Materials Research Corporation	Monocrystalline Al_2O_3 , MgO, CaI_2	Etch-pit, Crushing, Rupture	Room to 600 °C	Neutral, Oxidizing	Cleaved Single Crystal	Surface Residue, Fracture Surface, Time, Strength, Yielding

include a two-phased research, Part One dealing with single crystals and Part Two with polycrystals.

Four new tasks were initiated during this extension phase, two of which were dual tasks. The over-all organization of the tasks under active pursuit during the extension of the project, is given as Table II. As Table II shows, the even distribution of "in-house" and subcontract effort has been continued during the extension phase of this contract.

The same materials were used for experiments conducted on each Task to afford ready comparisons and provide background data for the individual research undertakings. Aluminum oxide and MgO were selected as the principal materials because of their comparatively ready availability both as single crystals and multicroystals in reasonably large sizes, the particularly simple crystallographic nature (ionic lattice) of MgO, and an extensive amount of literature available regarding their behavior. In this context, Al_2O_3 and MgO are regarded as "model materials"; if their phenomenological behavior is satisfactorily explored, it will open the way to an understanding of the anticipated performance of other brittle substances (nitrides, borides, carbides, silicides, intermetallics) intended for structural use in ultra-high temperature environments. During the current year, BeO has also been studied to some extent.

The proper organization and presentation of the results of a research program as broad as the current one always poses some difficult problems. To maintain the continuity of presentation, and still identify the specific problems attacked on each phase of the program, general information pertaining to the materials is described in Chapter II. Research carried out on this program is summarized in Chapter III. Each Task is described as an individual self-contained item. Thus, each of the task reports is identified in regard to principal investigator and research organization, contains an abstract and conclusions; figures, tables and references are identified by a prefix corresponding to the task number.

Table II
SUMMARY, RESEARCH TASKS ON CONTINUATION PHASE OF PROGRAM

Task	Principal Investigator	Ceramic Material	Experimental Technique	Temperature	Environment	Specimen	Parameters Measured
1. Size Effects: "The Zero Strength"	S. A. Borte, N. A. Weil, Armour Research Foundation	Polycrystalline BeO, MgO, Al ₂ O ₃	Rupture Tests, Surface Examination	Room, Elevated	Neutral, Oxidizing	Dogbones of Various Sizes and Finishes	Strength, Deformation, Fracture Surface
2. Effect of Strain Rate	J. W. Dally, Armour Research Foundation	Polycrystalline BeO, MgO, Al ₂ O ₃	Rupture Tests, Surface Examination	Room, Elevated	Air	Dogbones, Bar Rod	Fracture Surface, Strain Rate, Strain Rate
3. Effect of Non-Uniform Stress Fields	N. A. Weil, I. M. Daulton, Armour Research Foundation	Polycrystalline MgO, Al ₂ O ₃ , BeO	Photoelasticity, Rupture Tests	Room, Elevated	Air	Bar, Dogbones, Theta, Beam Disc	Volume, Strength, Stress Gradient
4. Effect of Microstructure	P. B. V. Evans, Armour Research Foundation	Polycrystalline Al ₂ O ₃ , MgO	Etch-plate Studies, Compression Tests	Room, 1000-1900°	Air	Solid Cylinder	Grain Size, Strength, Dislocation Density
5. Internal Friction Measurements: Part 1, Single Crystal; Part 2, Polycrystal Studies	P. D. Southgate, (Pt 1) L. M. Daulton, (Pt 2) Armour Research Foundation	Polycrystalline Al ₂ O ₃ , Monocrystalline MgO	Etch-plate Studies, Electron Microscopy, Ultrasonics	400-800	Inert Vacuum	Rod, Beam	Control Impurities, Annealing Treatment, Dislocation Densities, Damping, Strength
6. Effect of Surface Energy on Brittle Fracture	N. J. Pech, University of Durham	Monocrystalline MgO, Polycrystalline Al ₂ O ₃	Crack Propagation, Hertzian Crack, Creep, Cleavage	Elevated -196	Air, Liquid N ₂	Rod, Platelet, Bar	Creep Rate, Strength, Surface Energy
7. Fracture Mechanism	E. Orowan, Massachusetts Institute of Technology	Polycrystalline Al ₂ O ₃ , Monocrystalline MgO, CaF ₂	Microscopy, Inelastic X-ray Methods, Tensile and Torsion Tests	Room, Elevated	Air	Bar, Platelet, Dogbones	Plastic Deformation, Lattice Orientation, Dislocation Mobility, Strength
8. The Effects of Impurities	L. B. Cudger, University of Utah	Precipitated Polycrystalline Al ₂ O ₃ , Monocrystalline MgO	Crystallography, Microindentation, X-ray Methods, Tensile and Torsion Tests	Room, Elevated	Neutral, Oxidizing	Rods, Discs, Beams	Grain Size, Impurities, Strength, Diffusion
9. Static Fatigue: Delayed Fracture	R. J. Charles, GE Research	Polycrystalline MgO, Monocrystalline Al ₂ O ₃	Crystallography, X-ray Methods, Creep Tests	Room, to 1000°C	Neutral, Oxidizing, Dry H ₂ , Sat. Steam	Rod	Fracture Surface, Time, Strength, Yielding
10. Thermal Mechanical History	R. J. Charles, Honeywell Research	Monocrystalline MgO, Biscrystalline MgO	Etch-plate Studies, Electron microscopy, Photoelasticity	Room, 2000°C	Air	Crystal Beam	Strain Cycles, Time, Strength, Dislocation Densities
11. Surface Active Environments	G. T. Murray, Materials Research Corp.	Polycrystalline Al ₂ O ₃ , Monocrystalline Al ₂ O ₃ , CaF ₂	Rupture Tests, X-ray Diffraction, Microscopy	to 1000°C	Neutral, Oxidizing, Steam, H ₂	Crystal Beam	Plastic Strain, Fracture Surface, Strain Rate, Strength
12. Dislocation Studies in Polycrystalline Ceramic Materials	A. E. Gorum, Stanford Research Institute	Biscrystalline MgO, Polycrystalline MgO	Electron Transmission Microscopy	Room	Air, Vacuum	Thin Film Bulk	Dislocation Density and Mobility
13. Crack Propagation in Ceramic Materials: Part 1, Experimental Studies; Part 2, Theoretical Studies	W. F. Riley, (Pt 1) E. L. McDowell, (Pt 2) P. B. V. Evans, Armour Research Foundation	CR-39 Glass, Polystyrene	Multiple Spark-Gap Polariscope, Interferometer, Photoelasticity	Room	Air	Plates	Crack Velocity and Stress
14. Rheologic Behavior of Polycrystalline Bodies	P. B. V. Evans, Armour Research Foundation	Polycrystalline MgO, Ultra-fine Powder MgO	Compression Tests, Shearing	1200°C, 1700°C	Air	Cylinders	Ductility Strength
15. Effect of Porosity Part 1 Experimental Studies; Part 2, Theoretical Studies	L. M. Daulton, (Pt 1) N. A. Weil, (Pt 2) Armour Research Foundation	Low Porosity MgO and Al ₂ O ₃	Densimetry, Metallography, Creep-damping, Fracture tests	Various	Air	Beams	Density, Flexure Strength, Pore Size Damping, Elastic Constants

A complete description of all results obtained on those tasks which, having attained their objectives, will be completed and closed out at the conclusion of this research period. While this may involve a duplication of information already partially contained in ASD-TR 61-628, this course is pursued to give a rounded story of completed tasks. Tasks 1, 4, 9, 11 and 14 are in this category. On all other tasks, only the current year achievements are reported, and the work of the previous year is referenced where necessary.

It bears mentioning that Part Two of Task 15, the theoretical work on the effect of porosity on the mechanical properties of ceramics, was not scheduled to be performed as part of this contract. Rather, this work resulted from an internally sponsored ARF program, carried out in support of the research funded by ASD; because of its obvious close association with the current work, and the planned continuation of the effort on Task 15, the results of this study are included in this report.

II MATERIALS

Two oxides, Al_2O_3 and MgO , were originally studied; during the continuation of the program a third oxide, BeO , was added. In addition, ionic compounds such as KCl , NaCl and CaF_2 and such photoelastic materials as CR-39 and Plexiglas were used for exploratory purposes on several tasks. The Al_2O_3 investigated was of three forms: single crystals (sapphire) and two types of polycrystals. Magnesium oxide used was monocrystalline and high-density, high-purity polycrystalline. Only polycrystalline BeO was used.

Because the preparation, compaction and physical properties of the Al_2O_3 and MgO were discussed in such detail in ASD-TR 61-628, Pt I, they are noted only briefly here.

1. ALUMINUM OXIDE

Single-Crystal (sapphire) Al_2O_3 was supplied by the Crystal Products Section, the Linde Company Division of the Union Carbide Corporation. A representative composition is; Fe 1-10 ppm; Mg and Li 1-10 ppm; Mn, Sn, B undetected within measurement sensitivity of 10 ppm; Ag, Ca, Cr, Cu undetected within measurement sensitivity of 1 ppm; balance Al_2O_3 .

High Density Commercial Multicrystals, a proprietary composition labeled Wesgo AL-995, were supplied by the Western Gold and Platinum Corporation. The bulk specific gravity of the material is listed as 3.89 (theoretical: 3.996). Spectroscopic analysis of the material is as follows.

Semi-Quantitative Analysis, Wesgo AL-995*

Element	Amount Present (percent)
Al	Principal Constituent
Mg	0.3
Si	0.3
Ca	0.04
Fe	0.02
Ga	0.01
Ti	0.008
Cr	0.006
Ni	0.002
Cu	0.00005

*By Chicago Spectro-Service Laboratory, Inc.

Wesgo Al-995 is prepared from a starting powder using additions of approximately one percent plasticizer to strengthen the green compact and 0.25% MgO to inhibit grain growth during firing. The compact is cold-pressed and sintered by firing for 3 hr at 1700°C.

Ultra-High Density Multicrystals, trademarked Lucalox, were supplied by the Lamp-Glass Division of the General Electric Company. The semi-quantitative composition of the material is as follows.

Semi-Quantitative Analysis, Lucalox*

Element	Sample Crushed in Agate Mortar, Amount Present (percent)	"As Received", Not Mortared Amount Present (percent)
Al	Principal Constituent	Principal Constituent
Fe	0.07	0.002
Mg	0.15	0.15
Ti	0.01	Not Detected
Mn	0.001	Not Detected
V	0.004	Not Detected
Na	0.08	Not Detected
Cu	0.0003	Not Detected
Ni	0.0015	Not Detected
Ca	0.04	0.004
Cr	0.002	Not Detected
Ga	0.003	Not Detected
Si	0.03	0.03

* By Chicago Spectro-Service Laboratory, Inc.

2. MAGNESIUM OXIDE

Monocrystalline and polycrystalline magnesium oxides were used. Single crystals were procured from the Norton Company and from Semi-Elements, Inc. Because of the larger size, higher purity and greater supply reliability, Semi-Elements was the principal supplier. The Armour Research Foundation fabricated

the high-density sintered MgO and supplied investigators with specimens. Spectroscopic analyses of MgO follow.

Quantitative Analysis, Single Crystal Magnesium Oxide

Material Source		Impurity (ppm)							Max. Total Impurity, (percent)
		Al	Ca	Cr	Cu	Fe	Mn	Si	
Norton Co.	Range for 3 spec.	200-1000	600-1500	60-100	2	600	30-40	5-10	0.6
	Aver.	600	900	73	2	600	37	7	
Semi-Elements, Inc.		200	200	80	2	400	30	5	0.3

*By Chicago Spectro-Service Laboratory, Inc.

Semi-Quantitative Analysis, Cold-Pressed and Sintered Magnesium Oxide*

Element	Amount Present, (percent)
Mg	Principal Constituent
Al	0.05
Si	0.03
Ca	0.04
Fe	0.005
Cr	0.0003
Cu	0.0002

*Chicago Spectro-Service Laboratory, Inc.

3. BERYLLIUM OXIDE

The polycrystalline BeO was supplied by the Atomics International Division of North American Aviation, Inc. This material, developed by AI as part of a research program funded by the US Atomic Energy Commission, is hot-pressed, and contains somewhat less than 1 percent MgO used as sintering aid. Part of the MgO added, however, escapes as MgF_2 gas during hot-pressing, leaving an estimated 0.5-0.6% MgO in the final material. The average grain size of the material is about

50 microns and, since the MgO remaining in the sintered product is assumed to be fully soluble in BeO, the final structure of the polycrystalline material is single-phased. Neither the precise composition, nor the density or specific grain-size distribution for this material has been supplied by AI, despite of recurrent statements that such will be done. If such information is not received from AI in the near future, analysis of the material at hand will be secured locally.

III DISCUSSION

TASK 1 - EFFECT OF STRUCTURAL SIZE; THE "ZERO STRENGTH"

Principal Investigators: S. A. Bortz and N. A. Weil
Armour Research Foundation

ABSTRACT

A detailed study of the statistical fracture characteristics of four ceramic oxides, Wesgo and Lucalox, ARF MgO and Al BeO was undertaken. It was found that the Weibull theory provided a descriptive characterization of the cumulative distribution function of the fracture strengths of all materials studied, and predicted very adequately the variation of mean strength with specimen size.

The Weibull parameters σ_u , m , and σ_o were found to be greatly influenced by the test variables; test temperature, prior thermal history, surface finish, test atmosphere and specimen size. Specifically, grinding increases the value of m and lowers the mean strength. Annealing at 1700°C for 3 hr. increases the values of both m and σ_o , resulting in an average increase of about 15 percent in the mean strength; the latter effect is ascribed to a diminution of deleterious residual stresses during the annealing process. Increased testing temperatures lowered the strength of materials tested; at 1000°C the loss of mean strength amounted to 12-25 percent as compared to room temperature values.

Rather uniform values of the flaw density constant were derived for all materials, when arranged into groupings of as-received, ground and annealed categories at both test temperatures (20°C and 1000°C) explored. The zero strength was found to be generally less than one-half of the average strength. Lastly, a purposeful truncation of the extensive test series carried out on BeO showed that suppression of a comparatively small (less than 10 percent) of a large population consisting of 150 samples resulted in a complete change of the cumulative distribution function of the Weibull function from an apparent composite distribution to one of nearly gaussian character.

TASK 1 - EFFECT OF STRUCTURAL SIZE: THE "ZERO STRENGTH"

1. INTRODUCTION

The objective of this task is to investigate the applicability of the statistical theories of fracture to several ceramic oxides. These materials all exhibit what is commonly called "brittle fracture". They demonstrate essentially elastic behavior until fracture and give no warning of failure. Once the condition of fracture is initiated, failure is catastrophic. None of the materials exhibit a unique value of fracture stress. The value of the fracture stress has been observed to vary with size, stress state, temperature loading rate, and surface condition. Many experimenters have attempted to examine the random nature of the fracture stress to determine if this behavior is an inherent property of the material. If the behavior of the strength of a brittle material can be considered to be truly random then, theoretically, a description of its probable behavior can be obtained from an accurate plot of its frequency distribution curve. This information, in turn, can be used to construct a cumulative distribution curve which gives the probability of fracture for any stress. Thus the distribution curve gives a complete description of the strength of a material under the test conditions and allows for the choice of a stress determination from a probability of failure from zero through 100 percent.

The most frequently mentioned theory is the one developed by Weibull⁽¹⁻¹⁾. It is based on the weakest-link concept, i. e., failure in the material occurs when the forces of a critical flaw become large enough to cause crack propagation. In developing his theory Weibull assumed a normal distribution function relating the probability of fracture to actual stress observed at fracture. He found that this assumption did not truly fit the physical facts and attempted to correct the theory by proposing a semi-empirical distribution based on experimental data. From this distribution

function two basic material parameters can be determined, a constant m descriptive of the flaw density, and the stress level that the material can withstand with absolute assurance of freedom from failure, which is termed the zero strength, σ_u .

This task has attempted to investigate the applicability of Weibull's semi-empirical distribution function to the ceramic oxides selected and to derive values of the material parameters, under various conditions of test temperature, heat treatment, and surface conditions, as well as to confirm the effect of specimen size in these materials.

Previous work⁽¹⁻²⁾ on this task demonstrated that surface treatment, test temperature, and heat treatment have considerable effect on the material parameters. The present work attempts to complete this work and fill in the area not previously covered.

2. EXPERIMENTAL TECHNIQUES

A. Materials

The large number of specimens required for this investigation made the use of commercially obtainable oxides necessary. To assure material consistency companies supplying these specimens were required, where possible, to fabricate them from one batch and one firing.

Materials studied included two types of Al_2O_3 , Western Gold and Platinum Company (Wesgo) AL-995 and General Electric Lucalox; one grade of MgO manufactured at ARF because a commercial source which could produce the MgO specimens within the time and funding allotted was not found, and one type of BeO supplied by Atomics International.

B. Specimens

Because of the difficulty in making adequate tension studies bending tests were used to obtain test data. The study of size effects required that a controlled gage section be loaded in pure bending. This requirement is best met using a four-point loading system. To avoid any friction effects⁽¹⁻³⁾ under load, the specimens were loaded through their neutral axis. To ensure uniformity of denseness and to make the job of fabrication easier a flat coupon-type body was decided upon. After some investigation a final shape resembling a dogbone was selected. Figure 1-1 shows the shapes and dimensions adopted for the bulk of this program. Time and fabrication limitations reduced the study of BeO to the fixed volume type specimens under a study in Task 3. These consist of rectangular bars $1/3 \times 3/16$ in. and $1/4 \times 1/4$ in. in cross section. The rectangular section was tested on both faces and all specimens were loaded over a 2-in. gage section in pure bending.

C. Testing Conditions

The majority of experiments were performed at room temperature and at 1000°C. Attempts made to obtain data at 1750°C were abandoned because the test fixtures failed because of thermal shock. The time required to reduce this hazard for each test could not be realized because of the large number of specimen data required. Specimens were studied as combinations of the as-received, ground, and annealed conditions at 1750°C.

For this work a 30,000-lb Universal testing machine was used. The high temperature experiments were performed in a resistance type furnace. The test jig for the dogbone specimens is shown in Fig. 1-2, that for the rectangular bars in Fig. 1-3. The rollers shown in Fig. 1-3 were used to eliminate the friction effects. Data obtained using either test jig were compatible with each other. The main problem with the jig shown in Fig. 1-3 was that of keeping the rollers operational at high temperatures.

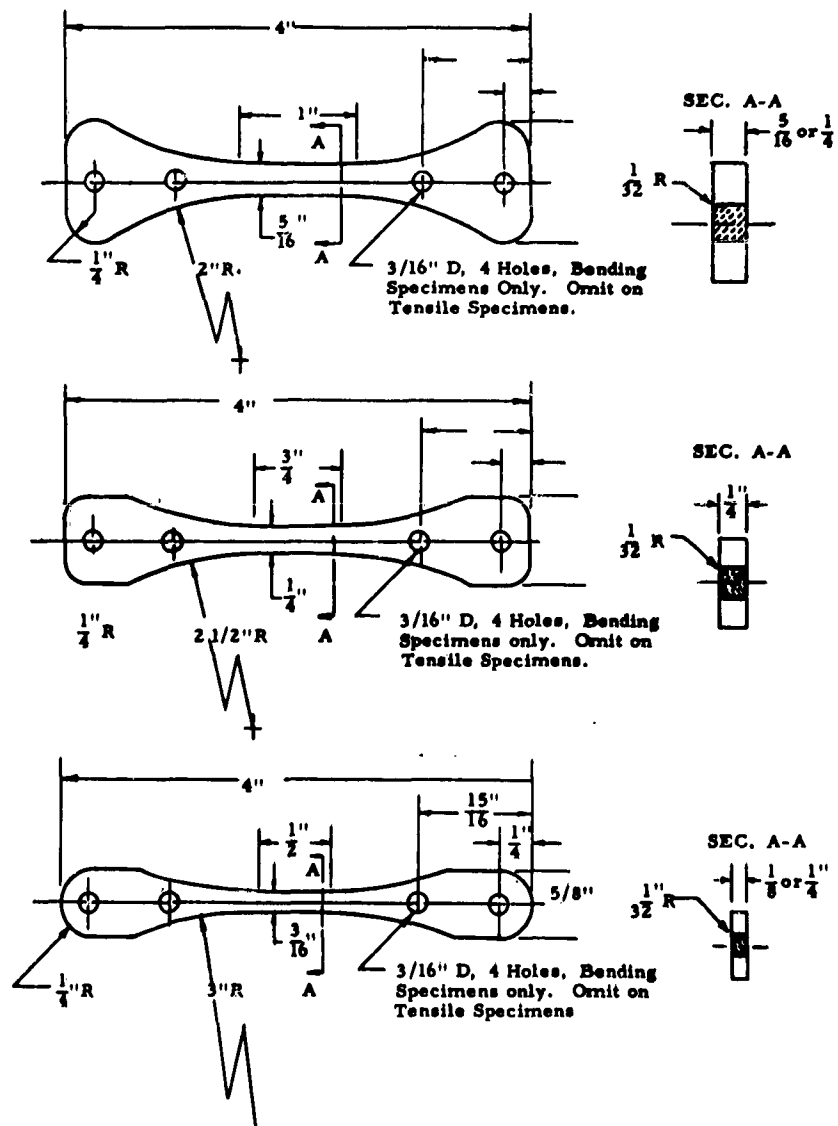


Fig. 1-1 DOGBONE SPECIMENS USED FOR TENSION AND BENDING

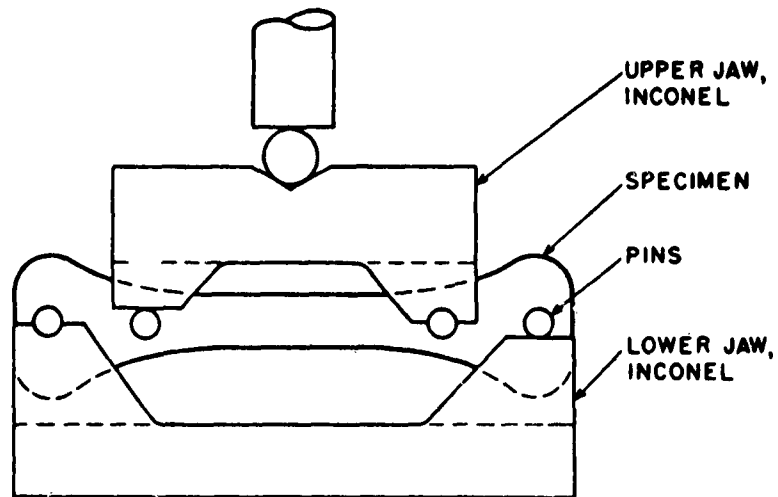


Fig. 1-2 FLEXTURE TEST SPECIMEN

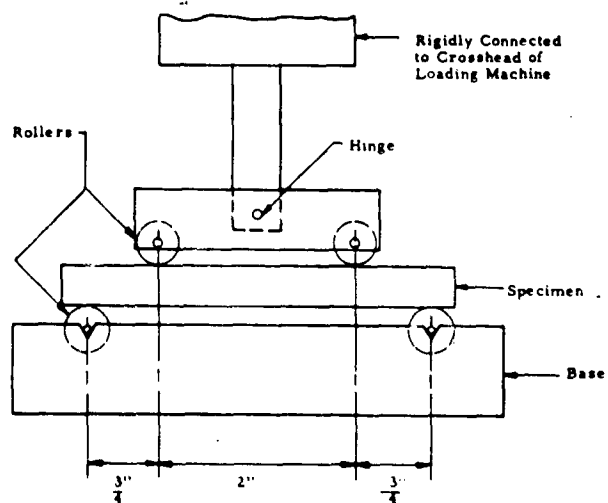


Fig. 1-3 LOADING FIXTURE USED TO TEST PRISMATIC BARS IN PURE BENDING

3. THEORETICAL CONSIDERATIONS

The Weibull theory^(1-1, 1-4) is based on the concept that brittle materials contain a large number of flaws, which lower the fracture stress in a material below the theoretical rupture stress. These flaws are assumed to be of random size and distribution throughout the body and to be the cause of scatter observed in the failure of a ceramic material. Starting with the expression for probability of fracture,

$$S = 1 - e^{-B} \quad (1-1)$$

the fundamental assumption of the Weibull theory is that the risk of rupture for uniaxial tension is given by

$$B = V \left(\frac{\sigma - \sigma_u}{\sigma_o} \right)^m \quad (1-2)$$

where V is a dimensionless number expressing the quantity of unit volumes subjected to uniform tension.

While for a beam of rectangular cross section, $b \times 2h$, subjected to pure bending over a length, L , the risk of rupture becomes

$$\begin{aligned} B &= \int_V f(\sigma) dV = \frac{bL}{\sigma_o^m} \int_{h_u}^h \left[\sigma \frac{y}{h} - \sigma_u \right]^m dy \\ &= \left[\frac{V}{2(m+1) \sigma_o^{mh}} \right] \left[\frac{(\sigma - \sigma_u)^{m+1}}{\sigma} \right] \end{aligned} \quad (1-3)$$

where m (the flaw density exponent) and σ_o are material constants, $V = 2bhL$ is the volume of beam under pure bending expressed in dimensionless numbers, σ is the bending stress at the extreme fiber, and $h_u = \sigma_u h / \sigma$ is the fiber distance from the neutral axis at which the stress equals the zero strength, σ_u .

Equations 1-1 and 1-2 can be rewritten in the form applicable to bending specimens

$$\left. \begin{aligned} \log \log \frac{1}{1-S} &= \log B + \log \log e \\ \log B &= (m+1) \log (\sigma - \sigma_u) - \log \sigma + \log \frac{V}{2(m+1) \sigma_o^m} \end{aligned} \right\} \quad (1-4)$$

where the logarithms are Briggs'. The expression for the probability of fracture, S , for a particular stress level, σ_n , can be calculated from

$$S = \frac{n}{N+1} \quad (1-5)$$

where N is the total number of specimens, and n is the specimen serial number listing the fracture is in an increasing order from 1 to N , (σ_n being the n^{th} fracture stress). The relation can therefore be written,

$$\log \log \frac{1}{1-S} = \log \log \frac{N+1}{N+1-n}$$

Equation 1-4 can now be restated as

$$\log \log \frac{N+1}{N+1-n} = (m+1) \log (\sigma - \sigma_u) - \log \sigma + \log \frac{V}{2(m+1) \sigma_o^m} + \log \log e \quad (1-6)$$

If $\sigma_u = 0$, the equation simplifies to

$$\log \log \frac{N+1}{N+1-n} = m \log \sigma + \log \frac{V}{2(m+1) \sigma_o^m} + \log \log e \quad (1-7)$$

For the case of pure tension a test plot is made first assuming $\sigma_u = 0$, and presenting results on a graph with $\log \log \left[(1-S)^{-1} \right]$ or $\log \log (n+1)/(N+1-n)$ as the ordinate and $\log \sigma$ as the abscissa. If the plot follows a straight line, σ_u is indeed equal to zero; if the resulting curve has a downward concave curvature, a trial value is taken for $\sigma_u > 0$ and the data are replotted using this time $\log (\sigma - \sigma_u)$ as the abscissa. If the curve reverses itself, the trial value of σ_u is too high and a new value, lower than the previous one, is chosen. The process is iteratively continued until a reasonably straight line plot is obtained, which corresponds to the correct value of σ_u . The slope of this straight line will yield m , while the intercept will have a value of $\log V - m \log \sigma_0 + \log \log e$, which allows for the determination of σ_0 once m and V are known.

For the case of pure bending, the procedure is quite similar, except that all graphs subsequent to the first one are presented in the coordinate system of

$$\log \log \frac{N+1}{N+1-n} + \log \sigma \text{ versus } \log (\sigma - \sigma_u) .$$

The value of σ_u is again determined by trial-and-error; the correct value is again the one that results in a straight line plot. For the correct value of σ_u the slope of the straight line will be $m+1$; with m thus determined and V known, σ_0 can then be determined from the value of the intercept given by $\log V - \log 2 (m+1) - m \log \sigma_0 + \log \log e$.

For the special case where σ_u is equal to zero the constants are obtained by plotting $\log \log \left[(N+1)/(N+1-n) \right]$ versus $\log \sigma$ as in the case for tensile specimens.

The method of plotting developed here for the case of bending is believed to be a novel contribution, reference available in the literature^(1-11, 1-12, 1-13) universally adopting the assumption that $\sigma_u = 0$. It should also be mentioned that if the first plot yields an upward concave curve, the results will not be reducible to a straight line under any assumption of $\sigma_u = 0$. Rather, this condition implies that the material is governed by different fracture mechanisms operative at various levels of fracture probabilities, and its statistical fracture behavior must then be represented by a set of "mixed" Weibull distribution parameters⁽¹⁻¹³⁾.

Attempts were made to develop a computer program for determining the material constants. The method described in full detail in Task 3, was based on a least-squares technique of curve fitting and would have provided firmer numerical material constants than graphical plots which are subject to subjective analysis. However, these techniques proved unsuitable with data available and, because of time considerations, the effort was abandoned.

After determining the materials constants, the theoretical effect of volume on the flexural specimens can be calculated and compared to the test data. The mean stress σ_m and variance a^2 of a group of specimens with a zero strength σ_0 is given by

$$\sigma_m = \sigma_u + \int_{\sigma_0}^{\infty} e^{-B} d\sigma, \quad (1-8)$$

and

$$a^2 = \int_{\sigma_u}^{\infty} e^{-B} d(\sigma^2) - \sigma_m^2$$

When Eq. 1-1 and 1-2 are substituted into these equations, the expressions for the mean strength and variance in uniaxial tension become

$$\sigma_m = \sigma_u + \sigma_o V^{-1/m} \Gamma \left(1 + \frac{1}{m}\right) \quad (1-9)$$

$$s^2 = \sigma_o^2 V^{-2/m} \left[\Gamma \left(1 + \frac{2}{m}\right) - \Gamma^2 \left(1 + \frac{1}{m}\right) \right] \quad (1-10)$$

where the Γ function is defined as

$$\Gamma(x) = \int_0^{\infty} z^{x-1} e^{-z} dz.$$

The equation which relates the size effect can then be written

$$\frac{\sigma_1}{\sigma_2} = \frac{\sigma_u + \sigma_o V_1^{-1/m} \Gamma \left(1 + \frac{1}{m}\right)}{\sigma_u + \sigma_o V_o^{-1/m} \Gamma \left(1 + \frac{1}{m}\right)} \quad (1-11)$$

For the case where $\sigma_u = 0$, the expression simplifies to

$$\frac{\sigma_1}{\sigma_2} = \left(\frac{V_2}{V_1} \right)^{1/m} \quad (1-12)$$

The significant features of the Weibull probability density function, assumed here to characterize the statistical strength of the ceramics drawn under study, were treated in detail in the previous year's report of this program⁽¹⁻²⁾, and need not be reiterated here. Nonetheless, in interpreting the results obtained, the following features of the Weibul function must be borne in mind:

(1) The value of the flaw density exponent m characterizes the nature and dispersion of flaws contained in the material. This flaw distribution is not measured, but rather inferred through the

observed dispersion of fracture strengths of the samples; a physical description of actual flaw sizes, if of interest, could be readily developed by means of the Griffith fracture criterion (with full awareness of the simplifying assumptions involved in the latter theory).

(2) The zero strength σ_u represents the limit stress below which the material is absolutely free from any risk of failure, regardless of the size of the specimen or structure. To a degree as covered in point (5), σ_u is also a measure of the inherent strength of the material.

(3) The only free parameters of the Weibull distribution of Eq. 1-1 and 1-2 are σ_u and m . The volume and applied stress, V and σ , represent actual conditions of test, and thus are variables rather than parameters. Also, σ_o is merely a normalizing factor, and is neither an independent parameter, nor can it be related to any identifiable physical property of the material.

(4) A low value of m indicates a material which either contains flaws of highly variable severity, or in which the flaws are very nonuniformly dispersed. Conversely, a high m value characterizes a material with a uniform distribution of highly homogeneous flaws. If two materials have identical values of V , σ_u and σ_o , the one with a lower m value will possess a higher mean stress. This can be readily confirmed by an inspection of Eq. 1-9, where the effect of m is far greater on the term $V^{-1/m}$ than on $\left(1 + \frac{1}{m}\right)$, the latter being close to 1 for all save very low values of m .

(5) For two materials with identical values of V , σ_o and m , the material having the higher value of σ_u will also have the higher mean stress as can be ascertained by an inspection of Eq. 1-9.

(6) Again, by Eq. 1-9, the mean stress will be the larger, the higher the numerical value of σ_o .

(7) By Eq. 1-10, the variance (or standard deviation) will increase with higher values of σ_o and decreasing values m ; this quantity is unaffected by the value of σ_u , as must be the case.

(8) From viewpoint of structural utilization or design, materials characterized by high values of σ_u , m and σ_o should be preferred. These conditions ensure a high mean stress σ_m . A high value of m , indicative of a homogeneous distribution of flaws, will also serve to narrow the range of fracture stresses corresponding to any desired level of risk of rupture, as Eq. 1-1 and 1-3 readily confirm, in fact, for $m = \infty$, there obtains $B = \infty$ and $S = 1$ for all values of σ , so that $\sigma_m = \sigma_u$, and the fracture probability abruptly changes from $S = 0$ for $\sigma < \sigma_u$ to $S = 1$ for $\sigma > \sigma_u$. High values of m also reduce the variance thereby contributing to the application of a lower safety factor in design for a stated value of the risk of rupture.

(9) The expressions contained in Eq. 1-9 and 1-10 are valid only for the case of uniaxial tension, and are not descriptive of fracture under pure bending. As it happens, for the latter case, Eq. 1-8 turns out to be nonintegrable; an approximate form of the mean fracture strength for pure bending was given in Ref. 1-9. In view of the approximate nature of the latter expression, and because it yields results very close to the case of pure tension, Eq. 1-9 has been utilized throughout this work for the calculation of mean fracture strengths from known values of σ_u , m , σ_o and V .

4. EXPERIMENTAL RESULTS

A. Selection of Population Samples

During the initial phases of the program, ⁽¹⁻²⁾ cells of five specimens were tested for each selected variable and combination of variables. The plan was to establish the material

parameters by statistically separating the variables and combining all the data into one distribution function. This presupposes that the variance for each cell comes from the same sample population. However, as the data were being tabulated, cells which should show similar strengths were discovered to indicate significant strength differences. This led to the conclusion that the population sampling was too small to provide accurate variable differences. The method of experimental approach was changed. The 0.047 - cu in. gage volume specimen population for each material was enlarged so that estimates of the material parameter could be made from a single group. The number of specimens required was estimated from the population sampling already obtained. The allowable error can be expressed in terms of confidence limits⁽¹⁻⁵⁾. If L is the allowable error in the samples and the results are not to exceed the 95 percent confidence limit, then

$$L = \frac{2 S}{\sqrt{n}} \quad (1-13)$$

where S is the standard deviation and n is the population size. From Eq. 1-9

$$n = \left(\frac{25}{L} \right)^2 \quad (1-14)$$

For a coefficient of error limited to 5 percent, a required population size of thirty to forty specimen results. A population size of sixty was established as more advisable, since it allows the rejection of invalid tests. In some cases specimens were lacking to meet this requirement and also fractures occurred out of the gage section so that certain specimen populations are less than this amount.

B. Data Acquisition and Presentation

With specimens and testing methods described in Section 2 experiments were conducted on the four materials entailed in this program,

Wesgo (AL-995) Al_2O_3

Lucalox Al_2O_3

ARF MgO

Al BeO

Variables explored included:

- (1) Test Temperature
- (2) Specimen Size
- (3) Prior Thermal History
- (4) Specimen Finish
- (5) Test Atmosphere

Variable (5) entailed experiments at room and elevated temperature conducted in testing environments represented by air, saturated steam and dry argon. As has been already noted, an analysis of variance conducted on the medium size specimens tested at room temperature showed that for the as-received material the environmental atmosphere had no significant effect on the fracture strength. Therefore, this variable was eliminated from all further tests, other than a modest exploration of its effect at 1000°C on Wesgo AL-995 samples represented by the very limited population of five samples each

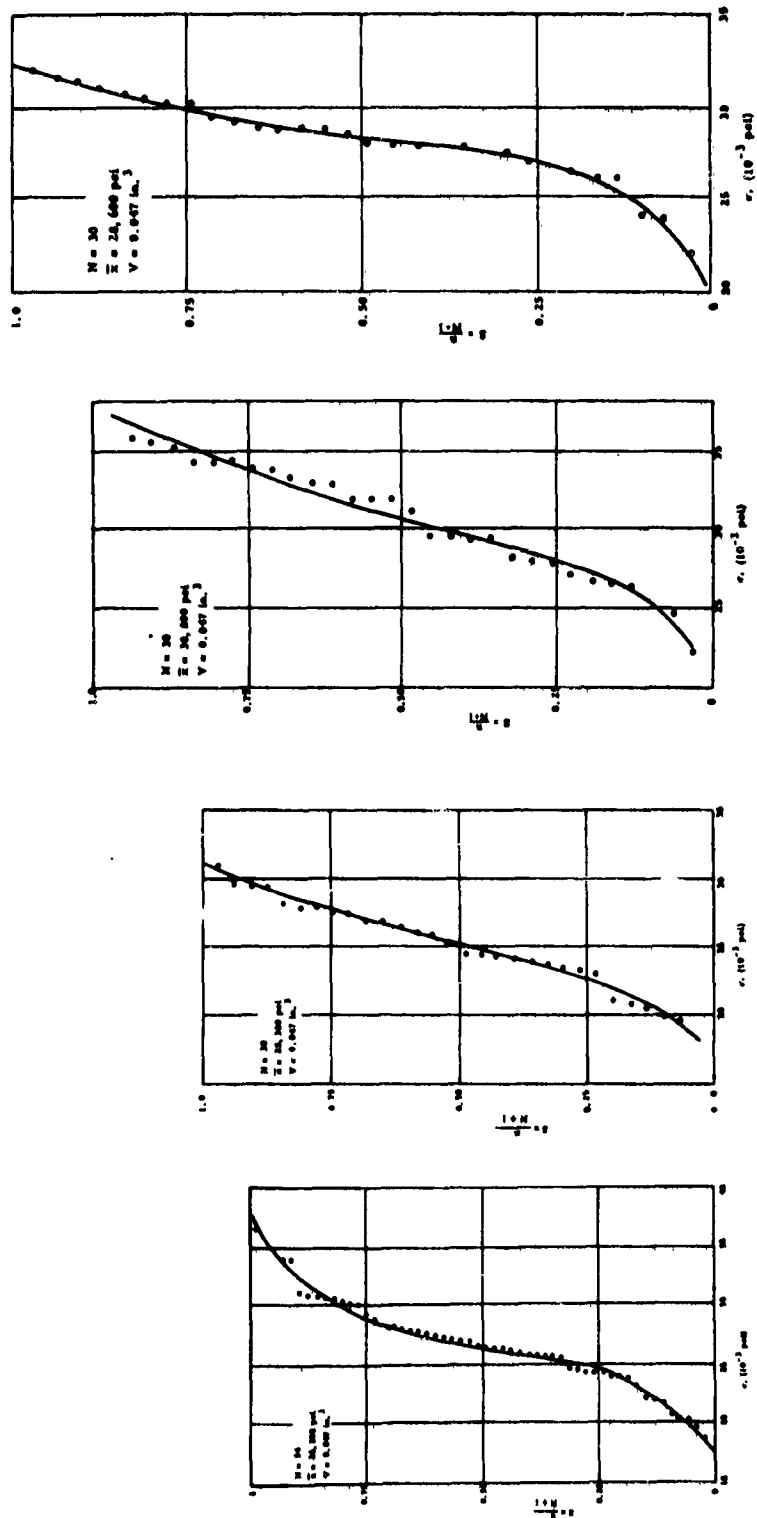
Specimen finish and prior thermal history were given a complete exploration for the Wesgo AL-995 tested at room temperature. Specimen finish consisted of the as-received condition and a "fine ground" finish; prior thermal history consisted again of the as-received condition, and an annealing treatment represented by soaking at 1700°C for 3 hr, followed by slow furnace cooling. Hence, the complete permutations for Wesgo AL-995 tested at room temperature cover the four cases of as-received, ground, annealed, and ground and annealed conditions. A modest amount of a comparable study was

also carried out on Wesgo AL-995 at 1000°C, but specimen limitations confined the experiments to population samples of groups of five, as reported later. No comparable studies were carried out on Lucalox, MgO or BeO, either because a sufficient number of specimens was not available, or because the specimens were shipped with an already ground finish (Lucalox, BeO).

The temperature levels investigated included room temperature and 1000°C., which were explored for all materials, save for BeO.

The primary test program, then, dealt with the effects of material composition, temperature, surface treatment, heat treatment and environmental atmosphere upon the Weibull parameters and statistical values descriptive of material properties. To obtain reasonably meaningful data, a minimum of 20 specimens was tested; actual population samples varied between 20 and 140 samples for the medium size specimens ($V = 0.047$ cu in). For sake of compactness of reporting, the results are presented in the form of cumulative distribution functions in Fig. 1-4 to 1-7 inclusive. With these data as the basis, Weibull plots were prepared for each test condition, using the graphical method described in Section 3. The resulting graphs are shown in Fig. 1-8 to 1-13, inclusive. Lastly, to summarize the results obtained, a condensed form of the resulting material parameters is presented in Table 1-I, which also contains other salient information of interest.

A second experimental program dealt with the effect of specimen size upon fracture strength. The volumetric variation of specimens chosen comprised an eight-fold range, from a test volume of 0.012 to 0.098 cu in.; most of the experiments were conducted on the "medium" specimen size having a gage volume of 0.047 cu in. The principal purpose of this work was to obtain an evaluation of the adequacy of the predictions of the Weibull theory for the effect of volume on resulting failure strength; this consideration entails no arbitrary assumptions, but constitutes a factual prediction of the theory as now formulated.



(a) As-received (b) Ground (c) As-received and Annealed (d) Ground and Annealed

Fig. 1-4 DISTRIBUTION CURVE OF BENDING STRENGTHS OF WESGO A1-995 IN AIR AT 20°C

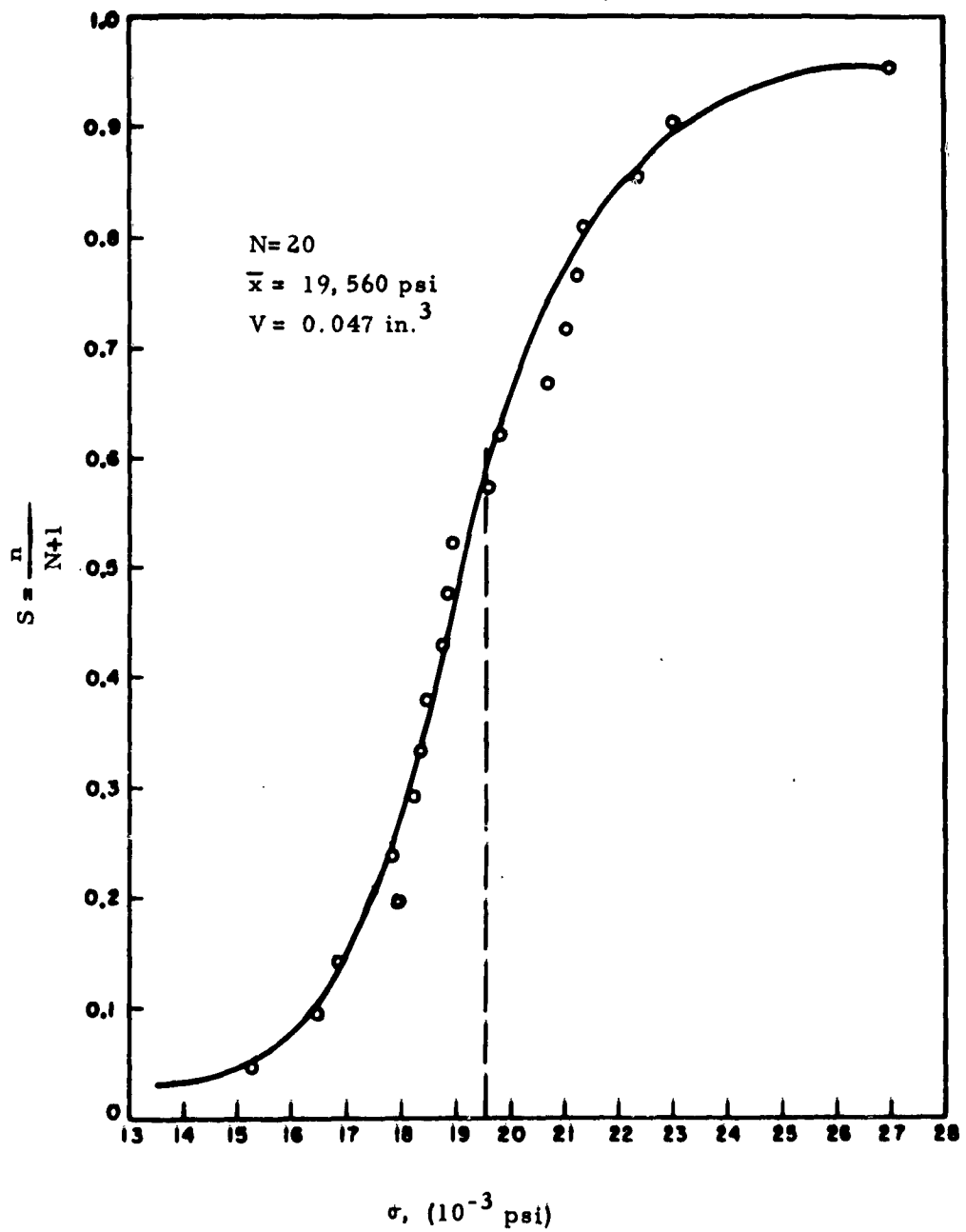
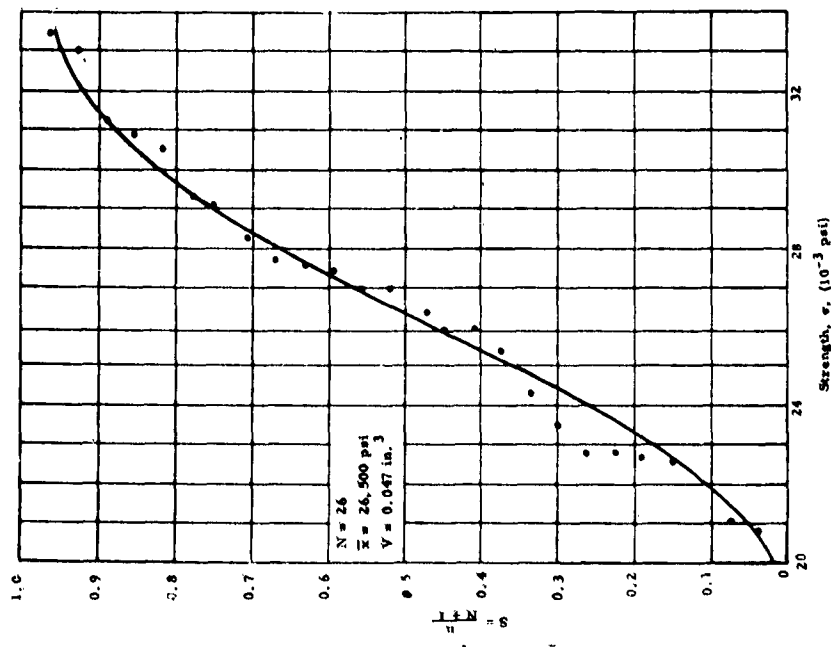
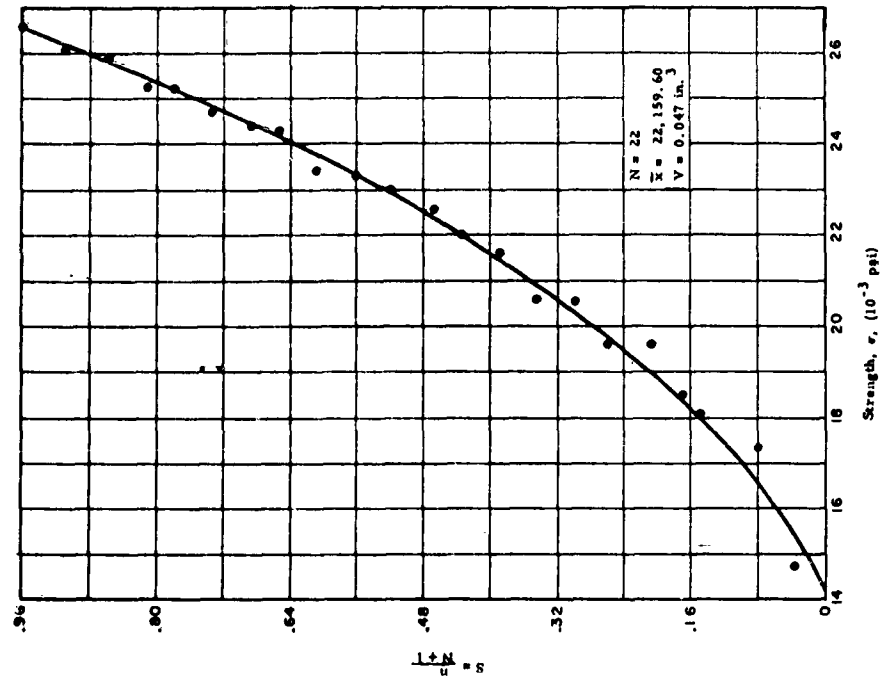


Fig. 1-5 DISTRIBUTION CURVE OF BENDING STRENGTHS, AS-RECEIVED WESGO AL-995 IN AIR AT 1000°C

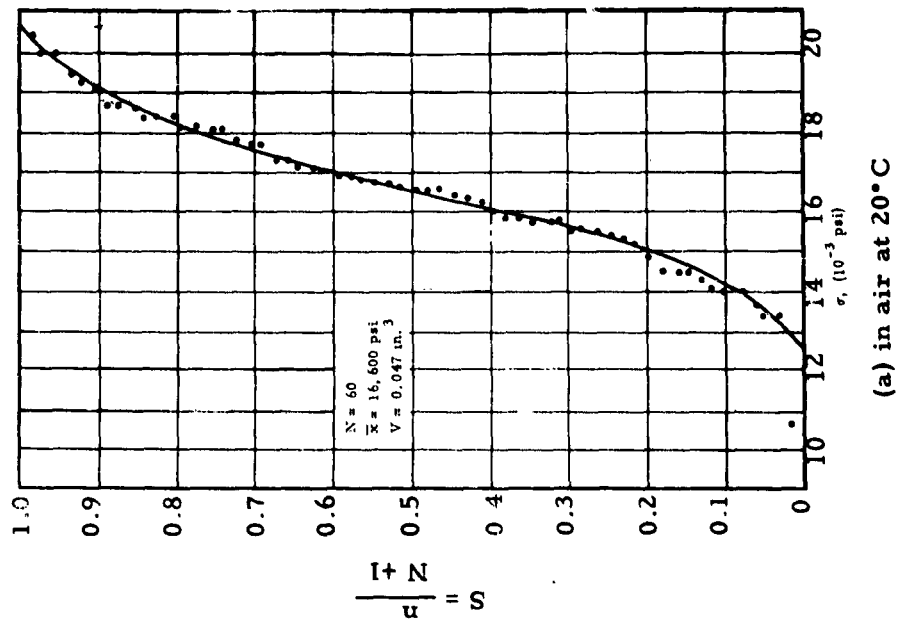


(a) in air at 20°C

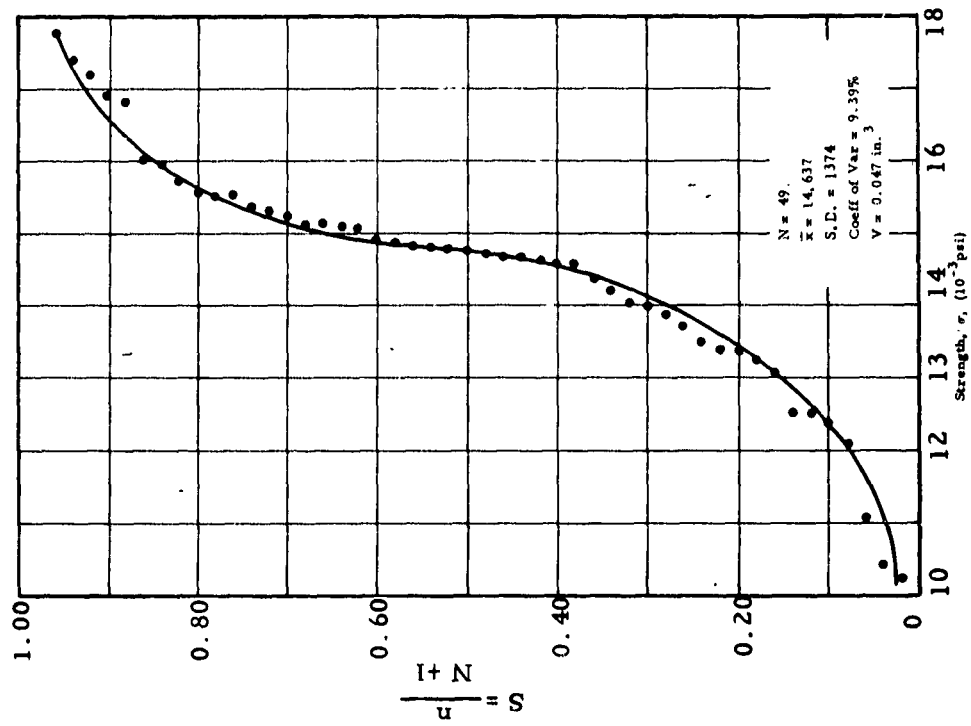


(b) in air at 1000°C

Fig. 1-6 DISTRIBUTION CURVES OF BENDING STRENGTHS, AS-RECEIVED LUCALOX

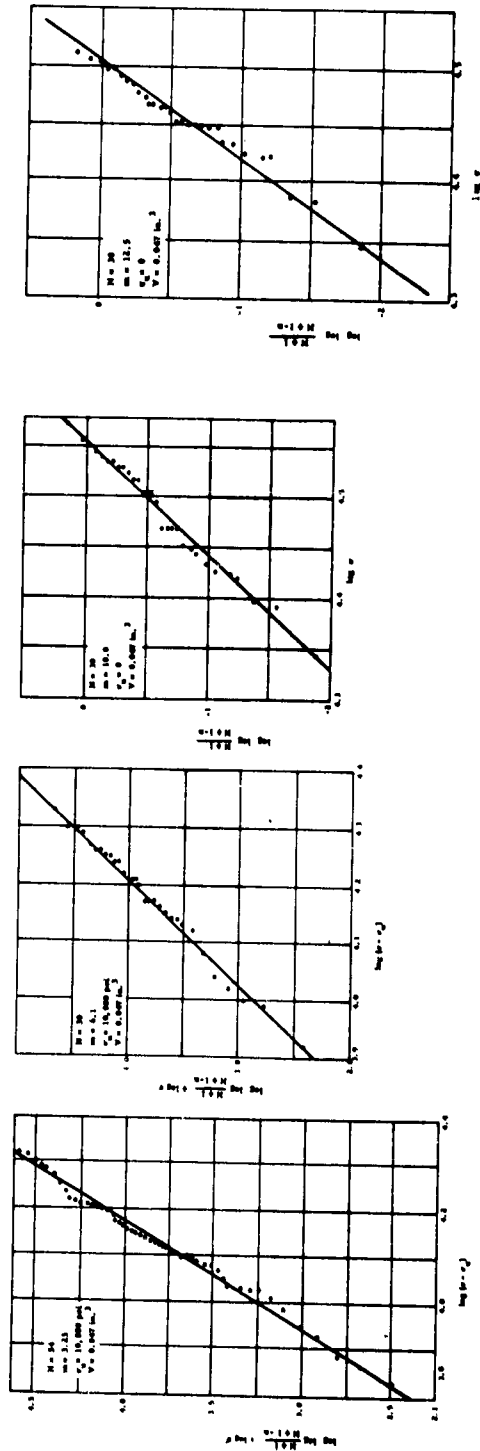


(a) in air at 20°C



(b) in air at 1000°C

Fig. 1-7 DISTRIBUTION CURVES OF BENDING STRENGTHS, AS-RECEIVED ARF
MAGNESIUM OXIDE



(a) As-received (b) Ground (c) As-received and Annealed (d) Ground and Annealed

Fig. 1-8 GRAPHICAL DETERMINATION OF WEIBULL PARAMETERS FOR WESGO ALUMINUM OXIDE IN AIR AT 20°C

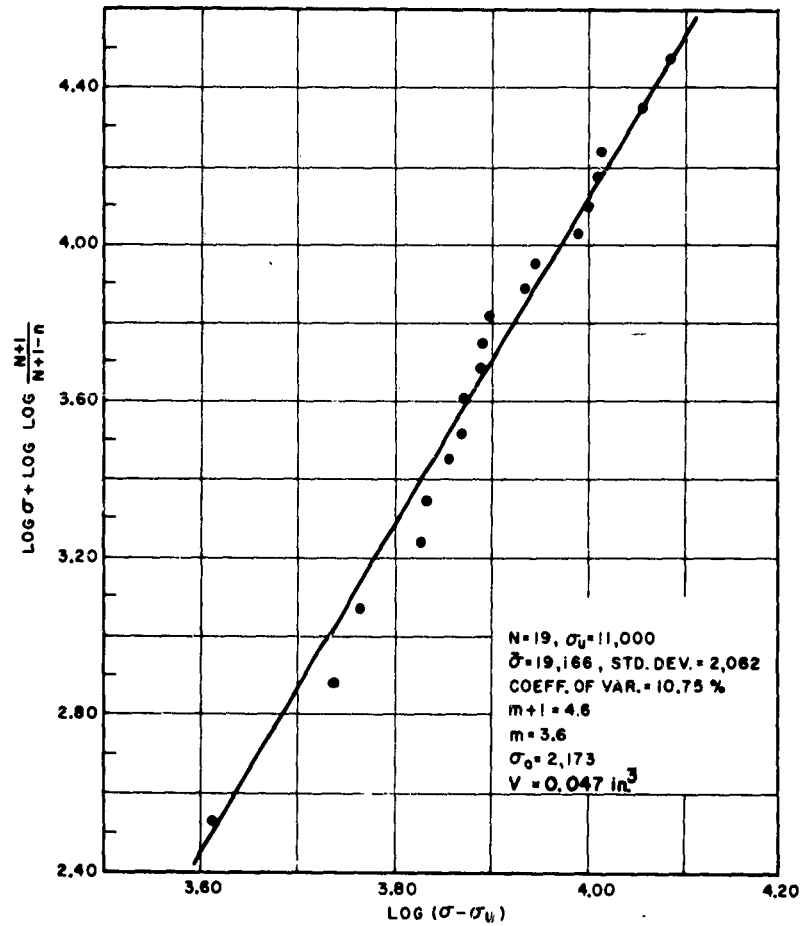


Fig. 1-9 GRAPHICAL DETERMINATION OF WEIBULL PARAMETERS, AS-RECEIVED WESGO AL-995 IN AIR AT 1000°C

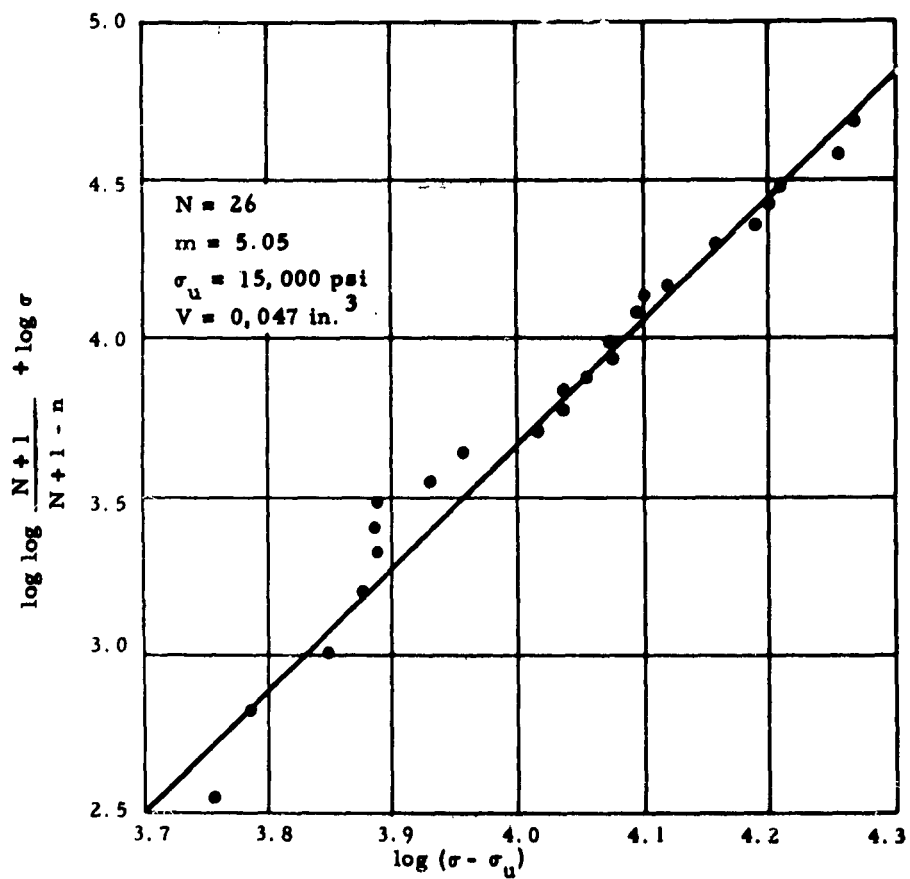


Fig. 1-10 GRAPHICAL DETERMINATION OF WEIBULL PARAMETERS, AS-RECEIVED WESGO AL-995 IN AIR AT 1000°C

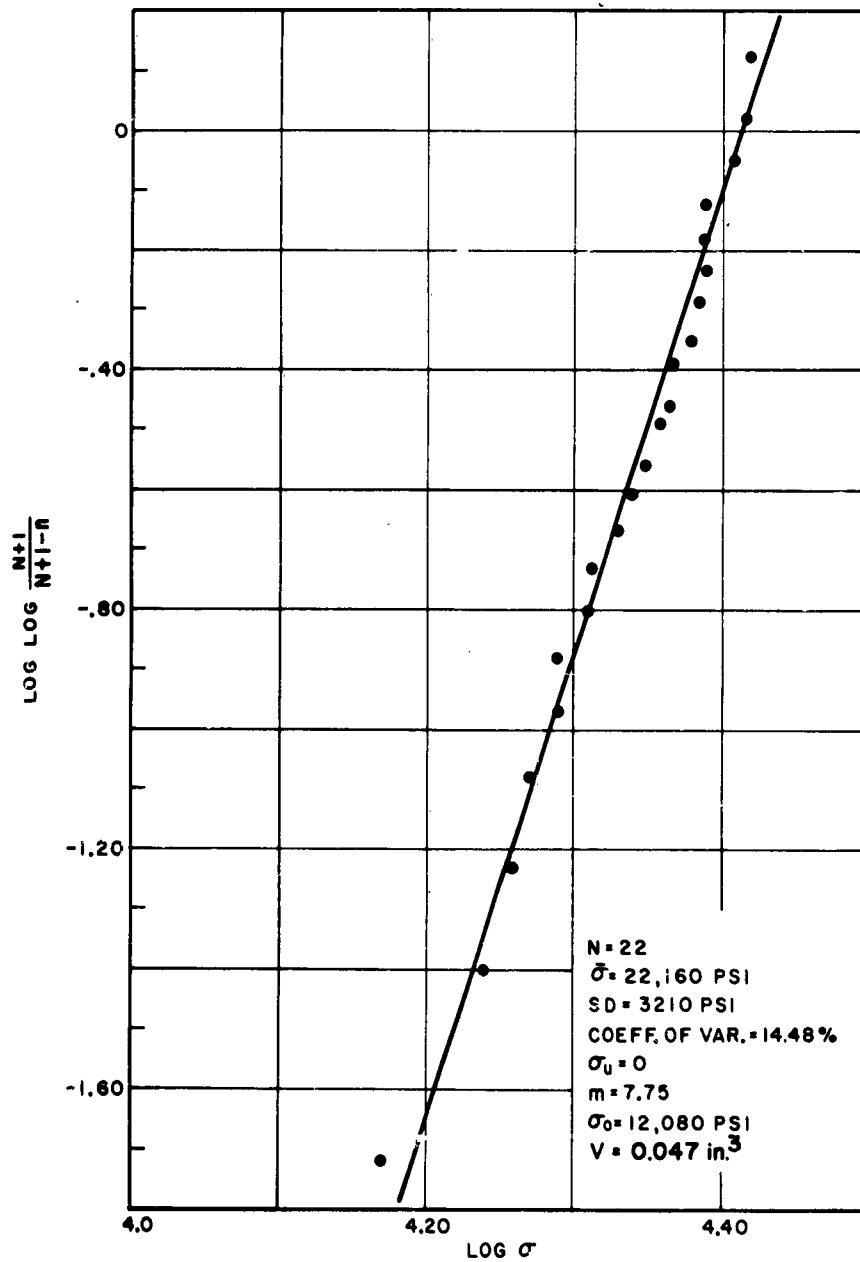


Fig. 1-11 GRAPHICAL DETERMINATION OF WEIBULL PARAMETERS, LUCALOX IN AIR AT 1000°C

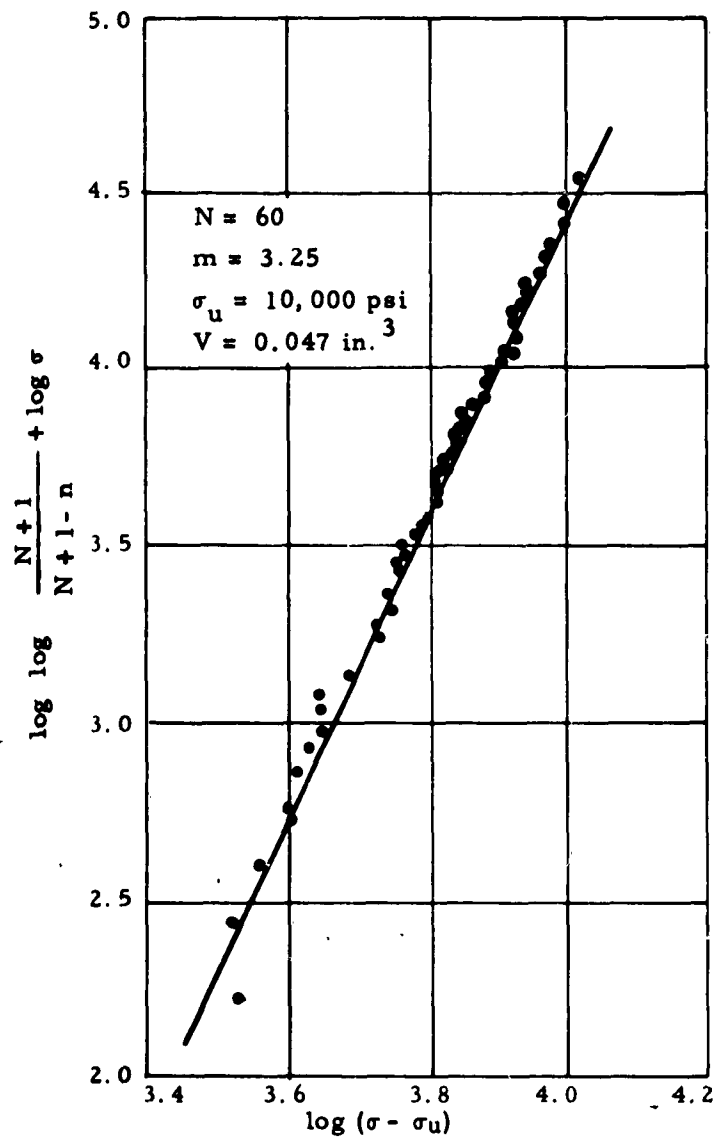


Fig. 1-12 GRAPHICAL DETERMINATION OF WEIBULL PARAMETERS, ARF MAGNESIUM OXIDE IN AIR AT 20°C

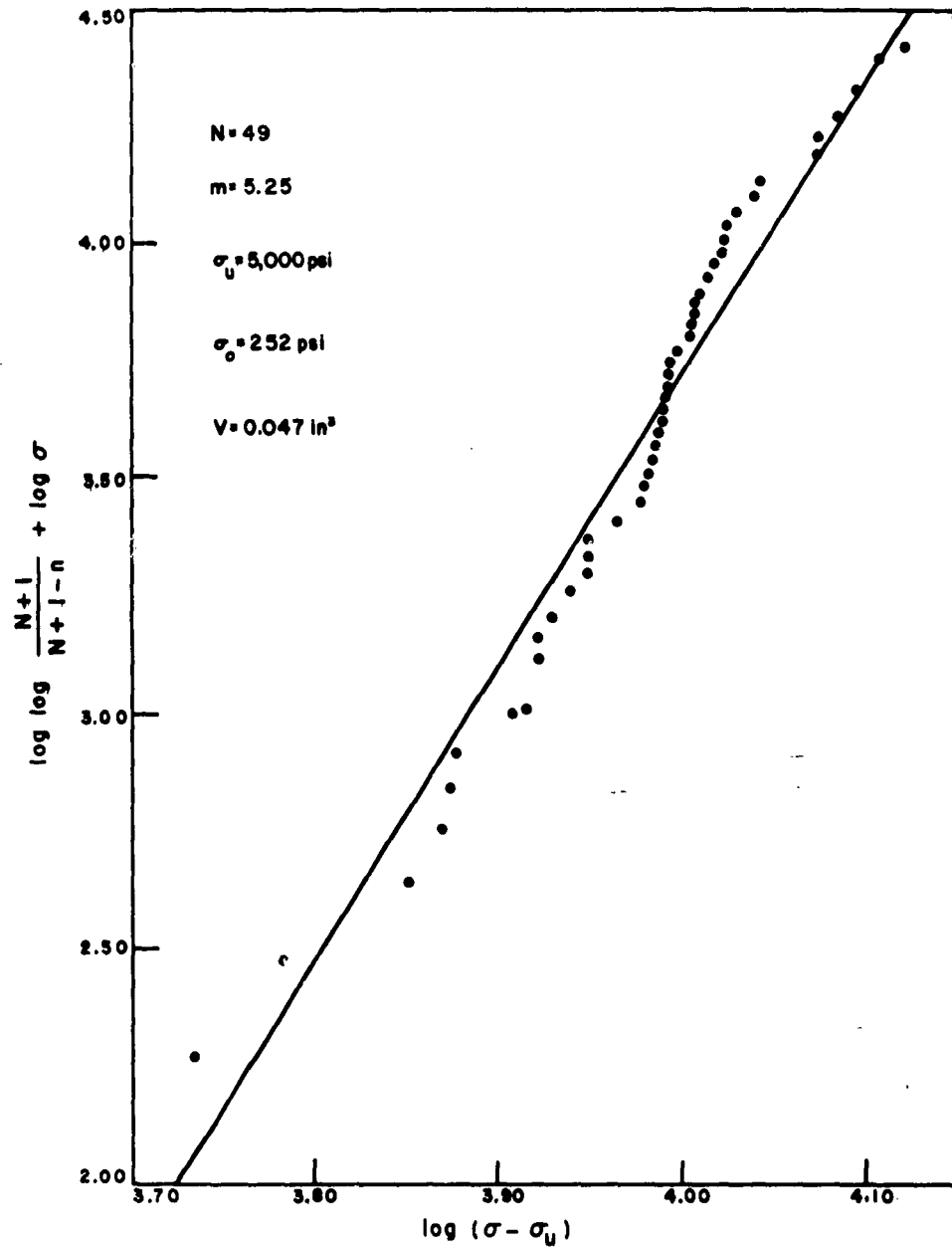


Fig. 1-13 GRAPHICAL DETERMINATION OF WEIBULL PARAMETERS, ARF MAGNESIUM OXIDE IN AIR AT 1000°C

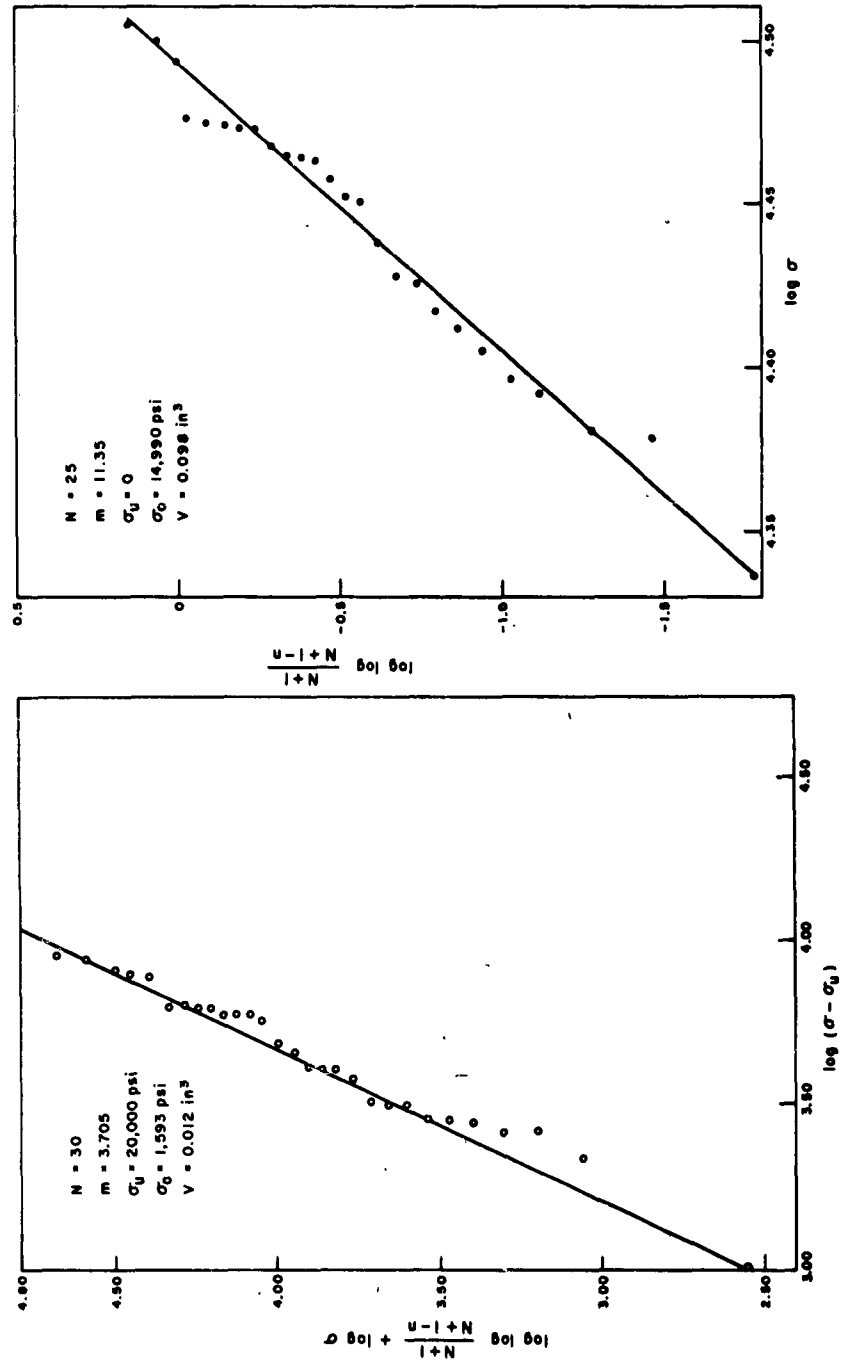
Table 1-1
SUMMARY, WEIBULL MATERIAL CONSTANTS FOR BEND TESTS OF SPECIMENS IN AIR
(0.047 cu in. Gage Volume)

Material	Temp., (°C)	Surface Treat- ment	Heat Treat- ment	Number of Specimens	Flaw Den- sity Constant, m	Zero Strength σ_u (10^{-3} psi)	Material Constant σ_o (10^{-3} psi)	Average Strength σ_m (10^3 psi)	Standard Devia- tion s_a (10^3 psi)	Coeffi- cient of Varia- tion (%)
Wesgo (AL-995) Al ₂ O ₃	20	As-received	None	54	3.23	10.0	3.24	26.3	1.28	4.87
	20	Ground	None	30	6.10	10.0	4.37	25.3	3.36	13.30
	20	As-received	Annealed at 1700°C	36	10.00	0.0	18.86	30.8	3.83	12.42
	20	Ground	Annealed at 1700°C	30	12.50	0.0	18.41	28.6	2.44	8.53
	1000	As-received	None	20	3.60	11.0	2.17	19.6	2.66	13.59
Lucalox Al ₂ O ₃	20	Ground	None	26	5.05	15.0	4.22	26.5	3.62	13.66
	1000			22	7.75	0.0	12.08	22.2	3.21	14.46
ARF	20	As-received	None	60	3.25	10.0	0.74	16.6	1.94	11.70
MgO	1000	As-received		49	5.25	5.0	0.25	14.6	1.38	9.45
Al BeO	20	Ground	None	140	7.35	0.0	8.82	15.6	2.50	16.02

Two experimental series were conducted to examine this condition. One series, already reported upon but not evaluated in the previous annual report⁽¹⁻²⁾, consisted of experiments on Wesgo AL-995 at 20° and 1000°C using, for the most part, population groups of five for each of the small (0.012 cu in) and large (0.098 cu in.) specimen sizes; results for the medium specimen size (0.047 cu in.) were taken from the main test series which constituted the bulk of the work on this program.

Because the population samples consisting of only five individuals proved highly inadequate for the construction of Weibull distributions, a new test series was conducted on the small and large specimen shapes at room temperature. For this series only the as-received Wesgo AL-995 was explored, and the BeO was not tested at all, since only the medium volume size of specimen was supplied by AI. To curtail the amount of presentation, only the final Weibull plots for this experimental series at room temperature are shown; these are presented in Fig. 1-14, 1-15 and 1-16.

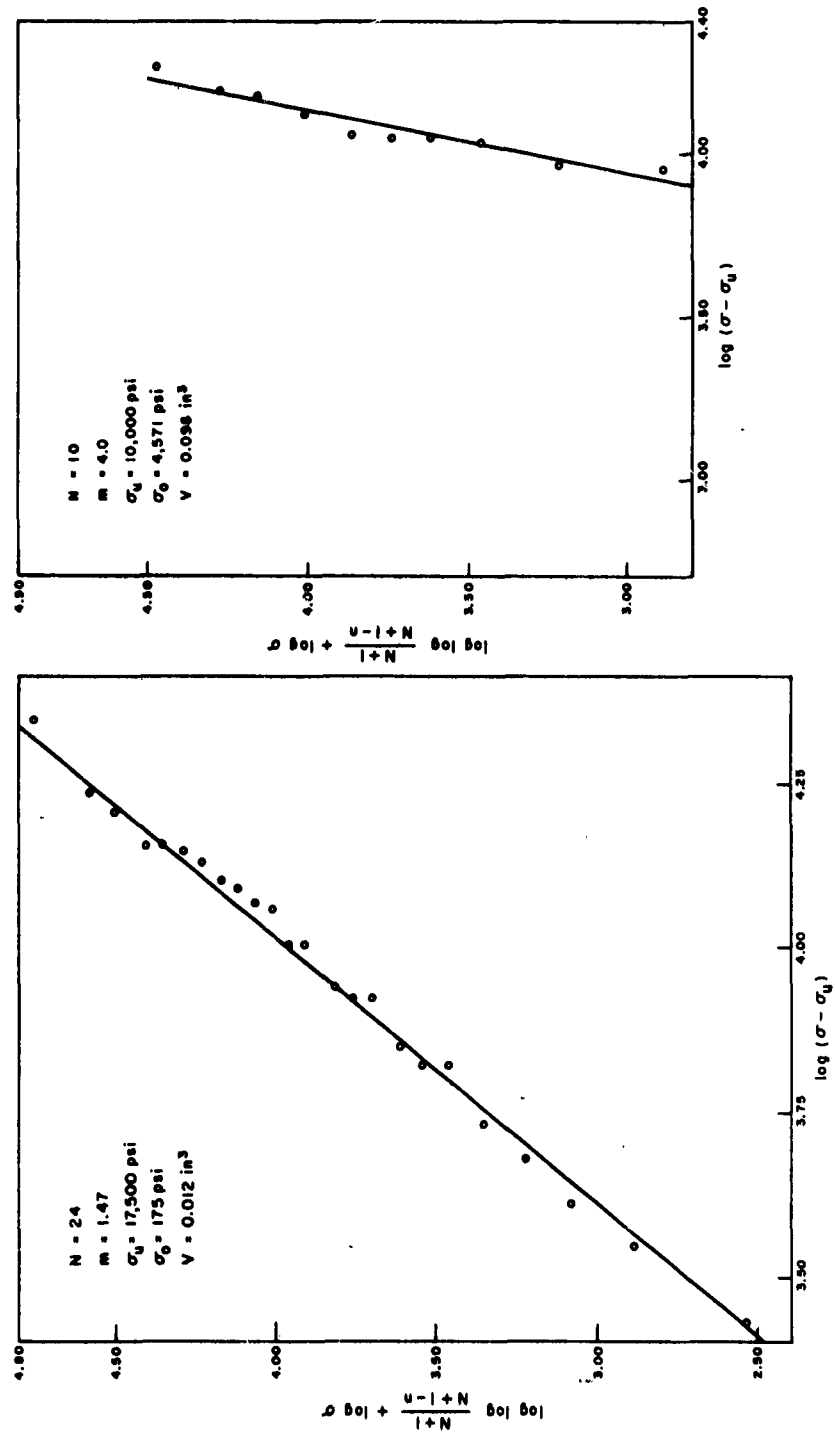
A second set of experiments, conducted at 1000°C, consisted of two separate series. The first series considered Wesgo AL-995 only; as has been presented in Table 1-II of the previous year's final report⁽¹⁻²⁾, experiments were conducted on all three specimen sizes under the three different environmental atmospheres at 1000°C. Acting on the results of room temperature tests, which showed that environmental atmosphere had little influence on the resulting fracture strength, data for the group of 5 contained in this test series were combined to consider solely the effect of specimen size. This was done in hope that the resulting groupings of 15 specimens would yield a sufficiently large population to allow a tentative evaluation of the Weibull parameters, even though it was known that 40-60 specimens are necessary for a reliable assessment of these constants.



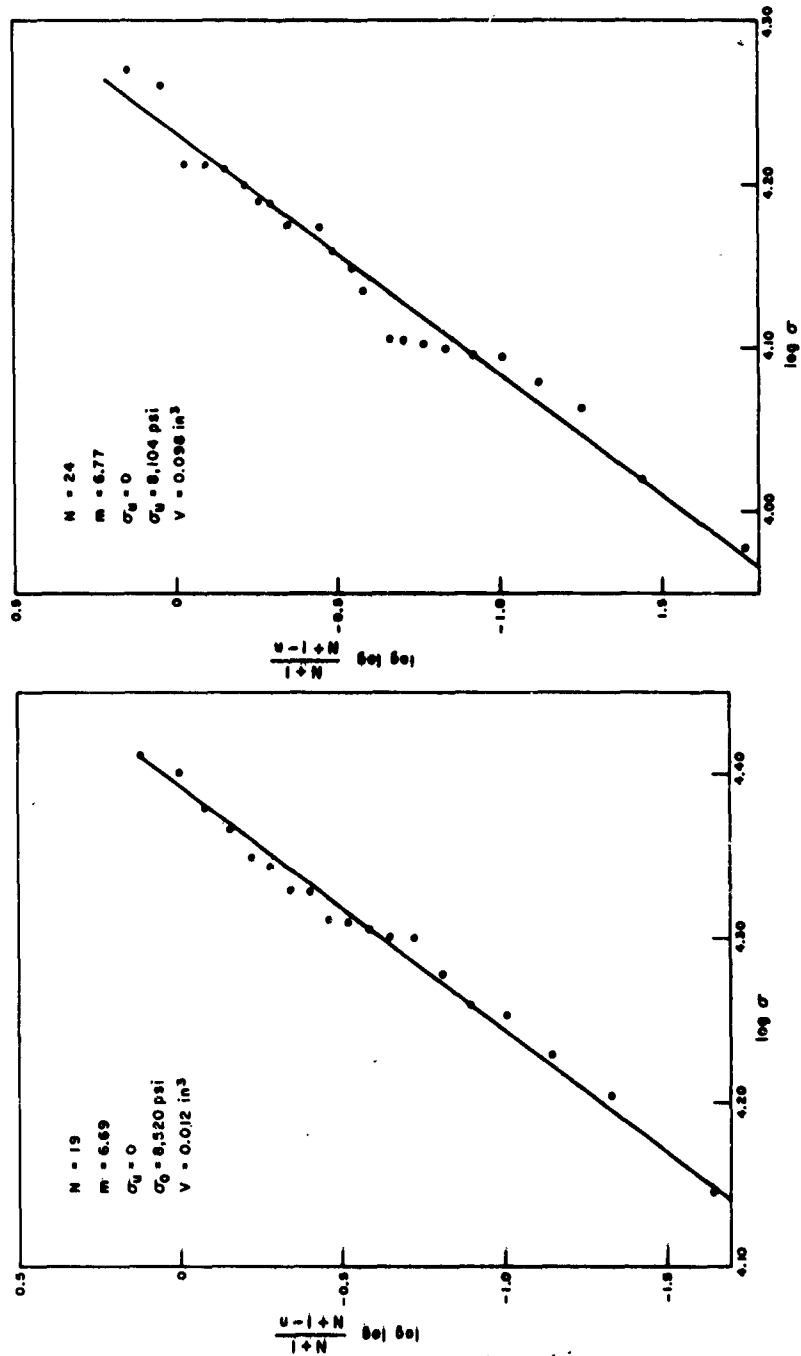
(a) Small Specimens

(b) Large Specimens

Fig. 1-14 GRAPHICAL DETERMINATION OF WEIBULL PARAMETERS,
AS-RECEIVED WESGO AL-995 IN AIR AT 20°C



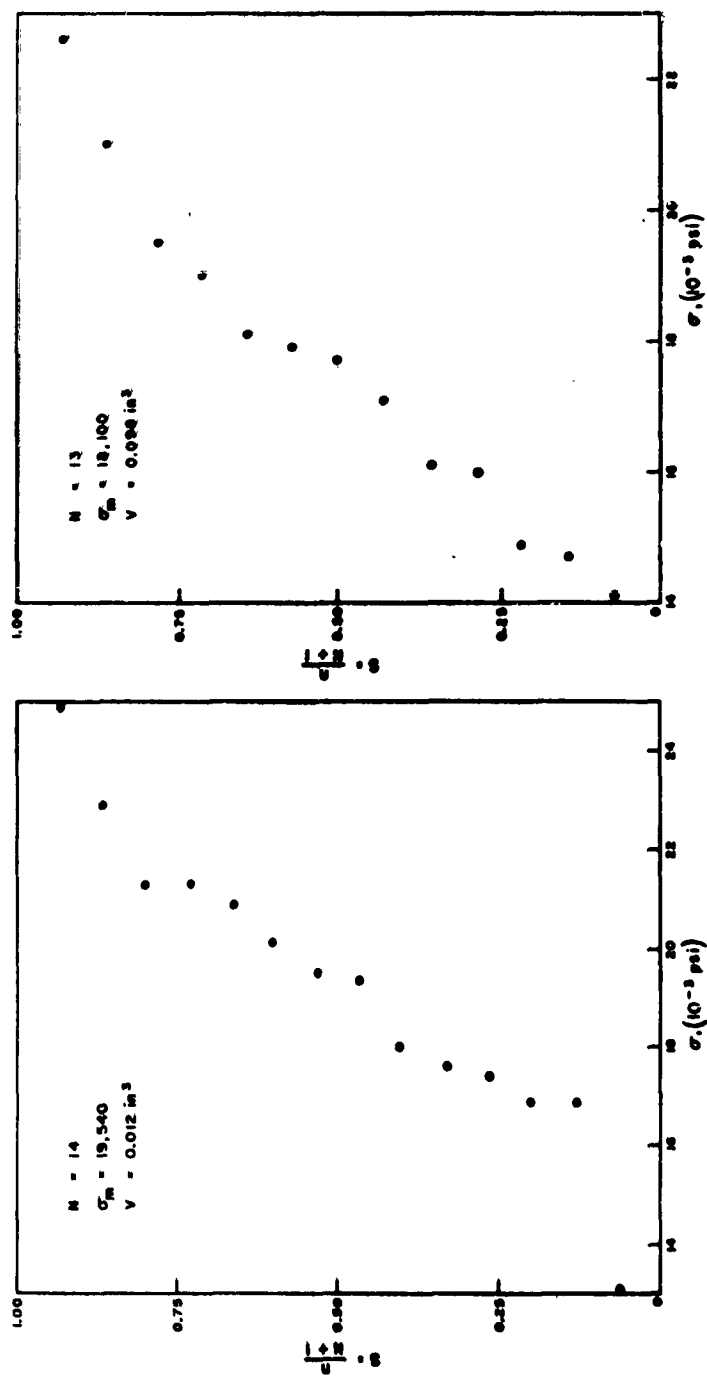
(a) Small Specimens (b) Large Specimens
 Fig. 1-15 GRAPHICAL DETERMINATION OF WEIBULL PARAMETERS,
 LUCALOX IN AIR AT 20°C



This was not the case. The data points were still insufficient to determine the Weibull parameters; the information was too sparse and the dispersion too large. Therefore, only cumulative distribution plots (Fig. 1-17, 1-18 and 1-19) were prepared for this test series and no attempt was made to reduce these data into the graphical presentation required for Weibull plots. While in this regard the results were disappointing, data are significant enough to allow for a credible determination of mean fracture strengths, used subsequently for the study of volumetric effects as predicted by the Weibull theory. Here it should be noted that the curve for the medium-sized, as-received Wesgo specimens is not included, since such information was already presented in Fig. 1-5 and 1-9. Also, no tests at 1000°C were conducted on ground and annealed Wesgo AL-995 for lack of available specimens; hence this information is lacking from the test series shown in Fig. 1-17 to 1-19.

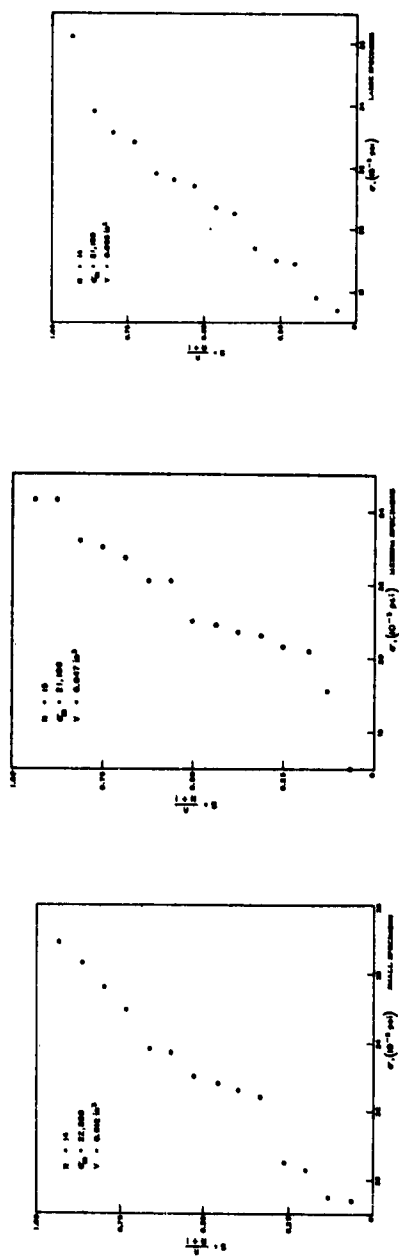
As contrasted to Wesgo AL-995, rather complete experimental work was carried out in the second 1000°C series on the other materials, allowing for the determination of detailed Weibull type plots. The exception was Lucalox, for which the small specimens could not be supplied by the vendor (G. E.), and for which only twelve large specimens were available for this experimental work. These, nonetheless, gave adequate distribution curves and are included in the graphs. The corresponding curves for this series are presented in Fig. 1-20 and 1-21. To reduce the details of presentation, again only the final Weibull plots are presented for this series; also, as stated, data for BeO could not be secured, since this material was supplied in only one volume.

To summarize the extensive data compiled in Fig. 1-14 to 1-21 the significant information derived from the test series on volumetric effects has been compiled in Table 1-II. As can be seen from this table, the Weibull parameters were left off for the cases where the number of experimental points proved insufficient to allow a detailed assessment of material properties



(a) Small Specimens (b) Large Specimens

Fig. 1-17 DISTRIBUTION CURVE, AS-RECEIVED WESGO AL-995 IN AIR AT 1000°C



(a) Small Specimens (b) Medium Specimens (c) Large Specimens

Fig. 1-18 DISTRIBUTION CURVE, GROUND, WESGO AL-995 IN AIR AT 1000°C

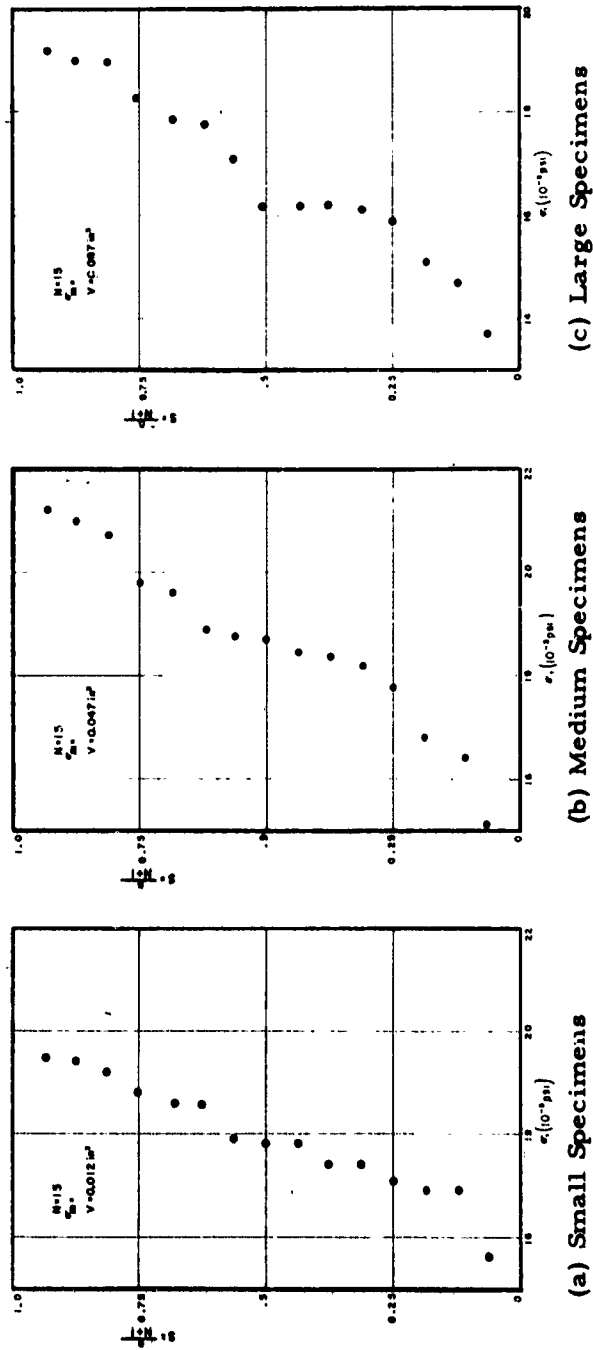


Fig. 1-19 DISTRIBUTION CURVE, ANNEALED WESGO AL-995 IN AIR AT 20°C

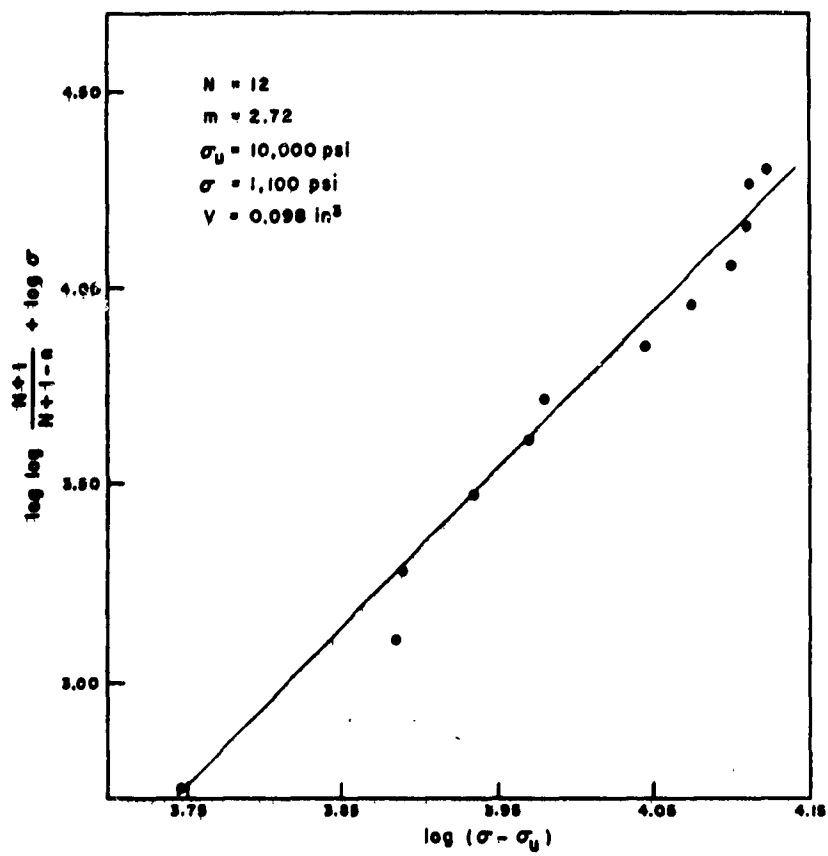
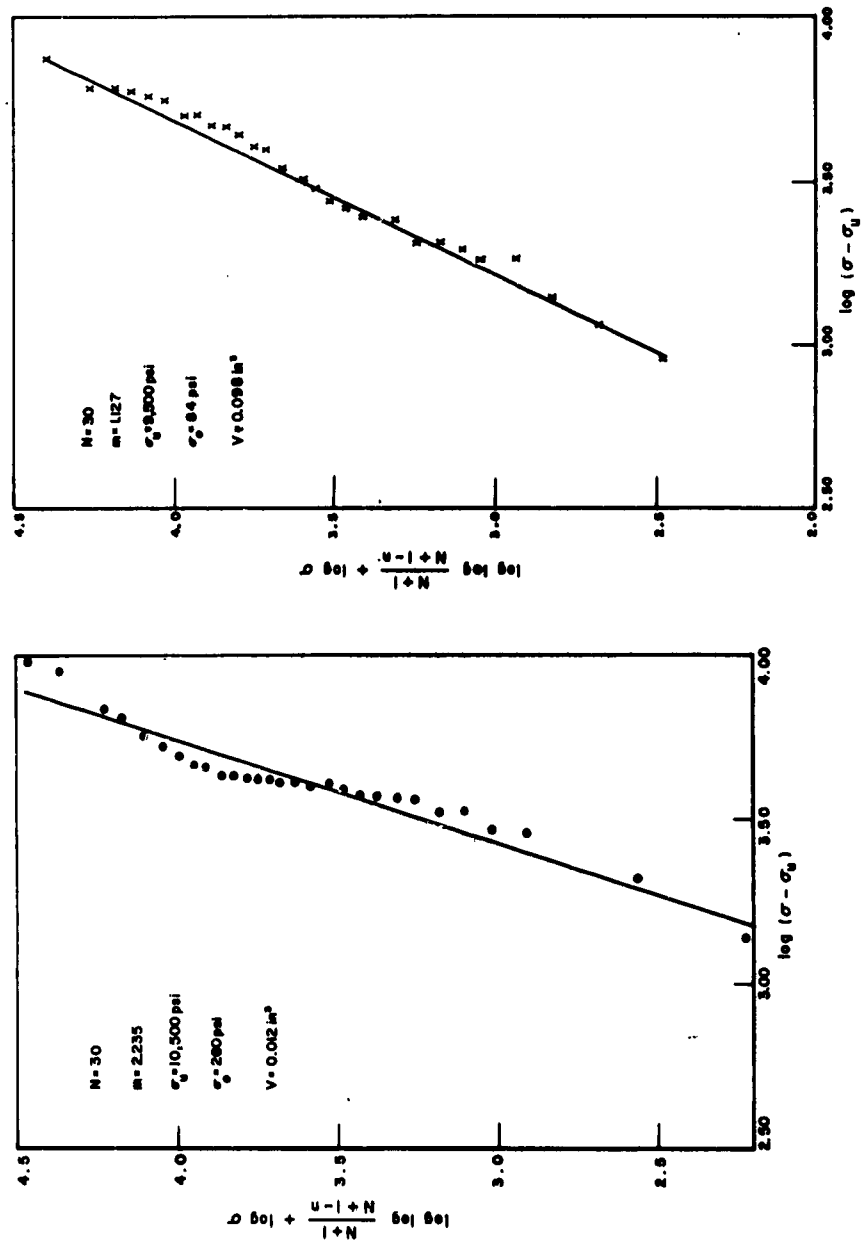


Fig. 1-20 DISTRIBUTION CURVE, LARGE LUCALOX SPECIMENS IN AIR AT 1000°C



(a) Small Specimens (b) Large Specimens

Fig. 1-21 GRAPHICAL DETERMINATION OF WEIBULL PARAMETERS,
ARF MAGNESIUM OXIDE IN AIR AT 1000°C

Table 1-II
SUMMARY, MATERIAL CONSTANTS FROM BEND TESTS OF SPECIMENS IN AIR

(Various Gage Volume)

Material	Temp. (°C)	Surface Treatment	Heat Treatment	Number of Specimens	Gage Volume (in. ³)	Weibull Parameters	Statistical Values				
						Flaw Density Constant, m	Zero Strength (10 ⁻³ psi)	Material Constant (10 ⁻³ psi)	Average Strength (10 ⁻³ psi)	Standard Deviation, s,	Coeff. of Variation, (%)
Wesgo AL-995 Al ₂ O ₃	20	As-received	None	30	0.012	3.70	20.0	1.59	28.8	2.23	7.73
				54	0.047	3.23	10.0	3.24	26.3	1.28	4.87
				25	0.098	11.35	0.0	15.0	27.7	2.54	9.16
		Ground	None	12	0.012	-	10.0	-	28.9	9.50	33.05
				30	0.047	6.10	-	4.37	25.3	3.36	13.30
				19	0.098	-	-	-	23.1	2.03	8.37
	1000	As-received	Annealed at 1700°C	5	0.012	-	-	-	34.6	3.50	10.10
				36	0.047	10.00	0.0	18.86	30.8	3.83	12.42
				5	0.098	-	-	-	27.1	2.5	9.22
		Ground	Annealed at 1700°C	5	0.012	-	-	-	25.6	2.81	11.00
				30	0.047	12.50	0.0	18.41	28.6	2.44	8.53
				4	0.098	-	-	-	27.8	2.75	9.88
20	As-received	None	14	0.012	-	3.60	-	19.5	2.88	14.75	
			20	0.047	-	-	2.17	19.6	2.66	13.59	
			13	0.098	-	-	-	18.1	3.16	17.45	
	Ground	None	14	0.012	-	-	-	22.8	2.27	9.97	
			15	0.047	-	-	-	21.1	1.97	9.32	
			14	0.098	-	-	-	21.1	2.37	11.23	
1000	As-received	Annealed at 1700°C	15	0.012	-	-	-	17.8	1.06	5.96	
			15	0.047	-	-	-	18.7	1.41	7.52	
			15	0.098	-	-	-	16.2	1.55	9.56	
	Ground	None	24	0.012	1.47	17.5	0.18	27.9	4.91	17.58	
			26	0.047	5.05	15.0	4.22	26.5	3.62	13.66	
			10	0.098	4.00	10.0	4.57	22.5	1.77	7.87	
Lucalox Al ₂ O ₃	20	Ground	None	22	0.047	7.75	0.0	12.08	22.2	3.21	
				12	0.098	2.72	10.0	1.10	20.3	2.52	12.43
				19	0.012	6.69	0.0	8.52	20.4	3.08	15.04
	1000	As-received	None	60	0.047	3.25	10.0	0.74	16.6	1.94	11.70
				24	0.098	6.77	0.0	8.10	14.1	2.30	16.32
				30	0.012	2.24	10.5	0.26	15.0	1.76	11.74
1000	As-received	None	49	0.047	5.25	5.0	0.25	14.6	1.38	9.45	
			30	0.098	1.13	9.5	0.09	13.1	1.83	13.99	

(i. e., for the results presented in Fig. 1-17 to 1-19.)

The curves and tables secured from these experiments form the basis of the evaluation of test results. To keep the main purposes of work on this task clearly defined, the treatment of the ensuing section is separated into sub-sections dealing with (1) parametric influences on the strength of ceramic substances, (2) a critical appraisal of the size effect predictions involved in the Weibull theory, and (3) an evaluation of the data derived from tests on BeO which led to interesting conclusions beyond those obtained from the other tests.

5. EVALUATION AND DISCUSSION OF EXPERIMENTAL RESULTS

A. Effect of Parametric Variables on Strength

Table 1-I and Fig. 1-8 to 1-13, upon which it is based, indicate clearly the primary finding of importance, notably that both of the independent Weibull parameters σ_u and m are highly variable with surface condition, heat treatment or testing temperature. Thus, these parameters cannot be considered to be constants at all, as has been often implied in the literature, but must be recognized as fluctuating with the thermal and mechanical history, testing temperature or surface finish applied to the specimen.

The room-temperature Wesgo AL-995 series shows that both grinding and annealing change the values of the Weibull parameters. Specifically, grinding serves to increase the m values, leaving the values of σ_u and σ_o relatively unaffected. Thus, from the theoretical considerations discussed in Section 3, the increased m value should result in lower strengths for the ground material. This is confirmed by the mean strength values displayed in Table 1-I, where the as-received specimens are seen to have somewhat higher σ_m values than their ground counterparts.

Annealing, on the other hand, induces a significant rise in the value of m , accompanied by an equally significant drop in σ_u which, in fact, invariably becomes zero in the annealed condition. The former effect is clearly indicative of a type of "flaw-healing" effect, since a higher m value is characteristic of a greater uniformity of flaw severity and distribution. In this regard, annealing might be assumed to act in the direction of eliminating the "worst" flaws interspersed comparatively infrequently in the as-received material, either through the mechanism of blunting the tips of atomically sharp cracks, or by means of removing a residual stress pattern from the material which is conducive to crack initiation in a narrow (probably surface) layer of the material.

At the annealing temperature of 1700°C employed in the present treatment, the latter mechanism appears to have more validity. As has been shown by the work conducted on Task 4⁽¹⁻²⁾, at 1600°C there is ample evidence of a pseudo-plastic flow in Al_2O_3 , as measured by the gross manifestations of a stress-strain curve. However, this apparent plasticity is the result of boundary layer viscosity while the grains themselves undergo only a rigid translation and rotation. Therefore, creep and the accompanying self-diffusion, which must lie at the base of any crack blunting mechanism, are unlikely to occur at these temperatures, unless the few worst cracks accounting for the low values of m in the as-received material and the resulting high variability of flaw dispersion, are all situated in an intergranular fashion. In the latter case, the cracks must all take the form of porosity between grains and self-diffusion, accompanied by crack blunting tendencies, becomes a valid mechanism, since grain boundary viscosity is detectable in this material at temperatures as low as 1400°C⁽¹⁻²⁾. Nonetheless pending proof that all the worst cracks are associated with interstitial porosity, this mechanism must be regarded with some reservation in attempting to account for the "flaw healing" effect accompanying annealing.

The removal of residual stresses is a more plausible hypothesis for this case. Such a stress system, if it exists, must consist of a high order of stress in the surface layer, accompanied by low stress levels of the opposite sign throughout the inner bulk of the material. Stress redistribution and relaxation is manifest at the earliest sign of gross plasticity existing in the material; in Al_2O_3 , the corresponding temperature at which this phenomenon begins to exhibit itself, might be put at about 1100°C on the basis the precipitous rise in the internal friction value of polycrystalline Al_2O_3 of this temperature, as obtained from studies conducted on Task 5. Once stress relaxation occurs, it will equally benefit all existing cracks, regardless of whether these take the form of surface scratches or intergranular porosity. Thus the flaw at the surface, whose effectiveness is enhanced by a high stress operating in a thin layer, lose their criticality upon removal of the residual stress pattern due to annealing. The consequence is that the flaw dispersion becomes more uniform, and the m value increases.

There is some evidence to support the latter argument by noting that grinding dropped the mean strength of the Wesgo AL-995 at 20°C for both the as-received and annealed condition. Since grinding can affect only the flaw density and severity existing at the surface, the lowering of strength incurred by grinding is strictly a surface-layer induced phenomenon. If this observation is generalized to the statement that the fracture of ceramic substances is always a surface-controlled phenomenon, the stress-relief mechanism acting to remove high residual stresses in a thin-surface layer by means of annealing takes on added validity.

It is interesting to note that, other things being equal, the increase in m and decrease in σ_u accompanying annealing should be expected to lower the mean strength. However, annealing is also accompanied by a pronounced increase in the value of σ_o . This factor, in turn, contributes to a sharp increase in

m to an extent, in fact, that is sufficient to outbalance the combined contributions of m and σ_u . The net result is that the annealed material shows a substantially higher (by 13 to 17 percent) mean fracture strength than the comparable as-received material.

The effect of the test temperature was studied using three materials, Wesgo AL-995, Lucalox and MgO using (Table 1-II) and two temperatures, room 20°C and 1000°C. The examination of these results permits the following comparisons.

The flaw density exponent m increases in each case as the temperature is raised, specifically from 3.23 to 3.60 for Wesgo AL-995, 5.05 to 7.75 for Lucalox Al_2O_3 and 3.25 to 5.25 for MgO. This increase, while significant, however, is far not as pronounced as that associated with annealing. The trend for both on the other hand, is similar, and could be ascribed to identical mechanisms, i. e. a diminution of the effectiveness of "worst" flaws extant in a shallow surface layer, by dint of a reduction of high level residual stresses locked up near the surface due to fabrication. The result is a leveling-out effect of the volumetric effectiveness of flaws, leading to a more uniform flaw dispersion and, hence, to a higher value. The testing temperature of 1000°C is far less effective in accomplishing this than the anneal treatment of 1700°C for 3 hr; it is likely that a test temperature of 1000°C induces only a modest redistribution of residual stresses, whereas the 1700°C anneal is effective in a nearly complete elimination of locked-up stresses. Hence, the changes in m values are correspondingly different.

In regard to the zero strength, σ_u remains virtually unaffected in Wesgo AL-995 by an increase in testing temperature from 20 to 1000°C. In Lucalox and MgO, however, the result is a sharp drop in σ_u at the higher test temperature.

As might be expected, these results taken together imply a significant decrease of mean strength at the higher temperature, based purely upon the theoretical considerations. This condition, in fact, is observed. The mean strength drops as the testing temperature is increased from 20 to 1000°C in all instances: by 25.5 percent for Wesgo AL-995 is, in fact, so pronounced that at 1000°C it becomes distinctively weaker than Lucalox, even though at room temperature the two materials have nearly identical average strengths.

In examining the parametric Weibull values characterizing these materials, it is found that the flaw-density exponents descriptive of the different ceramic oxides are grouped quite closely together, if care is taken to compare strictly identical conditions. Thus, for as-received unannealed materials, the m values range over the extremely narrow range of 3.23 for Wesgo AL-995 and 3.25 for MgO at room temperature. For ground material at 20°C, the results are 6.10 for Wesgo AL-995 5.05 for Lucalox and 7.35 for BeO. Likewise, at 1000°C, the results are: 3.60 and 5.25 for as-received materials, and 7.75 for the only ground material (Lucalox). As already seen, annealed Wesgo AL-995 at 20°C has m values ranging between 10.0 to 12.5.

One is almost tempted to generalize from these observations that for ceramic oxides fabricated in conformity with practices applicable to the materials studied here, the flaw density exponents can be characterized by:

- $m \approx 3.25$ for as-received material at room temperature
- $m \approx 6.0$ for ground material at room temperature
- $m \approx 11.0$ for annealed material at room temperature
- $m \approx 4.5$ for as-received material at 1000°C
- $m \approx 8.0$ for ground material at 1000°C

Naturally, any broad generalizations of this nature must be heavily tempered by an appreciation for the enormous variability of fabrication practices (and resulting material properties) possible with these materials, the comparative scarcity of data accumulated to date, and the relative freedom of choice with which Weibull parameters of a rather broad range can be fitted to a given set of data.

In the latter aspect, it is well to recall that Anthony and Mistretta⁽¹⁻¹⁵⁾ working with ATJ graphite derived m values of 7.5, 7.3, 14.5 and 7.8 at temperatures of 70, 2000, 2500 and 2750°F, respectively. While their work is subject to criticism because the broad generalization that $\sigma_u = 0$ for all cases is used, their finding of a nearly two-fold variation of m over the comparatively narrow temperature range of 2000 to 2750°F is remarkable. Unless ascribable to the sweeping simplifications or to an unknown mechanism operative in ATJ graphite at 2500°F, the results can only show the extreme variability that might be experienced in determining Weibull parameters even under controlled test conditions.

Beyond these clearcut conclusions, there is no apparent way in which either the temperature or the nature of the material affects the parameters σ_u or σ_o . Perhaps the only comment of interest that can be made is that the zero strength, if it exists, is nearly always less than 50 percent of the average strength. Any design, therefore, that is based on an allowable stress exceeding one-half of the average strength of ceramic materials, as determined from appropriately sized test specimens, is likely to incur at least some risk of failure of the completed structure under actual service conditions.

B. The Effect of Size on Strength

Experiments conducted to evaluate the effect of specimen size upon the specimen strength are summarized in Table 1-II, which is tabulated from Fig. 1-5, 1-9 and 1-14 to 1-21. As stated, no attempt was made to evaluate Weibull parameters where less than 20 specimens were tested*. In this connection it is well to recall that in excess of 50 specimens are generally required for a reliable determination of Weibull parameters; only three sets of experiments (as-received Wesgo AL-995 tested at 20°C and MgO tested both at 20°C and 1000°C, all for the medium specimen size) out of the total of 32 sets completed in this series satisfies this stipulation. Hence, the apparent values of the Weibull parameters derived from these experiments must be regarded with serious reservations and treated as approximate values only.

The test series itself had two primary purposes: (1) an examination of whether the Weibull parameters themselves were subject to variations with changes in specimen size, and (2) to examine the correctness of the Weibull theory regarding the effect of size upon the mean fracture strength of the structural piece.

In regard to the first consideration, the Weibull theory plainly predicts that, all other considerations remaining identical, the basic Weibull parameters (σ_u , m , σ_o) characterizing the material should not vary with the specimen size adopted for the experiments. This becomes obvious from the second of Eq. 1-4, where $\log V$ occurs merely as a numerical constant defining the value of $\log B$; it is further also evident from the description of the method of plotting the test results, as described in Section 3.

* Exceptions to this statement are large specimens ($V = 0.098 \text{ cu in.}$) of Mucalox at both test temperatures. Despite of a mere 10 and 12 specimens tested, the data points seemed consistent enough to allow for the determination of the apparent values of Weibull parameters.

A quick glance at Table 1-II readily shows that this postulate of the Weibull theory is contradicted by the results of the current task. Where complete test results exist, (e. g. for as-received Wesgo Al-995 at 20°C, Lucalox and MgO both at 20°C and 1000°C), all three Weibull parameters are seen to fluctuate over a broad range of values; moreover there is no consistent trend in the variation of either σ_u , m or σ_o with specimen size. This, in fact, points to the observation that a completely different set of Weibull parameters could have been adopted to characterize material behavior, depending on whether one chooses to accept the results obtained from the test series conducted on the small (0.012 cu in.) medium (0.047 cu in.) or large (0.098 cu in.) gage volume specimens.

These deductions, nonetheless, should not be taken as a negation of the validity of the Weibull theory, for two reasons. First, as has been already pointed out, the number of experimental data points are far too few in the overwhelming majority of conditions tested to allow for a credible determination of Weibull parameters. Secondly, the different specimen sizes used in these experiments were prepared in separate batches using, by force of necessity, different dies. Even though care was taken that the superficial characterizations (grain size and apparent density) coincided for the different gage volume specimens, it is an extremely strong probability that the different starting batches, dies, and possibly even the details of fabrication methods employed, resulted in different material characteristics for the various gage volume specimens utilized in this series. This argument is supported by Task 3 findings where identical gage volume (0.047 cu in) Wesgo AL-995 specimens, differing only in the shape of the cross section (and thus in the dies employed for their fabrication), yielded widely varying results for their Weibull parameters, despite of a sufficiently large number of specimens employed in each test series.

The second aspect of this test series, namely the validity of the Weibull theory's prediction of the effect of size upon the mean fracture strength, received much more adequate evaluation. This is for reasons that a set of eight to ten tests is generally regarded to be a statistically sufficiently large sample of population to allow for a credible evaluation of the mean value, regardless of the dispersion involved in the test results. As can be seen from Table 1-II, only in 4 cases out of 32 were less test specimens than this available for the calculation of the mean strength. For this purpose, therefore, the experiments reported in Table 1-II are regarded as having yielded fully significant results.

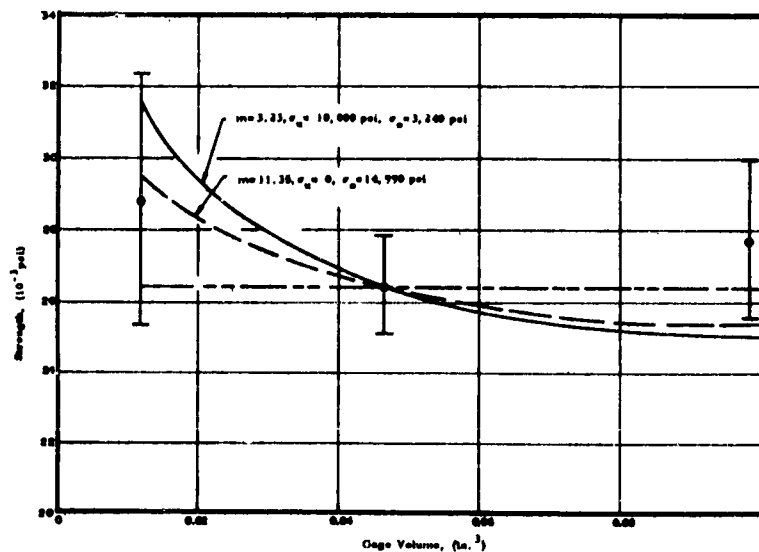
The theoretical predictions of volume upon mean strength were evaluated by using Eq. 1-11 for cases where $\sigma_u \neq 0$, and Eq. 1-12 for $\sigma_u = 0$ *. It should be recalled that in these equations V is dimensionless; hence, the equations will serve to predict the mean fracture strength σ_2 for any arbitrarily chosen value of specimen volume V_2 , provided the strength σ_1 corresponding to a basic specimen volume V_1 is known. In order to be consistent, the mean fracture strength determined for the median sized specimens ($V_1 = 0.047$ cu in.) was used to define the value of σ_1 , with σ_2 then calculated by substituting alternately $V_2 = 0.012$ cu in. or $V_2 = 0.098$ cu in. for the small or large specimen shapes, respectively. This choice was further recommended by the fact that the largest number of test points, leading to the most reliable determination of mean strength, existed invariably for the medium size specimens.

* It should be noted that Eq. 1-11 and 1-12 are rigorously valid only only for pure tension; no closed-form solution can be obtained for bending with the theory used. However, numerical calculations confirmed that these equations give very satisfactory predictions when used as approximate expressions for the case of pure bending, as well.

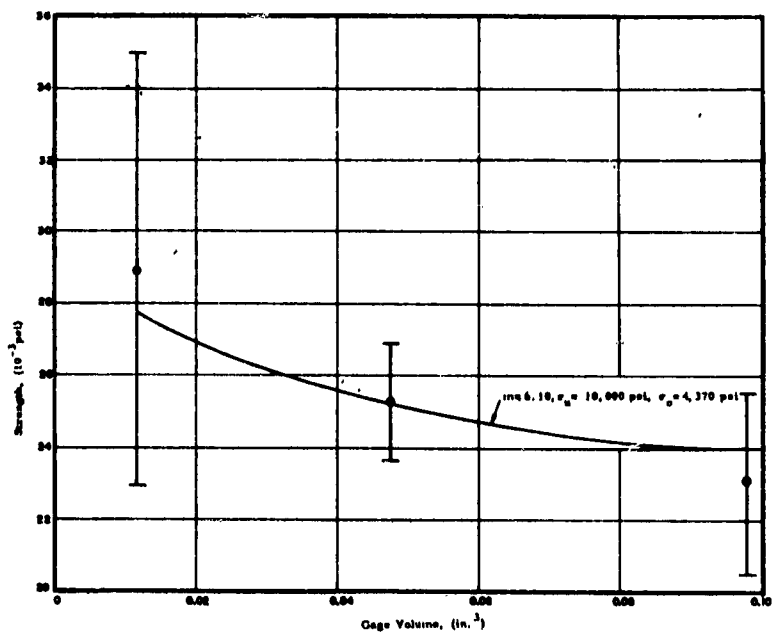
Similarly for greatest credibility, the Weibull parameters σ_u , m , σ_0 entering Eq. 1-11 or 1-12 were chosen to correspond to the median gage volume specimens. In addition, for the one case of the as-received Wesgo AL-995 tested at room temperature, calculations were also carried out using the Weibull parameters corresponding to the large specimens ($V = 0.098$ cu in.), since these were substantially different from those obtained for the other two gage volumes.

The results are presented in Fig. 1-22 to 1-24, inclusive. In these figures the results of theoretical calculations are shown in full lines, while the experimental data corresponding to the discreet values of $V = 0.012$, 0.047 and 0.098 cu in. are presented by the overall range of variations as well as the calculated mean value. It should be noted that the theoretical curves approach σ_u asymptotically as $V \rightarrow \infty$. Also, as mentioned, two theoretical curves are presented in Fig. 1-22(a) corresponding to the Weibull parameters of the medium and large specimen volumes, respectively.

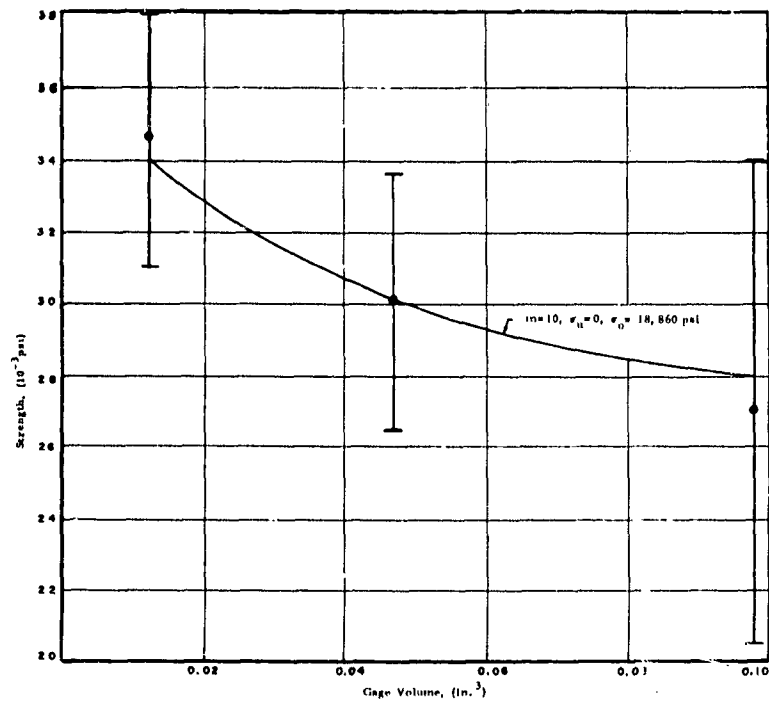
In general, the agreement between theory and experiments is very satisfactory. An almost perfect prediction is recorded in Fig. 1-22(b) and (c), 1-23(b) and 1-24(a). In most other instances the theoretical curve falls within the range of variation of the experimental results, the exceptions to this statement being presented by the small-sized specimens of Fig. 1-22(d) (4 tests only) and the large volume specimens of Fig. 1-23(a) (10 tests only). As a matter of general observations, therefore, it can be stated that these tests confirm the validity of the Weibull theory's predictions, insofar as the effect of specimen (or structural) volume upon mean fracture strength is concerned.



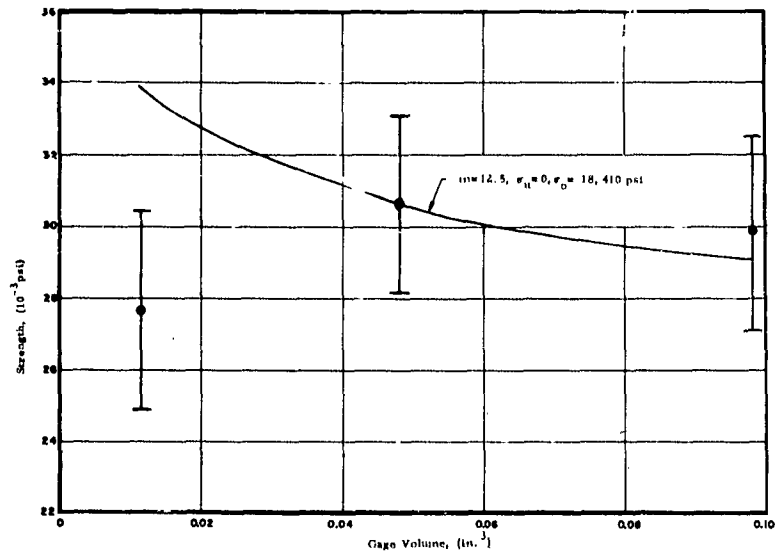
(a) As-Received



(b) Ground

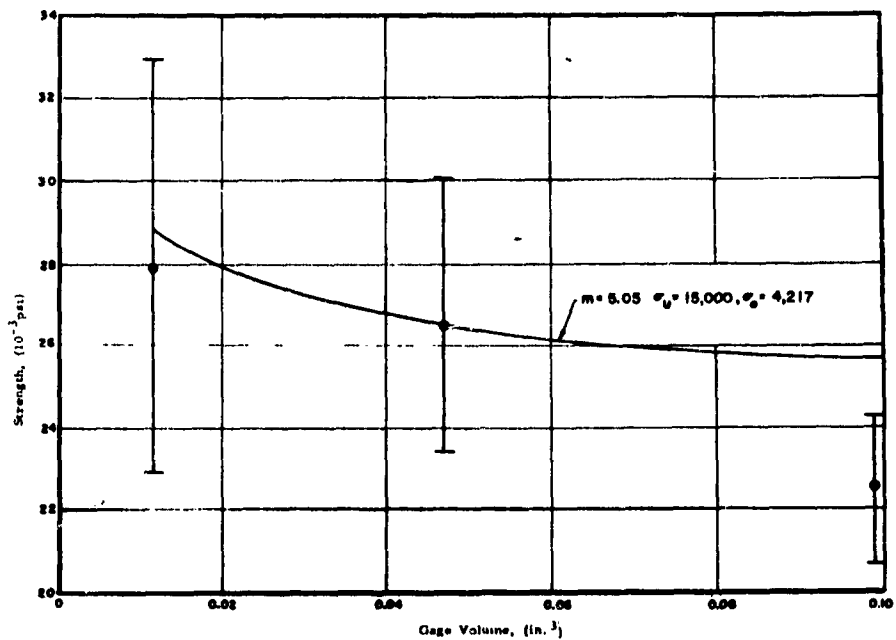


(c) Annealed

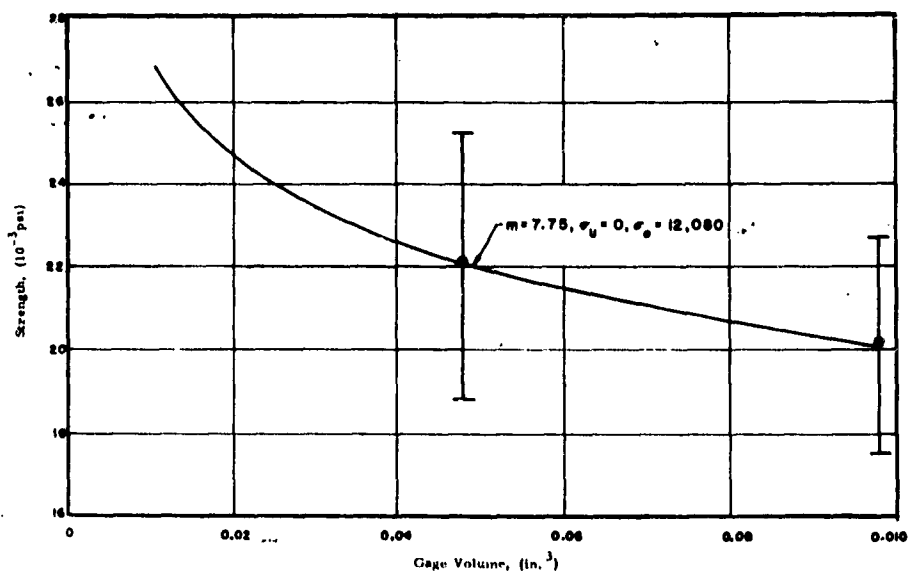


(d) Ground and Annealed

Fig. 1-22 COMPARISON OF THEORY AND EXPERIMENTS FOR SIZE EFFECTS IN WESGO AL-995 IN AIR AT 20°C

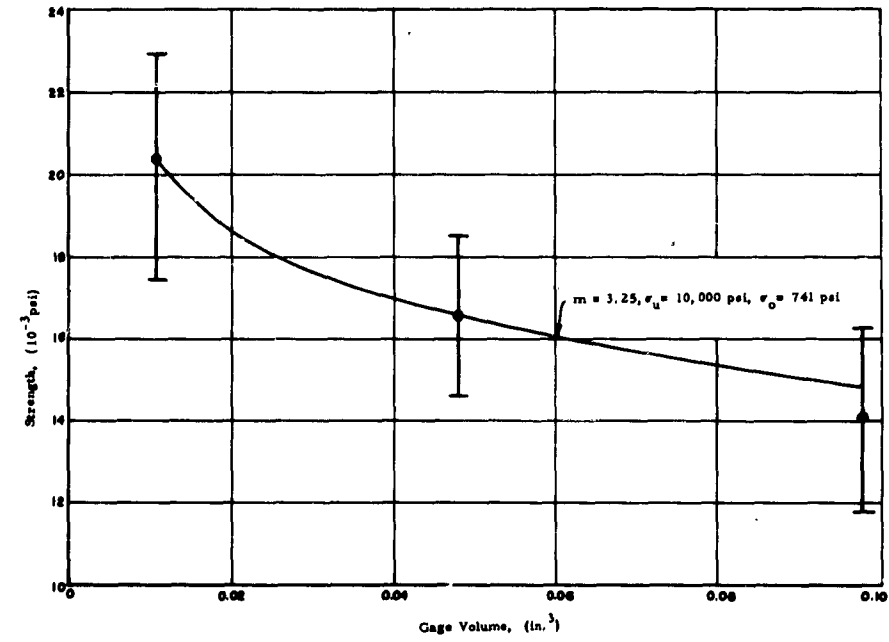


(a) in air at 20°C

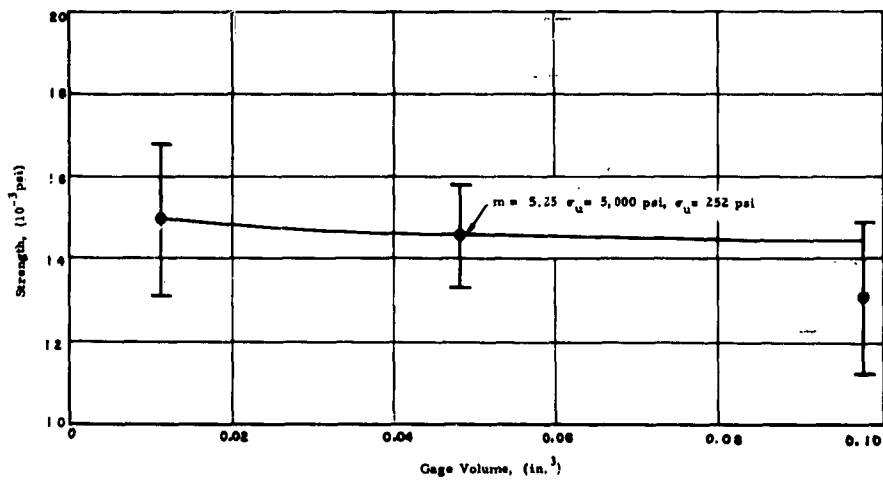


(b) in air at 1000°C

Fig. 1-23 COMPARISON OF THEORY AND EXPERIMENTS FOR SIZE EFFECTS IN LUCALOX



(b) in air at 1000°C



(a) in air at 20°C

Fig. 1-24 COMPARISON OF THEORY AND EXPERIMENTS FOR SIZE EFFECTS IN ARF MAGNESIUM OXIDE

C. The Beryllium Oxide Test Series

The experimental work conducted on the BeO specimens deserves special consideration for two reasons. First the specimens were not supplied according to specifications; neither volumetric variation, nor different grain sizes were rendered available to us for experimental work on BeO. This, however, enabled us to concentrate all of the effort on a searching study of the variability of predictions of material parameters, as derived from the Weibull theory, by testing all of the specimens under a single environmental condition: 20°C in air.

As mentioned, the BeO specimens were of two configurations: 3/16 by 1/3-in. and 1/4 by 1/4-in. in cross section, the latter coinciding with the medium specimen shape used in the main test series. The volume subjected to maximum stresses was the same for both specimen shapes. Fifty specimens each of the 1/4 by 1/4-in. and 3/16 by 1/3-in. specimens were tested for rupture strength, the latter utilized both in the edge-wise and flat-wise condition. Thus, a total of 150 tests were performed, in which the only variable was the stress gradient existing in the specimen; the test results, analyzed from a different viewpoint, are also reported in Task 3. As far as can be ascertained, the 100 specimens of 3/16 by 1/3-in. cross section came from a single batch; the 1/4 by 1/4-in. specimens were fabricated in a different batch.

The cumulative distribution functions (c. d. f.) for the three groups are shown in Fig. 1-25. The average fracture strengths for the 3/16 by 1/3-in. groups were 15,650 and 15,392 psi, respectively; that for the 1/4 by 1/4-in specimen was found to be 14,455 psi. As can be seen from Fig. 1-25, the distributions curves for the 3/16 by 1/3-in. specimens coincide very closely; however, the specimens having the square cross section produce a different distribution curve, particularly at the lower end of the strength values.

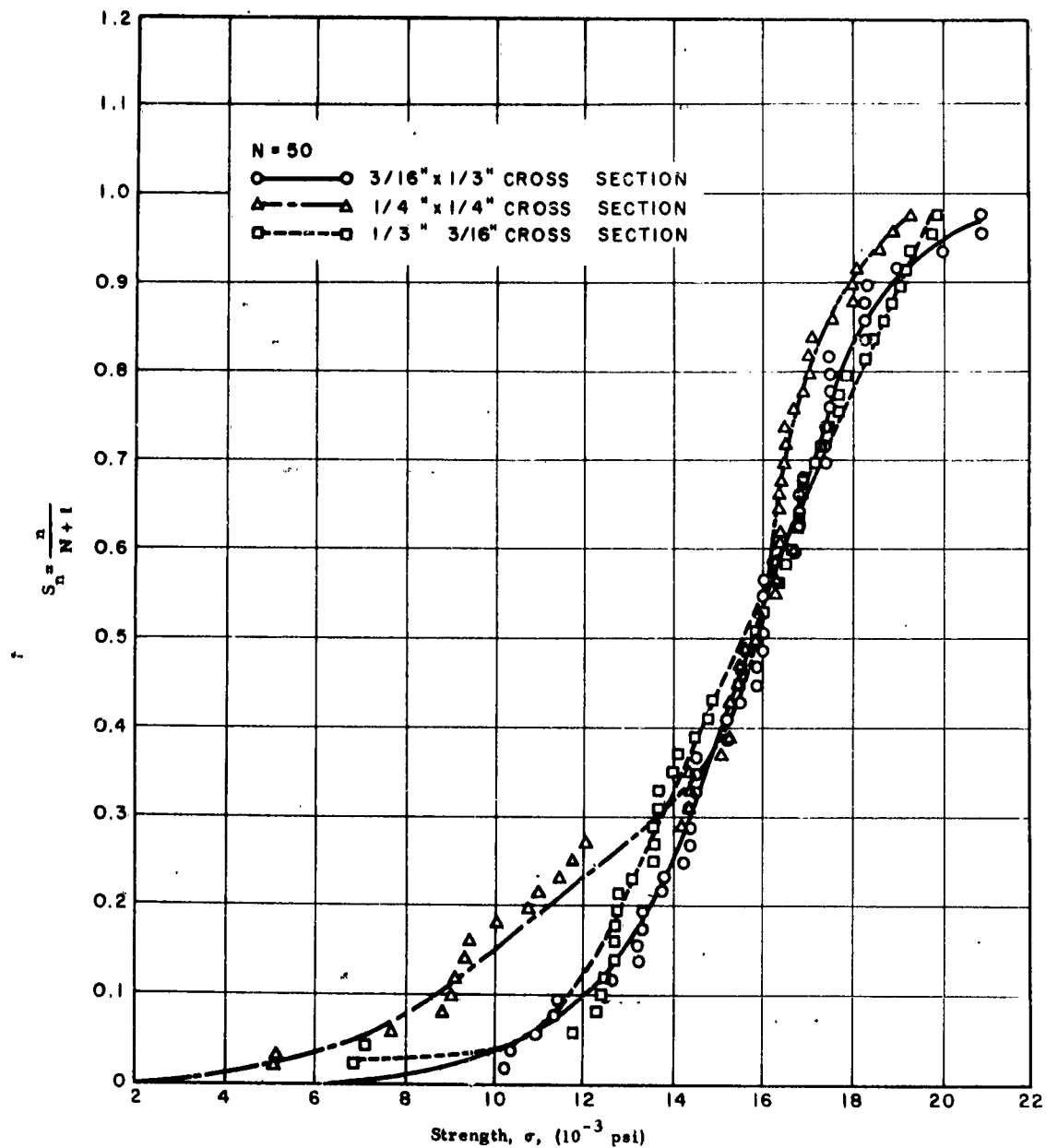


Fig. 1-25 CUMULATIVE DISTRIBUTION CURVES, THREE BERYLLIUM OXIDE SPECIMEN GROUPS OF THE SAME VOLUME IN AIR AT ROOM TEMPERATURE

The customary log-log plot of these distribution curves, based initially on the assumption that $\sigma_u = 0$, is presented in Fig. 1-26. It can be seen that the rectangular specimen shapes produce straight lines of slightly varying shapes. However, the square cross section specimens yield a curve which is concave upward which, as has been mentioned before, cannot yield a physically meaningful (non-negative) value of σ_u , regardless of the mathematical or graphical manipulations attempted. Weibull⁽¹⁻⁴⁾ terms this behavior as being that of a discontinuous anisotropic material; if the test points can be connected by two (or more) intersecting straight lines, a composite Weibull distribution would result, each straight segment characterizing the operation of a different failure mechanism.

An interesting change in the character of the data points results, however, when all 150 data points are lumped together to give a single distribution curve. This is shown in Fig. 1-27, and results in a smooth curve only slightly skewed toward the lower values. The log-log plot of this probability density curve, presented in Fig. 1-28, is still concave upward, signifying a discontinuous anisotropic material, for which no single physically meaningful value of σ_u exists. However, if the 10 lowest data points, contributing in the principal degree to the observed skewness, are dropped, and the remaining 140 data points are lumped in groups of about 7 to produce 19 unit probabilities (done merely for sake of convenience of plotting and presentation), the resulting c. d. f., shown in Fig. 1-29, is almost gaussian. Its log-log plot exhibited in Fig. 1-30, now produces a straight line for the assumption of $\sigma_u = 0$, and can be solved for the Weibull parameters characterizing this material. The m value of 7.35 so determined coincides the rectangular cross section groups determined in the log-log of Fig. 1-26. This is not altogether surprising, since 8 of the 10 data points dropped off at the skewed low-strength tail of the curve corresponded to the square specimen shapes, so that 98 of the remaining 140 data points originated from the rectangular specimen shapes.

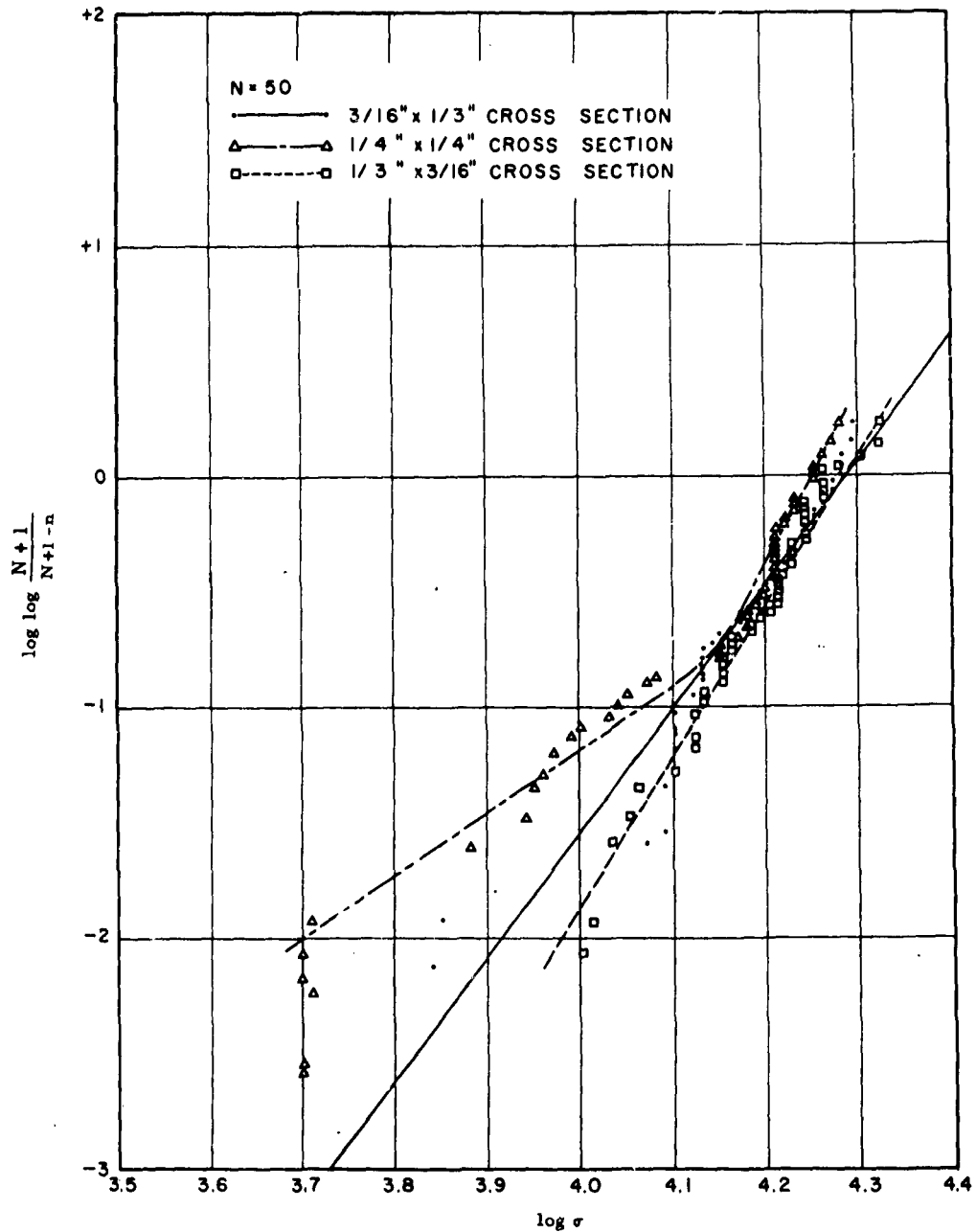


Fig. 1-26 GRAPHICAL DETERMINATION OF WEIBULL PARAMETERS,
 THREE BERYLLIUM OXIDE SPECIMEN GROUPS OF THE
 SAME VOLUME IN AIR AT ROOM TEMPERATURE

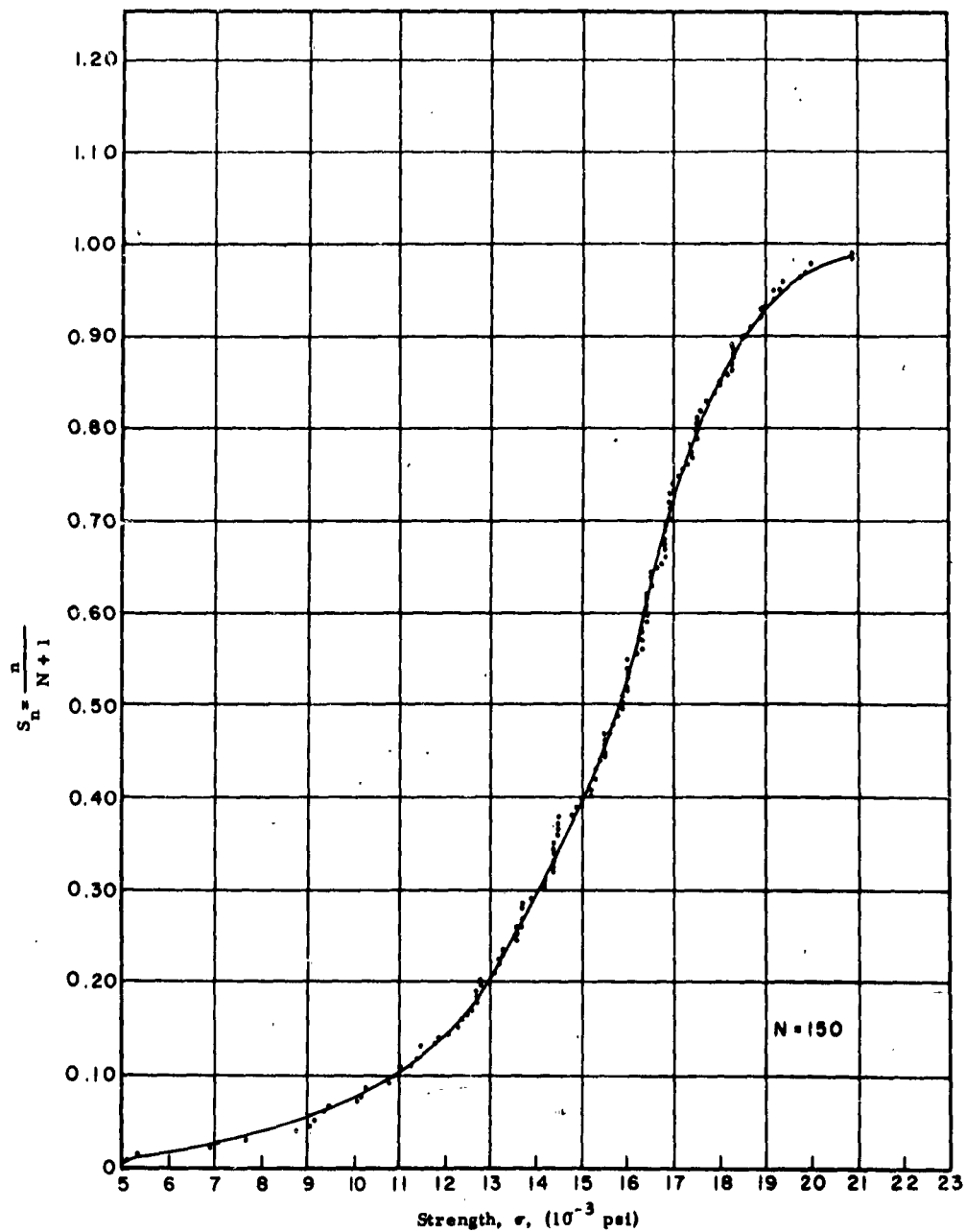


Fig. 1-27 COMBINED CUMULATIVE DISTRIBUTION CURVE, ALL BERYLLIUM OXIDE IN AIR AT 20°C

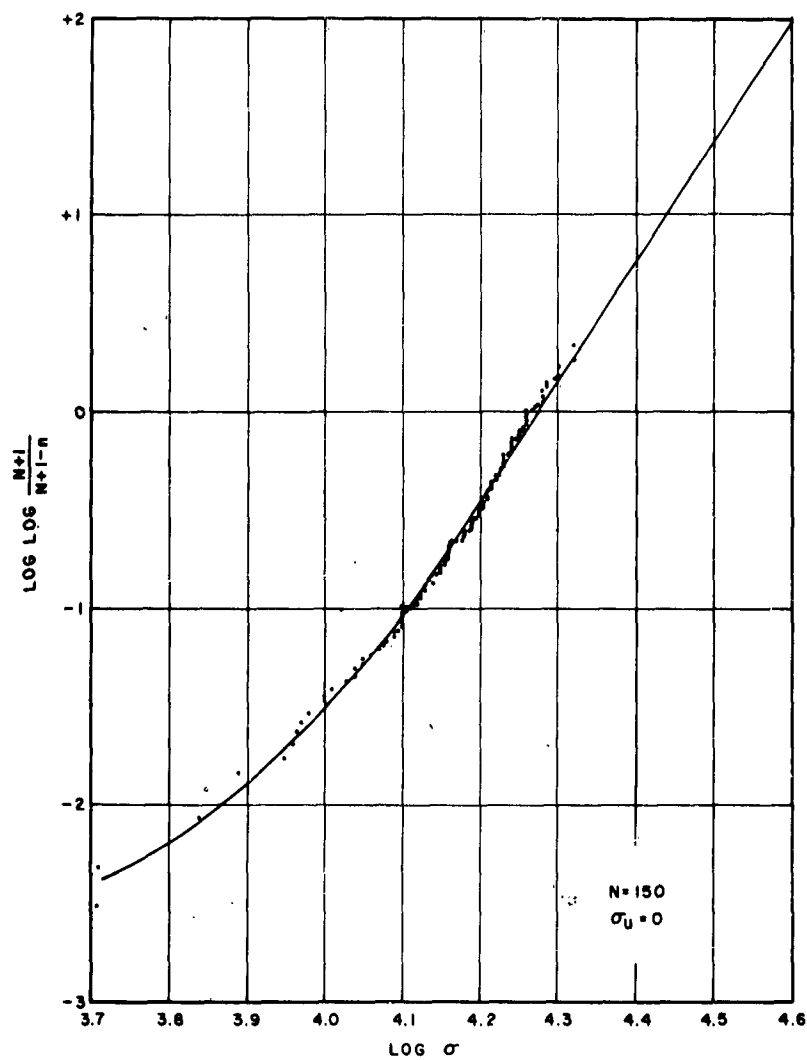


Fig. 1-28 GRAPHICAL DETERMINATION OF WEIBULL PARAMETERS,
 ALL BERYLLIUM OXIDE SPECIMENS IN AIR AT 20°C

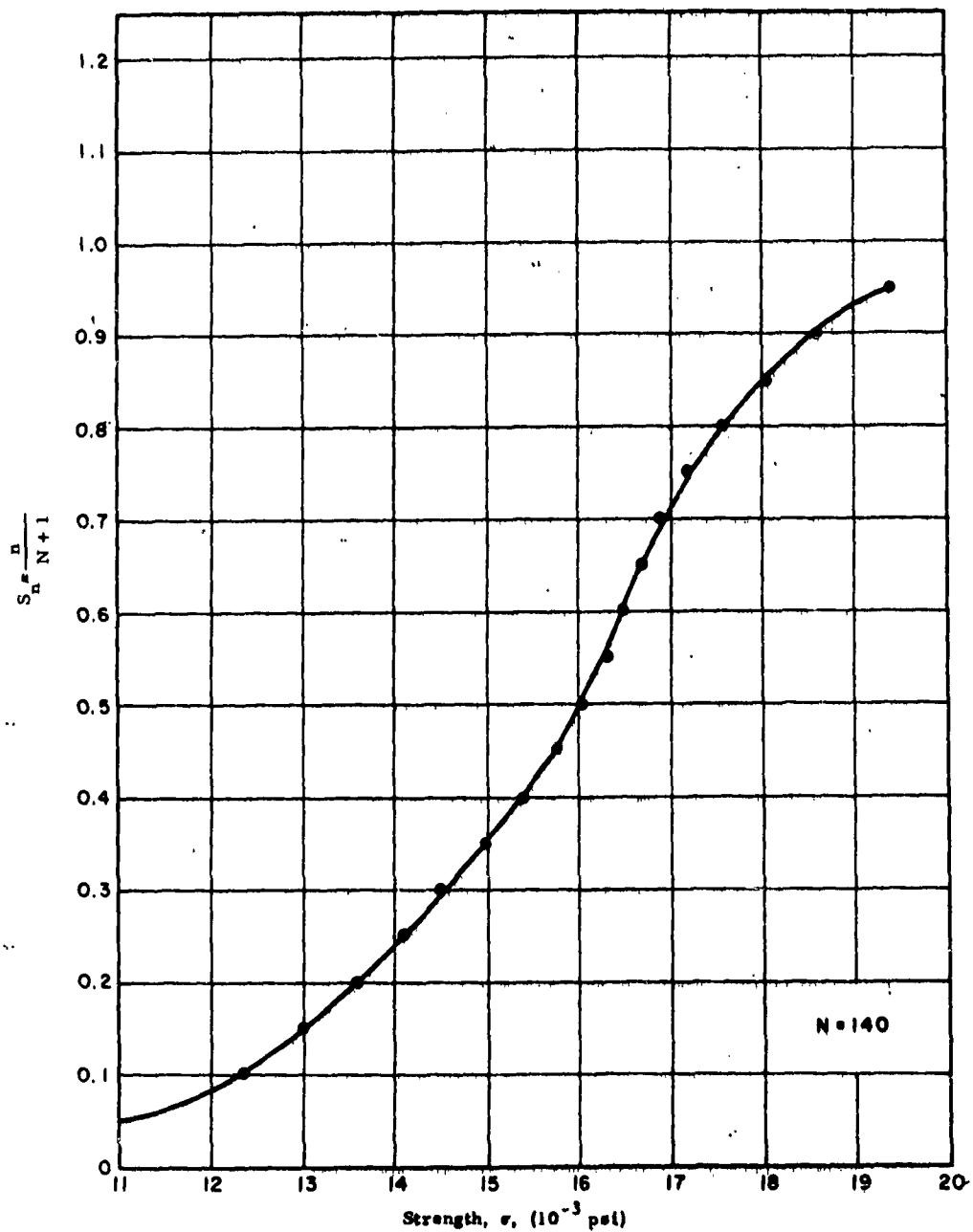


Fig. 1-29 COMBINED CUMULATIVE DISTRIBUTION CURVE. TRUNCATED SERIES OF ALL BERYLLIUM OXIDE SPECIMENS IN AIR AT 20°C

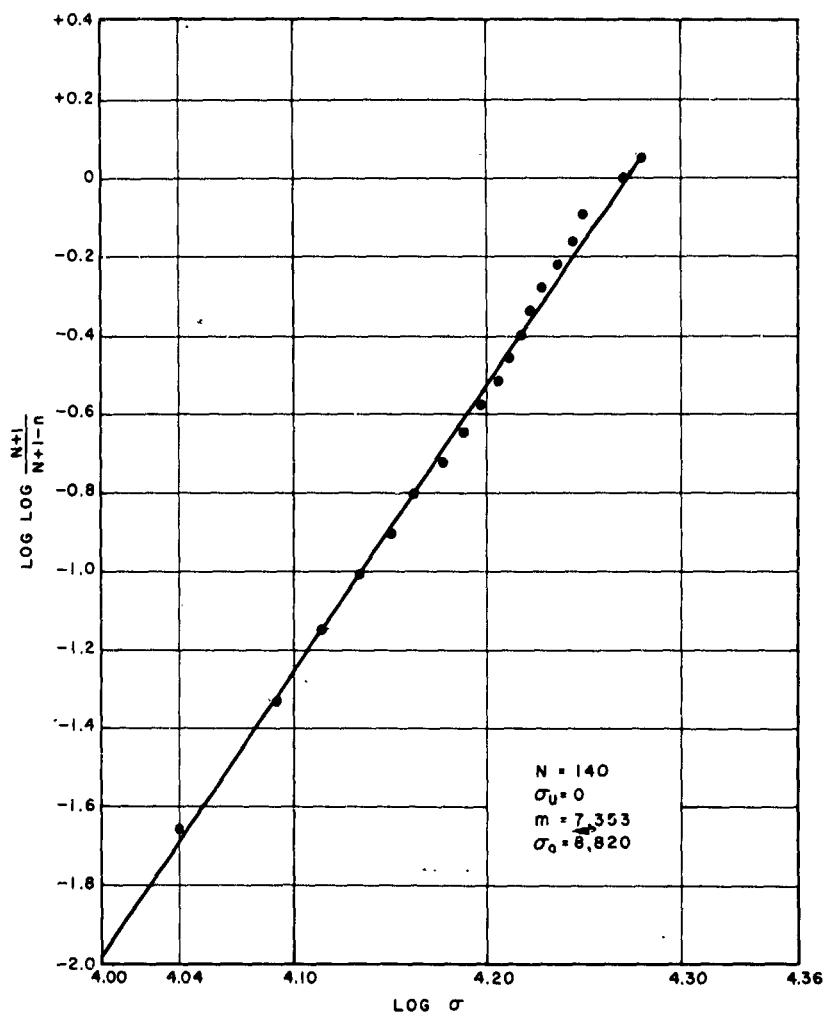


Fig. 1-30 GRAPHICAL DETERMINATION OF WEIBULL PARAMETERS, TRUNCATED SERIES OF ALL BERYLLIUM OXIDE SPECIMENS IN AIR AT 20°C

The manner of data manipulation and presentation previously discussed is very instructive, since it shows that large specimen populations of the same material, consisting of 50 units each with very similar average rupture strengths, can produce substantially differing material parameters. Moreover, when lumped together into a single population as large as 150 units, the character of the resulting c. d. f. can be radically changed by suppressing less than 10 percent of the population, even though, in this case, the population suppression was not of a random character.

6. CONCLUSION

The work described here was aimed at a thorough study of the probabilistic aspects of the fracture strengths of inorganic ceramic oxides, with particular reference to the applicability of the modified Weibull probability density function for describing the fracture characteristics of these brittle materials, and to derive values of the appropriate material parameters as influenced by test temperature, heat treatment, surface preparation and test atmosphere. An added part of the investigation was aimed at evaluating the predictions of the Weibull theory regarding the effect of structural size upon the average fracture strength of the object tested.

Dogbone-shaped specimens of three effective volumes were developed solely for purposes of these experiments. They were tested under conditions of four-point loading to develop pure bending in the critical gage section of the specimens. Experiments were conducted on four ceramic oxides, represented by Wesgo and Lucalox Al_2O_3 , ARF MgO and Al BeO. Variables explored during the studies included (1) the test temperature, (2) prior thermal history, (3) specimen surface finish, (4) test atmosphere, and (5) specimen size. The following conditions of these variables were investigated:

Test Temperature:	20 and 1000°C.
Prior Thermal History:	As-received or annealed at 1700°C for 3 hr.
Surface Finish:	As-received and ground.
Test Atmosphere:	Air, saturated steam and dry argon
Specimen Size:	0.012, 0.047 and 0.098 cu in.

As analysis of variance conducted on the medium size Wesgo AL-995 specimens tested at room temperature showed that for the as-received material the environmental atmosphere had no significant effect on fracture strength. Therefore, to limit the large number of specimen requirements already incorporated in the program, this variable was eliminated from most further tests. A thorough study of the test results obtained permit the following conclusions to be drawn.

(1) All Weibull parameters, as represented by σ_u , m and σ_o , vary substantially with surface condition, heat treatment and testing temperature for each of the materials included in this study. Therefore, these parameters cannot be considered true material constants, but must be taken as correct descriptors of material behavior for only a single (rigidly described) set of test or service conditions.

(2) Grinding serves to increase the value of the flaw density exponent, m , leaving the values of σ_u and σ_o relatively unaffected. This results in a lowered mean strength for the ground material. Since grinding can affect only the flaw density and severity existing at the specimen surface, these results appear to imply that fracture in ceramic substances is generally a surface-controlled phenomenon.

(3) The effect of an increased testing temperature (from 20 to 1000°C) is to induce a rise in the value of the flaw density exponent, which is again indicative of a flaw-healing effect ascribable to a reduction of adverse residual stresses. However, the effect of a 1000°C testing temperature in this regard is far more modest than that associated with a 1700°C annealing treatment, as stays constant or drops at the higher test temperature. These factors, taken together, result in a significant reduction of mean strength at 1000°C, which ranges from 12 to 25 percent, as compared to the room temperature values, for the material tested.

(4) Characterizations of the statistical dispersion of strength values of the brittle oxides by means of the Weibull theory were found to be quite applicable and descriptive. Even though the theory has shortcomings (i. e., a full fracture probability is not attained until the applied stress rises to infinity) and a reliable determination of its parameters requires a comparatively large number of tests, it defines the cumulative distribution function of the strength values of brittle oxides very well, and is perhaps the easiest yet most flexible three-parameter theory that can be used for this purpose.

(5) For the materials tested, the following m-values were found to characterize the materials: 3.25 for as-received material at room temperature, 6.0 for ground material at room temperature, 11.0 for annealed material at room temperature, 4.5 for as-received material at 1000°C and 8.0 for ground material at 1000°C. These findings, however, apply only to the test series conducted here, and their uncritical generalization to other cases does not appear warranted at the present state of knowledge.

(6) The zero strength, if it exists, is generally less than half of the average strength; design with ceramic materials should not be based on an allowable stress exceeding this value, unless one is prepared to accept a reasonable risk of rupture of the structural piece.

(7) The predictions of the Weibull theory, insofar as the effect of size on the average strength is concerned, were well supported by experimental results. At the same time, the slightly different batching and preparation techniques used in fabricating the specimen shapes for the volumetric effect studies resulted in wide variations of Weibull parameters for the same materials tested under identical conditions.

(8) A special test series conducted on BeO showed that a purposeful suppression of a comparatively small portion (less than 10 percent) of a large population, represented by 150 individuals, can completely change the character of the c. d. f. from an apparent composite Weibull distribution to one having a well-behaved and nearly gaussian character.

7. REFERENCES

1. 1 Weibull, W. A., "Statistical Theory of the Strength of Materials, "Ing. Vetenskaps Akad Handl, No. 151, Stockholm (1939)
1. 2 Weil, N. A., Studies of the Brittle Behavior of Ceramic Materials, Task 1, ASD-TR-61-628, (April 1962).
1. 3 Frocht, M. M., Photoelasticity, Vol. 1, pp. 380-381, Wiley and Sons, N. Y. (1951).
1. 4 Weibull, W. A., "The Phenomenon of Rupture in Solids, " Ing. Vetenskaps Akad Handl, No. 153, Stockholm (1939).
1. 5 Snedecor, G., Statistical Methods, pp. 501-502, Iowa State University Press, Ames, Iowa (1961).
1. 6 Daniels, H. E., "The Statistical Theory of the Strength of Bundles of Thread, " Proceedings of the Royal Society 183, 405-435 (1945).
1. 7 Weibull, W. A., "New Methods for Computing Parametrics of Complete or Truncated Distributions, " The Aeronautical Research Institute of Sweden, Report 58, Stockholm (February 1955).

(7) The predictions of the Weibull theory, insofar as the effect of size on the average strength is concerned, were well supported by experimental results. At the same time, the slightly different batching and preparation techniques used in fabricating the specimen shapes for the volumetric effect studies resulted in wide variations of Weibull parameters for the same materials tested under identical conditions.

(8) A special test series conducted on BeO showed that a purposeful suppression of a comparatively small portion (less than 10 percent) of a large population, represented by 150 individuals, can completely change the character of the c. d. f. from an apparent composite Weibull distribution to one having a well-behaved and nearly gaussian character.

7. REFERENCES

1. 1 Weibull, W. A., "Statistical Theory of the Strength of Materials, "Ing. Vetenskaps Akad Handl, No. 151, Stockholm (1939)
1. 2 Weil, N. A., Studies of the Brittle Behavior of Ceramic Materials, Task 1, ASD-TR-61-628, (April 1962).
1. 3 Frocht, M. M., Photoelasticity, Vol. 1, pp. 380-381, Wiley and Sons, N. Y. (1951).
1. 4 Weibull, W. A., "The Phenomenon of Rupture in Solids, " Ing. Vetenskaps Akad Handl, No. 153, Stockholm (1939).
1. 5 Snedecor, G., Statistical Methods, pp. 501-502, Iowa State University Press, Ames, Iowa (1961).
1. 6 Daniels, H. E., "The Statistical Theory of the Strength of Bundles of Thread, " Proceedings of the Royal Society 183, 405-435 (1945).
1. 7 Weibull, W. A., "New Methods for Computing Parametrics of Complete or Truncated Distributions, " The Aeronautical Research Institute of Sweden, Report 58, Stockholm (February 1955).

- 1-8 Duckworth, Schwope, "Mechanical Property Tests on Ceramic Bodies WADC TR 52-67.
- 1-9 Weil, N. A., Bortz, S. A. and Firestone, R. F., "Factors Affecting the Statistical Strength of Alumina," Research Conference on Structure and Properties of Engineering Materials, North Carolina State College, Raleigh, N. C., (March 12-13, 1962).
- 1-10 Salmassy, Duckworth, and Schwope, "Behavior of Brittle State Materials," WADC TR 53-50, Pt. I and II.
- 1-11 Kies, J. A., "Strength of Glass," NRL Report 5098 (April 3, 1958).
- 1-12 Kao, John H. K., "A Graphical Estimation of Mixed Weibull Parameters in Life-Testing of Electron Tubes," Technometrics, 1, No. 4, (November 1959).
- 1-13 Epstein, Benjamin, "Statistical Aspects of Fracture Problem", J. Appl. Phys. 19 (February 1948).
- 1-14 Bernbaum and Brodie, "Measurement of Tensile Strength of Brittle Materials," Brit. J. Appl. Phys., 10 (June 1959).
- 1-15 Anthony, F. M. and Mistretta, A. L., "Leading Edge Design with Brittle Materials," Paper No. 61-151-1845, IAS-ARS Mtg., Los Angeles (June 1961).

TASK 2 - EFFECT OF STRAIN RATE

Principal Investigator: J. W. Dally
Armour Research Foundation

ABSTRACT

The effect of strain rate on the fracture stress in bending has been studied for Lucalox Al_2O_3 , Wesgo AL-995, ARF MgO and Atomics International BeO. Strain rates in the range 10^{-7} sec^{-1} to 10^1 sec^{-1} at temperatures from 75° to 1800°F have been included in this investigation. At room temperature all of the materials show higher strength at increasing strain rates, except for Wesgo AL-995 which shows a small decrease. The rates of strength enhancement, as derived from a least squares linear data fit, were -328 psi per decade of strain rate for Wesgo, +997 psi for Lucalox, +415 psi for intermediate ARF MgO, +1130 psi for small size ARF MgO and +1030 psi per decade for Atomics International BeO.

The rate of strength increase with strain rate was more pronounced at elevated temperatures. At 1000°F Wesgo AL-995 and Lucalox showed a rate of strength increase of 4060 and 3960 psi per decade of strain rate, respectively. At 1800°F the comparable results were: Wesgo AL-995 8330 psi per decade, Lucalox 1510 psi, ARF MgO 20 psi and AI BeO at 1020 psi per decade.

A technique for achieving uniaxial tension in a state of dynamic loading has been evolved and is being extended to higher temperatures.

TASK 2 . EFFECT OF STRAIN RATE

1. INTRODUCTION

The purpose of this task is to study the effect of strain rate on the failure strength of polycrystalline Al_2O_3 , MgO and BeO in tension. The scope of the task includes strain rates from 10^{-7} per second to 10^2 per second, at temperatures from 75°F (nominal room temperature) to 1800°F .

During the initial contract period (June 1960 through October 1961) the principal effort was directed toward the development of uniaxial tension loading and measurement techniques. A great deal of effort was expended in the design of a tensile apparatus and measuring system which could reflect the true tensile strength of a brittle material. A state of pure tension through a direct, but highly refined "pull" technique was never achieved with the dog-bone type specimens. The difficulty of constructing such an apparatus arose from physical and mechanical constraints which could not be relaxed sufficiently to allow the development of a feasible test procedure.

While direct tension techniques have been very successful in studying the tensile properties of ductile or even semi-ductile materials, the use of such techniques for brittle materials has never been successful. Several procedures for indirect generation of a tensile state of stress in a brittle specimen have evolved. Development work on the attainment of a pure tensile stress state is now in progress by several laboratories. One of these techniques, applicable to the highest strain rates considered in this project, is currently under development at ARF with a portion of the results included in this report. The classical approach to the study of brittle materials in tension is the bend test in which the lower face of a bend specimen is in a state of pure tension.

In the first contract extension period (November 15, 1961 to November 15, 1962, emphasis was placed on the well established bend or rupture modulus technology. This development produced a bend fixture for four-point bending of dogbone specimens over a wide range of strain rates and temperatures.

2. STRAIN RATE EFFECTS IN BENDING

A. Bending Fixtures

A four-point bending apparatus was designed, built and modified to provide the most favorable condition of pure bending with a minimum of frictional constraint. Figures 2-1 and 2-2 show a typical bending fixture. The fixture consists of a pair of grips which attach to each end of the dogbone producing a variable section beam. Each grip contains two pins, one of which provides a loading point and the other a support point. In the resulting four-point loading system, the entire active portion of the specimen is in a region of constant bending moment. This puts the uniform reduced section of the dogbone in a state of pure bending. Care was taken to locate the pins so that the active contacting surfaces were all on the nominal neutral axis of the specimen. In addition to this, the pins were free to roll, thereby eliminating any friction contribution to the bending moment or induction of a net frictional tensile stress across the specimen cross section. One end of the load bar and one of the support pads contain pins perpendicular to grip pins. This assures point contacts at one end of both the loading bar and the support. This feature prevents the development of torsional stresses about the longitudinal axis of the dogbone since the fixture cannot ideally apply a torsional moment around this axis.

The type apparatus (several of which were built) was used over the entire spectrum of strain rates and temperatures. For strain rates from 5×10^{-7} to 1×10^{-2} per sec, the apparatus

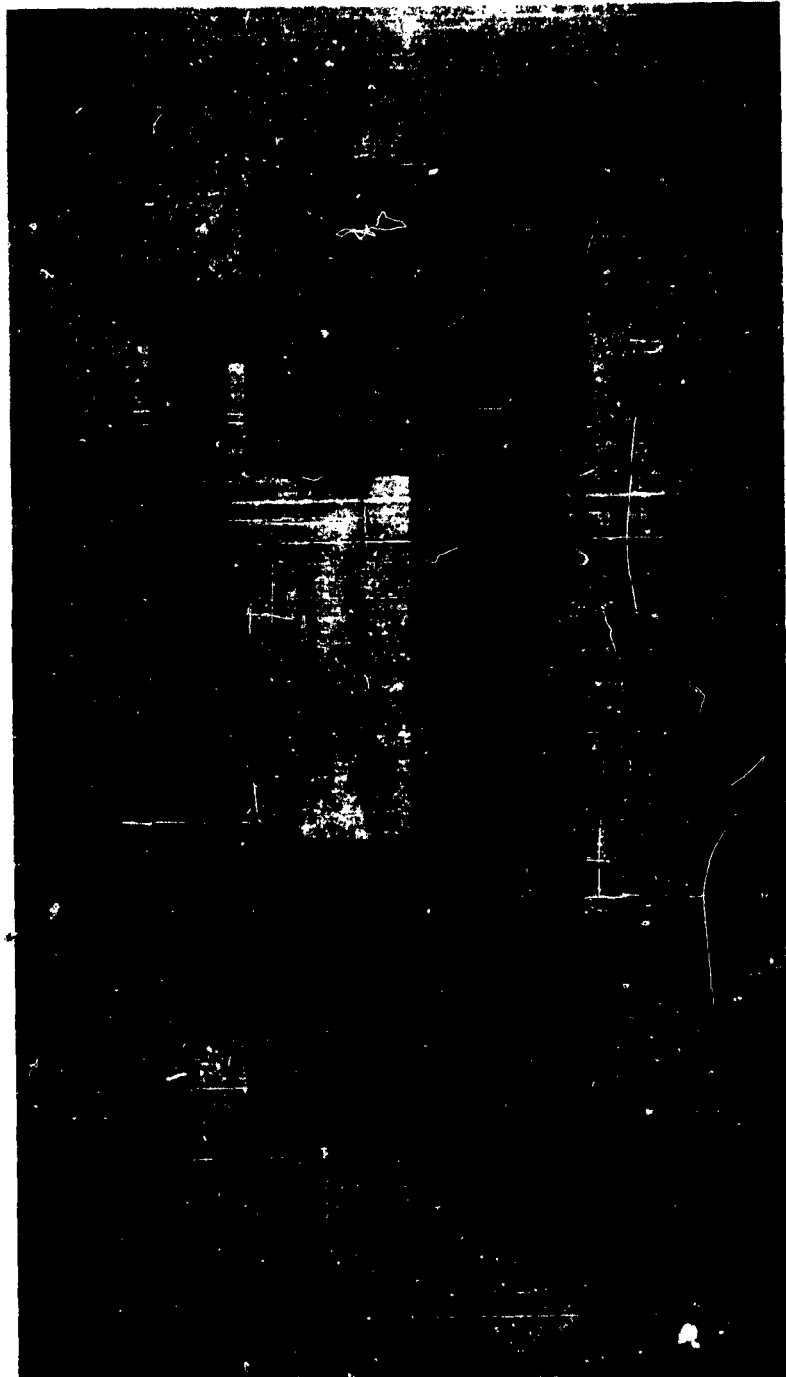


Fig. 2-1 BEND TEST APPARATUS FOR SMALL MAGNESIUM OXIDE SPECIMENS

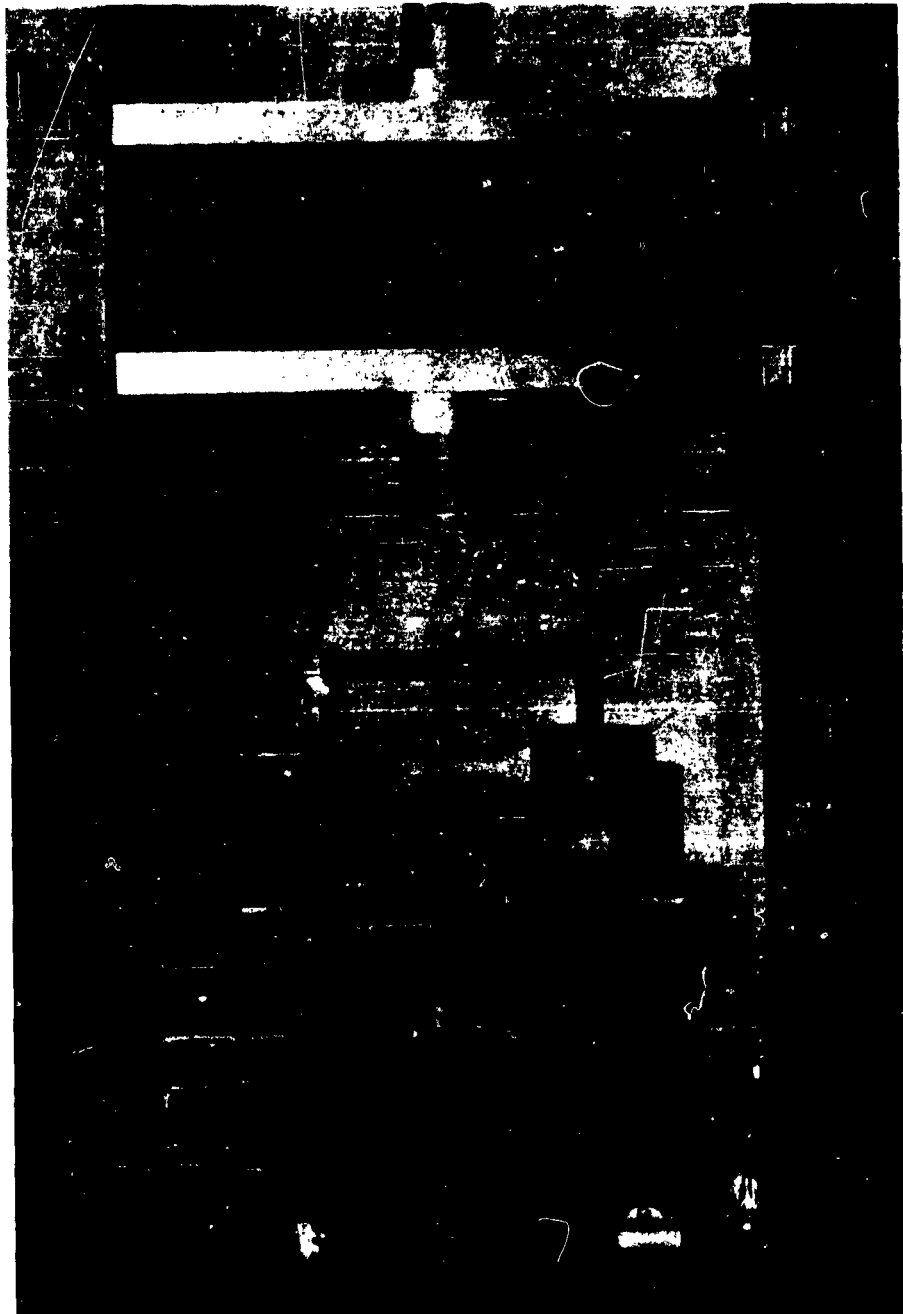


Fig. 2-2
TYPICAL BEND TEST APPARATUS POSITIONED IN UNIVERSAL
MACHINE FOR INTERMEDIATE SIZE DOGBONE SPECIMENS

was loaded in Riehle and Instron universal testing machines. Loading rates were varied from 0.0005 in. per min of cross head motion to 20 in. per min. For strain rates above 10^{-2} , a falling weight was used with the same bend fixture. Essentially, this apparatus consisted of a guide tube in which a weight was dropped from a prescribed height onto a loading ball at the center of the load bar. This impact can be controlled well enough to apply a reproducible load pulse giving a state of dynamic bending.

B. Elevated Temperature Furnace

Initial pilot tests were performed in the nichrome V wire-wound furnace described in reference 2-1. While the furnace was functional in the design temperature range, the temperature gradient along the specimen gage section (length of uniform cross section) was unacceptably large. In addition to this, after many cycles of temperature, a hot spot developed in the wire coil leaving serious doubts as to its reliability.

To circumvent some of the problems associated with the wire-wound furnace, a new furnace was designed around four silicon carbide Glo-bar * heating elements. The four heating elements are mounted in a firebrick furnace. This furnace was found to be far superior with regard to temperature gradient along the gage section, and also had improved over-all ruggedness and reliability. Photographs of the furnace in the assembled and opened conditions are shown in Fig. 2-3 and 2-4, respectively. The furnace is built in two notched halves to permit rapid specimen insertion and to cut down on over-all testing time. In the machine tests it was possible to attach the upper section of the furnace to the moving cross head, so that after a specimen is broken and the cross head raised to insert a new specimen, the furnace is opened

* Trade Name, The Carborundum Corporation.

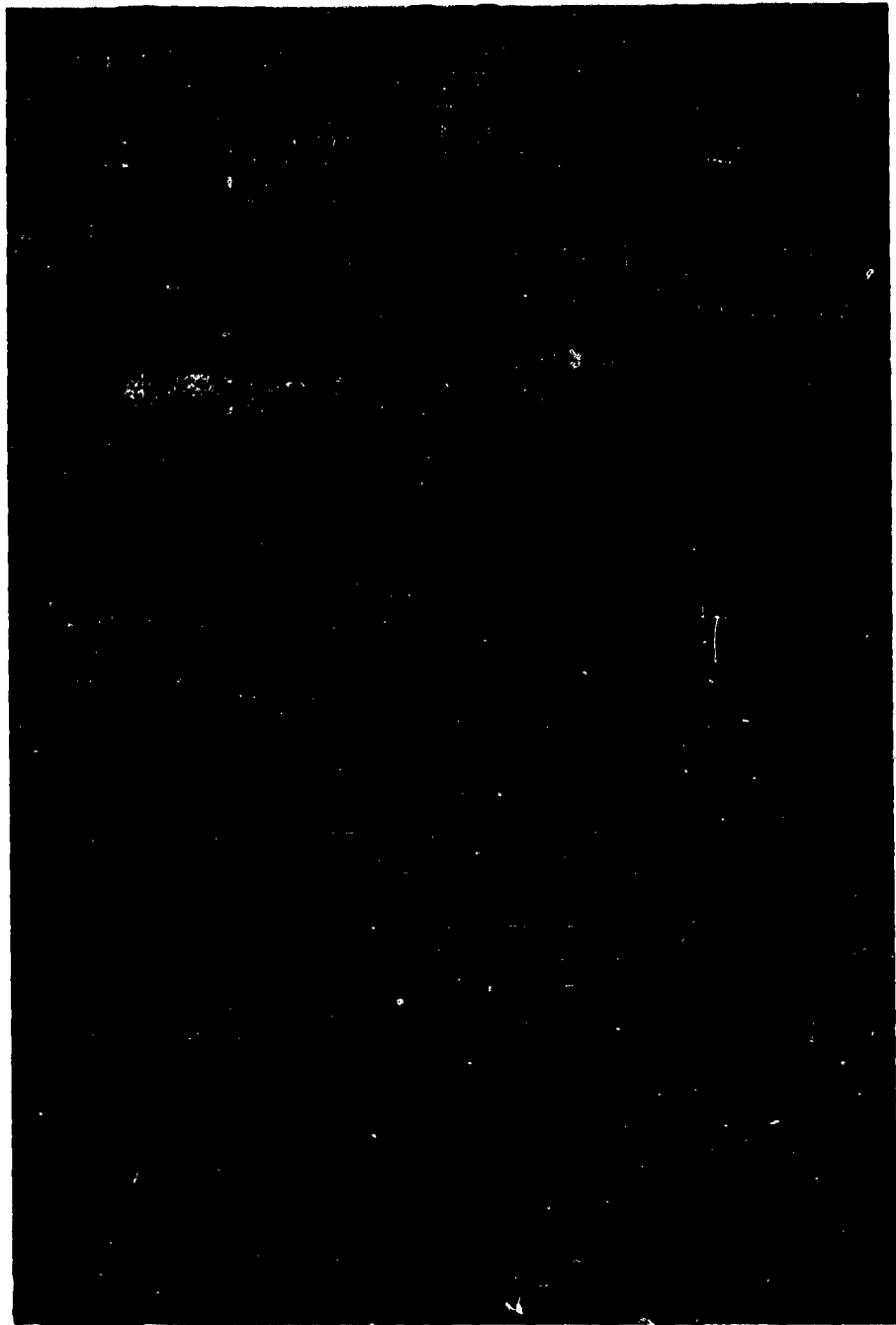


Fig. 2-3
TYPICAL BEND TEST APPARATUS IN CLOSED FURNACE

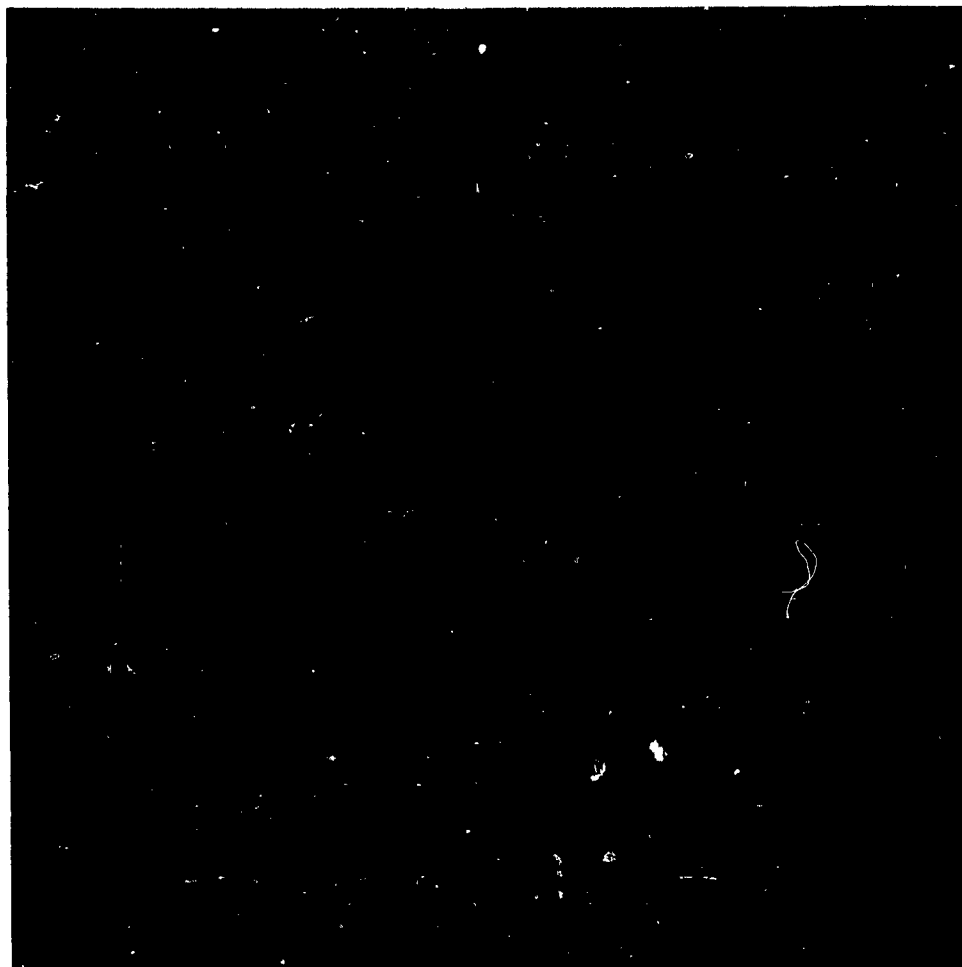


Fig. 2-4
TYPICAL BEND APPARATUS IN OPEN FURNACE

automatically. A plot of the temperature over the specimen gage length at a nominal temperature of 1800 °F is given in Fig. 2-5.

C. Measurement of Failure Loads and Strain Rates

As discussed, the mounted specimen is in a region of constant bending moment as long as the symmetry of the loading system is maintained. The symmetry condition was verified early in the bend test program; thereafter, a section of constant bending moment was assumed to exist for all tests since care was taken to maintain the symmetry of loading in each experiment.

The total failure load and time to failure are the only quantities needed to compute the failure stress and strain rate. The bending moment over the gage section can be computed directly from the total load, and the failure stress determined from the bending moment and the section modulus at the failure section. To compute the strain rate it was necessary to determine the time to failure and to assume a value for the modulus of elasticity of the material at the temperature in question.

Early in the bend test program modulus of elasticity determinations at room temperature were made for Wesgo AL-995, Lucalox, and ARF MgO, and found to agree well with the results of other investigations (reference 2-2, page 104, Fig. 24). At room temperature these modulus values were used to compute the failure stress for the drop tests as well as the strain rate for the other tests.

Values of the elastic modulus at elevated temperatures were obtained from the data given in Fig. 24 in reference 2-2. It should be pointed out that this procedure is sufficiently accurate at high temperatures because the log scale of strain rates on the final plots of failure stress versus log strain rate is quite insensitive to comparatively large percentage errors in the modulus of elasticity. The effect of a percentage error in the modulus is to shift the entire spectrum of points horizontally only a slight amount, hence it is of only minor importance.



For strain rates from 10^{-7} to 10^{-4} sec^{-1} , the measurement of failure load and time to failure by conventional means (chart records or load dial plus stop-watch) is acceptable over the whole temperature range. For strain rates of 10^{-3} to 10^2 per sec the system response requirements preclude the use of static recording and dynamic recording is required. All the recording in this regime was accomplished using a cathode ray oscilloscope with the load on the y axis and time following a trigger signal (on pulse rise) on the x axis in conjunction with a Polaroid back-scope camera. Load was transduced by a load cell and strain indicator, demodulated and low pass filtered for oscilloscope presentation.

Because of the difficulties encountered in attempting to measure load with transducers at the highest strain rate (drop test), specimens were individually instrumented with etched foil resistance strain gages mounted on the tensile face. Each strain gage was used as an active element in a four-arm d-c bridge. Strain pulses were recorded by oscilloscope photography, sweep being triggered by a microswitch contacted by the falling weight. This procedure requires that failure strength be computed from the known moduli at each temperature as discussed earlier. Extension of this technique to higher temperatures (1000°F and 1800°F) was not successful. The sensitivity of available high temperature strain gages in the region of 1000 microstrain full scale was not sufficient to meet the requirements. In addition, the program could not bear the high cost of procuring and mounting the requisite number of high temperature strain gages.

D. Specimens

The experiments on Lucalox and Wesgo AL-995 were performed using the intermediate sized dogbone depicted in Fig. 1-1. Part of the room temperature and all of the 1800°F work on ARF MgO was done using the same specimen

geometry. A series of room temperature tests was also run on small-size ARF MgO dogbones shown in Fig. 1-5 of reference 2-1). All of the experiments on Al BeO were carried out using 1/4 in. x 1/4 in. x 4 in. bars.

All specimens were used in the as-received* condition; they were stored from date of delivery until actual usage at atmospheric conditions in an air conditioned laboratory. Specimens for use at the higher temperatures, 1000°F and 1800°F, were equipped with thermocouples mounted in the center of the gage section at the neutral axis.

3. RESULTS

Summaries of the data for temperature of 75°F, 1000°F and 1800°F are given in Tables 2-I, 2-II and 2-III, respectively. In these tables, the strain rate, isothermal failure stress, standard deviation in failure stress, coefficient of variation and number of specimens are presented for each material. These data have been subjected to a linear least squares analysis to arrive at the failure stress versus log of strain rate plots shown in Fig. 2-6 through 2-16, and represented by the equation,

$$\sigma_F = A_0 + A_1 \ln \left(\frac{\dot{\epsilon}}{\dot{\epsilon}_0} \right) \quad (2-1)$$

where

σ_F is the failure stress

$\dot{\epsilon}$ is the strain rate

A_0 is the value of failure stress at a strain rate of $\dot{\epsilon}_0$, and

A_1 is the derived slope.

Since the lowest experimental strain rate was on the order of 10^{-7} sec^{-1} $\dot{\epsilon}_0$ was taken to be 10^{-7} . This normalization is arbitrary and does not change the line but only the form of the equation.

*The microstructure, physical dimensions, and surface finish of these specimens are described in reference 2-1.

Table 2-1

**SUMMARY, RESULTS OF STRAIN RATE EXPERIMENTS
AT ROOM TEMPERATURE**

Material	Strain Rate (sec ⁻¹)	Mean Failure Stress (psi)	Standard Deviation (psi)	Coefficient of Variation (%)	Number of Specimens
Wesgo AL-995	4 x 10 ⁻⁷	37,800	4700	12.4	8
	2 x 10 ⁻⁵	40,000	8400	21.0	8
	2 x 10 ⁻⁴	36,300	4000	11.0	9
	1 x 10 ⁻²	37,300	5200	13.9	10
	2 x 10 ¹	37,600	5000	13.3	8
Lucalox	4 x 10 ⁻⁷	28,500	2400	8.4	8
	2 x 10 ⁻⁵	26,000	3600	13.8	8
	1 x 10 ⁻⁴	28,300	3600	12.7	10
	1 x 10 ⁻²	31,100	6700	21.5	8
	2 x 10 ¹	30,300	3900	12.9	10
ARF MgO	5 x 10 ⁻⁷	16,900	2300	13.6	8
	2 x 10 ⁻⁵	14,300	2800	19.6	8
	2 x 10 ⁻⁴	16,700	2200	13.2	10
	9 x 10 ⁻³	14,800	2100	14.2	8
	2 x 10 ¹	17,800	1500	8.4	7
ARF MgO (Small Section)	7 x 10 ⁻⁷	17,000	1900	11.2	20
	1 x 10 ⁻⁴	18,000	1400	7.8	20
	1 x 10 ⁻²	17,700	1900	10.7	20
	3 x 10 ⁻¹	20,500	500	2.4	20
Al BeO	7 x 10 ⁻⁷	15,200	3800	25.0	20
	1 x 10 ⁻⁵	16,500	800	10.9	20
	5 x 10 ⁻⁴	16,600	3600	21.7	20

Table 2-II

SUMMARY, RESULTS OF STRAIN RATE EXPERIMENTS AT 1000 °F

Material	Strain Rate (sec ⁻¹)	Mean Failure Stress (psi)	Standard Deviation (psi)	Coefficient of Variation (%)	Number of Specimens
Wesgo AL-995	6 x 10 ⁻⁷	27,000	3300	12.2	20
	2 x 10 ⁻⁴	29,100	4900	16.8	20
	6 x 10 ⁻³	34,500	5700	16.5	20
Lucalox	8 x 10 ⁻⁷	21,600	3100	14.4	20
	2 x 10 ⁻⁴	25,600	1700	6.6	20
	7 x 10 ⁻³	28,400	5000	17.9	20

Table 2-III

SUMMARY, RESULTS OF STRAIN RATE EXPERIMENTS AT 1800 °F

Material	Strain Rate (sec ⁻¹)	Mean Failure Stress (psi)	Standard Deviation (psi)	Coefficient of Variation (%)	Number of Specimens
Wesgo AL-995	7 x 10 ⁻⁷	19,200	2000	10.4	20
	2 x 10 ⁻⁴	29,700	2300	7.7	20
	7 x 10 ⁻³	33,400	2700	8.2	16
Lucalox	7 x 10 ⁻⁷	19,900	2600	13.1	20
	1 x 10 ⁻⁴	22,500	4000	17.8	18
	8 x 10 ⁻³	22,500	5400	24.0	19
ARF MgO	1 x 10 ⁻⁶	13,600	1800	13.2	15
	3 x 10 ⁻⁴	14,900	1700	11.4	19
	9 x 10 ⁻³	13,400	1500	11.2	13
Al BeO	8 x 10 ⁻⁷	10,800	4200	38.9	20
	1 x 10 ⁻⁵	14,100	2400	17.0	20
	3 x 10 ⁻⁴	12,100	4000	33.1	20

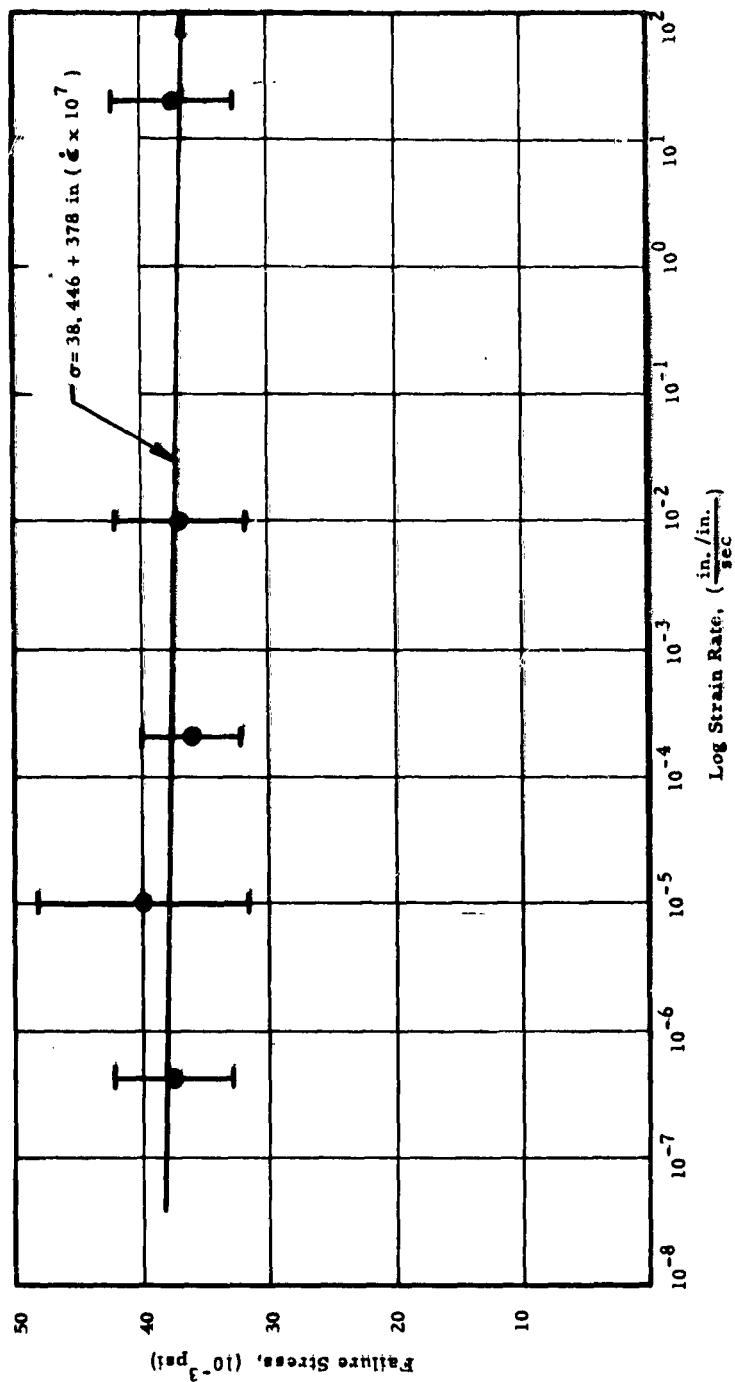


Fig. 2-6 FAILURE STRESS VERSUS STRAIN RATE, WESGO AL-995 AT ROOM TEMPERATURE, INTERMEDIATE-SIZE SPECIMEN

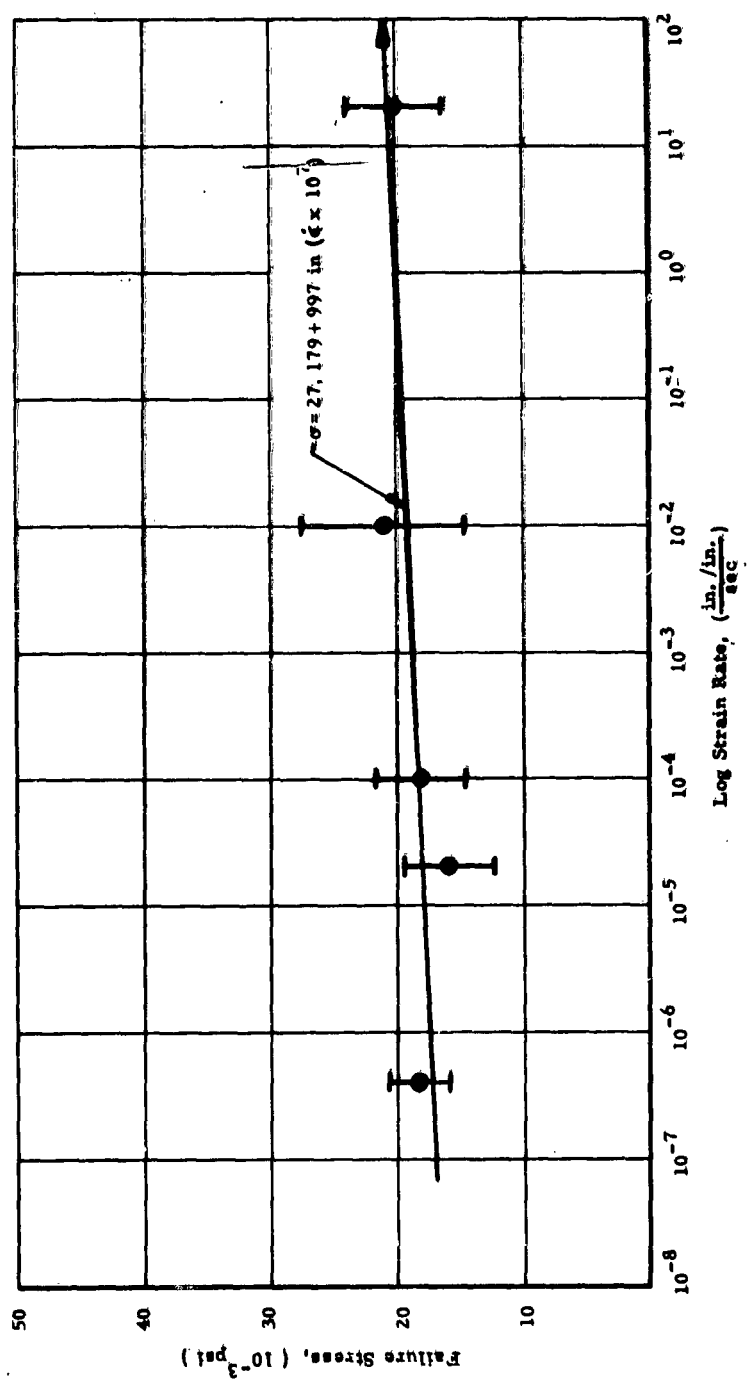


Fig. 2-7 FAILURE STRESS VERSUS STRAIN RATE, LUCALOX AT ROOM TEMPERATURE, INTERMEDIATE-SIZE SPECIMEN

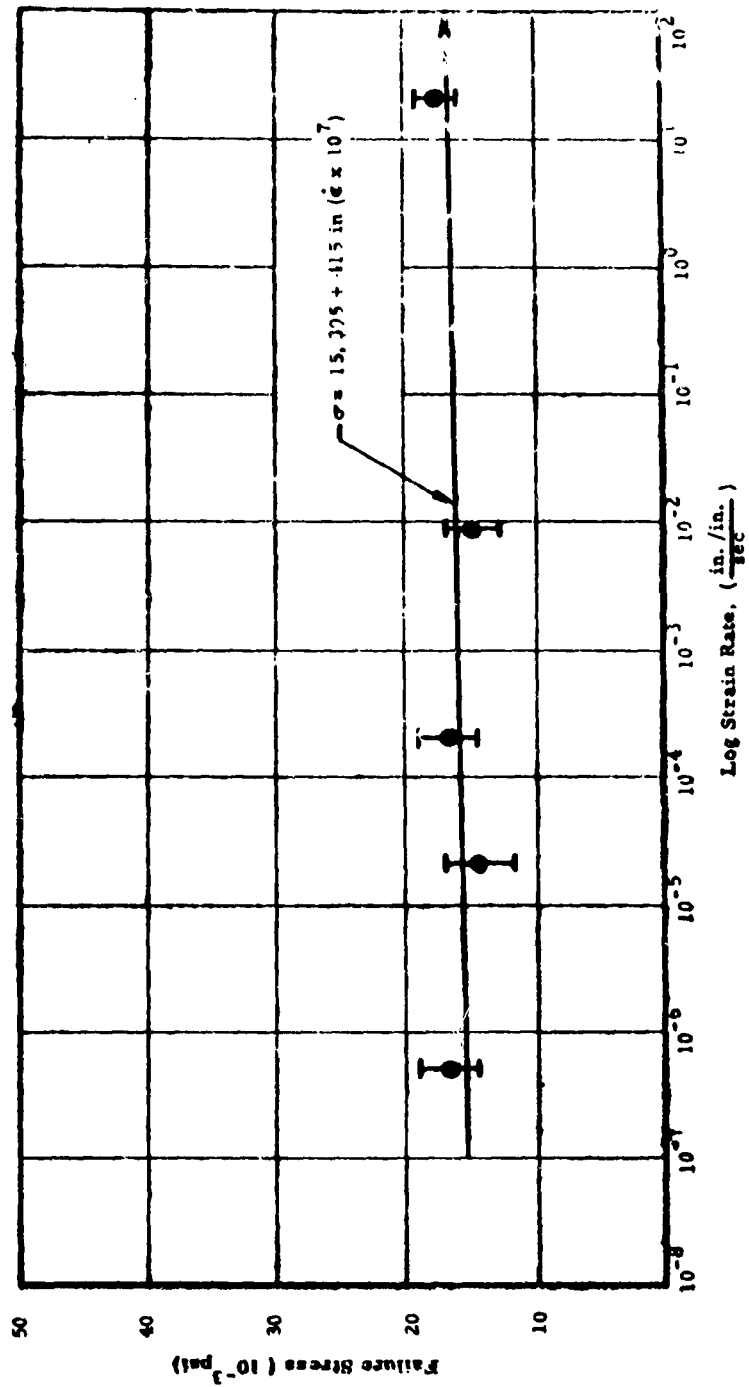


Fig. 2-8 FAILURE STRESS VERSUS STRAIN RATE, ARF MAGNESIUM OXIDE
AT ROOM TEMPERATURE INTERMEDIATE-SIZE SPECIMEN

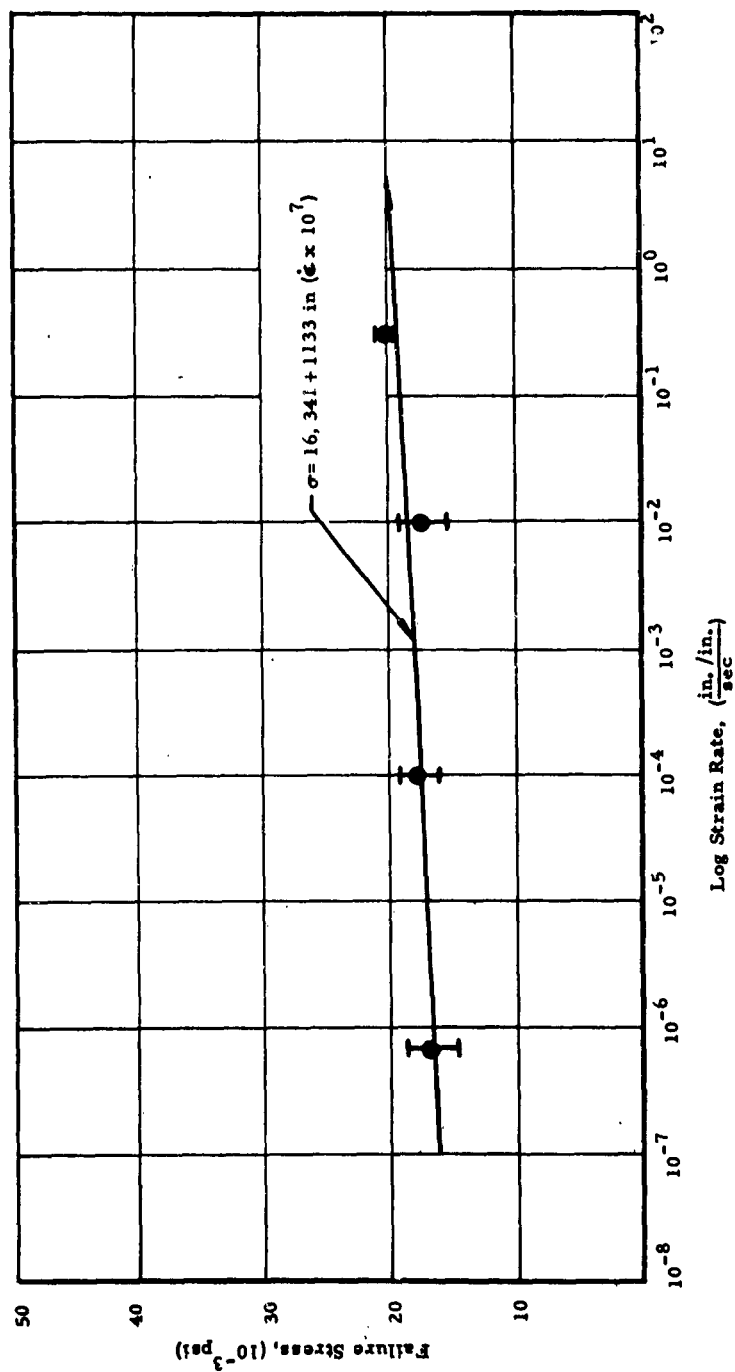


Fig. 2-9 FAILURE STRESS VERSUS STRAIN RATE, ARF MAGNESIUM OXIDE AT ROOM TEMPERATURE, SMALL-SIZE SPECIMEN

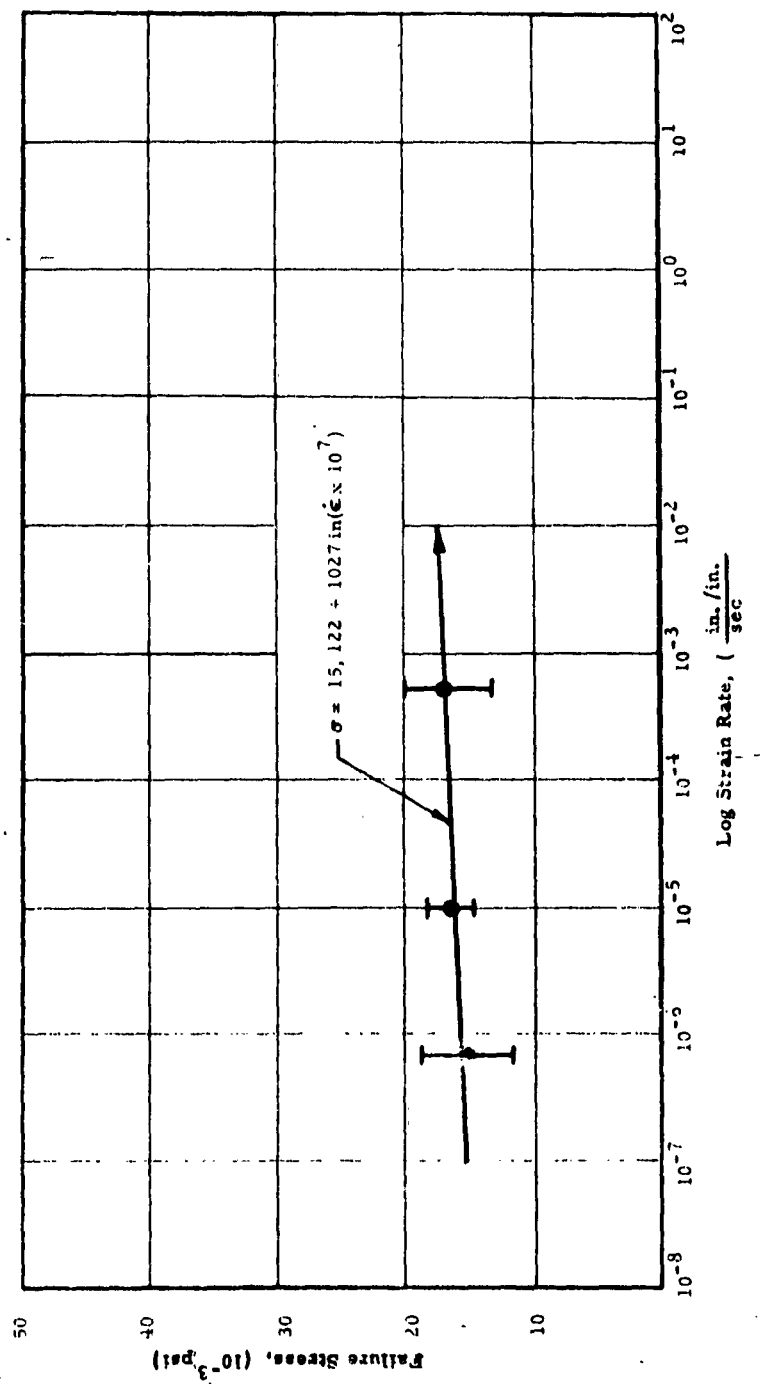


Fig. 2-10 FAILURE STRESS VERSUS STRAIN RATE, BERYLLIUM OXIDE AT ROOM TEMPERATURE, 1/4 IN. X 1/4 IN. X 4 IN. SPECIMEN

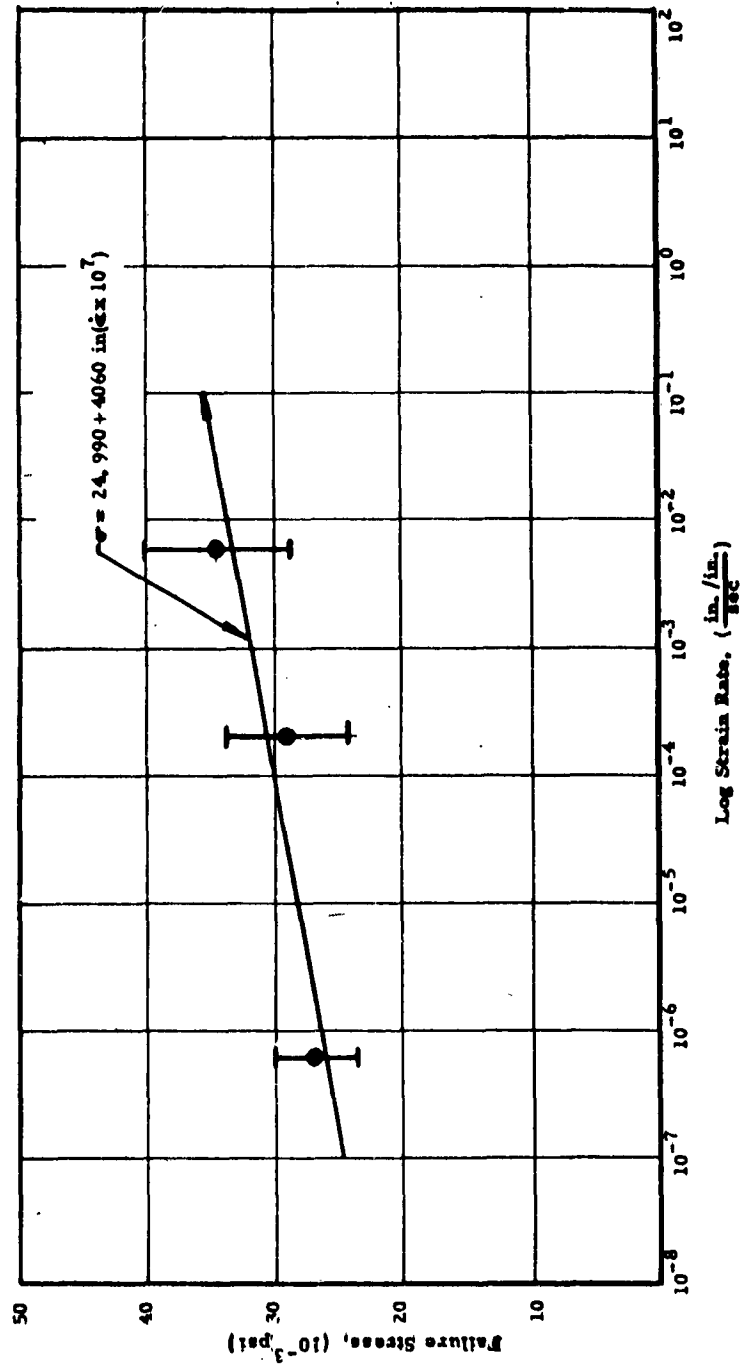


Fig. 2-11 FAILURE STRESS VERSUS STRAIN RATE WESGO AL-995 AT 1000°F
INTERMEDIATE-SIZE SPECIMEN

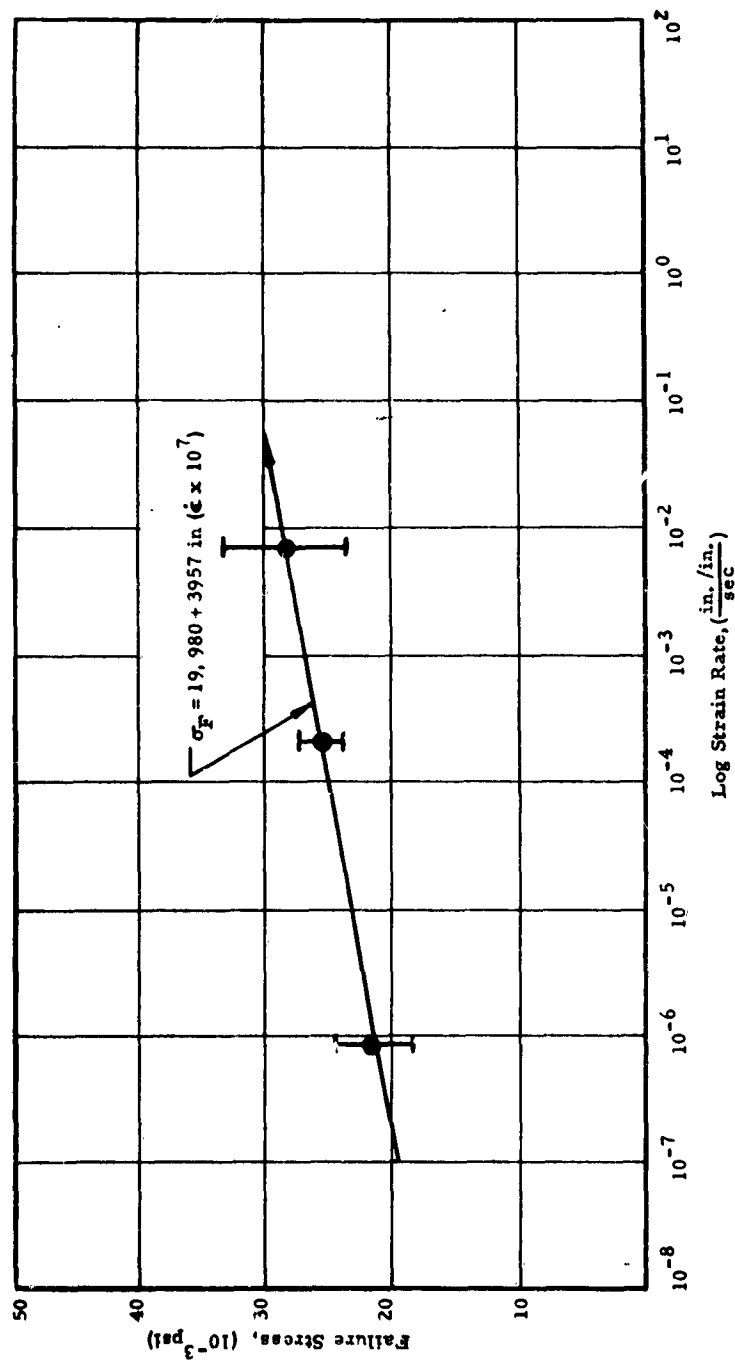


Fig. 2-12 FAILURE STRESS VERSUS STRAIN RATE, LUCALOX AT 1000°F
INTERMEDIATE-SIZE SPECIMEN

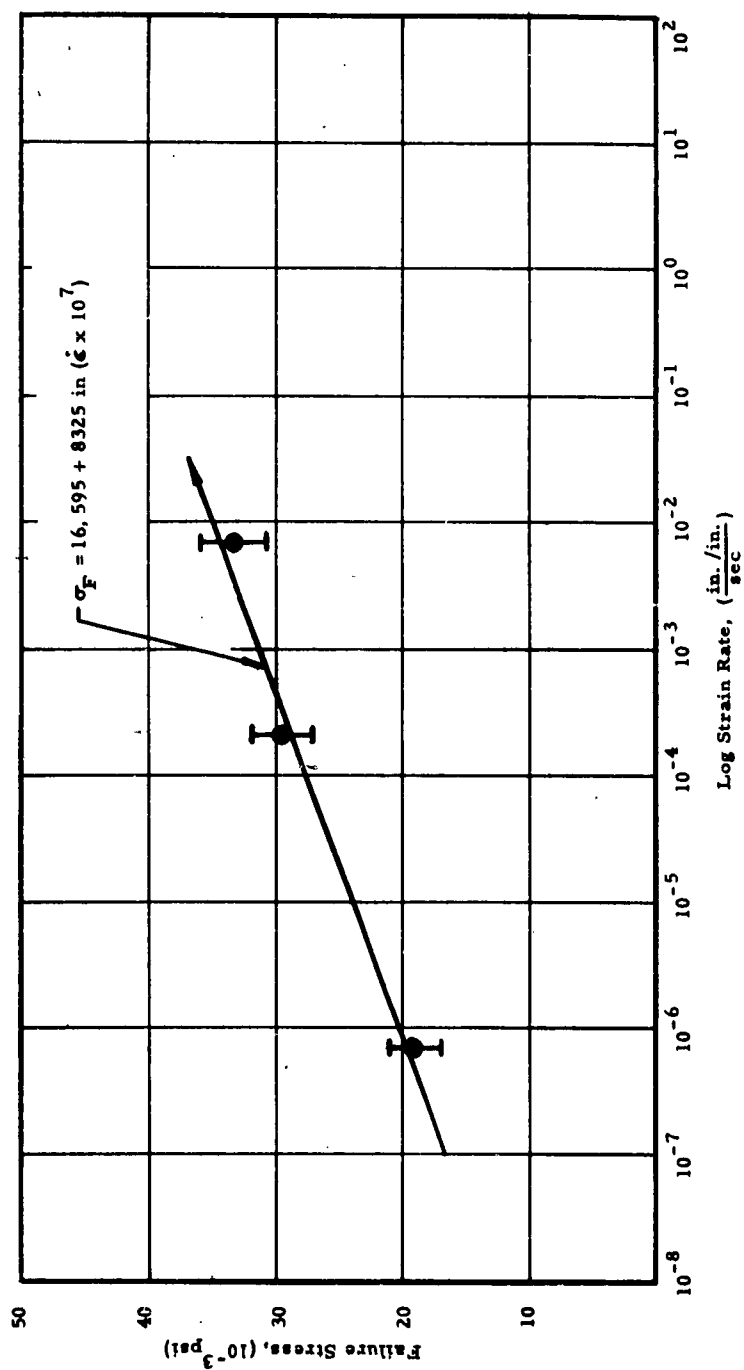


Fig. 2-13 FAILURE STRESS VERSUS STRAIN RATE WESGO AL-995 AT
1800°F INTERMEDIATE-SIZE SPECIMEN

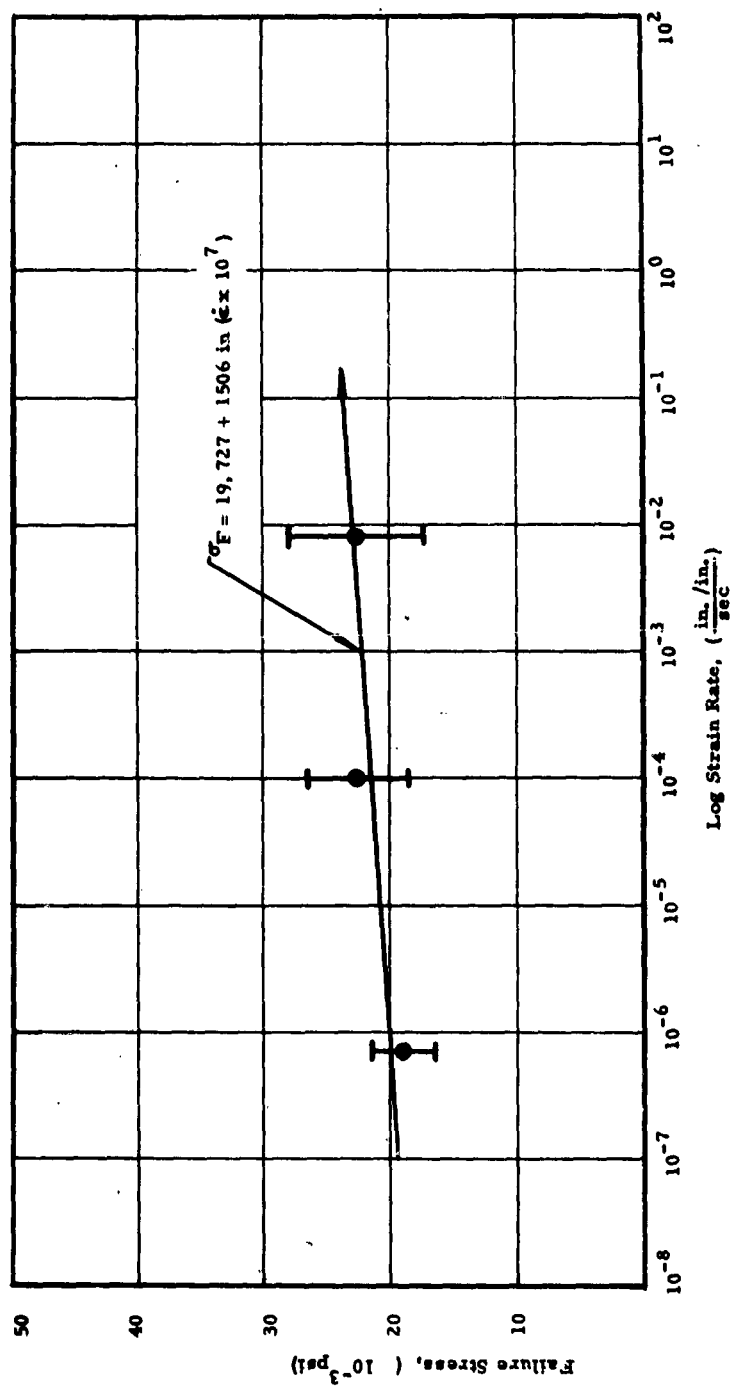


Fig. 2-14 FAILURE STRESS VERSUS STRAIN RATE, LUCALOX AT 1800 °F
INTERMEDIATE-SIZED SPECIMEN

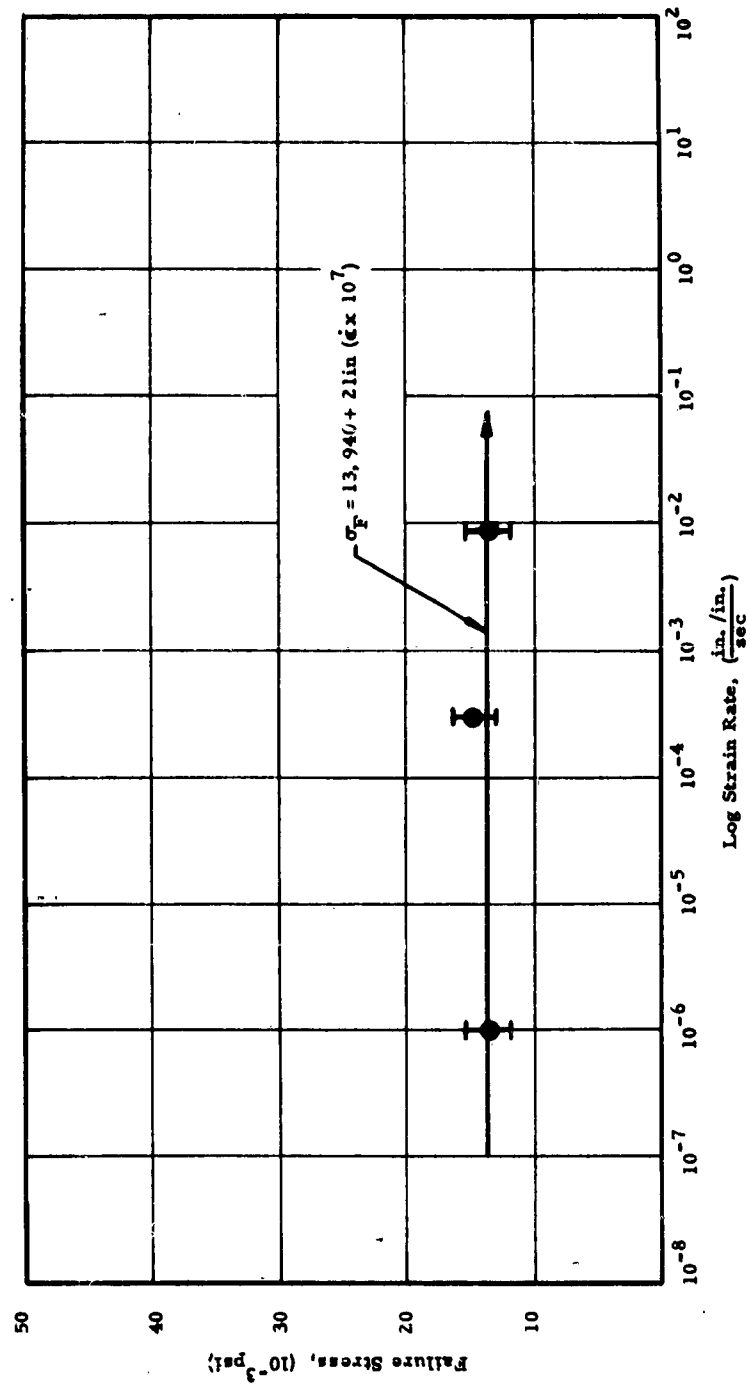


Fig. 2-15 FAILURE STRESS VERSUS STRAIN RATE, ARF MAGNESIUM OXIDE AT 1800°F INTERMEDIATE-SIZE SPECIMEN

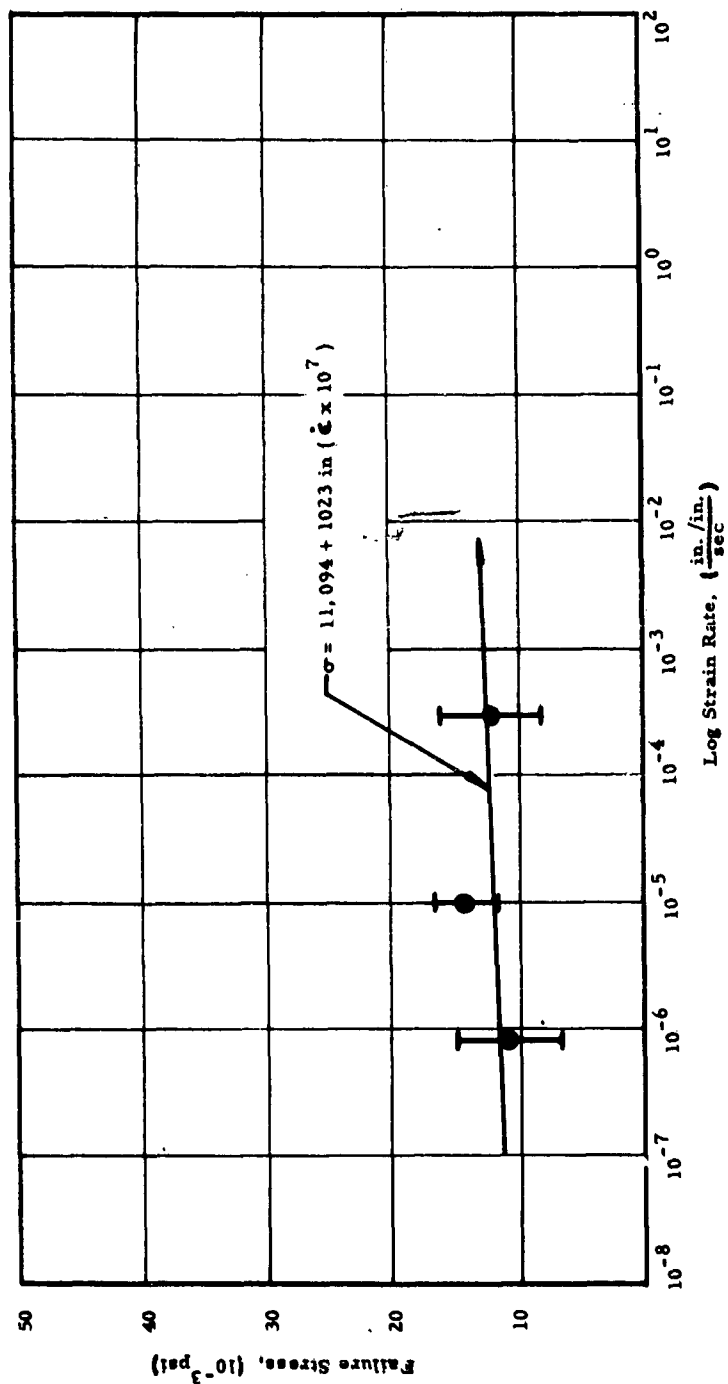


Fig. 2-16 FAILURE STRESS VERSUS STRAIN RATE, BERYLLIUM OXIDE
AT 1800°F 1/4 IN. X 1/4 IN. X 1/4 IN. SPECIMEN

On the basis of available Data this linear relationship appears to represent the most realistic fit to the experimental data points obtained. As more points are added either by expansion of the strain rate range or by filling in of the existing strain rate spectrum, a refinement for curves of a higher complexity than the simple semilogarithmic linearity may become appropriate.

The parameters from the least square fitting of the data are shown in Table 2-IV.

It is interesting to note that all of the materials except Wesgo AL-995 show an increase in failure strength with strain rate at room temperature. The value of this decrease is sufficiently small to leave some question as to its validity; this fact will be discussed in some more detail later in this task report.

At 1000°F the Wesgo AL-995 and Lucalox show a remarkably similar strain rate sensitivity, at 1800°F they show an equally remarkable difference with Lucalox which returns to near its room temperature in sensitivity. The ARF MgO and Al BeO show small strain rate dependence at 1800°F, quite similar to the behavior of Lucalox.

4. DISCUSSION

The basic strain rate effects are summarized in Table 2-IV. There are as yet, not enough different temperatures explored to allow for the derivation of a representative value of activation energy corresponding to a strengthening mechanism or mechanisms. The strain rate effects, or lack of them, will be discussed at each of the three test temperatures.

A. Room Temperature Behavior

At room temperature all of the materials, with the exception of Wesgo AL-995, show an increase of strength with strain rate. The decrease of strength in the case of Wesgo AL-995 is sufficiently small that it may not be of significance.

Table 2-IV

SUMMARY OF LINEAR FIT STRAIN RATE PARAMETERS

$$\sigma_F = A_0 + A_1 \ln \left(\frac{\dot{\epsilon}}{10^{-7}} \right)$$

Material	Temp. (°F)	A ₀ (10 ³ psi)	A ₁ (10 ³ psi)	Number of Strain Rates	Strain Rate Range (sec ⁻¹)
Wesgo AL-995	75	38.45	-0.33	5	4 x 10 ⁻⁷ to 2 x 10 ¹
	1000	24.99	4.06	3	6 x 10 ⁻⁷ to 6 x 10 ⁻³
	1800	16.60	8.33	3	7 x 10 ⁻⁷ to 7 x 10 ⁻³
Lucalox	75	27.18	1.00	5	4 x 10 ⁻⁷ to 2 x 10 ¹
	1000	19.98	3.96	3	8 x 10 ⁻⁷ to 7 x 10 ⁻³
	1800	19.73	1.51	3	7 x 10 ⁻⁷ to 8 x 10 ⁻³
ARF MgO (Int.size)	75	15.40	0.42	5	5 x 10 ⁻⁷ to 2 x 10 ¹
	1800	13.94	0.02	3	1 x 10 ⁻³ to 9 x 10 ⁻³
ARF MgO (Small size)	75	16.34	1.13	4	7 x 10 ⁻⁷ to 3 x 10 ⁻¹
Al BeO	75	15.12	1.03	3	7 x 10 ⁻⁷ to 3 x 10 ⁻⁴
	1800	11.09	1.02	3	8 x 10 ⁻⁷ to 3 x 10 ⁻⁴

Any explanation for an increase of strength with strain rate for brittle materials at room temperature must be based, to a fair extent, on conjecture. At room temperature almost no data exist with the exception of this work and that of Kingery and Pappis⁽²⁻³⁾ the latter study being performed at a single indeterminate strain rate (pendulum impact).

A tenable explanation for the room temperature behavior can be evolved using the known effects of dislocation mobility and dislocation pile-ups leading to crack nucleation. (2-4) In a basically brittle material there is strong evidence that failure is due to inherent cracks and their propagation under stress. The energetic requirements for crack growth in any material exceed the simple Griffith criterion based upon elastic energy only, by an amount corresponding to the energy dissipated by plastic work about the highly stressed tip of the propagating crack. If any amount of dislocation mobility, however small, exists, plastic flow at the tip of the crack is possible and will contribute to the observed fracture energy. Increasing strain rates increase the yield stress, and thus contribute to an increase of observed fracture strengths. The small size of the effect over the broad range the eight orders of strain, rate and the anomolous behavior of Wesgo Al_2O_3 make an exact interpretation very difficult. Extension of the strain rate by two more orders of magnitude and reduction of the scatter bands might provide sufficient information to permit firm conclusions to be drawn.

B. Behavior at 1000°F

The two materials tested at 1000°F, namely Lucalox and Wesgo AL-995, display a significant increase of strength with increasing strain rate. This is as expected, since dislocation mobility is enhanced by increased temperature and increased strain rate will accordingly decrease the time available for nucleation of plastic flow in regions of high shear stress. Once again, not enough points are available to tie down a dependence other than that displayed by the straight line approximations employed in Fig. 2-10 and 2-11.

C. Behavior at 1800°F

At 1800°F. Wesgo AL-995 shows a pronounced increase of strain rate. On the other hand, Lucalox Al_2O_3 , ARF MgO and Al Beo all show a very small strain rate effect, with A_1 equalling 1510 psi, 20 psi, and 1020 psi, respectively. The only possible explanation must be based on the relative purity of Wesgo AL-995 as compared with the other materials. It is possible that impurities precipitated at the grain boundaries in the other materials have caused a mechanism change. The Kingery and Pappis⁽¹⁰⁻³⁾ data reproduced in Fig. 2-17 show a drop of impact energy for Al_2O_3 at less than 1800°F which would tend to confirm the data for Lucalox, but leaves the question of the behavior of Wesgo AL-995 unanswered. The greater purity of Wesgo AL-995 as compared to Lucalox which used up to almost 1 percent MgO addition as a grain growth inhibitor, may be offered as a hypothetical explanation for the observed effect.

It is of interest to consider the work of Folweiler⁽²⁻⁴⁾ in light of the research performed on this program. Folweiler investigated creep effects at various cross head speeds for three point bending at temperatures ranging from 2600°F to 3270°F for Al_2O_3 having average grain sizes of 7, 13 and 34 microns. The corresponding strain rates were approximately 1.7×10^{-6} to $1.7 \times 10^{-3} \text{ sec}^{-1}$.

Folweiler's results show that the stress at which the Al_2O_3 will flow is linearly related to the strain rate over a very narrow range of stress (only at low stress levels). That is, the higher the strain rate, the higher is the stress required to cause plastic flow. In addition, Folweiler found that for Al_2O_3 with a grain size of 34 microns at 2600°F the stress required to cause plastic flow exceeded the fracture stress. These results indicate that essentially brittle behavior should be observed at temperatures below 2600°F and that strain rate effects on yield should be small.

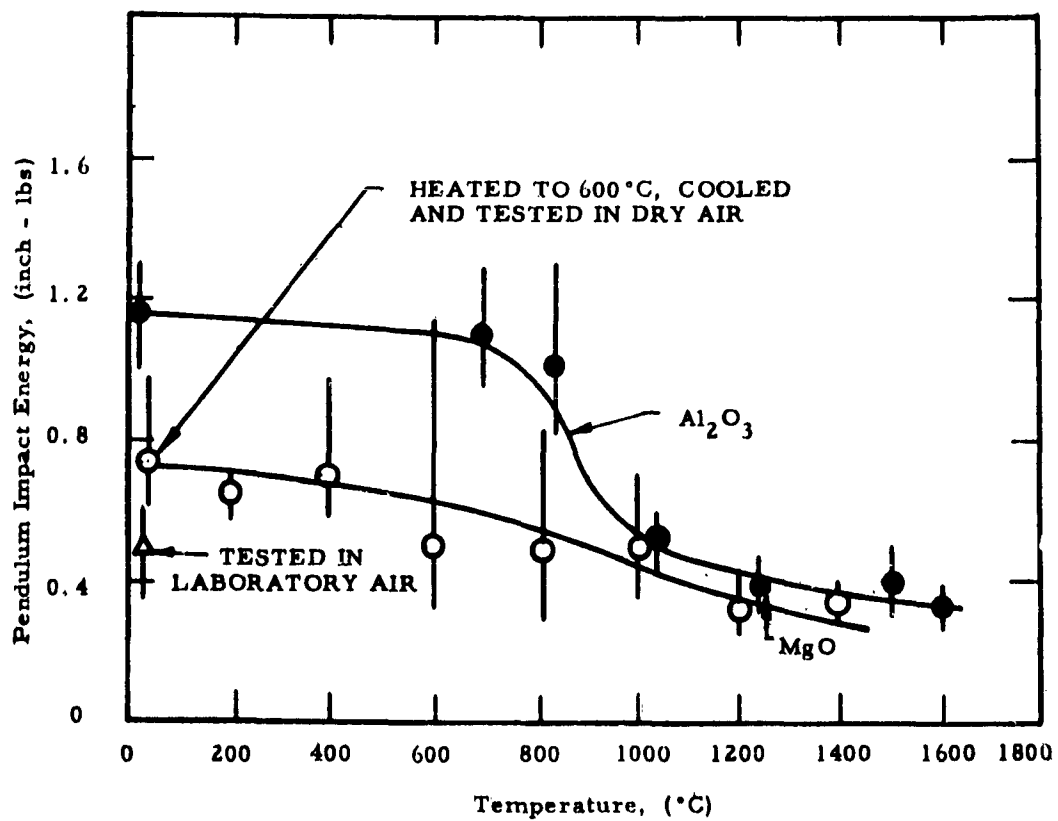


Fig. 2-17 IMPACT STRENGTH OF Al_2O_3 AND MgO

In addition, if the stress required to cause flow increases with an increasing strain rate, then a tendency toward brittle behavior should be exhibited at higher rates of strain. This behavior, however, may only become important at temperatures above 2600 °F.

In the work of Kingery and Pappis, the effect of temperature upon impact strength was studied. The work was performed on Al_2O_3 and MgO loaded as a three-point bend test, the impact load being applied by a pendulum striker. These investigators found the impact strength of Al_2O_3 to be essentially constant to about 1650 °F and then it decreased rapidly to about 30 percent of the room temperature value and thereafter remained constant to about 3000 °F. Magnesium Oxide was found to decrease slowly to about 50 percent of the room temperature value over the same temperature range. In no case did the authors notice any increase in impact strength at elevated temperatures where plastic deformation is known to occur for low strain rates. The authors suggest that the yield stress or flow stress may always be above the fracture stress for impact loadings at the temperatures considered.

In this investigation the failure strength seems to increase for Al_2O_3 at the temperatures and strain rates studied. However, additional studies are needed to reveal more information regarding the effect of strain rate on brittle materials at elevated temperatures; further work regarding completion of the experiment carried out to date, and an extension of the investigation to higher strain rates and temperatures is planned as part of the continuation work on this task.

5. PRELIMINARY INVESTIGATION OF A STRESS WAVE TECHNIQUE FOR DETERMINING THE TENSILE STRENGTH OF CERAMIC MATERIALS

A preliminary investigation of the stress wave technique was carried out during the course of the program. The purpose of this investigation was to establish the feasibility of the method for studying the effects of a uniform uniaxial state of tensile stress at very high strain rates in ceramic materials. It has been suggested that such a method of loading would provide a means for determining the ultimate tensile strength of ceramic materials if effects of strain rate on failure strength were small or negligible under these conditions. If, on the other hand, there is a strain rate effect in ceramics and if the nature of strain rate sensitivity can be established, the stress wave technique can still be used as the basic standard tension test for these materials. Such a technique also offers the opportunity to study the effects of strain rate on tensile strength in a region of strain rates substantially above that provided by ordinary testing machines and conventional impact tests.

Perhaps the most favorable aspect of the stress wave technique is the simplicity of the method coupled with the thorough background.⁽²⁻⁵⁾ A compression pulse is generated (by the explosion of a contacting pellet for example) at one end of a freely supported bar. This compression stress wave travels down the bar and is reflected as a tensile stress wave which, in turn, travels back toward the end at which the original compression pulse was generated. The phenomena of stress wave reflection at a free boundary is shown diagrammatically in Fig. 2-18.

As the tension wave is being formed at the free end during the reflection process, the tensile stress developed in the bar may exceed the tensile strength of the material; the bar will then fracture a short distance from the free end. Data collected during

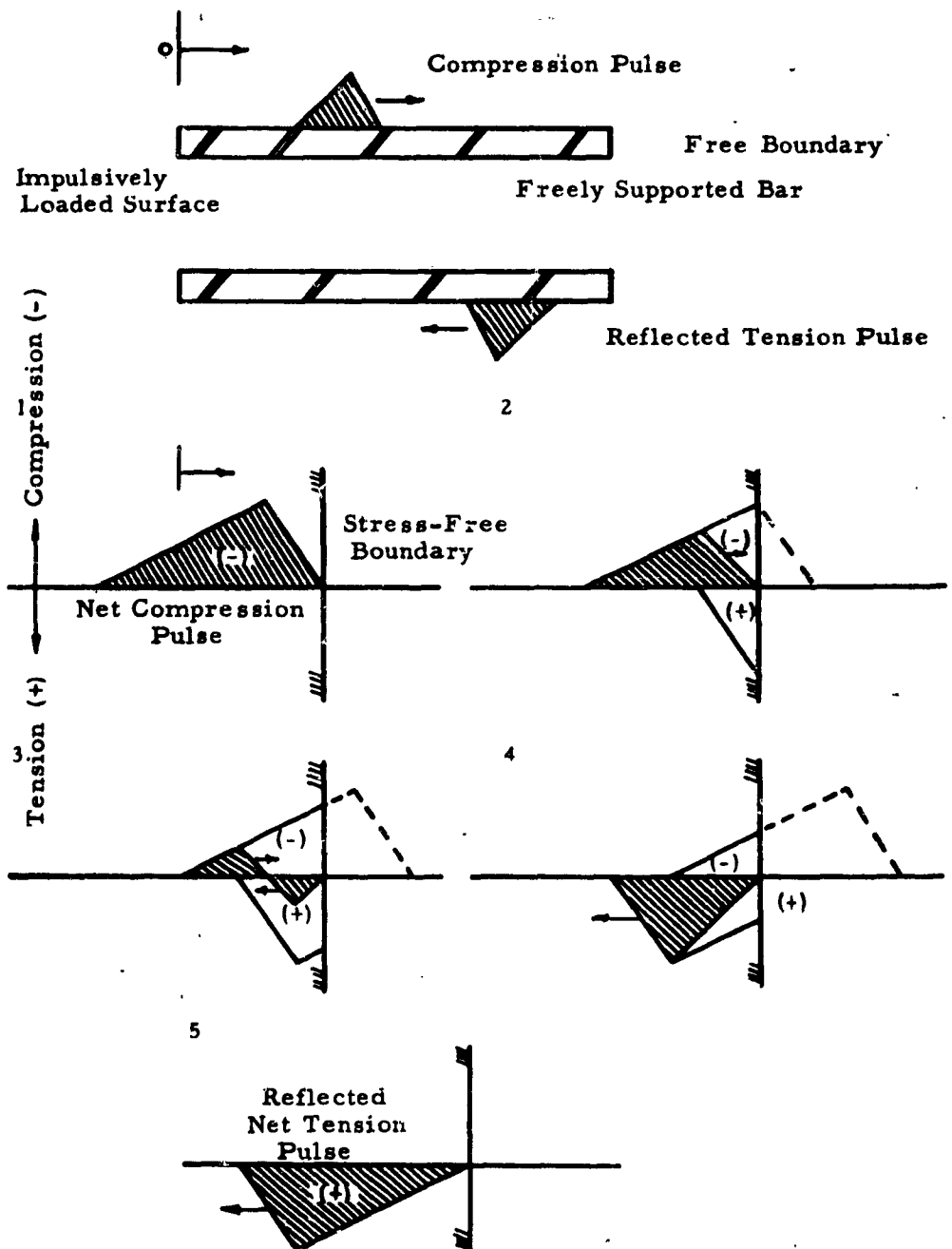


Fig. 2-18 STRESS WAVE REFLECTION AT A FREE BOUNDARY

such an experiment would indicate the strain rate, as well as the stresses and strains at the point of fracture.

Success using this technique depends upon minimizing the effects of geometrical dispersion, and pulse attenuation. Ideally, the incident and reflected waves are plane waves; this would ensure a uniform stress distribution over the entire cross section. Apparently this condition will be the case for stress wave pulse of a length of about ten times the nominal cross sectional dimensions; i. e. for pulses which are long as compared to the cross sectional dimensions of the specimen.

For cases where the dimensions of the cross section are large as compared to the length of the pulse, the phenomena of geometrical dispersion will occur. That is, a spherical wavefront will be generated and, as it travels down the bar, multiple reflection will occur from the longitudinal boundaries; these effects are then superimposed upon the principal wave thereby causing it to disperse. Needless to say, a state of pure tension cannot be obtained when the dispersion factor becomes important.

The degree of attenuation which will occur in a stress wave depends upon the material through which the pulse is being transmitted. If one considers a viscoelastic material it is possible to visualize what will happen to the pulse as it travels through the material. The strains and displacements are large upon impact stressing because the material has a low modulus of elasticity. As a result of the inherently large strains and viscoelastic behavior (loss of energy through internal friction) the pulse amplitude will be sharply reduced and the length of the pulse will be substantially increased continuously as the wave travels down the bar.

If continuous attenuation of the pulse occurs as it travels, one would have no simple means of knowing what its shape is at the failure section. However, the principle of attenuation is useful as it can be used to lengthen an incident pulse, thereby minimizing the effects of dispersion.

The pilot experiments carried out at ARF indicate quite clearly that the effects of dispersion and attenuation are minimal for Al_2O_3 . For these studies an Al_2O_3 ($1/4$ in. \times $1/4$ in. \times 4 in.) bar was provided with strain gages at two stations, one near the point of pulse generation and the other near the free end. With the use of an explosive (lead azide) a pulse was generated and monitored through the first reflection with a cathode ray oscilloscope. The results are shown in the form of inset photographs of oscilloscope traces in Fig. 2-19.

Both insets A and B show the incident and reflected pulses. Notice that both photos show a "clean" pulse for both incident and reflected conditions and these pulses are of the same length and amplitude. The pulses in A and B are not of the same size because the vertical scale calibration factors are different for the two strain gages.

The effects of dispersion are quite obviously absent, because:

- (1) both incident and reflected pulses are "clean".
- (2) both incident and reflected pulses are of the same amplitude and duration.
- (3) a crude calculation shows the pulse length to be about eight times the cross-sectional dimension.

Also the effects of attenuation are not important because both A and B show incident and reflected pulses to be of the same amplitude and duration. This would not have been the case if attenuation had occurred.

The ceramic materials therefore seem to be ideally suited for this technique and additional research is planned to perfect the technique and render it applicable as a useful tool of studying tensile fracture conditions at very high strain rates.

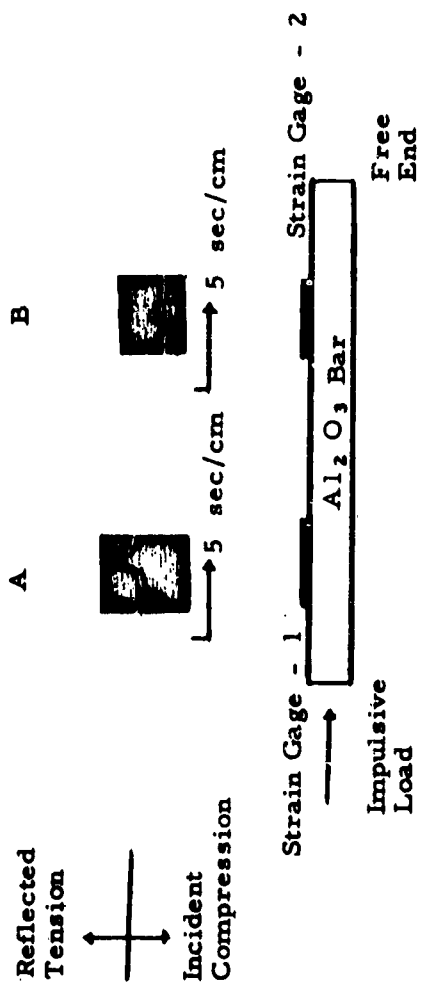


Fig. 2-19 STRAIN GAGE RECORDS OF PULSE PROPAGATION IN A POLYCRYSTALLINE Al_2O_3 BAR

6. SUMMARY

This task was organized to study the effect of strain rates upon the fracture strength of brittle ceramic oxides. Candidate materials included Al_2O_3 and MgO , to which BeO has been added at a later stage.

Work during the initial contract period concerned the development of experimental procedures for achieving uniaxial tensile loading in the brittle materials in question. Special equipment and recording techniques were developed for the range of strain rates from 10^{-7} to 10^1 sec^{-1} , but even the most refined techniques could not achieve pure uniaxiality of loading throughout the entire run of the experiment. The reason for this resides in the extreme brittleness of these materials, coupled with generally high values of Young's modulus. The maintenance of uniform tension in the specimen required a degree of concentricity of loading and straightness of the specimen which could not be achieved with current developments of the state of the art.

It was, therefore, decided to concentrate on the use of bending specimens for evaluating strain rate effects at various temperatures. The dogbone specimens in general used throughout this program were adapted for this purpose, and special end fixtures were designed which put the entire beam in a state of pure bending. The fixture, moreover, was provided with support conditions which allowed for the precise and unambiguous determination of loads (thereby stresses) and strain rates in the specimen. Furnaces which could be fitted about the existing loading equipment were constructed, capable of developing temperatures of 1000° and 1800°F with a good uniformity of thermal profiles about the gage section of the specimen. Extensive shake-down tests were carried out which proved the suitability and adequacy of the experimental apparatus and recording system over the entire range of strain rates and temperatures.

Experiments were carried out on Wesgo AL-995 and Lucalox, two specimen sizes of ARF MgO and AlBeO at room temperature for strain rates ranging from 10^{-7} to 10 sec^{-1} , eight decades of loading rates. Except for Wesgo AL-995, the results indicate a small increase of strength with strain rate at room temperature. It is hypothesized that a very small amount of dislocation mobility may support slip bond formation and plastic flow at the highly stressed areas around at the tips of propagating cracks, leading measurable plastic contribution to the surface energy and hence fracture stress. Higher loading rates normally have the effect of retarding dislocation mobility increasing the stress required to unlock dislocations from their impurity atmospheres serving as pinning points, and thereby raising the yield stress and the corresponding fracture stress. Higher temperature strain rate effects, namely at 1000°C are more significant. A similar explanation is more applicable as the increased temperature enhances dislocation mobility and thus plastic flow. The increased strength is a clear reflection of a greater resistance to slip bond formation and the development of plastic flow at increasing strain rates.

Unexplained anomalies exist at 1800°F for Lucalox, ARF MgO, and AlBeO. At this time it is not possible to advance a reasonable theory for these effects. Work on a dynamic loading technique for the attainment of a pure state of tension by use of reflective compression waves has indicated that both uniaxiality tensile loading and higher strain rates can be obtained in the extension phase of this task.

7. REFERENCES

- 2-1 Weil, N. A., Ed., Studies of the Brittle Behavior of Ceramic Materials, ASD-TR-61-628, April 1962.

- 2-2 Kingery, W. D. and Pappis, J., "Note on Failure of Ceramic Materials at Elevated Temperatures under Impact Loading", J. Am. Ceram. Soc., 39, No. 2, 64-6, (1956).
- 2-3 Folweiler, R. C., "Creep Behavior of Pore-Free Polycrystalline Aluminum Oxide", General Electric Research Laboratory, Report No. 60-RL-2590M, December 1960.
- 2-4 Washburn, J., "Mechanism of Fracture", pp. 108-128, Mechanical Behavior of Materials at Elevated Temperatures, J. E. Dorn, Ed., McGraw Hill Book Co. (New York 1961).
- 2-5 Davies, R. M., "A Critical Study of Hopkinson Pressure Bar" Roy. Soc. London Phil. Trans. 240, Series A 375 (1948).

TASK 3 - EFFECT OF NON-UNIFORM STRESS FIELDS

Principal Investigators: N. A. Weil and I. M. Daniel
Armour Research Foundation

ABSTRACT

The purpose of this program is to investigate the effect of non-uniform stress fields on the fracture characteristics of brittle materials, the principal aim being to determine whether the stress gradient existing at the location of fracture initiation has an independent effect upon the fracture strength.

To interpret experimental observations, extensive theoretical derivations were carried out for the risk of rupture of bend specimens based upon assumptions of the Weibull theory. This resulted in complete formulations for the probability of fracture of a prismatic beam subjected to a symmetrical four-point loading of arbitrary spacing, based upon either volumetrically dispersed or surface distributed flaw conditions. An analytical iteration procedure, aimed at determining the unique "best" set of material parameters by a computer solution was worked out; this method, however, failed to work in practice, possibly because of the many potential "best" set of answers that the solution may converge to.

Experiments were completed on Wesgo AL-995 at 20 °C and 1000 °C, and BeO at 20 °C, on prismatic beams having a nearly two-fold variation of extreme stress gradients. For this range, no effect of the stress gradient upon mean fracture strength or standard deviation could be discerned. Furthermore, fracture for these materials, using specimens with ground surfaces only, was found to be governed solely by a volumetric flaw distribution condition; the fortuitous and accidental mutual cancellation of superposed stress gradient and surface flaw effects must be ruled out on the basis of extensive experimental evidence already obtained.

TASK 3 - EFFECT OF NON-UNIFORM STRESS FIELDS

1. INTRODUCTION

The objective of this task was to determine the influence of non-uniform stress fields upon the fracture characteristics of brittle materials. The materials investigated during this phase of the program were Columbia Resin, polycrystalline Al_2O_3 , MgO , and BeO .

The simplest descriptor of stress distribution non-uniformity is the stress gradient, or the rate of change of the peak boundary stress along a line normal to the boundary. A specific objective, therefore, was to determine whether the stress gradient has an independent effect on the fracture stress.

The past research period⁽³⁻¹⁾ was primarily devoted to the development of experimental procedures and to the design, selection, and evaluation of specimens giving known stress gradients. A wide range of stress gradients was covered by using tensile, pure bending, ring- and theta-shaped specimens. It was known that in cases of complicated stress distributions, such as that in the ring specimens tested, a stress gradient along one line was not sufficient to describe the effective stress distribution. For this reason, a second parameter connected with stress distribution was introduced, notably the effective size or volume under high tensile stress. It was not possible, however, to segregate the effects of stress gradient from those corresponding to the effective size of the highly loaded region of the specimen.

The underlying theory used in this work is the statistical theory of failure based on the weakest link concept and using the Weibull distribution function.⁽³⁻²⁾ This theory uses two basic failure criteria, size and normal tensile stress; within the validity of these postulates it is capable of describing failure for any type of stress distribution, uniform or non-uniform, uniaxial or polyaxial.

Failure characteristics are described in terms of three material parameters, the zero (probability) strength, a flaw density exponent and a scale parameter. In practice, these parameters would be determined first from a simple test and the results would be applied to predict the probability of fracture of a given structural component of the same material.

The specific objective of this task is also equivalent to the investigation of the adequacy of the Weibull theory for predicting failure under conditions of non-uniform stress distribution. This is accomplished by comparing experimental results for specimens having various stress gradients but the same risk of rupture according to the theory. Another aspect of the investigation was to establish whether failure in the materials tested is governed by a volumetric or surface flaw distribution, and to establish procedures for determination of the corresponding material parameters.

These objectives were pursued by testing the simplest type of specimen, a prismatic beam under pure bending, since for this specimen the predictions of the Weibull theory are mathematically derivable and the stress distribution can be fully described by a stress gradient.

To understand the predictions of the theory and select suitable prismatic specimens, theoretical expressions were derived for the risk of rupture of prismatic beams under three- and four-point loading. This was done for materials whose failure is governed by volumetric and surface flaw distributions. Methods for the determination of material parameters were investigated. An analytical method, requiring the solution of a system of three equations, was presented. However, this system proved to be unwieldy, even for the computer. As a result recourse was made to the trial-and-error graphical method originally introduced by Weibull⁽³⁻³⁾ for the evaluation of material constants.

Prismatic specimens of different stress gradients but with identical risks of rupture (or effective size) were selected and tested under four-point loading. Materials used were Columbia Resin (CR-39), Wesgo Al_2O_3 (AL-995), MgO, and BeO. Results indicate that no stress gradient effect upon the mean failure stress and standard deviation exists. They also tend to show a volumetric flaw distribution rather than a surface one.

2. APPLICATION OF WEIBULL'S THEORY TO BENDING SPECIMENS

A. Risk of Rupture

The statistical theory of failure based on the Weibull distribution function uses two basic criteria of failure; size and tensile stress. Within the validity of these postulates and normal is capable of describing failure for any type of stress distribution, uniform or non-uniform, uniaxial or polyaxial. For a uniaxial stress field the probability of fracture in a material governed by volumetric flaw distribution is given by

$$S = \begin{cases} 1 - \exp \left[- \int_V \left(\frac{\sigma - \sigma_u}{\sigma_o} \right)^m dv \right] & \sigma \geq \sigma_u \\ 0 & \sigma < \sigma_u \end{cases} \quad (3-1)$$

where

$$B = \int_V \left(\frac{\sigma - \sigma_u}{\sigma_o} \right)^m dv = \text{risk of rupture} \quad (3-2)$$

and

σ_u is the zero probability strength (location parameter),
 m is the flaw density exponent (shape parameter), and
 σ_o is the scale parameter.

The last three parameters are associated with the material.

The mean failure stress is given by

$$\sigma_m = \sigma_u + \int_{\sigma_u}^{\infty} e^{-B} d\sigma, \quad (3-3)$$

and the variance by

$$a^2 = \sigma_u^2 + \int_{\sigma_u^2}^{\infty} e^{-B} d(\sigma^2) - \sigma_m^2. \quad (3-4)$$

From Eq. 3-1, it is seen that the theory does not make any special allowance for the non-uniformity of stress distribution. Each infinitesimal element of a specimen is considered to be under uniform tensile stress and the risk of rupture for the whole specimen is obtained by integrating the risk of rupture of each infinitesimal element over the volume of the specimen. The stress gradient does not enter as an independent parameter and all the non-uniformity effects seem to be accounted for by the risk of rupture. The question of whether the stress gradient has an independent effect on fracture stress is equivalent to the question of whether the Weibull theory is sufficient to predict failure for non-uniform stress fields.

In a material governed by surface flaw distribution, the risk of rupture is

$$B = \int_A \left(\frac{\sigma - \sigma_u}{\sigma_o} \right)^m dA. \quad (3-5)$$

To establish the dependence of the risk of rupture on the dimensions of a specimen, and to reach some conclusions regarding the validity of predictions of the Weibull theory, the risk of rupture was calculated for a general case of a prismatic beam under four-point loading. Derivations were made for both cases of volumetric and surface flaw distribution.

Material Governed by Volumetric Flaw Distribution

Case 1: $\sigma_u \neq 0$

The distribution of tensile stresses in the beam shown in Fig. 3-1 is

$$\begin{aligned}\sigma &= \frac{2k \sigma_b}{h L} yx \text{ for } 0 \leq x \leq \frac{L}{k} \text{ and } \left(1 - \frac{1}{k}\right)L \leq x \leq L \\ \sigma &= \frac{2\sigma_b}{h} y \text{ for } \frac{L}{k} \leq x \leq \left(1 - \frac{1}{k}\right)L.\end{aligned}\quad (3-6)$$

The risk of rupture is

$$B_b = B'_b + B''_b, \quad (3-7)$$

where B'_b corresponds to the central portion of the specimen subjected to uniform bending and B''_b refers to the outer portions. It can be shown that

$$\begin{aligned}B'_b &= bL \left(1 - \frac{2}{k}\right) \int_{y_u}^{h/2} \left(\frac{\frac{2\sigma_b}{h} y - \sigma_u}{\sigma_o}\right)^m dy = \\ &= \frac{V \left(1 - \frac{2}{k}\right)}{2(m+1)} \left(1 - \frac{\sigma_u}{\sigma_b}\right) \left(\frac{\sigma_b - \sigma_u}{\sigma_o}\right)^m, \quad (3-8)\end{aligned}$$

where

$$y_u = \frac{h}{2} \frac{\sigma_u}{\sigma_b}$$

and

$$\begin{aligned}B''_b &= 2b \int_x^{\frac{L}{k}} \int_{y_u}^{h/2} \left(\frac{\frac{2k\sigma_b}{hL} yx - \sigma_u}{\sigma_o}\right)^m dy dx, \\ B''_b &= \frac{2 b h L}{2(m+1) k \sigma_b \sigma_o^m} \int_{y_u}^{h/2} \frac{1}{y} \left(\frac{2\sigma_b}{h} y - \sigma_u\right)^{m+1} dy \quad (3-9)\end{aligned}$$

where

$$x = \frac{\sigma_u}{\sigma_b} \frac{h}{2} \frac{L}{ky} = \frac{y_u}{y} \frac{L}{k}$$

For the case where m has an arbitrary (non-integer) value, let $m = [m] + a$, where $[m]$ is the largest integer less than or equal to m ; then after some mathematical manipulation, the integral of Eq. 3-9 can be shown to have the value

$$\int_{y_u}^{h/2} \frac{1}{y} \left(\frac{2\sigma_b}{h} y - \sigma_u \right)^{m+1} dy = \sum_{r=0}^{[m]} \frac{(-\sigma_u)^r}{m+1-r} (\sigma_b - \sigma_u)^{m+1-r} + (-\sigma_u)^{[m]+1} \int_a \quad (3-10)$$

where

$$\int_a = \int_{y_u}^{h/2} \frac{1}{y} \left(\frac{2\sigma_b}{h} y - \sigma_u \right)^a dy. \quad (3-11)$$

By substitution of Eq. 3-10 and 3-11 into Eq. 3-9,

$$B''_b = \frac{V}{2(m+1)} \left(1 - \frac{\sigma_u}{\sigma_b} \right) \left(\frac{\sigma_b - \sigma_u}{\sigma_o} \right)^m \sum + \frac{V}{k(m+1)\sigma_b\sigma_o^m} (-\sigma_u)^{[m]+1} \int_a \quad (3-12)$$

where

$$\sum = \sum_{r=0}^{[m]} \frac{1}{m+1-r} \left(1 - \frac{\sigma_b}{\sigma_u} \right)^{-r}$$

Finally, by Eq. 3-7, we obtain

$$B_b = \frac{V}{2(m+1)} \left(1 - \frac{\sigma_u}{\sigma_b} \right) \left(\frac{\sigma_b - \sigma_u}{\sigma_o} \right)^m \left[1 - \frac{2}{k} + \frac{2}{k} \sum \right] + \frac{V}{k(m+1)\sigma_b\sigma_o^m} (-\sigma_u)^{[m]+1} \int_a \quad (3-13)$$

If m is an integer, i. e. if $m = [m]$ and $a = 0$, Eq. 3-13 reduces to

$$B_b = \frac{V}{2(m+1)} \left(1 - \frac{\sigma_u}{\sigma_b}\right) \left(\frac{\sigma_b - \sigma_u}{\sigma_o}\right)^m \left[1 - \frac{2}{k} + \frac{2}{k} \sum\right] \quad (3-14)$$

$$+ \frac{V}{k(m+1) \sigma_b \sigma_o^m} (-\sigma_u)^{m+1} \ln \frac{h}{2y_u}.$$

Special forms of this formula can be obtained by assigning values to the parameter k . The following special cases are of interest.

Pure Bending ($k = \infty$)

$$B_b = \frac{V}{2(m+1)} \left(1 - \frac{\sigma_u}{\sigma_b}\right) \left(\frac{\sigma_b - \sigma_u}{\sigma_o}\right)^m \quad (3-15)$$

Quadrant - Point Loading ($k = 4$)

$$B_b = \frac{V}{4(m+1)} \left(1 - \frac{\sigma_u}{\sigma_b}\right) \left(\frac{\sigma_b - \sigma_u}{\sigma_o}\right)^m \left[1 + \sum\right] \quad (3-16)$$

$$+ \frac{V}{4(m+1) \sigma_b \sigma_o^m} (-\sigma_u)^{m+1} \log \frac{h}{2y_u}$$

Third - Point Loading ($k = 3$)

$$B_b = \frac{V}{6(m+1)} \left(1 - \frac{\sigma_u}{\sigma_b}\right) \left(\frac{\sigma_b - \sigma_u}{\sigma_o}\right)^m \left[1 + 2 \sum\right] \quad (3-17)$$

$$+ \frac{V}{3(m+1) \sigma_b \sigma_o^m} (-\sigma_u)^{m+1} \ln \frac{h}{2y_u}$$

Three-Point Loading (Center-Point Loading; $k = 2$)

$$B_b = \frac{V}{2(m+1)} \left(1 - \frac{\sigma_u}{\sigma_b}\right) \left(\frac{\sigma_b - \sigma_u}{\sigma_o}\right)^m \sum \quad (3-18)$$

$$+ \frac{V}{2(m+1) \sigma_b \sigma_o^m} (-\sigma_u)^{m+1} \ln \frac{h}{2y_u}$$

Case 2: $\sigma_u = 0$

When $\sigma_u = 0$, both Eq. 3-13 and 3-14 reduce to

$$B_b = \frac{V}{2(m+1)} \left(\frac{\sigma_b}{\sigma_o} \right)^m \frac{k(m+1) - 2m}{k(m+1)}. \quad (3-19)$$

Again, we list below some typical cases of interest for specific values of k .

Pure Bending ($k = \infty$)

$$B_b = \frac{V}{2(m+1)} \left(\frac{\sigma_b}{\sigma_o} \right)^m \quad (3-20)$$

Quadrant-Point Loading ($k = 4$)

$$B_b = \frac{V}{2(m+1)} \left(\frac{\sigma_b}{\sigma_o} \right)^m \frac{m+2}{m+1} \quad (3-21)$$

Third-Point Loading ($k = 3$)

$$B_b = \frac{V}{6(m+1)} \left(\frac{\sigma_b}{\sigma_o} \right)^m \frac{m+3}{m+1} \quad (3-22)$$

Three-Point Loading (Center-Point Loading; $k = 2$)

$$B_b = \frac{V}{2(m+1)} \left(\frac{\sigma_b}{\sigma_o} \right)^m \frac{1}{m+1} \quad (3-23)$$

Material Governed by Surface Flaw Distribution

Case 1: $\sigma_u \neq 0$

For the same stress distribution described by Eq. 3-6 we have

$$\begin{aligned} B_b &= B'_b + B''_b \\ B'_b &= 2\left(1 - \frac{2}{k}\right) L \int_{y_u}^{h/2} \left(\frac{\frac{2\sigma_b}{h} y - \sigma_u}{\sigma_o} \right)^m dy + \left(1 - \frac{2}{k}\right) L b \left(\frac{\sigma_b - \sigma_u}{\sigma_o} \right)^m \\ &= \left(1 - \frac{2}{k}\right) L \left(\frac{\sigma_b - \sigma_u}{\sigma_o} \right)^m \left[\frac{h}{m+1} \left(1 - \frac{\sigma_u}{\sigma_b}\right) + b \right] \end{aligned} \quad (3-24)$$

and

$$\begin{aligned}
 B''_b &= 4 \int_x^{L/k} \int_{y_u}^{h/2} \left(\frac{2k\sigma_b}{hL} yx - \sigma_u \right)^m \frac{dydx}{\sigma_o} \\
 &+ 2b \int_{x_u}^{L/k} \left(\frac{k\sigma_b}{L} x - \sigma_u \right)^m dx \\
 &= \frac{4hL}{2k(m+1)\sigma_b\sigma_o^m} \int_{y_u}^{h/2} \frac{1}{y} \left(\frac{2\sigma_b}{h} y - \sigma_u \right)^{m+1} dy \\
 &+ \frac{2bL}{k(m+1)\sigma_b\sigma_o^m} (\sigma_b - \sigma_u)^{m+1}
 \end{aligned} \tag{3-25}$$

where

$$x_u = \frac{\sigma_u}{\sigma_b} \frac{L}{k}.$$

Then,

$$\begin{aligned}
 B_b &= \frac{L}{m+1} \left(1 - \frac{\sigma_u}{\sigma_b} \right) \left(\frac{\sigma_b - \sigma_u}{\sigma_o} \right)^m \left[\left(1 - \frac{2}{k} \right) h + \frac{2h}{k} \sum + \frac{2b}{k} \right] \\
 &+ \left(1 - \frac{2}{k} \right) \left(\frac{\sigma_b - \sigma_u}{\sigma_o} \right)^m Lb \\
 &+ \frac{2hL}{k(m+1)\sigma_b\sigma_o^m} (-\sigma_u)^{[m]+1} \Big|_a.
 \end{aligned} \tag{3-26}$$

If m is an integer, Eq. 3-26 reduces to

$$\begin{aligned}
 B_b &= \frac{L}{m+1} \left(1 - \frac{\sigma_u}{\sigma_b} \right) \left(\frac{\sigma_b - \sigma_u}{\sigma_o} \right)^m \left[\left(1 - \frac{2}{k} \right) h + \frac{2h}{k} \sum + \frac{2b}{k} \right] \\
 &+ \left(1 - \frac{2}{k} \right) \left(\frac{\sigma_b - \sigma_u}{\sigma_o} \right)^m Lb + \frac{2hL}{k(m+1)\sigma_b\sigma_o^m} (-\sigma_u)^{m+1} \ln \frac{h}{2y_u}
 \end{aligned} \tag{3-27}$$

Here again, it is of interest to list the same special cases mentioned previously.

Pure Bending ($k = \infty$)

$$B_b = L \left(\frac{\sigma_b - \sigma_u}{\sigma_o} \right)^m \left[\frac{h}{m+1} \left(1 - \frac{\sigma_u}{\sigma_b} \right) + b \right] \quad (3-28)$$

Quadrant-Point Loading ($k = 4$)

$$B_b = \frac{L}{m+1} \left(1 - \frac{\sigma_u}{\sigma_b} \right) \left(\frac{\sigma_b - \sigma_u}{\sigma_o} \right)^m \left[\frac{h}{2} + \frac{h}{2} \sum + \frac{b}{2} \right] \\ + \frac{1}{2} \left(\frac{\sigma_b - \sigma_u}{\sigma_o} \right)^m L b + \frac{2 h L}{4(m+1) \sigma_b \sigma_o^m} (-\sigma_u)^{m+1} \ln \frac{h}{2 y_u} \quad (3-29)$$

Third-Point Loading ($k = 3$)

$$B_b = \frac{L}{m+1} \left(1 - \frac{\sigma_u}{\sigma_b} \right) \left(\frac{\sigma_b - \sigma_u}{\sigma_o} \right)^m \left[\frac{h}{3} + \frac{2h}{3} \sum + \frac{2b}{3} \right] \\ + \frac{1}{3} \left(\frac{\sigma_b - \sigma_u}{\sigma_o} \right)^m L b + \frac{2 h L}{3(m+1) \sigma_b \sigma_o^m} (-\sigma_u)^{m+1} \ln \frac{h}{2 y_u} \quad (3-30)$$

Three-Point Loading (Center-Point Loading; $k = 2$)

$$B_b = \frac{L}{m+1} \left(1 - \frac{\sigma_u}{\sigma_b} \right) \left(\frac{\sigma_b - \sigma_u}{\sigma_o} \right)^m \left(h \sum + b \right) \\ + \frac{2 h L}{2(m+1) \sigma_b \sigma_o^m} (-\sigma_u)^{m+1} \ln \frac{h}{2 y_u} \quad (3-31)$$

Case 2: $\sigma_u = 0$

When $\sigma_u = 0$, both Eq. 3-26 and 3-27 reduce to

$$B_b = L \left(\frac{\sigma_b}{\sigma_o} \right)^m \left(\frac{h}{m+1} + b \right) \frac{k(m+1) - 2m}{k(m+1)} \quad (3-32)$$

For the specific values of k considered above, Eq. 3-32 yields:

Pure Bending ($k = \infty$)

$$B_b = L \left(\frac{\sigma_b}{\sigma_o} \right)^m \left(\frac{h}{m+1} + b \right) \quad (3-33)$$

Quadrant Point Loading ($k = 4$)

$$B_b = L \left(\frac{\sigma_b}{\sigma_o} \right)^m \left(\frac{h}{m+1} + b \right) \frac{m+2}{2(m+1)} \quad (3-34)$$

Third-Point Loading ($k = 3$)

$$B_b = L \left(\frac{\sigma_b}{\sigma_o} \right)^m \left(\frac{h}{m+1} + b \right) \frac{m+3}{3(m+1)} \quad (3-35)$$

Three-Point Loading (Center-Point Loading; $k = 2$)

$$B_b = L \left(\frac{\sigma_b}{\sigma_o} \right)^m \left(\frac{h}{m+1} + b \right) \frac{1}{m+1} \quad (3-36)$$

B. Relationship between Bending and Tensile Strengths

For a material governed by a volumetric flaw distribution, the risk of rupture in a tensile specimen is

$$B_t = V_t \left(\frac{\sigma_t - \sigma_u}{\sigma_o} \right)^m, \quad (3-37)$$

where V_t is the volume of the specimen. For a prismatic specimen under pure bending the risk of rupture is

$$B_b = \frac{V_b}{2(m+1)} \left(1 - \frac{\sigma_u}{\sigma_b} \right) \left(\frac{\sigma_b - \sigma_u}{\sigma_o} \right)^m. \quad (3-15 bis)$$

To compare mean failure stresses the risks of rupture given above must be substituted into Eq. 3-3 in order to compute σ_m for the two cases. However, this is quite involved for the case of pure bending, since for this loading case Eq. 3-3 does

not yield a closed form expression. A comparison of median failure stresses or, for that matter, any stresses of a given probability of fracture, is easily carried out by equating instead the risks of rupture corresponding to the different loading conditions.

$$V_t \left(\frac{\sigma_t - \sigma_u}{\sigma_o} \right)^m = \frac{V_b}{2(m+1)} \left(1 - \frac{\sigma_u}{\sigma_b} \right) \left(\frac{\sigma_b - \sigma_u}{\sigma_o} \right)^m$$

from which

$$\frac{\sigma_t - \sigma_u}{\sigma_b - \sigma_u} = \left[\frac{1}{2(m+1)} \frac{V_b}{V_t} \left(1 - \frac{\sigma_u}{\sigma_b} \right) \right]^{\frac{1}{m}}$$

or

$$\frac{\sigma_t}{\sigma_b} = \left[\frac{1}{2(m+1)} \frac{V_b}{V_t} \right]^{\frac{1}{m}} \left(1 - \frac{\sigma_u}{\sigma_b} \right)^{1 + \frac{1}{m}} + \frac{\sigma_u}{\sigma_b}. \quad (3-38)$$

For $\sigma_u = 0$, this expression reduces to

$$\frac{\sigma_t}{\sigma_b} = \left[\frac{1}{2(m+1)} \cdot \frac{V_b}{V_t} \right]^{\frac{1}{m}}. \quad (3-39)$$

In this case the relationship between median stresses is the same as that between mean stresses as can be shown easily. In the case of a classical material ($m = \infty$) Eq. 3-38 yields

$$\sigma_t = \sigma_b = \sigma_u.$$

For a material governed by surface flaw distribution, the risk of rupture in a tensile specimen of rectangular cross section ($b \times h$) is

$$B_t = 2 L (b + h) \left(\frac{\sigma_t - \sigma_u}{\sigma_o} \right)^m \quad (3-40)$$

For a prismatic specimen of the same dimensions under pure bending the risk of rupture is

$$B_b = L \left(\frac{\sigma_b - \sigma_u}{\sigma_o} \right)^m \left[\frac{h}{m+1} \left(1 - \frac{\sigma_u}{\sigma_b} \right) + b \right]. \quad (3-28)$$

not yield a closed form expression. A comparison of median failure stresses or, for that matter, any stresses of a given probability of fracture, is easily carried out by equating instead the risks of rupture corresponding to the different loading conditions.

$$V_t \left(\frac{\sigma_t - \sigma_u}{\sigma_o} \right)^m = \frac{V_b}{2(m+1)} \left(1 - \frac{\sigma_u}{\sigma_b} \right) \left(\frac{\sigma_b - \sigma_u}{\sigma_o} \right)^m$$

from which

$$\frac{\sigma_t - \sigma_u}{\sigma_b - \sigma_u} = \left[\frac{1}{2(m+1)} \frac{V_b}{V_t} \left(1 - \frac{\sigma_u}{\sigma_b} \right) \right]^{\frac{1}{m}}$$

or

$$\frac{\sigma_t}{\sigma_b} = \left[\frac{1}{2(m+1)} \frac{V_b}{V_t} \right]^{\frac{1}{m}} \left(1 - \frac{\sigma_u}{\sigma_b} \right)^{1 + \frac{1}{m}} + \frac{\sigma_u}{\sigma_b}. \quad (3-38)$$

For $\sigma_u = 0$, this expression reduces to

$$\frac{\sigma_t}{\sigma_b} = \left[\frac{1}{2(m+1)} \frac{V_b}{V_t} \right]^{1/m}. \quad (3-39)$$

In this case the relationship between median stresses is the same as that between mean stresses as can be shown easily. In the case of a classical material ($m = \infty$) Eq. 3-38 yields

$$\sigma_t = \sigma_b = \sigma_u.$$

For a material governed by surface flaw distribution, the risk of rupture in a tensile specimen of rectangular cross section ($b \times h$) is

$$B_t = 2 L (b + h) \left(\frac{\sigma_t - \sigma_u}{\sigma_o} \right)^m \quad (3-40)$$

For a prismatic specimen of the same dimensions under pure bending the risk of rupture is

$$B_b = L \left(\frac{\sigma_b - \sigma_u}{\sigma_o} \right)^m \left[\frac{h}{m+1} \left(1 - \frac{\sigma_u}{\sigma_b} \right) + b \right]. \quad (3-28)$$

Equating risks of rupture we obtain the relation:

$$\frac{\sigma_t}{\sigma_b} = \left[\frac{(m+1) \frac{b}{h} + \left(1 - \frac{\sigma_u}{\sigma_b}\right)}{2(m+1) \left(1 + \frac{b}{h}\right)} \right]^{\frac{1}{m}} \left(1 - \frac{\sigma_u}{\sigma_b}\right) + \frac{\sigma_u}{\sigma_b} \quad (3-41)$$

which, for $\sigma_u = 0$, reduces to

$$\frac{\sigma_t}{\sigma_b} = \left[\frac{(m+1) \frac{b}{h} + 1}{2(m+1) \left(1 + \frac{b}{h}\right)} \right]^{1/m} \quad (3-42)$$

C. Conclusion

From Eq. 3-13 it is seen that for materials whose fracture is governed by a volumetric flaw-density distribution, the only form in which the dimensions of the specimen enter the expression for the risk of rupture is their product giving rise to the total volume, V . An independent variation of length, width, and depth of specimen without a change in volume does not affect the risk of rupture and, therefore, the latter is independent of stress gradient.

The dependence of the risk of rupture on specimen dimensions is more complicated for the case of a material governed by a surface flaw distribution. For a given material σ_o , σ_u and m are constants. If one is, therefore, interested solely in the effect of depth and width upon the risk of rupture, h and b should be regarded as the only variables, while the length, L , and extreme fiber stress, σ_b , should be kept constant. Then, the risk of rupture for a pure bending specimen (Eq. 3-28) remains constant provided b and h satisfy the relationship

$$\frac{h}{m+1} \left(1 - \frac{\sigma_u}{\sigma_b}\right) + b = \text{constant.}$$

Substituting now $h = \frac{2\sigma_b}{g}$, where g is the stress gradient, there results

$$\frac{2\sigma_b}{g(m+1)} \left(1 - \frac{\sigma_u}{\sigma_b} \right) + b = \text{constant},$$

or

$$\frac{K_1}{g} + b = K \quad (3-43)$$

where

$$K_1 = \frac{2}{m+1} (\sigma_b - \sigma_u)$$

$K = \text{constant}.$

From Eq. 3-43 it follows that it is possible to vary the stress gradient without affecting the risk of rupture, provided the width b varies in such a manner that Eq. 3-43 is satisfied. This correlation involves the stress level σ_b . Given a stress σ_b it is possible to design specimens with different gradients but with the same risk of rupture or probability of failure at that stress.

The above derivation and resulting expressions make it clear that in this investigation strong preference should be given materials whose fracture initiation is governed solely by a volumetric flaw distribution. Materials with fracture governed exclusively by surface flaw distribution would complicate the investigation of stress gradient effects and should be avoided if possible. Materials governed partly by volumetric flaw distribution and partly by surface flaw distribution are unsuitable for the current investigation.

Further simplification would result if a material governed by volumetric flaw distribution is also characterized by $\sigma_u = 0$. Then, any type of bending test would be suitable for the determination of material parameters.

If $\sigma_u \neq 0$, material parameters can be uniquely determined only from a tensile or a pure bending test. This means that for four-point loading the loads should be as close to the supports as practicable, yet without incurring the risk of causing shear failures to develop next to the support points. In any case, only fractures occurring in the portion of the beam under constant bending moment should be regarded as being valid, and all tests resulting in fracture in the outer portions of the span (between supports and loading points) should be discarded from the statistical appraisal and evaluation of test results.

3. ANALYTICAL DETERMINATION OF MATERIAL PARAMETERS

For a specimen of a given material and geometry subjected to a given loading the probability of fracture at a given stress is expressed theoretically as a function of specimen geometry and material parameters. In practice, a number of specimens is tested and a value of the probability of fracture determined for the failure stress of each specimen. The problem, then, is to find those values of the material parameters which make the theoretical curve of probability of fracture fit the experimental points best. As before, we distinguish two types of materials, one for which the mode of failure is governed by volumetric and the other by surface flaw distribution.

A. Material Governed by Volumetric Flaw Distribution

The risk of rupture at a given stress, σ_n , of a prismatic specimen under pure bending is

$$B_n = \frac{V}{2(m+1)} \left(1 - \frac{\sigma_u}{\sigma_n}\right) \left(\frac{\sigma_n - \sigma_u}{\sigma_o}\right)^m \quad (3-44)$$

where,

V is gage volume of specimen,

σ_u is zero probability strength (location parameter),

m is flaw density exponent (shape parameter), and

σ_o is scale parameter.

The probability of fracture at the stress σ_n is

$$S_n = 1 - e^{-B_n}, \quad (3-45)$$

from which one can obtain

$$\begin{aligned} y_n = \ln \ln \frac{1}{1 - S_n} &= \ln B_n = \ln \frac{V}{2} - \ln(m+1) + (m+1) \ln(\sigma_n - \sigma_u) \\ &\quad - \ln \sigma_n - m \ln \sigma_o. \end{aligned} \quad (3-46)$$

The corresponding (estimated) value of this function of probability of fracture obtained experimentally is

$$Y_n = \ln \ln \frac{N+1}{N+1-n} \quad (3-47)$$

where

N is total number of specimens tested, and

n is the serial number of specimen (when specimens are ordered according to increasing failure stress σ_n).

According to the method of least squares, the curve of Eq. 3-46 will fit best the experimental points of Eq. 3-47 when

$$\sum_{n=1}^N (Y_n - y_n)^2 = \text{minimum}. \quad (3-48)$$

The necessary conditions for the existence of this minimum are

$$\begin{aligned}
 \sum_{n=1}^N (Y_n - y_n) \frac{\partial y_n}{\partial \sigma_u} &= 0 \\
 \sum_{n=1}^N (Y_n - y_n) \frac{\partial y_n}{\partial \sigma_o} &= 0 \\
 \sum_{n=1}^N (Y_n - y_n) \frac{\partial y_n}{\partial m} &= 0
 \end{aligned} \tag{3-49}$$

or,

$$\begin{aligned}
 \sum_{n=1}^N \left[\ell_n \ell_n \frac{N+1}{N+1-n} - \ell_n B_n \right] \frac{m+1}{\sigma_n - \sigma_u} &= 0 \\
 \sum_{n=1}^N \left[\ell_n \ell_n \frac{N+1}{N+1-n} - \ell_n B_n \right] \frac{m}{\sigma_o} &= 0 \\
 \sum_{n=1}^N \left[\ell_n \ell_n \frac{N+1}{N+1-n} - \ell_n B_n \right] \left[\frac{1}{m+1} - \ell_n \frac{\sigma_n - \sigma_u}{\sigma_o} \right] &= 0;
 \end{aligned}$$

which reduce to

$$\begin{aligned}
 \sum_{n=1}^N \left[\ell_n \ell_n \frac{N+1}{N+1-n} - \ell_n B_n \right] \frac{1}{\sigma_n - \sigma_u} &= 0 \\
 \sum_{n=1}^N \left[\ell_n \ell_n \frac{N+1}{N+1-n} - \ell_n B_n \right] &= 0 \\
 \sum_{n=1}^N \left[\ell_n \ell_n \frac{N+1}{N+1-n} - \ell_n B_n \right] \ell_n \left(\frac{\sigma_n - \sigma_u}{\sigma_o} \right) &= 0.
 \end{aligned} \tag{3-50}$$

B. Material Governed by Surface Flaw Distribution

The risk of rupture at a given stress, σ_n , of a prismatic specimen under pure bending is

$$B_n = L \left(\frac{\sigma_n - \sigma_u}{\sigma_o} \right)^m \left[\frac{h}{m+1} \left(1 - \frac{\sigma_u}{\sigma_n} \right) + b \right], \quad (3-51)$$

where,

L is gage length of specimen,

b is width, and

h is depth.

A theoretical relation between the probability of fracture, S_n , and the corresponding failure stress, σ_n , is

$$y_n = \ln \ln \frac{1}{1 - S_n} = \ln B_n = \ln L + m \ln (\sigma_n - \sigma_u) - m \ln \sigma_o + \ln \left[\frac{h}{m+1} \left(1 - \frac{\sigma_u}{\sigma_n} \right) + b \right]. \quad (3-52)$$

The corresponding experimental value is

$$Y_n = \ln \ln \frac{N+1}{N+1-n}. \quad (3-53)$$

Application of the least squares method yields Eq. 3-49, which in the present case can be written as

$$\begin{aligned} \sum_{n=1}^N \left[\ln \ln \frac{N+1}{N+1-n} - \ln B_n \right] \left[\frac{m}{\sigma_n - \sigma_u} + \frac{h}{\left[\frac{h}{m+1} \left(1 - \frac{\sigma_u}{\sigma_n} \right) + b \right] (m+1) \sigma_n} \right] &= 0 \\ \sum_{n=1}^N \left[\ln \ln \frac{N+1}{N+1-n} - \ln B_n \right] &= 0 \\ \sum_{n=1}^N \left[\ln \ln \frac{N+1}{N+1-n} - \ln B_n \right] \left[\frac{h \left(1 - \frac{\sigma_u}{\sigma_n} \right)}{\left[\frac{h}{m+1} \left(1 - \frac{\sigma_u}{\sigma_n} \right) + b \right] (m+1)^2} \right. \\ &\quad \left. - \ln \left(\frac{\sigma_n - \sigma_u}{\sigma_o} \right) \right] = 0 \end{aligned} \quad (3-54)$$

Equations 3-50 or 3-54, depending on the type of material, are solved for the three material parameters σ_u , σ_o and m . These are too involved for a conventional solution to be attempted and a computer solution is required.

The system of Eq. 3-50 was programmed for the computer but no convergence was obtained, probably because of the highly non-linear nature of the equations. To overcome these difficulties, a new equivalent system of equations was introduced. The development of this system for the case of a material governed by volumetric flaw distribution is described below.

Consider the ordered set of N failure stresses, $\sigma_1, \sigma_2, \dots, \sigma_N$ where $\sigma_1 \leq \sigma_2 \leq \sigma_3 \leq \dots \leq \sigma_N$. We seek to determine the Weibull constants σ_u , σ_o and m such that the function

$$f_n = 1 - e^{-B_n} \quad (3-55)$$

where

$$B_n = \frac{V}{2(m+1)} \frac{(\sigma_n - \sigma_u)^{m+1}}{\sigma_n \sigma_o} \quad (3-56)$$

best approximates the experimental data. In Eq. 3-55 and 3-56, n is the index and V is the volume of a prismatic specimen subjected to pure bending.

In the following, let

$$y_n = \frac{n}{N+1} \quad (3-57)$$

$$f_n = f_n(x; a, b, c) + 1 - e^{-B_n}$$

where,

$$x = \sigma_n$$

$$a = \sigma_u$$

$$b = \sigma_o$$

$$c = m$$

(3-58)

As a measure of the "best" choice of a , b , and c , we seek to minimize in some fashion the residuals V_n where

$$V_n = f_n - y_n; n = 1, 2, \dots, N. \quad (3-59)$$

A method of weighted averages, such as that of least squares is indicated. However, because Eq. 3-39 is highly-nonlinear in a , b , c , a solution of the resulting normal equations is difficult. The approach adopted consists of a least squares fit based on linearization of Eq. 3-59 in terms of correction factors to an initial estimate of a , b , c ⁽³⁻⁴⁾.

Let a_0 , b_0 , c_0 denote an initial estimate of a , b , c . The correction factors are

$$\begin{aligned} \alpha &= \Delta a_0 = a - a_0 \\ \beta &= \Delta b_0 = b - b_0 \\ \gamma &= \Delta c_0 = c - c_0 \end{aligned} \quad (3-60)$$

If the correction factors are sufficiently small, it is meaningful to expand $f_n(x; a, b, c)$ in a Taylor series about a_0 , b_0 , c_0 and retain only linear terms in α , β , γ . Thus, we may write

$$f_n(x; a, b, c) = f_n^0 + \alpha f_{n_a} + \beta f_{n_b} + \gamma f_{n_c} \quad (3-61)$$

where

$$\begin{aligned} f_n^0 &= f_n(x; a_0, b_0, c_0) \\ f_{n_a} &= \frac{\partial f_n(x; a_0, b_0, c_0)}{\partial a}; \text{ etc.} \end{aligned}$$

Substitution of the statement of Eq. 3-61 into 3-59 leads to

$$V_n = f_n^0 - y_n + \alpha f_{n_a} + \beta f_{n_b} + \gamma f_{n_c}; n = 1, 2, \dots, N \quad (3-62)$$

Equation 3-62, being linear in the correction factors, admits of the usual application of a least-squares fit. Thus, we seek to determine α , β , γ such that

$$\sum_{n=1}^N V_n^2 = \text{minimum.}$$

As necessary conditions, we require

$$\frac{\partial}{\partial a} \sum_{n=1}^N V_n^2 = \frac{\partial}{\partial \beta} \sum_{n=1}^N V_n^2 = \frac{\partial}{\partial \gamma} \sum_{n=1}^N V_n^2 = 0 \quad (3-63)$$

Upon differentiation, as indicated in Eq. 3-63, there results

$$\begin{aligned} a \sum_{n=1}^N f_{n_a}^2 + \beta \sum_{n=1}^N f_{n_a} f_{n_b} + \gamma \sum_{n=1}^N f_{n_a} f_{n_c} &= - \sum_{n=1}^N f_{n_a} (f_n^0 - y_n) \\ a \sum_{n=1}^N f_{n_a} f_{n_b} + \beta \sum_{n=1}^N f_{n_b}^2 + \gamma \sum_{n=1}^N f_{n_b} f_{n_c} &= - \sum_{n=1}^N f_{n_b} (f_n^0 - y_n) \\ a \sum_{n=1}^N f_{n_a} f_{n_c} + \beta \sum_{n=1}^N f_{n_b} f_{n_c} + \gamma \sum_{n=1}^N f_{n_c}^2 &= - \sum_{n=1}^N f_{n_c} (f_n^0 - y_n). \end{aligned} \quad (3-64)$$

Equations 3-64 are solved for the correction terms a , β , γ . The resulting a, b, c may be thought of as improved values of a_0, b_0, c_0 and the above process can be repeated until some criterion of convergence is satisfied.

Despite the linearization effected by this new system of equations the computer program did not prove successful, except in the case of CR-39 tests. The reasons for this lack of convergence are not fully understood. However, it is assumed that the lack of success with a suitable machine solution is ascribable to the nature of the Weibull theory, which appears to admit with almost equal facility a variety of widely divergent solutions. This, in fact, was noted in several computer trial runs, when the answer for a given set of test data could be made to converge with almost equal ease to different sets of Weibull constants.

4. EXPERIMENTAL RESULTS

Failure experiments were conducted on Columbia Resin (CR-39), a photoelastically sensitive amorphous polymer, Wesgo Al_2O_3 (AL-995), BeO doped with about 1 percent MgO, supplied by Atomics International and ARF MgO.

Of these, Wesgo AL-995 was tested both at room temperature and elevated temperature (1000 °C). Elevated temperature tests on BeO were in progress at the time of this writing. All room temperature tests, except those on BeO, were conducted in an Instron Model TT testing machine. Elevated temperature tests on Wesgo AL-995 and all tests on BeO were conducted in a hydraulic testing machine. Loading rate and environmental conditions were maintained constant during each of these tests.

All specimens were 4-in. long prismatic bars and were subjected to four-point loading with a gage length of 2 in. under pure bending and a distance of $3/4$ in. between loads and supports (Fig. 3-2). The presence of pure bending is demonstrated by the isochromatic fringe pattern in a CR-39 specimen shown in Fig. 3-3. For each of the ceramic materials three types of specimens were tested. These were prismatic bars of dimensions in the order of width, depth and length of $3/16$ in. x $1/3$ in. x 4 in., $1/4$ in. x $1/4$ in. x 4 in. and $1/3$ in. x $3/16$ in. x 4 in. These three specimens have different stress gradients (for the same extreme fiber stress) but the same gage volume and, therefore, according to the Weibull theory, the same probability of fracture.

A. Columbia Resin CR-39

This material was selected for preliminary work in establishing procedures and techniques. The first task was to obtain a stress-strain curve to failure and evaluate the degree of brittleness of the material. For this purpose, long (about 8-in. gage length) dogbone specimens were made and tested in an Instron

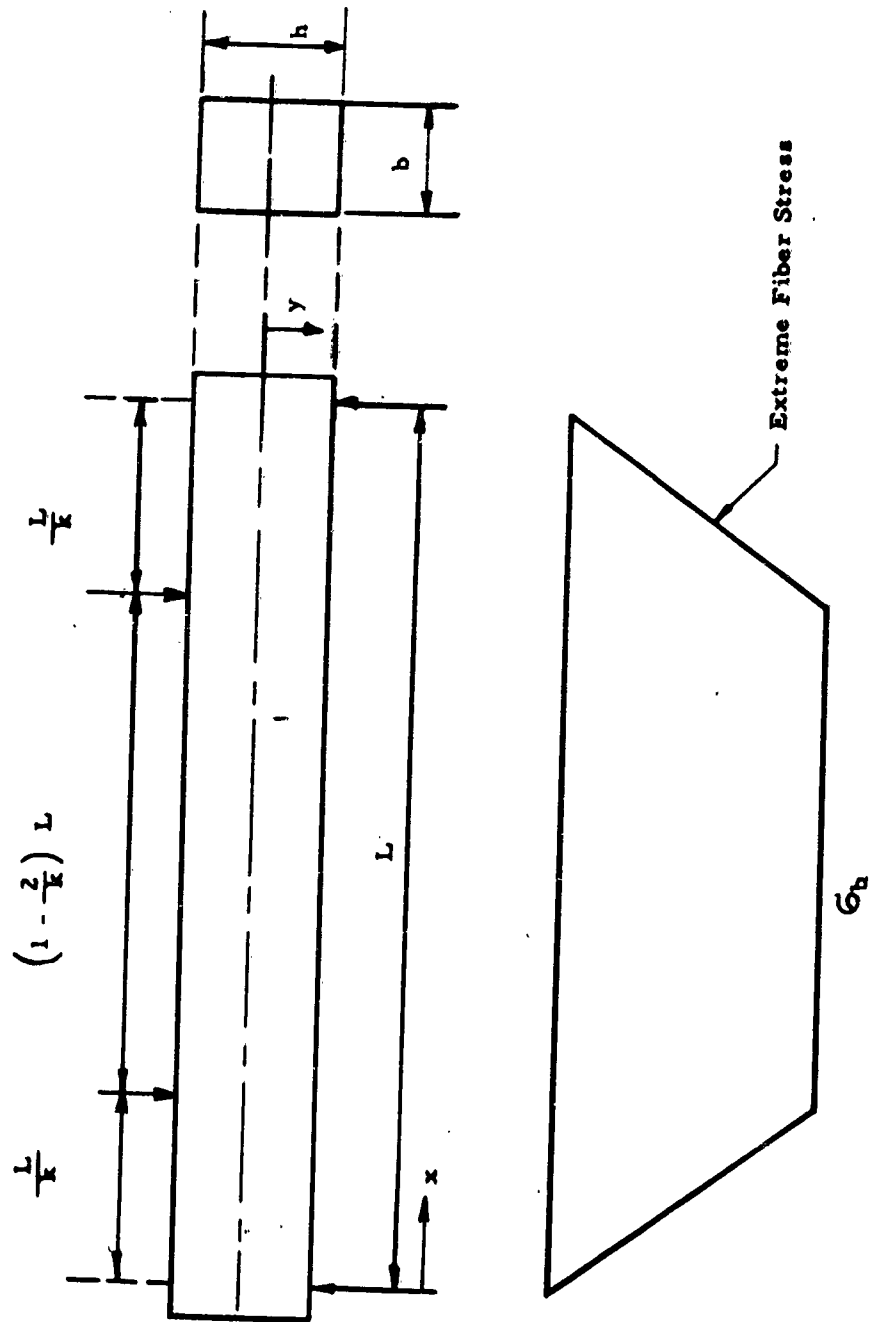


Fig. 3-1 PRISMATIC BEAM UNDER FOUR-POINT LOADING AND DISTRIBUTION OF EXTREME FIBER STRESS

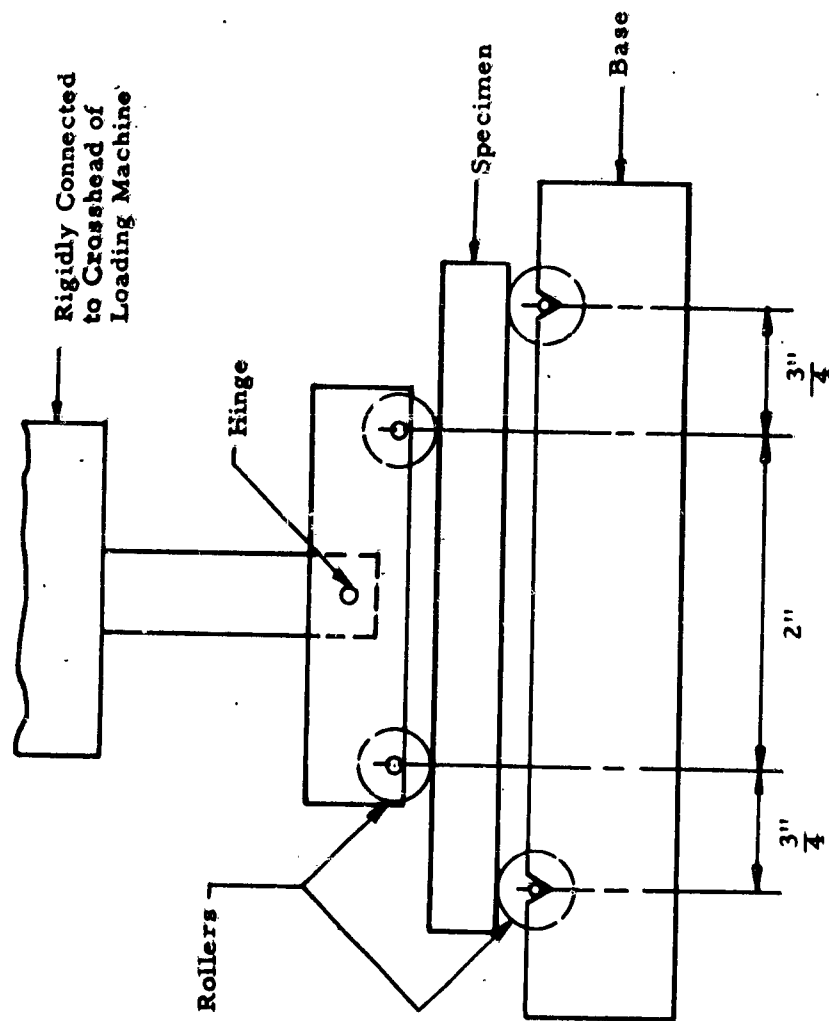
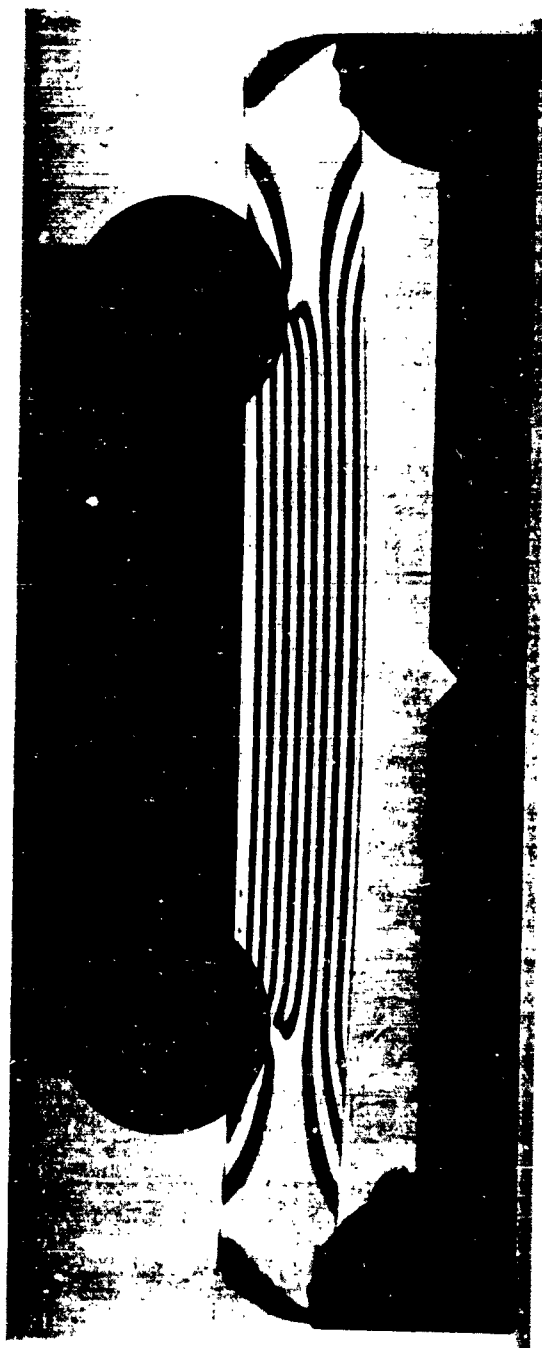


Fig. 3-2 SCHEMATIC DIAGRAM OF LOADING FIXTURE USED FOR TESTING PRISMATIC BARS IN PURE BENDING.



**Fig. 3-3 ISOCHROMATIC FRINGE PATTERN IN A CR-39 PRISMATIC SPECIMEN UNDER
FOUR-POINT LOADING**

testing machine. It was found that there is some deviation from linearity in the stress-strain relation near failure. The plastic flow that precedes failure would alter the stress distribution in the case of non-uniform stress fields. However, a statistical analysis such as Weibull's is applicable, provided the stress distribution at failure is known.

Thirty-six specimens 0.4 in. x 0.4 in. x 4 in. were cut from a 1/2 in. thick sheet of CR-39 with all surfaces of each specimen having a uniformly machined finish. These were tested in four-point bending at a crosshead speed of 1/2 in. per minute. A load versus crosshead deflection record was obtained and no deviation from linearity was noticed. Although this fact does not preclude localized non-linear deformation, the data were analyzed on the basis of linear elastic behavior to failure. The following results were obtained:

Mean failure stress:	σ_m	= 6,460 psi
Standard deviation:	a	= 1,060 psi
Variance:	a^2	= 1,123,600 (psi) ²
Coefficient of variation:	v	= 16.41 percent
Highest failure stress:	σ_{high}	= 8780 psi
Lowest failure stress:	σ_{low}	= 3670 psi.

The cumulative distribution curve of the failure stresses is shown in Fig. 3-4. A tendency of the points to follow a bimodal distribution may be explained by the fact that one group of failures occurs in the elastic linear region of the material while the group of high stress failures includes non-linear elastic and plastic deformation. The transition zone between these two groups is around 6,000 psi which is the zone of yielding of the material. The frequency curve could be obtained by graphically differentiating the cumulative distribution function of Fig. 3-4 since frequency of fracture at a given stress is proportional to the slope of the distribution curve at that stress. It can be seen from

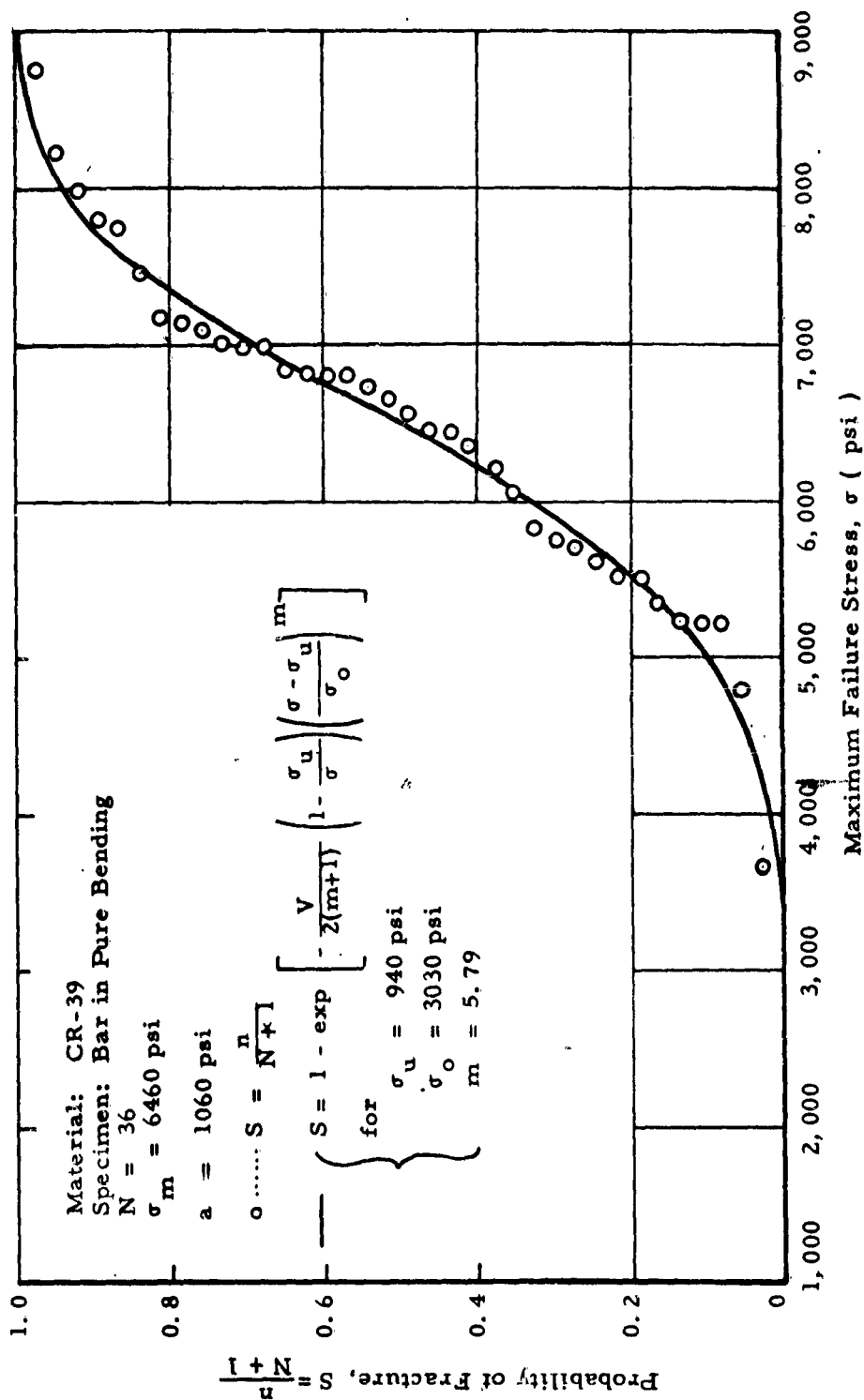


Fig. 3-4 COMPARISON OF EXPERIMENTAL VALUES WITH THEORETICAL CUMULATIVE DISTRIBUTION CURVE OF BEST FIT

Fig. 3-4 that this would result in a distribution skewed slightly toward the lower values. For typical brittle materials, in contrast, the plot would tend to be skewed toward the higher values.

Applying the analytical error minimization process described previously, the computer programming resulted in the following values for the material constants of CR-39:

$$\begin{aligned}\sigma_u &= 940 \text{ psi} \\ \sigma_o &= 3030 \text{ psi} \\ m &= 5.79\end{aligned}$$

Figure 3-4 illustrates the closeness of fit between the theoretical curve for the cumulative distribution function and the experimental points. As can be seen, the agreement is very satisfactory. It should be remarked, however, that the nature of the fitting criterion used (minimization of least squares) does not necessarily guarantee a best fit in other respects; e. g. the derivative of the cumulative distribution function which provides the probability density function may not show an equally satisfactory correlation.

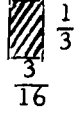
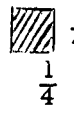

B. Wesgo Aluminum Oxide AL-995

Sixty specimens of each of the three types described were tested at room temperature in the Instron machine at a crosshead rate of 0.02 in. per min. The experimental results are assembled in Table 3-1. It should be noted that specimens A and C are identical in shape, except for one being tested "edge-on", the other "flatwise". These specimens were fabricated using the same dies, and assumed to have been made from the same batch. In contrast, specimen B has a different cross section and must be pressed in a different die, therefore, these specimens were made in a different batch. The significance of these observations will become evident.

Figure 3-5 shows the cumulative distribution curves for the failure stresses of these specimens. The specimen shapes and dimensions were selected such that the volume subjected to pure

Table 3-I

EXPERIMENTAL RESULTS
OF WESGO AL-995 AT ROOM TEMPERATURE

Specimen Type	A	B	C
Dimensions (in.)	$\frac{3}{16} \times \frac{1}{3} \times 4$	$\frac{1}{4} \times \frac{1}{4} \times 4$	$\frac{1}{3} \times \frac{1}{16} \times 4$
Cross Section (in.)	 $\frac{1}{3}$ $\frac{3}{16}$	 $\frac{1}{4}$ $\frac{1}{4}$	 $\frac{3}{16}$ $\frac{1}{3}$
Gage Volume, V, (cu in.)	0.125	0.125	0.125
Number of Specimens Tested, N	60	60	60
Mean Failure Stress, σ_m , (psi)	29,770	31,850	29,750
Standard Deviation σ , (psi)	2,250	2,210	1,800
Coefficient of Variation, v, (%)	7.57	6.94	6.05
Mean Stress Gradient at Failure (psi/in.)	178,620	254,800	317,340
Lowest Failure Stress, σ_{low} , (psi)	23,540	24,910	25,540
Highest Failure Stress, σ_{high} , (psi)	33,800	36,430	33,980

Material: Wesgo AL-995
 Specimen: Bar in Pure Bending
 N = 60

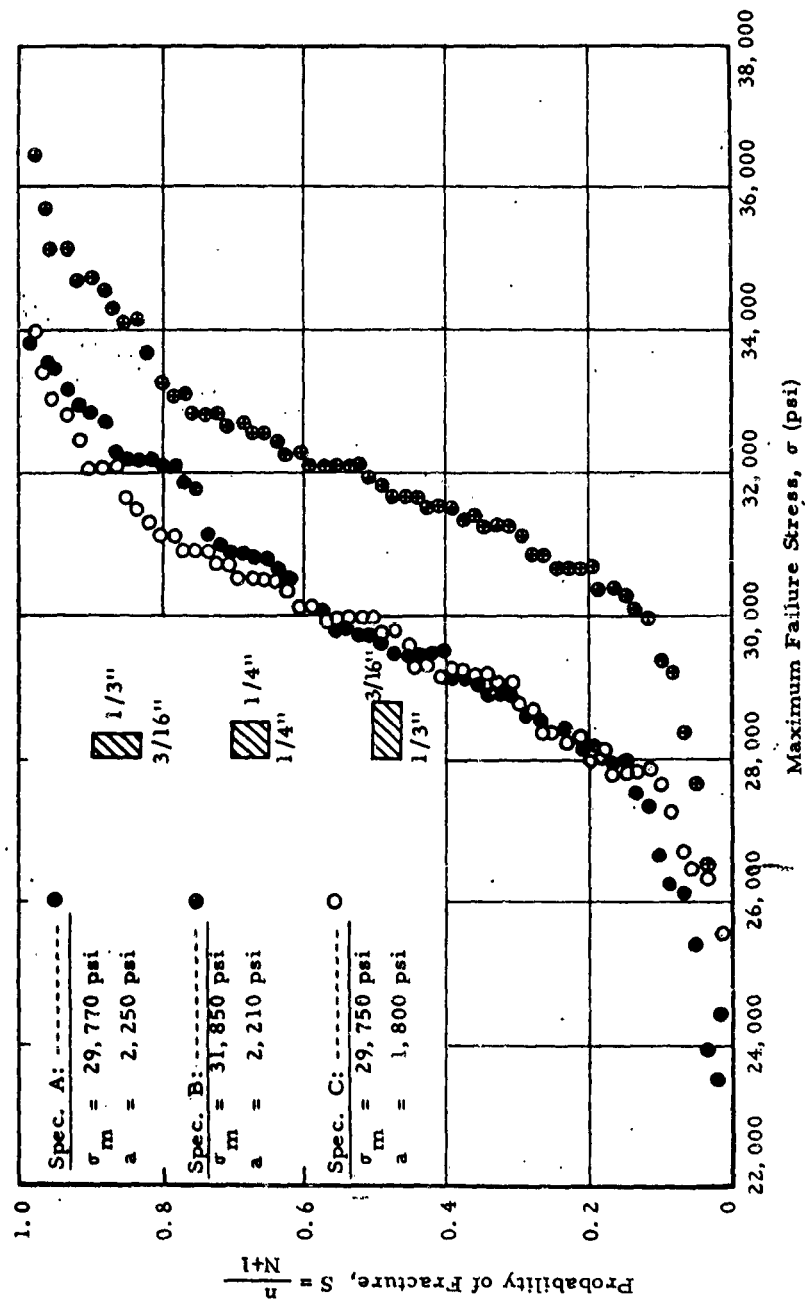


Fig. 3-5 CUMULATIVE DISTRIBUTION CURVES OF FAILURE STRESSES IN WESGO AL-995 UNDER PURE BENDING

bending is identical for each configuration. The only parameter varied was the stress gradient. The most significant result seems to be the fact that specimens A and C with the largest variation in stress gradient seem to have almost identical cumulative distribution functions. The significance of this result is two-fold: first it suggests that there is no gradient effect on failure stress, at least for the range of gradients studied; and second, that the material is governed by a volumetric flaw distribution. The latter can be explained by the fact that in specimens A and C the effective volumes are the same while the effective surface areas are different. The contingency that a fortuitous combination of mutually opposing surface flaw distribution and stress gradient effects would tend to cancel each other is highly improbable. The fact that specimen B with an intermediate value of stress gradient shows a higher mean failure stress than either A or C must be attributed to a difference in the batch of ceramic powders used for pressing these specimens or manufacturing procedure employed. Later experiments on a new order of Wesgo AL-995(not reported here) indicate that differences in strength and elastic properties from batch to batch may be appreciable.

A combined probability density curve was obtained for specimens A and C by graphically differentiating the cumulative distribution curve (Fig. 3-6). The mode was found to be almost identical with the mean of $\sigma_m = 29,760$ psi. It can be seen also from the shape of the curve that the skewness is imperceptible and that a normal (Gaussian) distribution function might be a good approximation. A Gaussian distribution has actually been applied by Frenkel and Kontorova⁽³⁻⁵⁾ to describe the fracture strengths of brittle materials.

The trial and error graphical method suggested by Weibull was used in this case for the determination of material parameters. For a volumetric flaw distribution these parameters satisfy the equation

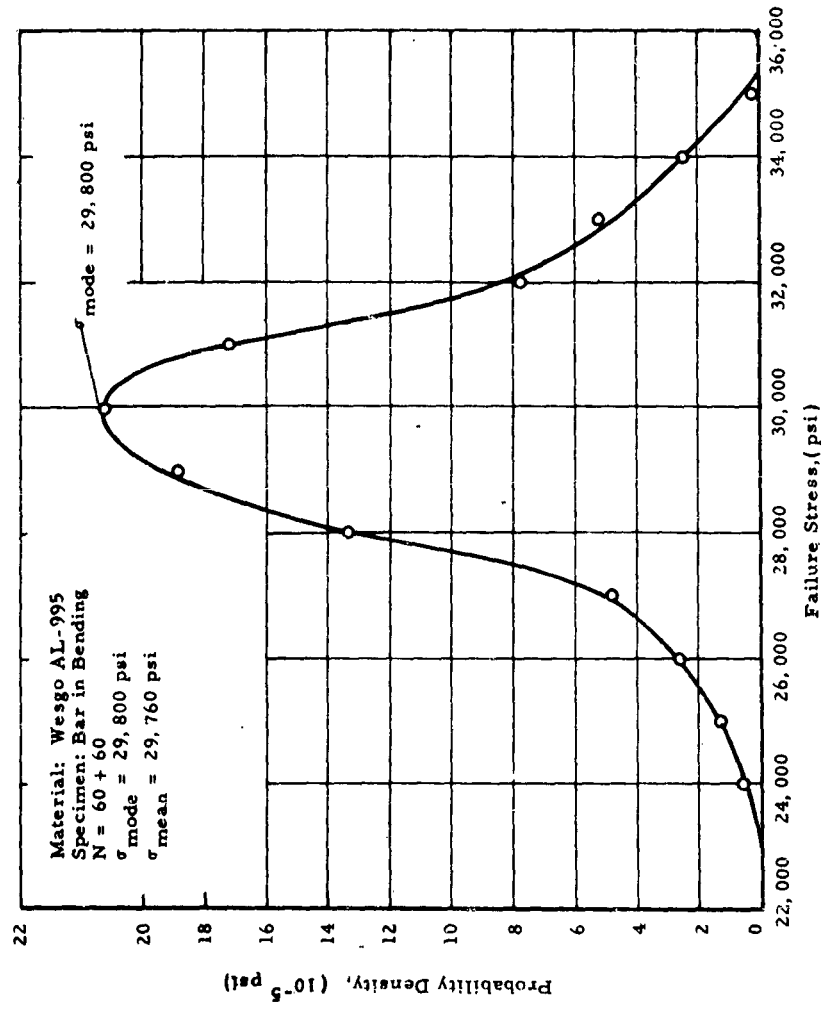


Fig. 3-6 PROBABILITY DENSITY CURVE OF FAILURE STRESSES IN WESGO AL-995 BENDING SPECIMENS A AND C

$$\begin{aligned} \log \log \frac{N+1}{N+1-n} &= (m+1) \log (\sigma - \sigma_u) - m \log \sigma_o - \log \sigma \\ &+ \log \frac{V}{2(m+1)} + \log \log e \end{aligned} \quad (3-65)$$

(The logarithms here are referred to base 10.)

The recommended procedure is to plot $\left[\log \log \frac{N+1}{N+1-n} + \log \sigma \right]$ versus $\log (\sigma - \sigma_u)$. The value of σ_u has to be obtained by trial and error until a straight line results for the correct value of this parameter. Values of σ_u lower than the correct one would result in curves concave downward, values higher than the correct one would give curves concave upward. Once a straight line plot is obtained, $(m+1)$ is determined as the slope of this line and σ_o is found by substituting all, by now known, quantities into Eq. 3-65.

To improve the accuracy of this graphical determination, a smooth curve was drawn through the Fig. 3-5 data points corresponding to specimens A and C. Then, $\log \log \frac{N+1}{N+1-n}$ was replaced by $\log \log \frac{1}{1-S}$ where the S values are ordinates of the curve drawn. The above mentioned plot was obtained for values of σ_u equal to 0, 5,000 psi, 10,000 psi, 15,000 psi, 20,000 psi and 25,000 psi. In all cases except the last, the resulting curve was concave downward, indicating an assumed value of σ_u lower than the correct one. For $\sigma_u = 25,000$ psi, a reasonably straight line was obtained. As a further refinement for an estimate of the value of σ_u the following procedure was adopted;

For each of the assumed values of σ_u the highest and the lowest values of m were obtained from the end slopes of the curves $\log \log \frac{1}{1+S} + \log \sigma$ versus $\log (\sigma - \sigma_u)$. These enveloping values of m , called respectively m_1 and m_2 , were plotted versus the assumed σ_u values (Fig. 3-7). The correct value of σ_u is obtained from the point of intersection of the m_1 and m_2 curves. This gave the values of σ_u and m . This final value of σ_u was used in the $\log \log \frac{1}{1+S} + \log \sigma$ versus $\log (\sigma - \sigma_u)$ plot

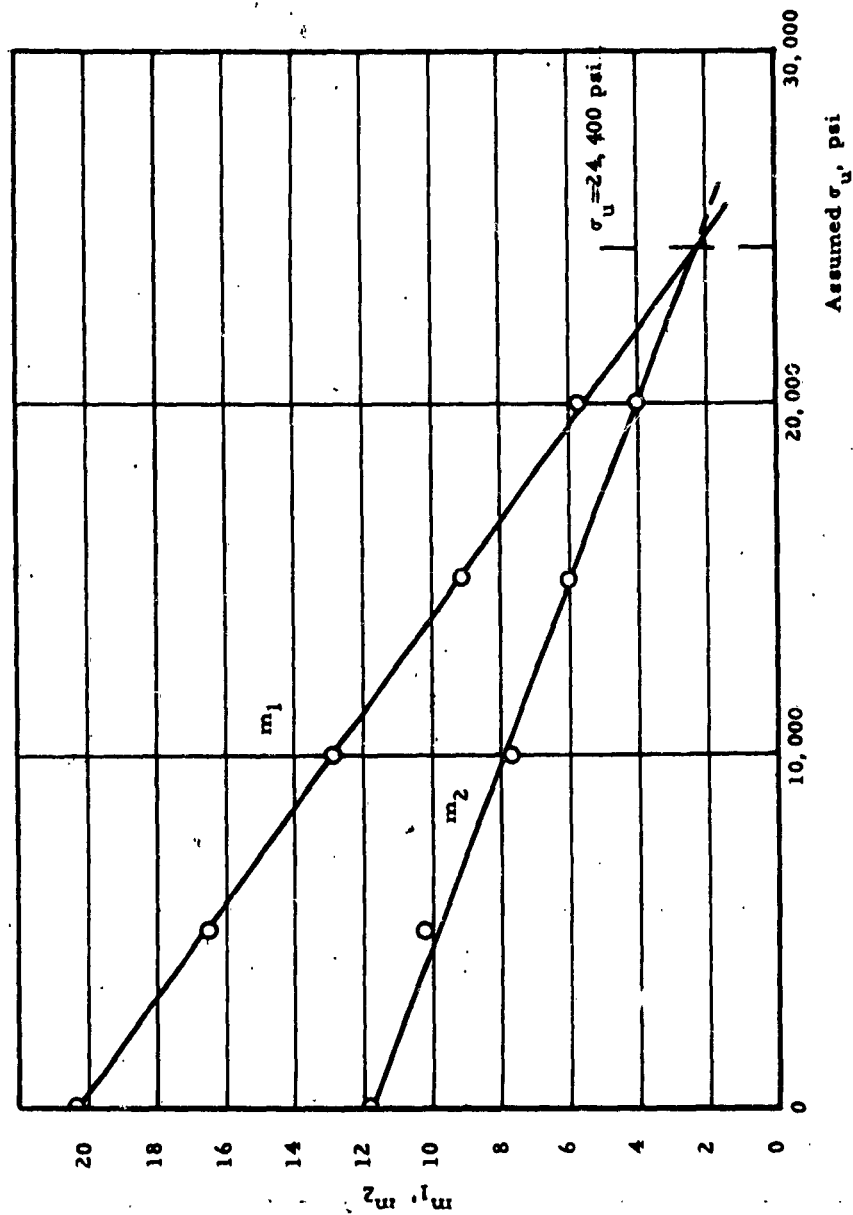


Fig. 3-7. VARIATION OF TWO EXTREME VALUES OF m (TAKEN FROM END SLOPES OF CURVES) WITH ASSUMED VALUE OF σ_u FOR WESGO AL-995 AT ROOM TEMPERATURE

(Fig. 3-8) and the following values of the parameters were obtained:

$$\sigma_u = 24,400 \text{ psi}$$

$$m = 2.4$$

$$\sigma_o = 560 \text{ psi.}$$

This value of σ_u , however, appears high, especially in view of the fact that two of the $\frac{3}{16}$ in. x $\frac{1}{3}$ in. specimens failed at stresses below 24,000 psi. There is no doubt, however, that the above values of the parameters represent the best over-all fit to the set of experimental data obtained for this material.

A similar series of tests on Wesgo AL-995 was conducted at 1000°C. Experimental results for specimens A and C are assembled in Table 3-II. Data on specimen B were also obtained; although they were consistent in themselves they gave a mean value much lower than that for specimens A and C. As in the case of room-temperature tests there is no significant difference between the mean failure stresses from the two gradients studied. Besides, the effect of the elevated temperature used seems to be nil as the mean failure stresses are remarkably close to those obtained at room temperature.

Figure 3-9, shows the cumulative distribution curve for these tests. A procedure similar to that described for the room temperature tests was adopted for the graphical determination of the material parameters. Figure 3-10 depicts the variation of values of the parameter m obtained for assumed values of σ_u . Three different values m_1 , m_2 and m were obtained for each σ_u . These were obtained from the end slopes and a mean slope of the curves $\log \log \frac{1}{1+S} + \log \sigma$ versus $\log (\sigma - \sigma_u)$. Final values of σ_o and m were obtained from the coordinates of the common intersection point of the three σ_u versus m lines. This value of σ_u was used in the plot of Fig. 3-11 from which the following values of the parameters were obtained:

$$\sigma_u = 18,200 \text{ psi;} \quad m = 5.4; \quad \sigma_o = 4,500 \text{ psi.}$$

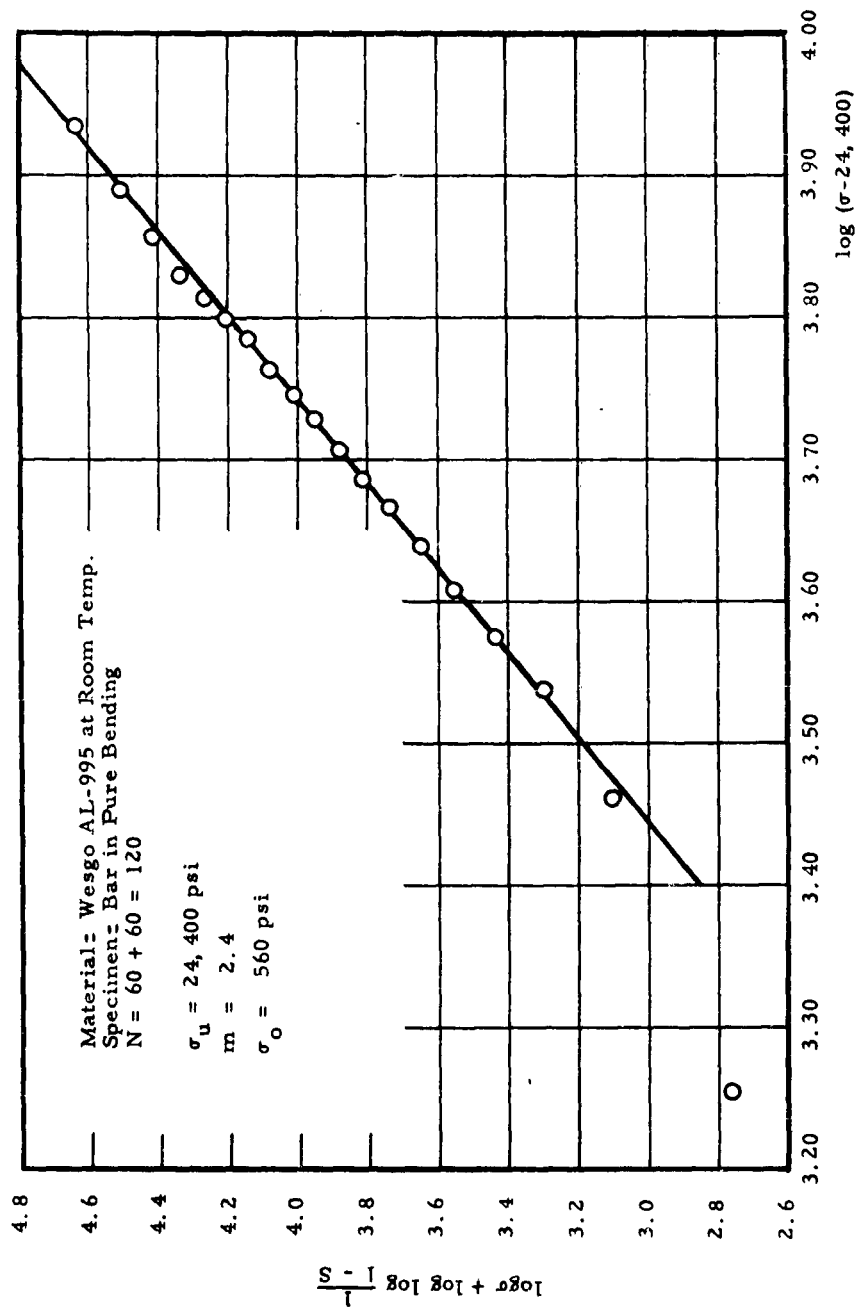




Fig. 3-8. GRAPHICAL DETERMINATION OF MATERIAL PARAMETERS FOR WESGO AL-995 AT ROOM TEMPERATURE

Table 3-II

EXPERIMENTAL RESULTS OF WESGO AL-995 AT 1000°C

Specimen Type	A	C
Dimensions (in.)	$\frac{3}{16} \times \frac{1}{3} \times 4$	$\frac{1}{3} \times \frac{3}{16} \times 4$
Cross Section (in.)	 $\frac{1}{3}$ $\frac{3}{16}$	 $\frac{3}{16}$ $\frac{1}{3}$
Gage Volume (cu in.)	0.125	0.125
Number of Specimens Tested, N	52	60
Mean Failure Stress, σ_m , (psi)	29,780	29,710
Standard Deviation, σ , (psi)	2,120	2,000
Coefficient of Variation, v , (%)	7.12	6.73
Mean Stress Gradient at Failure (psi/in.)	178,680	316,910
Lowest Failure Stress, σ_{low} , (psi)	25,060	24,960
Highest Failure Stress, σ_{high} , (psi)	33,700	33,790

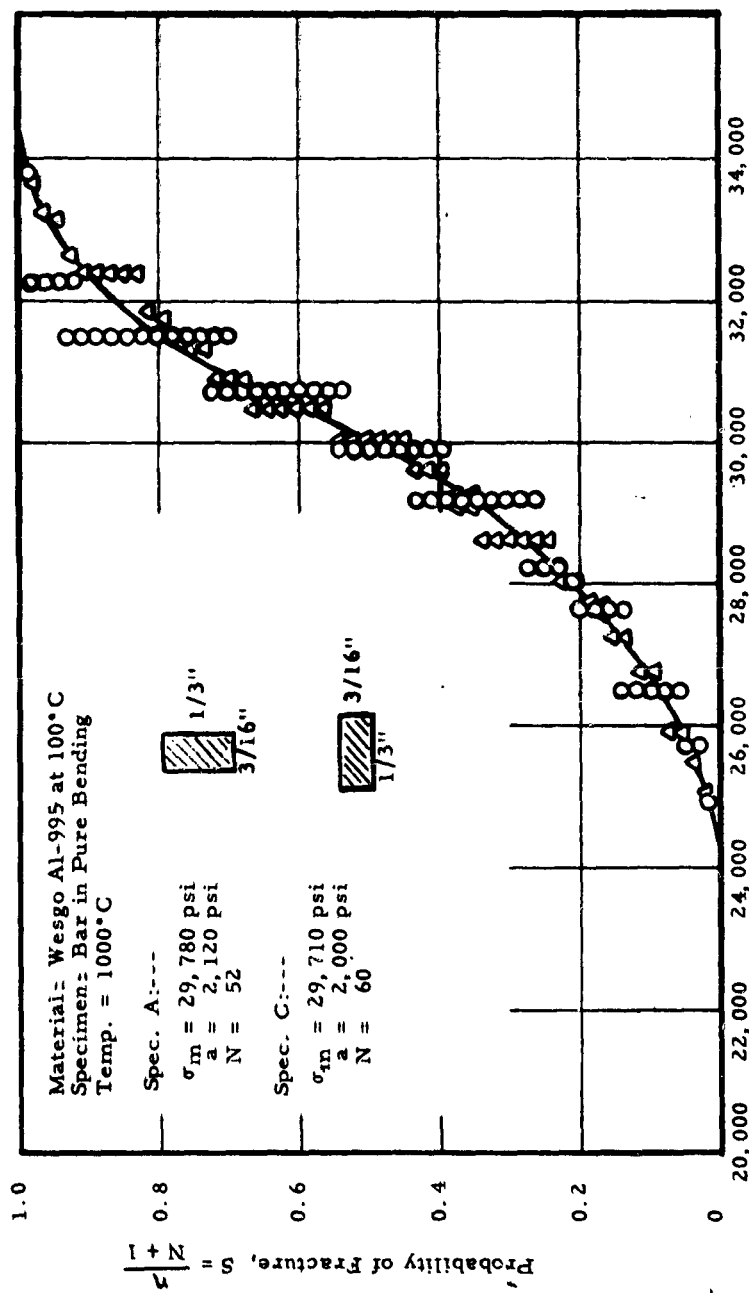


Fig. 3-9. CUMULATIVE DISTRIBUTION CURVES OF FAILURE STRESSES IN WESGO AL-995 UNDER PURE BENDING AT 1000°C

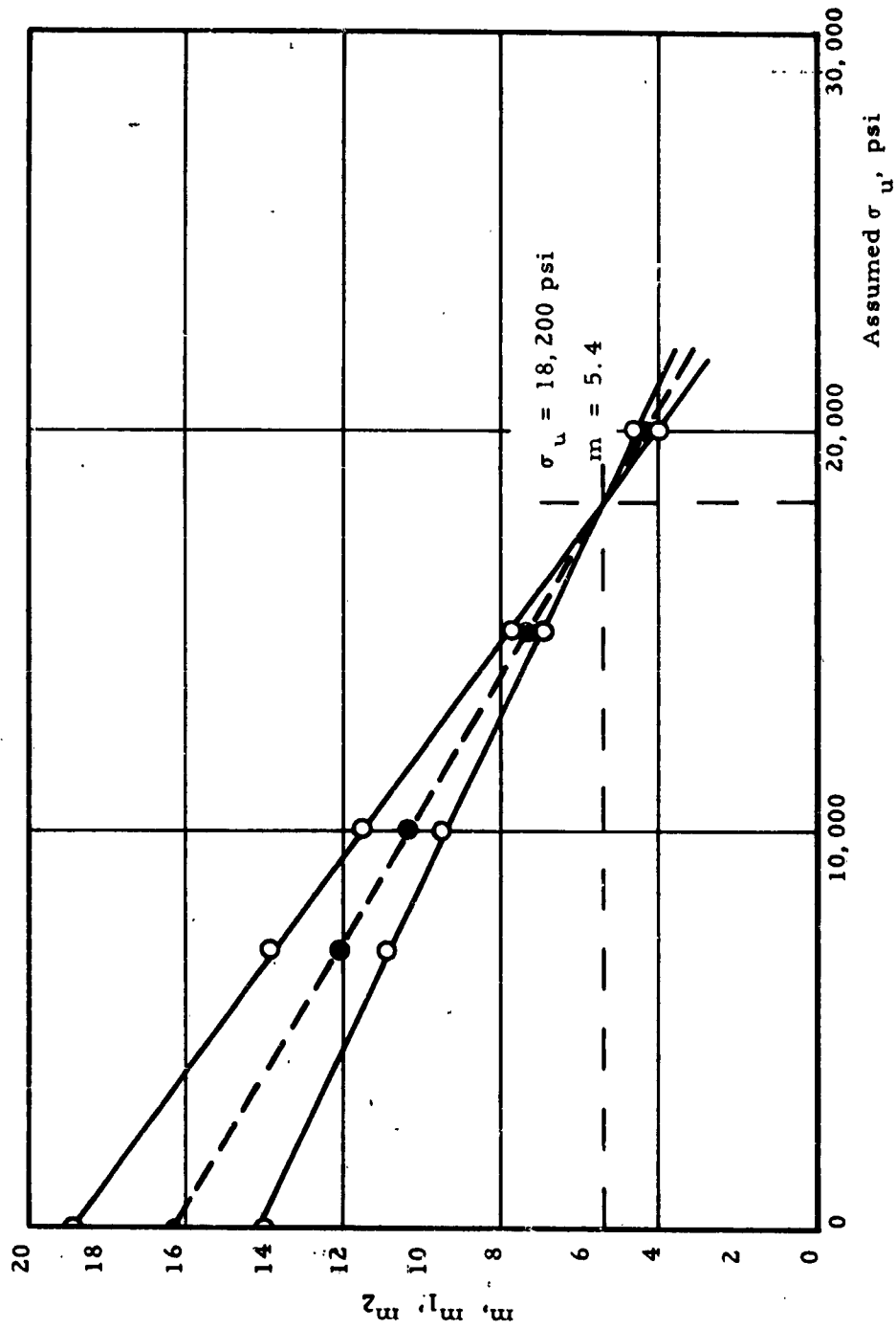


Fig. 3-10. VARIATION OF AVERAGE AND EXTREME VALUES OF m (WITH ASSUMED VALUE OF σ_u FOR WESGO AL-995 AT 1000°C

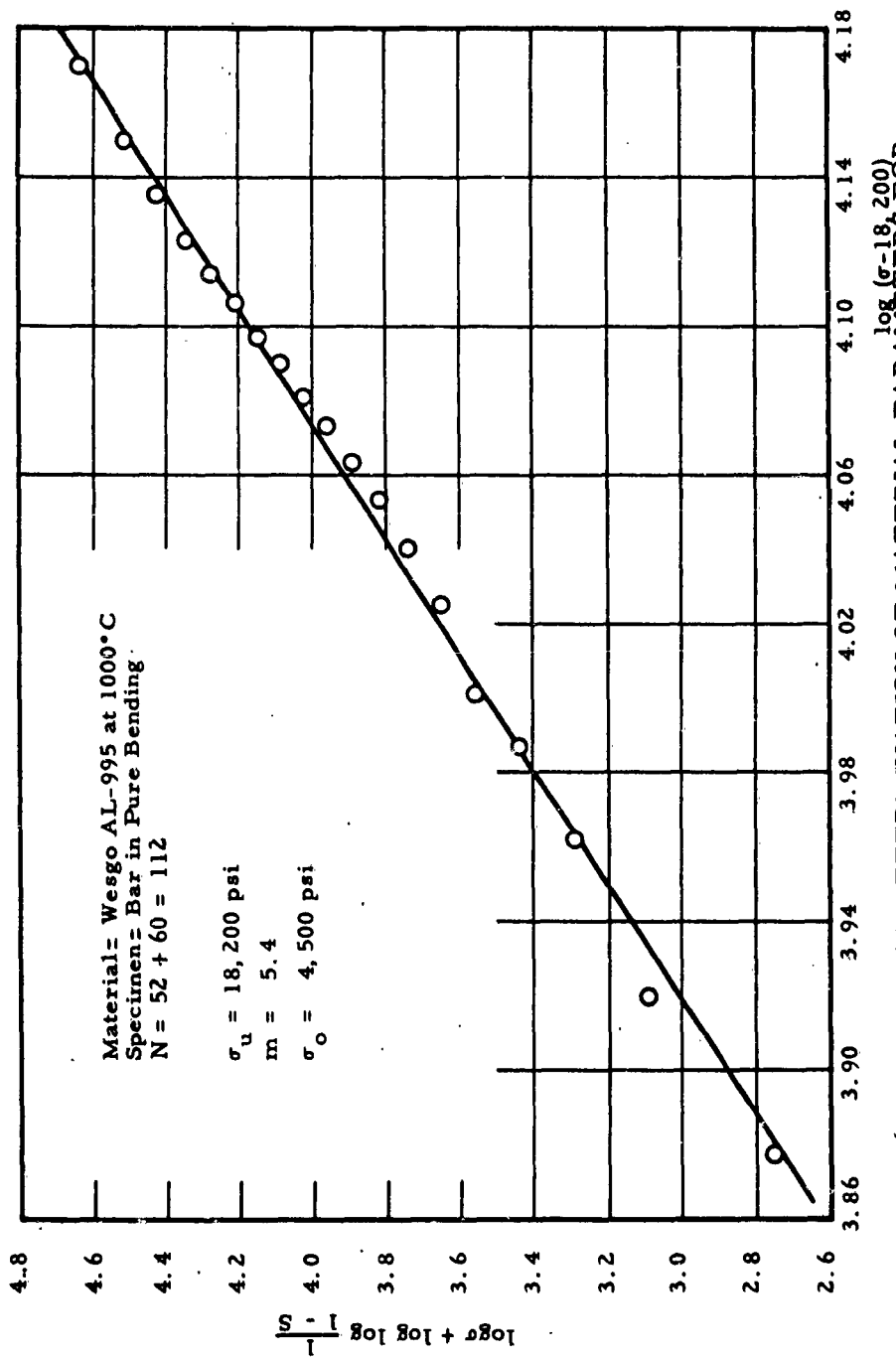


Fig. 3-11. GRAPHICAL DETERMINATION OF MATERIAL PARAMETERS FOR
 WESGO AL-995 AT 1000°C

C. Beryllium Oxide

A series of $\frac{3}{16}$ in. x $\frac{1}{3}$ in. x 4 in., $\frac{1}{4}$ in. x $\frac{1}{4}$ in. x 4 in., $\frac{1}{3}$ in. x $\frac{3}{16}$ in. x 4 in. BeO specimens were tested at room temperature. Experimental results are assembled in Table 3-III. As in the case of the Al_2O_3 , there is no stress gradient effect evident. The mean failure stresses of all three specimens are close. The variability, however, is higher than that of Al_2O_3 . Here, the coefficient of variation ranges from 14.74 percent to 16.34 percent. This increased variability of failure stresses shows in the cumulative distribution curves plotted in Fig. 3-12. The data points lie on a wide S-shaped band. The points corresponding to the $\frac{1}{3}$ in. x $\frac{3}{16}$ in. x 4 in. specimens lie near the middle of this band. By drawing a curve through these points a reasonable cumulative distribution function was obtained and the graphical method of parameter determination was applied. To average out the results for all three types of specimens, a cumulative distribution curve (Fig. 3-13) was obtained by combining the results of all tests. This seems justified in view of the fact that the mean and standard deviation were about the same for all three specimens. The conventional $\log\log \frac{1}{1-S}$ versus $\log \sigma$ plot for the two alternative cumulative distribution curves is shown in Fig. 3-14. The resulting curve is clearly a straight line (especially in the case of the $\frac{1}{3}$ in. x $\frac{3}{16}$ in. x 4 in. specimen) which indicates a value of σ_u equal to zero. The values of the material parameters obtained are:




$$\sigma_u = 0$$

$$m = 7.25$$

$$\sigma_o = 7,800 \text{ psi.}$$

Table 3-III

**EXPERIMENTAL RESULTS OF BERYLLIUM OXIDE
AT ROOM TEMPERATURE**

Specimen Type	A	B	C
Dimensions (in.)	$\frac{3}{16} \times \frac{1}{3} \times 4$	$\frac{1}{4} \times \frac{1}{4} \times 4$	$\frac{1}{3} \times \frac{3}{16} \times 4$
Cross Section (in.)	 $\frac{1}{3}$ $\frac{3}{16}$	 $\frac{1}{4}$ $\frac{1}{4}$	 $\frac{3}{16}$ $\frac{1}{3}$
Gage Volume (cu in.)	0.125	0.125	0.125
Number of Specimens Tested, N	48	42	50
Mean Failure Stress, σ_m , (psi)	15,740	15,540	15,650
Standard Deviation, σ , (psi)	2,320	2,540	2,530
Coefficient of Variation, v , (%)	14.74	16.34	16.17
Mean Stress Gradient at Failure (psi in.)	94,440	124,320	166,930
Lowest Failure Stress, σ_{low} , (psi)	11,830	8,870	10,210
Highest Failure Stress, σ_{high} , (psi)	19,900	19,320	21,000

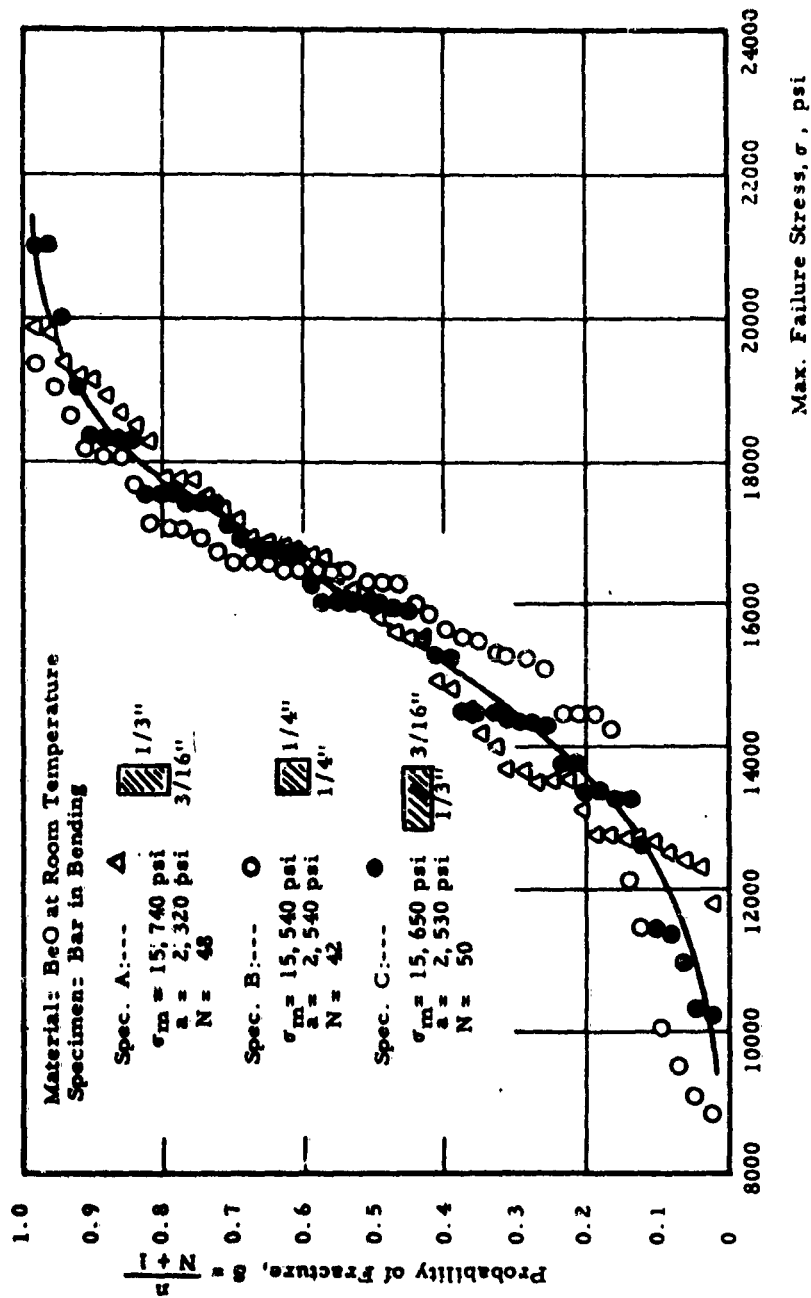


Fig. 3-12. CUMULATIVE DISTRIBUTION CURVES OF FAILURE STRESSES IN BERYLLIUM OXIDE UNDER PURE BENDING AT ROOM TEMPERATURE (3 TYPES SPECIMENS PLOTTED SEPARATELY)

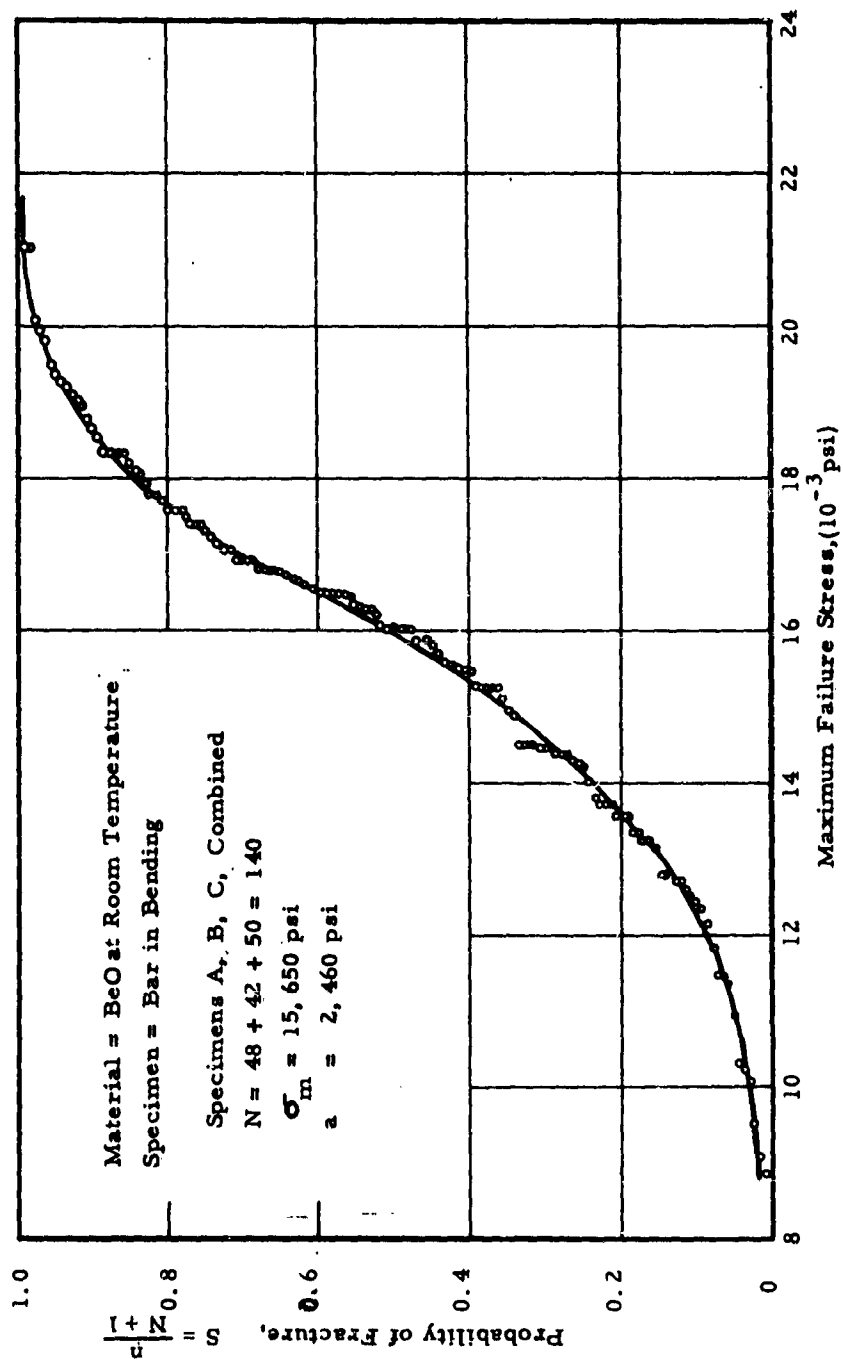


Fig. 3-13. CUMULATIVE DISTRIBUTION CURVE OF FAILURE STRESSES IN BERYLLIUM OXIDE UNDER PURE BENDING AT ROOM TEMPERATURE (3 Types of Specimens Combined)

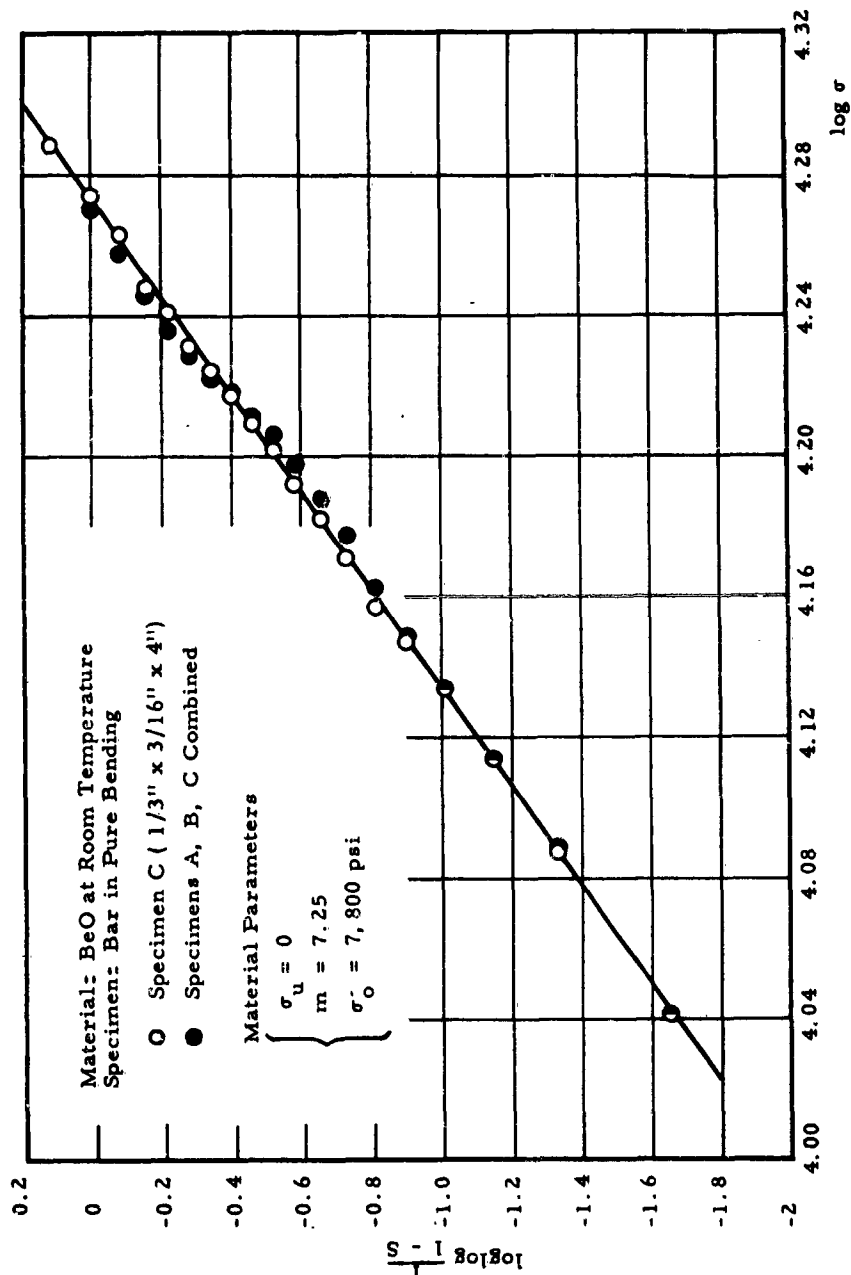


Fig. 3-14. GRAPHICAL DETERMINATION OF MATERIAL PARAMETERS FOR BERYLLIUM OXIDE AT ROOM TEMPERATURE

D. Magnesium Oxide (ARF)

A similar series of tests was conducted using MgO specimens. While the data have not been completely analyzed some preliminary results are given in Table 3-IV.

Table 3-IV

PRELIMINARY RESULTS OF BEND TESTS
ON ARF MAGNESIUM OXIDE AT ROOM TEMPERATURE

Specimen Type	A	B	C
Specimen Dimensions (in.)	$\frac{1}{3} \times \frac{3}{16} \times 4$	$\frac{1}{4} \times \frac{1}{4} \times 4$	$\frac{3}{16} \times \frac{1}{3} \times 4$
Number of Specimens, N _t	50	50	50
Mean Failure Stress, σ_m , (psi)	14,430	16,520	15,060
Standard Deviation, σ (psi)	2,380	1,660	2,250
Coefficient of Variation v, (%)	16.50	10.04	14.93

Although the mean failure stresses here are somewhat different, it is not clear whether this is an indication of a stress gradient effect, especially in view of the higher variability of the results. The differences may not be significant at all or they may indicate a surface effect. The latter may be due to the fact that not all surfaces in the specimens were ground.

5. CONCLUSION

The results of the experimental work described are summarized in Table 3-V. Even though this work is not yet complete, it is sufficiently extensive to lead to reasonably well founded conclusions. The prismatic pure-bending specimens used here proved a simple and effective means of studying the stress gradient effect. The specimens used gave almost a 2 to 1 ratio of extreme stress gradients. The gage volume was the same in all three types of

specimens and, as a result, the effective size (arrived at either by Weibull's theory or by an arbitrary definition based on a given percentage of the extreme fiber stress) was the same.

Table 3-V

SUMMARY OF BASIC WEIBULL MATERIAL PARAMETERS
FOR COMPLETED TEST SERIES

Source and Material	Test Temperature, (°C)	Weibull Parameters		
		σ_u (10^3 psi)	m	σ_o (10^3 psi)
Wesgo AL-995	20	24.4	2.4	0.56
Wesgo AL-995	1000	18.2	5.4	4.50
BeO	20	0	7.25	7.80

The results on Wesgo AL-995 and BeO prove that the stress gradient does not have an independent influence on the mean failure stress and standard deviation, at least for the range of stress gradients investigated. This proved to be the case both at room temperature and at elevated temperature (1000 °C) for the Al_2O_3 . This result is in full accordance with the Weibull theory. The latter does not make any special allowance for the stress gradient, but it accounts for the non-uniformity of stress distribution by assigning a risk of rupture to each infinitesimal element. The risk of rupture for the entire specimen is then obtained by a volume integration. According to Weibull⁽³⁻⁶⁾, the stress gradient should not have an independent effect when it is moderate but it is conceivable that it might, when the effective size (linked to the stress gradient) is of the order of the grain size or of the order of volume elements between "weak points".

Another conclusion reached from the Al_2O_3 and BeO specimens tested is that failure in these materials is governed by a volumetric flaw distribution. This was evidenced by the fact that

specimens having the same effective volume but different effective surfaces gave the same average failure stress. This, as discussed previously, can only be attributed to a volumetric flaw distribution rather than to an improbable combination of mutually cancelling stress gradient and surface effects. This is not surprising, however, since these specimens had been ground in order to obtain the dimensional tolerances requested. It is believed that specimens with "as-fired" surfaces would show appreciable surface effects.

The determination of unique and fundamental material properties is still a difficult problem. The analytical procedure specifically developed in an attempt to evolve unique numerical answers did not lend itself to a computer solution. The graphical trial and error method originally suggested by Weibull is still the most convenient method. Some suggestions for improving the accuracy of this method were offered in the text, but the method is still not entirely free of misinterpretations, the result of subjective judgment. The only way to increase the reliability of the graphical determination of material parameters is to obtain perfectly homogeneous and isotropic materials and conduct a large number of failure tests under well controlled experimental conditions.

Work on the stress gradient effect and the type of flaw distribution governing failure is expected to continue in the extension phase of the program. The range of stress gradients investigated will be extended by testing specimens of cross sections $\frac{1}{8}$ in. x $\frac{1}{2}$ in. and $\frac{1}{2}$ in. x $\frac{1}{8}$ in. A more systematic procedure for the investigation of the type of flaw distribution is contemplated, by simultaneously varying effective size and surface of specimen. Work on MgO and BeO at high temperature will be continued and completed. Lucalox will be another grade of Al_2O_3 to be investigated. In addition to the influence of temperature, the influence of annealing on the stress gradient effect will be studied.

7. REFERENCES

- 3-1 Weil, N. A., Ed., Studies of the Brittle Behavior of Ceramic Materials, ARF Final Report 8203-16 October 1961.
- 3-2 Weibull, W., "A Statistical Distribution Function of Wide Applicability", J. Appl. Mech. 18, 293-297 (1951).
- 3-3 Weibull, W., "A Statistical Theory of the Strength of Materials", Ing. Vetenskaps Akad. Handl., 151, (1939); "The Phenomena of Rupture in Solids", ibid, 153, (1939).
- 3-4 Scarborough, J. B., Numerical Mathematical Analysis p. 46, Johns Hopkins Press, Baltimore, 3rd Ed. (1955).
- 3-5 Fränkel, J. I., and Kontorova, T. A., "A Statistical Theory of the Brittle Strength of Real Crystals", J. Phys. USSR, 7, 108 (1943).
- 3-6 Weibull, W., Private communication.

TASK 4 - EFFECT OF MICROSTRUCTURE

Principal Investigator: P. R. V. Evans

A B S T R A C T

The fracture behavior of polycrystalline MgO and Lucalox Al_2O_3 over a limited grain size range was studied under uniaxial compression in between 1000 and 1900°C. The fracture strength of both oxides showed a marked dependence on temperature and grain size. Microscopical examination showed that the fracture path was essentially intercrystalline in Lucalox and MgO at high temperatures. However, there was evidence of mixed transgranular and intercrystalline fracture in some of MgO specimens at the lower test temperatures.

While the grain size (d) fracture strength (σ_F) data involved scatter which was considerable at low temperatures, average results were found to fit the Petch equation $\sigma_F = \sigma_0 + kd^{-1/2}$ at all temperatures tested. The parameter k was found to decrease with increasing temperature as might be expected and at any given temperature, was greater for Lucalox than MgO. Contrary to expectations, σ_0 , which is considered to represent a measure of the fractional stress imposed by the host lattice on mobile dislocations, most frequently increased with increasing temperature.

No brittle-ductile fracture transition temperature was observed in either oxide. However, at high temperatures, stressing was accompanied by extensive grain rotation and grain boundary sliding imparting an apparent ductility to both materials.

TASK 4 - EFFECT OF MICROSTRUCTURE

1. INTRODUCTION

The metal oxides offer considerable promise as structural materials for advanced applications particularly where strength at high temperatures is required. In this latter respect their general superiority over metals is well known. However, one of the major problems associated with the use of these oxides is their extreme brittleness especially at temperatures below about $1/2 T_m$ (T_m = melting point, °K). In recent years some effort has been devoted to developing a better understanding of the nature of this brittleness and the relationship between stress, temperature, grain size and porosity. Although such knowledge is still incomplete, significant advances have been made.

In a detailed review of the dependence of mechanical strength of brittle polycrystalline materials on porosity and grain size, Knudsen⁽⁴⁻¹⁾ derived a relationship of the form:

$$S = KG^{-a} e^{-bP} \quad (4-1)$$

where

S is the strength of porous brittle material,

G is the mean grain diameter,

P is the specimen porosity,

e is the base, of Napierian logarithm, and

k, a and b are constants.

Crandall, et al⁽⁴⁻²⁾ studied the fracture strength in transverse bending as a function of grain size in Al_2O_3 . Since all specimens were of near theoretical density, porosity was eliminated as a variable. Although only three grain-size levels were examined, the relationship

$$S = 86000G^{-1/3} \quad (4-2)$$

was found to hold between fracture strength, S (psi) and grain size, G, (microns).

In more recent work, Spriggs and Vasilos⁽⁴⁻³⁾ investigated the influence of porosity and grain size on the transverse bend strength for polycrystalline Al_2O_3 and MgO . The testing was confined to room temperature. These investigators showed that the effect of porosity on strength was of the type previously suggested by Knudsen⁽⁴⁻¹⁾ and Duckworth⁽⁴⁻⁴⁾. On extrapolating to zero porosity, the variation of strength with grain size for the two oxides was found to be:

$$\text{Al}_2\text{O}_3 \quad S = 86000 G^{-1/3} \quad (4-3)$$

$$\text{MgO} \quad S = 75000 G^{-1/2} \quad (4-4)$$

for fabricated and machined specimens over a limited grain size range, while an expression of

$$S = 50000 G^{-1/6} \quad (4-5)$$

was obtained for specimens heat treated to yield much broader grain size range.

Comparison of equations (3) and (2) indicates that the data for Al_2O_3 is identical with the previous findings of Crandall, et al.⁽⁴⁻²⁾ Of course, these equations represent empirical relationships between the different variables that influence strength at a given temperature and do not provide information regarding the nature or mechanism of fracture in these polycrystalline materials.

In recent years work by Stroh⁽⁴⁻⁵⁾, Cottrell⁽⁴⁻⁶⁾, Petch⁽⁴⁻⁷⁾ and others^(4-8, 4-9) on cleavage fracture in so-called semi-brittle materials* such as many of the b c c metals at cryogenic temperatures has lead to significant advances in understanding of the mechanisms involved.

The success of these current theories dealing with the atomic mechanisms of cleavage fracture in metallic lattices prompted an extension of this thinking to a study of fracture behavior in ceramic materials. This approach, used in this task to study fracture in

* i. e., those crystalline materials which undergo some plastic deformation, although this may be extremely small, before fracture.

polycrystalline Al_2O_3 and MgO , centers around the Petch equation relating fracture strength, σ_F , and grain size, d ,

$$\sigma_F = \sigma_0 + kd^{1/2} \quad (4-6)$$

where σ_0 represents the frictional stress on an unlocked dislocation and k is a constant directly related to the surface energy associated with the formation of the fracture surfaces. This equation is particularly useful in studying fracture behavior since it separates the factors controlling σ_F into three components. Furthermore, the equation is based on a dislocation model for fracture and the parameters in the equation may therefore be interpreted in terms of this model.

In addition to studying the influence of d on σ_F over a broad range of temperatures, the experimental work was aimed at investigating the existence of a ductile-to-brittle transition temperature of the type observed in b c c metals. Previous work^(4-10, 4-11) demonstrated that non-metallic single crystals do exhibit a ductile-to-brittle transition behavior which, in general, is very gradual compared with metals. Kronberg⁽⁴⁻¹²⁾, however, showed that in the case of Al_2O_3 the transition temperature was relatively sharp and sensitively related to strain rate.

The influence of porosity on strength was not investigated in this study. Porosity, except for two grain-size levels in the Al_2O_3 specimens was held as low as possible and constant throughout. This permitted a direct determination of the influence of grain size without having to compensate for variations in porosity in different specimens.

Some of the experimental detail and results presented here have been reported before⁽⁴⁻¹³⁾ but are included so as to render this report complete in its present form.

2. MATERIALS

A. Polycrystalline Magnesium Oxide

All the MgO specimens tested were produced by hot pressing and subsequently grinding to a cylindrical shape 1 in. long by 1/2 in. diameter, such that the end faces were square to within 0.001 in. of the specimen axis. Details of the hot-pressing procedure were reported previously:⁽⁴⁻¹³⁾ The surface finish resulting from grinding was smooth and reproducible. The required variation in grain size was achieved by high-temperature annealing of hot pressed material at either 1700° and 1900°C for three hours. The grain size results, given in Table 4-I, were determined by quantitative metallographic methods using the equation

$$D = \frac{1.075}{M} \sqrt{\frac{A}{N}} \quad (4-7)$$

where

M is the magnification,

A is the area (sq cm),

N is the number of grains in area, A, and

D is the average grain diameter (cm).

Table 4-I

GRAIN SIZE OF MAGNESIUM OXIDE SPECIMENS

Condition	Average Grain Diam., d, (mm)	Average Grain Diam, d ^{-1/2} (mm ^{-1/2})
As-Hot Pressed	0.022	6.9
Annealed at 1700 °C for 3 hr	0.043	4.8
Annealed at 1900 °C for 3 hr	0.070	3.8

The annealing temperature - grain size data indicate that the rate of grain growth in these specimens was considerably lower than is normally encountered in polycrystalline MgO (see, for example, Daniels, Lowrie, Gibby and Curler⁽⁴⁻¹⁴⁾). The reason for the marked reluctance for grain growth to occur in this material is not clearly understood; grain boundary impurities, such as carbon picked up during hot pressing in graphite dies, probably play an important role in this phenomenon.

The chemical analysis of as hot-pressed and annealed materials is given in Table 4-II. These data indicate that, within the limits of accuracy of the analytical method, high-temperature annealing produced small changes in the impurity content of the oxide. The possible extent to which these changes influenced subsequent mechanical behavior is not known.

The relatively high carbon content of the hot-pressed material is attributed to contamination from the hot pressing dies referred to above, and its incomplete removal during the subsequent decarburization treatment.⁽⁴⁻¹³⁾

Typical microstructures of the as hot-pressed and the 1900°C annealed materials are given in Fig. 4-1 and 4-2, respectively. In both cases the grains are equiaxed and of uniform size. The densities of test specimens ranged from 99.4 to 99.7 percent of theoretical; the small amount of porosity being confined in general to the grain boundaries and particularly grain corners.

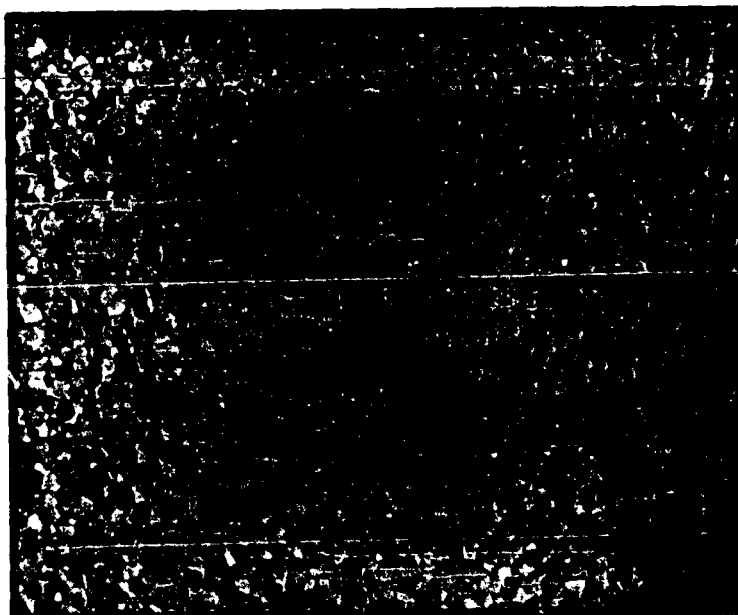
B. Polycrystalline Aluminum Oxide

The polycrystalline Al_2O_3 specimens were supplied by the General Electric Company, Cleveland, Ohio under the trade name Lucalox at five grain-size levels (see Table 4-III). The chemical analysis of Lucalox is given in Table 4-IV. In the as-received condition the specimens were 1 in. long by 1/2 in. diameter, with the end faces square to the specimen axis to within

Table 4-II
CHEMICAL ANALYSIS OF HOT-PRESSED AND ANNEALED MAGNESIUM OXIDE

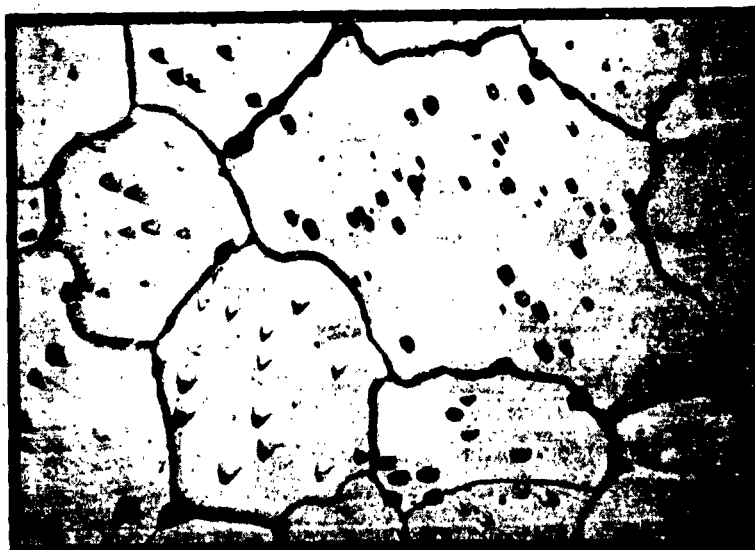
Element	Concentration (w/o) *		
	As Hot-Pressed	Annealed at 1700 °C	Annealed at 1900 °C
Mg	Principal constituent	Principal constituent	Principal constituent
Ca	0.5	0.03-0.3	0.03-0.3
Al	0.005-0.05	0.0005-0.005	0.0005-0.005
Fe	0.005-0.05	0.003-0.03	0.003-0.03
Si	0.005-0.05	0.0005-0.005	0.001-0.01
Ti	0.001-0.01	Trace < 0.0005	0.0005-0.005
Cr	0.0001-0.001	Trace < 0.0001	Trace < 0.0001
Cu	0.0001-0.001	Trace < 0.0001	0.0001-0.001
Li	Not detected < 0.03	Not detected < 0.03	Not detected < 0.03
C	0.018	Not determined	Not determined

* With the exception of the carbon determination, the analysis is semi-quantitative.



X 250

Fig. 4-1
AS HOT-PRESSED POLYCRYSTALLINE MAGNESIUM OXIDE
Etched in 5% Sol. HCl in Alcohol Grain Size = 0.02-0.025 mm



X 500

Fig. 4-2
POLYCRYSTALLINE MAGNESIUM OXIDE HOT-PRESSED AND
ANNEALED AT 1900 °C
Etched in 50% H₂SO₄ + 50% Sol. NH₄Cl held at 50 °C

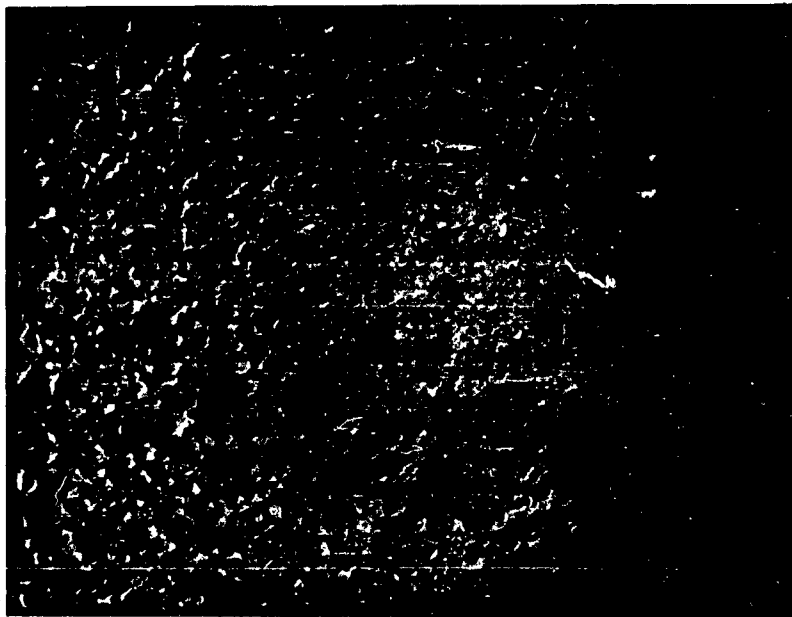
0.001 in. During preliminary tests it was discovered that the loading capacity of the compression testing unit was not adequate to produce fracture in these specimens at temperatures below 1900 °C. They were, therefore, centerless ground to 3/8-in. diameter to reduce the cross sectional area and thus the load at fracture. Subsequent testing at 1000 °C necessitated a further reduction in specimen diameter to 1/4 in. Although the height to diameter ratio for these specimens varied from 2 to 4 it was not thought to influence significantly any comparison made between the tests data collected at a 1000 °C and the higher temperatures.

Table 4-III
GRAIN SIZE AND DENSITY DATA, LUCALOX SPECIMENS

Nominal Avg. Grain Diameter, (mm)	Measured Avg. Grain Diameter, d, (mm)	Measured Avg. Grain Diameter, $d^{-1/2}$, (mm ^{-1/2})	Density, (g/cc)
0.005	0.004	15.7	3.85
0.01	0.018	7.3	3.94
0.03	0.040	5.1	3.98
0.05	0.047	4.5	3.98
0.10	0.10	3.2	3.98

The microstructure of Lucalox is illustrated in Fig. 4-3 and 4-4. The grain size in these structures, as in all specimens, was uniform and the presence of porosity is clearly evident in the fine grain material (Fig. 4-3). As for the MgO material, grain size determinations were made on a series of selected samples using Eq. 4-7.

The density of the Lucalox varied with grain size as the data in Table 4-III indicated. Theoretical density was approached at the coarser grain-size levels while falling to about 97.22 per cent of theoretical for the 0.004-mm material. Since porosity



X 250

Fig. 4-3
PHOTOMICROGRAPH OF LUCALOX AT 0.005 mm Grain Size.
(Note small amount of intergranular porosity characteristic
of the finer grain specimens, unetched)



X 150

Fig. 4-4
PHOTOMICROGRAPH OF LUCALOX. LITTLE EVIDENCE OF
POROSITY; MATERIAL APPROXIMATELY OF THEORETICAL
DENSITY. Unetched. Grain Size = 0.05 mm

Table 4-IV
SEMI-QUANTITATIVE SPECTROCHEMICAL
ANALYSIS OF LUCALOX

Element	Concentration (w/o)
Al	Principal constituent
Fe	0.07
Mg	0.15
Ti	0.01
Mn	0.001
V	0.004
Na	0.08
Cu	0.0003
Ni	0.0015
Ca	0.04
Cu	0.002
Ga	0.003
Si	0.03

has a pronounced influence on strength properties, its presence in the fine grain samples must be considered in the final analysis of the mechanical property data.

The dimensions of the compression test specimens were chosen with three considerations in mind:

- (1) the specimens should be stubby enough to avoid the possibility of elastic buckling. This requirement is amply satisfied, since elastic buckling is seldom of concern below "slenderness ratios" of 60;

- (2) The L/D ratio should be large enough to avoid any distortion of data resulting from friction effects exerted at the specimen-platen interface (these effects, resulting in an apparent increase in compressive strength owing to the frictional constraint, become significant only below L/D ratios of 2:0); and
- (3) to satisfy the dimensional allowances of the available high-temperature testing machine which could accept specimens only up to 1-1/4 in. in height. The specimen size selected satisfied all of these requirements.

Each specimen was carefully calipered to determine its actual diameter and cross sectional area prior to testing.

3. APPARATUS AND TESTING PROCEDURE

The high-temperature-compression testing apparatus was built around an existing high-temperature resistance furnace. (4-15) A sectional view of the apparatus is given in Fig. 4-5. Testing was carried out in a helium atmosphere and, with a tantalum heating element, the furnace was capable of temperatures up to 2200 °C. The rate of heating and cooling of specimens was closely controlled by manual adjustment, this being necessary in the case of MgO, which is particularly sensitive to thermal shock. It was also thought that controlled heating rates would tend to reduce the possibility of thermal cycling damage to the Lucalox rams used in the testing of Lucalox specimens.

The compression specimen was positioned in the uniform temperature zone of the furnace and the load applied through the bottom ram by a screw jack. The screw jack was driven by a 1/2-hp variable speed d-c motor through a 50:1 reduction gear. The load was measured by a resistance strain gage load cell which was directly recorded on a Speedomax recorder. The

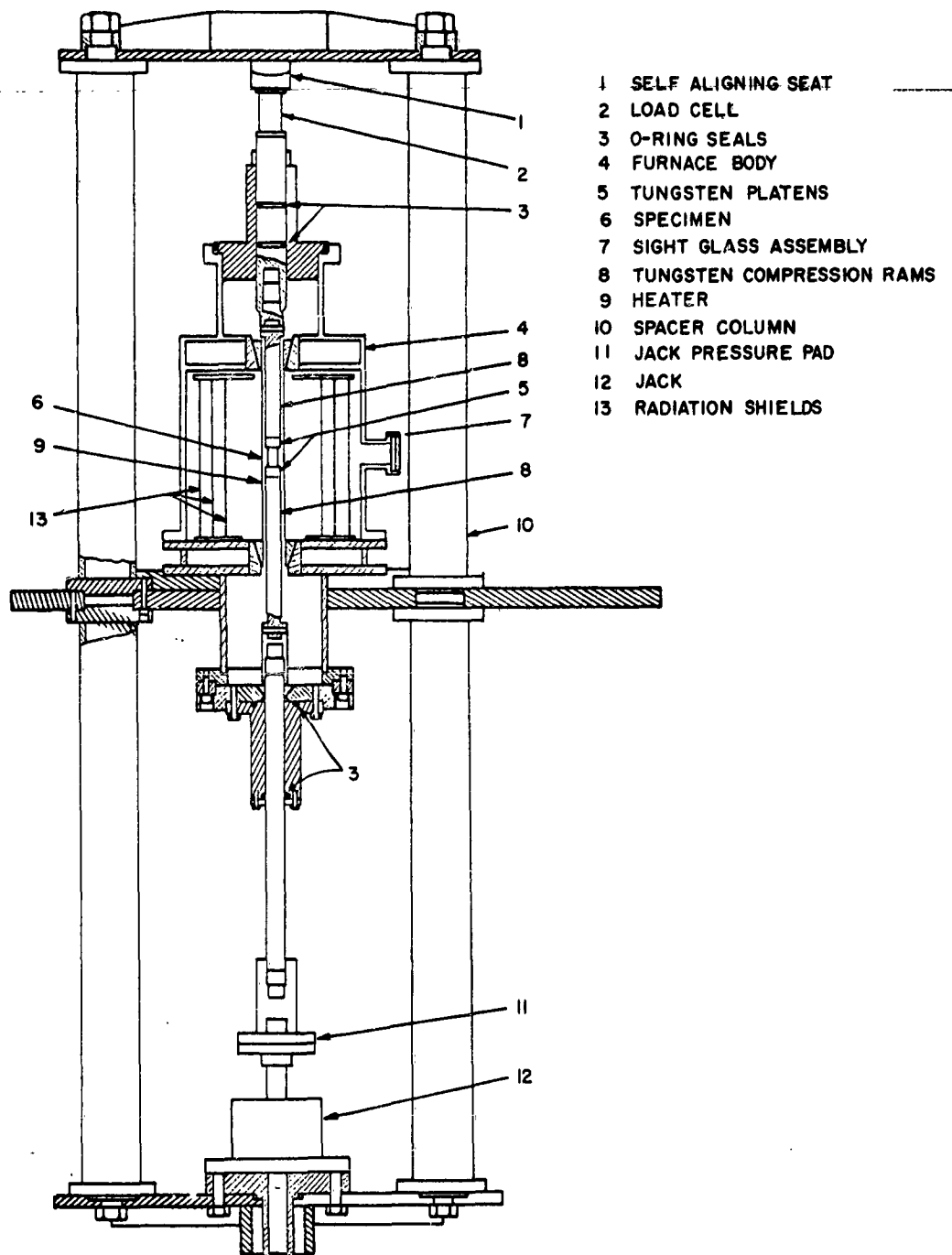


Fig. 4-5 HIGH TEMPERATURE COMPRESSION TESTING APPARATUS

screw jack speed was held constant at 6.8×10^{-2} in. per min resulting in a relatively constant strain rate of 6.8×10^{-2} in. per in. per min (1.13×10^{-3} sec⁻¹).

Two major problems were encountered in building the apparatus and in carrying out the compression tests; (1) obtaining axial alignment of the rams and (2) selection of a suitable ram material that would withstand the extremely severe temperature-stress condition involved.

The alignment problem was overcome by improved engineering design.

After a series of preliminary experiments it was decided to try both tungsten and Lucalox as ram materials, since both materials were commercially available in shapes suitable for this application. A set of 3/4-in. diam. tungsten rams have proved satisfactory for testing MgO up to 1600 °C, although the specimens did cause a small amount of localized deformation of the tungsten at the ram-specimen interface. The depth of penetration observed was about 0.0005-0.001 in. To avoid damaging the ends of the rams in this way, flat tungsten discs were always placed between the specimens and the rams. These discs were readily removed after each test, ground to yield a flat surface, and re-used for further testing.

Tungsten rams even up to 1-in. diam. were found completely inadequate for the testing of Lucalox where higher test temperatures were to be studied. It was, therefore, decided to use Lucalox rams for this phase of the work. Rods, 1-in. diam. were employed together with 1/4-in. thick discs which formed the working surfaces of the compression unit and thus reduced the possibility of damaging the rams. The rams were friction fitted into steel grips as illustrated in Fig. 4-6. Although this material has proved satisfactory from a mechanical standpoint, these desirable strength properties appear to deteriorate at high temperatures.



Fig. 4-6
LUCALOX RAMS, DISCS AND A COMPRESSION TEST
SPECIMEN USED IN THE HIGH TEMPERATURE COM-
PRESSION TESTING EXPERIMENTS

Between two and five specimens of a given grain size were tested at each temperature, the larger numbers being used at the low temperatures where the scatter in fracture stress data was greatest.

4. RESULTS

A. Magnesium Oxide

The compression testing of hot-pressed MgO was carried out at three grain-size levels (see Table 4-I) in the temperature range 1000°-1600°C. The fracture strength data are summarized in Fig. 4-7, and illustrate the dependence of strength on temperature and grain size. As the results indicate, the scatter in experimental data increase with decreasing test temperature, leading to overlapping of the strength values for the different grain-size levels at 1000°C. However, the average results do indicate a decrease in strength with increasing grain size.

The relationship between σ_F and $d^{-1/2}$ is given in Fig. 4-8. Using the mean values of σ_F at the different grain-size levels, the data yield essentially linear plots, in agreement with the Petch equation. The constants σ_0 and k for these temperatures are given in Table 4-V. However, as this table shows, no regular dependence of σ_0 on temperature can be noted.

Table 4-V

VALUES OF THE PARAMETERS σ_0 AND k
FOR MAGNESIUM OXIDE DETERMINED
USING THE PETCH EQUATION

Temperature, (°C)	σ_0 (psi)	k (psi/mm ^{-1/2})
1000	3,500	4,700
1300	8,500	2,150
1600	2,200	1,960

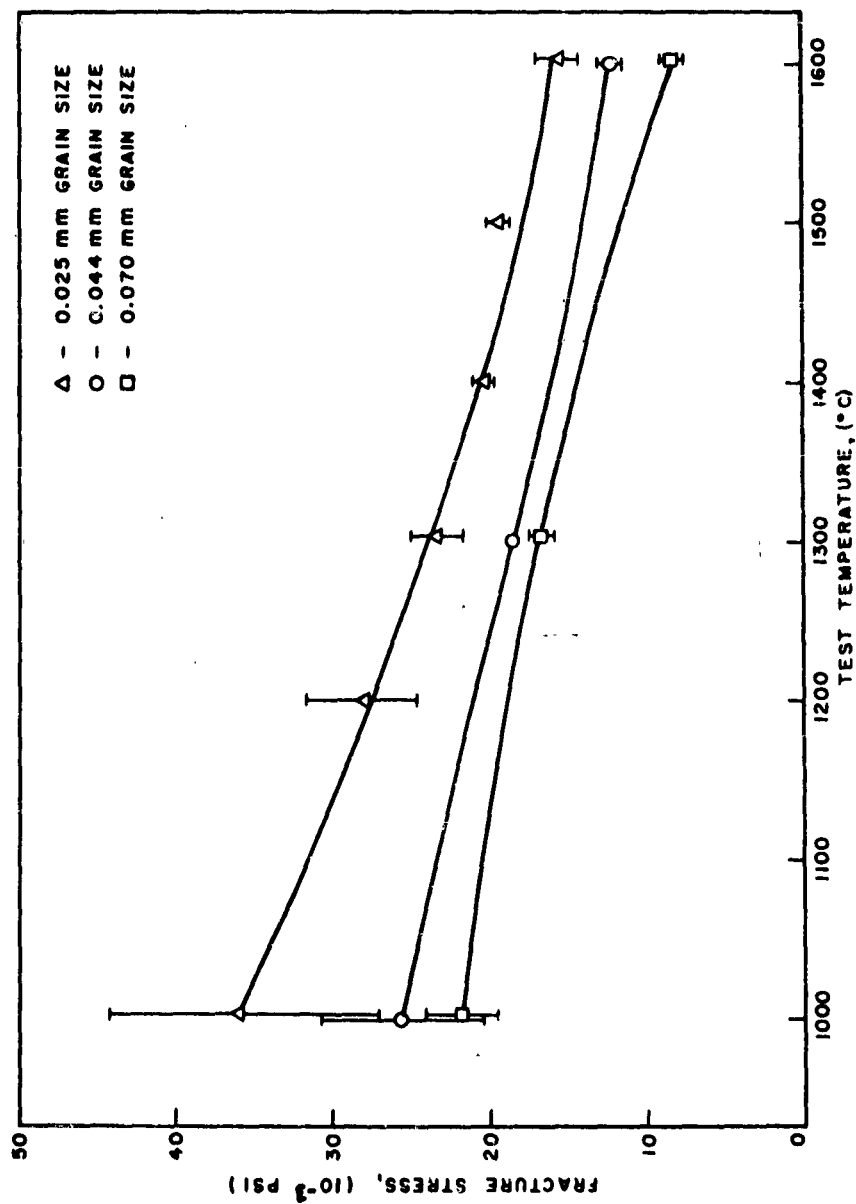


Fig. 4-7 VARIATION OF FRACTURE STRENGTH WITH TEMPERATURE FOR MAGNESIUM OXIDE AT THREE GRAIN-SIZE LEVELS

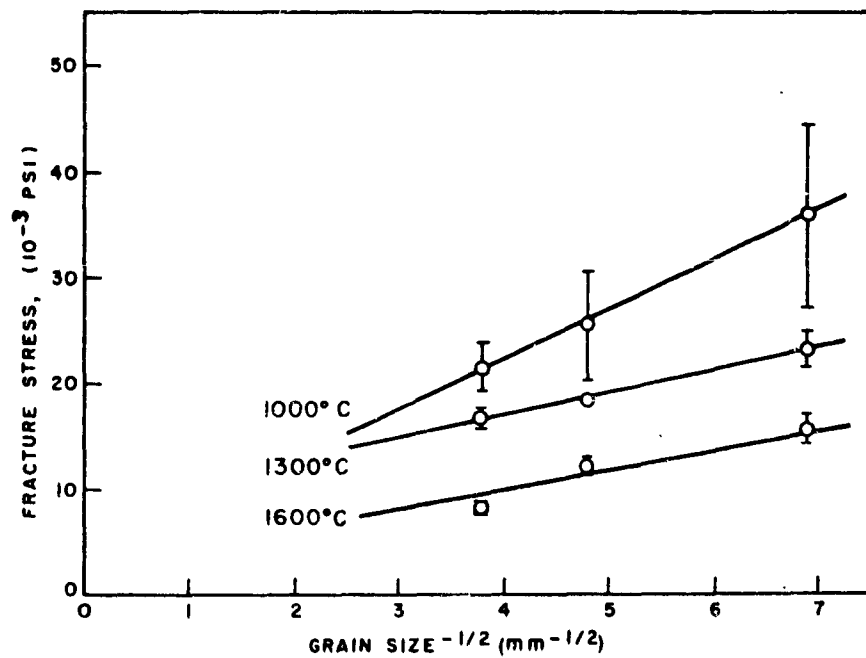


Fig. 4-8 PETCH-TYPE ANALYSIS FOR MAGNESIUM OXIDE IN THE TEMPERATURE RANGE 1000° - 1600°C

Some typical autographic load-compression curves for the fine grain specimens are given in Fig. 4-9. The fracture stress in these tests was taken as the point where the elastic portion of the curve deviated from linearity (F_1 , F_2 etc. in Fig. 4-9) since this represented the initiation of microscopically visible cracks. At low temperatures complete fracture occurred at this point (curve 1, Fig. 4-9) while at higher temperatures (1400°C and above) fracture in the fine grain specimens resulted after varying amounts of apparent plastic deformation. The extent of this apparent plastic strain showed a general increase with increasing temperature. Microscopic evidence indicated that this deformation was associated with extensive grain boundary sliding accompanied by the rigid rotation of grains and the formation of intergranular cavities, i. e., micro cracks. At these temperatures microscopical evidence indicated that the crack nuclei did not grow catastrophically but joined together as the compression test progressed, ultimately resulting in the collapse of the specimen. This apparent plastic deformation, thus, did not represent true ductility as is observed in metals and, as will be seen, was found to occur in the finer grain Al_2O_3 specimens. The 0.043-mm and 0.07-mm MgO specimens were completely brittle at all test temperatures, exhibiting load-compressive strain curves similar to curve 1 in Fig. 4-9.

Microscopic examination of polished and etched* specimens after testing indicated that the fracture path in the 0.022-mm grain size material was intergranular at all temperatures (see Fig. 4-10 and 4-13). Intergranular fracture also predominated in the 0.043-mm and 0.07-mm specimens but there was evidence of some transgranular cracks in the fracture pattern. These transgranular cracks were most frequently observed at the lower

* Etching was performed using a mixture of equal parts of sat. NH_4Cl solution and conc. H_2SO_4 maintained at 50°C.

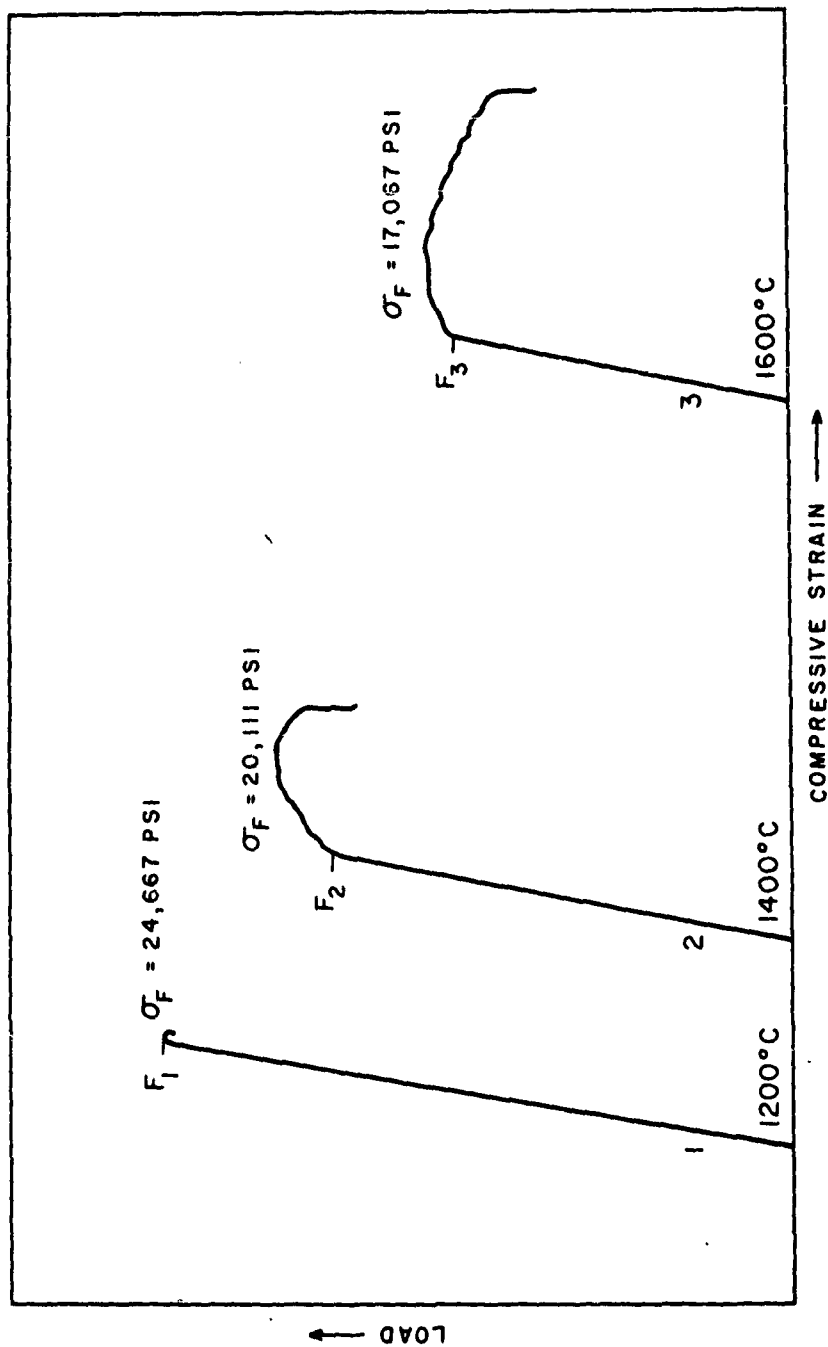
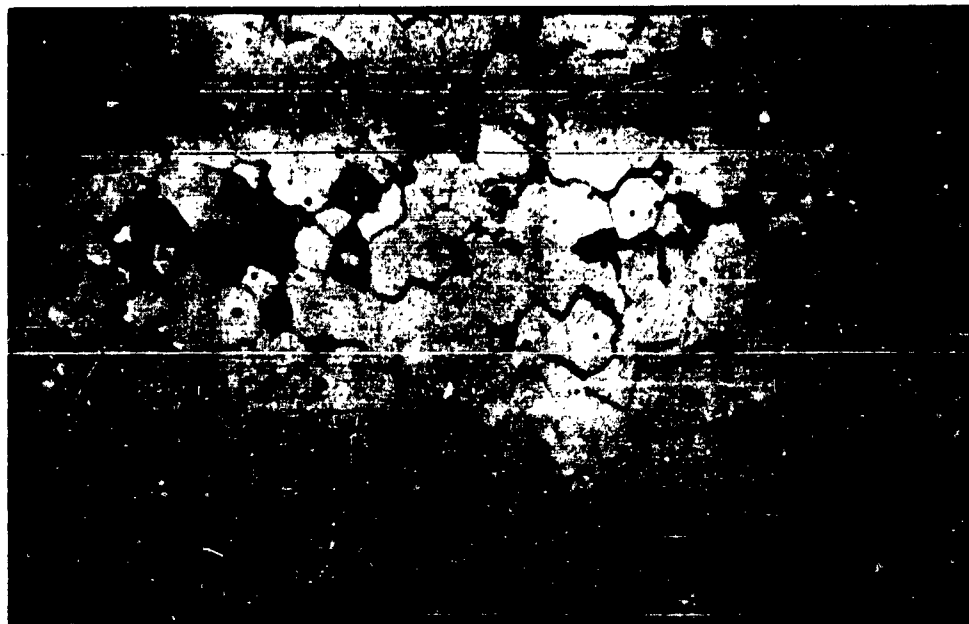


Fig. 4-9 AUTOGRAPHIC RECORDS OF LOAD-STRAIN CURVES OF POLYCRYSTALLINE MAGNESIUM OXIDE AT VARIOUS TEST TEMPERATURES



X 500

Fig. 4-10
INTERGRANULAR FRACTURE IN POLYCRYSTALLINE
MAGNESIUM OXIDE, COMPRESSION TESTED AT 1000°C.
Grain Size = 0.022 mm



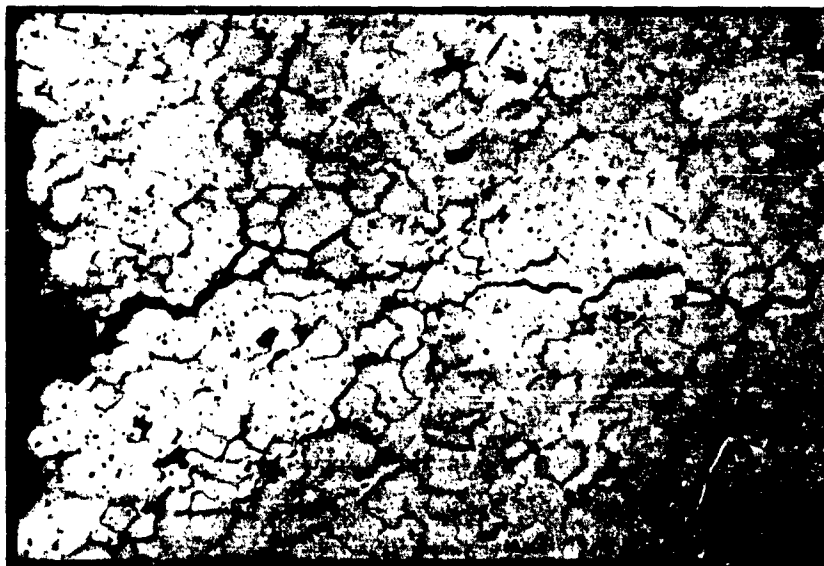
X 500

Fig. 4-11
INTERGRANULAR AND TRANSGRANULAR FRACTURES IN
MAGNESIUM OXIDE, COMPRESSION TESTED AT 1000°C.
Grain Size = 0.043 mm



X 500

Fig. 4-12
INTERGRANULAR AND TRANSGRANULAR FRACTURE IN
MAGNESIUM OXIDE, COMPRESSION TESTED AT 1000°C.
Grain Size = 0.007 mm



X 250

Fig. 4-13
INTERGRANULAR FRACTURE AND SOME EVIDENCE OF
GRAIN CHANGE IN SHAPE IN MAGNESIUM OXIDE AFTER
COMPRESSION TESTING AT 1600°C. Grain Size = 0.004 mm

test temperature in the 0.07-mm material. Typical example of mixed intergranular and transgranular cracking are illustrated in Fig. 4-11 and 4-12; the large black areas in these photomicrographs are due to grains pulled out during mounting and polishing.

Examination of grain shape in fractured specimens suggested that the MgO grains with the exception of the 0.022-mm specimens did not undergo any gross plastic deformation at any temperature. There was evidence in this material tested at 1600 °C that individual grains were exhibiting some plasticity (see Fig. 4-13).

The type of fractures obtained in the compression tests, shown in Fig. 4-14 through 4-16, illustrate the marked change in fracture geometry with test temperature. The specimens deformed at 1600 °C (Fig. 4-16) often buckled during testing which might suggest that the loading was not uniaxial. An alternative explanation is that the onset of "plastic deformation" is accompanied by grain-boundary shearing along a preferred direction in the specimen. Further strain develops this localized shearing at the expense of other possible directions until fracture is ultimately reached. A similar effect has been observed in the Lucalox specimens (see Fig. 4-21).

Surface blistering of specimens has been observed at 1400 °C and above, increasing in severity with temperature. The extent of blistering varied from specimen to specimen and in some cases did not occur. The blistering was thought to be due to the presence of unstable impurities in the MgO.

B. Aluminum Oxide (Lucalox)

The compression testing of Lucalox was carried out in the range 1000 °C-1900 °C at five grain size levels (see Table 4-III). The variation in fracture strength with temperature, given in Fig. 4-17 and 4-18, clearly shows the superior strength of Lucalox compared with MgO at least between 1000 ° and 1600 °C. The data



Fig. 4-14
POLYCRYSTALLINE MAGNESIUM OXIDE COMPRESSION
SPECIMEN FRACTURED AT 1200°C. Grain Size = 0.022 mm

Fig. 4-15
POLYCRYSTALLINE MAGNESIUM OXIDE COMPRESSION
SPECIMEN FRACTURED AT 1400°C. Grain Size = 0.022 mm



Fig. 4-16
POLYCRYSTALLINE MAGNESIUM OXIDE COMPRESSION
SPECIMEN FRACTURED AT 1600°C. Grain Size = 0.022 mm
(Note Surface Blistering and Buckling of Specimen)

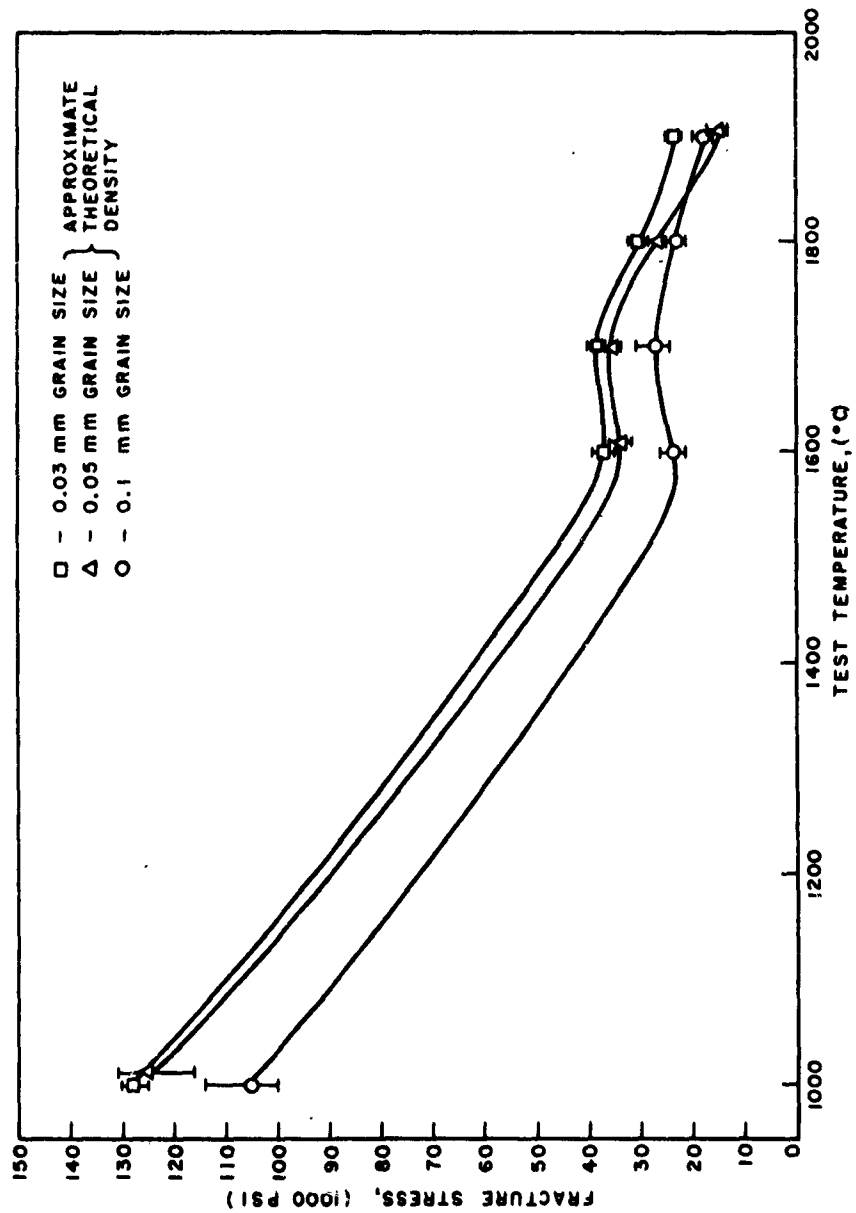


Fig. 4-17 VARIATION OF FRACTURE STRENGTH WITH TEMPERATURE FOR LUCALOX OF NEARLY THEORETICAL DENSITY

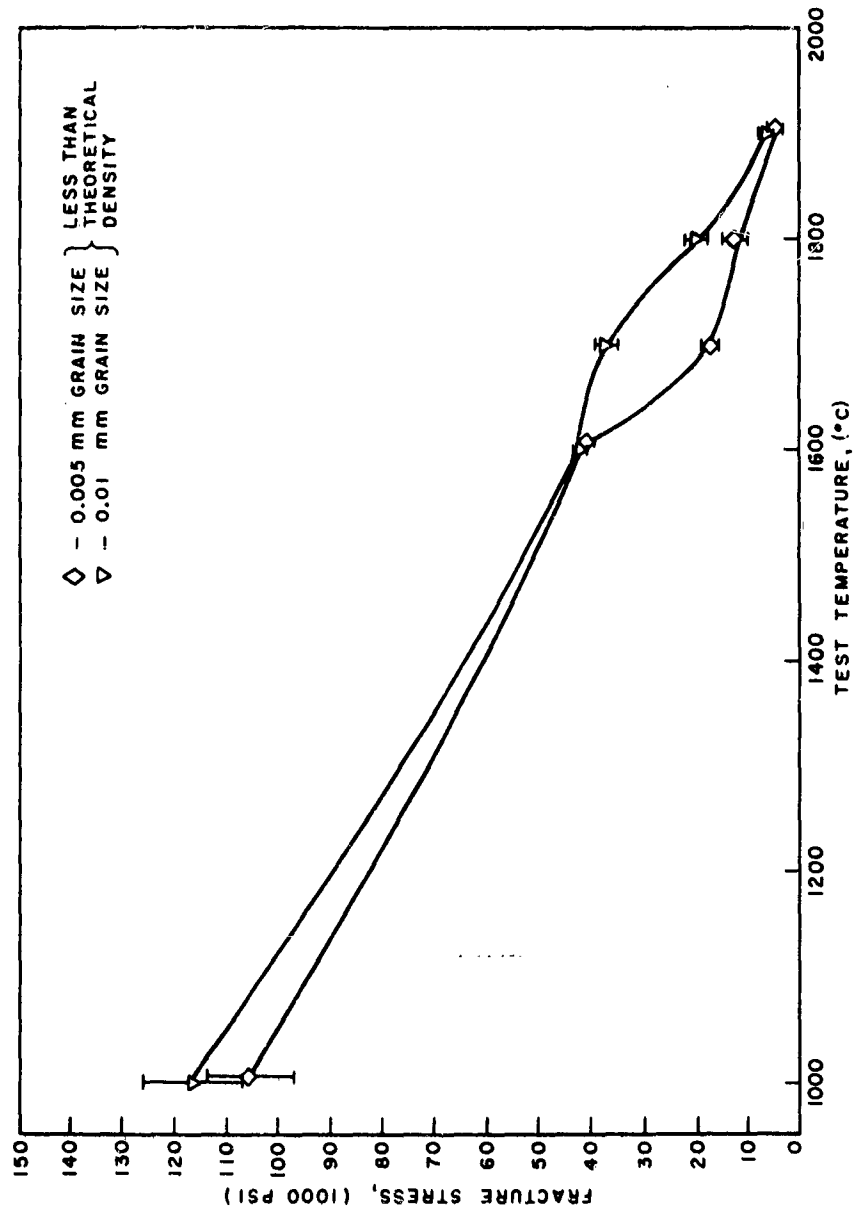


Fig. 4-18 VARIATION OF FRACTURE STRENGTH WITH TEMPERATURE FOR LUCALOX CONTAINING POROSITY

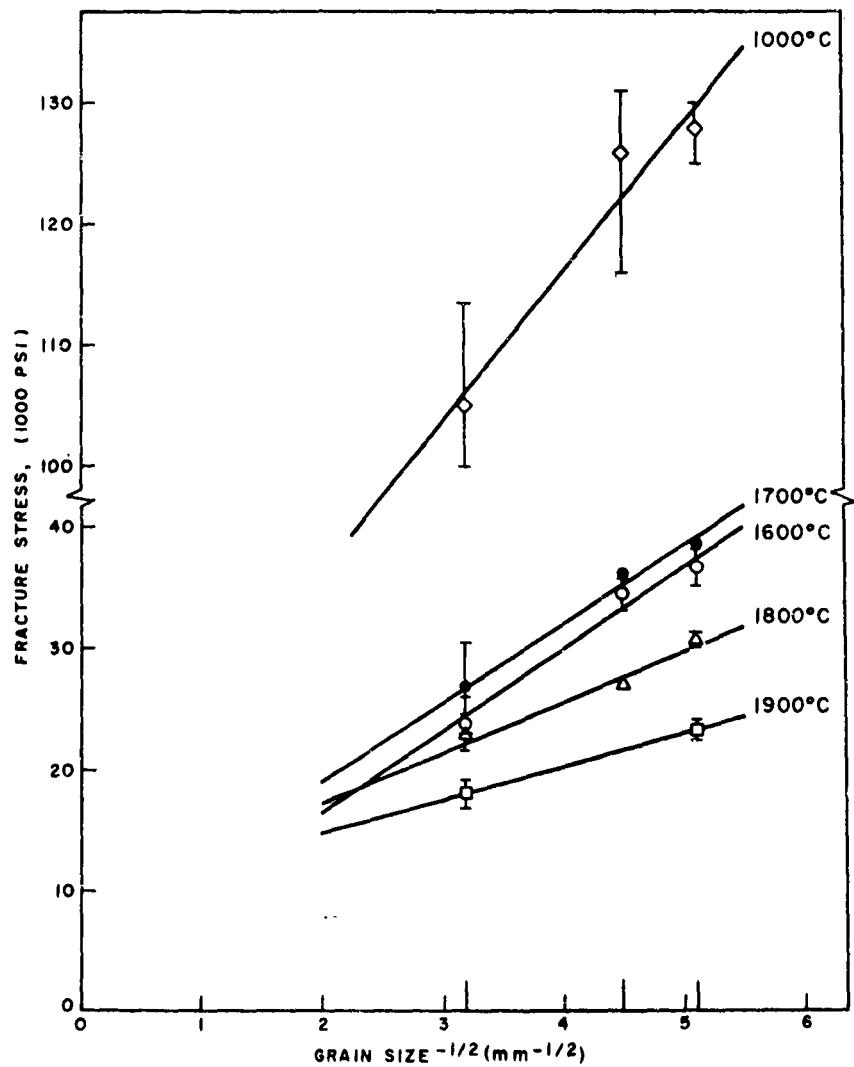


Fig. 4-19 PETCH-TYPE ANALYSIS FOR LUCALOX IN THE TEMPERATURE RANGE 1000° - 1900°C

for the 0.004-mm and 0.018-mm specimens are plotted separately (Fig. 4-18) since they contained significant amounts of porosity and thus cannot be compared directly, from the standpoint of grain-size effects, with the fully dense material.

The data indicate that, like MgO, the strength of Lucalox is both temperature and grain-size dependent. Up to 1600°C this dependency is what would be anticipated with increasing grain size and temperature leading to corresponding reductive in σ_F . Above 1600°C the strength of the fine grained materials containing porosity falls off very rapidly, with the result that, at 1900°C, they have the lowest strength of all specimens tested. Also, the fully dense specimens exhibited a slight increase in σ_F at 1700°C compared with 1600°C and thus is thought to be a real effect although the cause is not known.

The relationship between σ_F and $d^{-1/2}$ for the fully dense specimens at the various test temperatures is given in Fig. 4-19. Again, the data for the porous specimens have been omitted. As in the case of MgO, the data are limited and considerable scatter in σ_F exists at the lower test temperatures. It cannot be concluded decisively, therefore, that the $\sigma_F - d^{-1/2}$ results agree with the linear relationship implied by Eq. 4-6. However, straight lines have been drawn through the data points and the corresponding values for the constants σ_0 and k are given in Table 4-VI. The significance of these results will be discussed in the next section.

At all test temperatures the 0.1-mm, 0.047-mm and 0.04-mm specimens were completely brittle and fractured into many small pieces. The 0.018-mm and 0.004-mm specimens did exhibit apparent ductility at 1800°C and 1900°C in a similar way to that observed in fine grain MgO (curve 3, Fig. 4-9).

Figures 4-20 through 4-22 show the marked change in fracture characteristics with temperature at the 0.004-mm grain-size

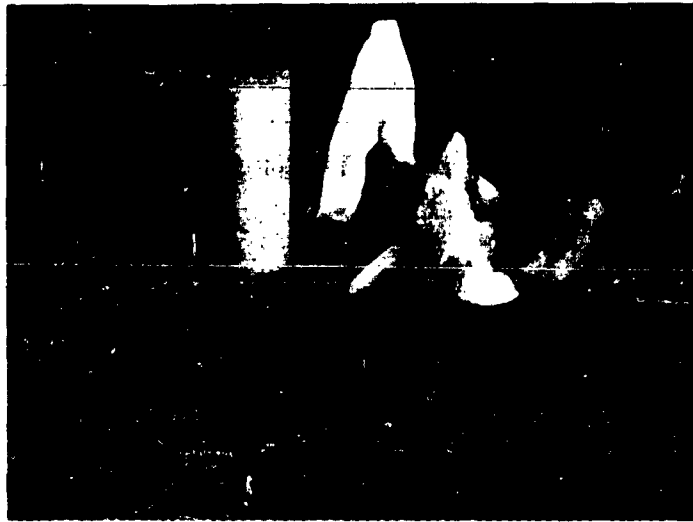


Fig. 4-20
LUCALOX SPECIMENS BEFORE AND AFTER TESTING IN
COMPRESSION AT 1600 °C. Grain Size = 0.004 mm



Fig. 4-21
LUCALOX SPECIMENS BEFORE AND AFTER TESTING
IN COMPRESSION AT 1700 °C. Grain Size = 0.004 mm

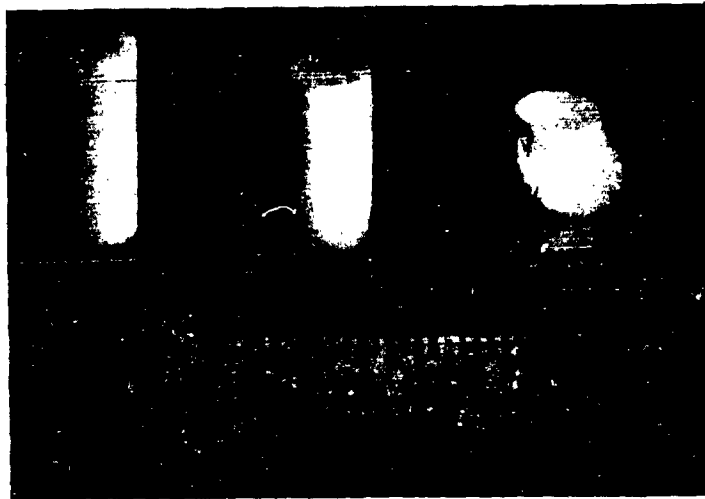


Fig. 4-22
LUCALOX SPECIMEN BEFORE AND AFTER TESTING IN
COMPRESSION AT 1900 °C. Grain Size = 0.004 mm

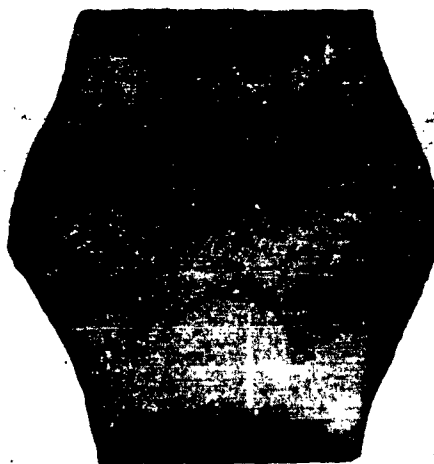


X 4

Fig. 4-23
CROSS SECTION OF LUCALOX SPECIMEN COMPRESSION
TESTED AT 1900 °C ILLUSTRATING THE NON-UNIFORM
STRAIN PATTERN AND THE ZONES OF MAXIMUM SHEAR
STRAIN. Grain Size = 0.004 mm



Fig. 4-22
LUCALOX SPECIMEN BEFORE AND AFTER TESTING IN
COMPRESSION AT 1900°C. Grain Size = 0.004 mm



X 4

Fig. 4-23
CROSS SECTION OF LUCALOX SPECIMEN COMPRESSION
TESTED AT 1900°C ILLUSTRATING THE NON-UNIFORM
STRAIN PATTERN AND THE ZONES OF MAXIMUM SHEAR
STRAIN. Grain Size = 0.004 mm

Table 4-VI

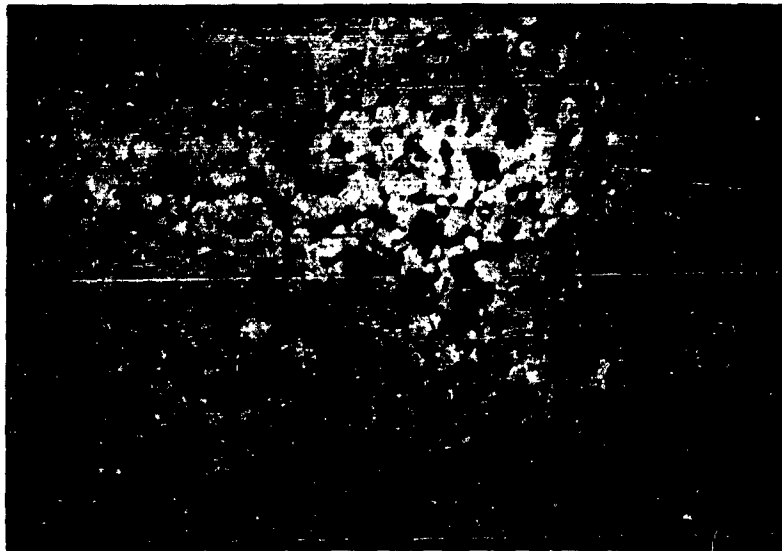
VALUES OF THE PARAMETERS σ_o AND k
FOR LUCALOX DETERMINED USING THE PETCH EQUATION

Temperature (°C)	σ_o (psi)	k (psi/mm ^{-1/2})
1000	66,000	12,500
1600	3,000	6,740
1700	6,000	6,500
1800	8,750	4,150
1900	9,200	2,760

level. The apparent ductile behavior of this material is illustrated in Fig. 4-22. Metallographic evidence of specimen deformed at 1900°C showed that deformation within the specimen was markedly heterogeneous with extensive intergranular cavities and fissures concentrated in regions of maximum shear (see Fig. 4-23 and 4-24). In those regions restrained from flowing, adjacent to the compression rams, the microstructure showed little change (Fig. 4-25). In addition, there was no evidence of any change in grain shape as a result of compression which suggests that the Lucalox grains did not undergo any gross plastic deformation.

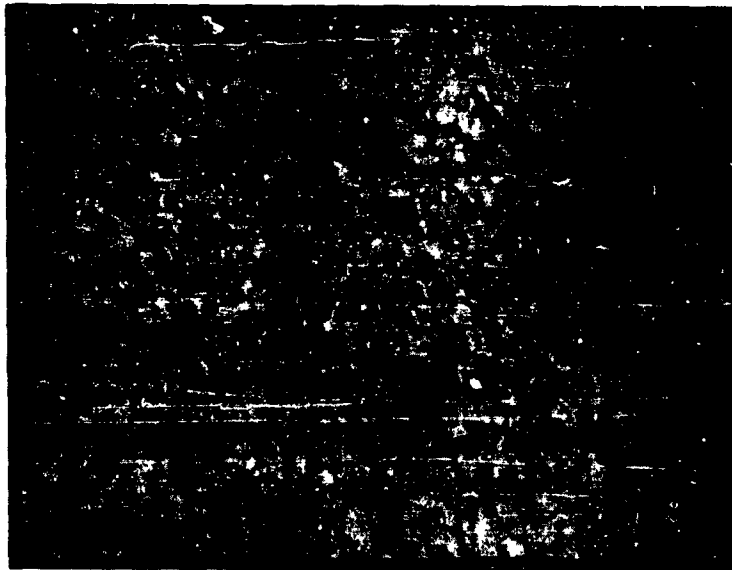
5. DISCUSSION

The experimental data clearly show that the brittle fracture strength of polycrystalline MgO and Lucalox (Al_2O_3) increases with decreasing grain size and decreasing temperature in the range 1000°-1600°C. Above 1600°C, some of these grain size-strength trends for Lucalox are reversed. The behavior of these ceramic oxides between 1000°-1600°C is identical in nature to that of brittle metals. As a result one is tempted, in the light of this and previous work (see, for example, references 4-16, 4-17, and 4-18), to account for the fracture characteristics of



X 250

Fig. 4-24
 PHOTOMICROGRAPH SHOWING THE EXTENSIVE POROSITY
 THAT DEVELOPS IN REGIONS OF MAXIMUM SHEAR IN
 LUCALOX, COMPRESSION TESTED AT 1900 °C.
 Grain Size = 0.004 mm



X 250

Fig. 4-25
 PHOTOMICROGRAPH OF AN AREA ADJACENT TO THE
 PLATEN-SPECIMEN. Interface Showing has Pictorial
 Constraint, Prevents Formation of Intergranular Cavitation
 Taken from Specimen Shown in Fig. 4-23

polycrystalline oxides in terms of current fracture theory: that some prior plastic deformation occurs to produce dislocations which, in turn, can generate crack nuclei. Since this slip need only be very limited, it is often difficult to detect it experimentally. Although the generation of glide dislocations in these oxides is more difficult than in metals, it has been demonstrated on single crystals of both MgO and Lucalox, that this is feasible at the temperatures and stresses under consideration.

When the crack nucleus has formed it may propagate intergranularly or transgranularly. In this study, fracture generally propagated by the intergranular mode indicating that, assuming some prior slip, the intergranular cohesive strength of hot pressed polycrystalline MgO and Lucalox controls mechanical strength in the range 1000°-1600°C. Stokes and Li⁽⁴⁻¹⁹⁾ reached a similar conclusion in room-temperature tensile tests on bi- and tri-crystals of MgO produced by hot-pressing techniques. The low intergranular cohesion in these materials is probably due to the presence of small amounts of residual porosity in the grain boundaries remaining after fabrication. Furthermore, grain boundaries often serve as sinks for impurities which can also lead to a lowering of intergranular cohesive strength.

It is clearly evident that the method of fabricating polycrystalline ceramic bodies must have an extremely important and often predominating influence on their mechanical behavior. All powder methods of fabricating have the inherent disadvantage of residual porosity, sometimes immeasurably small and, also, possible pick-up of impurities. Thus, the true intergranular cohesive strength is never reached in such materials. Further work investigating the properties and determining the nature of grain boundaries in ceramic materials to include the influence of conventional and new fabrication techniques is much needed at this time.

No transition from brittle to ductile behavior with increasing test temperature was observed in either MgO or Lucalox. In this respect these polycrystalline oxides were unlike many metals which exhibit this transition in fracture mode with temperature. It is interesting to note, however, that ductile-brittle transitions have been observed in single crystals of MgO⁽⁴⁻¹⁰⁾ and Al₂O₃⁽⁴⁻¹²⁾ suggesting that a temperature dependent transition in fracture mode is an inherent characteristic of these oxides. The fact that a transition was not noted in this investigation is attributed to the interplay between intergranular cohesive strength, its temperature dependence and the difficulty of producing grain-to-grain slip.

The brittleness characteristic of MgO and Lucalox at the lower test temperatures gave way to apparent ductile behavior with increasing temperature and decreasing grain size. This was considered to be due to a decrease in intergranular cohesion with increasing temperature so that a stage was reached when the applied stress led to extensive grain boundary sliding and the formation of intergranular cavities, i. e., cracks. Crack growth then occurred by the linking up of small intergranular cracks as the applied stress increased and under such conditions catastrophic brittle fracture propagation was completely suppressed.

The Petch-type analysis of the grain-size data for MgO and Lucalox must be examined with caution because of the limited number of grain sizes studied and the scatter in fracture stress results observed at the lower temperatures.

Averaging the fracture stress values at all test temperatures yielded linear relationships between σ_F and $d^{-1/2}$, indicating the following points of interest:

- (1) The values of k for both oxides show a decrease with increasing temperature, i. e., σ_F becomes less grain-size dependent. According to Stroh:⁽⁴⁻⁵⁾

$$k = \sqrt{\frac{6\pi\gamma G}{1-\nu}} \quad (4-8)$$

where

γ is the effective surface energy associated with fracture,

G is the shear modulus, and

ν is Poisson's ratio.

γ includes a contribution resulting from plastic work in the vicinity of the crack (γ_p), in addition to the true surface energy (γ_T). Since γ_p should increase with temperature, it is difficult to explain the behavior of k in terms of a decrease in γ . Assuming that ν varies only slightly with temperature, possible changes in G must be considered. The data in Table 4-VII shows that G falls rapidly for both oxides in this temperature range and can account, in part at least, for the temperature dependence of k .

Table 4-VII

VARIATION IN SHEAR MODULUS WITH TEMPERATURE
FOR MAGNESIUM OXIDE AND ALUMINUM OXIDE

Reference	Material	Fabrication Procedure	Porosity, % of Voids	Temperature (°C)	Shear Modulus, (psi x 10 ⁶)
4-20	MgO	Hot pressed - 2500 psi, Fired 1830 °C for 5 hr	2	30	16.7
				1100	10.3
				1200	8.4
				1400	5.2
4-21	Al ₂ O ₃	Fired at 1885	3	RT	18.1
				1050	15.4
				1350	9.8
				1550	5.5

- (2) The grain-size dependence of σ_F for Lucalox is more pronounced than for MgO at any given temperature in agreement with the work of Spriggs and Vasilos.⁽⁴⁻³⁾ This effect may be related to the significant difference in G for these oxides if the other parameters in Eq. 4-8 are assumed to be relatively similar for the two materials.
- (3) The values derived for σ_0 for both oxides show, with two exceptions, a surprising and unexpected increase with temperature. Since σ_0 represents the frictional resistance imposed by the lattice on a mobile dislocation it is to be expected that this parameter would decrease with temperature. The exceptions to this pattern were found in Lucalox where between 1000 °C and 1600 °C σ_0 drops rapidly and from 1300 ° to 1600 °C in MgO. However, the value of 66,000 psi at 1000 °C for Lucalox appears abnormally large.

6. CONCLUSION

The fracture strengths in uniaxial compression of both polycrystalline MgO and Lucalox of high density showed a marked temperature dependence in the range 1000 °-1600 °C and 1000 °-1900 °C, respectively. This variation in strength was also accompanied by a change in the mode of fracture which showed a similar trend in both oxides.

The fracture strengths of MgO and Lucalox were shown, in general, to increase with decreasing grain size at any given temperature. This dependence was more pronounced in Lucalox than MgO. The fine grain Lucalox specimens were exceptions to this behavior in the range 1600 °-1900 °C. This was attributed, in part at least, to the presence of porosity and a concomitant change in fracture mechanism.

Microscopic examination of fractured specimens of both Lucalox and fine-grain MgO indicated that failure always occurred by intergranular fracture. The medium and coarse grain MgO exhibited mixed intergranular and transgranular fracture paths although the former mode did predominate.

The fracture stress data indicated that Lucalox is considerably stronger than MgO. At 1000°C, Lucalox has about three times and at 1600°C, twice the fracture strength of MgO.

The fracture stress-grain size data were subjected to a Petch-type analysis. Because of the limited amount of data and scatter in the fracture stress results obtained at low-test temperatures, it cannot be concluded with certainty that the Petch equation holds. However, averaging of test data did yield linear plots between σ_F and $d^{-1/2}$. The constant k decreases with increasing temperature for both MgO and Lucalox while at any given temperature, it is always higher for Lucalox. The behavior of σ_0 was unexpected since it generally increased with increasing temperature.

There was evidence of apparent ductility in both MgO at 1600°C and Lucalox at 1900°C. However, in the case of Lucalox, the ductility was traceable to a grain boundary sliding mechanism rather than gross plastic deformation of the bulk material. In polycrystalline MgO this mechanism may also have been operative although metallographic evidence did suggest that some true plastic deformation of the grains may also have occurred. It appears, therefore, that the possibility of obtaining true ductility is greater in polycrystalline MgO than Lucalox. This conclusion might reflect basic differences in the slip mechanisms and the crystallographic structures of these oxides.

7. REFERENCES

- 4-1 Knudsen, F.P., J. Am. Ceram. Soc., 42, No. 8, 376 (1959).
- 4-2 Crandall, W.B., Chung, D.H., and Gray, T.J., "The Mechanical Properties of Ultra-Fine Hot-Pressed Alumina", North Carolina State College, Raleigh, North Carolina, March 1960, Interscience Publishing, New York, 1961.
- 4-3 Spriggs, R.M., and Vasilos, T., "Effect of Grain Size and Porosity on Transverse Bend Strength and Elastic Modulus of Hot-Pressed Alumina and Magnesia", Presented at the 63rd Annual Meeting, Am. Ceram. Soc., Toronto, 1961.
- 4-4 Duckworth, W., "Discussion of Ryshkewitch Paper", J. Am. Ceram. Soc., 36, No. 2, 68 (1953).
- 4-5 Stroh, A.N., Advances in Physics 6, 418 (1957).
- 4-6 Cottrell, A.H., Trans. AIME, 212, 192 (1958).
- 4-7 Petch, N.J., "The Ductile-Cleavage Transition in Alpha-Iron" in Fracture, B.L. Averbach, et al, ed. John Wiley and Sons, N.Y. (1959).
- 4-8 Gilman, J.J., "Cleavage, Ductility, and Tenacity in Crystals" in Fracture, B.L. Averbach, et al, ed. John Wiley and Sons, N.Y. (1959).
- 4-9 Low, Jr., J.R., Deformation and Flow of Solids, p. 60, Springer-Verlag, Berlin (1956).
- 4-10 Murray, G.T., J. Am. Ceram. Soc. 43, 330 (1960).
- 4-11 Johnson, T.L., Stokes, R.J., and Li, C.H., 5th Technical Report Nonr-2456 (00) NR-032-451, July 1959.
- 4-12 Kronberg, M.L., J. Am. Ceram. Soc. 45, 274 (1962).
- 4-13 Weil, N.A., ed., Studies of the Brittle Behavior of Ceramic Materials, ASD-TR-61-628, April 1962.
- 4-14 Daniels, A.V., Lowrie, Jr., R.C., Gibby, R.L., and Cutler, I.B., J. Am. Ceram. Soc., 45, 282 (1962).

- 4-15 Domagala, R.F. and McPherson, D. J., Trans AIME, p. 238, February 1954.
- 4-16 Westwood, A. R. C., Phil. Mag 6, 195 (1961).
- 4-17 Clarke, F. J. R., Sambell, R. A. J. and Tattersall, M. G., Trans. British Ceram. Soc. 61, 61 (1962).
- 4-18 Johnston, T. L., Li, C. H., and Stokes, R. J., p. 341, Strengthening Mechanisms in Solids, ASM, Metals Park, Ohio (1962).
- 4-19 Stokes, R. J., and Li, C. H., 6th Technical Report, ONR Research Project Nonr-2456 (00) NR-032-451, June 1962.
- 4-20 Ryshkewitsch, E., J. Am. Ceram. Soc., 34, 322, (1951).
- 4-21 Wygant, J. F., J. Am. Ceram. Soc., 34, 374 (1951).

TASK 5 - INTERNAL FRICTION MEASUREMENTS

Principal Investigator : P. D. Southgate and L. M. Atlas
Armour Research Foundation

ABSTRACT

On Part One of this Task the internal friction of single crystal MgO was studied to determine, in particular, the effect of anneal time and temperature, stress amplitude and dislocation density upon dislocation damping in the material.

The activation energy of dislocation pinning during anneal was found to be 2.3 or over a temperature range of 400° to 700°C. A construction involving curve translation is suggested which permits collapsing the whole temperature range onto a single anneal curve, valid for the entire range. Evidence strongly indicates that the dislocation pinning process is ascribable to the diffusion of vacancies to the dislocations.

Attempts to explain the experimental results in terms of existing theories were not successful. Analytical models examined included the stretched string model of Koehler and Granato-Lucke and the abrupt kink model of Brailsford. Comparisons were developed for three measurements: (1) temperature dependence, (2) amplitude dependence, and (3) the annealing kinetics of internal friction.

Information was also gathered on the room temperature creep behavior of MgO crystals, and work on dislocation damping behavior below room temperature has begun.

Damping studies on polycrystalline commercial Wesgo Al_2O_3 , constituting the work on Part Two of this program, showed that at temperatures below 800°C the relaxation process resembles that in alkali-free glass. Between 800°C and 1350°C, damping appears to be controlled by the motion of impurity cations, which gradually gives way to the diffusion of O_2 vacancies as the temperature is increased. The formation of a single relaxation peak in this material appears to be prevented; instead Q^{-1} exhibits a continued rise with increasing T . In creep studies carried out to 1300°C, the deformation rate appears to be controlled by the diffusion of Al ions.

TASK 5 - INTERNAL FRICTION MEASUREMENTS

Part One: Studies on Single Crystals

Principal Investigator: P. D. Southgate
Armour Research Foundation

I. INTRODUCTION

The dynamic properties of dislocations in ceramic materials are being investigated along three major lines. First, the fundamental origin of the damping force on a dislocation in an otherwise perfect lattice is being sought. Secondly, the mechanism of diffusion of point defects in the crystal to dislocation sites, and the consequent pinning of dislocations during an anneal at elevated temperatures is being investigated. Thirdly, a study is being made of the nature of non-linearity of forces acting on a dislocation line, which apparently allow increased ease of motion once the dislocation has moved away from its equilibrium position under the action of an applied stress. All these features of dislocation motion are related to the degree of brittleness of the material: their relevance has been discussed in the introduction to the previous report⁽⁵⁻¹⁾.

Internal friction measurements form a valuable tool for determining both the damping forces and the forces required to break a dislocation away from its equilibrium position. In this task we are measuring internal friction between 10 and 50 kc/s from -195°C to 1000°C in material which has been plastically deformed at room temperature to introduce dislocations. Studies have been confined entirely to single crystal MgO of commercial purity. The results are analyzed in terms of three phenomena: (1) the temperature dependence of the logarithmic decrement measured at low amplitudes of oscillation, which is independent of amplitude (2) the reduction of this amplitude-dependent damping during anneal at temperatures in the range 400° - 700°C (3) the nature of the amplitude dependence of damping. In each case, experimental results are compared with existing theories; the agreement is often

found unsatisfactory. Further theoretical developments, given in sections 5-8 and 5-9 are based on similar models of dislocation motion to those used in the past.

The damping and break-away forces measured by internal friction may be taken to be very similar to those operating to dissipate the energy of a moving crack, since in both cases the motion of the dislocation is fairly small. On the other hand, it should be pointed out that both the damping and the break-away forces operating during gross slip of the material will be of a different nature, since in this case we are dealing with a general rearrangement of the dislocation network. Each dislocation will be constantly intersecting other dislocations and lattice defects as it moves through the lattice, and consequently the energy dissipated during these intersections will be added to that dissipated by dislocation motion through an ideal lattice.

2. SPECIMEN DEFORMATION

Dislocations were introduced into the specimens by bending at room temperature. The bend technique is essentially as described in the previous report on this program⁽⁵⁻¹⁾, creep being allowed to occur under constant load. A displacement gage was added to the apparatus (shown in Fig. 5-1) so that creep curves could be plotted. The strain gages mounted on the ring are connected in a bridge, the output of which is fed through a d-c amplifier to a recorder. Relative displacement of tubes connected to opposite sides of the ring will unbalance the bridge, producing recorder displacement.

There is a considerable advantage in using specimens of dumb-bell form, since then, during flexural oscillation, the bending moment is almost constant along the center section. Furthermore, dislocations may conveniently be introduced by plastic bending in a more uniform manner than in a straight bar. The technique used

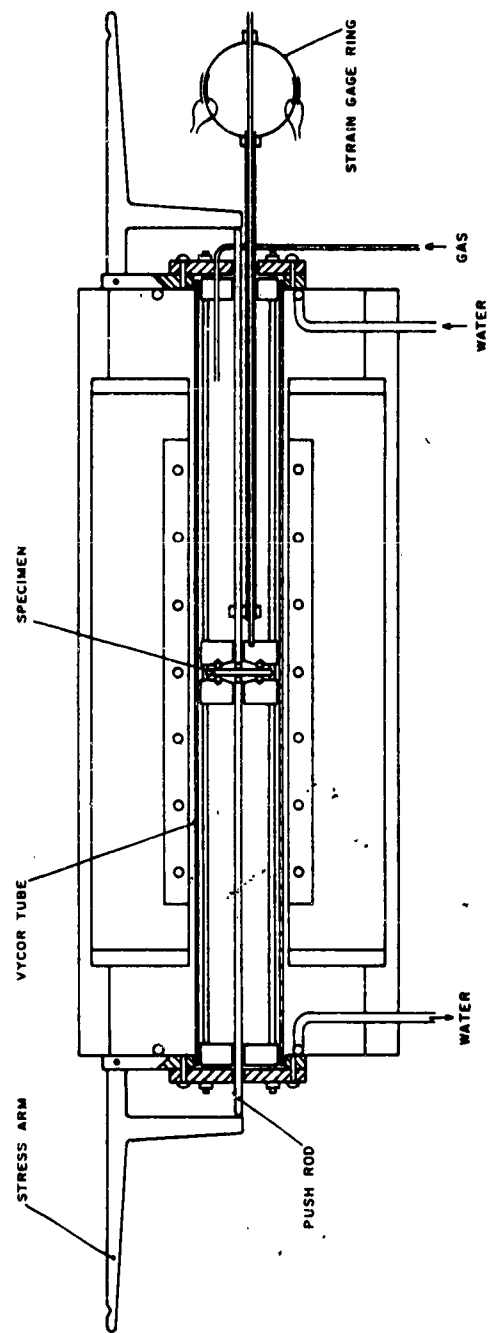


Fig. 5-1 APPARATUS FOR DEFORMING BAR SPECIMENS AND MEASURING CREEP CURVES

is shown in Fig. 5-2. The bar is initially cleaved to shape and the further cutting and drilling carried out with an ultrasonic tool. Initially a portion is cut from one side of the center section. Three-point bending at high temperature follows, the resulting slip line pattern being approximately indicated in the figure. Finally the other side of the center section is removed, the material thus cut away just including the neutral axis. Since the dislocation density increases now nearly linearly across the center section, the average dislocation density across the specimen should remain constant, if the section is thinned from both sides by a chemical etch to reduce the resonant frequency. Thus a study of internal friction as a function of frequency for a given dislocation density may be readily carried out using only one specimen. Care has to be taken to etch away sufficient surface material, so that none of the layer that has suffered additional working after deformation resulting from the ultrasonic machining process remains.

The data for this series of experiments are assembled in Table 5-I. Specimens prefixed 109 and 111 were obtained from Semi-Elements, Inc. and have a somewhat lower impurity content than the remainder which originated from the Norton Company. All were in the form of bars with the axis in the $[100]$ direction. The stress, σ_1 , quoted in column 7 of the table, an approximation, is derived on the assumption of a constant stress across the specimen during slip. Derivation of the outer fiber strain also is approximate, since it depends on the extent of the deformation along the bar. Studies of the dislocation pattern as revealed by etch-pits show that usually the slipped region extends along about 1.5 times the specimen thickness. In the arbitrary assumption that the strain in this region is constant, the outer fiber strain, ϵ_1 , becomes equal to one-third of the angle of bend, independent of the specimen thickness. However, the ratio of strained to unstrained material will be proportional to the thickness.

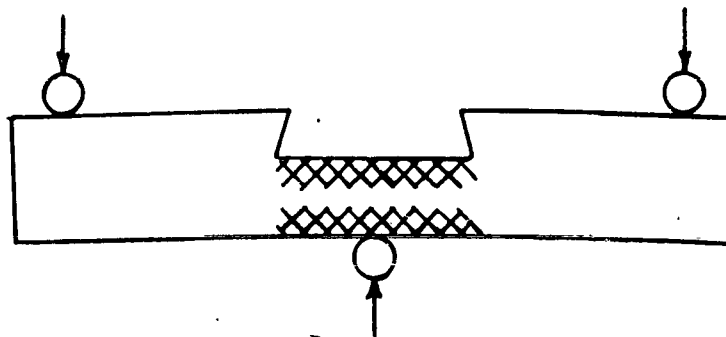
Table 5-1
BENDING DATA ON SINGLE CRYSTAL SPECIMENS

Specimen	Total Bend Angle (deg)	Thickness (mm)	Width (mm)	Weight (mm)	Total Outer Fiber Strain	Approximate Average Stress
1074	1.2	2.97	4.9	12.9	0.7	1.1
1092	4.0	2.25	3.7	6	2.3	1.8
1093	0.44	2.1	3.7	4.5	0.26	1.5
1094	0.55	2.5	3.7	6	0.32	1.4
				6.5		1.6
				7		1.7
1095	6	2.4	3.8	6	3.5	1.6
1112	Small	1.8	3.2	4.2	Small	1.5
1113	4.3*	1.5	3.4	3.06	2.5	1.5
1114	2.8*	1.2	3.3	2.0	1.6	1.6
1115	2.7*	1.05	3.3	1.38	1.6	1.5
1225	0.8	2.08	3.0	10	0.47	1.6
1233	2.1	3.0	4.75	6.5	1.2	0.7
1234	2.4	3.2	4.75	8	1.5	0.75

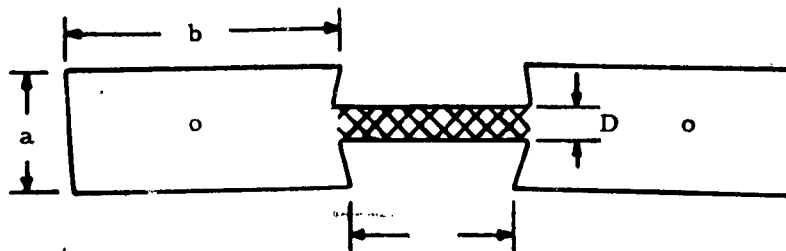
* Bend reversed.



(a) First Cut



(b) Bending, Showing Approximate Distribution of Slip Planes



(c) Second Cut, Further Thinning of Bridge Section Maintains Average Dislocation Density

Fig. 5-2 FABRICATION SEQUENCE FOR PLASTICALLY DEFORMED DUMBELL SPECIMENS

Three creep curves taken over about an hour on different MgO crystals are shown in Fig. 5-3. All show two stages of creep, both of which are approximately linear on a strain versus log time plot. There seems to be no direct correlation between creep rate and stress, since the specimen showing the slowest creep rate in the later stages in fact had the greatest applied stress. Analysis of these specimens for purity has not yet been carried out, so it is not clear whether the different behavior is due to purity difference. However, it is interesting that the logarithmic creep law is obeyed over these extended times. Figure 5-4 shows curves for specimens deformed over shorter times. If a specimen was loaded in stages, each stage is plotted separately, a fresh zero of time being taken as each extra load is applied. Here, considerable variation of behavior is observed; however, there is again a tendency for logarithmic creep behavior. The most highly strained specimen shows clear signs of strain hardening after 1.6 percent deformation.

3. DISLOCATION DAMPING ABOVE ROOM TEMPERATURE

Previous work has shown a broad peak in internal friction which is due to dislocation damping above room temperature. Further measurements have been made now which confirm the existence of this peak in more specimens, and show that its shape is unchanged as the total damping is reduced by anneal. Figure 5-5 demonstrates this in a specimen subjected to three stages of anneal. The lowest curve is flatter than the rest since a constant background damping has been added to the internal friction, reducing the total variation. The plotted points represent the internal friction at low amplitudes; at higher amplitudes, the internal friction always increased. The nature of the amplitude dependence, as well as possible interpretations of the temperature variation of damping, will be discussed later.

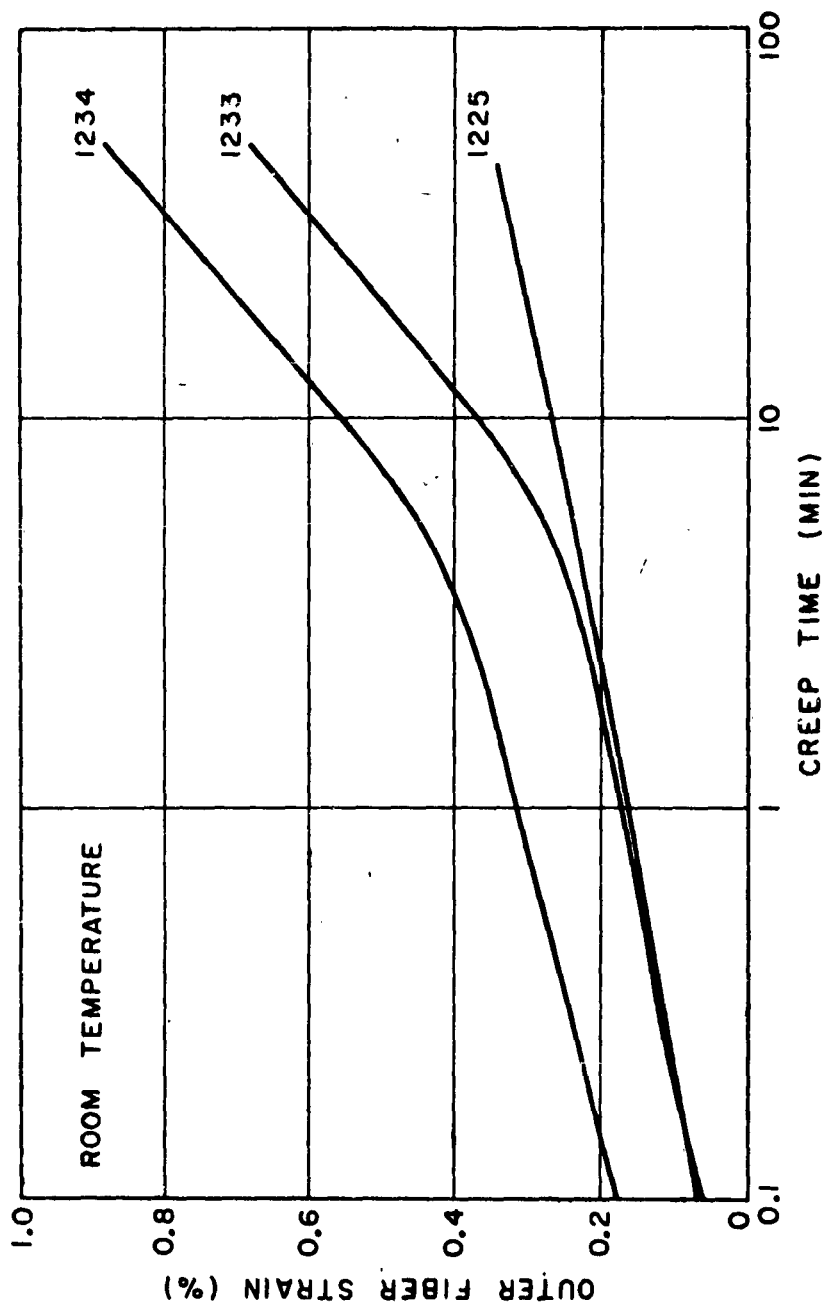


Fig. 5-3 CREEP CURVES ON THREE SPECIMENS DEFORMED IN BENDING
(Stress Values as in Table 5-1)

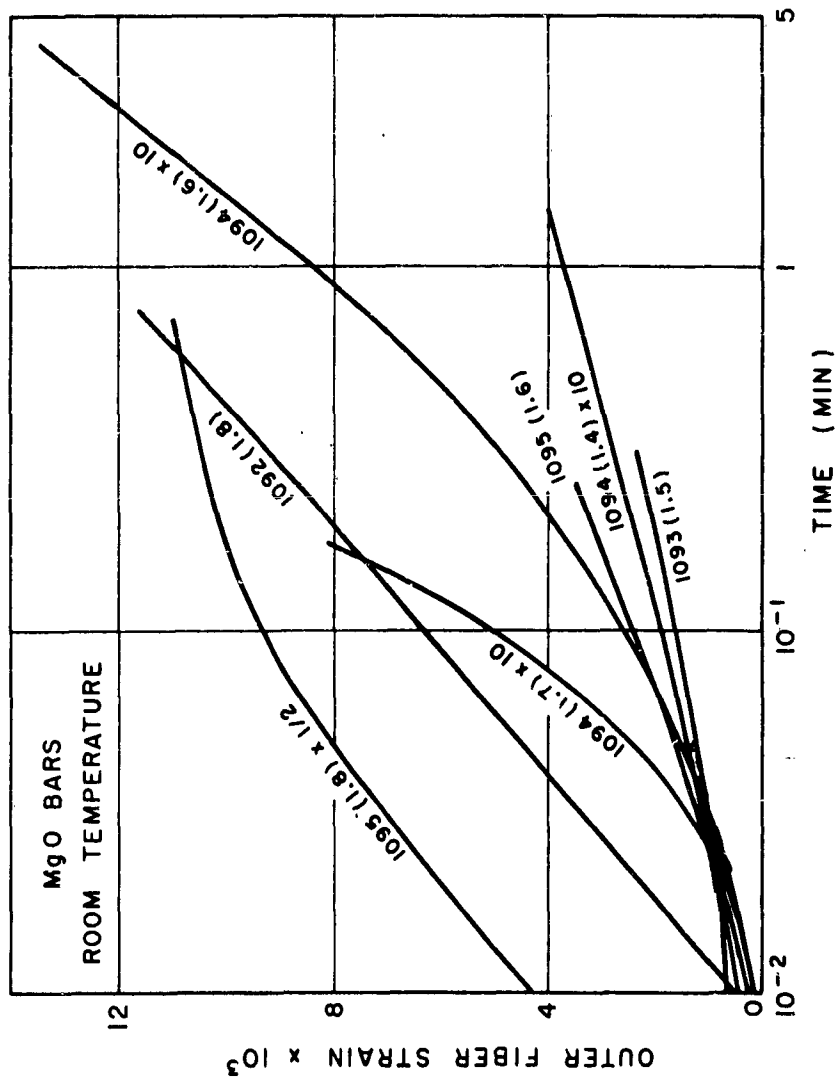


Fig. 5-4 EARLY STAGES OF CREEP FOR SEVERAL SPECIMENS
(Stress Values as in Table 5-1)

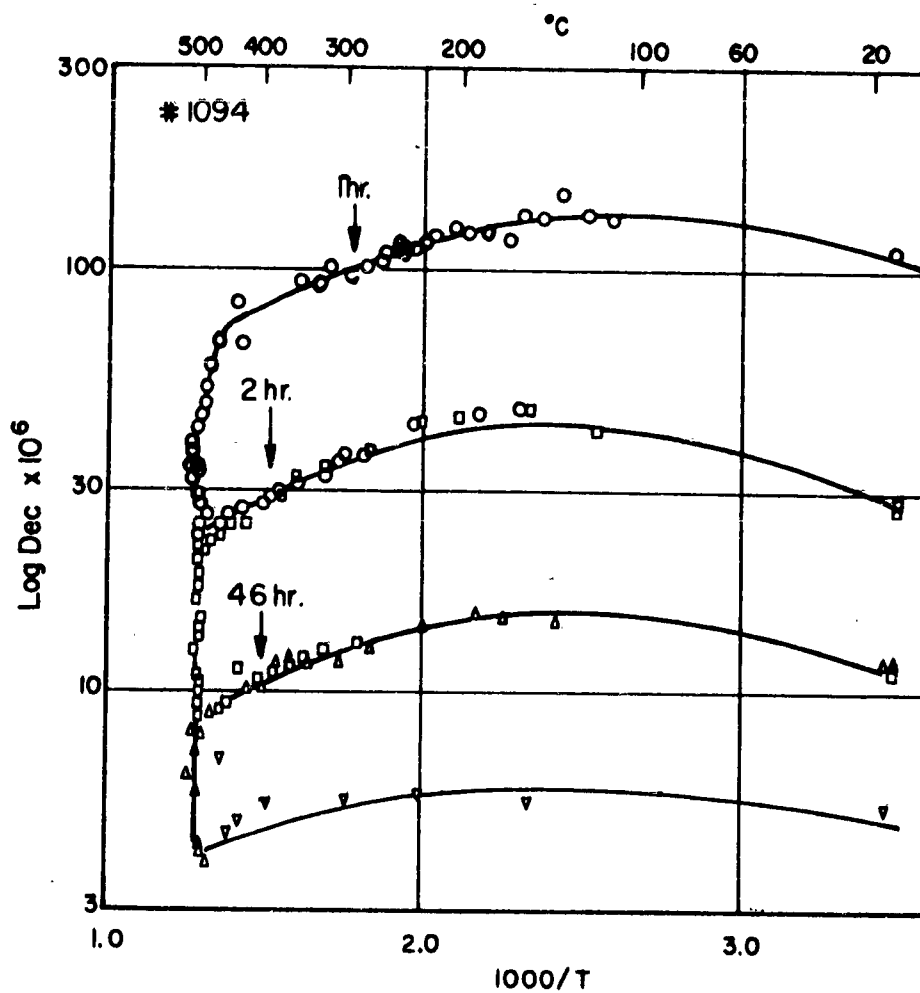


Fig. 5-5 TEMPERATURE DEPENDENCE OF LOGARITHMIC DECREMENT FOR A SPECIMEN, TAKEN AT SEVERAL STAGES OF ANNEAL

4. ANNEALING OF DISLOCATION DAMPING

A. Pinning by Vacancies

Work in other ionic crystals has shown that dislocation damping usually decreases as annealing occurs. This effect has been interpreted as being due to pinning of the dislocation at points along its length by cation vacancies. Bauer and Gordon^(5-2, 5-3) have investigated the pinning in NaCl, KCl, KBr, KI as vacancies are created by x-ray irradiation, and find that the results fit the Granato-Lucke theory for internal friction as a function of free dislocation segment length. The vacancies were created adjacent to the dislocation, and their effectiveness in pinning depended upon whether or not they had captured electrons and become F-centers. The earlier measurements of Gordon and Nowick⁽⁵⁻⁴⁾ on annealing of internal friction in NaCl were analyzed by Granato, Hikata and Lucke⁽⁵⁻⁵⁾, who showed that they fitted the concept of diffusion-limited precipitation of vacancies generated in the bulk, obeying a Cottrell-Bilby $t^{2/3}$ law.

In MgO, the vacancies which play the major role are anion vacancies. Hence, they cannot form F-centers, as do the vacancies in alkali halides, and their state of ionization cannot be so readily observed by optical means. In addition, since they are created by the deformation they will always lie within the slip bands, although not necessarily immediately adjacent to a dislocation. Depending upon the mechanism one favors in alkali halides, one would expect x-ray irradiation to form vacancies either adjacent to dislocations or uniformly throughout the bulk material. Thus some differences are to be expected between annealing of irradiated NaCl and deformed MgO.

B. Analysis of Results

An extensive series of measurements were carried out on two crystals which were bent through about 5 deg. Figures 5-6 and 5-7 show the results of a series of anneals at differing temperatures, a new zero of the time scale being taken for each change of temperature. A background damping has been assumed equal to the logarithmic decrement measured after a prolonged anneal at the highest temperature, and this has been subtracted from the total logarithmic decrement before plotting Fig. 5-6 and 5-7. It is reasonable to suppose that the background is due mainly to acoustic radiation along the specimen support wires. It will thus remain constant during the anneal, and depend only slightly upon temperature.

It will now be shown that the anneal curves may be synthesized into a single composite curve by a suitable scaling procedure. We start by assuming that the effect of temperature on the anneal process is to alter its rate, without changing its form. Then, any anneal curve may be assigned a time zero, the effective time of all previous anneals. Additionally, in this analysis we assume that the temperature dependence is governed by a single activation energy. Thus, to obtain the zero time of an anneal at temperature T_1 following anneals of periods $t_2, t_3 \dots$ at temperatures $T_2, T_3 \dots$, we add effective times:

$$t_0 = t_2 e^{\exp \frac{H}{k} \left(\frac{1}{T_1} - \frac{1}{T_2} \right)} + t_3 e^{\exp \frac{H}{k} \left(\frac{1}{T_1} - \frac{1}{T_3} \right)} + \dots$$

where H is the activation energy. If a composite curve corresponding to an anneal at T_0 is being produced, the time scale of the curve must then be shifted by a factor

$$\exp \frac{H}{k} \left(\frac{1}{T_1} - \frac{1}{T_2} \right)$$

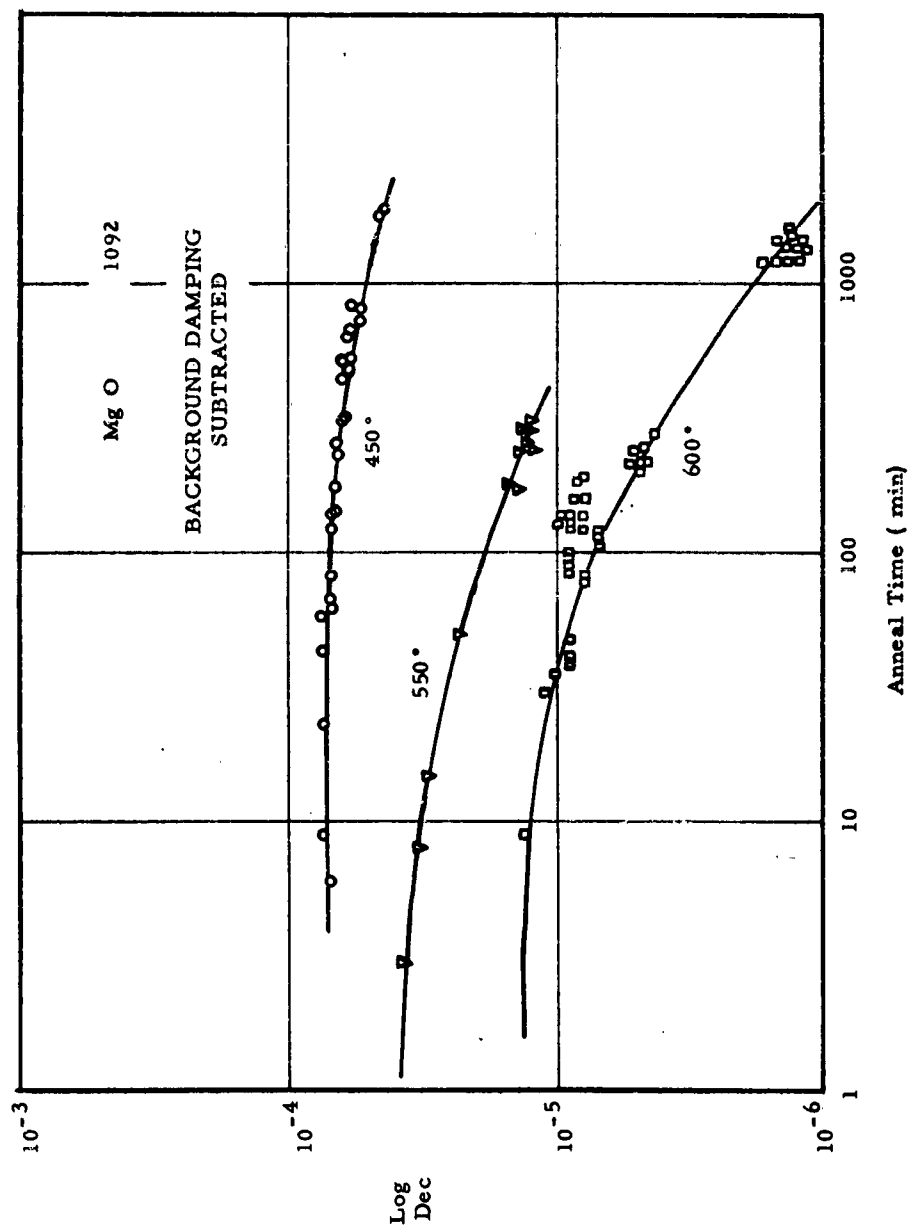


Fig. 5-6 ANNEALING OF DISLOCATION DAMPING IN SPECIMEN 1092

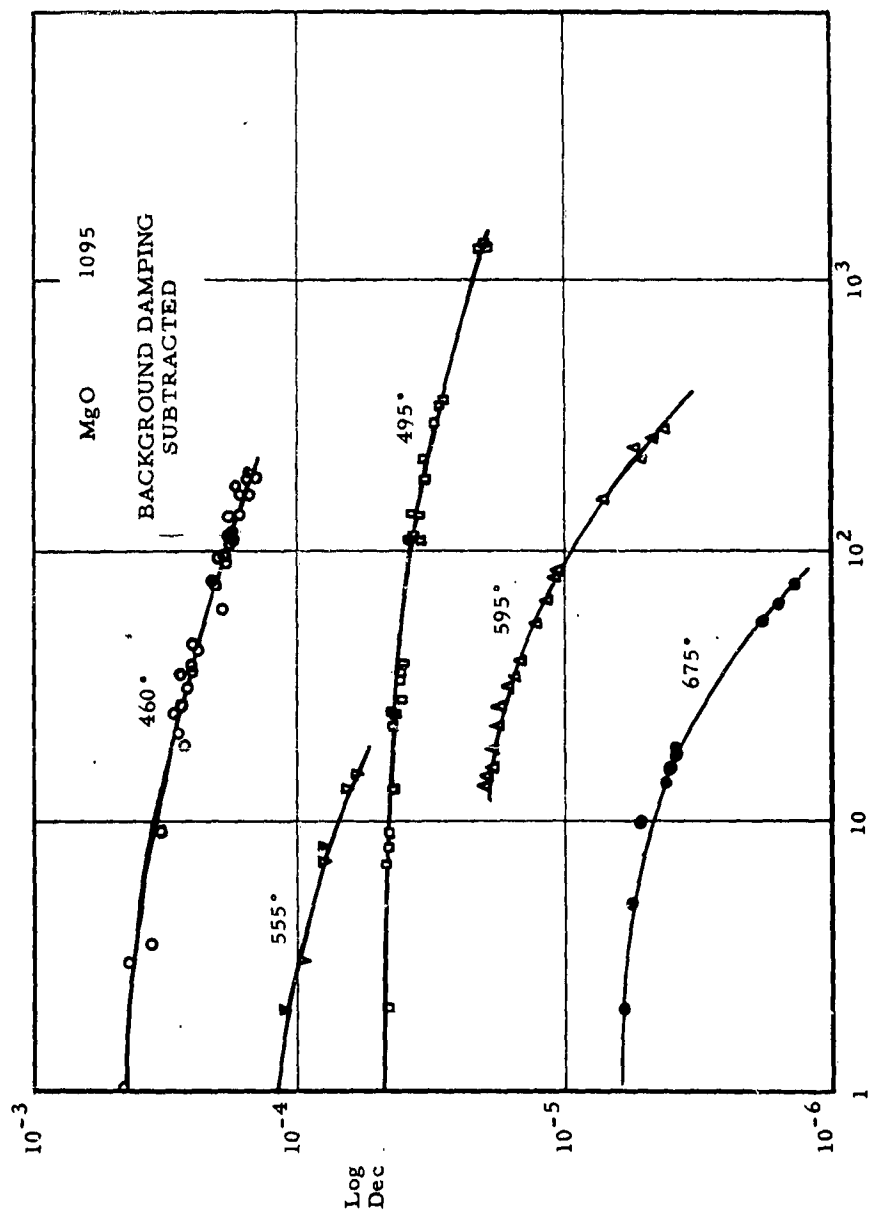


Fig. 5-7 ANNEALING OF DISLOCATION DAMPING IN SPECIMEN 1095

Finally, an adjustment must be made in the magnitude of the logarithmic decrement to allow for the temperature variation which is independent of annealing. This adjustment may be made either by fitting the beginning of one anneal curve to the end of the previous one, or by reference to the temperature dependence curves of Fig. 5-7. The whole procedure is illustrated in Fig. 5-8. Two imaginary anneal curves at temperatures T_1 and T_2 are shown. Stage 1 is then the initial subtraction of background damping; 2, compensation for temperature dependence; 3, the addition of the zero time due to previous anneals; and 4, the shift which is due to temperature dependence of anneal rate. The activation energy H is chosen so that after the shift a continuous curve is formed. Figures 5-9 and 5-10 now show the result of the procedure applied to the previous anneal curves, using an activation energy of 2.3 ev. In both cases, a composite curve which is straight, except in the final stages, and has a slope of $1/2$, is obtained. The fit is good over the whole of the temperature range.

Treatment along similar lines of the less complete and accurate annealing curves obtained previously is shown in Fig. 5-11. Again, a line of slope $1/2$ is obtained along the majority of the anneal. For specimens 1114 and 1115, however, an initial flat portion of the curve is seen. The magnitude of the damping at any time is very roughly proportional to the outer fiber strain produced during plastic deformation, with the exception of specimen 1074, which shows an anomalously low damping for which no explanation can be offered at the present time. During the annealing of specimen 1094, it was held at 400°C for a period of 2 hr, and later for 46 hr; no reduction in log decrement was observed during these periods, and indeed they turn out to represent only very short equivalent times at 500°C .

The activation energy of 2.3 ev which has been used in producing the composite anneal curves is probably reliable to ± 0.2 ev.

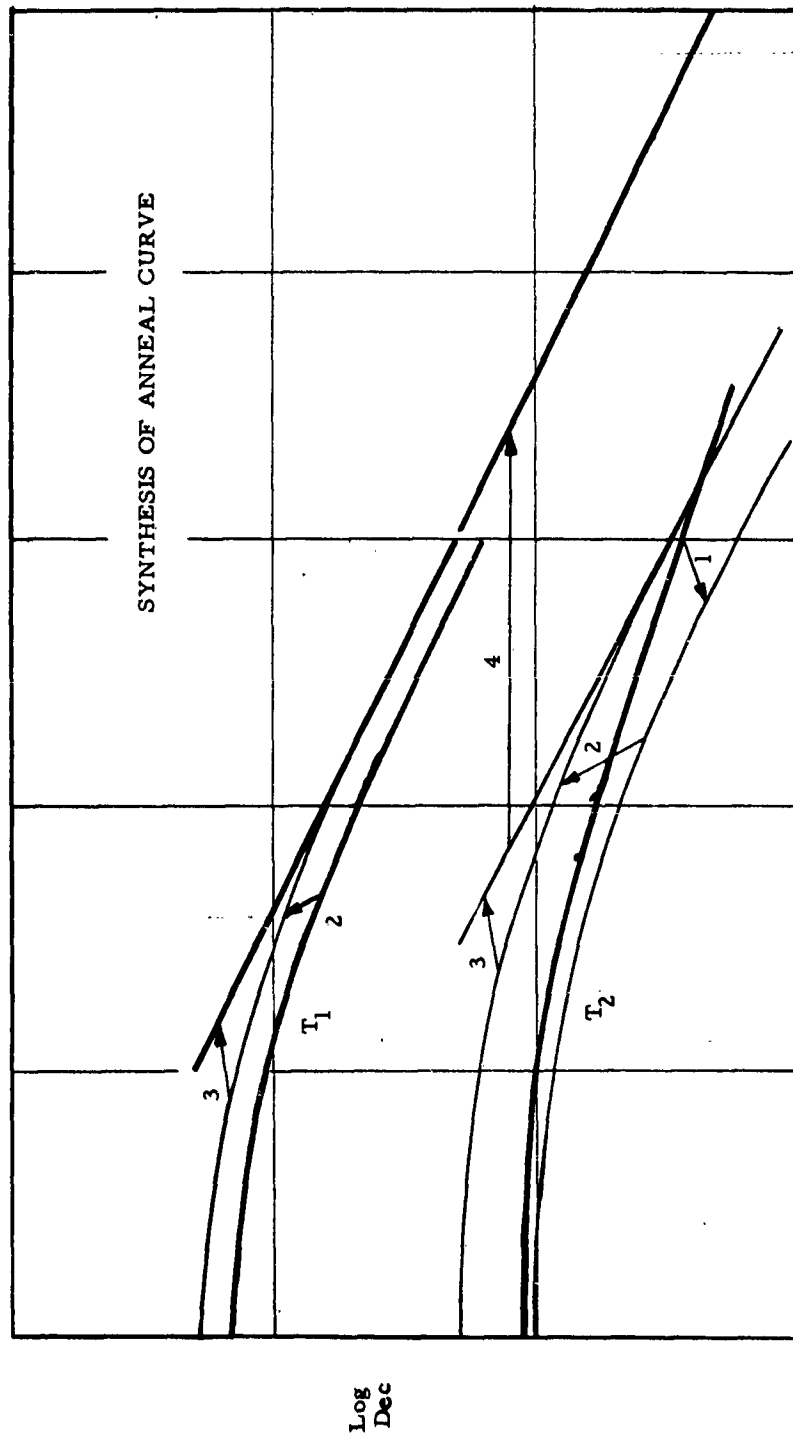


Fig. 5-8 METHOD OF ANNEAL CURVE SYNTHESIS

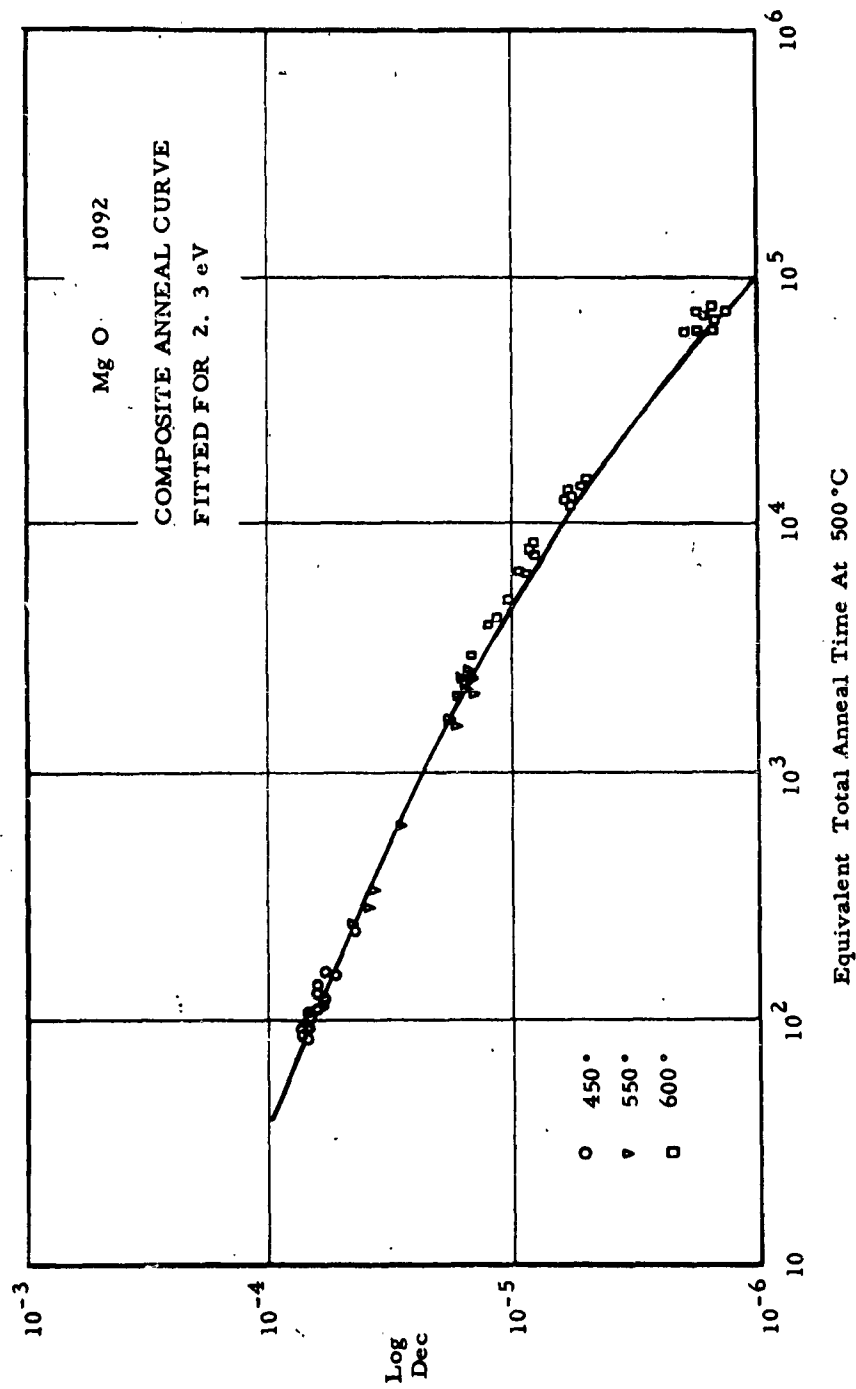


Fig. 5-9 COMPOSITE ANNEAL CURVE FOR SPECIMEN 1092

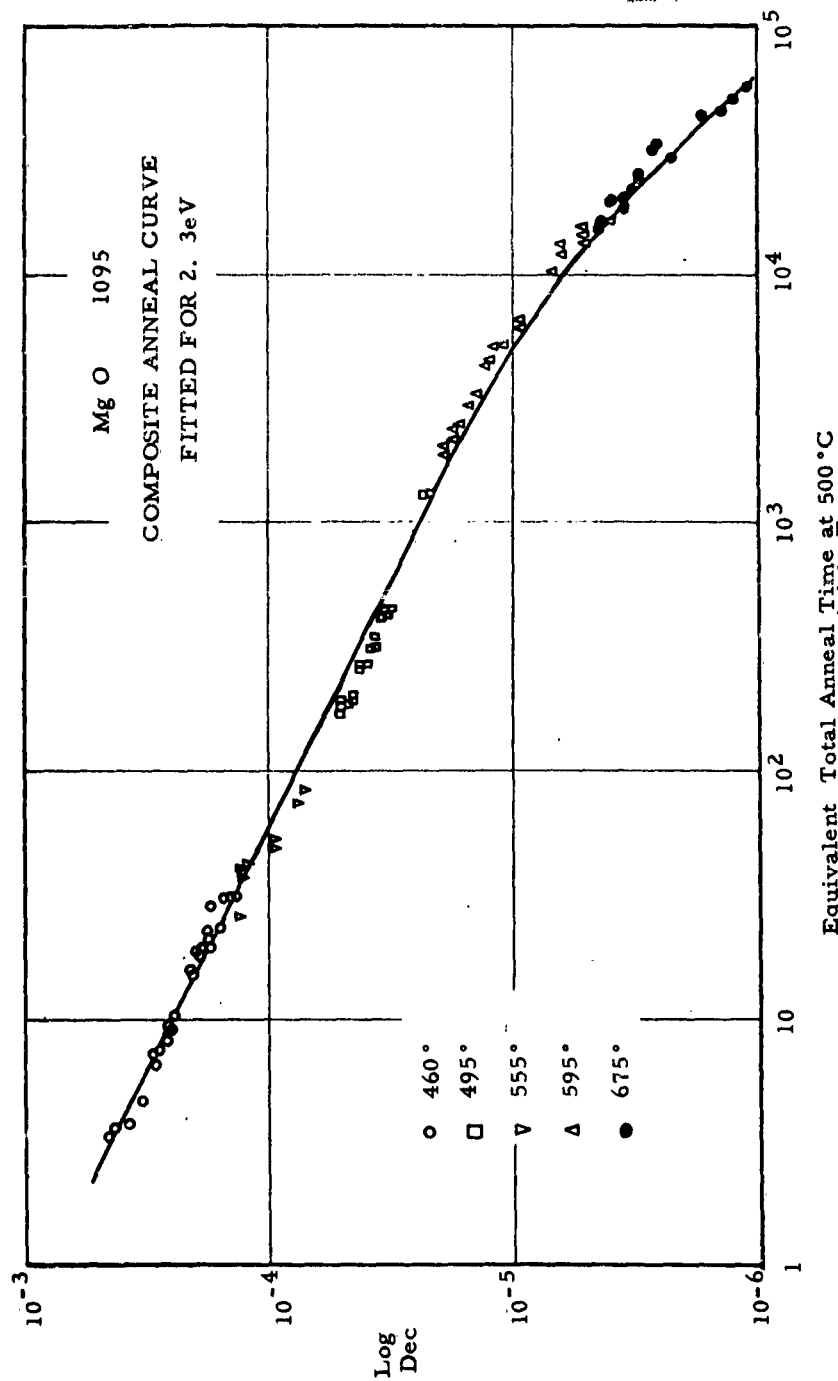


Fig. 5-10 COMPOSITE ANNEAL CURVE FOR SPECIMEN 1095

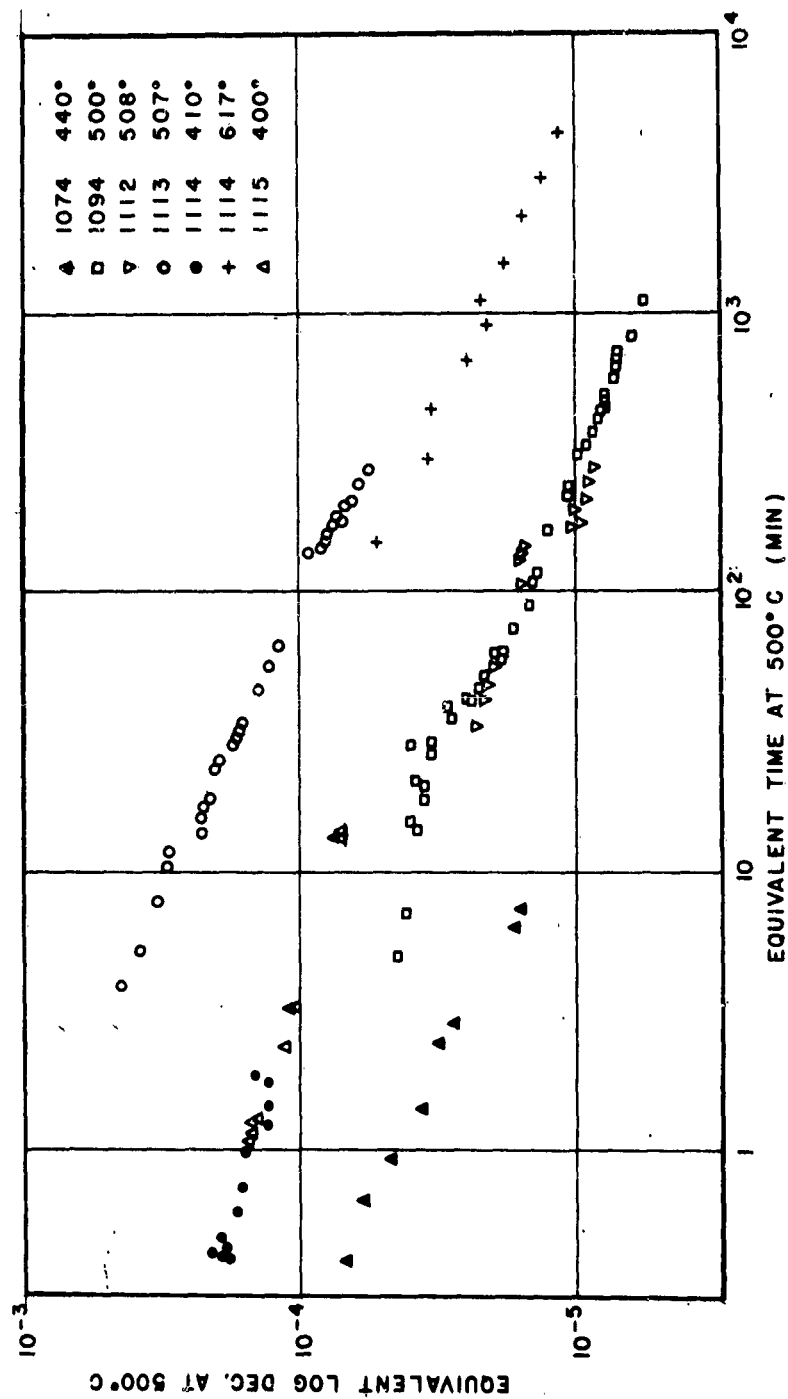


Fig. 5-11 ANNEAL CURVES FOR SEVERAL SPECIMENS CONVERTED TO THE EQUIVALENT 500°C CURVE

Considerable weight is, therefore, lent to the hypothesis of pinning by vacancy migration, since 2.1 ev is the energy of vacancy motion derived from vacancy-impurity pair relaxation, discussed in subsection 5-5. Some idea of the distance traveled by the vacancies may be gained by considering that the log decrement is reduced to about one-tenth after 100 min at 500°C. In this time, the vacancies will have made $1.5 \times 10^{14} \times \exp(-2.1/kT) \times 60 \times 100 = 2.3 \times 10^4$ jumps, which, as a random walk, would take them about 1000\AA . This is of the order of magnitude of the spacing of dislocations; in other words, it is quite possible for all the vacancies in the deformed material to precipitate on dislocations during the time of anneal.

C. Anomalous Precipitation Kinetics

It soon becomes clear on investigation that the analysis of Granato Hikata and Lucke, which used the $t^{2/3}$ precipitation law, and which appeared to fit the NaCl results, cannot fit the MgO results. It is not clear whether this indicates any fundamental difference in the modes of pinning in NaCl and in MgO. The NaCl results are taken over only one decade of time, and indeed, if they are plotted in the same way as the data of Fig. 5-9, they give an approximately straight line of about the same slope. Thus, it is possible that the agreement obtained by Granato et al⁽⁵⁻⁵⁾ is fortuitous.

Subsequent work on diffusion-limited precipitation on dislocations by Bullough and Newman⁽⁵⁻⁶⁾ shows that after a short initial period, the defect density will be linearly dependent on time, rather than on the two-thirds power given by Cottrell and Bilby. Now, the internal friction is proportional to the fourth power of the length of free dislocation segments between pinning points, according to the Koehler-Granato-Lucke theory^(5-7, 5-8). Therefore, if the precipitating defects remain isolated, the internal friction would be expected to be proportional to the inverse fourth power of the time over most of the range. The initial stage in which existing pinning

points are important can be shown to be of brief duration. This prediction is strongly at variance with the observed $t^{-1/2}$ law, and so it is evident that the model used for NaCl cannot be applicable. There are several possible reasons for this. First, precipitation may be limited by causes other than diffusion along a concentration gradient, such as electrostatic interactions, which may vary as the proportion of ionized vacancies changes. Secondly, the pinning points may not be isolated vacancies but clusters, which increase in size more rapidly than fresh clusters are nucleated. If this is the explanation, it would imply that the cluster density varies as the $1/8$ power of the cluster size. For impurities the electron microscope observations of Venables⁽⁵⁻⁹⁾ show how clustering can occur along the dislocation line; but whether vacancies behave in a similar manner has yet to be confirmed. Thirdly, the simple application of the Koehler-Granato-Lucke theory to give a ℓ^4 variation of internal friction may be incorrect. The expression of this theory for log decrement, at least in the frequency region where inertial effects of the dislocation may be ignored, is

$$\Delta = \frac{8G^2}{\pi^3 C} \Lambda \ell^2 \frac{\omega \tau \ell}{1 + \omega^2 \tau^2 \ell^2} \quad (5-2)$$

where the relaxation time is

$$\tau \ell = \frac{\ell^2 B}{\pi^2 C}$$

Here G is the shear modulus; a , the atomic spacing; Λ , the dislocation density; ℓ , the free dislocation segment length; B , the damping constant per unit length of dislocation; and C , the line tension. Thus, for small damping constants, $\omega \tau \ell \ll 1$ and $\Delta \propto \ell^4$; but for large damping constants, Δ is independent of ℓ . It is possible that we are working in the latter range, and that the relatively slow variation of log decrement with vacancy precipitation reflects a change of damping constant due to buildup of a cloud around the dislocation, rather than an effect ascribable to a

reduction of ℓ . Further analysis of the frequency dependence of logarithmic decrement is required to elucidate this point, so that the location of the $\omega\tau_{\ell} = 1$ condition may be sought. The interpretation is very much clouded by lack of knowledge of the temperature dependence of the damping constant. Discussion of the point will be given in subsection 5-8 where consideration is given a model in which the damping constant originates in thermally generated dislocation kinks.

5. POINT DEFECT RELAXATION AND VACANCY DIFFUSION

It was previously reported⁽⁵⁻¹⁾ that some MgO specimens showed a pronounced internal friction peak in the region of 200°C, which exhibited all the features of a relaxation peak. Further investigation of this peak has been carried out on a project separately funded by ARF. It now is evident that the interpretation originally suggested, that the peak is due to relaxation of impurity-vacancy pairs is in error, and that the mechanism is, in fact, operative at a higher temperature. Figure 5-12 shows the peak near 200°C ("D-peak") on a corrected temperature scale. From an analysis of its shape and of the shift with varying frequency for twelve specimens, it appears that the activation energy of the process giving rise to the peak is 0.64 eV and, hence, the relaxation frequency is of the form $1.8 \times 10^{11} \exp(-0.64/kT)$. The pre-exponential factor is an order of magnitude lower than that usually found for point defect relaxation processes, which indicates that some other type of mechanism may be operating, possibly one which involves the cooperative motion of several atoms. A search was made for a correlation between the height of the peak and the proportion of a number of impurities in the specimens, including Cr and Fe, but no correlation was found. Discussion of the mechanism is not pursued here, as this would lead us too far from the general purpose of the study.

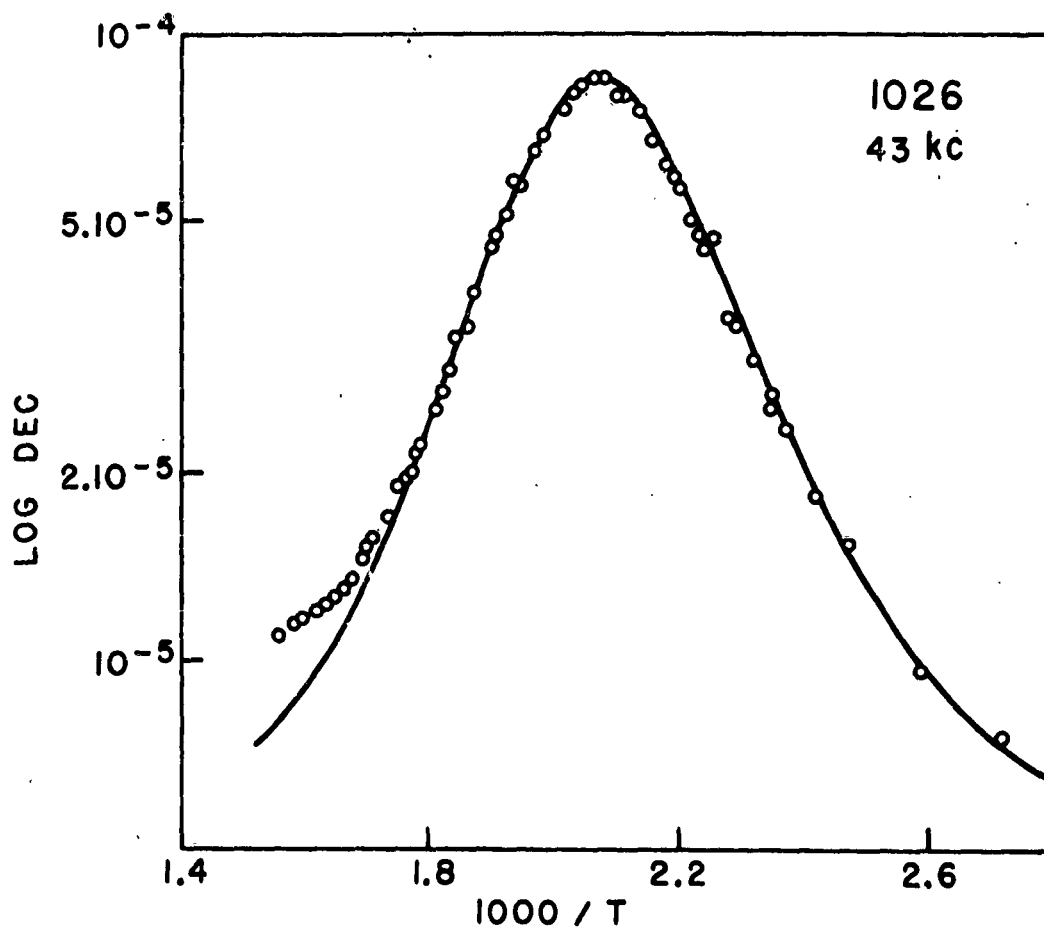


Fig. 5-12 RELAXATION PEAK NEAR 200 °C TAKEN AT 43.2 KILOCYCLES
SPECIMEN 1026

A second, which is now believed to be due to relaxation of Cr-vacancy pairs, is shown in Fig. 5-13. The specimen used in these measurements was doped with about 0.05 percent Cr, and only this specimen shows a peak of this size. Comparison with Figures 5-26 and 5-27 of reference 5-1 shows that the same peak, of reduced height, is indeed visible in specimens 1026 and 1074 which contained about 0.01 percent Cr. Specimens doped with Fe show no analogous peak. This is not surprising, since if the specimen is heated to the range in which a peak may be expected, all the Fe is converted to the divalent state, and any nearby vacancies would no longer be electrically bound to the iron.

The theory of Lidiard⁽⁵⁻¹⁰⁾ predicts that a vacancy-impurity peak would not be a simple relaxation peak, since there are a number of different kinds of vacancy motion between nearest neighbor and next-nearest neighbor positions having slightly different activation energies. To a first approximation, the total logarithmic decrement may be regarded as compounded of three peaks as indicated in Fig. 5-13. The slope of the low-temperature shoulder gives an activation energy of about 2.1 ev, which agrees with that derived from the shift with frequency. It is this activation energy, then, which is that of cation vacancy motion close to trivalent Cr, and the activation energy of motion for free cation vacancies may be expected to be close to this. No other direct estimate of the energy of motion of vacancies in MgO is known. The pre-exponential frequency factor is 1.5×10^{14} .

It is interesting to consider the results for the activation energy of diffusion of transition metal impurities in MgO obtained by Wuensch and Vasilos⁽⁵⁻¹¹⁾ using radioactive tracer methods. All these energies were close to 2 ev; while the exponential factor in the diffusion constant, normally near 0.1, was of the order 10^{-5} . The value of pre-exponential factor was taken to indicate

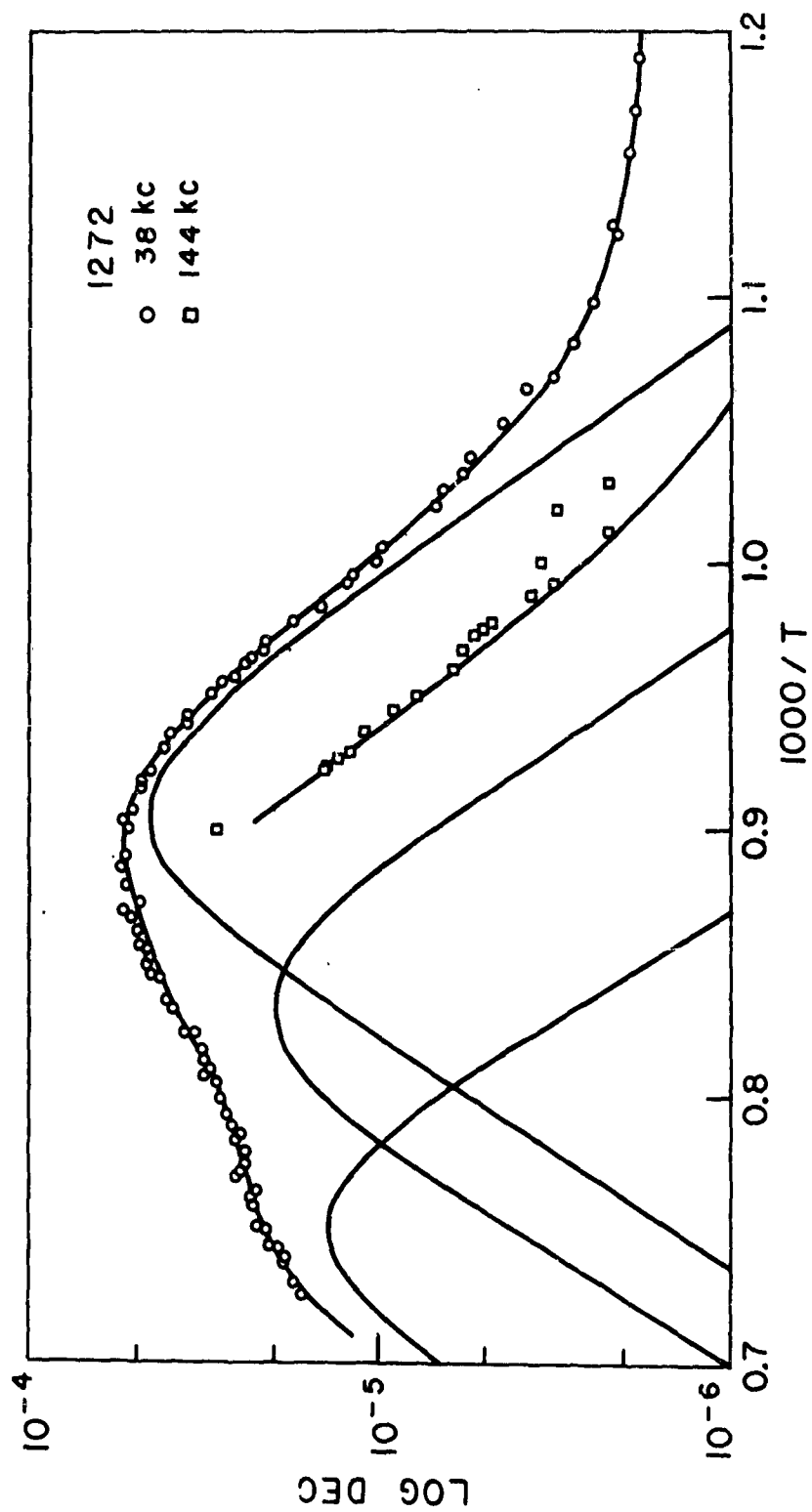


Fig. 5-13 RELAXATION PEAK DUE TO CHROMIUM-VACANCY PAIR RELAXATION IN CHROMIUM-DOPED SPECIMEN 1272

a very low value of entropy of diffusion. However, since we now have the value 2.1 ev for the energy of vacancy motion alone, it seems very possible that in the temperature range in which the diffusion measurements were made, the vacancy concentration was being held constant by some requirement of charge neutrality. The impurity diffusion energy would then approximately equal that of vacancy motion. At higher temperatures, the vacancy concentration would increase due to thermal activation, so that the diffusion energy would equal that of vacancy motion plus that of vacancy formation. If this is the case, the low value of pre-exponential factor in the former temperature range loses the special significance assigned to it. We may examine the validity of the hypothesis by observing that the energy of self-diffusion of Mg measured by Lindner and Parfitt⁽⁵⁻¹²⁾ is 3.4 ev, and hence the formation energy of vacancies will be $3.4 - 2.1 = 1.3$ ev. The expected vacancy concentration at 1000°C will then be about $\exp(-1.3/kT)$, or 10^{-3} . With such a concentration of trivalent impurities, the vacancy concentration would be held at a similar value below 1900°C; however, there is some doubt whether the specimens used in the diffusion studies did contain such a high impurity concentration.

6. DAMPING BELOW ROOM TEMPERATURE

An apparatus which will allow measurement of internal friction below room temperature was constructed. A semi-diagrammatic section is given in Fig. 5-14, and a photograph in Fig. 5-15. The method of operation is the same as for the high temperature apparatus, and the same electronic drive and detection equipment is used in conjunction with the apparatus. The high temperature furnace has been replaced by a double-vessel cryostat, with the inner vessel or the space between the inner and the outer being

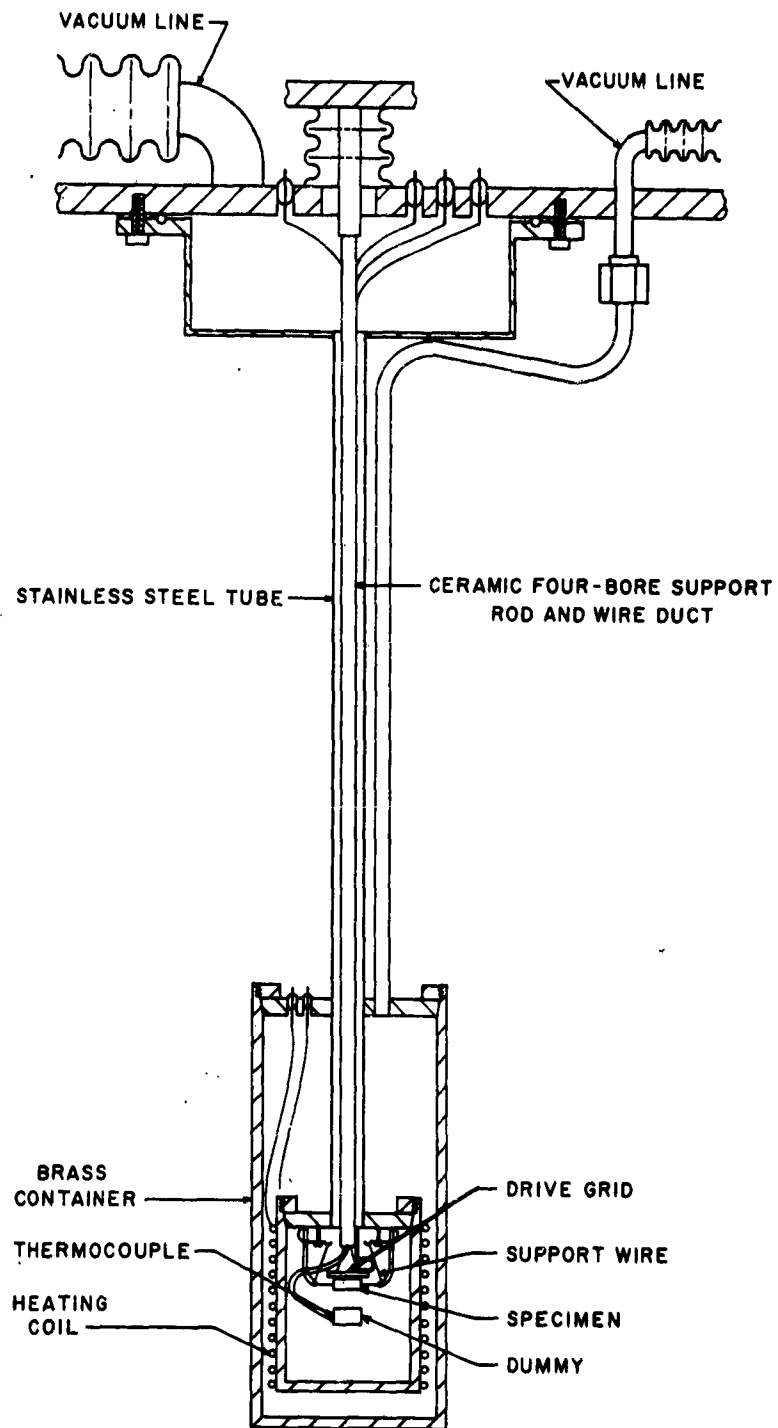


Fig. 5-14 SECTION OF LOW TEMPERATURE APPARATUS

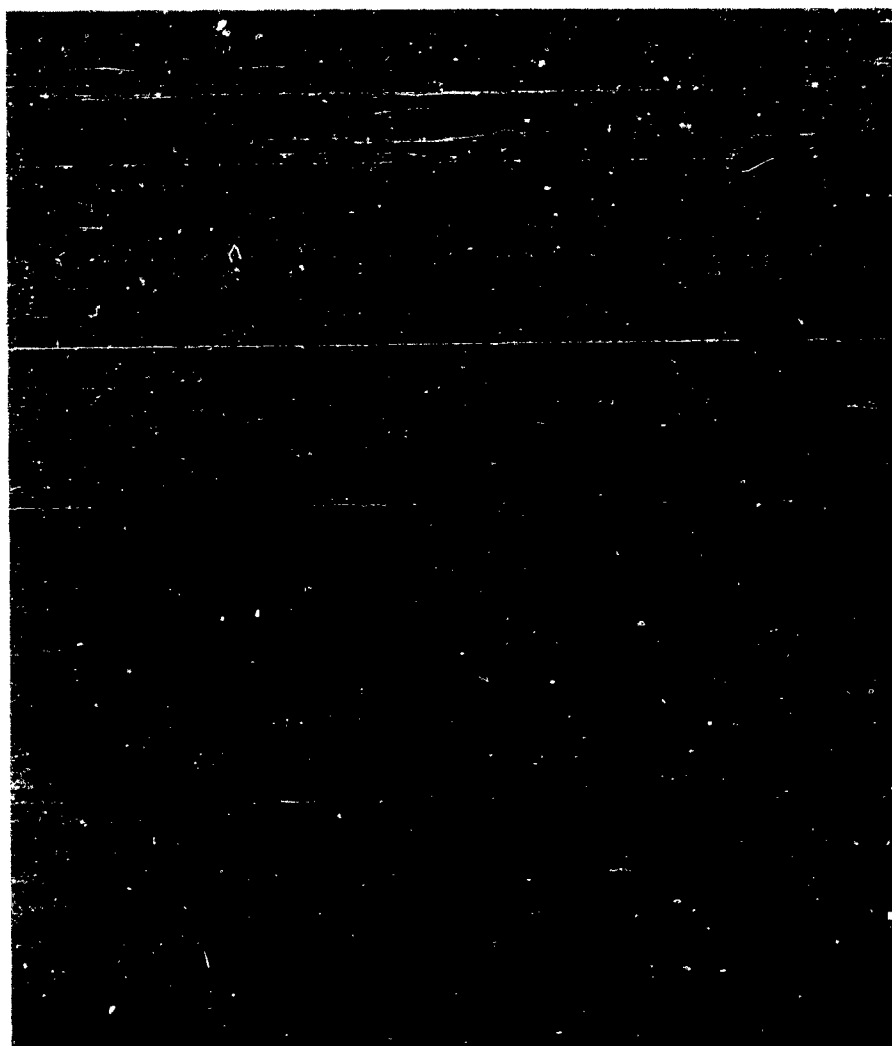


Fig. 5-15
LOW TEMPERATURE APPARATUS (INVERTED FOR EASY SPECIMEN MOUNTING)

capable separately of being evacuated or filled with helium exchange gas. The outer vessel is surrounded by liquid N_2 . The temperature of the inner space may then be controlled by filling the intermediate space with helium to cool it, or by evacuating the space to isolate the inner container and using the heater to warm it. Calibration of the frequency-temperature curve of the specimen is achieved by filling the inner vessel with a helium pressure of approximately 0.1 torr. This is sufficient to give reasonable thermal contact between the specimen and the dummy which contains the thermocouple, without damping the specimen acoustically to a degree that would induce an appreciable frequency shift to occur.

The drive grid is fabricated using a standard photographic transfer and etch technique to produce a copper film of the correct form on an epoxy resin sheet base. This allows a grid of very high sensitivity to be produced since small uniform spacings can be readily achieved.

A series of measurements were made on three specimens using this apparatus. The curves obtained are not presented here, as their significance is not clear. Two dumbbell specimens were measured in flexural vibration, but it seems likely that the nodal suspension was not sufficiently accurately placed. As a consequence, a rather large damping was observed which showed very little variation between $20^{\circ}C$ and $-195^{\circ}C$, in both a bent and an as-grown specimen. An undeformed specimen of simple bar form showed a series of peaks at -90 , -110 , and -140 deg, but the repeatability of these is in doubt, and their amplitude was small. Hence, comparison with the peaks observed at -30 deg by Chang⁽⁵⁻¹³⁾ is not yet possible.

7. THEORY OF DISLOCATION DAMPING

Calculations were performed with three different objectives in view. The first was to consider the effects of some modifications, made by Southgate⁽⁵⁻¹⁴⁾ to a theory of dislocation motion originally worked out by Brailsford⁽⁵⁻¹⁵⁾. The second objective concerned an exploration of the temperature dependence of the amplitude independent dislocation damping in MgO in terms of the Brailsford theory. Finally, an investigation of the dislocation breakaway theory of Granato and Lucke⁽⁵⁻⁸⁾ was made.

8. THEORY OF AMPLITUDE INDEPENDENT DAMPING

A. The Brailsford Model

Brailsford's model is based on the assumption that the dislocation tends to lie in potential valleys which follow close-packed crystal directions. Displacement of the dislocation between adjacent valleys is made by abrupt kinks. The form of such a dislocation is shown in Fig. 5-16. In this figure, x denotes a close-packed crystal direction and a is the separation of adjacent potential valleys. There are two types of kinks. Those in Fig. 5-16 will be called "left" kinks. Kinks of the opposite sense (which would carry the dislocation from the upper-left to the lower-right of the figure) will be called "right" kinks.

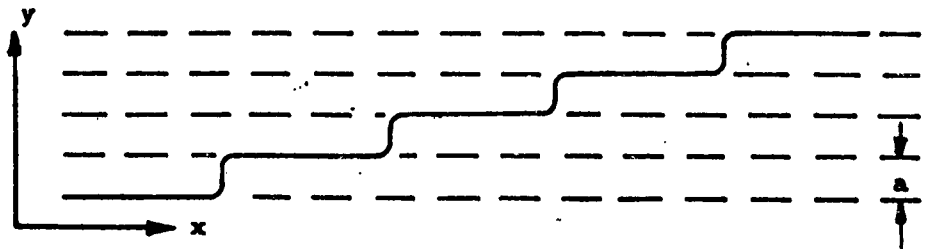


Fig. 5-16 SCHEMATIC DRAWING OF A DISLOCATION

Kinks may be produced by thermal activation. If the end points of the dislocation are pinned, they must be produced in pairs of a right and left kink. If the end points of the dislocation are pinned in different potential valleys, there will be kinks present at 0°K; this is the case shown in Fig. 5-16. The kinks are assumed mobile. Under the influence of an external force or of a nonuniform distribution, there will be a current of kinks diffusing along the dislocation. When this motion leads to the collision of a right and left kink, the kinks annihilate each other. In equilibrium, the right and left kink currents must separately vanish and the generation and recombination rates must be equal.

Consider a dislocation with end points pinned at $x = 0$ and $x = L$. In general, we will suppose the end points to be pinned in different potential valleys. Let the number of left and right kinks in the element of length between x and $x + dx$ be $n(x)dx$ and $p(x)dx$ respectively. The kink generation rate per unit length in the x -direction is taken to be independent of x and will be denoted by g . The recombination rate is taken to be rn_p , where r is also independent of x . The kink densities satisfy the continuity equations

$$\frac{\partial p}{\partial t} + \frac{\partial I_p}{\partial x} - g + rn_p = 0 \quad (5-3)$$

$$\frac{\partial n}{\partial t} + \frac{\partial I_n}{\partial x} - g + rn_p = 0$$

where I_p and I_n are the right and left kink currents respectively. If F is the force per kink on the right kinks ($-F$ on the left kinks), the kink currents are

$$\begin{aligned} I_p &= F\mu p - D \frac{\partial p}{\partial x}, \\ I_n &= -F\mu n - D \frac{\partial n}{\partial x} \end{aligned} \quad (5-4)$$

where μ is the mobility and D the diffusion coefficient of the kinks. These are assumed to satisfy the Einstein equation

$$\frac{D}{\mu} = kT \quad (5-5)$$

In equilibrium

$$I_p = I_n = 0 \quad (5-6)$$

and

$$g = rnp \quad (5-7)$$

In addition to setting up the equations in this manner, Brailsford makes the reasonable assumption that an external shear stress σ produces a force on the kinks of

$$F = \sigma ab \quad (5-8)$$

where b is the magnitude of the Burgers vector.

B. Modification of Brailsford's Theory

Southgate⁽⁵⁻¹⁵⁾ modified Eq. (5-8) by considering the force resulting from the stress field surrounding the dislocation. He assumed that the stress field energy is that of a tube which follows the average dislocation direction and that this energy is computed from elastic continuum theory. If the dislocation line is curved, and the stress field energy per unit length of dislocation, or line tension, is E_0 there must be added to Eq. (5-8) the term

$$\frac{E_0 a}{\rho}$$

where ρ is the radius of curvature of the dislocation.

In terms of the kink densities

$$y(x) = a \int_0^x (n-p) dx \quad (5-9)$$

Thus, assuming $\frac{\partial y}{\partial x} \ll 1$,

$$F = \sigma ab + E_0 a \frac{\partial^2 y}{\partial x^2} = \sigma ab + E_0 a^2 \frac{\partial}{\partial x} (n-p) \quad (5-10)$$

The effect of this modification was considered for the case in which only one type of kink is present, in particular for the case $n(x) = 0$. Here we wish to consider the possibility that both $n(x)$ and $p(x)$ are non-vanishing. The situation which is of interest is that of a small, uniform applied stress, which varies so slowly with time that the system is approximately in equilibrium at all times. To clarify the meaning of this last requirement we write

$$n = n_0 + \Delta n \quad p = p_0 + \Delta p,$$

when, since σ is small, $\Delta n \ll n_0$ and $\Delta p \ll p_0$.

Then, neglecting second-order terms,

$$np = n_0 p_0 + n_0 \Delta p + p_0 \Delta n.$$

Now, for a system in equilibrium, we have, from Eq. (5-7),

$$np = n_0 p_0$$

Thus, by the requirement that the system lie approximately in equilibrium, we mean that

$$n_0 \Delta p + p_0 \Delta n$$

is at most of the second order of smallness so that

$$np \doteq n_0 p_0 \quad (5-11)$$

(Note that separately $n_0 \Delta p$ and $p_0 \Delta n$ are of the first order of smallness).

Now, substituting Eq. (5-10) in Eq. (5-4), one obtains

$$\begin{aligned} I_p &= \sigma ab\mu p + E_o a^2 \mu p \frac{\partial}{\partial x} (n-p) - D \frac{p}{x}, \\ I_n &= -\sigma ab\mu n - E_o a^2 \mu n \frac{\partial}{\partial x} (n-p) - D \frac{\partial n}{\partial x}. \end{aligned}$$

With the aid of Eq. (5-11), one can eliminate $n(p)$ from the expression for I_p (I_n). Neglecting second-order terms and using Eq. (5-5) leads to the results

$$\begin{aligned} I_p &= \sigma ab\mu p - D' \frac{\partial p}{\partial x} \\ I_n &= -\sigma ab\mu n - D' \frac{\partial n}{\partial x} \end{aligned} \quad (5-12)$$

where

$$D' = D \left[1 + \frac{E_o a^2 (n_o + p_o)}{kT} \right] \quad (5-13)$$

Thus, we see that, to first order, the effect which the additional term in Eq. (5-10) involving the line tension has on the currents is a modification of the effective value of kink diffusion coefficient. For a reasonable rate of kink generation, $a(n_o + p_o)$ may be about 0.1; and the diffusion coefficient will be enhanced by a factor of about 50.

Now let us consider the case of a constant applied stress. If the system is in equilibrium under the applied stress, Eq. (5-6) will be satisfied and Eq. (5-11) will be satisfied to all orders. The effect of the stress is to change the kink densities n and p and this, in turn, causes an increase in the average length and energy of the dislocation. From Eqs. (5-6), (5-11) and (5-12), we have

$$\begin{aligned} n &= n_\lambda e^{-\lambda x}, \\ p &= p_\lambda e^{\lambda x}, \quad n_\lambda p_\lambda = n_o p_o \end{aligned} \quad (5-14)$$

where

$$\lambda = \frac{\sigma ab\mu}{D'}$$

The values of n_λ and p_λ can be obtained from Eq. (5-14) and the boundary condition

$$\Delta y(L) - a \int_0^L (\Delta n - \Delta p) dx = 0$$

The equation will be satisfied if the end points of the dislocation are pinned.

The average length of the dislocation is given by

$$\ell = \int_0^L \left[\left(\frac{\partial y}{\partial x} \right)^2 + 1 \right]^{1/2} dx \quad (5-15)$$

where

$$y = y_0 + \Delta y.$$

The first-order terms in $\Delta \ell$ vanish because of the boundary conditions $\Delta y(L) = \Delta y(0) = 0$ and the fact that $\partial y_0 / \partial x$ is constant. Thus the leading term in $\Delta \ell$ is

$$\Delta \ell = 1/2 \int_0^L \left(\frac{\partial \Delta}{\partial x} \right)^2 dx = \frac{a^2}{2} \int_0^L (\Delta n - \Delta p)^2 dx \quad (5-16)$$

Using the values of n and p from Eq. (5-14), one obtains, for small applied stress (i.e., small λ),

$$\Delta \ell = \frac{a^2 L^2}{24} (n_0^2 + p_0^2) \lambda^2. \quad (5-17)$$

The change in energy depends on the change in kink densities in two ways. First, if each kink has an energy ϵ_k , there will be a change in energy

$$\epsilon_k \int_0^L (\Delta n + \Delta p) dx.$$

Secondly, under the action of the stress, the kinks will pile up at either end of the dislocation. To calculate the change in energy which is due to this piling up, consider the kinks which were originally in the element of length dx at the point $x - 1/2 \Delta x$ and which moved to the point $x + 1/2 \Delta x$ when the stress was applied. The change in energy of these kinks is

$$1/2 F (n-p) \Delta x \, dx,$$

where we have taken the average force on the kinks to be $F/2$ and have assumed that the change in the kink densities is small. This leads to a change in the energy of the dislocation line of

$$1/2 \int_0^L F(n-p) \Delta x \, dx.$$

Now

$$(n-p) \Delta x = \frac{\Delta y}{a} = \int_0^L (\Delta n - \Delta p) \, dt.$$

Thus, the total change in the energy of the dislocation is

$$\Delta E = \epsilon_k \int_0^L (\Delta n + \Delta p) dx + 1/2 \int_0^L F \int_0^x (\Delta n + \Delta p) \, dt \, dx. \quad (5-18)$$

Again taking the values of n and p from Eq. (5-14) and using Eq. (5-17), one obtains for small stress

$$\Delta E = \frac{\Delta \ell}{n_o^2 + p_o^2} \left[\frac{4\epsilon_k n_o p_o}{a^2 (n_o + p_o)} + \frac{kT}{a^2} (n_o + p_o) + 4E_o n_o p_o \right] \quad (5-19)$$

This disagrees with the result obtained by Brailsford [Eq. (19) of reference (5-15)] which is

$$\Delta E = \frac{\epsilon_k}{a^2 (n_o + p_o)} \Delta \ell$$

Brailsford's results contains neither the term in E_o , which appears because of the modification made in Eq. (5-10), nor the term in kT which should appear even in the case $E_o = 0$. In addition, his term in ϵ_k does not agree with that in Eq. (5-19). In the limit, as $\epsilon_k \rightarrow \infty$ Brailsford's results predicts that $\Delta E \rightarrow \infty$. This does not appear to be correct, since in this limit no kinks can be excited and hence there is no change in energy. In the limit of infinite ϵ_k , there will be

only built-in kinks, so that either n_o or p_o must vanish. In fact, Brailsford indicates that the product $n_o p_o$ vanishes exponentially as $\epsilon_k \rightarrow \infty$. Hence, the term in ϵ_k in Eq. (5-19) vanishes in this limit, as expected.

C. Application of Brailsford's Theory to Magnesium Oxide

An attempt was made to see if Brailsford's theory would explain the broad peak in the temperature dependence of the logarithmic decrement in MgO. If one assumes that all of the dislocations have the same length and neglects the modification made in Eq. (5-10), Brailsford's theory gives for the decrement at small stress amplitude the expression

$$\Delta = \Delta(L, T) \frac{\omega \tau_L}{1 + \omega^2 \tau_L^2} \quad (5-20)$$

where

$$\Delta(L, T) = \frac{8Ga^2 b^2 L^3}{\pi^4 V k T (n_o + p_o)} \quad (5-21)$$

and

$$\tau_L = \frac{L^2}{D\pi} \quad (5-22)$$

Here ω is the angular frequency, V is the volume and G the shear modulus of the sample. Brailsford considers the diffusion to be thermally activated so that

$$D = D_o \exp\left(-\frac{W}{kT}\right) \quad (5-23)$$

If one supposes that only built-in kinks are present, $n_o + p_o$ is independent of temperature and the decrement will have a maximum at a temperature to given by

$$\exp\left(-\frac{W}{kT_o}\right) = \frac{\omega L^2}{\pi^2 D_o}$$

In a plot of Δ versus $10^3/T$, the half-width of the peak is given approximately by

$$\frac{10^3 k}{W} \ln \left(\frac{2 + \sqrt{3}}{2 - \sqrt{3}} \right).$$

There are three quantities appearing in the preceding equations whose magnitudes are not known in advance. These are the loop length, L , the diffusion activation energy, W , and the equilibrium kink density, p_0 , (assuming only right kinks are present). To compare theory and experiment, these quantities were chosen so that the theoretical and experimental curves agreed in the position and magnitude of the maximum and in the half-width. For example MgO 1115, discussed in reference (5-9), the following values were obtained;

$$W = 0.11 \text{ eV}$$

$$L = 1.3 \times 10^4 \text{ \AA}$$

$$p_0 = 1.8 \times 10^{-14} \text{ \AA}^{-1} = 1.8 \times 10^{-6} \text{ cm}^{-1}.$$

The values of W and L are quite reasonable, but the value of p_0 is much too small. It would imply that a negligible number of kinks make the entire contribution to the decrement.

Attempts were made to obtain better agreement with experiment by considering the thermal generation of kinks, the effect of the stress field energy E_0 , and the possibility of a distribution of dislocation lengths. None of these factors, however, give a significant improvement in the agreement.

D. Effect of a Localized Charge Cloud

One mechanism which might produce additional damping is the formation of a charge cloud around a dislocation which is also charged. The cloud could be produced by trapped charge carriers

or, since MgO is an ionic crystal, by an excess of vacancies of one sign (cf. reference 5-16). Analysis of the effect of such a cloud is rendered difficult by the fact that the parameters, such as vacancy formation and diffusion energies, which determine the configuration of the cloud are not well known. The effect of the charge cloud, however, can be expected to depend strongly on its configuration. In particular, if the radius of the cloud is small compared to the amplitude of vibration of the dislocation, so that the dislocation can break away from the cloud, one would expect an amplitude dependence in the damping. On the other hand, if the radius is large, the cloud might exert only a small force on the dislocation.

Because of these difficulties, these investigations were dropped pending further experimental results which might help to clarify the situation.

9. AMPLITUDE DEPENDENT DAMPING

A. Outline of the Granato-Lucke Theory of Dislocation Break-Away

Granato and Lucke⁽⁵⁻⁸⁾ assume that the crystal contains a network of dislocations and that each dislocation is strongly pinned at its points of intersection with other dislocations. Between these network pinning points, the dislocations are further pinned by impurities. The length L_N between network pinning points is taken to be the same for all dislocations, but a distribution of lengths, with average length L_C , is assumed between impurity pinning points. At larger amplitudes the dislocation will break away from the impurities and vibrate between network pinning points. This breakaway produces an amplitude dependent damping.

To determine the strain produced by the vibrating dislocation, Granato and Lucke postulate that dislocations behave like a stretched

string with a line tension C . Consider a single dislocation loop which breaks away at a shear stress, σ_1 . Neglecting the small strain produced by bowing of loops L_c before breakaway, we have, for increasing $|\sigma|$, the dislocation strain

$$\epsilon_d = \begin{cases} 0, & \sigma \leq \sigma_1 \\ \frac{8b^2 L_N^3}{\pi^4 C} \sigma, & \sigma > \sigma_1, \end{cases} \quad (5-24)$$

Once one point has broken away, the remainder must also do so, and the loop length will be L_N for decreasing σ

$$\epsilon_d = \frac{8b^2 L_N^3}{\pi^4 C} \sigma. \quad (5-25)$$

The energy loss per cycle is given by

$$\begin{aligned} \Delta W &= \oint_{\text{cycle}} \epsilon_d d\sigma \\ &= \frac{8b^2 L_N^3 \sigma_1^2}{\pi^4 C} \end{aligned}$$

The decrement which is due to a single dislocation loop, which breaks away at stress σ_1 , is thus

$$\delta(\sigma_1) = \frac{\Delta W}{2W} = \frac{G\Delta W}{\sigma_0^2} = \frac{8Gb^2 L_N^3 \sigma_1^2}{\pi^4 C \sigma_0^2} \quad (5-26)$$

where σ_0 is the amplitude of the stress and W is the energy per unit volume of the sample. It is assumed that the whole material has an applied periodic shear stress in the glide plane of the dislocation. Now let $n(\sigma)d\sigma$ be the number of loops per unit volume that break away at stresses between σ and $\sigma + d\sigma$. Then the total decrement is

$$\Delta = \int_0^{\sigma_0} \delta(\sigma_1) n(\sigma_1) d\sigma_1 = \frac{8Gb^2 L_N^3}{\pi^4 C \sigma_0^2} \int_0^{\sigma_0} \sigma_1^2 n(\sigma_1) d\sigma_1. \quad (5-27)$$

To determine the function $n(\sigma)$, we observe that a dislocation breaks away from an impurity when the force exerted on the impurity by the line tension of the dislocation is greater than the binding force. Consider two adjacent loops of length l_1 and l_2 . The force on the impurity at the intersection of the two loops is

$$\frac{4b\sigma}{\pi} (l_1 + l_2).$$

Thus, breakaway occurs if $l_1 + l_2$ is greater than the breakaway length

$$L = \frac{f_m}{4\pi\sigma}$$

where f_m is the binding force.

Let the probability that before breakaway a loop has length between l and $l + dl$ be $P(l) dl$. For a given σ (and hence L), the probability that two adjacent loops, of length l_1 and l_2 have not broken away is

$$I = \int_0^L \int_0^{L-l_1} P(l_1) P(l_2) dl_2 dl_1.$$

The probability that a network length has not broken away is I^ν , where $\nu = L_N/L_C - 1 = L_N/L_C$ is the number of loops in the whole dislocation line and hence the probability that the whole line has broken away is $M = 1 - I^\nu$. In terms of this quantity

$$n(\sigma) = \frac{\Lambda}{L_N} \frac{dM}{d\sigma} = - \frac{\Lambda \gamma}{L_N \sigma^2} \frac{dM}{dL}, \quad (5-28)$$

where Δ is the total dislocation length per unit volume and $\gamma = \pi f_m / 4b$. For small σ , $I \approx 1$ so it is convenient to write

$$I = 1 - J$$

where $J \ll 1$. Then

$$M = 1 - (1 - J)^{\nu} \approx \nu J$$

Thus

$$n(\sigma) = - \frac{\gamma \Delta}{L_c \sigma^2} \frac{dJ}{d\sigma} = \frac{\gamma \Delta}{L_c \sigma^2} \frac{dI}{d\sigma} \quad (5-29)$$

To evaluate the derivative, we make the change of variables

$$\begin{aligned} \ell_1 &= q - \ell \\ \ell_2 &= \ell \end{aligned}$$

In terms of these variables

$$I = \int_0^{\ell} \int_0^q P(q-\ell) P(\ell) d\ell dq \quad (5-30)$$

which is just the probability that $\ell \leq \ell_1 + \ell_2 \leq \ell + d\ell$.

Combining Eqs. (5-27), (5-29) and (5-30), we have

$$\Delta = \frac{8Gb^2 \gamma \Delta L_N^3}{\pi^4 C L_c \sigma_0^2} \int_0^{\sigma_0} \int_0^{\ell} P(\ell - \ell) P(\ell) d\ell d\sigma.$$

Finally, making the change of variable

$$\sigma = \frac{\gamma}{\ell}$$

and letting $\lambda = \gamma / \sigma_1$, so that λ is the breakaway length corresponding to the maximum stress occurring during the cycle, we have

$$\Delta = \frac{8Gb^2 \Delta L^3}{\pi^4 C L_c} \lambda^2 \int_{\lambda}^{\infty} \frac{1}{\ell^2} \int_0^{\ell} P(\ell - \ell) P(\ell) d\ell d\ell \quad (5-31)$$

B. Analysis of Experimental Results on Amplitude Dependent Damping

The preceding discussion has been in terms of the shear stress σ . In an actual experiment the sample is subjected to a longitudinal stress, Σ ; and one measures: the total longitudinal strain, $\epsilon = \Sigma/E$, where E is Young's modulus. The shear and longitudinal stresses are related by

$$\sigma = R\Sigma,$$

when R is a geometrical factor which takes into account the orientation relations between the longitudinal axis of the crystal, the slip direction and the direction of the normal to the slip plane. In our case $R = 1/2$. For a sample in longitudinal stress, the energy W is the denominator of Eq. (5-26) should be

$$W = \frac{\Sigma_o^2}{2E} = \frac{\sigma_o^2}{2R^2 E}.$$

The rest of the discussion remains unchanged so that Eq. (5-31) now becomes

$$\Delta = \frac{8R^2 E b^2 \Lambda L_N^3}{\pi^4 C L_c} \lambda^2 \int_{\lambda}^{\infty} \frac{1}{\lambda'^2} \int_0^{\lambda'} P(\lambda' - \ell) P(\lambda) d\ell d\lambda', \quad (5-32)$$

Granato and Lucke use the exponential distribution of loop length derived by Koehler⁽⁵⁻⁷⁾

$$P(\ell) = \frac{1}{L_c} \exp(-\ell/L_c) \quad (5-33)$$

Application of this form to Eq. (5-32) gives an expression for Δ such that a plot of $\log \Delta \epsilon_o v \cdot 1/\epsilon_o$ should be a straight line. Figure 5-17 shows that this is clearly not so. A similar example was given in reference 5-1. In Fig. 5-17, the amplitude dependent decrement ΔH was obtained by subtracting the amplitude independent decrement measured at low amplitudes, from the total decrement.

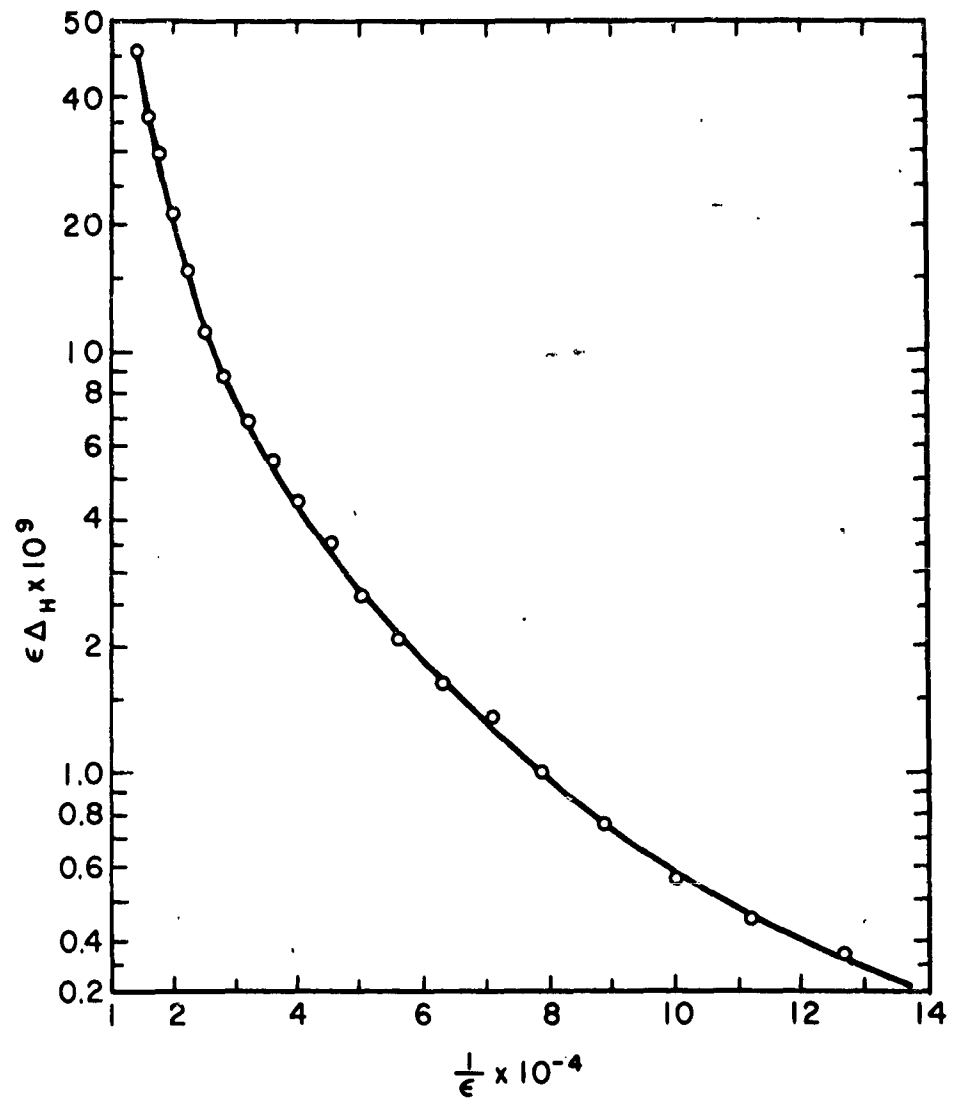


Fig. 5-17 PLOT OF AMPLITUDE DEPENDENT COMPONENT OF DAMPING. (On the Granato-Lucke Theory this Should be a Straight Line)

One possible difficulty with the theory is that the actual distribution of loop lengths differs from the exponential distribution used by Granato and Lucke. An attempt was, therefore, made to obtain information about the distribution from the measured decrement. Since only a small range of the curve of Δ versus λ is known, it is not possible to determine the distribution function $P(\ell)$. However, it is possible to obtain information about the distribution of the sum of lengths of pairs of loops. Let $Q(\lambda) d\lambda$ be the probability that $\lambda \leq l_1 + l_2 \leq \lambda + d\lambda$; we recall that

$$Q(\lambda) = \int_0^\lambda P(\lambda - \ell) P(\ell) d\ell.$$

From Eq. (5-32) we see that

$$Q(\lambda) = - \frac{\pi^4 C L_c}{8 R^2 E b^2 \lambda L_N^3} \lambda^2 \frac{d}{d\lambda} \left(\frac{\Delta}{\lambda^2} \right). \quad (5-34)$$

To use Eq. (5-34), it is necessary to estimate the magnitudes of the parameters which appear in it. The binding force between the dislocation and an impurity atom was assumed to be due to an elastic interaction between the dislocation and impurities lying directly above the dislocation. Then from Cottrell's theory⁽⁵⁻¹⁷⁾,

$$f_m = \frac{4Gb\epsilon' r^3}{\rho^2},$$

where r is the radius of the solvent atom, ϵ' is the difference in solute and solvent radius, divided by the solvent radius, and ρ is the distance of the impurity from the dislocation. For the line tension, a good estimate is⁽⁵⁻¹⁴⁾

$$C = Gb^2$$

We thus find the relation

$$\lambda = \frac{\pi}{R} \frac{G}{E} \frac{\epsilon' r^3}{\rho^2} \frac{1}{\epsilon_0} \quad (5-35)$$

and

$$Q(\lambda) = \frac{\pi^3}{8R} \frac{L_c}{L_N} \frac{1}{L_N^2} \frac{\rho^2}{r^3} \frac{d}{d\epsilon_0} (\Delta \epsilon_0^2) \quad (5-36)$$

We now take the values: $E = 2.45 \times 10^{12}$ dyne/per sq cm, $G = 1.5 \times 10^{12}$ dyne per sq cm, $b = 2.8 \text{ \AA}$, $\rho = 2 \text{ \AA}$, $r = 1 \text{ \AA}$, $L_c = 10^3 \text{ \AA}$, $L_N = 5 \times 10^4 \text{ \AA}$, $\Lambda = 10^5 \text{ cm}^{-2}$. The low value of dislocation density reflects the fact that the specimen under consideration had never been deliberately deformed, such mobile dislocations as are present having been introduced incidentally during cleaving and machining.

Using Eqs. (5-35) and (5-36), we obtained $Q(\lambda)$ from a measured curve of Δ versus ϵ_0 . The result is shown in Fig. 5-18. All the factors involved in calculating the abscissa are known fairly accurately with the exception of the misfit parameter ϵ' ; hence, it is plotted in terms of λ/ϵ' . Because measurements were made only at relatively small stresses, which correspond to large breakaway lengths, only the tail of the distribution has been obtained. Nevertheless, the result indicates a very sharp cut-off, much sharper than that given by the exponential distribution. Assumption of the reasonable value 0.1 for ϵ' gives a cut-off near 0.14μ , which is of the magnitude to be expected. The cut-off value suggests that L_c should perhaps be smaller than the 0.1μ which we used. The magnitudes of $Q(\lambda)$ do not have much significance since they depend strongly on the value of L_N , which can only be estimated crudely.

As this point, the results suggest that the Granato-Lucke theory may be valid provided an appropriate distribution of loop lengths is used. However, further investigation will be necessary to determine whether the required distribution is meaningful. Extension of the amplitude of measurement may show whether we are dealing with a sharply peaked function or whether the portion derived is the

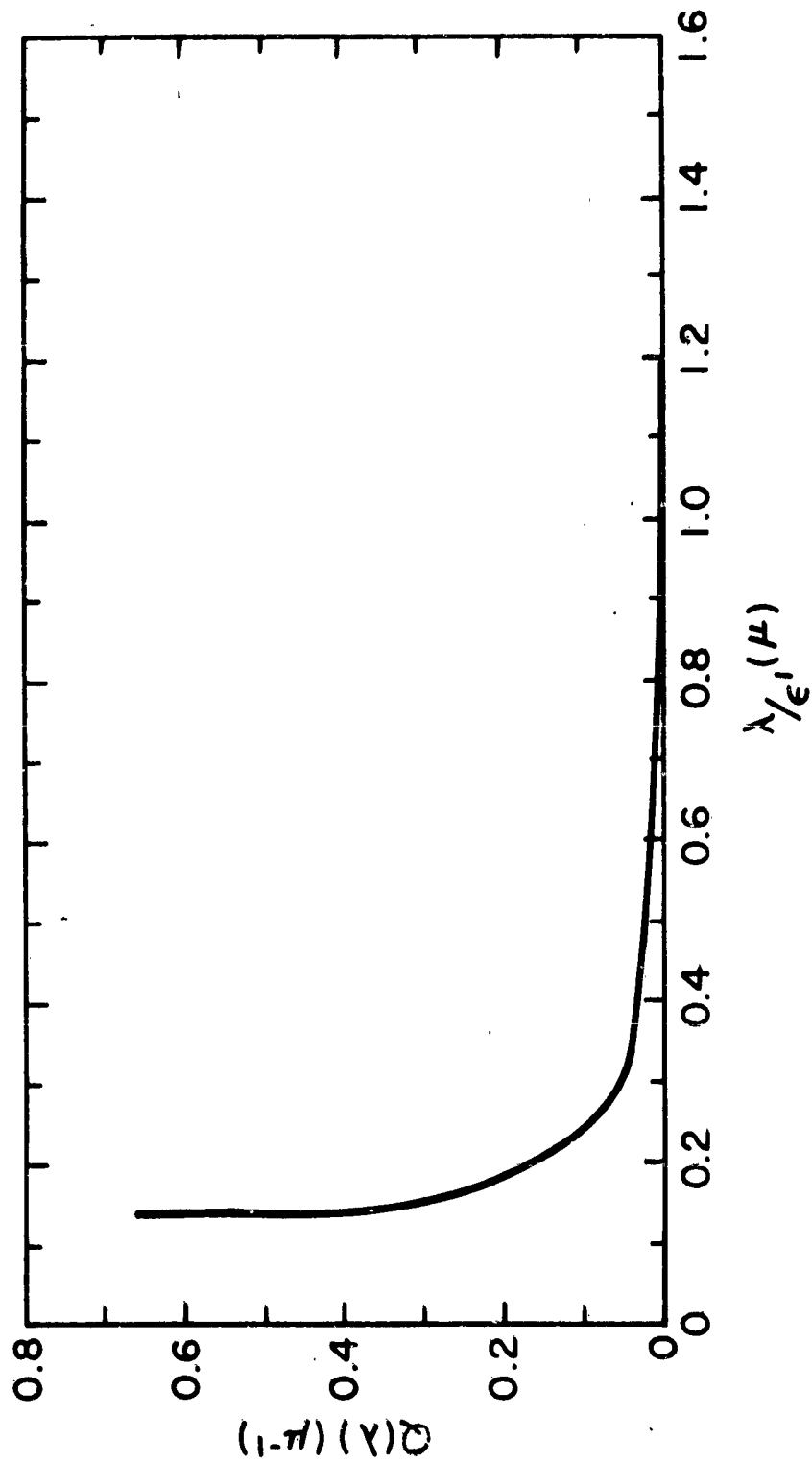


Fig. 5-18 DERIVED PROBABILITY DISTRIBUTION FOR SUM OF ADJACENT LOOP LENGTHS BETWEEN POINT DEFECT PINNING LOCATIONS

tail of a continuously decreasing distribution. In either case, a strong ordering force is required during precipitation of the pinning points along the dislocation, since a sharp cut-off on the length distribution implies an abnormal regularity of pinning points. At this time, it is difficult to see how the ordering force arises, and the possibility must be borne in mind that the mechanism of amplitude dependence may be totally different from that developed in the Granato-Lucke model.

10. CONCLUSION

The data presented in this report augment considerably the previously available information on dislocation damping in MgO. Probably the most significant conclusion reached is the determination of an activation energy of approximately 2.3 eV for the process of dislocation pinning during anneal between 400° and 700°C. From the way in which this activation energy can be used to convert to a common curve, anneal curves taken over the whole temperature range, it may be deduced that a single anneal process is taking place over the whole range. Comparison of the activation energy with that of vacancy motion around Cr impurities suggests strongly that the dislocation pinning process is ascribable to the diffusion of vacancies to the dislocations.

Interpretation of the data in terms of a detailed model raises difficulties. The models which have been examined are the stretched-string model proposed by Koehler and developed by Granato and Lucke, and the abrupt-kink model of Brailsford. These models are closely related in the case where no dislocation kink pairs are thermally generated. Attempts have been made to use them to explain three types of observation: the temperature dependence of

the internal friction measured at low vibration amplitudes; the dependence of internal friction upon amplitude of vibration; and the annealing kinetics of the low-amplitude internal friction. In each case, the theories are found to fit, only if certain assumptions which are sufficiently unusual to cast doubt on the validity of the theories are made. The assumptions are as follows:

- (1) The broad peak centered around 200°C found in deformed specimens can be fitted on the abrupt-kink theory, in which case it is analogous to the Bordoni peak observed in many metals. However, to affect the fit, a ridiculously low value of the average angle between the dislocation line and the lattice plane, about 10-13, must be assumed.
- (2) On the Granato-Lucke theory of amplitude-dependent damping caused by break-away of the dislocation from pinning points along the length, the exact form of amplitude dependence depends on the statistical distribution one assumes for the pinning point spacing. The theory has been extended so that it is possible to deduce the distribution curve for the spacing of next nearest neighbor pinning points. Application to a typical curve of damping versus amplitude showed that a distribution having a very rapid cut-off was required for the theory to be valid. It is difficult to see how such a distribution might arise, if pinning is indeed caused by point defects or clusters of defects which have condensed on the line.
- (3) The stretched-string theory assumes a damping force per unit length on the dislocation line which is independent of the free dislocation length. The internal friction derived from the model is either independent of free dislocation length, or proportional to the fourth power, depending upon whether the damping force is high or low. Now the theory of diffusion limited precipitation of point defects onto a dislocation gives a defect density which is approximately proportional to the time of precipitation over most of the period. Hence, free dislocation lengths should vary inversely as the time, and the internal friction independent of time or inversely as the fourth power. The observations reported here have shown that, in fact, the variation is as the inverse root of the time. One could effect a fit by assuming a variable clustering of impurities, but the assumption is somewhat artificial.

The failure of these theories to give an immediately satisfactory account of the dislocation behavior leads one to examine alternative models of a different nature. One such model depends on the fact that dislocations in ionic materials are charged and hence tend to accumulate a charge cloud of opposite sign, which may consist of vacancies or of trapped charge carriers. This charge cloud will greatly modify the restoring force on a dislocation from that given by the elastic line tension, increasing its value and rendering it non-linear. Extra damping forces will be introduced by oscillation of the charge cloud. However, the consequences of this model have yet to be worked out.

Information has also been gathered on creep of MgO at room temperature under constant load. There is considerable scatter in the data, which is felt to reflect intrinsic differences in the material. However, specimens whose creep was allowed to occur for more than a few minutes showed a steady increase of strain, varying as the logarithm of the time. After about 10 min, a change of creep rate occurred so that a new logarithmic law having a higher proportionality factor was followed.

Some measurements of internal friction were made below room temperature, but so far no peak analogous to that reported by Chang at 15 mc/s has been seen.

It is evident that there are still experimental data which should be gathered to extend the present findings. The following are suggested as the most significant:

- (1) Extension of the anneal studies to discover the maximum range over which the 2.3 ev energy is the dominant one.
- (2) Measurements of similar specimens over a wider frequency range, so that the frequency dependence of amplitude independent damping may be determined and compared with the predictions of the stretched-string theory.

- (3) Comparison of a relatively pure specimen with one doped with an impurity such as Fe which may be modified to exist either in the divalent or trivalent state. This should indicate the relative importance of elastic as compared to electrostatic interactions between impurities and dislocations.
- (4) Investigation of other cubic ionic materials such as NaCl to show how closely analogous their behavior is to that of MgO, and indicate whether the double-charged nature of the ions in MgO is causing any fundamental difference of behavior.
- (5) Continuation of measurements below room temperature.

Part Two: Studies on Polycrystalline Crystals
Principal Investigators: L. M. Atlas
Armour Research Foundation

11. INTRODUCTION

Ceramic bodies used in structural applications in the past frequently contained two or more phases -- commonly a crystalline compound embedded in a vitreous matrix. Many of the electrical and mechanical properties of such aggregates were clearly dominated by the characteristics of the cementing matrix, and by those of the interface between it and the crystalline grains. With the advent of relatively pure single phase ceramics, however, the properties of polycrystalline aggregates become increasingly more dominated by those of their constituent single crystals. This has prompted an increasing tendency to explain the mechanical behavior of apparently single phase ceramics in terms of single crystal slip processes.

Nevertheless, even the purest of present-day oxide ceramics really contains two types of material: (1) relatively ordered material within the individual grains, and (2) highly disorganized layers, in which many impurities may be concentrated, at the grain surfaces and contacts. As a result, an elastic movement in commercial single phase polycrystalline oxides still appears

to occur at or near the grain contacts. This is probably true not only at high temperatures, but for unheated ceramics as well. Thus, Hanna and Crandall⁽⁵⁻¹⁸⁾ found a clear relationship between the internal friction (Q^{-1}) and the mean grain surface area of MgO ceramics measured at room temperature. Moreover, the magnitude of Q^{-1} in these ceramics, and in Al_2O_3 also, is ten or more times higher than that observed for single crystals (see Task 5, Part I). Since diffusion rates are extremely low in Al_2O_3 and MgO at room temperature, dislocation movements are likely to be the agents of slip; however, these processes are controlled by the stress inhomogeneities at the grain boundaries, and they may actually be concentrated in the grain contact zones.

At high temperatures, diffusion (either directly or through its control of dislocation climb) appears to be the rate limiting factor for slip in fine grained ceramics (Beauchamp, Baker and Gibbs⁽⁵⁻¹²⁾ and Warshaw and Norton⁽⁵⁻¹³⁾).

The dependence of creep rate on grain size indicates that it too is governed by the grain boundaries, although it may actually take place in the surface layers and/or through the grain bulk. For the steady state creep of polycrystalline Al_2O_3 , the diffusion of oxygen vacancies appears to occur mainly in the grain surface layers. Thus, Warshaw and Norton found that diffusion constants calculated by applying the Nabarro-Herring^(5-21, 5-22) relation to creep in Al_2O_3 ceramics were several orders of magnitude higher than those obtained by Oishi and Kingery⁽⁵⁻²³⁾ from measurements of oxygen diffusion in single crystals. Diffusion of oxygen at the grain surfaces is so rapid that creep rates in Al_2O_3 and BeO appear to be limited by the migration of aluminum and beryllium cations (cf. Paladino and Coble⁽⁵⁻²⁴⁾ for Al_2O_3).

For coarse-grained Al_2O_3 ceramics, Warshaw and Norton found that the strain rate dependence on stress is not linear, and they suggested that intragranular dislocation movements may contribute significantly to the creep deformation.

High temperature damping in fine-grained oxide ceramics is also considered to be produced, or at least limited by diffusion (Chang⁽⁵⁻²⁵⁾). Stress differences at the grain boundaries provide the driving force for this diffusion as it does for dislocation movements at lower temperatures. Unlike creep, however, damping need not be limited by the diffusion of a particular species. Therefore, movements of cations and anions both at the surface and through the grains, may contribute separately or additively to the dissipation of energy. Another point of difference from steady state creep arises from the fact that in damping the mechanical stress varies periodically with a certain maximum amplitude. The diffusion takes the form therefore, of a flip-flop or oscillatory motion similar to dipole rotation in a ceramic dielectric. Since the diffusion path length is limited in the oscillatory process, Q^{-1} reaches a maximum with rising T and then falls off to form a relaxation peak (see discussion in Part I of Task 5, and also the work of Kirby on glass⁽⁵⁻²⁶⁾). Commonly, the peaks representing the separate relaxation times tend to overlap, or else diffusion of a single species may, with rising temperature, progressively penetrate into deeper regions of the grain. The result of the first effect would be to diffuse a sharp peak into broad zones of high damping, while the second might, at high temperatures, produce a steadily rising internal friction over a relatively long temperature interval.

From the above discussion, creep and internal friction might be expected to have the following response to the influence of impurities and oxygen and hydrogen environments: (1) If the diffusion of aluminum ions is the controlling factor in creep, hydrogen and divalent cation impurities such as Mg^{++} (both of which tend to increase the concentration of oxygen vacancies or reduce the number of cation vacancies) should tend to lower the creep rate. This agrees with the experience of Beauchamp, Baker and Gibbs, who noted that additions of ionic Mg and Mn did retard the creep of Al_2O_3 -- in apparent violation of the commonly accepted model

that creep is controlled by the diffusion of oxygen vacancies; (2) If the surface diffusion of oxygen vacancies is faster than the bulk diffusion of aluminum ions, the former make the dominant contribution to Q^{-1} over some interval of T . In this region, hydrogen and divalent cations should serve to augment the energy dissipation processes.

To study these effects further, and to examine the relationships between damping and creep processes in a commercial high Al_2O_3 ceramic, the temperature dependence of Q^{-1} and creep in annealed and unannealed Wesgo AL-995 were measured in oxygen and hydrogen atmospheres.

12. EXPERIMENTAL METHODS

Damping and creep measurements were carried out on Wesgo AL-995 and Morganite Triangle RR Al_2O_3 rods 6 in. long by 1/4 in. diameter, having a curved gage section (3-in. radius) 1/4 in. wide and 1/10 in. thick at its thinnest point. Three types of Wesgo AL-995 specimens were examined: (1) as received from the supplier, (2) annealed in H_2 at 1800°C for 2 hr, and (3) annealed in O_2 at 1800°C for 2 hr. The untreated specimen was subsequently measured in air, while the others were exposed to the same gases as were used during annealing.

Internal friction measurements were performed near 20 c/s by measuring the decay of flexural vibration presumably caused by damping in the gage section. A specimen was fastened at the bottom end, either by being cemented with a water-cooled steel fixture with an epoxy compound or, later, with a combination of cement and a Swagelok fitting*. Only the central section of the rod was heated by a small platinum-wound furnace fitted with both thermocouples and a direct sight port for pyrometer measurements. The top of the rod was fastened into a rigid plastic tube which served as a pendulum extension arm for

* Crawford Fitting Company, Cleveland, Ohio.

magnifying the deflection. The entire apparatus could be enclosed in an outer steel case fitted with a flexible plastic bag at the top. This permitted control of the internal atmosphere, while at the same time allowing the pendulum arm and transformer core to be moved from the outside. Specimens were set into vibration through the plastic bag by the action of an external solenoid pusher on an extension of the pendulum arm. When the solenoid current was on, its core displaced the pendulum arm a controlled distance; after the current was shut off, the spring loaded core retracted and allowed the specimen to oscillate freely. For creep experiments, the Al_2O_3 bars were subjected to a constant flexural load of 50 g by means of a weight suspended through a simple pulley system from the pendulum arm.

Bending movements of the specimen were maintained by a linear variable differential transformer whose core was fastened near the top of the pendulum arm. The primary of the transformer was supplied with a 2000 c/s voltage, and the output of the secondary was demodulated by a Daytronic Model 300BF Differential Transformer Indicator. For damping measurements, the fluctuating demodulated output was introduced to a Bruel and Kjaer High Speed Level Recorder, which plotted logarithmically the decay of the output envelope. For creep measurements, the output was traced directly by a recording millivoltmeter.

To calculate the internal friction from a level recorder trace (which was generally linear), the slope was first converted to a reverberation time (RT) by means of a special protractor. Reverberation time was then transformed into Q^{-1} by

$$Q^{-1} = \frac{4.40}{RT \times \text{Frequency}} \quad (5-37)$$

Bending displacements of the Wesgo AL-995 specimens were converted to units of tensile strain in the outermost fibers of the gage section by means of a calibration curve obtained by strain gage measurements at room temperature. The stress in this area (3400 psi) was calculated from the beam formula:

$$S = \frac{6 WL}{bd^2} \quad (5-38)$$

where S is the stress

W is the load applied at the free end of the beam

L is the distance from the loading point to the gage section

b is the width of the gage section

d is the thickness of the gage section.

Use of Eq. 15-38 implies that there is no significant stress concentration in the gage section because of its curvature. According to Peterson's⁽⁵⁻¹⁹⁾ curves this assumption is warranted for the 3-in. radius of curvature of gage sections used in this program.

The system described had a sensitivity of 0.1 in. on the recording chart = 0.001 in. of pendulum deflection (at a point 14 in. from the gage section) = 3.4 microinches/inch maximum strain in the gage section. Its main limitation was a relatively high level of background damping (probably localized in the lower specimen grip) which corresponded to a Q^{-1} of about 1.5×10^{-3} . Although this masks the damping values obtainable with polycrystalline specimens at room temperature, the specimen damping rose above this background level at just a few hundred degrees Centigrade.

13. EXPERIMENTAL RESULTS

Curves of Q^{-1} versus T for the Wesgo AL-995 specimens are shown in Fig. 5-19 (as-received), Fig. 5-20 (annealed and measured in O_2) and Fig. 5-21 (annealed and measured in dry H_2). A partial damping curve for the Morganite Al_2O_3 is included for comparison in Fig. 5-19. Creep results are presented in Fig. 5-22 in the form of a semilog plot of steady state creep rate versus $1000/T^\circ K$. A comparison of the creep and damping curves, and an examination of the effects produced by annealing and by changing the surrounding gas reveals the following interesting features:

(1) A specimen annealed and measured in O_2 has about twice the creep rate of one exposed to H_2 ; yet there is no significant change of activation energy. Since O_2 tends to create cation vacancies and to eliminate oxygen vacancies, this behavior is consistent with creep being limited in both specimens by the diffusion of aluminum ions rather than oxygen vacancies.

(2) Annealing the Wesgo AL-995 at a temperature about $100^\circ C$ higher than was used for firing causes the activation energy of steady state creep to drop to about one-half of its original value (76-82 kcal/mole as compared to 165 kcal/mole), and raises the creep rate at lower temperatures. Since the decrease of U is independent of the surrounding gas, it appears to arise from effects produced by the heating itself. These effects might include: (a) the thickening of a semi-vitreous impurity-rich surface layer as it absorbs more Al_2O_3 , (b) grain growth, (c) increased solution and homogenization of impurity cations which are soluble in Al_2O_3 , (d) evaporation of volatile impurities, (e) the thermal creation of anion and cation vacancies and cation interstitials, and (f) the additional pinning of dislocations. Of these, (b), (c), and (d) would tend to raise U by reducing both the area of grain surface and the concentration of impurities in

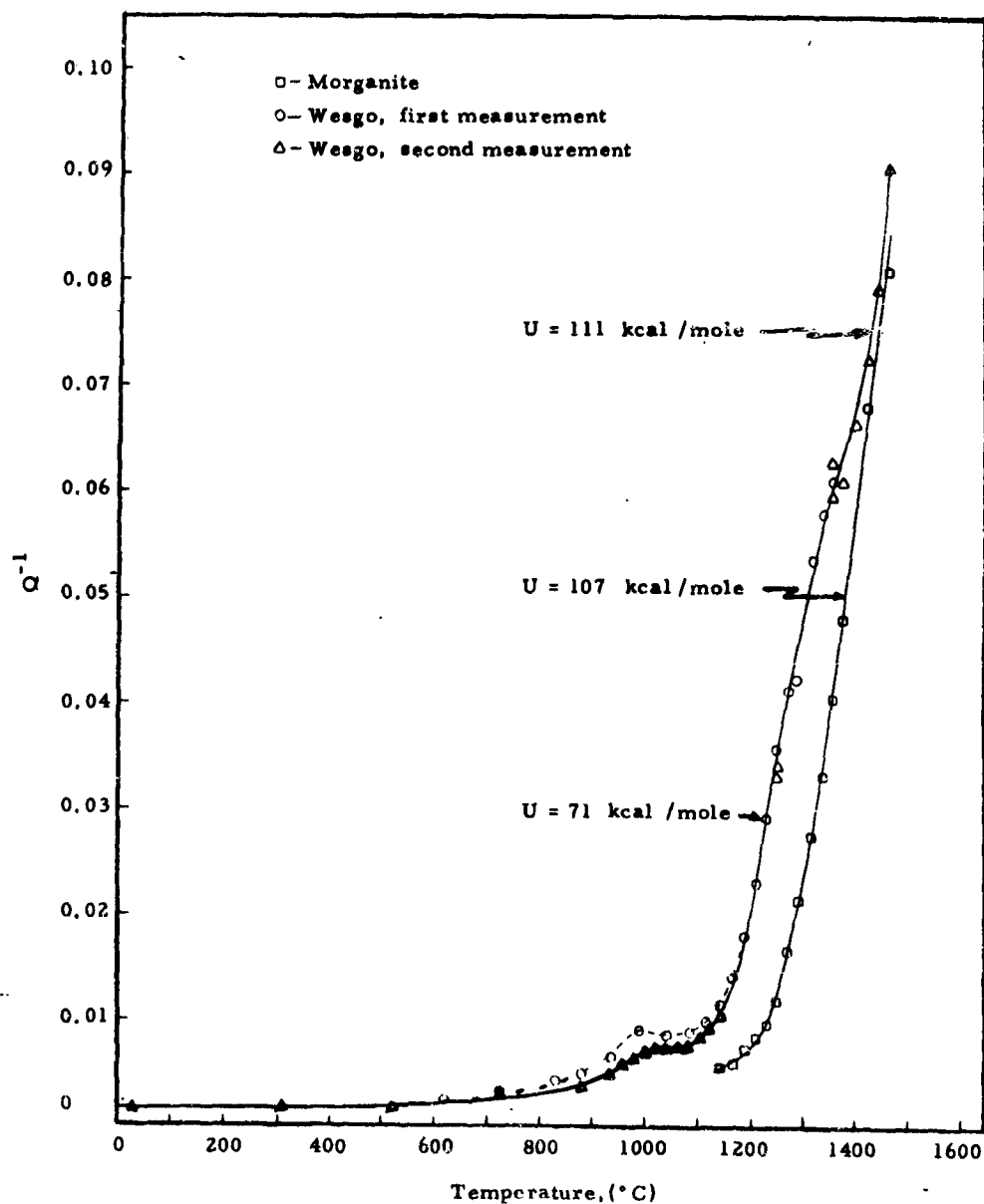


Fig. 5-19 DAMPING DECREMENT Q^{-1} AS A FUNCTION OF TEMPERATURE, WESGO AL-995 AND MORGANITE MEASURED IN AIR
 Wesgo AL-995: 22 cycles/sec at 30°C
 Morganite: 20 cycles/sec at 30°C

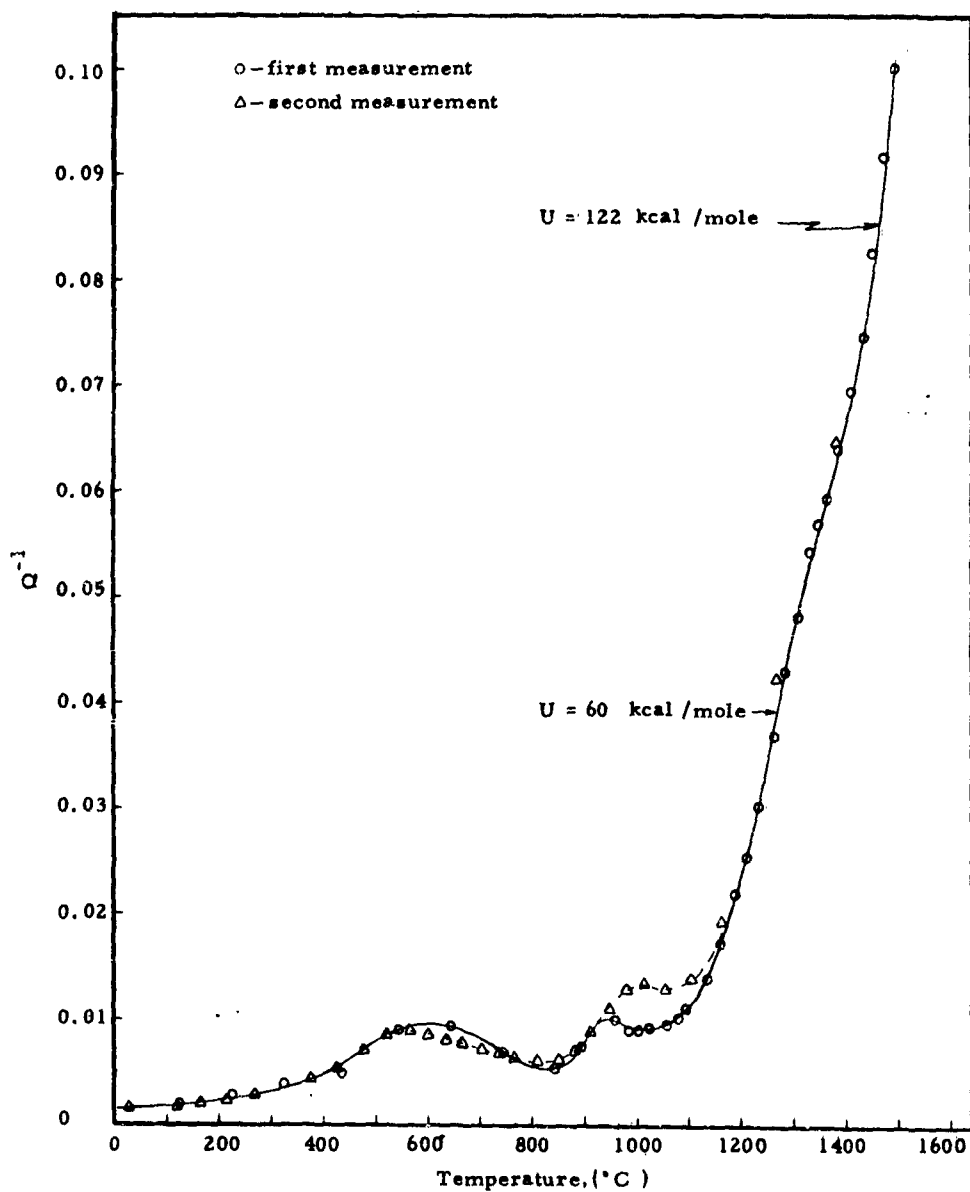


Fig. 5-20 DAMPING DECREMENT Q^{-1} AS A FUNCTION OF TEMPERATURE, WESGO AL-995 ANNEALED AND MEASURED IN OXYGEN (19 cycles/sec at 30°C)

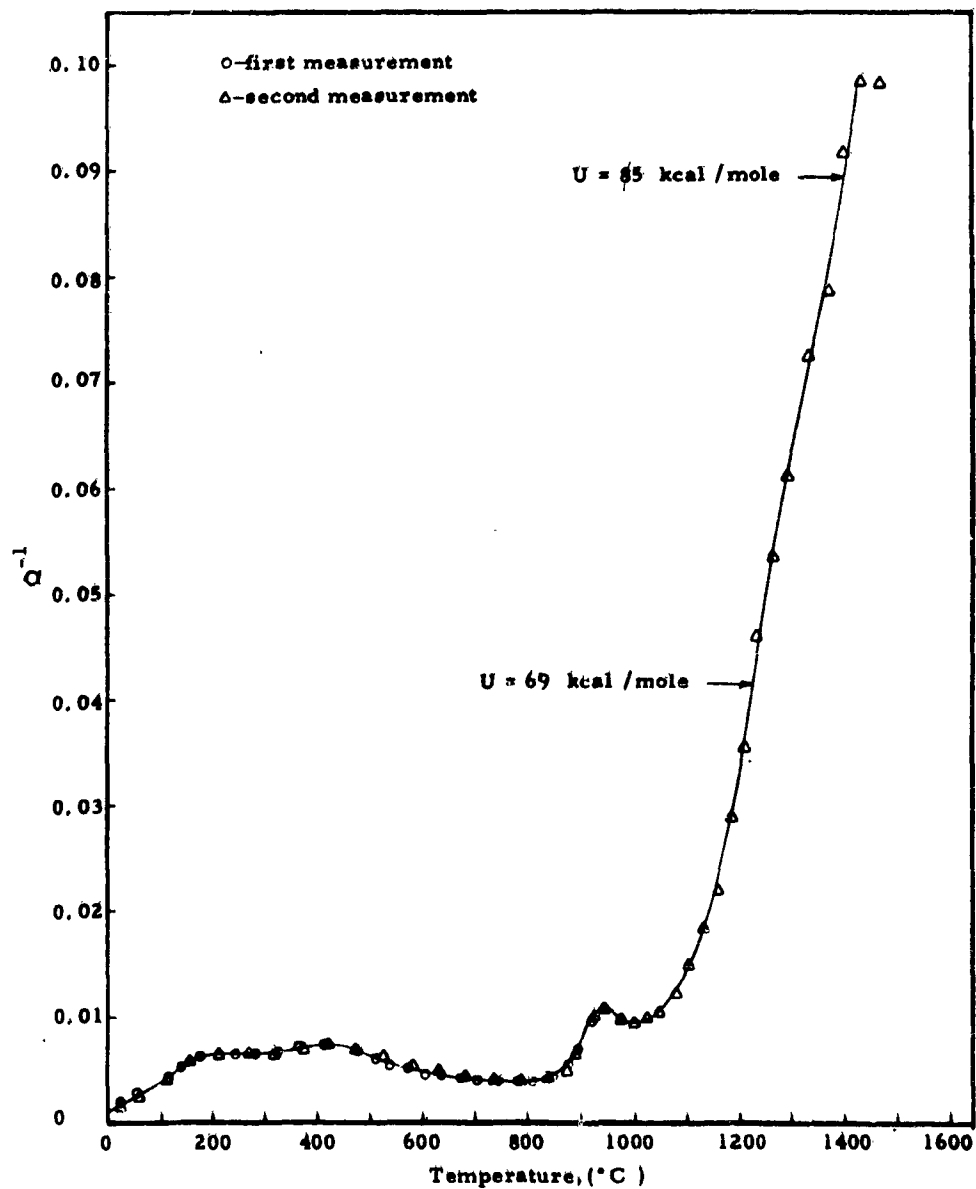


Fig. 5-21 DAMPING DECREMENTS Q^{-1} AS A FUNCTION OF TEMPERATURE, WESGO AL-995 ANNEALED AND MEASURED IN HYDROGEN (19 cycle/sec at 30°C)

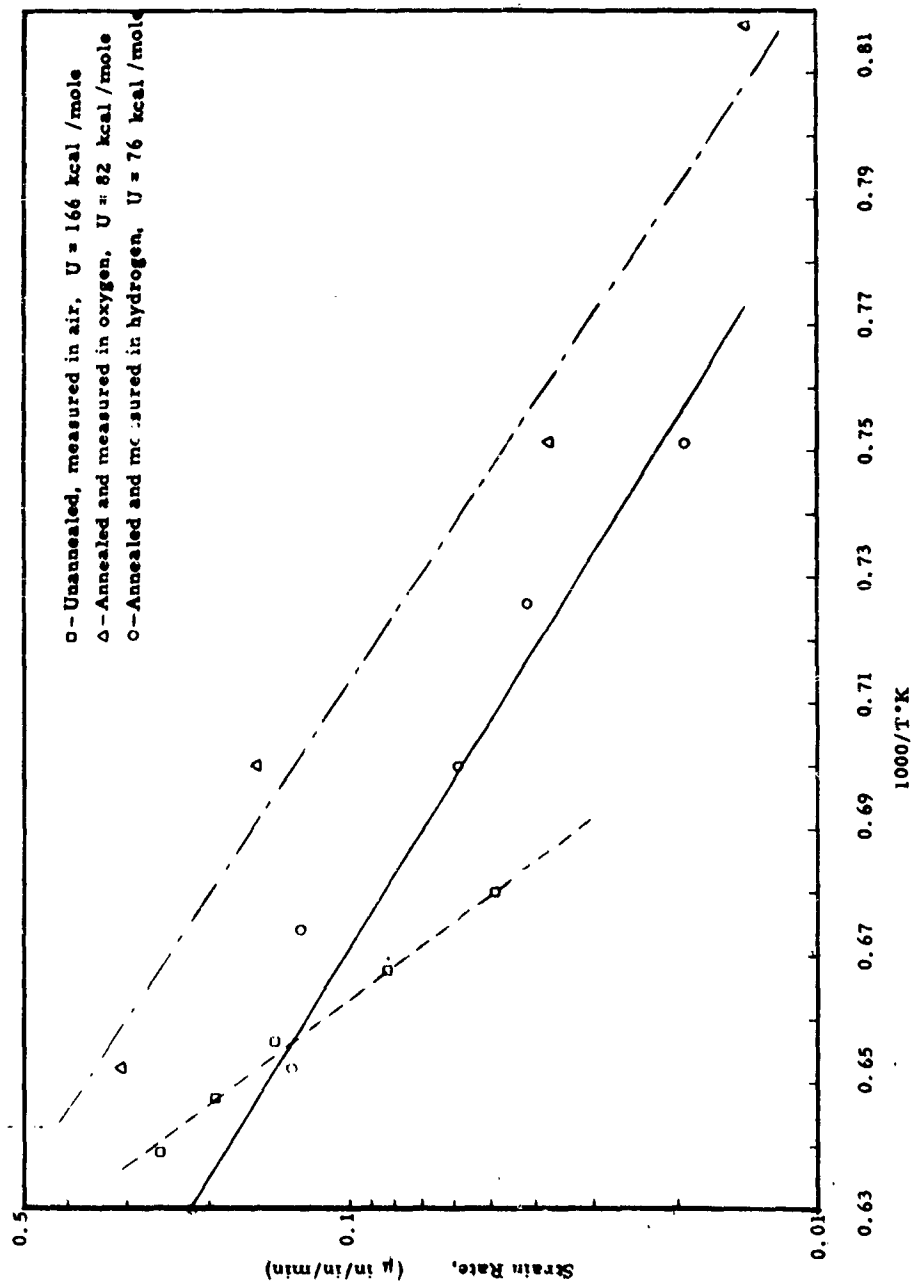


Fig. 5-22 ARRHENIUS PLOTS, STEADY STATE CREEP RATES FOR WESGO AL-995 Al_2O_3

that ration. Processes (a), (e), and (f) might all lower U, but in the case of (e), any defects frozen in after the annealing treatment should tend to disappear by equilibration at the lower temperatures of the creep experiments. Additional dislocation pinning would make diffusion relatively more dominant, but would only serve to subtract from the total pool of deformation processes; this does not explain the higher creep rate of the annealed specimens. On the other hand, increased development of an impurity-rich layer would not be reversible (although some devitrification might occur during the creep runs) and it would tend to increase creep rates. Since Wesgo AL-995 contains about 0.5 percent of impurities (mainly SiO_2 and MgO), this layer may well be thick enough after annealing at 1800°C for it to serve as the site of most of the creep diffusion occurring at the temperatures studied.

In the unannealed specimens -- which had been heated to only 1700°C -- the high value of U suggests that the impurity layer is so thin or poorly developed that it does not control creep. Although the surface diffusion of oxygen vacancies may still occur primarily in this layer, the movement of aluminum ions appears to be through the alumina itself. Furthermore, the bulk Al_2O_3 may contribute to the deformation through slip processes other than diffusion. The presently measured U of 165 kcal/mole for the unannealed Wesgo specimen (average grain size about 40 microns) lies between Warshaw and Norton's extremes of 130 kcal/mole for fine-grained Al_2O_3 (3-13 microns) and 185 kcal/mole for coarser materials (50-100 microns). Although additional corroboration is needed from the dependence of creep rate on stress, the above results suggest that dislocation movements do contribute to the creep of unannealed Wesgo AL-995.

(3) In an oxidizing atmosphere, the internal friction of an annealed bar is generally higher up to about 1250°C than for an as-received specimen. Below 800°C, this increased Q^{-1} takes the form of a broad maximum peaking near 600°C. The gentle rise on the low temperature side of this peak has a superficial resemblance in shape and magnitude of Q^{-1} to the damping curves of alkali-free glasses (Ryder and Rindone⁽⁵⁻²⁸⁾). A second peak occurs between 950 and 1000°C for both annealed and as-received specimens but is somewhat more highly developed in the former. Above 1050°C, Q^{-1} rises exponentially, except for a change of slope near 1350°-1400°C. Below the irregularity, the temperature dependence of Q^{-1} corresponds to $U = 60$ kcal/mole for the annealed bar, and $U = 71$ kcal/mole for the as-received specimen. Above the inflection, U rises to 122 kcal/mole and 111 kcal/mole for the two bars -- closer to the activation energy determined from the creep of an unannealed specimen.

These results are consistent with the model that below about 1250° to 1350°C, energy is dissipated mainly in a thin, impurity-rich, and possibly vitreous surface zone, and that at higher temperatures it penetrates progressively into the Al_2O_3 itself. This transition is not seen in the creep data -- probably because the creep experiments were conducted at temperatures at and below 1300°C.

The Q^{-1} versus T curve of Morganite Al_2O_3 does not show an inflection, and has a slope corresponding to the upper portions of the other damping curves. Since Triangle Al_2O_3 is purer than Wesgo Al_2O_3 , this provides some additional support for the important role played by a surface impurity layer.

(4) In an H_2 atmosphere, the damping curve of an annealed specimen differs from the curve measured in O_2 in the following respects: (a) The low temperature zone below $800^\circ C$ is characterized by an overlapping double maximum (peaking at about 200° and $430^\circ C$) which has an even closer resemblance to the glass curves of Ryder and Rindone (b) The exponential rise of Q^{-1} in H_2 is apparently displaced to somewhat lower temperatures (c) The change of slope near $1350^\circ C$ is not as great in H_2 as in O_2 -- corresponding to a rise of U from 69 kcal/mole to only 85 kcal/mole. Furthermore, on the evidence of only one point, it appears possible that there may be another change of slope between 1400° and $1450^\circ C$.

The displacement of the exponential portion of the damping curve to lower temperatures by H_2 suggests that damping in this region is caused or limited by the surface diffusion of O_2 vacancies rather than by the movement of Al ions, as in creep. This agrees with the concept that the diffusion of the slower species -- in this case the cations -- limits the large scale transfer of material in creep (because of space charge effects), but does not retard the small displacements involved in damping.

The relative insensitivity to different atmospheres of the small peak near $950^\circ C$ suggests that it may be of impurity origin -- possibly the oscillation of impurity cations (e.g., Mg^{2+}) or the rotation of pairs such as Mg^{2+} - O_2 vacancy, or Mg^{2+} - Si^{4+} . Changes in the "glass" peak at low temperatures may reflect atmosphere control of the cation/ O_2 ratio in the vitreous surface layer.

(5) Despite a similarity of vibration frequencies to those used by Chang, none of the specimens of this program show the well developed relaxation peak that Chang found at about $1100^\circ C$. However, Chang observed this peak only for very pure Al_2O_3 ;

upon adding Cr_2O_3 or La_2O_3 impurities, his internal friction curves takes on the appearance of those shown in Fig. 5-19 to 5-21.

14. CONCLUSION

Summarizing the above observations, it appears that up to about 1300°C , creep in an unannealed commercial 99.5 percent Al_2O_3 ceramic is controlled largely by the diffusion of Al ions with possibly some contribution from dislocation processes. In specimens annealed at higher than the firing temperature, Al ion diffusion continues to control creep but it appears to take place largely in a surface zone rich in impurities.

At low and moderate temperatures, damping in Wesgo AL-995 is characterized by relaxation processes which resemble those occurring in an alkali-free glass. Above 800°C , however, damping may be controlled first by the oscillatory movement of impurity cations, possibly paired with O_2 vacancies, and later by the diffusion of O_2 vacancies. Up to about 1350°C , this seems to occur in an impurity-rich surface zone, but above that temperature, the process apparently penetrates deeper into the Al_2O_3 itself. This prevents the formation of a simple relaxation peak characterized by a single relaxation time, and produces instead, a continued rise of Q^{-1} with T, and an increase of U.

15. REFERENCES

- 5-1 Weil, N. A., Ed., Studies of the Brittle Behavior of Ceramic Materials, ASD-TR-61-628, April, 1962.
- 5-2 Bauer, C. L., and Gordon, R. B., J. Appl. Phys. 33, 673 (1962).
- 5-3 Bauer, C. L., and Gordon, R. B., J. Appl. Phys. 31, 945 (1960).
- 5-4 Gordon, R. B., Nowick, A. S., Acta Metall. 4, 514 (1956).
- 5-5 Granato, A., Hikata, A., Lucke, K., Acta Metall. 6, 470 (1958).

- 5-6 Bullough, R., Newman, R. C., Phil. Mag. 6, 405 (1961).
- 5-7 Koehler, J. R., Imperfections in Nearly perfect Crystals (W. Shockley, Ed.) New York, J. Wiley and Sons (1954).
- 5-8 Granato, A., Lucke, K., J. Appl. Phys., 27, 583 (1956).
- 5-9 Venables, J. D., Phys. Rev. 122, 778 (1961).
- 5-10 Lidiard, A. B., Defects in Crystalline Solids, Phys. Soc. (London) 261 (1955).
- 5-11 Wuensch, B. J., Vasilos, T., J. Chem. Phys. 36, 2917 (1962).
- 5-12 Lindner, R., Parfitt, G. D., J. Chem. Phys. 26, 182 (1957).
- 5-13 Chang, R., J. Appl. Phys. 32, 1127 (1961).
- 5-14 Southgate, P. D., Technical Report No. ASD-TR-62-431, March 1962.
- 5-15 Brailsford, A. D., Phys. Rev. 122, 778 (1961).
- 5-16 Eshelby, J. D., et. al: Phil. Mag. 3, 75 (1958).
- 5-17 Cottrell, A. H., Dislocations and Plastic Flow in Crystals: Oxford University Press, London (1953).
- 5-18 Hanna, R. and Crandall, W. B., "Dissipation of Energy by the Grain Boundaries", Astia Doc. 274 956, OTS, U. S. Dept. of Commerce (May 1962).
- 5-19 Beauchamp, E. K., Baker, G. S. and Gibbs, P., "Impurity Dependence of Creep Aluminum Oxide", ASD TR 61-481 (April 1962).
- 5-20 Warshaw, S. I. and Norton, F. N., "Deformation Behavior of Polycrystalline Aluminum Oxide", J. Am. Ceram. Soc., 45 (10) 479-486 (1962).
- 5-21 Nabarro, F. R. N., "Deformation of Crystals by Motion of Single Ions" pp. 75-90 in Rept. Conf. Strength of Solids (U. of Bristol) July 1947 (pub. 1948).
- 5-22 Herring, C., "Diffusional Viscosity of a Polycrystalline Solid" J. Appl. Phys. 21 (5), 437-45 (1950).
- 5-23 Oishi, Y. D. and Kingery, W. D., "Self Diffusion of Oxygen in Single Crystal and Polycrystalline Aluminum Oxide", J. Chem. Phys. 33, 480-86 (1960).

- 5-24 Paladino, A. E. and Coble, R. L., "High Temperature Kinetic Processes in Aluminum Oxide" Pres. at 64th An. Meeting of Am. Ceram. Soc., New York, N. Y. paper No. 2-2s-62, (April 1962).
- 5-25 Chang, R., "High Temperature Creep and Anelastic Phenomena in Polycrystalline Refractory Oxides" J. Nucl. Materials, 1, 174-81 (July 1959).
- 5-26 Kirby, R. L., (a) "Internal Friction in Glass: I Theoretical Aspects", J. Soc. Glass Technol. 37 (174) 7-26T (1953).
(b) "Mechanical Relaxation of Alkali Ions in a Borosilicate Glass," Loc. Cit. 39, 385-93 T (1955).
(c) "Relaxation Processes in Glass," Trans. Faraday Soc. 52, 131-42 (1956).
- 5-27 Peterson, R. E., "Stress Concentration Design Factors", J. Wiley and Sons, New York, N. Y. (1953).
- 5-28 Ryder, R. J. and Rindone, G. E., "Internal Friction of Simple Alkali Silicate Glasses Containing Alkaline Earth Oxides: I-Experimental Results" J. Am. Ceram. Soc., 43 (12) 662-69 (1960).

TASK 6 - EFFECT OF SURFACE ENERGY

Principal Investigator: N. J. Petch

ABSTRACT

This work is concerned with the determination of the effect of surface energy in the fracture strength of brittle materials, particularly as concerns the differences between true (elastic) values and the effective surface energy accompanying crack propagation. The problem was approached by the utilization of three techniques (1) crack propagation studies in plates containing pre-drilled cracks, (2) absorption isotherm determinations, and (3) zero-creep determinations at elevated temperatures.

Crack propagation studies carried out on Al_2O_3 , MgO and glass plates containing pre-drilled cracks showed that the apparent surface energy increases pronouncedly in all three materials as the temperature is lowered from 20°C to -196°C . Subject to the substantial plastic deformation required to initiate a running crack; because of the greater resistance to dislocation mobility at lower temperatures, such plastic deformation calls for higher stresses, and leads to higher values of the apparent effective surface energy.

Studies of the lowering of surface energy which is due to the absorption of CO_2 , H_2 and H_2O on Al_2O_3 powders showed that the effects ascribable to the first two substances are completely negligible. Water vapor lowers the surface energy by about 7 percent and fracture stresses by about 4 percent. This, however, is insufficient to account for observed effects; the possibility of the added existence of a chemical reaction is currently under investigation.

Preliminary results for the determination of "zero creep" rates on Al_2O_3 at 1900°C show surface energy values of 890 ergs per sq cm in excellent confirmation of previously published results. An extension of the technique to a broader range of temperatures is currently in progress.

TASK 6 - EFFECT OF SURFACE ENERGY

1. INTRODUCTION

In the theory of fracture, the term "surface energy" acquires a wider than normal usage. Most commonly the term refers to the reversible or true surface energy; however, often it is also assumed to include the "effective" surface energy associated with fracture. This concept, introduced by Orowan, is intended to describe Griffith's energy balance criterion for the growth of a crack when that growth induces plastic deformation at the crack.

In metals, where the formation of a crack nucleus seems to be caused by dislocation processes, the true surface energy is probably the significant term at the absolute beginning of the crack formation. However, this stage is probably never detected in fracture observations commencing at a critical crack size such that there is an extensive stress field around the crack in which plastic deformation takes place.

In a very brittle material, such as glass, it has for long been supposed that fracture involves the purely elastic spreading of a pre-existing crack, involving only the true surface energy term. However, even this view may require revision in view of the recent experimental findings of Marsh which appear to show that the fracture of glass fibers is associated with a catastrophic flow process, rather than the attainment of the theoretical bond strength.

It is with this interplay between true and effective surface energies as significant terms in the fracture of inorganic oxide ceramics that the present work is concerned.

From the work reported in 1961⁽⁶⁻¹⁾, three main lines of investigation emerged.

- (1) Direct estimation of the effective surface energy in crack propagation from the stress required to extend pre-formed cracks in thin plates.
- (2) Measurements of the lowering in surface energy resulting from absorption of CO_2 , H_2 and H_2O on Al_2O_3 and the possible relation of this to static fatigue
- (3) Measurement of the true surface energy at high temperature from the stress required to prevent surface contraction

2 THE FRACTURE OF PRE-CRACKED PLATES

A. Central Cracks

Most of the work on this phase of the program concerned fracture studies on thin plate specimens $5 \times 3 \times 0.1$ cm in size that contained a centrally-placed elliptical crack with the major axis perpendicular to the applied tension. The cracks, in general, were ultrasonically drilled and had a tip radius of the order of 10^{-3} cm, which was the sharpest that could be manufactured by this technique.

Initially these plates were loaded by fixing them across the arms of a U-jig as was described in the previous phase report on this program⁽⁶⁻¹⁾. However, the axi-ality of stressing was found to be unsatisfactory with this device and a new system was developed. In this approach, the tension was applied to the plates by means of two straps, $2 \times 11 \times 0.005$ in in size. The two ends of each strap were connected to opposite faces of the long edge of the plate, forming a loop. This loop passed over a 1-in diam roller; in addition, two smaller rollers pressed against the strap so that the separation of the two arms of the loop was reduced to 1 mm equaling the specimen plate thickness (Fig 6-1). This system automatically equalizes the load applied to each face, leading to a very satisfactory axi-ality of stressing, as shown in Fig 6-2, which presents the stresses on the two faces of the plate

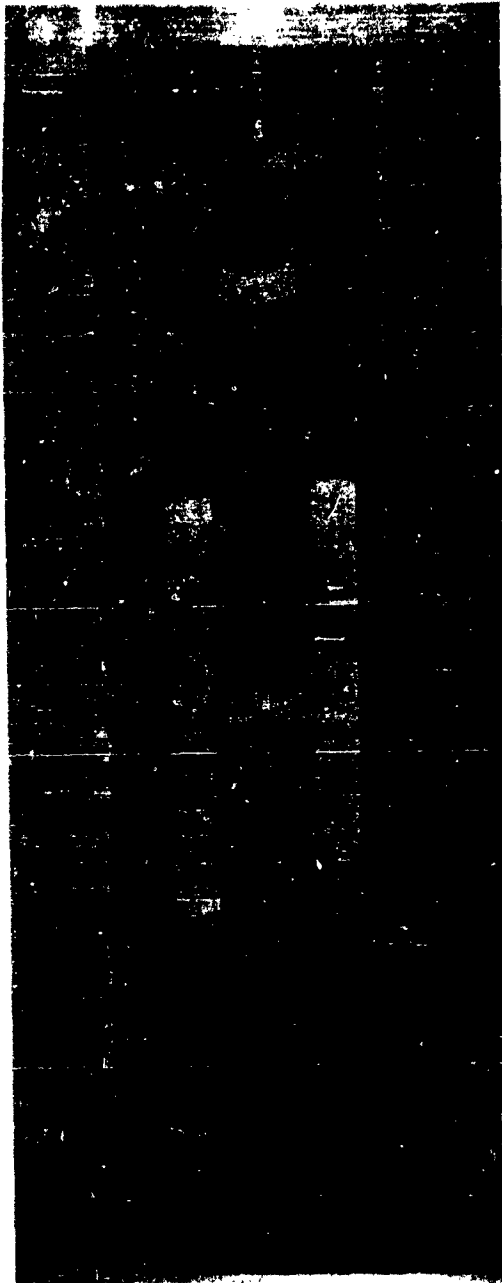


Fig. 6-1
LOADING SYSTEM USED TO OBTAIN UNIAXIAL
TENSION OF THIN PLATES

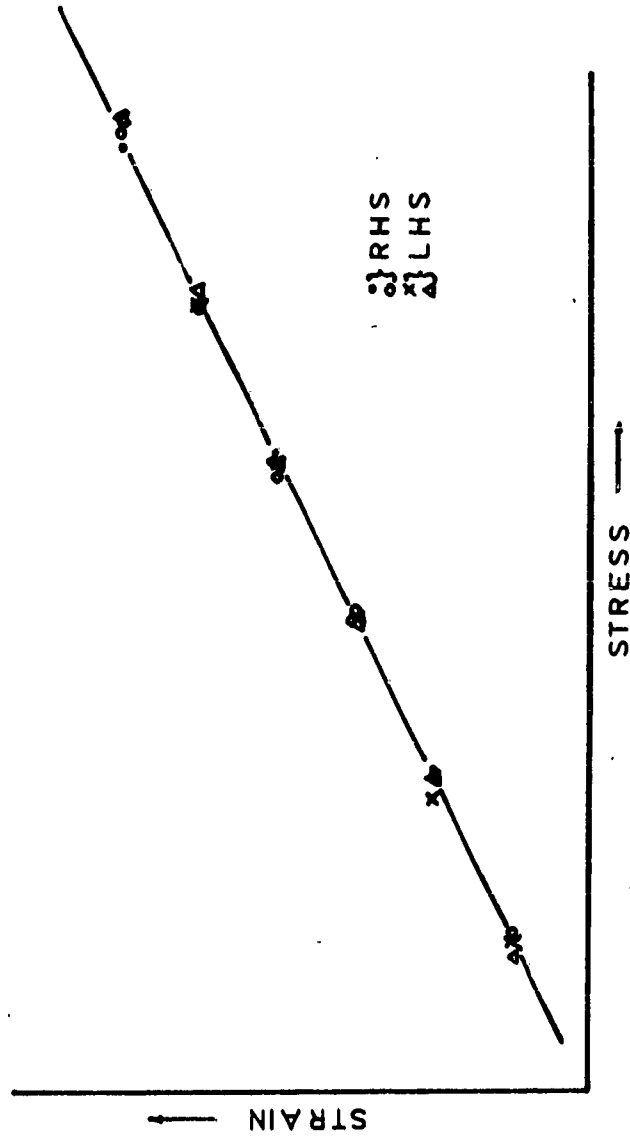


Fig. 6-2 MEASUREMENTS ON THE AXIALITY OF LOADING ACHIEVED USING THE DEVICE IN FIGURE 6-1

obtained by strain gauges.

A standard cross-head velocity of 4.8×10^{-4} in. per min was used in all measurements; because of the elasticity of the loading jig, this value was found to correspond to a strain rate of about $5 \times 10^{-5} \text{ min}^{-1}$.

The plates were fractured at a variety of temperatures. This required that the strap material have a similar coefficient of thermal expansion to the specimen, otherwise thermal stresses set up at the joint could lead to premature fracture. Mild steel was a satisfactory strap material for MgO, but for glass and Al_2O_3 an iron-nickel alloy "Nilo 42" was used. Low temperature measurements were made in liquid nitrogen and in acetone-solid CO_2 . Silicone oil baths were used above room temperature.

The results of these fracture stress measurements are shown in Fig. 6-3, 6-4, and 6-5, and are expressed in terms of $\sigma_f^2 c$, where σ_f is the fracture stress in dynes per sq cm and c is the half-length of the original crack.

Before these measurements were carried out, it was thought possible that, although the macroscopic radius of curvature of the drilled crack was obviously too great to satisfy conditions for a true Griffith crack, the actual surface might be so irregular that effectively Griffith crack propagation might occur in these very brittle materials. However, assuming reasonable values for the reversible surface energy, it is apparent that the observed fracture stresses are too high for this to be true. The surface energies calculated on the assumption of ideal Griffith crack behavior are shown in Table 6-I.

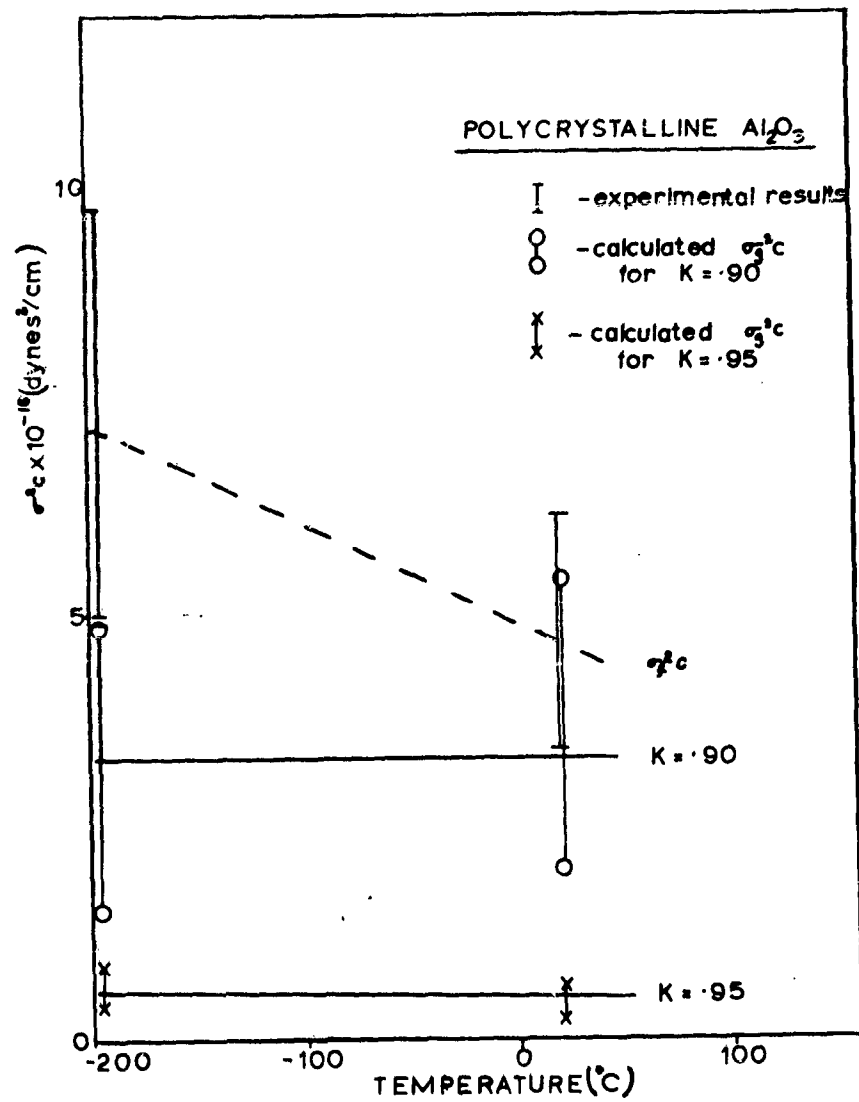


Fig. 6-3 MEASURED VALUES OF σ_z^2 FOR ALUMINUM OXIDE AND DEDUCED VALUES OF σ_z^2 FOR VARIOUS VALUES OF K

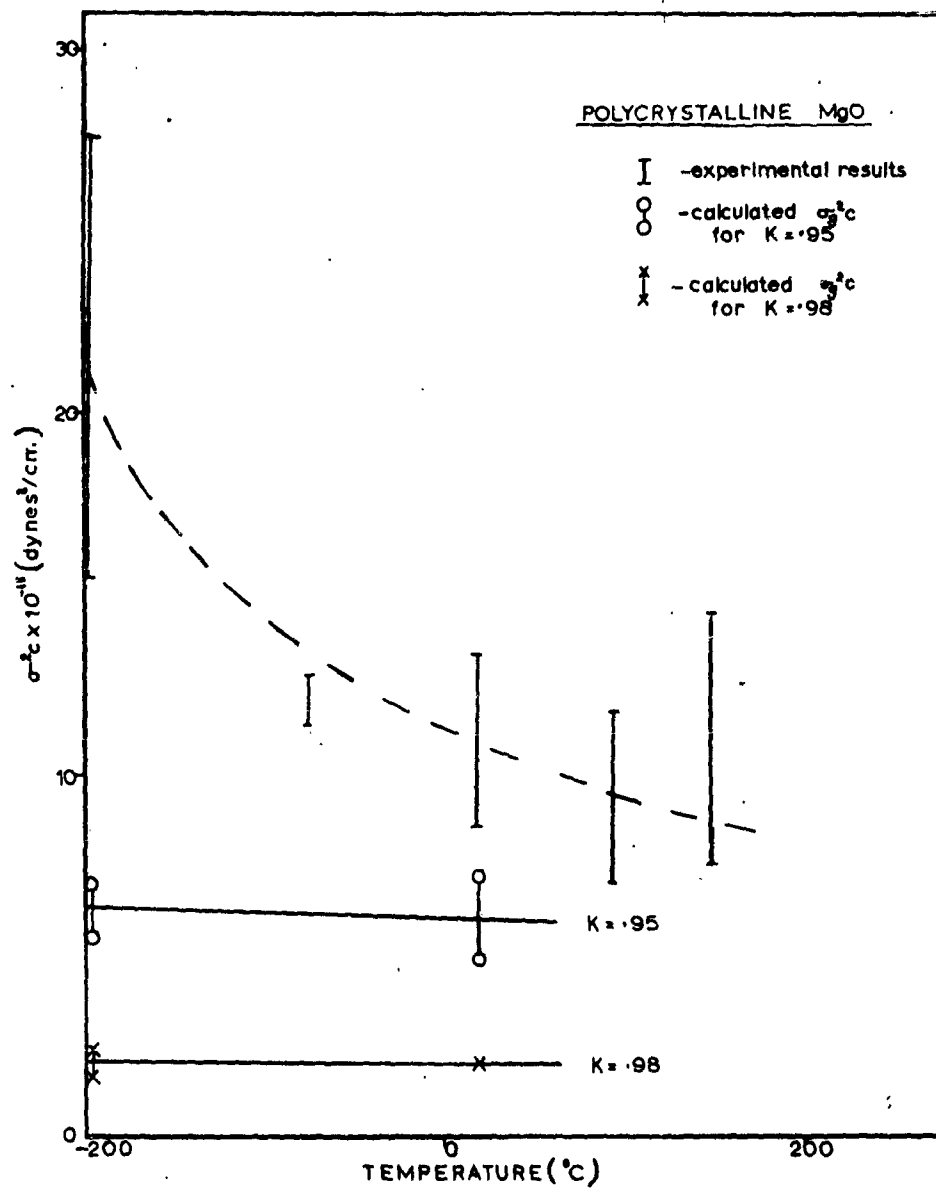


Fig. 6-4 MEASURED VALUES OF $\sigma_{12}^2 c$ FOR MAGNESIUM OXIDE AND DEDUCED VALUES OF $\sigma_{12}^2 c_0$ FOR VARIOUS VALUES OF K

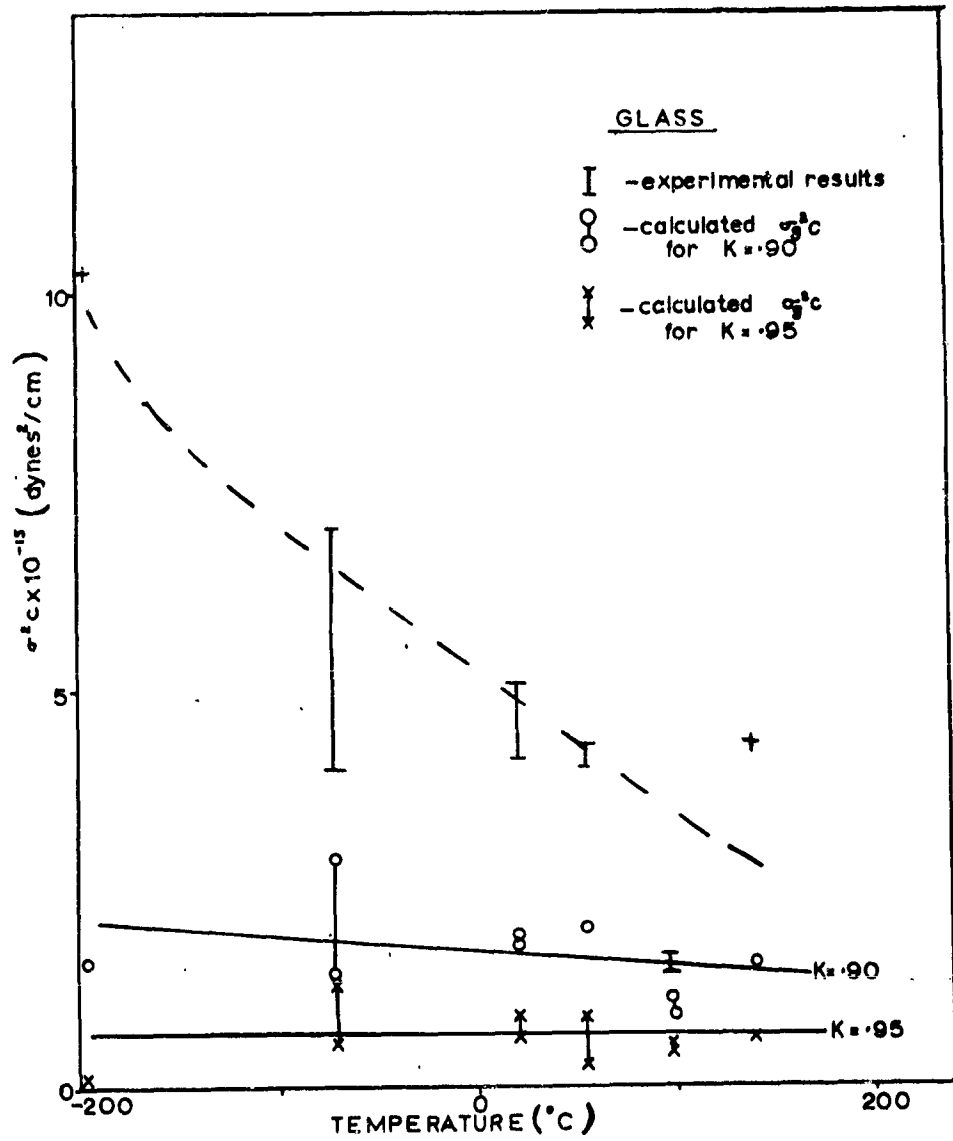


Fig. 6-5 MEASURED VALUES OF $\sigma_f^2 c$ FOR GLASS AND DEDUCED VALUES OF $\sigma_g^2 c_o$ FOR VARIOUS VALUES OF K

Table 6-I

SURFACE ENERGIES CALCULATED ASSUMING IDEAL
GRIFFITH CRACK BEHAVIOR

Material	Range of $\sigma_f^2 c$	Surface energy, γ , (ergs/cm ²)
Al ₂ O ₃	$3.4 \times 10^{16} - 10^{17}$	$2-6 \times 10^4$
MgO	$7 \times 10^{15} - 2.5 \times 10^{16}$	$4.2 - 17 \times 10^3$
Glass	$1.5 \times 10^{15} - 10^{16}$	$4-26 \times 10^3$

The explanation of the high fracture stress could lie simply in the bluntness of the cracks, the actual propagation being purely elastic. If this were so, the effective curvature of the crack tip can be estimated on the assumption that the theoretical strength has to be reached at the crack tip. Then, the criterion for fracture is given by

$$\sigma_{th} \sim \left(\frac{\gamma E}{a} \right)^{\frac{1}{2}} = 2\sigma_f \left(\frac{c}{\rho} \right)^{\frac{1}{2}}$$

where σ_{th} is theoretical strength, γ is true surface energy, E is Youngs' Modulus, a is the interatomic spacing and ρ is the tip curvature. Table 6-II gives ρ values calculated in this way from typical fracture stresses at room temperature.

It is evident that although the cracks do not behave as Griffith cracks, they do behave as if they had effectively much sharper radii than their nominal values (10^{-3} cm). Even for a circular hole in Al₂O₃, the calculated was only 2×10^{-6} cm.

As Fig. 6-3, 6-4 and 6-5 show, there is a pronounced increase in the value of $\sigma_f^2 c$ for all three materials, as the temperature is lowered from 20°C to -196°C. This marked increase in $\sigma_f^2 c$ between room temperature and -196°C indicates that the observed

Table 6-II

CALCULATIONS FOR EFFECTIVE CRACK RADII

Material	Theoretical Strength σ_f (dynes/cm ²)	Half-length c, (cm)	Young's Modulus E, (dynes/cm ²)	Surface Energy, γ , (ergs/cm ²)	Tip Curvature, ρ , (cm)
Al ₂ O ₃	6.2×10^8	0.16	3.75×10^{12}	2.5×10^3	2×10^{-7}
MgO	2.3×10^8	0.165	2.6×10^{12}	1.2×10^3	2×10^{-7}
Glass	1.7×10^8	0.162	6×10^{11}	10^3	5×10^{-7}

fracture stresses cannot be explained simply by changes in the bluntness of the crack tip, since the only temperature dependent terms available in Eq. (6-1) are the elastic surface energy, Young's modulus and a , and none of these are sufficiently temperature sensitive to explain the observed variation in fracture stress.

There seem to be two possible explanations of the temperature dependence of the fracture stress.

(1) That the observed fracture is affected by the existence of static fatigue. At low temperatures, there might be less lowering of the fracture stress by fatigue during the duration of the loading to fracture.

(2) The process of extending these drilled cracks may require an initial temperature sensitive step, in which either the macroscopic crack is sharpened or a cleavage crack nucleus is formed at its tip by some dislocation process. The temperature-dependence of the fracture stress could then arise through a temperature-dependence of the stress required for dislocation movement.

At present we prefer alternative (2), although the critical test of whether the temperature dependence persists under stringent vacuum conditions has not yet been made. Equipment for this purpose is being assembled currently.

B. Crack Branching

The fracture experiments described were invariably characterized by a branching of the propagating crack. In glass specimens the details of the propagation are clearly identifiable by the following stages: at first the fracture surface has a mirror appearance; then a hackle develops which becomes gradually coarser until crack branching occurs. The branches then go through a mirror-hackle-re-branch cycle. The lower the temperature, the higher the fracture stress and the sooner crack branching occurs.

The mathematics of crack propagation has been well developed by Yoffe⁽⁶⁻²⁾, Craggs⁽⁶⁻³⁾ and Berry⁽⁶⁻⁴⁾. In our experiments, the ratio of the area, A , of the plate to the circular area with the crack length as diameter is ~ 150 . Treatment of the fracture as occurring under constant stress is then justified.

From Berry, the velocity, v , of a crack when it has grown to a semi-length, c , from an initial c_0 under a stress σ_f is given by

$$v^2 = \frac{2\pi}{k} \cdot \frac{E}{d} \left(1 - \frac{c_0}{c}\right) \left(1 - (n-1) \frac{c_0}{c}\right)$$

where k is a constant, E is Young's modulus, d is the density and n is given by

$$n = 2 \left(\frac{\sigma_g}{\sigma_f} \right)^2.$$

Here, σ_g is the Griffith critical stress for c_0 and σ_f is the actual fracture stress.

If branching occurs at a critical velocity, which is some fraction of the maximum theoretical velocity $\sqrt{\frac{2\pi}{k} \cdot \frac{E}{d}}$, then,

$$\left(1 - \frac{c_0}{c}\right) \left(1 - (n-1) \frac{c_0}{c}\right) = K,$$

where K is a constant.

Thus, if K were known, it would be possible to find n and σ_g , the fracture stress for a Griffith crack of semi-length c_0 . This, then could be another method of analyzing the fracture stresses to obtain the surface energy corresponding to Griffith crack propagation, since the surface energy, γ , is then given by

$$\gamma = \frac{\sigma_g^2 \pi c_0}{2E}. \quad \text{This method should give a value of the}$$

surface energy independent of tip geometry so long as the crack is approximately elliptical with a reasonably small minor axis. This latter condition is necessary since Wundt and Wynne⁽⁶⁻⁶⁾ showed that if a good part of the material at a circle inscribed on the crack as diameter were removed, Griffith propagation condition is altered.

To carry through this analysis a value for K is required. Wells and Roberts⁽⁶⁻⁵⁾ have estimated the maximum terminal velocity as $0.38 \sqrt{E/d}$, which for a Poisson's ratio of $1/3$ is $\sim 0.6 c$, where c is the shear wave velocity. Yoffe showed that crack branching should occur at velocities approaching $0.6 c_2$. On this basis, \sqrt{K} should be slightly less than unity.

Figures 6-3, 6-4, and 6-5 give $\sigma_g^2 c_0$ values derived using assumed values of K within the range of 0.85-0.95. The experimental data is in Table 6-III along with the γ values. The principal interest in this method of analyzing the fracture measurements lies not so much in the absolute values of γ deduced, which depend rather sensitively on the value of K chosen, but rather in the fact that reasonable values of K indicate little temperature dependence of γ . Thus, when γ is deduced from crack branching, little temperature dependence is indicated, but, when deduced from the stress required to initiate crack propagation, there is considerable

Table 6-III

-284-

temperature dependence. This is further evidence suggesting that the initiation of crack propagation at the drilled cracks involves some temperature-dependent process whereas, once the crack begins to travel, only a temperature-independent surface energy is involved.

C. Cantilever Loading of an Edge Crack

Some additional measurements have been made on 3 x 1 x 0.1 cm polycrystalline specimens containing an ultrasonically drilled edge crack 1-cm long parallel to the long edge of the specimen. This was loaded by pins put through the two arms of the crack, which consequently bend approximately as cantilevers. This follows the method used originally by Obreimov and applied by Gilman to the propagation of cleavage cracks in single crystals. In the present case, the shape of the specimen, governed by dimensions developed for other purposes, did not justify the neglect of the shear strain energy; hence calculated results for surface energy values, shown in Table 6-IV for polycrystalline MgO and Al_2O_3 , are apt to be on the high side. The interesting point is not so much the actual values, as the fact that these are independent of temperature. Gilman and Guernsey⁽⁶⁻¹²⁾ have investigated photoelastically the stress system in this form of loading and shown that it is much more localized than that corresponding to a plate containing an internal crack. Thus, the effect of dislocation movement on the apparent surface energy may not be so marked.

D. Discussion and Conclusion

From results derived to date it appears that a stopped cleavage crack can be re-started with the consumption of about work equaling roughly the true surface energy at the temperature range in question in these experiments. Measurements on crack branching suggest that a running crack also consumes only the true, nearly temperature independent, surface energy. However, initiation

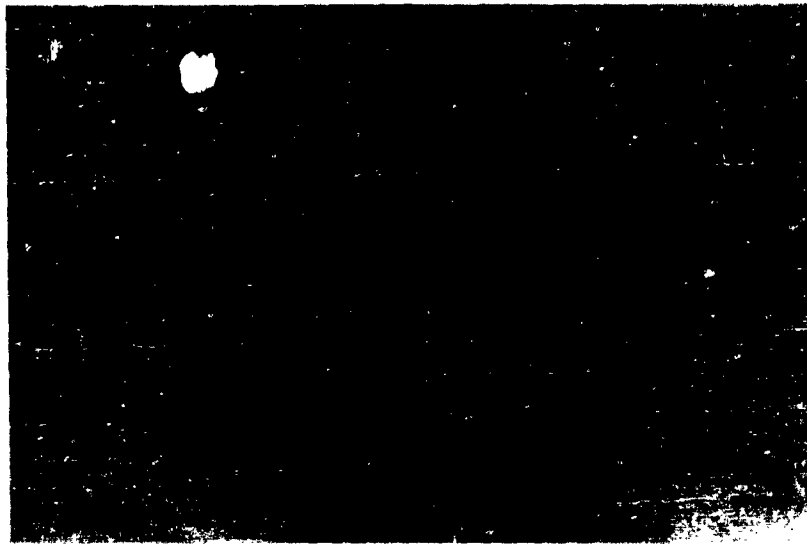
Table 6-IV
SURFACE ENERGY VALUES FROM EDGE CRACKS
IN POLYCRYSTALLINE SPECIMENS

Temperature (°C)	Apparent Surface Energy, γ , (ergs/cm)	
	Al ₂ O ₃	MgO
90	23, 100	-
20	-	6, 175
20	19, 650	5, 400
20	19, 200	4, 361
-196	23, 840	5, 470
-196	-	5, 240
-196	-	7, 360

of propagation with blunter cracks within a plate requires a higher temperature-dependent, "effective" surface. As has been suggested here, this appears to require some dislocation process to initiate the propagation. This process might involve direct sharpening of the crack tip, or the production of a cleavage nucleus in the vicinity of the tip.

There already exists clear evidence of the generation of dislocations at the tip of slowly moving cleavage cracks (Gilman⁽⁶⁻⁷⁾, Tetelman⁽⁶⁻⁸⁾). Figure 6-6 shows the dislocation movement that occurs when a crack in MgO is stopped by running into a compression region. It is clear that the fast running crack does not induce any discernable dislocation movement, while the slowly moving crack initiates substantial dislocation coalescence and associated plastic flow at the crack tip.

If the higher effective surface energy for starting the propagation of the blunter cracks merely reflected some plastic work associated with propagation of the crack, then this plastic



x 40

(a) Fast running portion of crack showing no associated plastic deformation



x 100

(b) Slow running portion of crack showing associated plastic deformation

Fig. 6-6

CLEAVAGE CRACK IN MAGNESIUM OXIDE SINGLE CRYSTAL STOPPED
BY RUNNING INTO ZONE OF COMPRESSIVE STRESSES
Etchant = 50% Sat. NH_4Cl 50% HNO_3

work should decrease as the temperature is lowered. However, the experimental evidence is that the effective surface energy increases as the temperature is lowered. Thus, the important aspect of plastic deformation in the present case seems to be not so much that a plastic work factor will be added to the effective surface energy, but that plastic deformation is necessary before propagation is possible and this will require a higher stress at lower temperatures and so appear in the calculations as a higher effective surface energy at lower temperatures.

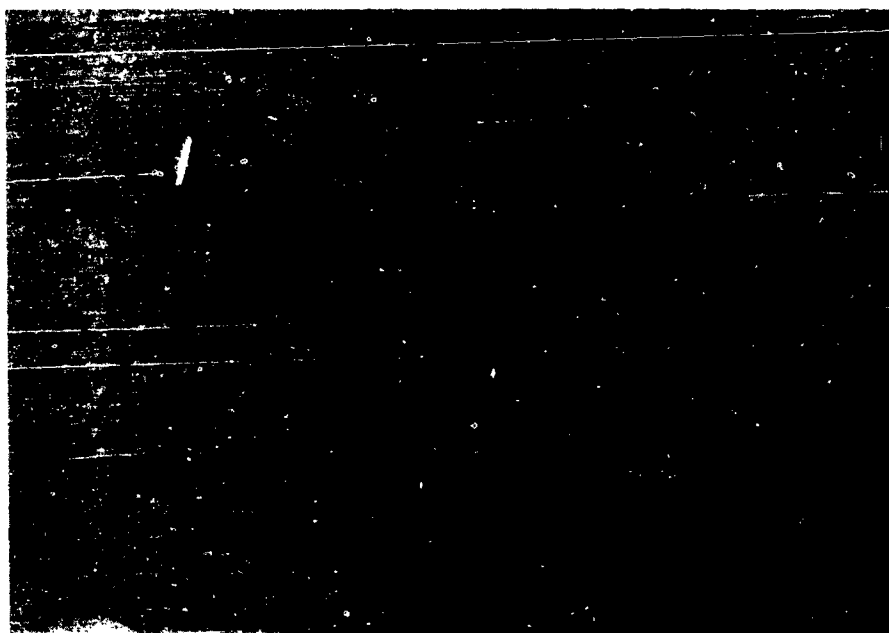
This possible importance of dislocation movement in the propagation of the blunter cracks clearly suggests the need for micrographic evidence of the events surrounding crack propagation. Preliminary work of this nature has been carried out. The normal plates used for the ultrasonically drilled cracks proved too fine grained for satisfactory microscopical examination. However, two large grained MgO plates have now been examined. These show a 3.5 fold change in fracture stress between room temperature and -196°C .

An electron micrograph of the fracture surfaces, prepared with an etchant of 50:50 concentrated HNO_3 and saturated NH_4Cl at 70°C , is shown in Fig 6-7. So far, only the general etching features of the fracture surfaces have been examined. Prominent features are the hillocks that appear to be associated with precipitate particles. Similar observations have been made by Ghosh and Clark⁽⁶⁻¹⁰⁾ and in thin films by Bowen⁽⁶⁻¹¹⁾. Sub-grain boundaries and dislocation arrays are also observed. Of more immediate interest is, of course, the structure in the immediate locality of the drilled crack tip. However, even at these grain sizes, it has so far proved difficult to get satisfactory replicas specifically of these areas. Work aimed at the resolution of these questions is currently in progress.



x 16,000

(a) Etch hillocks associated with precipitate particles



x 8,000

(b) Dislocation arrays

Fig. 6-7

ELECTRON MICROGRAPHS OF POLYCRYSTALLINE MAGNESIUM OXIDE
FRACTURE SURFACES ILLUSTRATING NORMAL ETCHING FEATURES

Etchant = 50% Sat. NH_4Cl , 50% conc HNO_3

3. LOWERING OF SURFACE ENERGY

The final report of the previous of this program⁽⁶⁻¹⁾ presented results obtained for the lowering of surface energy on a sample of fused bauxilite by adsorption of CO_2 , but this powder had a rather low specific surface area; hence the adsorption determinations were rather inaccurate and not well reproducible.

An Al_2O_3 powder of much higher specific surface area has since been obtained and used in adsorption determinations. X-ray examination has revealed that this ultra-microid polishing Al_2O_3 has a γ crystal structure, the α - Al_2O_3 as opposed to structure of the bauxilite used previously. This material also contained some impurities, and was characterized by a hexagonal crystal structure of unit cell dimensions $a = 4.756 \text{ \AA}$ and $c = 12.960 \text{ \AA}$. Despite this difference, however, it was decided to examine adsorption isotherms for this material and if possible obtain a more accurate value for the lowering of surface energy

A. Experimental Techniques

Adsorption of Carbon dioxide and Hydrogen

For determinations of the adsorption of CO_2 and H_2 on the ultra-microid Al_2O_3 , the volumetric apparatus previously employed on the bauxilite material was used. The extremely flocculent nature of the powder, however, resulted in pronounced difficulty in outgassing, because of the eruption of the powder and its rapid transfer from the adsorption chamber into the capillary tubes and manometer. This difficulty was overcome by employing an adsorption cell subdivided by means of five thin glass platforms on which the powder could be distributed in reasonably thin layers (Fig 6-8). As a result, vacuum outgassing at 300°C could be carried out without difficulty. After an outgassing period of 12 hr adsorption measurements were carried out by adding small



Fig. 6-8
PARTITIONED ADSORPTION CELL

measured volumes of CO_2 (or H_2) from the gas burette and determining the pressure in the adsorption system when equilibrium had been attained.

The specific surface area of the powder was first determined by adsorption of CO_2 with the reaction tube immersed in a cardice-acetone mixture (-78°C). A BET plot of the results gave a value of 46.5 sq meters per gram for the specific surface area.

Adsorption of CO_2 and H_2 at ambient temperature were then measured in a similar manner.

Adsorption of Water Vapor.

Because of the low saturation vapor pressure of water at ambient and lower temperatures, the measurement of adsorption isotherms for water vapour presents difficulties. The volumetric method was abandoned in favor of the less sensitive but more practicable gravimetric method. In adopting this change it was considered that the sensitivity of the gravimetric method would be sufficient if adequate adsorption occurred to give an appreciable reduction in surface energy.

A helical silica spring balance having a sensitivity of about 20 cm per gram was used to detect the change in weight on adsorption. The powder sample (weighing 0.6-0.8 gram) was held in an aluminum foil bucket suspended from the spring by a glass fiber. Movement of the lower end of the spring under load was measured by a cathetometer reading to 0.05 mm.

The problem of equilibrium pressure measurement was overcome by utilizing the variation in saturation vapor pressure of water at various temperatures. A steel tube containing ice was placed in the lower end of the glass tube enclosing the silica spring and was immersed in a cardice-acetone bath until the powder sample had been outgassed at about 300°C . The pressure of water vapor over ice at -78°C is 0.00056 torr. After the sample had been outgassed for 2 or 3 hr, the water vapor pressure in the system was

increased by simply replacing the cardice-acetone bath by one containing CCl_4 and cardice. By using a selection of constant temperature baths up to ambient temperature the vapor pressure could be varied and the increase in weight of the powder sample determined when equilibrium was reached at each pressure. A description curve could be obtained by reversing the procedure. The use of a steel container for the ice in the system obviated the cracking of the glass tube which otherwise occurred on re-freezing after heating almost to ambient temperature.

To assess whether any irreversible chemical reaction with the powder occurred, an adsorption isotherm was determined in one case increasing the vapor pressure to 3.88 torr, followed by a reducing to 0.00056 torr, and then a repeated increase. Results in the second run were identical with the first, within the range of experimental error, so that the occurrence of any such chemical reaction can be ignored, at least within 3 hr duration of the present experiments at ambient temperature.

B. Discussion of Results

Adsorption of carbon dioxide

The results obtained for the adsorption of CO_2 on ultra-microid Al_2O_3 at -78°C and 19°C are shown in Fig 6-9. Since the curve for -78°C did not show a distinct plateau corresponding to monolayer formation as was previously obtained for the bausilite sample, a BET plot was employed for calculation of specific surface area. Even with the increased specific surface area compared with the bauxilite powder, the adsorption only amounted to 4.3 cu cm (at NTP) per gram at 700 torr pressure.

Various methods of plotting the adsorption results were examined to obtain a suitable isotherm for integration to give the surface energy lowering. With these more accurate results the Langmuir plot no longer gave a linear variation of p/v with p , where V is the volume of gas (at NTP) adsorbed at an equilibrium

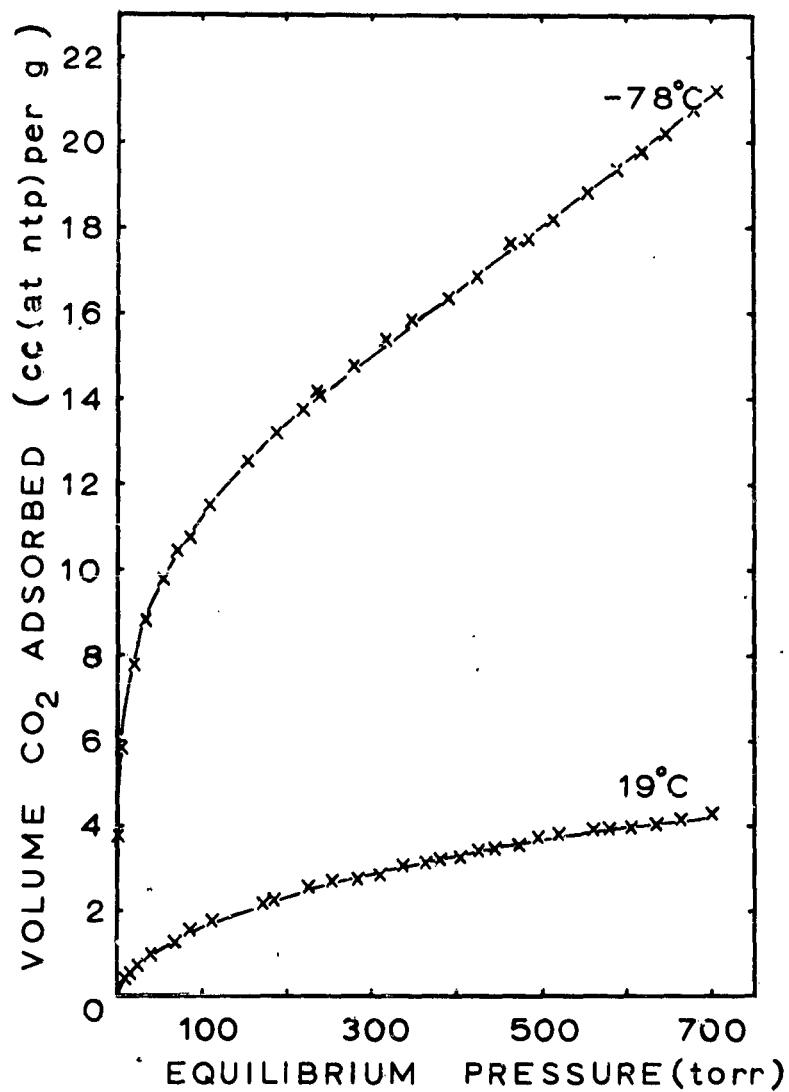


Fig. 6-9 ADSORPTION CURVES FOR CARBON DIOXIDE ON
ULTRA-MICROD ALUMINUM OXIDE AT -78 AND 19°C

pressure p . Plotting of results as $\log p$ vs $\log V$, as presented in Fig. 6-10, however, showed close adherence to a Freundlich isotherm with the adsorption at 19°C obeying the equation

$$V = 0.145 p^{0.52} \quad (6-2)$$

when the volume adsorbed is in cubic centimeters at NTP and p is in torr. If G is the number of gram molecules of gas adsorbed per unit area, then

$$G = 0.139 \times 10^{-10} p^{0.52} = cp^n \quad (6-3)$$

where c and n are constants for a particular temperature. If adsorption takes place at temperature T ($^\circ\text{K}$) from a gas at pressure p , the change in surface energy produced is given by

$$d\gamma = -GRTd\log p \quad (6-4)$$

and, therefore,

$$\begin{aligned} \gamma_o - \gamma &= RT \int G d\log p \\ &= RT \int cp^n d\log p \\ &= RT \cdot \frac{c}{n} \cdot p^n = 0.267 \times 10^{-10} RT p^{0.52} \end{aligned} \quad (6-5)$$

The lowering in surface energy associated with adsorption of CO_2 at a partial pressure of 10 torr is thus 2.15 ergs per sq cm and the variation in lowering of surface energy with pressure is represented in Fig. 6-11. The value at 10 torr is in reasonable agreement with that of 0.80-1.13 erg cm per sq cm obtained for a fused bauxilite sample at this partial pressure⁽⁶⁻²⁾.

Adsorption of Hydrogen

The amount of H_2 adsorbed on the ultra-microid Al_2O_3 at ambient temperature was even considerably less than that of CO_2 . At a pressure of 670 torr only about 0.20 cu cm H_2 (at NTP) were adsorbed per gram of powder. No appreciable lowering of surface energy could be ascribed to this condition.

pressure p . Plotting of results as $\log p$ vs $\log V$, as presented in Fig. 6-10, however, showed close adherence to a Freundlich isotherm with the adsorption at 19°C obeying the equation

$$V = 0.145 p^{0.52} \quad (6-2)$$

when the volume adsorbed is in cubic centimeters at NTP and p is in torr. If G is the number of gram molecules of gas adsorbed per unit area, then

$$G = 0.139 \times 10^{-10} p^{0.52} = cp^n \quad (6-3)$$

where c and n are constants for a particular temperature. If adsorption takes place at temperature T ($^\circ\text{K}$) from a gas at pressure p , the change in surface energy produced is given by

$$d\gamma = -GRTd\log p \quad (6-4)$$

and, therefore,

$$\begin{aligned} \gamma_0 - \gamma &= RT \int G d\log p \\ &= RT \int cp^n d\log p \\ &= RT \cdot \frac{c}{n} \cdot p^n = 0.267 \times 10^{-10} RT p^{0.52} \end{aligned} \quad (6-5)$$

The lowering in surface energy associated with adsorption of CO_2 at a partial pressure of 10 torr is thus 2.15 ergs per sq cm and the variation in lowering of surface energy with pressure is represented in Fig. 6-11. The value at 10 torr is in reasonable agreement with that of 0.80-1.13 erg cm per sq cm obtained for a fused bauxilite sample at this partial pressure⁽⁶⁻²⁾.

Adsorption of Hydrogen

The amount of H_2 adsorbed on the ultra-microid Al_2O_3 at ambient temperature was even considerably less than that of CO_2 . At a pressure of 670 torr only about 0.20 cu cm H_2 (at NTP) were adsorbed per gram of powder. No appreciable lowering of surface energy could be ascribed to this condition.

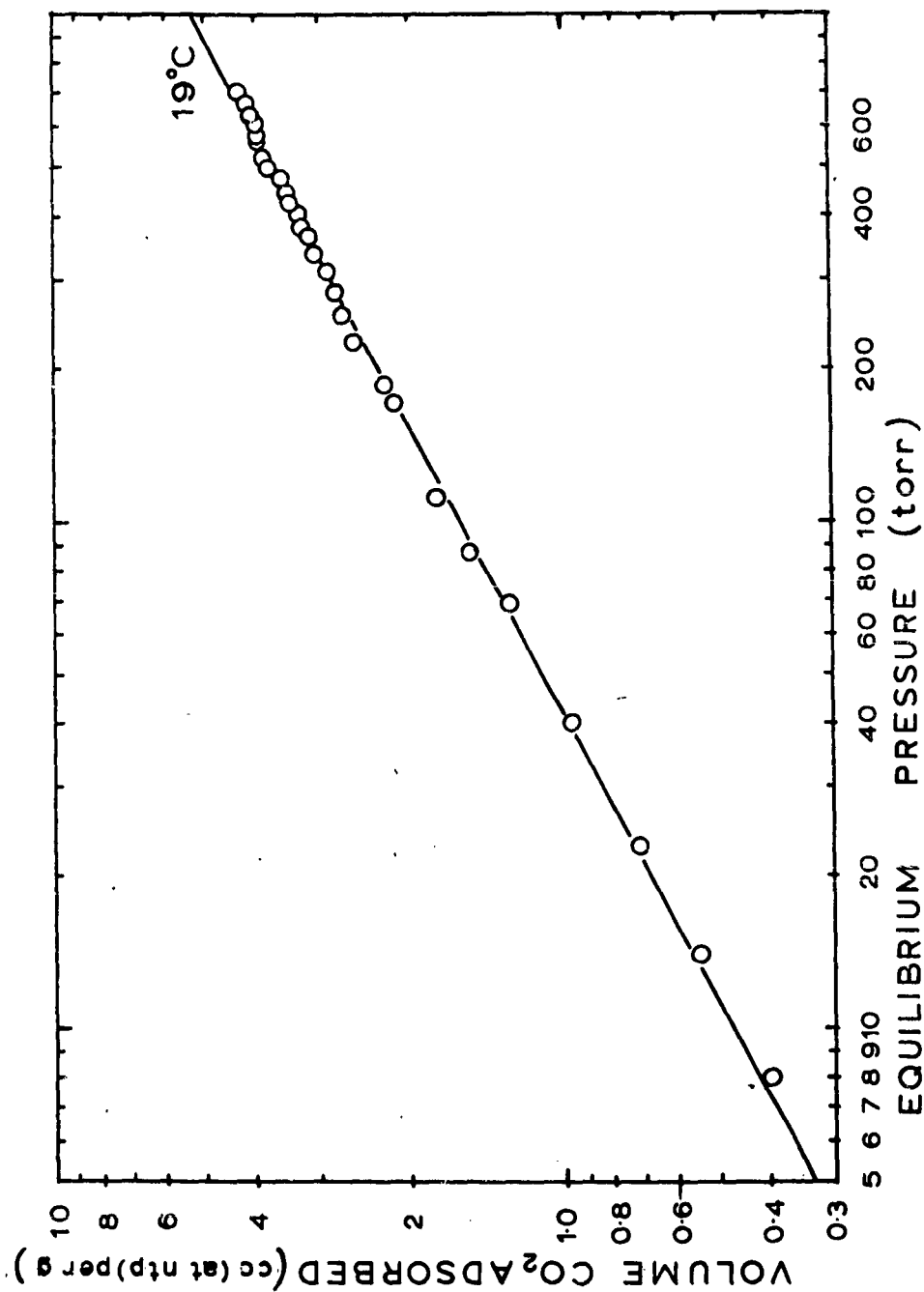


Fig. 6-10 FREUNDLICH PLOT FOR ADSORPTION OF CARBON DIOXIDE ON ULTRA-MICROID ALUMINUM OXIDE AT 19°C

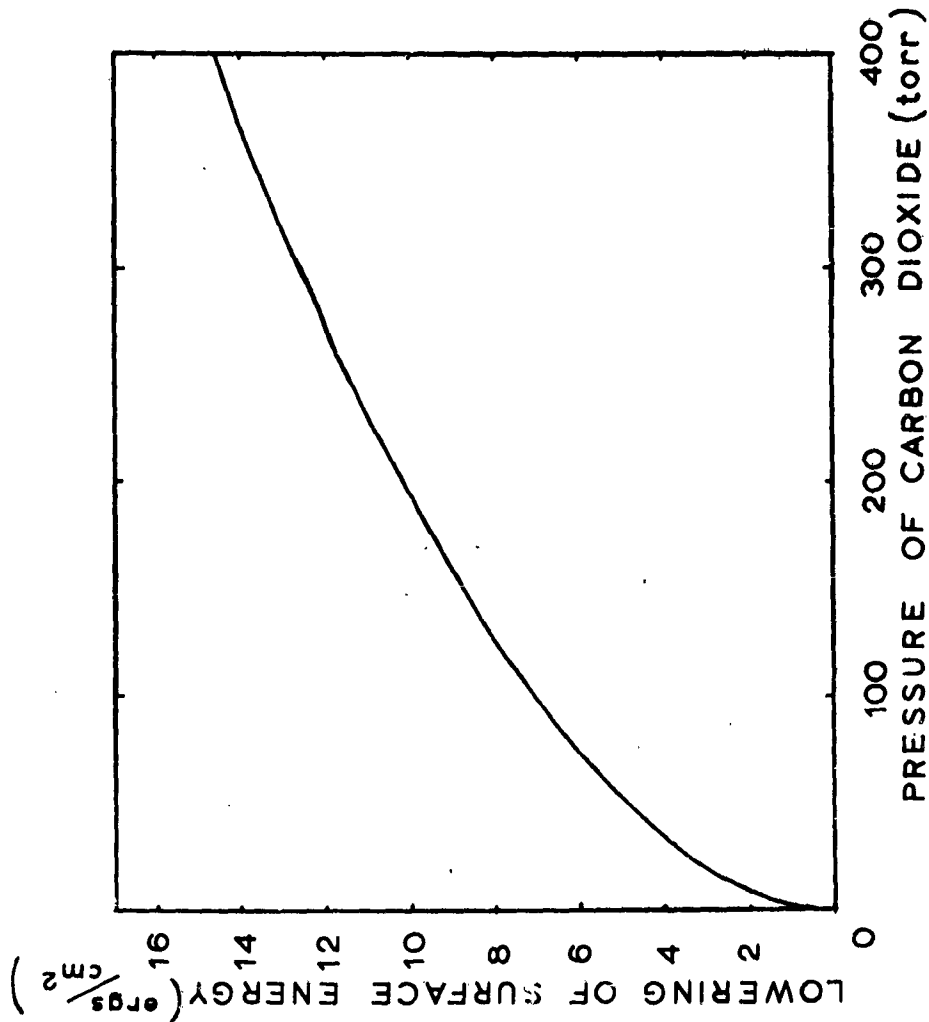


Fig. 6-11 LOWERING OF SURFACE ENERGY OF ALUMINUM OXIDE AS A RESULT OF ADSORPTION OF CARBON DIOXIDE AT DIFFERENT PARTIAL PRESSURES

Adsorption of Water Vapor

The method employed here seriously limits the number of experimental points on any adsorption curve which can be obtained. However adsorption results are reasonably reproducible at least up to pressures approaching saturation, as can be seen from Fig. 6-12.

As well as can be ascertained from results at such a limited number of pressures the adsorption obeys a Langmuir plot up to 0.6 of saturation pressure. Results for adsorption at 14°C and 19°C are in good agreement up to this point and a common line has been drawn through the combined results by the least squares method (Fig. 6-13). The slope of this line and its intercept on the pressure/adsorption per unit area axis are respectively $\frac{1}{G_s}$ and $\frac{1}{AG_s}$; where G_s and A are the constants in the Langmuir expression relating the number of moles per unit area adsorbed at a pressure, p ,

$$G = G_s \frac{A p}{1 + A p} \quad (6-6)$$

For adsorption from a gas at pressure, p , and temperature, T ,

$$d\gamma = -GRT d \log p \quad (6-4 \text{ bis})$$

and substitution for G from (6-6) and integration gives

$$\gamma = \gamma_0 - G_s \log (1 + A p)$$

The reduction in surface energy resulting from adsorption of water vapor at 5 torr calculated from this is 134 ergs per sq cm.

Taking the lowering of surface energy by adsorption of water vapor at 5 torr as 140 ergs per sq cm and the true surface energy of Al_2O_3 as ~ 2000 ergs per sq cm, the ratio of lowered to original surface energy is 0.93.

The lowering of surface energy produced by adsorption of CO_2 or H_2 on Al_2O_3 is negligible and would have no detectable

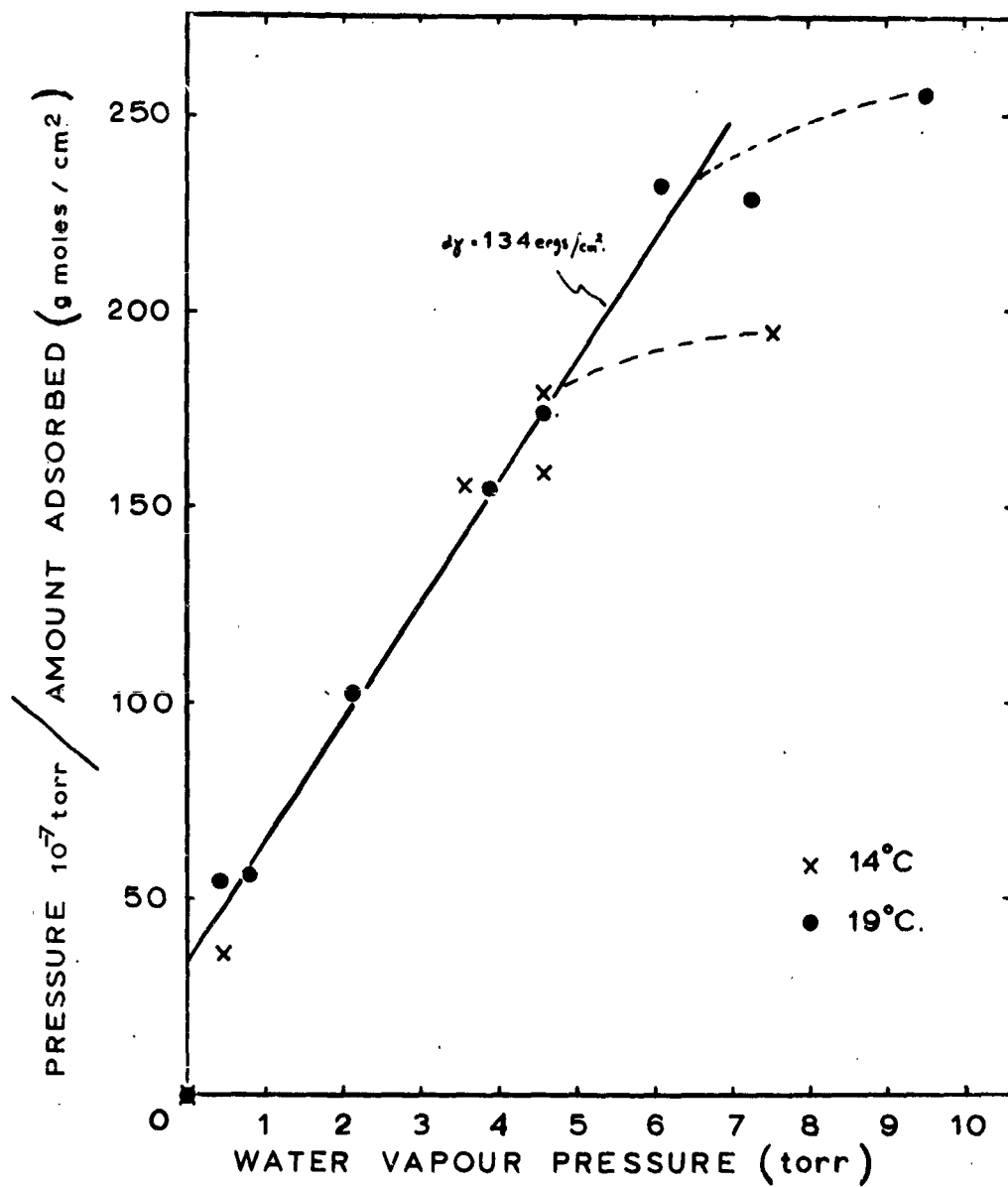


Fig. 6-12 ADSORPTION CURVE FOR WATER ON ULTRA-MICROID ALUMINUM OXIDE AT AMBIENT TEMPERATURE

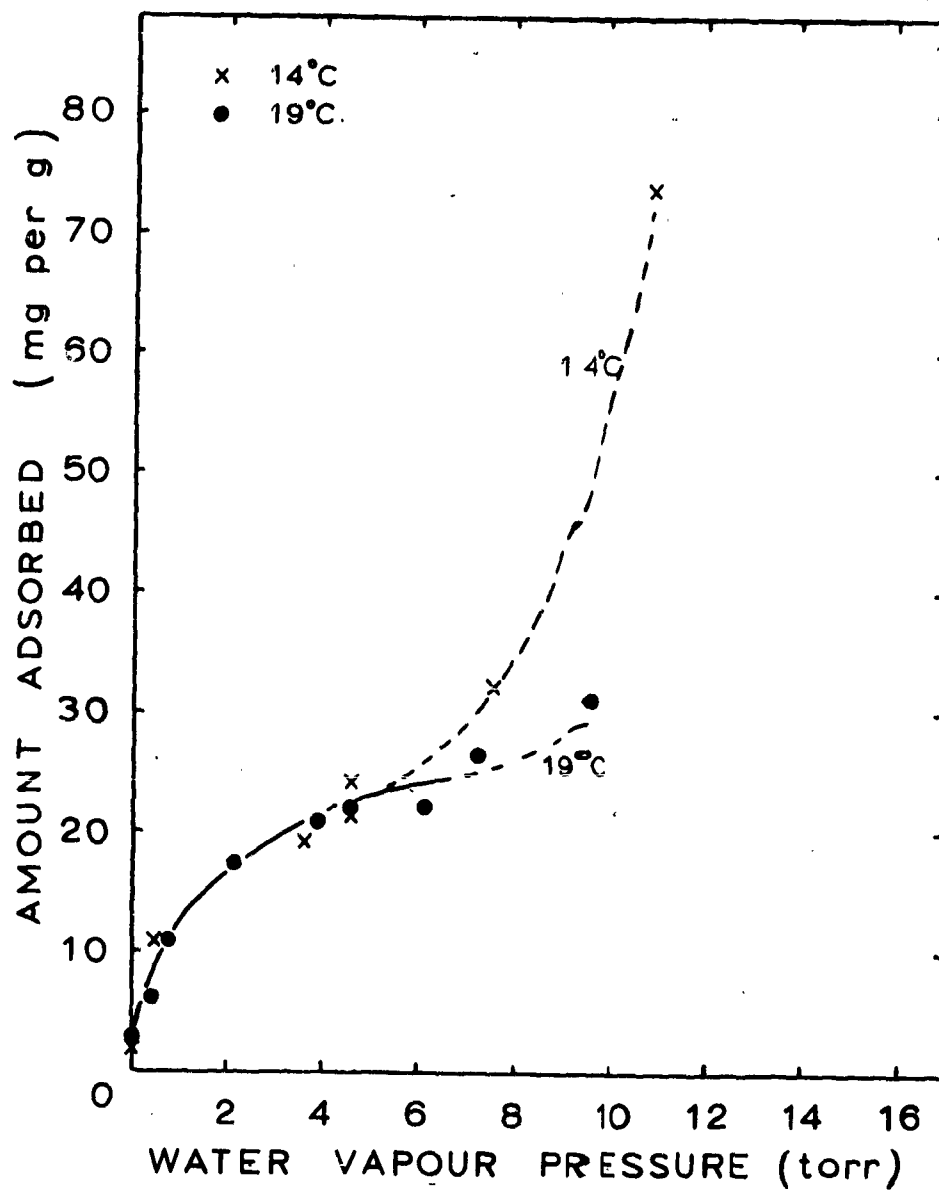


Fig. 6-13 LANGMUIR ISOTHERM FOR ADSORPTION OF WATER ON ULTRA-MICROID ALUMINUM OXIDE AT AMBIENT TEMPERATURE

effect on the fracture stress. This suggests that delayed fracture effects are induced by the presence of moisture alone in the environment. The delayed fracture effects observed by Charles⁽⁶⁻¹⁾ in a dry hydrogen atmosphere could then only be attributed to residual moisture.

If the Orowan criterion⁽⁶⁻¹³⁾ for brittle fracture:

$$\sigma_f = \left(\frac{E\gamma}{2c} \right)^{\frac{1}{2}}$$

is considered to apply to the fracture of Al_2O_3 , then σ_f is proportional to γ , so that

$$\frac{\sigma_1}{\sigma_0} = \sqrt{\frac{\gamma_1}{\gamma_0}}$$

where γ_0 and γ_1 are the original and lowered surface energies and σ_0 and σ_1 are the original and lowered fracture stresses. From the measurements of adsorption of water vapor $\frac{\gamma_1}{\gamma_0}$ (at 5-torr pressure) is 0.93, therefore $\frac{\sigma_1}{\sigma_0} = 0.96$. Thus, the lowering of fracture stress attributable to the lowering of surface energy by the adsorption of water vapor is only about 4 percent, whereas the lowering in fracture stress in moist air, as compared with vacuum, observed by Charles⁽⁶⁻¹⁾ was about 30 percent.

Some further factor must therefore be involved; the obvious suggestion is chemical reaction. However, the reversibility of the adsorption after a period of 3 hr rules out any reasonably rapid reaction and Pearson⁽⁶⁻¹⁴⁾ did observe delayed fracture after shorter periods at certain stresses, although period of several days were required at lower stresses. It will, nevertheless, be necessary to carry out a similar determination leaving the water vapor in contact with the alumina powder for a similar period to that involved in Charles' fracture stress determinations.

4. SURFACE ENERGY OF ALUMINUM OXIDE FROM THE STRESS REQUIRED TO PREVENT SURFACE CONTRACTION

The surface energy of Al_2O_3 at 1900°C has been estimated from measurements of the change in length of thin rod specimens after various times at various stresses, the latter being chosen so that both contraction and extension were observed. By plotting the strain rate against stress, the stress corresponding to equilibrium (zero rate) has been interpolated. The load which just balances deformation arising from the stress which is due to surface energy can then be used for determining the surface energy, since

$$w = \pi r \gamma_s - n \pi r^2 \gamma_b$$

where w is the balancing load, r the radius of the rod, γ_s the surface energy, n the number of grains per unit length of rod and γ_b the grain boundary tension.

An evacuated graphite resistor furnace has been used for heating the specimens, which were suspended from the lid of an Al_2O_3 crucible located in the bore of the resistor element, as was described in more detail in the final report of the previous phase⁽⁶⁻¹⁾. Strain measurements were made between gauge marks 2 cm apart with the aid of a measuring microscope having 0.001 cm. graduations. The stress on the specimen arises from the weight of material below the mid-point of the gauge length and it may be varied by using different lengths of rod below the lower gauge mark.

The only modification made in the apparatus since the previous description has been the incorporation of an iridium-40 percent iridium/rhodium thermocouple for temperature measurement, replacing the optically temperature recorder used previously. The thermocouple is introduced through a vacuum seal in the base of the furnace and extends up the bore of the resistor being sleeved with a thoria sheath and an outer molybdenum tube. Through a hole

drilled in its bottom, the hot junction protrudes into the Al_2O_3 crucible.

A. Results

The strain curves so far available are shown in Fig. 6-14 and the plot of strain rate against stress in Fig. 6-15. In calculating the surface energy, it is necessary to know not only the stress for zero creep, but also the number of grains per unit length of rod and the grain boundary tension. The grain size of the rods has not yet been accurately determined since the rods are required for further measurements, nor has the grain boundary energy been measured. However, visual inspection suggests that the grain size is about the same as the rod diameter and for the grain boundary energy we can assume, as has frequently been found to be the case, that

$$\gamma_b/\gamma_s \approx 0.4$$

The interpolation of the stress for zero creep from Fig. 6-15 cannot be made with high accuracy because of the paucity and scatter of available data. However, the minimum value of this stress is 15×10^4 dynes per sq cm and the maximum value 24.5×10^4 dynes per sq cm. These correspond to surface energies of 690 and 1090 ergs per sq cm respectively, with a mean of 890 ergs per sq cm.

B. Discussion

The mean result of 890 ergs per sq cm at 1900°C compares favorably with that of 900 ergs per sq cm at 1850°C quoted by Norton and Kingrey⁽⁶⁻¹⁵⁾, although this correspondence may well prove to be fortuitous in the light of the further measurements contemplated.

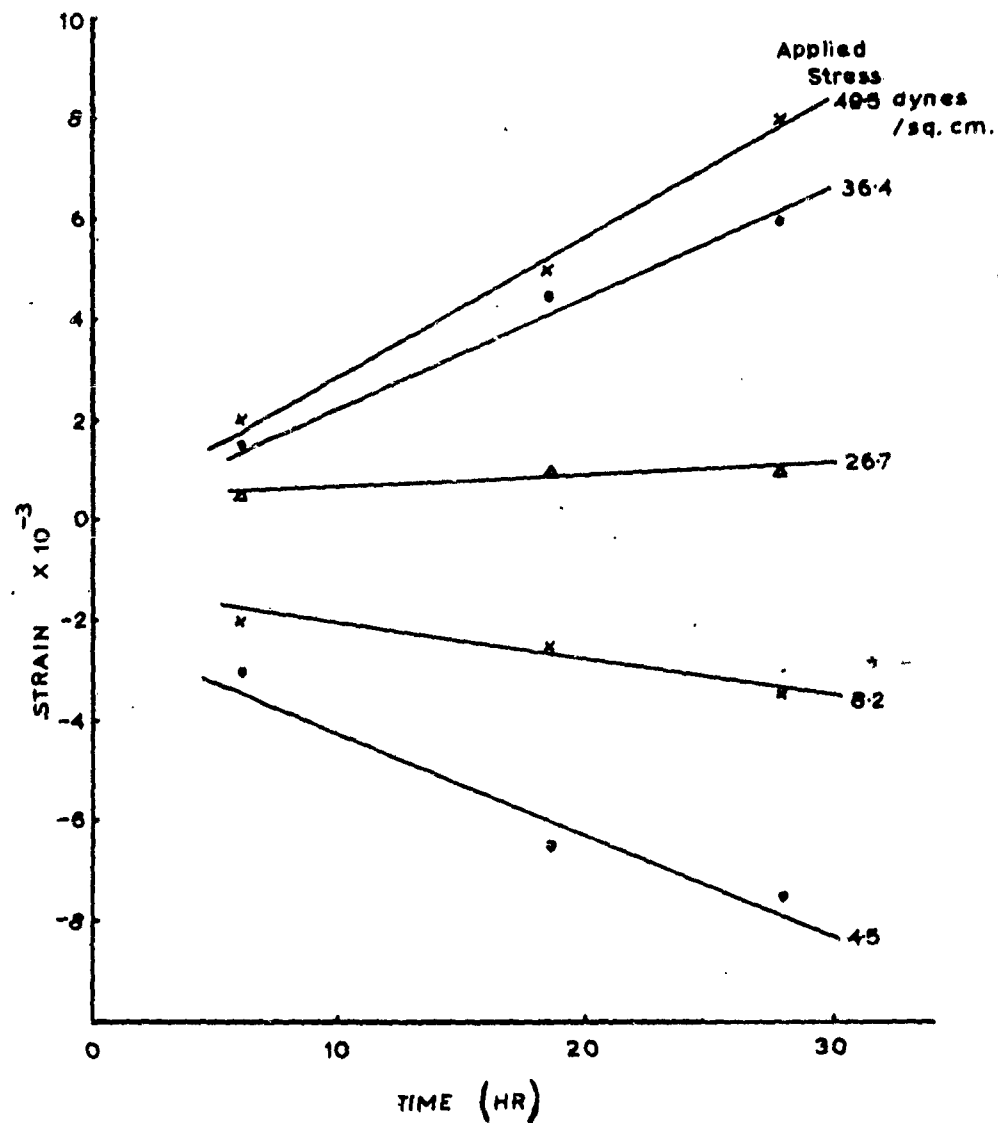


Fig. 6-14 CONSTANT STRESS CREEP CURVES FOR ALUMINUM OXIDE AT 1900°C

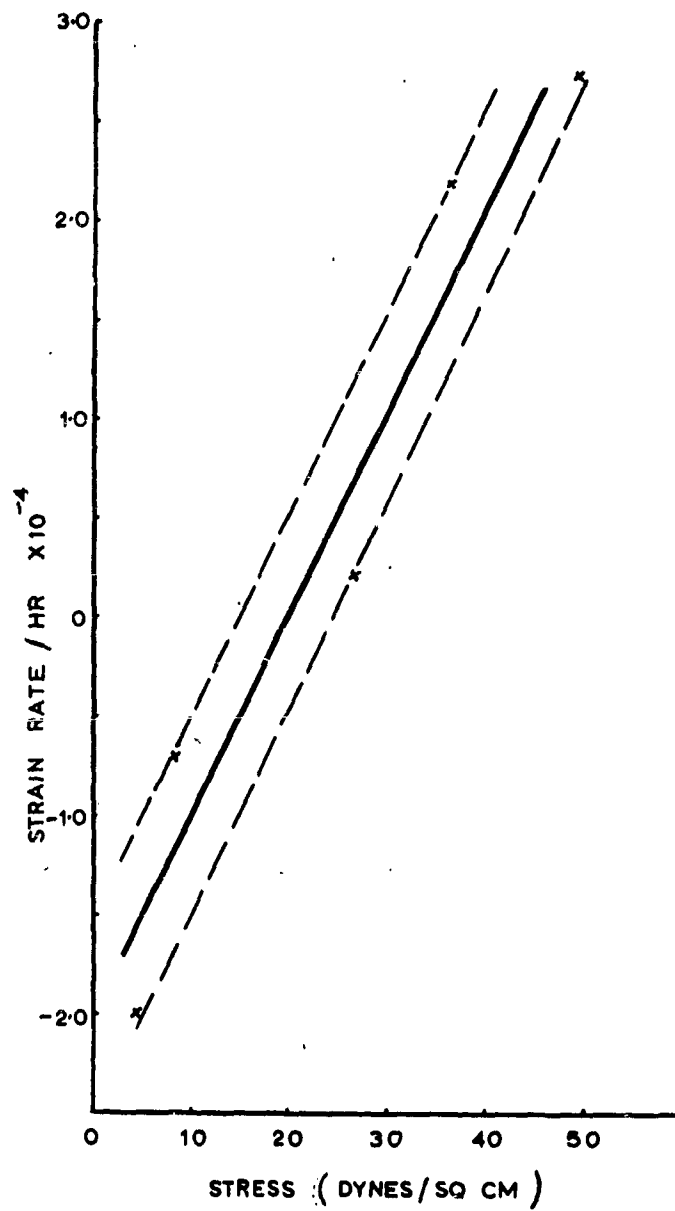


Fig. 6-15 CREEP RATE AS FUNCTION OF STRESS FOR ALUMINUM OXIDE AT 1900°C

There are a number of possible sources of error in this work, apart from those already mentioned or those inherent in measuring small strains at 1900°C. The two most important sources of such errors are concerned with the purity of the Al_2O_3 used and with the time at temperature. The purity of the Al_2O_3 (quoted as 99.5%) is doubtful because of the observations that, although white when received, the specimens became grey after heating; furthermore, the degree of vacuum in the furnace chamber is impaired by the presence of Al_2O_3 . The time involved in heating specimens to temperature is important at the present stage simply because it is, cumulatively, of the same order as the time that specimens have been held at temperature and the times shown in Fig. 6-15 refer only to time at temperature. Because of outgassing problems and the cracking of crucibles by thermal stress it is necessary to employ times of 2-3 hr in heating specimens to the operating temperature. This problem will be avoided in future runs by employing longer holding times and so reducing the heating time to insignificance.

It is apparent that, the technique having been finally established, measurements should now be made in which the stress range is extended so that the interpolation of the stress for zero strain rate can be made with greater confidence. The temperature sensitivity of the surface energy should be studied; this will also serve as an additional check on overall accuracy. These measurements should be made on samples of Al_2O_3 of controlled purity, and indeed arrangements have been made for the supply of such material by Professor B. Cutler, University of Utah.

5. REFERENCES

- 6-1 Weil, N. A., Ed., "Studies of the Brittle Behavior of Ceramic Materials", ASD-TR-61-628, April 1962.
- 6-2 Yoffe, E. H., Phil. Mag., 42, 739 (1951).
- 6-3 Craggs, J. W., J. Mec. Phys. Solids, 8, 66 (1960)
- 6-4 Berry, J. P., J. Mec. Phys. Solids, 8, 194 (1960)
- 6-5 Roberts, D. K. and Wells, A. A., Engineering, 820 (1954)
- 6-6 Wynne, D. H. and Wundt, B. M., Amer. Soc. Mech. Eng., 80, 1643 (1958).
- 6-7 Gilman, J. J. et al, J. App. Phys., 29, 601 (1958).
- 6-8 Tetleman, Seattle Conf. on Fracture, Aug. 1962.
- 6-9 Clarke, F.J.P., Special Ceramics, Heywood and Co. London, (1961).
- 6-10 Ghosh, T. K. and Clarke, F.J.P., Brit. J. App. Phys., 12, 44 (1961).
- 6-11 Bowen, Brit. Ceram. Soc. Conf. on Mech. Properties of Non-Metallics, October 1962.
- 6-12 Gilman, J. J. and Guernsey, R., J. Exp. Stress. Anal., 18, 50 (1961).
- 6-13 Orowan, E., Welding Journal Res. Suppl. 34, 157s (1955).
- 6-14 Pearson, S., Proc. Phys. Soc., London, 69B, 1293 (1956).
- 6-15 Norton, W. and Kingery, W., J. Am. Ceram. Soc. 42 (1959).

TASK 7 - FRACTURE MECHANISMS

Principal Investigator: E. Orowan
Massachusetts Institute of Technology

ABSTRACT

The purpose of the present work is to study the processes which lead to fracture in high temperature refractory oxides, particularly Al_2O_3 and MgO . The work progressed along two distinct lines: studies of multicrystalline bodies of Al_2O_3 and MgO at various temperatures, and microscopic and x-ray studies of fracture mechanisms in MgO single crystals.

Studies on polycrystalline MgO bodies in torsion at room temperature yielded stresses 20 percent lower than those obtained at ARF previously in bending. This anomaly was traced to the existence of impurities and pores in this material, whose stress concentrating effect in torsion far more pronounced than in bending or tension. At temperatures running to 1500°C , the MgO specimens showed considerable weakening, the mode of fracture gradually changing from a brittle toward a ductile type; this behavior was principally traced to grain boundary sliding.

Work on MgO crystals clearly established the importance of the high stresses produced by kinking, which are instrumental in crack nucleation under certain circumstances. Crack initiation was also traced to the arrest of dislocation bands by an obstacle band, and to the simultaneous widening of two conjugate dislocation bands where cracks are nucleated by stresses in finite tilt boundaries. It was found that dislocations gliding along a blocked band actually penetrate some distance into the conjugate obstacle band, rather than piling up at its boundary. This explains why the Zener crack forming mechanism seldom governs crack nucleation. The formation of conjugate slip bands can also lead to crack formation by the creation of high tensile stresses in the turn band intersection zone. This mechanism is counteracted by an accommodation mechanism which effectively dissipates the high shear strain concentration of impinging turns.

TASK 7 - FRACTURE MECHANISMS

1. INTRODUCTION

The purpose of the present work is to contribute to the understanding of the processes which lead to the fracture of high temperature refractory materials particularly Al_2O_3 and MgO .

The characteristic difference between metallic and non-metallic materials is the narrow range of transition between almost complete brittleness and ductility in the latter. In the high temperature range, the material may be too soft to be practically useful; this is the case with MgO . In this case, the range of usefulness can be extended upwards by the incorporation of a hard phase. In the low temperature range of nearly complete brittleness, the material can still become useful if its strength (fracture stress) can be sufficiently increased - e. g., by the incorporation of crack arresters; an example for this possibility is Pyroceram. What appears most attractive at first sight is the extension of ductility to lower temperatures, in order to relieve stress concentrations. This is occasionally possible: if the lack of ductility is due to the absence of mobile dislocations, it may be increased by the introduction of such dislocations. The crucial point, however, is whether the introduction of mobile dislocations can increase the ductility without giving rise to crack formation or propagation.

In 1934 it became clear⁽⁷⁻¹⁾ that the observed low strength of NaCl crystals could not be explained if they were assumed as essentially brittle and behaving according to the Griffith theory of crack propagation. It was suggested therefore,

that crack propagation occurred by a mechanism based on plastic deformation, that is, on the movement of dislocations. Since 1949 additional mechanisms have been suggested⁽⁷⁻²⁾ through which cracks might arise as a consequence of plastic deformation. Thus plastic deformation is no longer regarded as an unqualified blessing; it can make stress concentrations harmless, but it may also produce or propagate cracks. It is necessary, therefore, for practical engineering purposes, to understand the mechanism of fracture in order to know whether, for improving the mechanical properties of the material, plastic deformation should be promoted or counteracted.

Table 7-I gives a survey of the main possibilities of increasing the resistance to fracture. In substantially brittle materials, there are only two ways of increasing the strength: (1) cracks can be avoided by careful manufacture and fabrication; or they can be removed, if surface cracks, by dissolution of the surface layer; or they can be neutralized by a tangential compressive stress at the surface; (2) the resistance to crack propagation can be increased by the introduction of obstacles such as grain boundaries, inclusions, or by the use of a composite material.

In more or less ductile materials, fracture can be counteracted either by increasing ductility to the point at which it is sufficient for removing stress concentrations, or by reducing ductility if it is more important to inhibit a plastic crack formation or propagation mechanism. The choice between these opposite measures requires the knowledge of the fracture mechanisms that may act in the material and at the temperature in question.

Naturally, the practical use of a material at high temperatures may be limited by its low yield stress (softness) rather than its low fracture stress (weakness). In this case as

Table 7-1
POSSIBLE METHODS FOR IMPROVING THE STRENGTH OF REFRACTORY MATERIALS

Principle	Method	Remarks
(1) Prevention of cracks	Careful fabrication Removal of surface cracks by dissolution Residual skin compression	Acid polishing of glass; effective only if surface cracks alone are important, and if subsequent damage can be prevented. Tempering of glass; nitriding or shot-peening of steel to improve fatigue strength. Effective only if surface cracks alone are important. Important, practical measures
(2) Increasing the resistance to crack propagation	Finer grain Dispersed polyphase material Composite material	Feasible only with a few materials, mostly single crystals
(3) Leveling down of stress concentrations by plastic deformation; beneficial only if plastic deformation does not produce cracking	Introduction of dislocations by localized pressure Introduction of dislocations by deformation at elevated temperature	Probably a factor in the "breaking down" of ingots by rolling
(4) Prevention of crack origination or propagation by counteracting plastic deformation. Beneficial only if reduction of ductility does not cause embrittlement.	Increasing the yield stress by alloying additions, hard inclusions, etc.	Possible in specific cases

mentioned, the yield stress has to be increased by alloying or by the incorporation of hard particles by precipitation or by mechanical mixing.

The work described here progressed along two lines. The first line of attack was a study of the strength of polycrystalline MgO and Al_2O_3 specimens as a function of temperature, up to the highest temperatures of practical interest. The main part of this work was the design and construction of an elevated temperature testing machine capable of loads up to 5,000 lb. So far, the heating element used is made of tantalum, and the highest temperature at which experiments were carried out was $1,500^\circ\text{C}$; the use of tungsten elements may permit an extension of the temperature range to the neighborhood of $2,200^\circ\text{C}$.

The second part of the study was a microscopic and x-ray study of the mechanism of fracture, mainly in single crystal MgO, but also including alkali halide crystals. The crystals were compressed, extended or bent in devices that could be placed on the microscope stage, so that the development of photoelastic patterns and slip lines during deformation could be observed; after deformation, or between two stages of deformation, the crystal could be etched to reveal dislocations or studied by imaging x-ray photography.

2. WORK WITH POLYCRYSTALLINE SPECIMENS

A. Design of the High Temperature Testing Machine

The machine was originally designed for use in tension and compression, with the possibility of carrying out bending tests by means of an auxiliary attachment to the grips. The tensile specimens were to be dogbones used for bending tests at the

Armour Research Foundation. However, most of the specimens were more or less warped, requiring a change-over to torsion tests, and a corresponding modification of the testing machine. The original tension-compression machine will be described first followed by a presentation of the machine as modified for torsion tests.

In the tension-compression machine, the specimen was strained by a mechanical gear and the load measured by electric resistance gage load cells. Heating of the specimen is accomplished by an electric resistance furnace with a vertical tubular heating element split vertically in two halves from the top nearly to the bottom. This makes it possible to observe the specimen during the test; it also doubles the length of the current path and reduces by half the cross section, so that the heating current is halved for the same heater power. The heating element is made of tantalum sheet; if higher temperatures, up to nearly 4,000°F, are required, a heating element of tungsten can be used. The heating element is surrounded by three sets of molybdenum radiation shields (concentric cylinders around the tube, circular plates above and below). Heating element, radiation shields, specimen, and grips are in an evacuated steel vessel with chromium plated and buffed interior walls. Both the walls of the steel vessel and the pulling rod are water cooled. The power supply is a saturated core transformer of 25-kva capacity.

Figure 7-1 shows a vertical and a horizontal section of the machine, and a vertical view. The machine is built up on a frame consisting of a base (7), two vertical steel columns of 2-in. diam, and a head-piece (5), giving a total height of approximately 6 ft. Two steel columns (4) are suspended from the head-piece; their lower ends carry a heavy steel disc (3)

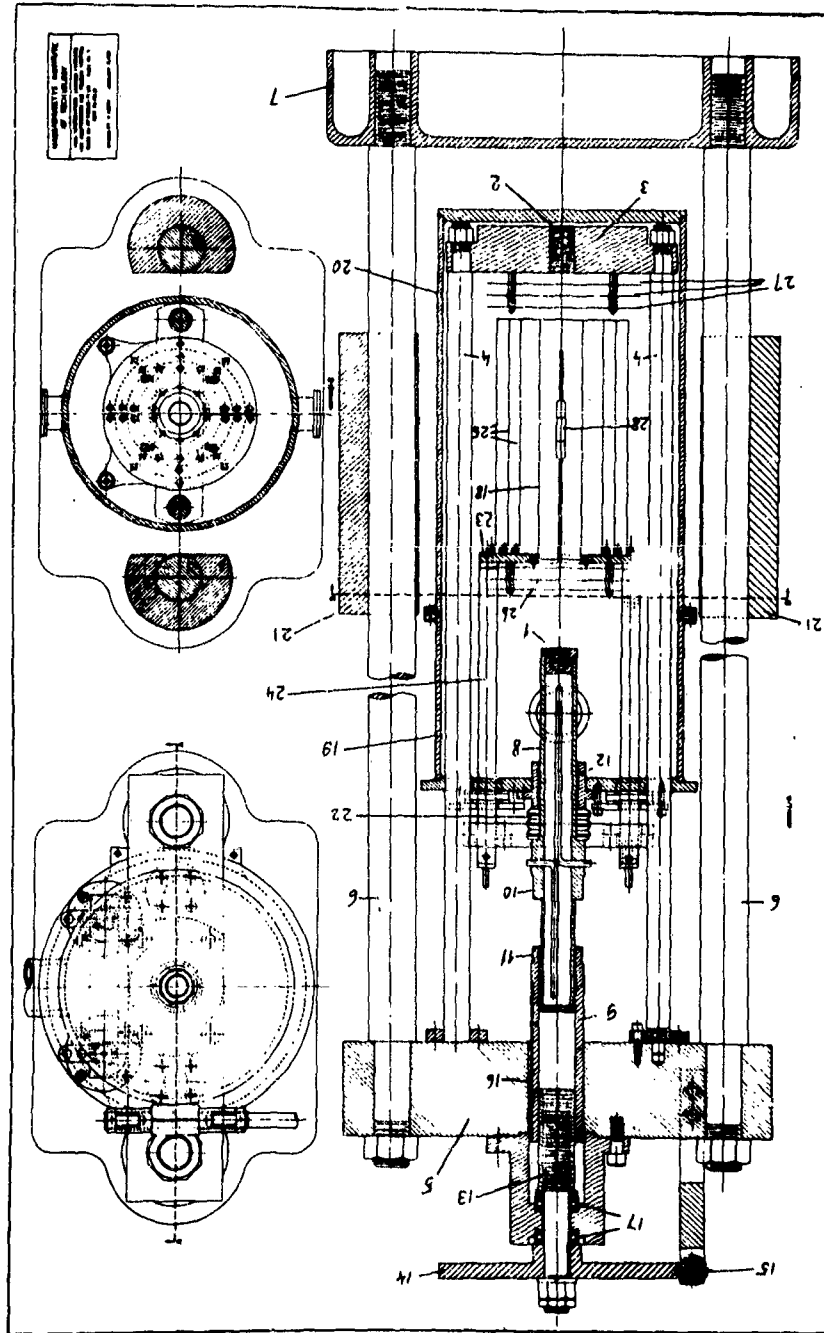


Fig. 7-1 HIGH-TEMPERATURE VACUUM FURNACE FOR USE WITH 5000LB TESTING MACHINE

with a central threaded hole (2) into which the lower (fixed) specimen grip is screwed. The upper grip is screwed into a threaded plug (1) closing the lower end of the lower part of the pulling (or compressing) rod (8). This hollow rod is water-cooled in a way seen in the drawing. It slides in the thick-walled tube (9) which is the upper part of the pulling rod and has an internal thread engaging the threaded rod (13). The tube is prevented from rotating by the key (16), so that it is lifted or lowered when the threaded rod is rotated by the pinion wheel (14) and the pinion (15). The pinion is supported on a swiveling block so that it can be disengaged if the pulling rod is to be moved rapidly.

The two parts (8) and (9) of the pulling rod are connected by a thin-walled tube or thin strips, the ends of which are screwed to (8) and (9) at the points (10) and (11); the connecting tube or strips (not shown in the drawing) carry the resistance gages and act as a dynamometer. Thin (and, if required, bent) strips are used for very low loads; thick strips or a relatively thick-walled tube for high load ranges. As is indicated in the drawing, the lower part of the rod is guided in the upper part by three vertical rows of steel balls in a single cage; similarly, the lower part of the rod is guided in the bush (12) of the vacuum vessel by three rows of steel balls. In this way, the friction is reduced to a value between $1/2$ oz. and 1 oz., and the rod is guided with no perceptible play. Consequently, it can be used for compressing specimens as well as for pulling them, without much danger of buckling at the sliding joint of the two parts (8) and (9).

A "Bellofram" rolling rubber diaphragm was used to establish a vacuum seal between the pull rod and the tank.

In Fig. 7-1, it can be seen that the vacuum vessel consists of a short upper and a long lower part bolted together by flanges with a sealing rubber O-ring between the flanges. To obtain access to the specimen and the heating element, the lower part can be lowered as shown in Fig. 7-2. It is balanced by a weight sliding on one of the main columns (in Fig. 7-1, two counterweights, each on one of the columns, were planned); the vessel can be lowered by unbolting the connection and turning the hand-wheel seen in Fig. 7-2.

The heating element (18) of tantalum sheet is 60 mils thick, and the upper horizontal and the cylindrical radiation shields (26) and (25) are supported by two heavy molybdenum plates (23) carried by water-cooled copper rods (24), which are introduced through the top of the vacuum vessel electrically insulated and vacuum-sealed. Above the vessel the two busbars (24) are bracketed together by an insulating bar. The vertical section and the vertical view in Fig. 7-1 show the position of the vacuum connection; the horizontal section (lower right) shows the two observation windows in the lower part of the vessel. The vacuum diffusion pump, of course, is permanently attached to the upper part of the vessel, as seen in Fig. 7-2.

For reasons already mentioned, it was decided to carry out the experiments on dogbones in torsion. Therefore, the initial design of the machine was modified in the manner shown in Fig. 7-2 and 7-3.

In torsion, the torque is produced by rotating a fork (29) made up of a pair of short levers, so that the latter pressed against a pair of radial rods of a capstan (30). The fork is rotated by a worm and worm wheel (31) driven by a motor with a two-speed drive (32). The torque is measured by means of resistance

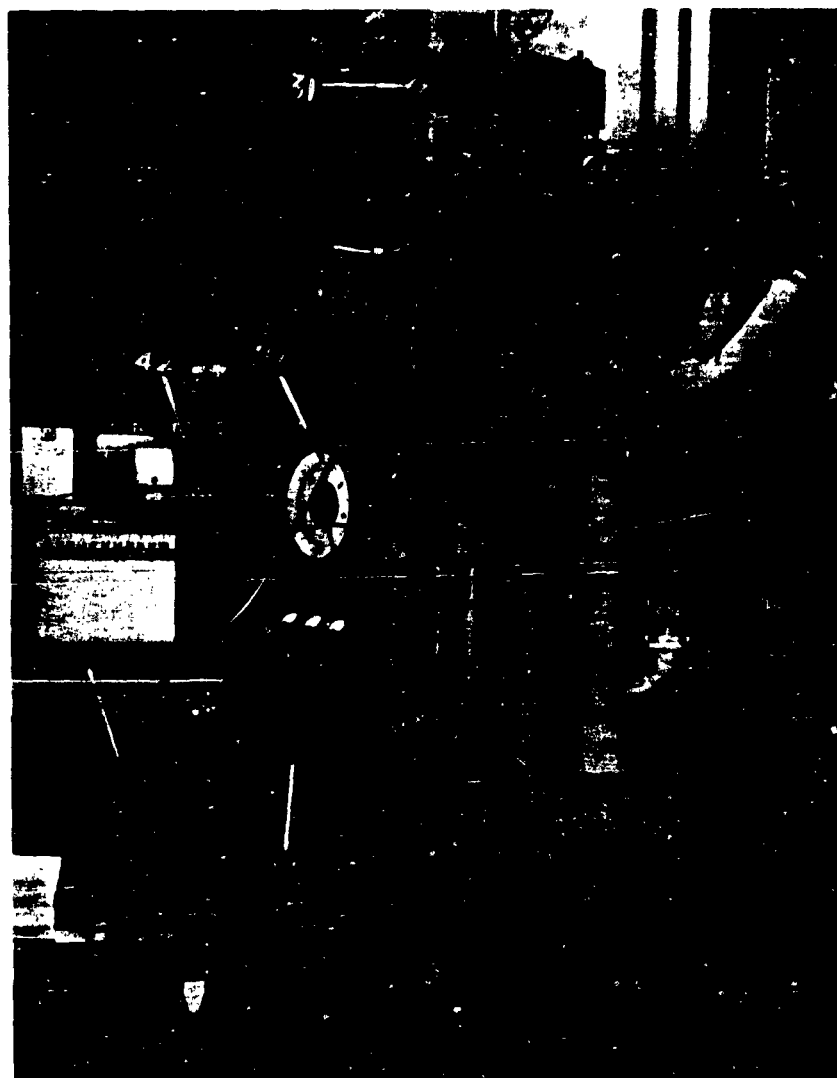


Fig. 7-2
HIGH TEMPERATURE TESTING FACILITY

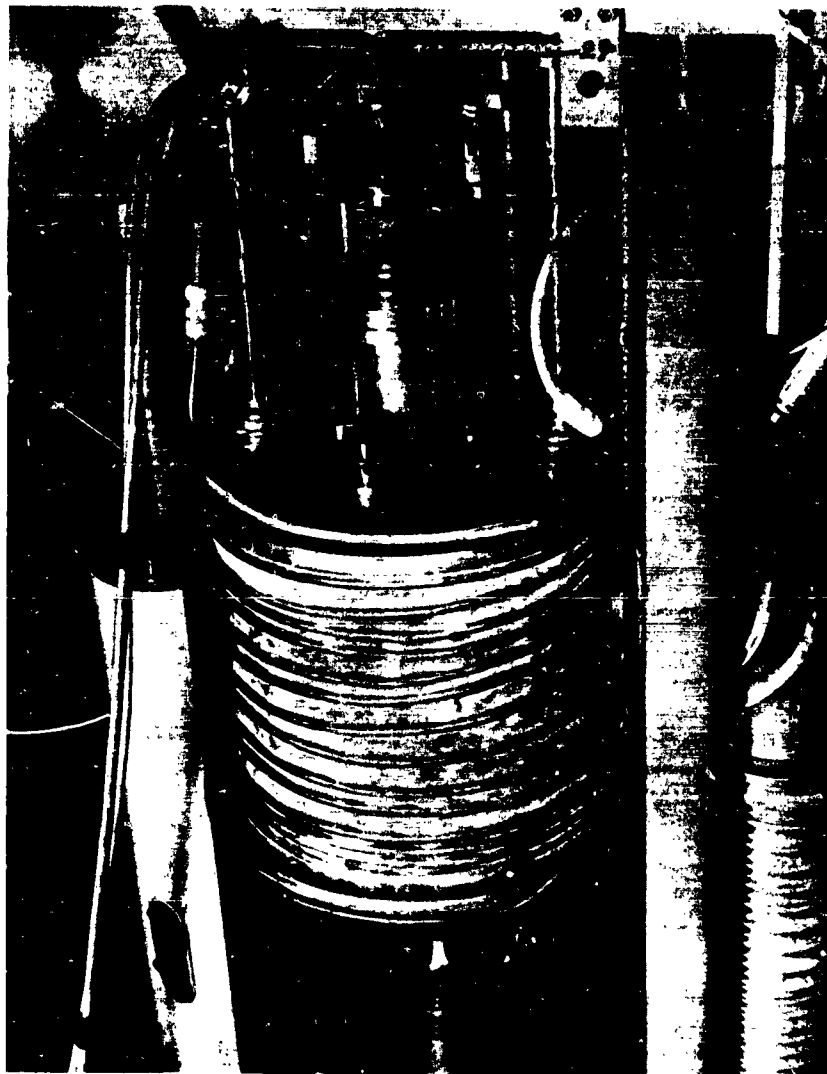


Fig. 7-3
UPPER PART OF TESTING MACHINE

strain gages mounted on the two levers of the fork. The torque assembly is sketched out in Fig. 7-4. The capstan is the upper termination of the twist rod (33). It is radially supported by two ball bearings. A collar (34) is connected with the capstan by means of a thin rubber tube (Gooch tubing) covering the gap (35). The bushing is guided by a thrust bearing and is free to rotate in an O-ring seal (36). This arrangement involving the floating collar permits a certain amount of twist without significant friction, primarily through the elastic deformation of the rubber collar. Rotation of the collar in the O-ring seal allows for large adjustments to take care of initial differences in specimen thickness.

The specimens were twisted by molybdenum grips (37), as shown in Fig. 7-5, with broached rectangular holes slightly larger than the cross section of the heads of the specimen. The torque was applied to the specimens through the rounded ends of two tungsten pins inserted into each grip and protruding into the broached hole. This assured contact in a horizontal plane in bowed specimens and eliminated superimposed bending.

Since it is very difficult to measure the twist of the specimen directly, the rotation of the capstan relative to the frame of the machine has been measured by means of a flexible phosphor-bronze leaf spring fixed at one end to the frame of the machine with the other end bearing against an arm on the capstan. The displacement of the end of the cantilever is measured as the change in curvature of the cantilever by means of resistance strain gages mounted on the latter. Both the torque and the twist were recorded with a Honeywell recorder (38) seen in Fig. 7-2. Figure 7-2 also shows the power transformer (39), the Honeywell temperature indicator-controller (40), the vacuum gage (41) and indicator (42).

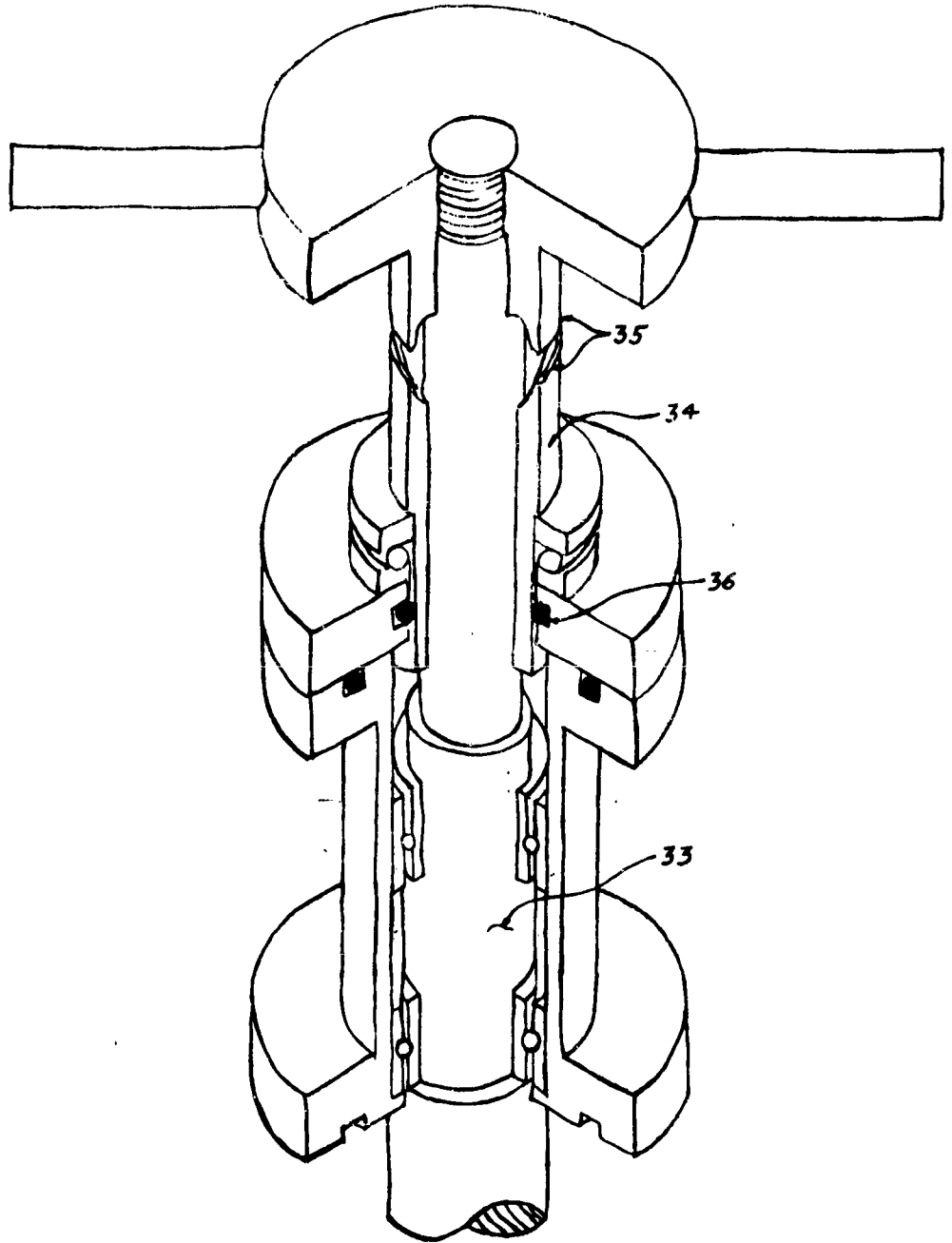


Fig. 7-4 TORQUE ASSEMBLY



Fig. 7-5
CENTRAL PART OF INSIDE OF TESTING MACHINE

The temperature is measured by means of a tungsten -- tungsten-rhenium thermocouple bearing against the specimen at the lower grip. The temperature is controlled by switching between two levels of heating current. This gives a very uniform control of temperature in the specimen with a practically insignificant ripple.

B. Dogbone Specimens

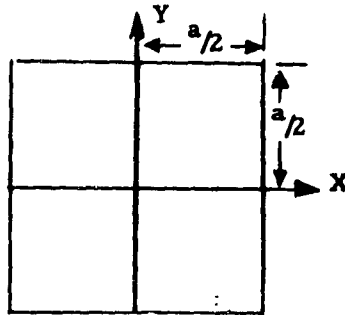
As noted, the dogbone specimens have an approximately square cross section over the gage section. The stress distribution in a purely elastic twisted square rod is given by:

$$\tau_{zx} = \frac{-48 \pi^3 M}{a^3} \frac{\sum_{n=0}^{\infty} \frac{(-1)^n}{(2n+1)^2} \frac{\sinh k_n y}{\cosh k_n a/2} \cos k_n x}{\pi^5 + 96\pi \sum_{n=0}^{\infty} \frac{1}{(2n+1)^4} - 384 \sum_{n=0}^{\infty} \frac{\tanh k_n a/2}{(2n+1)^5}}$$

$$\tau_{zy} = \frac{12 \pi^3 M}{a^4} \frac{\pi^2 x - 4a \sum_{n=0}^{\infty} \frac{(-1)^n}{(2n+1)^2} \frac{\cosh k_n y}{\cosh k_n a/2} \sin k_n x}{\pi^5 + 96\pi \sum_{n=0}^{\infty} \frac{1}{(2n+1)^4} - 384 \sum_{n=0}^{\infty} \frac{\tanh k_n a/2}{(2n+1)^5}}$$

$$\text{where: } k_n = \frac{(2n+1)\pi}{a}$$

and



The variation of the principal tensile stress on the surface of the specimen, along a line perpendicular to its axis is plotted in Fig. 7-6; the abscissa is the distance from one edge, the width of the face being a . The dotted curve has been calculated from the elastic solution of the torsion problem; for the sake of interest, the stress at the surface of a twisted rod with square cross section has actually been measured and the result compared with the calculation. For this purpose, a square rod of an aluminum alloy of the 7075 - T6 type, heat treated to maximum hardness, of a cross section 2-in. square, has been loaded in a torsion testing machine, and the tensile stresses at the surface measured by electric resistance gages of 1/8-in. length, cemented to the face of the rod at 45 deg to its axis. Seven gages were spaced at 1/4-in. on one face of the specimen; another gage, also oriented at 45 deg to the axis, was cemented in the center of a face at 90 deg to the first face. The stresses read from the gages are represented by the dots in the figure; the full curve fits the measured points according to visual judgment.

If the cross section deviates from a square, and becomes a rectangle, the stresses on the long side rise to higher levels than on the narrow side. Figure 7-7 shows the ratio of the maximum tensile stresses on the long side (σ_B) to those on the

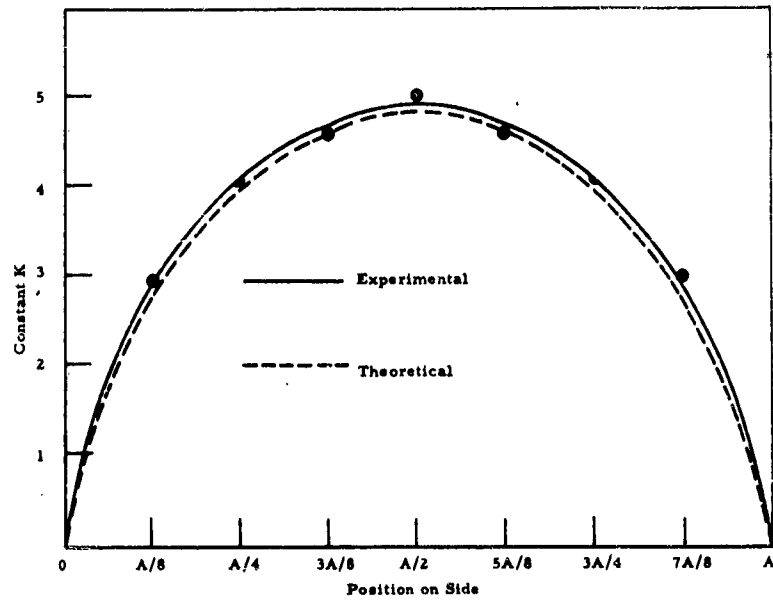


Fig. 7-6 DISTRIBUTION OF TENSILE STRESS ACROSS THE SIDE OF A SQUARE SHAFT IN TORSION $\sigma = \frac{KM}{A^3}$

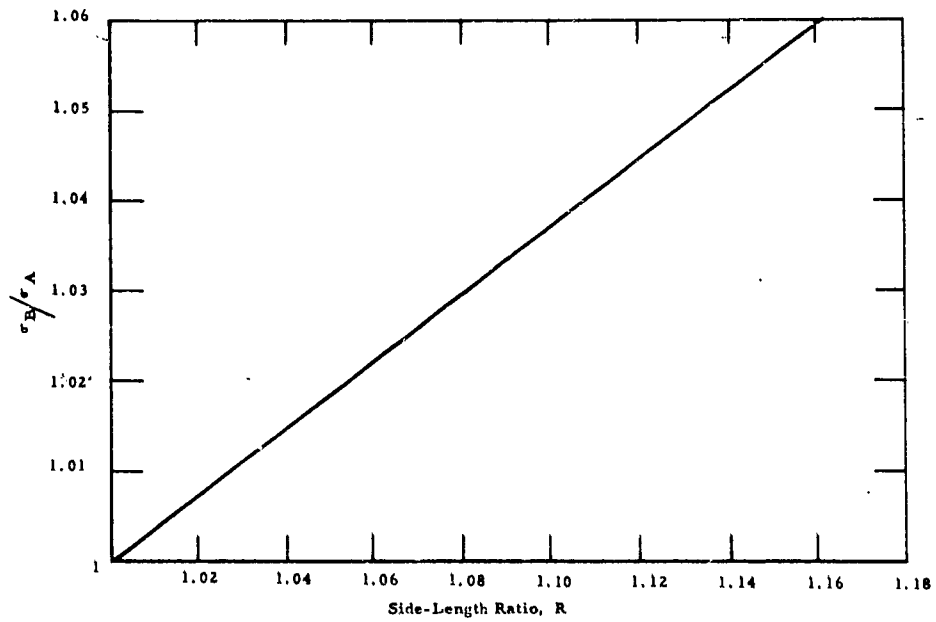


Fig. 7-7 RATIO OF MAXIMUM STRESSES ON LONG SIDE (σ_B) AGAINST SHORT SIDE (σ_A) FOR RECTANGULAR BARS IN TORSION

narrow side (σ_A) as a function of the ratio, R , of the lengths of the two sides. Figure 7-8 gives the highest tensile stress in the specimen (in the center of the long side acting across a plane at 45 deg to the axis); the ordinate C is the factor to be multiplied by the torque M and divided by the cube of the width A of the narrower face in order to give the maximum stress in the wider face. The cross sections of the specimens used were, in general, not quite square; the maximum stress was calculated, therefore, on the basis of the curve in Fig. 7-8.

Two batches of dogbones were received. The first shipment consisted of ten MgO and ten Al_2O_3 specimens. * The ten MgO specimens, referred to as Group I, had a rough and scaly surface and were considerably bowed and twisted. Their average cross sectional area was somewhat less than 1/16 sq. in. These specimens are referred to hereafter as small specimens. The specimens had what appeared to be a parting line (a very flat re-entrant wedge) on the side surface following roughly the median plane as shown in Fig. 7-9. The ten Al_2O_3 specimens, referred to as Group II, had a somewhat larger cross sectional area, and a smoother satiny surface; these specimens were considerably less distorted. No trace of a "parting line" could be detected on the Group II specimens.

In addition to the curvature and the parting line, the majority of the specimens contained one or more of a variety of

* No explanation accompanied the shipment. Since the test results to be discussed in Subsection 4 indicated two distinct kinds of behavior, scratch hardness tests were made; they indicated that one half of the twenty specimens was Al_2O_3 , the other half MgO.

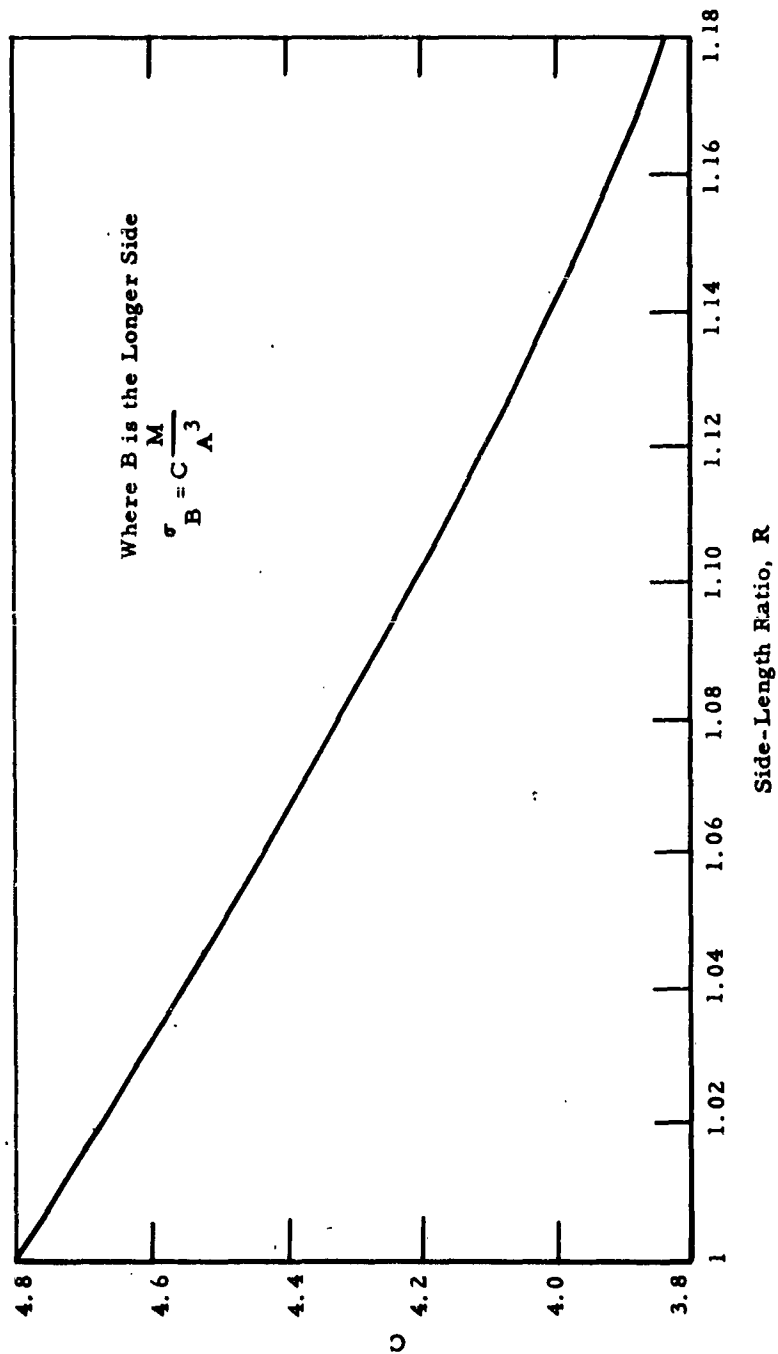


Fig. 7-8 MAXIMUM STRESS IN RECTANGULAR BAR UNDER TORSION, AS FUNCTION OF SIDE-LENGTH RATIO

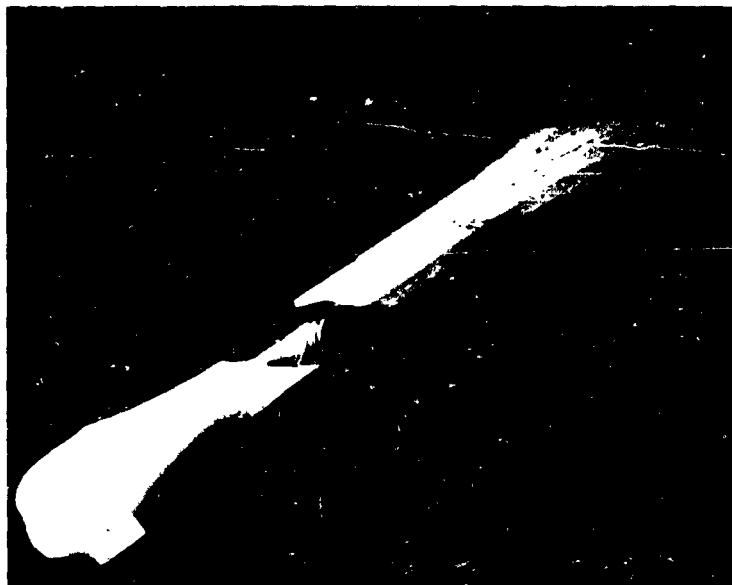


Fig. 7-9
MAGNESIUM OXIDE DOGBONE SHOWING "PARTING LINE"
AND STEPED FRACTURE SURFACE



Fig. 7-10
TYPES OF CRACKS PRESENT IN
ARF MAGNESIUM OXIDE DOGBONES

defects. A common type of defect was a crack either in the plane across the direction of pressing, such as the ones seen in Fig. 7-10, or more frequently along the edge, the crack penetrating into the interior of the specimen. Other defects were: colored spots (brown, orange-yellow, green), which were frequently observable on the surface or slightly under the surface of the specimens. As will be discussed, fracture originated often from these sites of impurities. All specimens contained varying numbers of surface pits and scales. The cross section of the specimens often deviated markedly from that of a square.

A second batch of one-hundred and fifty MgO dogbones was received later. Although the size of the specimens in this batch was larger (0.1 sq. in.), their quality was similar to those in the first batch. These specimens of larger cross sectional area will be referred to hereafter as large specimens.

C. Experimental Results

Torsion Experiments at Room Temperature

The results of the torsion experiments at room temperature of the first batch are given in Table 7-II. The first half of the table shows the results on the small MgO specimens. The first three specimens were tested in grips without the two pins mentioned in Subsection 2B; there was therefore a certain amount of superimposed bending stress, which is reflected in the scatter of the measured stresses and also in appreciable deviations from 45 deg of the angle between the fracture surface origin and the specimen axis. The remaining six specimens were loaded by means of the rounded pins described above, eliminating the bending stress. The angle between the fracture surface and the specimen axis was remarkably close to 45 deg.

Table 7-II
TESTS ON DOGBONES IN TORSION AT ROOM TEMPERATURE

Specimen	Fracture Stress (10^{-3} psi)	Angle Between Fracture Face and Specimen Axis (deg)	Origin of Fracture
I. DOGBONES WITH "PARTING LINE" AND ROUGH FACES (MgO)			
A. WITH A BENDING COMPONENT PRESENT			
1	19.4	39	FACE
2	12.6	53	FACE
3	13.1	53	FACE
B. WITH BENDING COMPONENT REMOVED			
4	12.5	45	SIDE
5	13.7	44	SIDE
6	14.2	44	SIDE
7	9.8	44	SIDE
8	15.3	46	SIDE
9	12.3	45	SIDE
II. DOGBONES WITHOUT "PARTING LINE" (Al_2O_3)			
1	36.5	SHATTERED	FACE
2	32.7	44	FACE
3	33.5	45	SIDE
4	30.4	45	SIDE
5	26.0	47	SIDE
6	33.2	SHATTERED	FACE
7	35.4	44	FACE
8	30.5	44	FACE
9	30.3	SHATTERED	FACE
10	32.6	46	FACE
SUMMARY			
Group Number	Average Stress (10^{-3} psi)	Standard Deviation (10^{-3} psi)	Coefficient of Error (%)
I-B	13.0	1.9	15.0
II	32.1	3.0	9.3

These specimens had a somewhat rectangular cross section; the thickness in the plane of the dogbone was larger by as much as 10 percent than the thickness at a right angle to it. It is to be noted that fracture in these six specimens did not originate on the wider face where the tensile stress must have been somewhat larger, but on the narrow side containing the longitudinal parting line.

In Group I, specimens nearly all traces of the fracture surface had a small kink at the parting line as shown in Fig. 7-9. The mean fracture stress for this group was 13,000 psi, which is about 25 percent lower than the value of 16,000 obtained in the Armour Research Foundation. These lower values are of considerable interest, especially in view of the fact that the most highly stressed part of the surface in the torsion specimens is less than in the bending specimens of Armour; for this reason, a higher strength might be expected in torsion. Consequently, these lower values may be the result, either of a plane of weakness associated with the "parting line," or of certain defects having a higher stress concentration in torsion than in tension or compression (see below).

No information about the way in which the manufacturing process gives rise to the parting line has so far been available. It is of interest that the strength impairing property of this defect could not have been detected by tension or bending experiments, but only with torsion experiments.

The second half of Table 7-II gives the results for the Al_2O_3 specimens. The mean fracture stress of this group was 32,100 psi, which is about 20 percent higher than the average value of 26,300 psi obtained in bending experiments at Armour.

These specimens had a very nearly square cross section; the origins of fracture were more uniformly distributed between face and side, and no kinks were observed at the fracture origin.

Of the second batch of (large) MgO dogbones, forty-nine were tested in torsion at room temperature. The results of tensile fracture strengths are presented as a "cumulative" probability distribution in Fig. 7-11 by the solid curve. The results of the earlier torsion experiments of the first batch (small specimens) are given as the six points marked by "x" in Fig. 7-11. The sixty tensile fracture stresses of small specimens obtained in bending at room temperature by the Armour Research Foundation are entered in Fig. 7-11 as the dotted cumulative probability curve. The fracture strengths in torsion are similar to those of the small specimens. Their average strength is 13,600 psi, and the distribution has a standard deviation of 1,830 psi. The average bending strength of small specimens measured by the Armour Research Foundation was 16,600 psi with a distribution having a standard deviation of 1,940 psi. Figure 7-11 shows that the MgO specimens are considerably weaker in torsion than they are in bending. To make certain that no differences in material or manufacturing techniques were responsible for this difference in strength, five large dogbone specimens were broken in four-point bending. The fracture stresses are given in Table 7-III; they do not differ significantly from the values measured at the Armour Research Foundation.

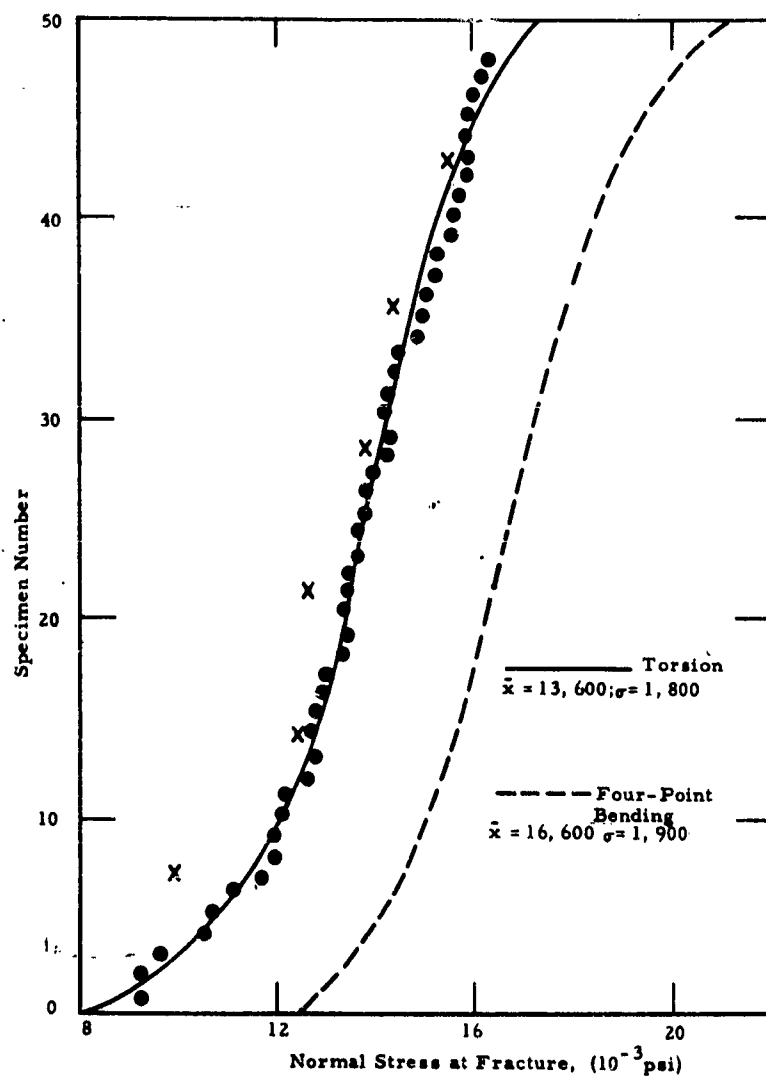
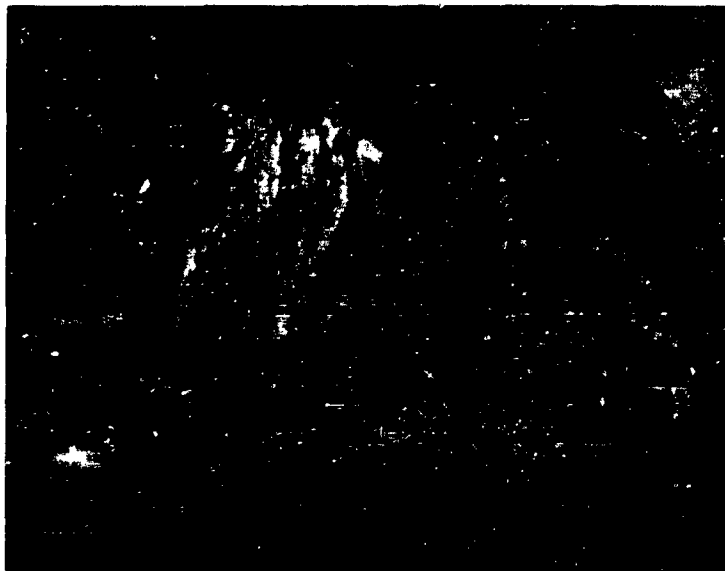


Fig. 7-11 DISTRIBUTION OF FRACTURE STRENGTHS OF AS-RECEIVED ARF MAGNESIUM OXIDE AT ROOM TEMPERATURE

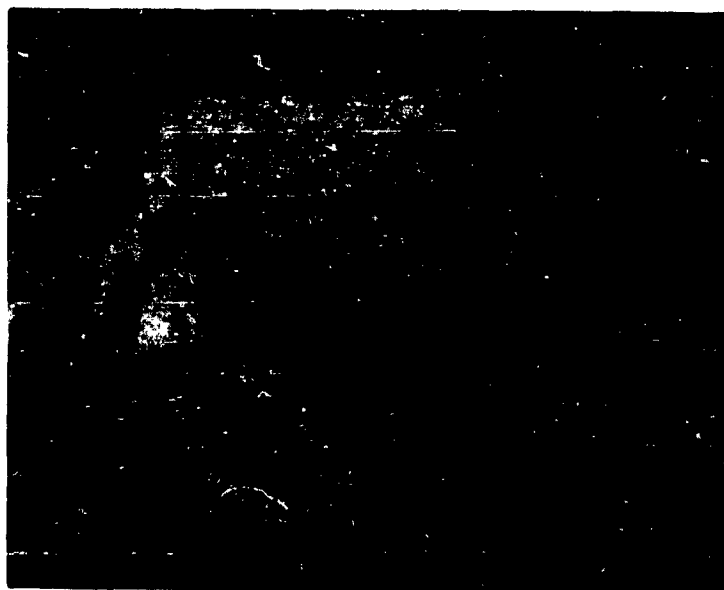
Table 7-III
FRACTURE STRENGTHS OF ARF MAGNESIUM OXIDE AT ROOM TEMPERATURE

	Twist Rate	Normal Fracture Stress (psi)	Average Normal Fracture Stress (psi)	Standard Deviation (psi)
	0.057°/min.	49 specimens	13,600	1,800
Torsion		15,500		
Four-Point Bending		15,600	16,200	530
		15,900		
		16,100		
		18,100		

It seems certain, then, that differences between the batch used in these experiments and the batches used at Armour could not be made responsible for the higher strength observed in bending. On the other hand, the difference cannot be attributed to the testing machine, because the tensile strengths derived from the torsion tests for Al_2O_3 specimens were considerably higher than those obtained from the bending tests at ARF. One circumstance that may be relevant is that in the majority of the MgO specimens, fracture originated at a more or less spherical cavity at or near the surface. Such cavities are visible in the photographs shown in Fig. 7-12. The peculiarity of a spherical cavity is that its stress concentration factor under a tensile stress is lower than that under shear stress; more explicitly, if $+\sigma$ and $-\sigma$ are the principal stresses in a biaxial state of stress, the highest tensile stress at the wall of a spherical cavity is $\frac{2}{1.8-\nu}$ times higher than the highest tensile stress at the cavity wall if a uniaxial tensile stress σ is acting. This has the simple reason that, in uniaxial tension, the stresses tangential to the wall of the cavity will vary as shown in Fig. 7-13a; around the diameter parallel to the applied tension, the tangential stress is compressive, while it is tensile along the equator. Evidently, if a tensile stress and a perpendicular compressive stress are applied, the tensile stresses generated around the poles of the compression axis are superposed on the (higher) tensile stress at the equator around the tension axis, and the maximum tensile stress at the wall of the cavity is higher than if the tensile stress were acting alone. Calculation leads to the ratio just mentioned; if Poisson's ratio is assumed as 0.2, its numerical value is 1.25. This happens to be close to the ratio $16,600/13,600 = 1.22$ of the tensile strengths derived from bending tests to those derived from torsion tests.



(a) at
brown
spot



(b) at
yellow
spot

Fig. 7-12
FRACTURE ORIGIN

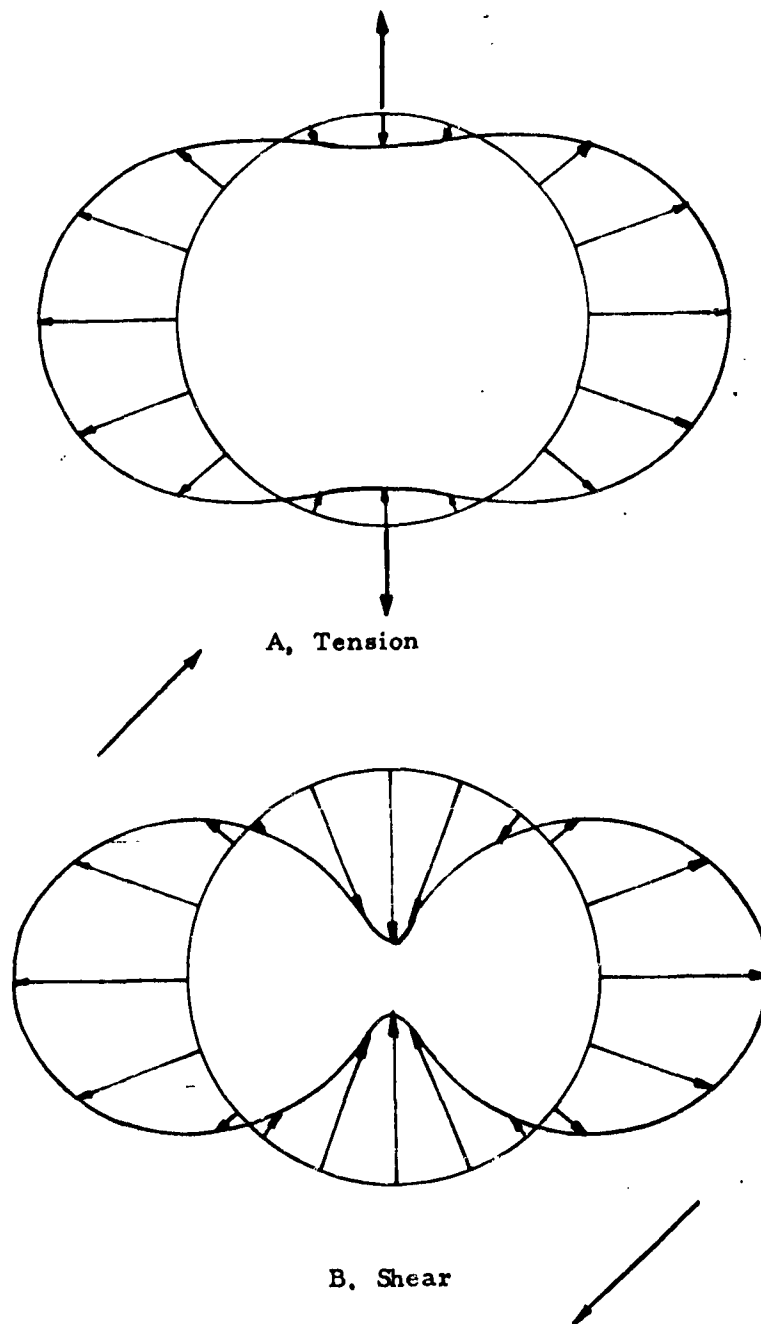


Fig. 7-13
DISTRIBUTION OF NORMAL STRESS AT THE CIRCUMFERENCE
OF A SPHERICAL CAVITY

On the other hand, no spherical cavities were observed in Al_2O_3 specimens; since Al_2O_3 is less plastic at the sintering temperature, it may be assumed that any cavities that may be present are likely to be crack-like in shape. With a crack-shaped cavity, the stress concentration factors would not differ significantly in tension and torsion; but there are two circumstances that may introduce a difference. First, if the orientation of the cracks is not random, they may lie so as to weaken the material more if the tensile stress is at 90 deg to the specimen axis than when it is at 45 deg.

Secondly, it is not unreasonable to expect that the crack surfaces will be rough so that there may be friction between the walls of the crack, arising from mechanical interlocking. If then the cracks are almost normal to the axis of the specimen, the propagation of the crack by an axial tension is not hindered by friction effects. In torsion, however, such a crack has to propagate against the wall friction.

Torsion Experiments on Polycrystalline Magnesium Oxide at Elevated Temperatures

A number of torsion experiments were performed in an Ar atmosphere at 400°C, 1200°C, and 1500°C at the standard twist rate, which was 0.057° per min. Two experiments at 1200° and 1500°C were also performed at a twist rate of 1.4° per min. The results are given in Table 7-IV.

Table 7-IV
RESULTS OF EXPERIMENTS ON MAGNESIUM OXIDE DOGBONE
SPECIMENS AT ELEVATED TEMPERATURES

Temperature (°C)	Twist Rate (deg/min)	Normal Fracture Stress* (psi)	Average Normal Fracture-Stress (psi)	Standard Deviation (psi)
400	0.057	15,200	14,700	1,300
	0.057	16,800		
	0.057	13,900		
	0.057	13,700		
	0.057	14,200		
1200	0.057	6,500	8,700	1,700
	0.057	8,000		
	0.057	9,700		
	0.057	10,400		
	1.4	8,600		
1500	0.057	2,100	—	—
	1.4	4,100		

* As is discussed the specimens show considerable nonelastic deformation at elevated temperatures, so that these normal stress values should be considered as moduli of rupture in torsion.

It is important to realize that fracture stresses in Table 7-IV have been calculated on the basis of the stress distribution in a twisted elastic bar. Since, as will be seen, the specimens show strong relaxation effects at elevated temperatures, the elastic calculation is unrealistic and the values given in Table 7-IV, particularly at the temperatures 1200 and 1500°C, can not be regarded as representing the true fracture stress. Moreover, if the material showed ideally plastic behavior (no strain hardening) at a high temperature, and the stresses could be calculated from the stress distribution in an ideally plastic twisted square rod, the maximum stress obtained could not be a fracture stress, because this stress would have acted from the beginning, through the entire stage of plastic torsion, without causing fracture. Consequently, the fracture could not have been of the brittle type, governed by a critical tensile stress condition

Figure 7-14 shows that, in fact, the type of fracture changes with the temperature. The first of the three fractured specimens shown broke at room temperature; the surface of fracture is almost exactly at 45 deg to the axis. The second specimen was tested at 1200°C; the surface of fracture is irregular, and, on the whole, its angle to the axis is smaller. The third specimen was broken at 1500°C, and the fracture surface is close to being at right angles to the axis than at 45 deg to it. In other words, at 1500°C, the orientation of the surface of fracture is much closer to that observed in shear fracture than that in a brittle fracture.

The numerical evaluation of the tests at the elevated temperatures, therefore, is made impossible by the circumstance that the stress distribution is not that in an elastically twisted rod, nor, in general, that in a twisted rod of ideally plastic material.

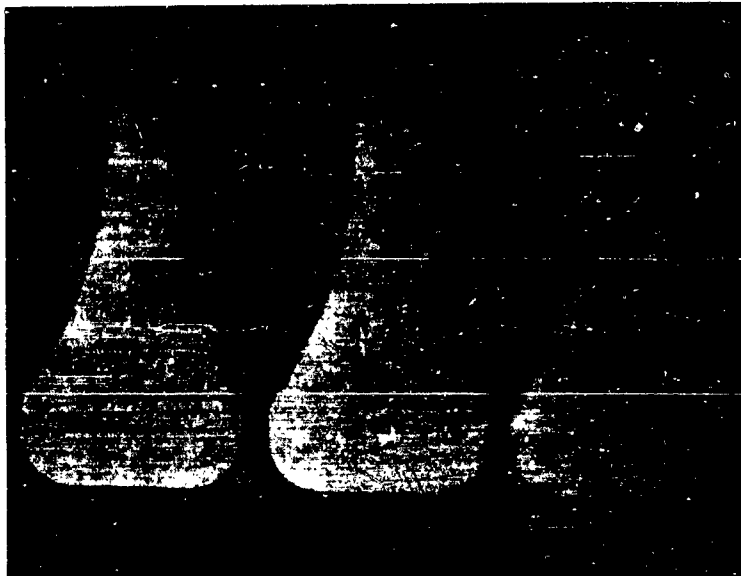


Fig. 7-14
CHANGE OF POSITION OF FRACTURE SURFACE WITH TEMPERATURE

Of greater fundamental importance is that the character of the fracture changes from the brittle to a ductile type as the temperature rises. This means that the maximum tensile stress fracture condition ceases to be valid. It was pointed out⁽⁷⁻³⁾ that ductile fractures do not obey any critical stress fracture condition; in other words, there is no single value of a ductile strength (or, there is no ductile strength as a quantity that can be regarded as characteristic of the material).

Naturally, the strain rate influences the fracture mechanism in the same way as the temperature. Increased strain rate is approximately equivalent to a reduced temperature. Only a few experiments could be carried out in this direction. At 1200°C, increase of the strain rate by a factor of 25 did not seem to influence the nominal fracture stress, while in two tests at 1500°C, the nominal strength rose from 2, 100 psi to 4, 100 psi as the strain rate was increased by a factor of 25.

In summing up, it can be said that the torsion test (or, for that matter, the bending test) can not be evaluated, and the true maximum stress can not be obtained when the material is noticeably plastic. The true stress at fracture could be found in the plastic range from a tensile test. However, this would not represent a fracture stress (strength) characteristic of the material from which its behavior under other types of loading could be calculated, because the maximum tensile stress fracture condition is not valid in the plastic range where the fracture changes from the brittle to a ductile type. At very high temperatures, the problem becomes one of creep fracture ("stress rupture"); under a general state of stress practically nothing is known about its solution. In simple tension at very high temperatures, the fracture strain is usually approximately constant in creep fracture tests; in the intermediate temperature range (between room temperature and very high temperatures) not even this simple approximate rule holds.

For polycrystalline MgO a temperature of 800°C appears to be the approximate limit of substantially elastic behavior; however, this is not meant to imply that plastic deformation can safely be neglected at lower temperatures. Figure 7-15 shows torque versus twist curves of MgO dogbone specimens; it shows that the curve for 400°C deviates considerably from the substantially elastic curve at 20°C. The deviation is not merely a consequence of the temperature dependence of the elastic modulus; the torque twist plot is distinctly curved. Whether the entire deviation from the initial tangent was due to permanent deformation could not be ascertained, since the experiment ended with fracture.

Table 7-IV shows a point of interest in connection with the slight plastic deformation observed at 400°C. The mean nominal fracture stress (normal stress) from five specimens at 400°C is 14,700 psi with a standard deviation of 1,300 psi; at room temperature, the mean value is 13,600 with a standard deviation of 1,800 psi. There is a possibility that the difference may be significant; if so, the simplest explanation would be to attribute it to the reduction of stress concentrations by the plastic deformation indicated by Fig. 7-15.

Figure 7-16a shows the surface of fracture of a specimen broken at 1200°C. It is quite different from the fracture surface at room temperature, although this is not clearly visible on the photograph. The microscopic observation shows very suggestively that the fracture was not a simple crack propagation process, but that the grains have been pulled apart, apparently by the weakness of the grain boundaries at the high temperature. This is illustrated also in Fig. 7-16b, which shows a partly broken specimen with a branching surface of fracture obtained at 1200°C.

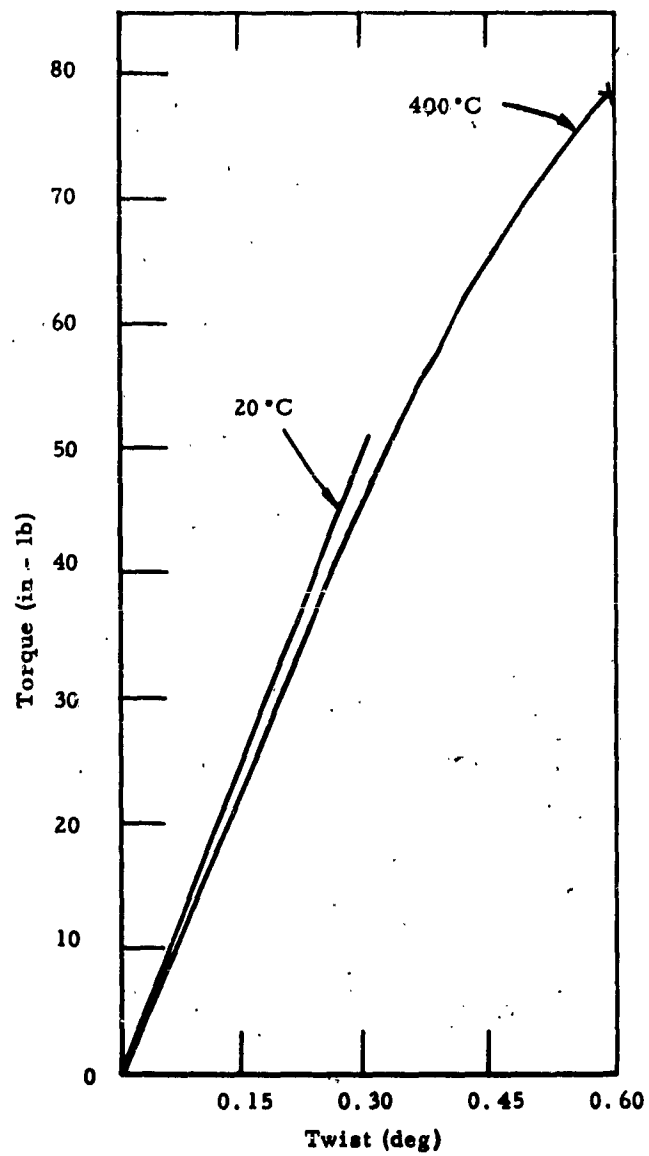


Fig. 7-15 TORQUE VS TWIST FOR POLYCRYSTALLINE MAGNESIUM OXIDE 20°C AND 400°C



(a)
complete
fracture



(b)
incomplete
fracture
showing
forking

Fig. 7-16
Fig. 7-16 MAGNESIUM OXIDE FRACTURE SURFACES AT 1200°C

If the weakness of polycrystalline MgO at higher temperatures is due to the grain boundaries, as Fig. 7-16 strongly indicate, a point of great practical importance arises. In an unpublished investigation, one of the participants in the present work, E. Orowan, found many years ago that commercial lead comes apart cleanly along the grain boundaries if it is carefully heated over a gas flame and pulled by hand. The question was whether this was due to the inherent weakness of the grain boundaries as sites of atomic disorder, or to small amounts of impurity lodged in the grain boundaries and depressing the melting point. The experiment was repeated with spectroscopically pure lead, and the effect could not be reproduced. Although commercial lead is an exceptionally pure metal, impurities accumulated in the grain boundaries did produce a radical change in its high temperature fracture behavior. Another similar instance is the plastic deformation of polycrystalline ice in glaciers. It seems that the creep of temperate-zone glaciers (in which the ice is approximately at the pressure melting point) is largely due to grain boundary sliding caused by a slight reduction of the melting point at the boundary, resulting from accumulated impurities, of which NH_4NO_3 , formed from air by atmospheric electric discharges, seems to be the most important. The high temperature creep fracture behavior of a polycrystalline material, therefore, may be determined by traces of impurities concentrated in the grain boundaries.

From what has been said about colored specks present in the MgO specimens, it is clear that impurities are present in visually observable quantities; the question is whether the use of a purified material would lead to a radical improvement in creep fracture strength. To answer this question would require experiments with very pure MgO; the important point shown by the present

work is that the weakness of polycrystalline MgO may possibly be due largely to small amounts of impurities. Naturally, even if this weakness would be remedied, MgO would still retain the disadvantage of considerable intracrystalline softening at higher temperatures.

Relaxation Experiments

As mentioned, the MgO specimens showed considerable plastic deformation at temperatures approaching 1000°C. A number of relaxation tests have been carried out to obtain some orientation about the phenomenon. These tests consisted in applying a torque at the higher rate given by the drive of the testing machine (1.4 deg twist per minute), stopping the drive, and recording the decrease of the torque. One of the relaxation curves obtained at 1500°C is shown in Fig. 7-17. It is useful to compare such a relaxation curve with that of purely Newtonian viscous relaxation characterized by

$$M = M_0 \exp(-t/\theta)$$

where M_0 is the initial magnitude of the moment and θ the time constant of the relaxation. If the logarithm of the moment M/M_0 is plotted against the time, t , a straight line is obtained. Figure 7-18 shows the logarithm of M/M_0 plotted against t . The curve is not a straight line, but seems to consist of three straight portions, the slopes of which diminish with the time. This is to be expected. Being a crystalline material, MgO ought to show non-Newtonian viscosity of the type encountered with metals in the hot creep range. Up to the "creep limit," the creep rate is very small, and then it begins to rise very rapidly. In other words, the effective coefficient of viscosity increases rapidly with decreasing load, and time constant which determines the slope of the logarithmic plot ought to increase in the course of the relaxation process. This is just what has been observed.

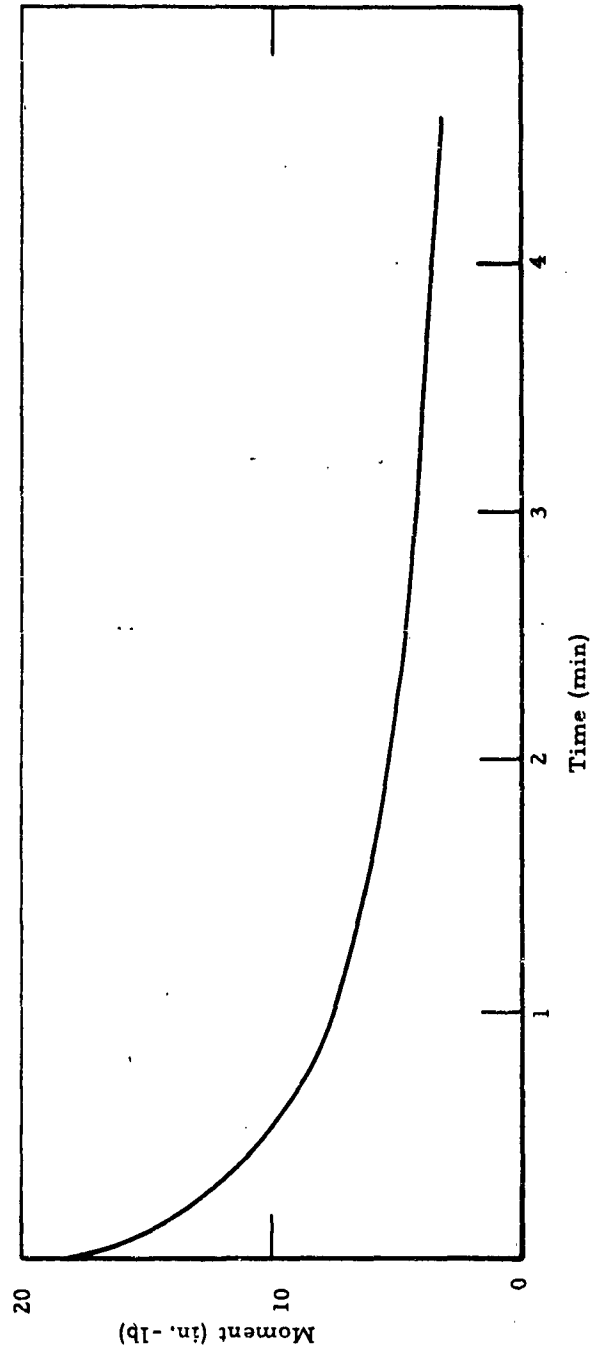


Fig. 7-17 RELAXATION CURVE FOR ARF MAGNESIUM OXIDE AT 1500 °C IN TORSION

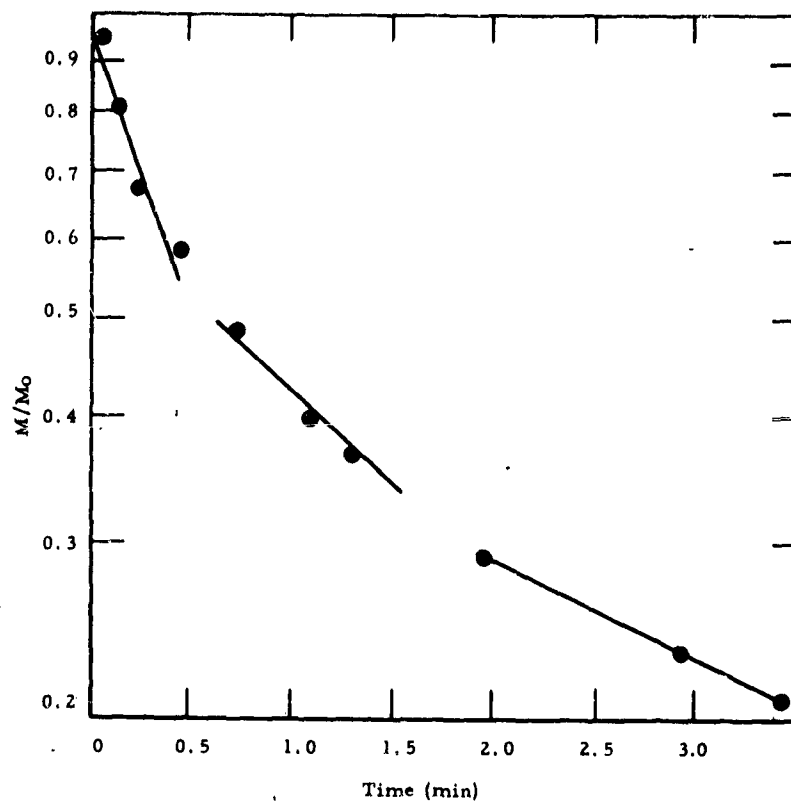


Fig. 7-18 M/M_0 Vs t FOR RELAXATION OF ARF MAGNESIUM
OXIDE AT 1500°C

It is conventional to compute the activation energy from the temperature dependence of a creep process. Figure 7-19 shows the relaxation rate plotted over the reciprocal of the absolute temperature for seven temperatures between 900 and 1500°C; the experimental points are grouped around a straight line with considerable scatter. The slope of the line corresponds to an activation energy of about 0.7 ev. In view of the uncertainties of the experiments, not too much weight is attached to this value. In experiments with another specimen, at three different initial torques, the scatter was too strong and no plausible curve could be fitted. It is intended to clarify the matter by means of further creep tests in tension at constant load.

Because the polycrystalline MgO specimens were warped, they were not suitable for tensile tests; for this reason, torsion tests were carried out. At room temperature, the maximum tensile stress at fracture was almost 20 percent lower in torsion tests than in four-point bending tests; with Al_2O_3 specimens, on the other hand, the tensile strength derived from torsion tests was higher than that from bending tests. The majority of the MgO specimens contained roughly spherical cavities at which many fractures originated. This may account for the lower strength in torsion, since the stress concentration at such a cavity is higher under an applied shear stress than under a tensile or compressive stress.

At temperatures approaching 1000°C, the MgO specimens showed considerable plastic deformation, and the mechanism of fracture gradually changed from the brittle type towards a ductile type. This meant that the maximum tensile stress could no longer be evaluated by means of calculations referring to elastic materials. Moreover, even if the stress at fracture

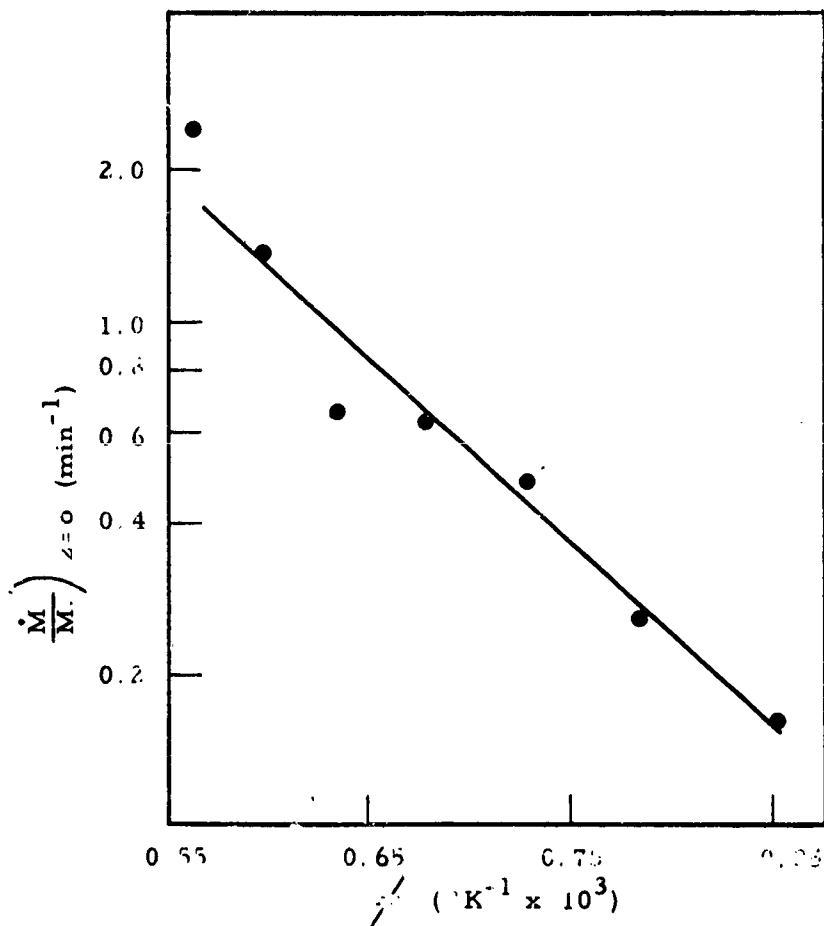


Fig. 7-19 $\frac{\dot{M}}{M}$ $z=0$ Vs $\frac{1}{T}$ FOR ARF MAGNESIUM OXIDE IN THE RANGE 900°C - 1500°C A = 0.7eV

could be calculated, ductile fractures are not governed by a critical tensile stress (or shear stress) condition.

The high temperature fractures seem to indicate that much, if not most, of the deformation, as well as the fracture itself, is likely to be due to grain boundary sliding. Since boundary sliding may be accelerated by impurities accumulated at the boundaries, the possibility is presented that the inferior mechanical behavior of MgO at high temperatures could be partly or mainly due to small amounts of impurities.

3. EXPERIMENTS ON SINGLE CRYSTALS OF MAGNESIUM OXIDE

It was recognized early that the tensile cleavage strength of NaCl crystals was much too low to be explained on the basis of the Griffith theory, and that plastic deformation must play a fundamental role in the fracture mechanism; the proposition that cracks of subcritical size could propagate with the help of the tensile stresses of edge dislocations approaching the tip of the crack was advanced nearly 30 years ago. ⁽⁷⁻¹⁾ Recently, it was proposed ^(7-4, 7-5) that such a mechanism would be responsible for the formation of cracks in MgO observed by Parker and his collaborators in 1957.

Between 1948 and the present time, attention was concentrated on the nucleation of cracks by the interaction of individual dislocations, or a few dislocations, with obstacles such as grain boundaries, or with other dislocations. The formation of cracks by the piling up of edge dislocations at a grain boundary was suggested by Zener ⁽⁷⁻²⁾, mathematically investigated by Stroh ^(7-6, 7-7), and observed in MgO crystals by Westwood ⁽⁷⁻⁸⁾ and by Stokes, Johnston, and Li ⁽⁷⁻⁹⁾. The formation

of cracks by the fusion of edge dislocations was suggested by Cottrell⁽⁷⁻¹⁰⁾; although similar mechanisms were used to explain crack formation in single crystals, (7-9, 7-11, 7-12) there is no conclusive evidence available in this respect. Slip across a low-angle boundary was suggested as a mechanism of crack formation by Orowan⁽⁷⁻¹³⁾, and quantitatively investigated by Stroh⁽⁷⁻¹⁴⁾; its operation was observed by Gilman⁽⁷⁻¹⁵⁾ and by Deruyttere and Greenough⁽⁷⁻¹⁶⁾. That the intersection of twin bands can lead to crack formation has been known since 1868⁽⁷⁻¹⁷⁾; the importance of twinning in the brittle fracture of iron has been recently demonstrated by Low⁽⁷⁻¹⁸⁾, Hull⁽⁷⁻¹⁹⁾, Edmondson⁽⁷⁻²⁰⁾ and others.

The following investigation was undertaken for clarifying the processes which lead to the formation and propagation of cracks in single crystals of MgO. It has shown the importance of crack formation due to stresses produced by kinking at the intersection of slip bands.

A. Preparation of Specimens

Large chunks of MgO crystals were purchased from the Norton Company. The color of the raw crystals varied considerably; however, this does not seem to have a significant effect on fracture and therefore, chemical analyses were not made.

The raw crystals were cleaved to the desired sizes and shapes; if chemical polishing was required, this was done by continuous agitation in boiling orthophosphoric acid followed by a succession of rinses in boiling water (to prevent thermal shock), methanol and ether. The etch reported by Stokes, Johnston, and Li⁽⁷⁻⁹⁾, consisting of five parts of a saturated solution of NH_4Cl in water, one part H_2SO_4 , and one part of water, was used to reveal dislocations. This etch differentiates between "grown-in" and fresh dislocations.

Slender compression and tension specimens of square cross sections (3 mm x 3 mm) were initially mounted with epoxy cement in brass collars. In the case of compression, this eliminated undesirable spalling fractures at the compression faces. A simpler technique used in later experiments consisted of producing a slight convexity on the ends of the crystals by acid polishing. This not only eliminated spalling fracture, but also made subsequent etching and x-ray investigations more convenient. The crystals equipped with brass collars were compressed or extended in a specially constructed microscope stage testing machine. The crystals with bulged ends were compressed in a small, stiff machinist's vise. All loading experiments were carried out on the stage of a polarizing microscope, so that continuous observation of the development of deformation was possible.

The majority of the experiments was carried out in compression to arrest the growth of cracks. Some tension and bending experiments were also performed. These did not show any feature that could not be studied more conveniently in compression.

B. Features of Plastic Deformation in Magnesium Oxide Crystals

If carefully cleaved MgO crystals are intensively acid-polished, all surface irregularities in the form of cleavage steps, cracks, and of fresh dislocations introduced by superficial plastic deformation can be removed. Such acid-polished crystals may fracture when bent at a high stress without any sign of plastic deformation⁽⁷⁻²¹⁾. If polishing is not carried out to such an extent, or if mobile dislocations have been

produced at the surface by mechanical surface damage, it is possible to limit deformation to a few dislocation.* In this manner, the development of a few band intersections can be studied in detail.

Figure 7-20 shows the surface of a moderately polished crystal after two stages of compression, each followed by a step of etching. The dark central portions of the intersecting dislocation bands show the width after the first stage of compression; the somewhat lighter portions represent the lateral growth of the bands during the second stage of compression. The part of the thin diagonal band within the broad band is uniformly sheared over; no discontinuity of the shear is apparent at the boundary between the primary and secondary portions of the broad-band. This shows that, as in the case of Luders bands in mild steel, additional deformation occurs only at the boundary of a widening band, but not inside the band. The band widens by "infecting" neighboring slip planes with dislocations, injected into

* Dislocation-filled bands in MgO crystals are usually called "slip bands". However, their nature differs fundamentally from slip bands in the traditional sense of the word, which arise in an already dislocation-filled crystal by the gradual concentration of slip in bands (or "zones") (in cubic face-centered crystals, in the third stage of plastic deformation). To avoid confusion, the deformation bands of the type occurring in LiF and MgO, may be called dislocation bands, or after their discoverers, Gilman-Johnston bands.

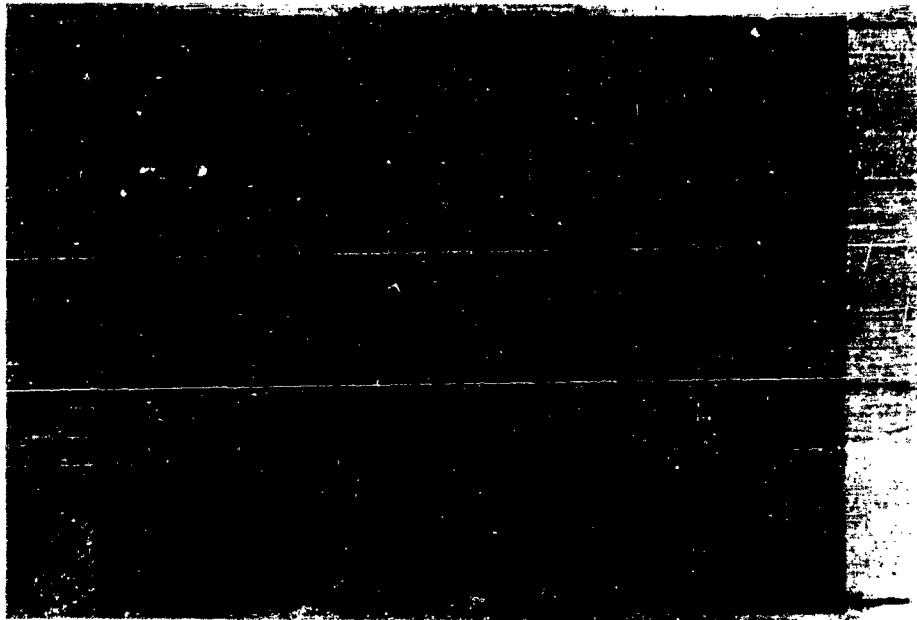


Fig. 7-20
LATERAL GROWTH OF DISLOCATION BANDS DURING TWO STAGES OF
COMPRESSION, EACH FOLLOWED BY A STAGE OF ETCHING

them apparently by double cross slip.**

Within the band, the dislocation density is such that the resulting strain hardening makes further deformation in the band impossible until the stress is raised above the magnitude required for widening the band. The shear strain in the band is conveniently determined by measuring the angle introduced into an intersecting conjugate*** slip line (single row of etch pits)

** The current term for this process is "dislocation multiplication." However, it occurs usually by double cross slip, in which case the number of non-connected dislocation loops does not necessarily increase; what is "multiplied" is:

- (1) the length of the loops;
- (2) the number of dislocation etch-pits observed;
- (3) the number of active slip planes.

Now, (1) the length increases also when a simple loop expands;
(2) the number of observed etch-pits may increase if a simple loop becomes wavy and gives multiple intersections with the plane of sectioning;
(3) the number of active slip planes does not increase when a Frank-Read "source" operates in one plane, a process also called dislocation multiplication.

To avoid ambiguities, therefore, it is convenient to refer to the process here considered as the infection of neighboring slip planes with dislocations, a term first used for this purpose in Ref. (7-22).

It may be remarked here that the term "dislocation source" involves similar ambiguities. A Frank-Read double "source" may increase the number of non-connected loops in a slip plane, but this is not an essential point; a single "source," and in many cases the double "source," merely increases the length of a dislocation loop, without increasing the number of loops or infecting other slip planes. It was for this reason that the term Frank-Read "dislocation mill" was suggested(7-13) to replace "dislocation source."

***A pair of slip systems in which the slip direction of one is normal to the plane of the other will be called conjugate.

as it crosses a wide band (see Fig. 7-27). It can also be determined, somewhat less accurately, from the tilt produced in a cube face (cleavage face) where it is intersected by a dislocation band with a slip direction at 45 deg to the cube face. Such measurements show that the shear angle is, on the average 5 deg, and may vary between 4.8 deg and 5.3 deg.

In the early stages of deformation, the dislocation bands are narrow, and they can easily cut through each other. As they widen, however, they become increasingly effective obstacles to intersecting slip. The reason why the width of a dislocation band determines its effectiveness as an obstacle is a question of fundamental importance; a possible answer will be discussed below. When a band becomes wide enough to make penetration by intersecting bands practically impossible, the segments of the intersecting bands begin to widen more or less independently from each other. If the segments of a band acquire different widths in this manner, high internal stresses are bound to arise. It will be seen that the internal stresses arising from the independent broadening of band segments are the cause of crack formation in many cases.

When the dislocation bands have widened sufficiently to give rise to independent widening of the conjugate band segments, the crystal becomes subdivided into regions in which further deformation takes place preponderantly by the widening of one parallel set of dislocation bands (out of the four possible sets). It seems that this subdivision into regions is a consequence of the constraint exerted upon the crystal by the grips of the testing machine, in connection with the tendency of the crystal to operate only one set of bands in one region. The operation of only one set in the whole crystal would result in a relative

transverse movement of the grips; since the testing machine used does not permit this, different slip planes become active in different regions, so that the resulting transverse movement of the ends of the crystal is cancelled, and only the longitudinal movement remains.

At a given moment, therefore, each region contains an active set of dislocation bands and a conjugate substantially inactive set. Since slip in the segments of the active set (each segment lying between two neighboring inactive bands) can not fully penetrate the inactive bands, the shear in the areas of intersection has to take place largely, if not entirely, by slip on the slip planes of the inactive system, by the movement of edge dislocations already present in the inactive band. In other words, the deformation takes place by slip in the active segments and by kinking in the prisms of intersection of the active with the inactive bands.⁽⁷⁻²³⁾ Figure 7-21 shows this schematically; A is the active band, I the inactive one; full lines indicate active slip planes, and dotted lines the quiescent slip planes of the inactive band. The lattice rotation at the intersections can be recognized from Berg-Barrett imaging x-ray photographs of deformed MgO crystals. Figure 7-22a shows a low-magnification optical photograph of a vertically compressed and then etched crystal, while Fig. 7-22b is the imaging x-ray photograph of the same crystal face^{*}. On the optical photograph made with incident light, the dislocation bands appear dark because they are saturated with dislocation etch-pits; on the x-ray photograph, they are dark because of decreased

* The top $[010]$ edge of the crystal (in the coordinate system of Fig. 7-25) was parallel to the x-ray plate and normal to the x-ray beam. The Bragg reflection is from the $[201]$ planes, and the radiation is copper $K\alpha$.

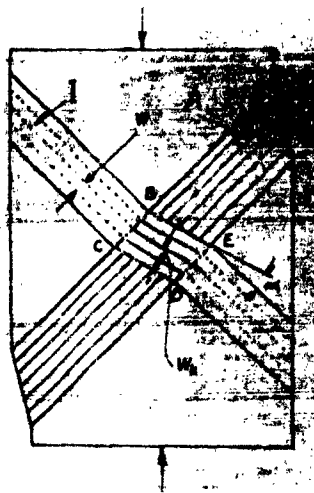


Fig. 7-21
FORMATION OF A KINK AT AN INTERSECTION OF
TWO CONJUGATE DISLOCATION BANDS



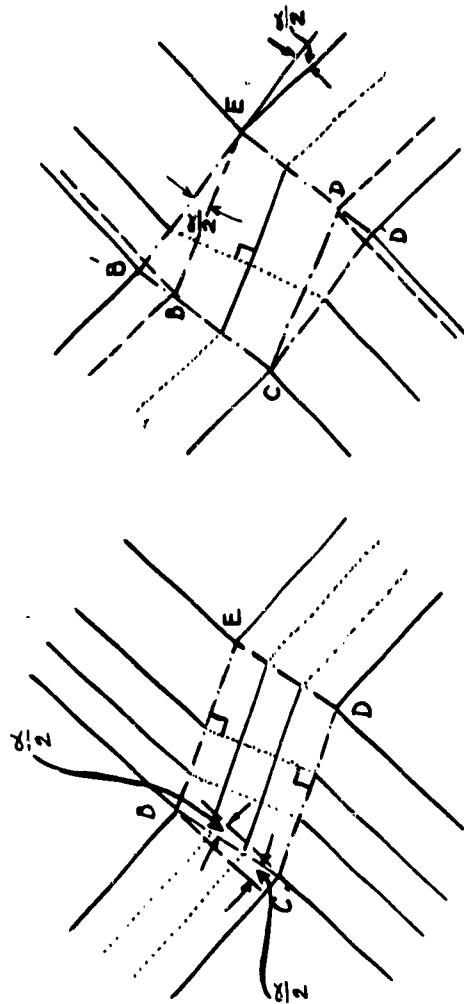
Fig. 7-22
LATTICE ROTATION AT INTERSECTIONS OF CONJUGATE
DISLOCATION BANDS; (a) Dislocation bands on cube face in
visible light, (b) Berg-Barrett X-ray back reflection from
(120) planes showing detail of same surface

primary extinction. However, the intersections are white on the x-ray photograph, showing that the lattice orientations in these areas have changed, as a rule, the reflections from the intersections can be found as dark patches close by, and, as mentioned above, the amount of displacement indicates lattice rotations of the order of 4 or 5 deg.

In Fig. 7-21, the dash-dotted lines represent the observed boundaries of the intersection of the active dislocation band with the inactive band. The solid lines inside the intersection and the dotted lines outside the intersection. The solid lines inside the intersection on the other hand represent the lattice planes of the kinked intersection, corresponding to dotted lines of the external portions of the inactive band. The lattice planes of the intersection which would correspond to the solid lines of the active band have not been drawn in, to avoid confusion, these lines would have appeared at right angles to the solid lines of the intersection. Evidently, one of the four dash-dotted boundaries of the intersection bisects the angle between corresponding crystallographic planes of the intersection and the rest of the crystal. All four of these boundaries are of a simple tilt nature -- being made up of edge dislocations of only one type. Therefore they grossly violate the fundamental condition of accommodation of a tilt boundary, and should give rise to large microscopic stresses. If W is the thickness of the glide lamellae of the inactive dislocation band, the corresponding lamellae of the kinked intersection would be compressed to the width $W_k = W \cos \alpha$, if the dash-dotted boundaries BC and DE are at right angles to the dotted lamellae as shown in Fig. 7-21. Similar reasoning with regard to the boundaries BE and CD would establish that the atomic planes of the intersection must be extended to a strain of $1/\cos \alpha$ in the BE

direction, if the boundaries BE and CD are parallel to the solid lines of the intersection. If elastic adjustments outside the kink were disregarded and Hooke's Law assumed valid, a high compressive stress would be present in the intersection parallel to the active band, and an equal tensile stress parallel to the conjugate inactive band.

These non-accommodation stresses could be cancelled in principle by additional kinking in the area of the band intersection. The boundaries BC and DE can be easily displaced into a position of full accommodation by additional growth of the active band, as shown in Fig. 7-23a. This would result in an offset of the boundaries of the active dislocation band across the inactive one. Such offsets are indeed observed in many intersections. Accommodations of the boundaries BE and CD would appear to be possible by the displacement of these boundaries into positions BE' and CD', accompanied by additional growth of the inactive band, as shown in Fig. 7-23b. The resulting dash-dotted boundaries of the intersection would now be fully accommodated, and the interior of the intersection would have undergone a rigid body rotation. Evidently the required displacement of the boundaries BE and CD into positions BE' and CD', as well as the additional growth of the inactive dislocation band for producing the accommodated configuration can be accomplished only by a shear stress opposite in sign to that applied. That is, the slip required for eliminating the non accommodation stresses of the boundaries BE and CD is opposed by the applied stress. Consequently, the kink stresses can not be eliminated so long as a given shear stress is maintained; with increasing deformation, they oppose further deformation increasingly, and so they are a contributory factor to strain hardening. The kink stresses are directly observable between crossed polarizers; and the rotation in the kinked intersection gives



(a)

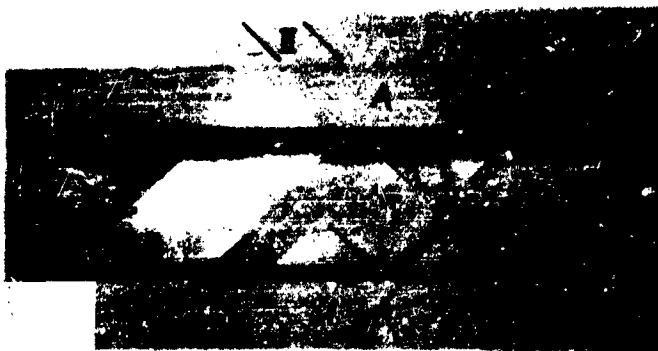
(b)

Fig. 7-23
POSSIBLE MODES OF ELIMINATION OF THE KINK NON-ACCOMMODATION
STRESSES AT AN INTERSECTION OF TWO DISLOCATION BANDS

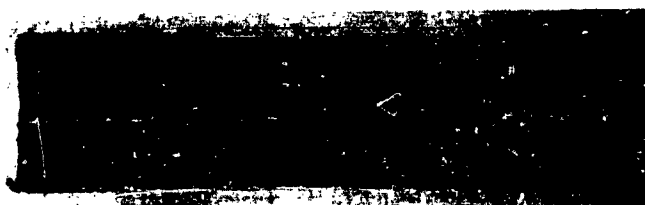
rise to microasterism. As is seen from Fig. 7-23b, the kink stresses can be relieved only by reversing the stress and producing opposite slip in one of the conjugate sets of slip bands. Opposite slip is promoted by the kink stresses, and its result is a reduction of the component of strain hardening due to the non-accommodation of intersection kinks. The first circumstance gives rise to a Bauschinger effect; the second to a permanent softening (lowering of the stress-strain curve) on strain reversal. Thus, the non-accommodation stresses play at least a contributory role in the reversal (Bauschinger, etc.) effects.

The internal stresses arising in the course of deformation may finally arrest slip in the active bands and re-start slip in the formerly inactive ones; in this case, kinking continues in the expanding area of intersection of the two bands by slip on the planes of the formerly active band. An example of this is seen in Fig. 7-24a to c. Figures 7-24a and 7-24b show the optical micrograph and the Berg-Barrett x-ray photograph* respectively, of an acid-polished crystal, which was provided with two opposite knife-edge indentations at A and A' to nucleate dislocation bands. The large intersection of the dislocation bands is shown at a higher magnification in Fig. 7-24c (optical micrograph). The intersection consists of three regions marked by arabic numerals. The center region I was formed by kinking of band II, while I was the active band widening by slip. Later, II became the active band, and the kinked regions 2 and 3 were added to the intersection. In

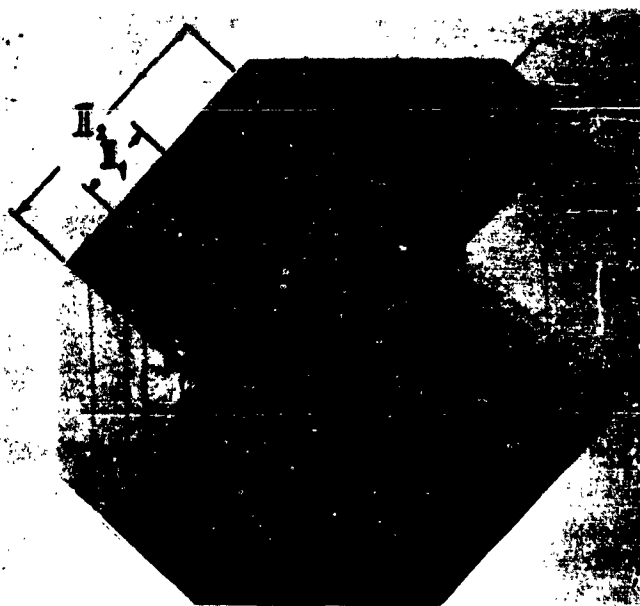
* The long $[100]$ edge (in the coordinate system of Fig. 7-25) was parallel to the x-ray plate and normal to the x-ray beam. The Bragg reflection is from the (021) planes.



(a) Cube face
in visible light;
Note crack at
point A



(b) Berg-Barrett
X-ray back re-
flection from (02T)
planes showing
twofold lattice
rotation at the
large intersection



(c) Enlarged view of
same intersection as
pointed out in B; Note
boundaries between
areas 1, 2, and 3

Fig. 7-24
TWOFOOLD LATTICE ROTATION AT AN INTERSECTION OF TWO
CONJUGATE DISLOCATION BANDS, AND CRACK NUCLEATION
BY SIMULTANEOUS ACTION OF TWO DISLOCATION BANDS

these regions, the lattice rotation is opposite to that in region 1: it is evident from Fig. 7-21a and 7-23 that the lattice rotation in the intersection kink is opposite if the other conjugate dislocation band operates under the same shear stress. This is confirmed by the imaging x-ray photograph Fig. 7-24b, where the reflection from the band intersection is split up into three spots. The spots representing regions 2 and 3 are displaced relatively to that from 1, and the corresponding rotations of the lattice are opposite. The kinking of regions 2 and 3 occurred suddenly, accompanied by a drastic change of the photoelastic pattern. In spite of the very high stresses indicated by the birefringence, no crack was formed.

C. Tension and Compression in the Kinks

Figure 7-21 shows that in a non-accommodated kinked (one in which the kink boundaries do not bisect the tilt angle of the neighboring lattices) intersection between an active and inactive dislocation band, there is a tensile stress in the direction of the operative slip planes of the kink, and a compressive stress normal to these planes. It was mentioned in the preceding section that the two stresses would be equal in magnitude if Hooke's Law remained valid and if the surroundings of the kink were indeformable. Under realistic conditions, the two stresses must be approximately equal if the intersecting bands are of equal width, so that their intersection is a square; in this case, a nearly plane state of stress exists, and the stress perpendicular to the plane of Fig. 7-21 is approximately zero.

The situation is very different, however, if the intersecting bands differ considerably in width. If the kinked (inactive) dislocation band (I in Fig. 7-21) is very narrow, the tensile stress in its direction (normal to the active band) is of the same order as if

the surrounding material were rigid. The compressive stress normal to the band (parallel to the active dislocation band A), however, is very small because the transverse expansion of the band is not hindered much by the elastic reaction of the embedding matrix. The stress at right angles to the plane of the figure (parallel to the line of intersection of the two bands) is then considerable, and it is tensile, because it arises by the hindering of the Poisson contraction corresponding to the tensile stress in the direction of the narrow kink band.

If the number of independently deforming regions in the crystal is large enough, widening can continue in only one set of dislocation bands without necessitating any widening of the conjugate set. In this case, the widening dislocation bands will eventually fuse into a homogeneously sheared domain in which the shear angle is about 5 deg the typical shear strain in a dislocation band. As this takes place, the kinked intersections of the widening bands with the inactive conjugate bands will join up and form long, straight, and highly birefringent kinked bands. This is illustrated in the sequence of Fig. 7-25. Several such birefringent kinked bands can be seen in Fig. 7-26, showing clearly the sharp bend in the segments of the narrow bands captured by the broad, active band. Although their mode of for-

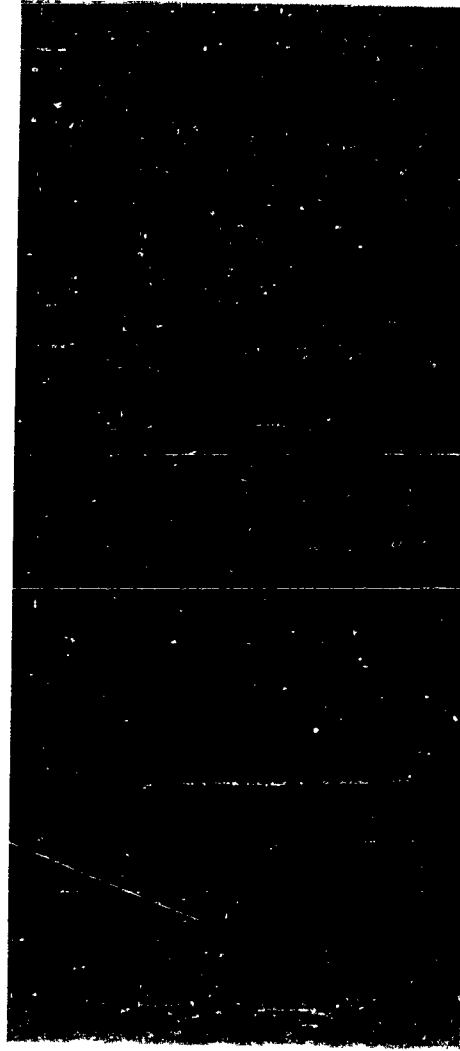


Fig. 7-25

FORMATION OF A KINK BAND OUT OF THE CAPTURED PORTION OF
THE NARROW DISLOCATION BAND UNDER THE IMPOSED SHEAR OF
THE BROADENING BAND



Fig. 7-26
BIREFRINGENT KINK BANDS (Direction of polarizer and analyzer axes were parallel to the cube edges, i.e., edges of the figure)

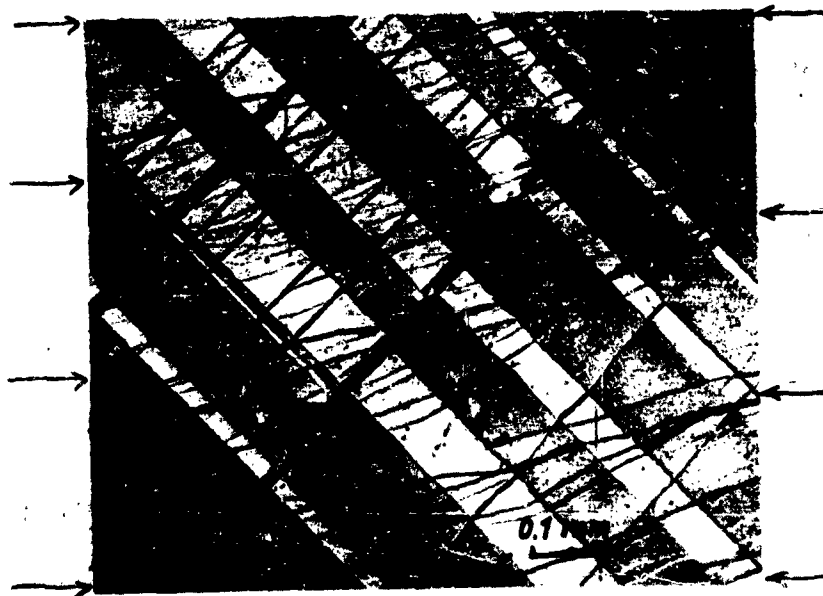


Fig. 7-27
CRACK FORMATION DUE TO SHARP VARIATION IN SHEAR ANGLE
IN DISLOCATION BANDS (Note the variation of widths in the wide bands)

mation differs from the familiar kink joints* in aluminum and zinc, they produce very similar effects.

The nature of the residual stress in the long kinked bands was investigated by the polarizing microscope and a Berek compensator. Let the system of coordinates be chosen so that the x-axis is perpendicular to the birefringent lamella L (Fig. 7-25), the y axis lies in the lamella and in the plane of the figure, and the z axis is perpendicular to the plane of the figure. It may be expected, then, that all stress components except σ_{xx} are different from zero. In the median plane of the band, however, only σ_{yy} , σ_{zz} , and σ_{yz} are likely to be considerable. Thus, a sighting along the cube direction (z direction) permits the measurement of σ_{yy} , while another sighting at right angles,

* If a crystal with potential slip lamellae, as shown in Fig. 7-28a, is extended, as in Fig. 7-28b, by slip only in region B without any deformation in regions A, the crystal is said to have kinked, and the interior of the band B is called a kink band^(7-24, 7-25). The result of kinking then is a lattice rotation of the slipped region inside a kink band relative to the unslipped part of the lattice. Starting with a crystal with slip lamellae oriented as shown in Fig. 7-29a, the same relative lattice rotation of Fig. 7-28b can be achieved by compression, so that slip occurs only in regions B (Fig. 7-29b). In this case, region B undergoes the lattice rotation, and therefore, are the kink bands, while region A, which does not deform, retains its original lattice orientation. In spite of this difference all long and narrow bands of both types have been commonly called kink bands. As this distinction between the two types of bands is not trivial, it is proposed that the name kink band apply only to the first type of band, while the second type of band in which the interior undergoes no deformation be called a kink joint.

along the face diagonal (y direction) would give σ_{zz} .

Although the first measurement is easily carried out in air, the second necessitates immersion of the crystal in methylene-iodide ($n = 1.738$) to overcome refraction effects.

Investigation of the sign of the residual normal stress in a large number of long kinked bands, in this manner, established that both σ_{yy} and σ_{zz} were tensile in all bands, regardless of the magnitude or sign of the average plastic strain in the crystal, that is, whether the crystal was extended or compressed. Assuming that the stress σ_{yy} in the platelet results principally from the uniform shear of the surrounding regions by slip on the (110) dodecahedral planes, which are initially perpendicular to the kinked band (refer to Fig. 7-25) and that the stress σ_{zz} is the plane strain stress preventing Poisson contractions, the relation between the measured relative retardation, $\Delta\eta$, and the stress, σ_{yy} , can be readily derived from the phenomenological theory of crystal photoelasticity. This gives,

$$\sigma_{yy} = - \frac{2}{\eta_0^3} \frac{\Delta\eta}{p_{44} s_{44}} \quad (7-1)$$

$$\sigma_{zz} = - \frac{2}{\eta_0^3} \frac{s_{12} \Delta\eta}{p_{44} s_{44} 11} \quad (7-2)$$

where $n_o = 1.736$ is the refractive index of the unstrained crystal, $p_{44} = -0.096$ is the strain optical constant for shear, and $s_{11} = 4.01 \times 10^{-13}$ sq cm per dyne, $s_{12} = -0.93 \times 10^{-13}$ sq cm per dyne, $s_{44} = 6.46 \times 10^{-13}$ sq cm per dyne are the three elastic compliances of MgO⁽⁷⁻²⁶⁾.

Measurements of $\Delta\eta$ in five different bands of a deformed MgO crystal* gave for σ_{yy} a value of 1.75×10^9 dyne per sq cm with negligible scatter (that is, $\Delta\eta$ was equal for all bands).

Reliable determinations of σ_{zz} were not possible because of the warping or bending of the platelets, which made it impossible to get a clear view through the band in the direction of the face diagonal. The sign of the stress was recognized only after cleaving the crystal in half along the axial (010) (Fig. 7-25) plane. This permitted a clear sight as well as a measurement of σ_{zz} . Since the cleavage resulted in considerable relaxation of the σ_{yy} stress component, however, no significance could be attached to the measurements of the magnitude of σ_{zz} .

D. Crack Formation in Magnesium Oxide Crystals

All compression experiments were terminated after the detection of the first crack. The method of detection relied

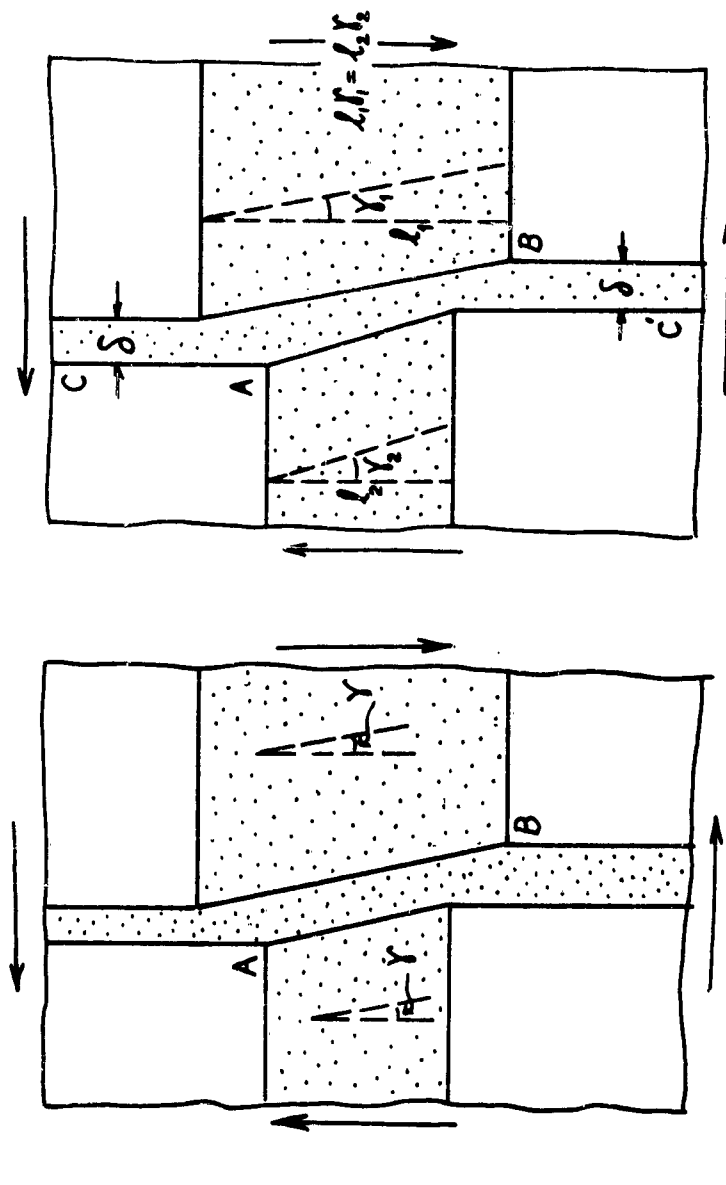
* As described in the early stages of deformation of MgO crystals, when dislocation bands broaden, there is no relation between the macroscopic average plastic strain and the strain inside dislocation bands, which is nearly constant. Thus, the kinked segments of the narrow dislocation bands will be subjected to a constant lattice rotation independent of the macroscopic plastic strain.

on visual observation of the specimen in polarized light. Cracks normal to the surface of observation would reveal themselves as a short dark line or spot in the highly colorful photoelastic pattern, while cracks parallel to the surface of observation could be detected by the formation of longitudinal crack channels appearing suddenly as bright streaks in the field of view

Although, as will become clear later, there is only one basic mechanism of crack formation, it is possible to classify the various types of observed cracks into three groups, examples of which will now be discussed in order of decreasing frequency of occurrence.

Cracks Resulting from Differences of Shear Strain in Segments of a Dislocation Band

It was commonly observed that widths of slip bands could change abruptly across an intersecting conjugate band, as shown in Fig. 7-27. As can be seen from this figure, this has lead to crack formation practically in every case. It is evident from the sketch of Fig. 7-28a that if the shear strain were the same on both sides of the band, cracks would have arisen in the corner B; in reality, however, they occurred at A. Examination of the density of etch pits in the bands in Fig. 7-29a and b, which are enlarged views of bands similar to those in Fig. 7-27 (observed in another crystal), show that the shear strain must be considerably smaller in the wider segment of the band. This was directly confirmed by measurement of the angle introduced into a conjugate row of dislocations intersecting the wide band. These measurements showed that the product of the width and the shear strain in each segment of the band was approximately constant. That is, the displacement between the two sides of the band is the same in all segments, wide or narrow; this is

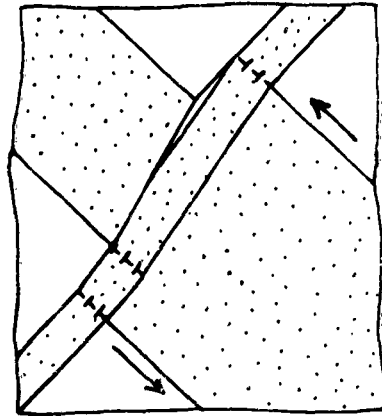


(a) Situation requiring very high normal stress across narrow band at point B, if shear angle was the same throughout the wide band

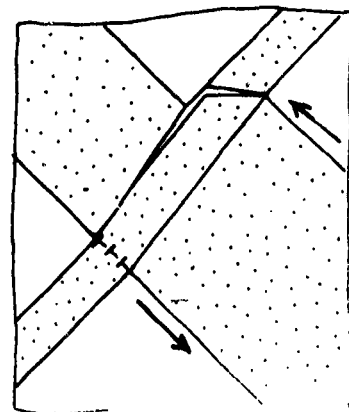
(b) Real situation with different shear angles for right and left hand sides of the wide band causing normal stresses across thin band at point A

Fig. 7-28

CRACK FORMATION RESULTING FROM VARIATION OF SHEAR ANGLE IN THE BROADENING BAND

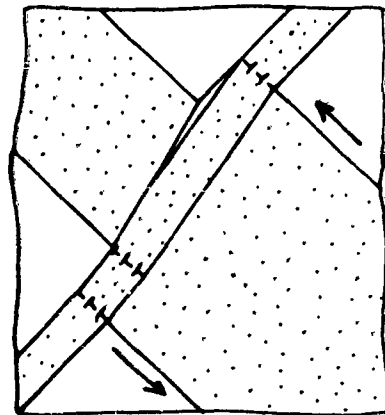


(a) Crack formation accompanied by the formation of a kink boundary to delineate the rotation in the quadrangle

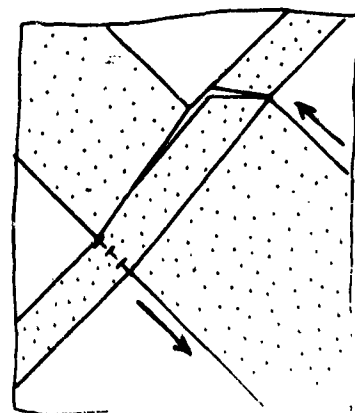


(b) Lattice rotation bounded by the extension of the crack

Fig. 7-29
CRACK FORMATION RESULTING FROM VARIATION
IN SHEAR STRAIN



(a) Crack formation accompanied by the formation of a kink boundary to delineate the rotation in the quadrangle



(b) Lattice rotation bounded by the extension of the crack

Fig. 7-29
CRACK FORMATION RESULTING FROM VARIATION
IN SHEAR STRAIN

indicated in Fig. 7-28b. The highest tensile stress must then occur at A where the crack is actually observed. After the formation of a crack at A, parallel to the edge of the intersecting band, it has a tendency to change its direction on further propagation by swining into the cleavage plane (100). This is seen in Fig. 7-29b.

Cracks Resulting from the Arrest of a Dislocation Band by an Obstacle Band

If an intersecting dislocation band is very wide, it does not suffer kinking in the entire area of intersection, but only in the neighborhood of the boundary that is "hit" by the intersected band. The dislocations of the intersected band penetrate into the intersecting band to a limited extent, and, in addition, kinking is also observed, the intensity of which decreases towards the interior of the intersecting band. This is seen in Fig. 7-30 where a very wide band (only a part of its width is visible in the photograph) intersects a number of narrower (vertical) bands. It is seen how the intensity of kinking in the wide band decreases with the distance from its boundary; light streaks where its boundary is hit by the intersected bands indicate higher dislocation densities, that is, a piling of dislocations of the intersected band. This is shown schematically in Fig. 7-31, in which the horizontal row indicates piled-up dislocations, and the two vertical rows kink dislocations; the size of the symbols \perp and T indicates the density of dislocations at a given point of the row.

The horizontal row of piled-up dislocations in Fig. 7-31 represents a low angle boundary. If the vertical band could stand at the angle demanded by this boundary, no macroscopic stress would arise. However, the band is embedded between bands of undeformed material which, by opposing its low-angle tilt, exert

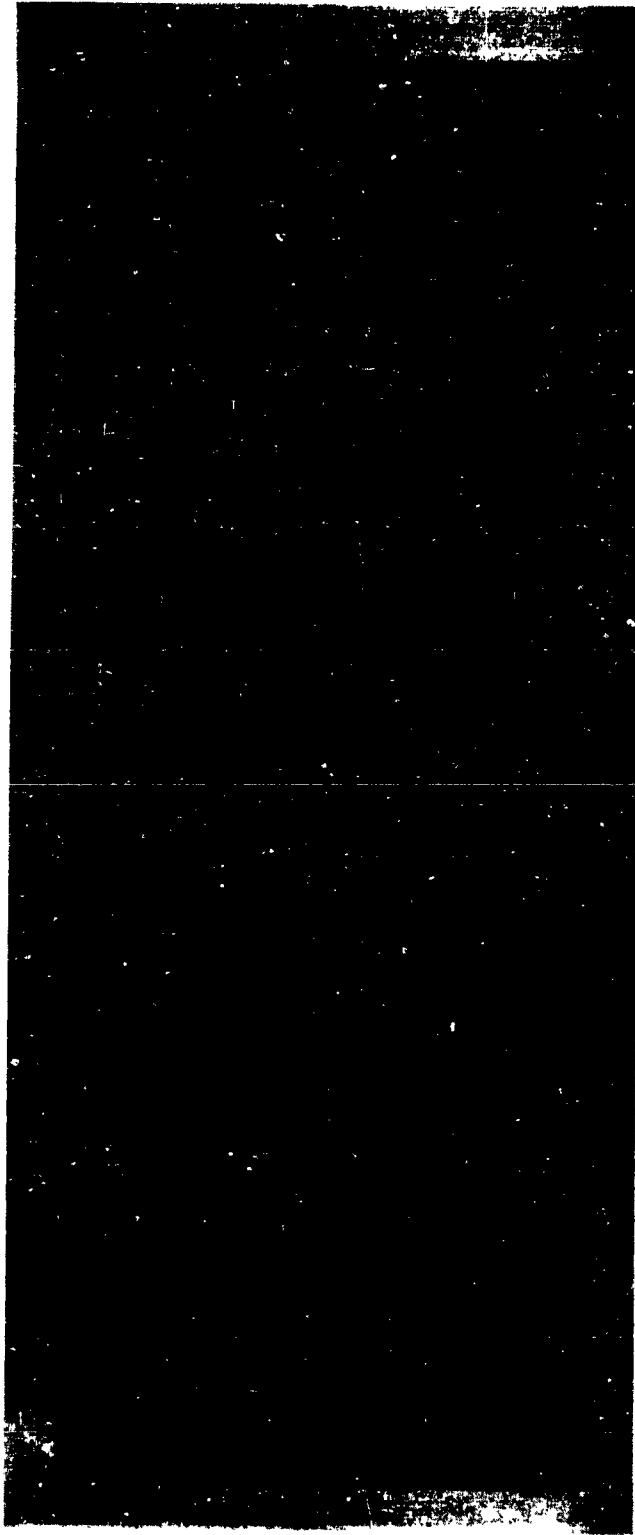


Fig. 7-30
CRACK FORMATION BY THE ARREST OF HOMOGENEOUS SHEAR IN
VERTICAL BANDS BY EXTENSIVE HOMOGENEOUSLY SHEARED REGION

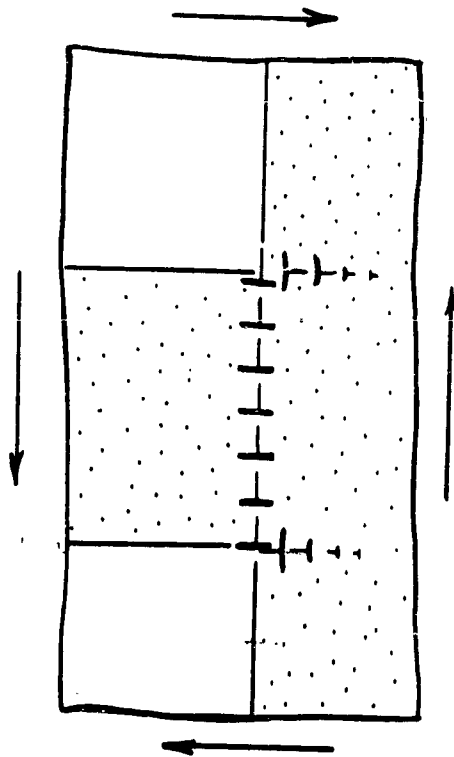


Fig. 7-31
 DISLOCATION ARRANGEMENTS SHOWING INCOMPLETE KINK
 ACCOMMODATION FOR THE ARRESTED BANDS OF FIG. 7-30

a bending moment on it. From the direction of the shear recognized in Fig. 7-30 (indicated by framing arrows), it follows that the tensile side of the bent vertical bands is where cracks are actually visible.

The crack across the third band from the right, which formed first, has been embedded into the horizontal band, which continued to widen before cracks formed across the remaining five bands. In the case of this band, the presence of the crack made the formation of a vertical kink boundary possible inside the growing horizontal band. Propagation of the primary cracks across cleavage planes at 45 deg, giving them the shape of a letter S, occurred later, before the crystal could be unloaded.

The third crack from the left and the one on the extreme right, after having propagated along the cleavage plane for some distance, have gone back again into the dodecahedral plane. This suggests that the presence of the many dislocations in the dodecahedral slip planes of the dislocation bands reduces the cohesion across that plane almost to the level of the cleavage plane. In addition, there is a decrease of cohesion in the kink planes, as has been observed by Mugge in 1898⁽⁷⁻²⁴⁾. In Fig. 7-30, the original cracks have arisen along (horizontal) kink planes; the photograph, however, does not indicate whether, in addition to the macroscopic bending stresses, a weakening of the kink planes (attributed by Mugge to microscopic bending stresses in the kink lamellae) was also present.

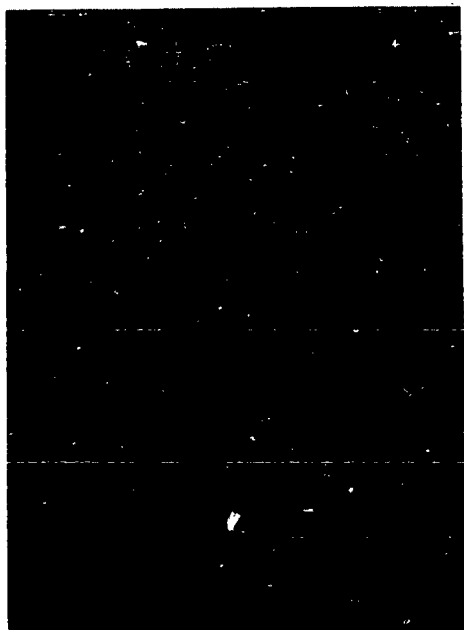
Stokes, Johnston, and Li^(7-9, 7-11, 7-27) were the first to observe cracks of the type seen in Fig. 7-11 in MgO; they attributed them to the cooperative action of a number of parallel dislocation pile-ups in the intersected dislocation band. Why this interpretation is unsatisfactory will be discussed below.

Cracks Resulting from the Simultaneous Widening of Two Conjugate Bands

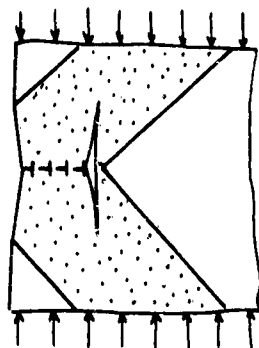
In highly polished crystals with very few slip sources a conjugate pair of dislocation bands can emanate from the same surface defect, and the widening of these bands may then represent the entire slip activity. An example of such simultaneously widening conjugate dislocation bands can be seen in Fig. 7-24a, as the two orthogonal bands II and III. This has led to the formation of a crack at point A, at the corner of the rigid-elastic wedge between the bands; the plane of the crack is parallel to the direction of compression. An enlarged view of this crack is seen in Fig. 7-32a. A low angle boundary is visible on the convex side of the crack, as indicated by an arrow, and sketched in Fig. 7-32b. This is also confirmed by the overlapped reflections in the Berg-Barrett photograph of Fig. 7-24a.

The mechanism of formation of this crack is shown in the sequence of Fig. 7-33. If the crystal is sectioned along a plane bisecting the angle between the two dislocation bands and is then allowed to deform freely inside the dislocation bands, the two parts will distort as shown in Fig. 7-33a. As the penetration of the dislocations of one band into the conjugate band is physically not permitted, the slanted surfaces of the cut faces will be bent outward when the two halves are joined together. This would lead to the observed crack, as shown in Fig. 7-33b. Cracks of this type have apparently been observed first by Reusch in 1867⁽⁷⁻²⁸⁾ in compressed rock salt crystals.

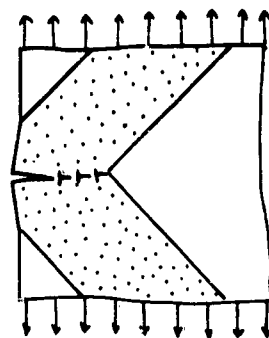
If compression is continued after the crack has formed, spalling fracture invariably results. An example is shown in Fig. 7-34.



(a) Enlarged region of point A in crystal of Fig. 7-24 a



(b) Sketch of terminated tilt boundary arising from the homogeneous shear of the wide bands; Note overlap on the Berg-Barrett reflection of Fig. 7-24 b



(c) Same mechanism leading to crack formation normal to stress direction in tension

Fig. 7-32
CRACK FORMATION BY THE SIMULTANEOUS BROADENING OF
TWO CONJUGATE DISLOCATION BANDS

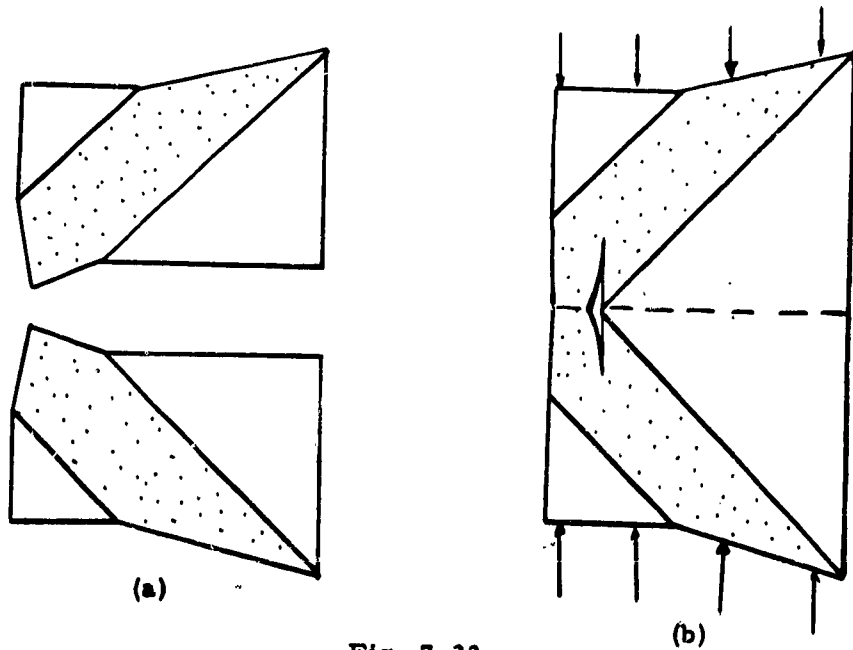


Fig. 7-33

MODEL OF CRACK FORMATION FOR THE COMPRESSION
CASE OF FIG. 7-32 a and b



Fig. 7-34

SPALLING FRACTURE IN A COMPRESSED CRYSTAL RESULTING
FROM A CRACK OF THE KIND SHOWN IN FIG. 7-32 a and b

If the crystal has been pulled in tension instead, evidently the distortions of the sectioned crystal would be as shown in Fig. 7-35a. If these halves are put together, large tensile stresses are required to bring the oppositely slanted surfaces together. This would then lead to the formation of a crack starting from the surface. The low angle boundary which would form in this case is shown in Fig. 7-32c. A crack of this type has been reported by Parker⁽⁷⁻²⁹⁾.

The crack shown in Fig. 7-36 is a rare hybrid. Here the shear strain is the same in regions A and B of the growing wide band on opposite sides of the obstacle band, indicated with an arrow, and the additional shear displacement of the wider portion A of the growing band is compensated by a kind of "stitching" shear in region C on the slip planes conjugate to those of the wide band. The overhand of part A of the wide band has been accommodated by formation of a kink boundary in the narrow obstacle band. This has transferred the highly stressed region to the other side of the narrow obstacle band. This crack shows a striking similarity to a type of crack observed in kinked zinc crystals by Gilman⁽⁷⁻¹⁵⁾.

E. Discussion of Results

a. Deformation

Magnesium Oxide, in common with other ionic crystals of the rock salt structure, deforms by glide primarily on dodecahedral planes in the direction of the face diagonal. In the commercially obtainable MgO crystals, the grown-in dislocations are firmly anchored to the lattice by, most likely, impurities.

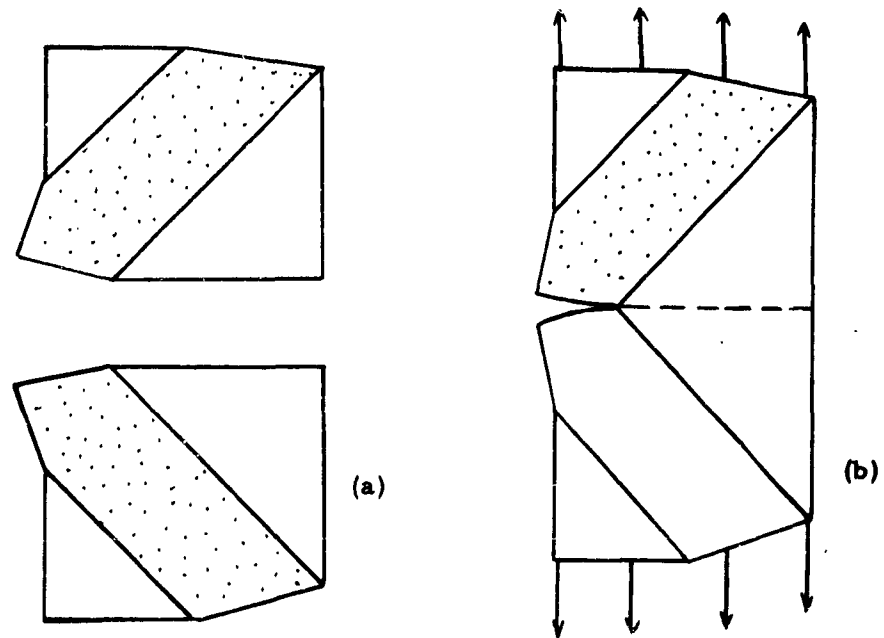


Fig. 7-35

MODEL OF CRACK FORMATION FOR THE TENSION CASE OF FIG. 7-32c

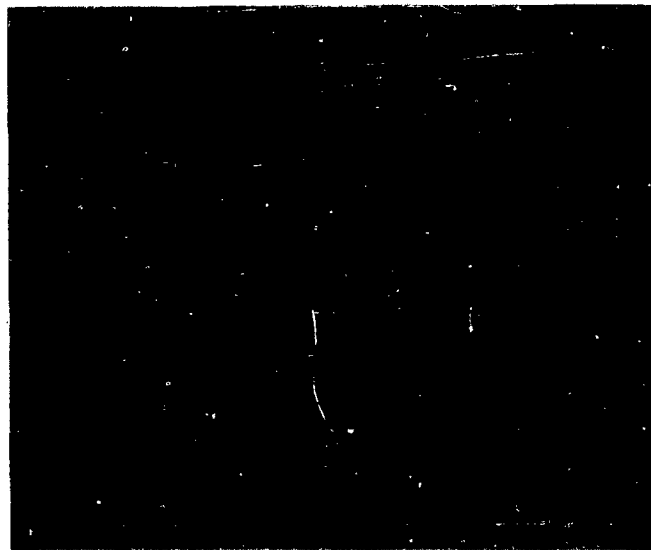


Fig. 7-36

CRACK FORMATION BY INHOMOGENOUS DISTRIBUTION OF SHEAR

This necessitates the generation of fresh slip dislocations at the edges of dislocation bands by a process of dislocation sprouting (multiplication), qualitatively described by Johnston and Gilman⁽⁷⁻³⁰⁾ for LiF crystals*.

The dislocation density, ρ , inside unobstructed portions of dislocation bands was determined by direct count and found to be 10^8 lines per sq cm on the average. As the distribution of pits inside a band is quite isotropic, it was assumed that the spacing of slip lines in a band is

$$w = \rho^{-1/2} = 10^{-4} \text{ cm} = 1\mu$$

* Although the conditions for dislocation sprouting (multiplication) are still not fully understood, a minimum requirement for it is that there exist highly stressed and normally less favored cross slip planes connecting the preferred slip planes connecting the preferred slip planes. In the rock salt structure, both the cube planes and octahedral planes fulfill the requirement. In most of the commonly performed experiments of extension and compression along a cube direction, however, all cube planes are unstressed and can, therefore, not serve as cross slip planes. Evidently, thermal activation can not alter this conclusion.

It is possible that the chief requirement for dislocation sprouting by the double cross slip mechanism is a critical resolved shear stress on the octahedral plane. The fact that this necessary stress may only be achieved at stress levels where the dislocations move with an appreciable velocity on the dodecahedral planes would also explain the apparent velocity threshold observed by Gilman and Johnston⁽⁷⁻³¹⁾.

To produce the observed shear strain γ of about 0.1 radians in a slip band, it would be necessary that, on the average, $\eta = W\gamma/b \approx 350$ dislocations move through the crystal in every active slip plane inside a dislocation band. Once this occurs, the active slip plane hardens, and no further slip takes place in it by the applied stress alone, as long as undeformed regions exist in the crystal into which slip can expand. As was discussed above, further slip can be enforced locally inside an already hardened band by the shear stress concentration of a widening conjugate dislocation band, which leads to kinking at the intersection.

The mean free path λ of a glide dislocation was calculated from the relation $\lambda = V/b\rho$, where γ is the shear strain inside a dislocation band, and b is the magnitude of the Burgers vector. This was found to be 1.2×10^{-2} cm.

From the above results, it must be concluded that a freshly released dislocation glides, on the average, a distance of 10^{-2} cm, where it finds an obstacle which it can not overcome, and its useful life is thus terminated. This simple life history leads to a number of important conclusions (1) the inactivation rate of dislocations is equal to the multiplication rate, (2) the number of dislocations in motion at any one time is constant and may differ only if the rate of straining or the temperature of straining is varied, (3) the obstacles stopping the motion of dislocations do not preexist, but are manufactured by the dislocation itself, possibly in the process of cross slipping into an octahedral plane. Although the initial net spacing ($\rho_0^{-1/2} = 10^{-2}$ cm) is about equal to the mean free path of a dislocation, this can not serve as an obstacle, as it had to be overcome in the first place. This sequence of events in MgO is very similar to that in the easy glide deformation of

copper reported by Young⁽⁷⁻³²⁾, and appears to be representative of all ductile crystals in which single slip is possible.

Stowell⁽⁷⁻³³⁾ has studied "kink bands" in extended crystals of AgCl and concluded that the thin and straight birefringent bands were platelets of crystal composed of dodecahedral planes that were stressed only in their own plane. For small average plastic strains, he found these platelets in residual compression in the direction of the face diagonal, and in residual tension along the cube edge. For large plastic strains, the sign of both of these stresses was reversed. To account for these observations, he suggested second order effects due largely to the core of the dislocations.

In MgO, the widening of active dislocation bands of a deforming region, gradually extended all kinked intersections with inactive orthogonal dislocation bands into birefringent kinked bands. The two residual principal normal strains ϵ_{yy} and ϵ_{zz} were found to be tensile, regardless of the sign or magnitude of the average plastic strain.

A simple explanation can be given for the observed residual strains in both MgO as well as in AgCl, without straining the argument. With reference to the coordinate axes of Fig. 7-25, consider a plastically undeformable platelet embedded at 45 deg to the direction of extension in a matrix which is to undergo a homogeneous plastic strain ϵ . Specifically, we consider a (110) platelet which has hardened by having undergone slip on (110) planes and that the resulting dislocation density on these planes strongly inhibits plastic deformation on any other intersecting slip plane. This platelet is inserted in a cubic crystal with (010) and (001) side faces, pulled in the $[100]$ direction.

If the plastic deformation in the matrix is achieved by slip on (110) planes in the $[110]$ direction, the (110) platelet will be subjected to a tensile strain $\epsilon_{yy} = \epsilon^2$ in its plane. Such plastic deformation of the matrix will create plane strain conditions, so that the elastic contraction of the platelet will be prevented by the matrix and, disregarding end effects, ϵ_{zz} in the platelet would be zero. Thus, a relative retardation measurement will give positive residual strain values for both ϵ_{zz} and ϵ_{yy} (relative to ϵ_{xx}). In MgO, the strain in the matrix is inhomogeneous; it occurs only in widening dislocation bands where it is constant and of magnitude of $\gamma = 0.1$ radians. Hence the strains $\epsilon_{yy} = \gamma^2/2$ and $\epsilon_{zz} = 0$ in the portion of the platelet captured inside a widening dislocation band, and zero outside. As the slip planes and slip directions are initially normal to the platelet, the same state of residual elastic strains would be produced in the platelet, regardless of whether the crystal is extended or compressed.

If the plastic deformation in the matrix is achieved by slip on at least two systems, such as (110) 110 and (101) $[101]$, plastic contractions in the direction (Fig. 7-25) will be possible. For the most ideal case, if the matrix deforms plastically as a structureless material with uniform lateral plastic contractions, the embedded platelet will be subjected to strains

$$\epsilon_{yy} = \frac{1}{4}\epsilon \quad \therefore \quad \epsilon_{zz} = -\frac{1}{2}\epsilon$$

by the deforming matrix. This latter case is that of AgCl, at large average plastic strains.

If the plastic deformation in the matrix is achieved by slip on (110) planes in the $[110]$ direction, the (110) platelet will be subjected to a tensile strain $\epsilon_{yy} = \epsilon^2$ in its plane. Such plastic deformation of the matrix will create plane strain conditions, so that the elastic contraction of the platelet will be prevented by the matrix and, disregarding end effects, ϵ_{zz} in the platelet would be zero. Thus, a relative retardation measurement will give positive residual strain values for both ϵ_{zz} and ϵ_{yy} (relative to ϵ_{xx}). In MgO, the strain in the matrix is inhomogeneous; it occurs only in widening dislocation bands where it is constant and of magnitude of $\gamma = 0.1$ radians. Hence the strains $\epsilon_{yy} = \gamma^2/2$ and $\epsilon_{zz} = 0$ in the portion of the platelet captured inside a widening dislocation band, and zero outside. As the slip planes and slip directions are initially normal to the platelet, the same state of residual elastic strains would be produced in the platelet, regardless of whether the crystal is extended or compressed.

If the plastic deformation in the matrix is achieved by slip on at least two systems, such as (110) 110 and (101) $[101]$, plastic contractions in the direction (Fig. 7-25) will be possible. For the most ideal case, if the matrix deforms plastically as a structureless material with uniform lateral plastic contractions, the embedded platelet will be subjected to strains

$$\epsilon_{yy} = \frac{1}{4} \epsilon \quad \therefore \quad \epsilon_{zz} = -\frac{1}{2} \epsilon$$

by the deforming matrix. This latter case is that of AgCl, at large average plastic strains.

A comparison of these estimated magnitudes with the previously given measured values for MgO and those of Stowell on AgCl shows that in reality, the (110) platelet permits the passage of a limited number of dislocations through it on planes other than the (110) slip planes.

Stowell's initial compressive σ_{yy} and tensile σ_{zz} stresses and their reversal can not be explained as satisfactorily. In any event, the core effects, which he proposes to account for the compressive residual stresses (his Read effect) would not appear to bear any relation to the stresses inside the birefringent bands. If it was to be otherwise, all low angle tilt boundaries should produce strong birefringent effects in rock salt crystals, which is certainly not the case.

As was mentioned, Stowell's thin, straight, and birefringent bands should more properly be called kink joints, as they differ fundamentally from the conventional kink bands observed in NaCl by Brilliantow and Obreimow⁽⁷⁻³³⁾ and in KCl by Schutze⁽⁷⁻³⁴⁾. The kinked bands resulting from elongated kinked intersections of two dislocation bands in MgO are a limiting case of conventional kink bands. In them slip takes place on slip planes parallel to the long boundaries. When the widening dislocation bands sweep through the whole width of the crystal, and the kinked intersection with the captured inactive orthogonal band goes completely through the crystal, the short kink boundaries would leave the crystal, and the kinked bands would be indistinguishable from the kink joints. It is for this reason that the narrow birefringent bands in MgO have been named kinked bands in preference to kink bands.

The lattice rotation at dislocation band intersections, resulting from the conversion of slip in the active dislocation band into kinking in the inactive one, has the direction shown by x-ray asterism of the microscopic type. The resulting configuration is in principle identical to the one suggested by Burgers⁽⁷⁻³⁵⁾. Asterism of this type differs fundamentally from the macroscopic asterism which results from the bending of the slip lamellae⁽⁷⁻³⁶⁾.

b. Crack Initiation at Dislocation Band Intersections

The uniform shear strain inside the dislocation bands in MgO and their lateral growth makes their behavior strikingly similar to that of twin bands in b c c or h c p metals. Thus, these observations reported here do not only clarify the belabored subject of crack formation in MgO single crystals, but also contribute to the understanding of crack formation by intersection of deformation twins in b c c metal single crystals, and the origin of the often very puzzling spalling fractures occurring in compression.

Previous attempts to explain crack nucleation have largely relied on the cooperative effect of a long train of edge dislocations, such as the Eshelby, Frank, Nabarro⁽⁷⁻³⁷⁾ dislocation pile up. Stroh's analysis^(7-6, 7-7) of the conditions for crack nucleation by this mechanism established that about 1,000*

* The number of necessary dislocations in the pile up for the nucleation of a crack at its tip by the Zener mechanism is roughly equal to the ratio of the Young's modulus to the yield stress in tension.

edge dislocations on either one or several closely spaced active slip planes have to be arrested by an impenetrable obstacle to form a stable cleavage crack. These predictions have been confirmed in experiments by Westwood⁽⁷⁻⁸⁾ and Stokes, Johnston and Li⁽⁷⁻³⁸⁾ on MgO bicrystals, where the edge dislocations are made to pile up at the grain boundary. In single crystals, no such strong obstacles exist. A number of intricate dislocation reactions have, therefore, been proposed to furnish sessile obstacle dislocations strong enough to block the motion of the large number of required cooperating slip dislocations. Stroh⁽⁷⁻³⁹⁾ has argued that such efforts can not be fruitful, as no single sessile dislocation can support more than a small fraction of these required slip dislocations.

In MgO single crystals, similar conditions hold, that is, obstacles such as conjugate dislocation bands are not completely impenetrable. A considerable number of the obstructed dislocations of a blocked band actually penetrate partially into the conjugate obstacle band. This makes it impossible for very long dislocation pile-ups to form. The stress amplification is, therefore, insufficient, and no crack forms. This result follows from the earlier statement that, on the average, 350 dislocations move through any active slip plane inside a band. Thus, if the cause of the fracture was to be a Zener crack, dislocation bands of only three rows of pits would have been sufficient to nucleate a crack.

The evidence presented above indicates that cracks in MgO are nucleated by the stresses of a finite tilt boundary, formed in the process of widening of the dislocation bands. We now discuss the cases presented in Subsection D in somewhat greater detail.

Consider first the formation of cracks resulting from an inhomogeneous shear strain inside a dislocation band, as in Fig. 7-29a. This intersection, which is also sketched out in Fig. 7-28a and 7-28b, is made up of a dislocation arrangement of the type shown in Fig. 7-37a.

The total number of dislocations is the same for the two segments AC and BD. Thus, no long range stress field will result from the arrangement. There will, however, be local stress fields of range l_2 or l_1 , resulting from the inhomogeneous arrangement of dislocations, which leaves regions such as AE and CF free of dislocations. We note that the arrangement of Fig. 7-37a is equivalent to the sum of two dislocation arrangements of Fig. 7-37b and 7-37c. The homogeneous arrangement of Fig. 7-37b represents an included grain, free of stresses of range longer than W , the spacing of slip lines (dislocation rows) inside a band*. The arrangement of Figure 18c, however, will have stresses of a range of order l_2 . The tensile stress acting across the boundary at a distance c from point A, can be obtained by summing the stress fields of the individual edge dislocations. It is to first order quantities,

$$\sigma = \frac{\gamma_2 \mu}{2 \pi (1 - \nu)} \ln \frac{l_2}{c} \quad (7-3)$$

where μ is the average shear modulus and l_2 the width of the narrow portion of the band. These stresses can be relieved by a crack of the type shown in Fig. 10a.

* We consider here, for simplicity, the boundaries fully accommodated, that is, they are symmetrically situated with respect to the lattice on both sides. This will not be the case in MgO, where kink non-accommodation stresses are always present. As will be shown in the Appendix, such kink non-accommodation stresses can not lead to the formation of cracks on the boundaries of the intersection.

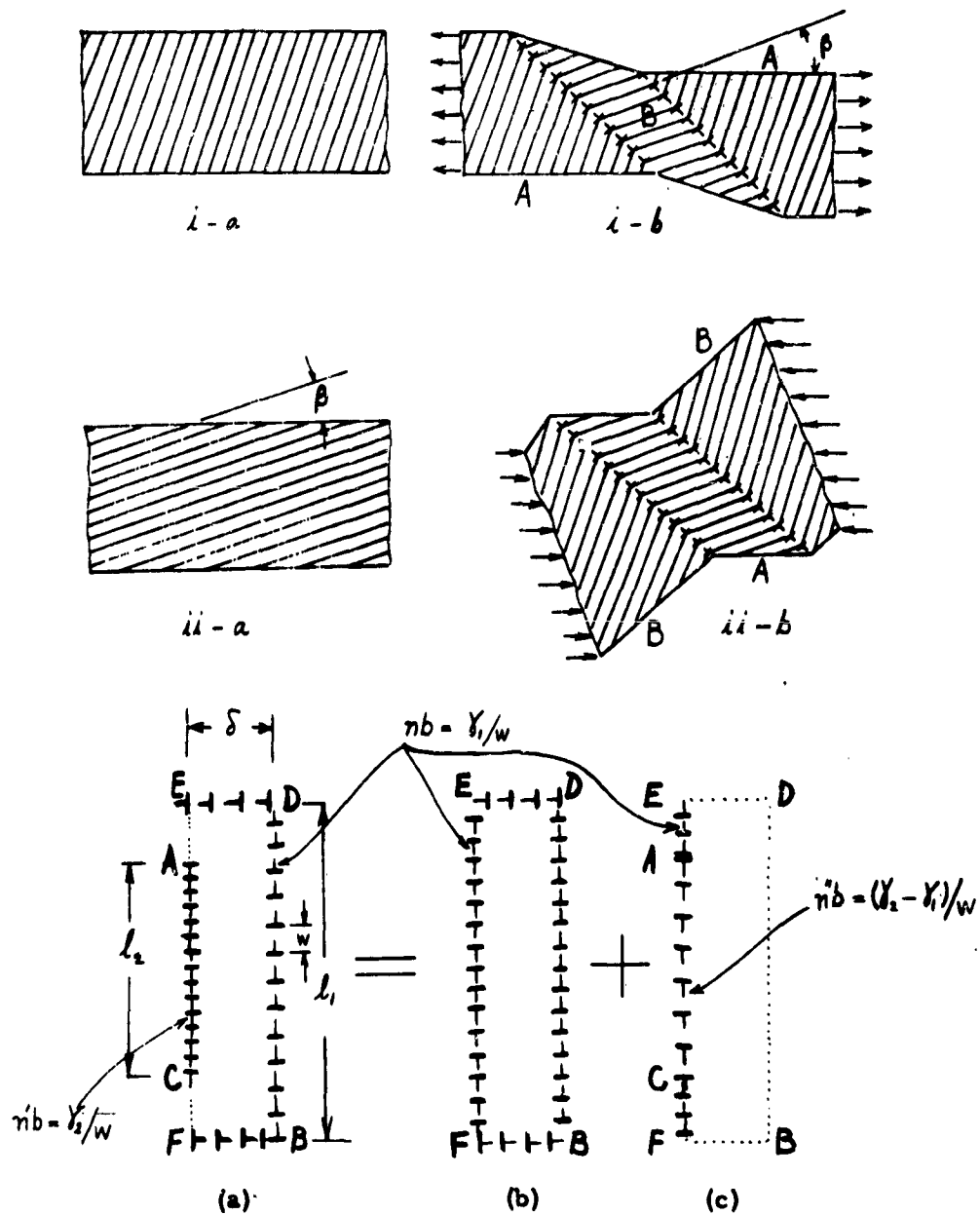


Fig. 7-37

ANALYSIS OF STRESSES PRESENT IN THE CASE OF CRACK FORMATION BY THE MECHANISM ILLUSTRATED IN FIG. 7-29 a

The case of Fig. 11 is far simpler. Here, a horizontal tilt boundary has formed, as shown in Fig. 12. Such a boundary will produce a high tensile stress acting across the plane of the boundary at A. This tensile stress, at a distance c from point A, can be obtained again by the summation of the stresses of individual dislocations in the boundary. It is,

$$\sigma = \frac{\gamma\mu}{2\pi(1-\nu)} \ln \frac{1}{c} \quad (7-4)$$

This stress can be relieved by the type of crack shown in Fig. 7-30.

The case of Fig. 7-32 is no different from the two discussed above. Depending upon whether the superimposed stress is tensile or compressive, there appear to be two possibilities for relieving the local stresses of such a boundary. The tensile stress acting across the boundary at a distance c from the surface in Fig. 7-32c is identical to that given in Eq. (7-4)*.

The tensile stress acting at a distance c from the end of the boundary and across a plane normal to the boundary, as in the compression case of Fig. 7-32b, would be,

$$\sigma = \frac{\gamma\mu}{2(1-\nu)} \ln \frac{\sqrt{2}}{e c} \quad (7-5)$$

If these tensile stresses are to lead to the formation of a stable crack, they would have to equal or exceed, for all distances c , the nominal tensile stress necessary to hold the elliptical crack of half length c in unstable equilibrium, that is,

$$\frac{\gamma \mu}{2 \pi (1-\nu)} \ln \frac{1}{c} \gg \frac{\sigma_c}{2} \sqrt{\frac{a}{2c}} \quad (7-6)$$

where σ_c is the ideal tensile cohesion and $a/2$ is the interionic distance between Mg^{++} and O^{--} .

Since the curvature of the stress field (as a function of c) on the left hand side of the inequality (7-6) is always smaller than that on the right hand side, it is sufficient to equate the stress fields at the point $c = a/2$. This gives for the critical width of the dislocation band

$$l = \frac{a}{2} \exp \left(\frac{2\pi (1-\nu^2) \sigma_c}{E \gamma} \right) \quad (7-7)$$

where E is Young's modulus. Accurate values for the ideal tensile cohesion for crystalline materials are not available. They are usually estimated from crude models, which can not claim any accuracy. As the band width is very sensitively dependent upon the ratio σ_c/E , an accurate evaluation of Eq. (7-7) is not possible. For instance, if σ_c/E is taken in the range $\frac{1}{10} - \frac{1}{\pi}$ the critical band width would vary between $6 \cdot 10^{-6}$ cm and 10 cm. This very strong dependence of the width of the band on the ratio σ_c/E explains why experimentally a large variation is observed in the width of the bands, which in one mode or other have resulted in the formation of cracks. This is presumable due to small local variations in the effective ideal strength, σ_c .

As was mentioned earlier, Fig. 7-29 and 7-30 show

* We have neglected here the effect of the free surface, which would reduce the stresses by a factor of order unity.

that in nearly every case there is some dissipation of the stress field of the finite tilt boundary by incomplete kinking in the obstructing band. The two diffuse kink boundaries inside the intersection of Fig. 7-29a and the streaks in the heavily slipped region at the extensions of the arrested bands are very clear cases. As soon in Fig. 7-31, the incomplete kink accommodation attempts to taper off the tilt boundary by gradually decreasing kinking in the obstructing region. When full kink accommodation is possible in the obstructing band, such as the case of Fig. 7-24, no significant long range tensile stresses will remain, and a crack will not be nucleated. In the case of (Fig. 7-22) kink accommodation is crystallographically not possible, and fracture will invariably result.

There are thus two effects competing against each other: formation of a finite tilt boundary with high accompanying tensile stresses, and kink accommodation tending to eliminate the high stresses of the tilt boundary.

An immediate extension of these observations would be to the case of crack nucleation by twin band intersections. Crack nucleation resulting from the obstruction of one twin by the boundary or another is especially common in body-centered cubic crystals, and has been observed by many investigators. The twinning shear strain $= 1/2$ in a b c c lattice is very large in comparison with the shear strain in a dislocation band in MgO. It would, therefore, lead to the formation of a crack almost as soon as the path of the impinging twin is obstructed by the primary twin. Examination of twin intersections in b c c crystals has shown that, although cracks are commonly observed, uncracked intersections are equally, if not more, common. This is due to the possibility of dissipating the shear strain concentration of the impinging twin by an accommodation mechanism. The untwinning

of a portion of the obstructing twin by the impinging twin can lead to full accommodation in some cases where the twin direction of the two twins are parallel. This case which has been observed first by Smith, Dee, and Young⁽⁷⁻⁴⁰⁾ in meteoric iron, is a trivial case, as the shear displacement of the impinging twin has no component normal to the boundary of the obstructing twin and would, therefore, not tend to produce a tension crack. A second, more common, and more effective mechanism of accommodation would appear to be the kinking of the portion of the obstructing twin band subjected to the concentrated shear strain of the impinging twin. The formation of another twin or a slip band on the opposite side of the kinked obstructing twin, would then eliminate nearly all the strain concentration. As the (112) composition plane of the twins in b c c crystals is also a good slip plane, kinking of the interior of a twin should be a distinct possibility. Hull⁽⁷⁻¹⁹⁾ has observed unambiguously some kinked twin intersections of this type in silicon iron.

It is attractive to offer the mechanism of crack formation in MgO also for the formation of an internal crack in the tension experiment. Consider the necked portion of a plane strain specimen shown in Fig. 7-38a. Further deformation might be expected to concentrate in the two slip bands approximately at 45 deg to the tensile axis. As the shear stress on the sides of the bands facing the constriction of the neck will be higher than on the sides which face the shoulders, the bands will preferentially widen by consuming the approximately right triangular blocks at the constriction. If the deformation of one band can not fully go through its conjugate, diffuse tilt boundaries are bound to form as shown in Fig. 7-38b. The stresses resulting from such

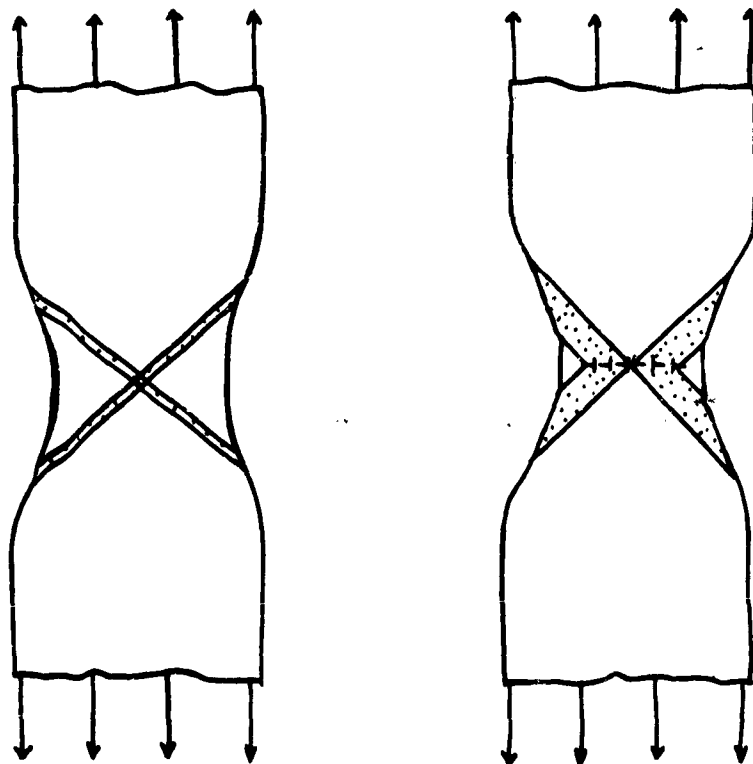


Fig. 7-38

**PROPOSED MECHANISM OF CRACK FORMATION IN THE PLANE
STRAIN TENSION EXPERIMENT**

diffuse boundaries may then reach very high values at the center of the neck and lead to the nucleation of a transverse crack. Naturally, if the material is impure, and highly inhomogeneous, holes may open up at the neck before any genuine crack nucleation mechanism can become active. On the other hand, if the deformation bands remain essentially transparent to each other, no diffuse tilt boundaries will form, and the specimen will continue to thin to a knife edge and rupture.

4. APPENDIX

The kink non-accommodation stresses at an intersection of two dislocation bands, such as those in Fig. 7-21 and 7-23, lead to stresses, which are not of a nature to cause crack formation at the boundaries of the intersection. We show this by a method consisting of sectioning, freely deforming, and sticking together blocks of the crystal in a fashion used by Eshelby⁽⁷⁻³⁷⁾ in the treatment of inhomogeneities.

Considering the case of Fig. 7-21, we first let the crystal plastically shear homogeneously inside the narrow band of width δ until the maximum shear strain γ is attained, as in Fig. 7-39a. Then, as shown in Fig. 7-39b, we cut out and remove from the narrow band, a parallelepiped segment with corner angles, $\gamma/2$, and length, l , equal to the width of the wide band to be introduced in the vertical direction. Then, as shown in Fig. 7-39c, we let the crystal with the hole plastically shear homogeneously inside the wide band until again the maximum shear angle is attained. To reintroduce the cut out parallelepiped block back into the hole, which has now been distorted into a mirror image shape, it is necessary: a) that

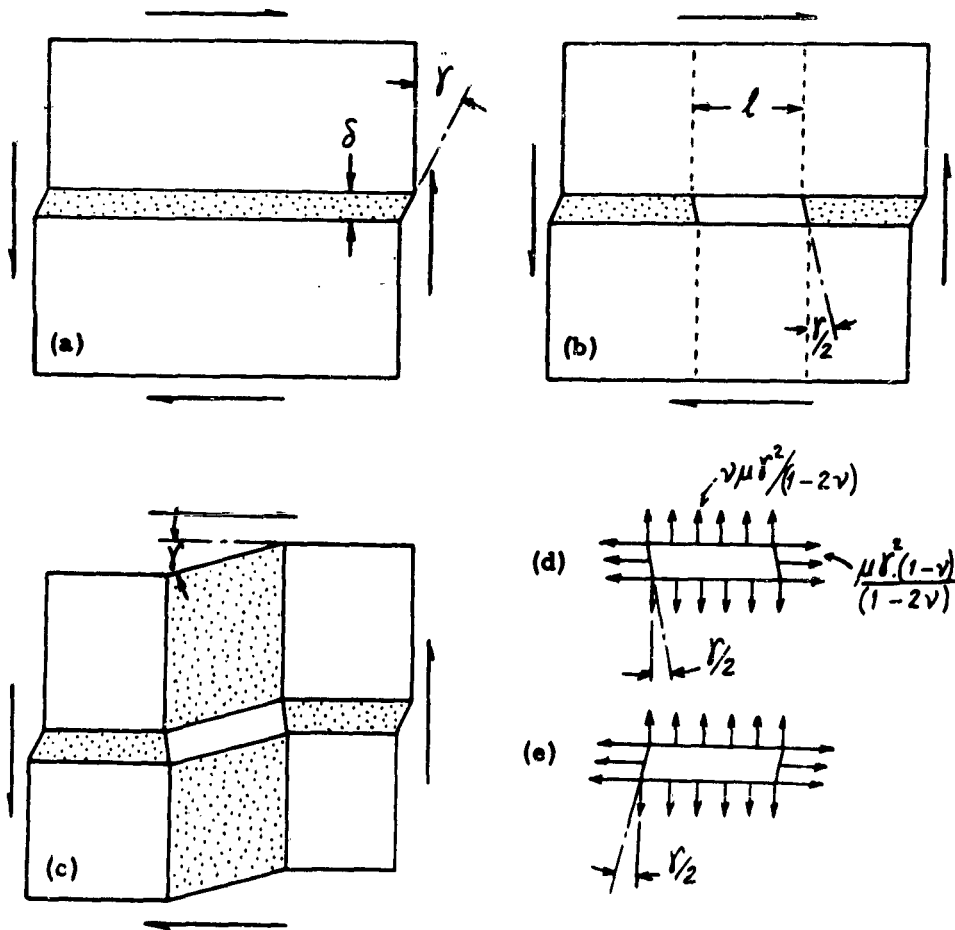


Fig. 7-39
 NORMAL STRESSES ARISING IN THE QUADRANGLE OF AN INTER-
 SECTION, WHICH IS DUE TO LATTICE ROTATION

we apply normal surface stresses $\frac{\mu\gamma^2(1-\nu)}{1-2\nu}$ and $\frac{2\mu}{1-2\nu}\gamma^2$ on the short and long faces respectively, and b) plastically shear the strip homogeneously along planes parallel to the long edge by an angle of γ , so that the parallelepiped is transformed into its mirror image. Note that this is the shear, which is permitted physically inside the narrow band. To complete the process, we add volume forces of $-\frac{\mu\gamma^2(1-\nu)}{1-2\nu}$ and $-\frac{2\mu}{1-2\nu}\gamma^2$ to the crystal along the short and long faces of the parallelogram. The calculation of the stresses at any point inside the crystal can now be performed by straight forward superposition of distributed volume forces. Such integration is, however, not necessary, since it is obvious from equilibrium considerations that the normal stresses across the edges of both the narrow band and the wide band will be compressive, and thus, cannot lead to formation of cracks along these planes. The above argument is based on the consideration that the two short boundaries inside the narrow band are in their position of symmetry, that is, the plane of the tilt wall bisects the angle γ in the narrow band. This configuration minimizes the elastic energy inside the quadrangle before it is inserted back into the crystal.

5. REFERENCES

- 7-1 Orowan, E., Proc. of Intern. Conference on Phys., 2, 81, The Physical Society, London (1934).
- 7-2 Zener, C., Fracturing in Metals, 3-31, American Society for Metals, Cleveland (1949).
- 7-3 Orowan, E., Nye, J. F., and Cairns, W. J., Testing of Materials, Part I, H. M. Stationery Office, London, (1952).

- 7-4 Orowan, E., Fracture, (Averback et al, editors), Technology Press and J. Wiley and Sons, Inc., New York (1959).
- 7-5 Clarke, F. J. P., New Scientist, London, 16(1962).
- 7-6 Stroh, A. N., Proc. Roy. Soc., London, A223, 404 (1954).
- 7-7 Stroh, A. N., Proc. Roy. Soc., London, A232, 548 (1955).
- 7-8 Westwood, A. R. C., Phil. Mag., 6, 195, (1961).
- 7-9 Stokes, R. J., Johnston, T. L. and Li, C. H., Phil. Mag., 3, 718, (1958).
- 7-10 Cottrell, A. H., Trans. AIME, 212, 192, (1958).
- 7-11 Stokes, R. J., Johnston, T. L. and Li, C. H., Phil. Mag., 4, 920, (1959).
- 7-12 Biggs, W. D., and Pratt, P. L., Acta Met., 6, 694, (1958).
- 7-13 Orowan, E., Dislocations in Metals, (M. Cohen, Editor), 191, American Institute of Mining and Metallurgical Engineers, New York (1954).
- 7-14 Stroh, A. N., Phil. Mag., 3, 597 (1958).
- 7-15 Gilman, J. J., J. Metals, 6, 621 (1954).
- 7-16 Deruyttere, A. and Greenough, G. B., Inst. Metals, 84, 337 (1956).
- 7-17 Rose, G., Abh. Preussische Akademie der Wissenschaften, 57 (1868).
- 7-18 Low, J. R., Acta Met., 5, 405 (1957).
- 7-19 Hull, D., Phil. Mag., 3, 1, 368 (1958)
Hull, D., Acta Met., 8, 11 (1960).
- 7-20 Edmondson, B., Proc. Roy. Soc., London, A264, 176 (1961).

- 7-21 Stokes, R. J., Private Communication.
- 7-22 Orowan, E., Z. Physik, 89, 634 (1934).
- 7-23 Argon, A.S., and Orowan, E., Nature, 192, 447 (1961).
- 7-24 Mugge, O., Neues Jahrbuch fur Mineralogie, etc., 1, 71 (1898).
- 7-25 Orowan, E., Nature 149, 643 (1942).
- 7-26 Krishnan, R.S., (Editor), Progress in Crystal Physics, 1, 89, 128, S. Viswanathan, Madras (1958).
- 7-27 Stokes, R. J., Johnston, T.L. and Li, C.H., Phil. Mag., 4, 137 (1959).
- 7-28 Reusch, E., K. Akademie der Wissenschaften, Berlin, Monatsberichte, 11, 222 (April 1867).
- 7-29 Parker, E., Fracture, (Averbach, et. al., Editors), 181, Technology Press and J. Wiley and Sons, Inc., New York (1959).
- 7-30 Johnston, W.G., and Gilman, J.J., J. Appl. Phys., 21, 632 (1960).
- 7-31 Gilman, J.J., and Johnston, W.G., Dislocations and Mechanical Properties, p. 116, (Fisher et al, Editors), J. Wiley and Sons, Inc., New York.
- 7-32 Young, F.W., J. Appl. Phys., 33, 963 (1962).
- 7-33 Brilliantov, N.A., and Obreimov, I. W., Phys. Z. Sowjetunion, 6, 587 (1934).
- 7-34 Stowell, H.H., Phil. Mag., 7, 677 (1962).
- 7-35 Schutze, W., Z. Physik, 76, 135 (1932).

- 7-36 Burgers, J. M., Proc. Phys. Soc., London, 52, 23 (1940).
- 7-37 Orowan, E., and Pascoe, K. J., Nature, 148, 467 (1941).
- 7-38 Eshelby, J. D., Proc. Roy. Soc., London, A241, 376 (1957).
- 7-39 Stokes, R. J., Johnston, T. L. and Li, C. H., Phil. Mag., 7, 23 (1962).
- 7-40 Stroh, A. N., Fracture, (Averbach et. al., Editors), 117, Technology Press and J. Wiley and Sons, Inc., New York (1959).
- 7-41 Smith, S. W. J., Dee, A. A., and Youn, J., Proc. Roy. Soc., London, A121, 501 (1928).

TASK 8 - IMPURITY INFLUENCES

Principal Investigator: I. B. Cutler
University of Utah

ABSTRACT

The objective of this task is to study the effect of carefully controlled additions of selected impurities on the mechanical properties of high purity polycrystalline MgO and Al_2O_3 . Successful refinements were carried out to improve specimen purity of oxides prepared with predetermined amounts of doping elements. The removal of a surface layer by chemical etching, or testing in a liquid N_2 environment, was found to increase the strength of undoped polycrystalline MgO bodies.

Ferric oxide and Cr_2O_3 additions (up to 2×10^4 ppm) had a consistently deleterious effect on MgO; Al_2O_3 and TiO_2 decreased the strength only at concentrations in excess of 10^3 ppm, while ZrO_2 and SrO left the room-temperature strength of MgO largely unaffected. At elevated temperatures, a significant weakening was noted only for TiO_2 concentrations exceeding 10^3 ppm; other additions, had no discernible influence on the elevated temperature strength of MgO which, however, was greater in all instances than room temperature values at identical concentration levels.

Aluminum oxide tested at 1050°C , was shown to have been weakened by increasing concentrations of MgO; TiO_2 served to reduce the strength only at concentrations in excess of 100 ppm. Doping with Cr_2O_3 , Fe_2O_3 and Na_2O had no perceivable effect on the strength of Al_2O_3 at elevated temperatures. The weakening effect of TiO_2 was also confirmed in room temperature experiments. In contrast to MgO, the room-temperature strength of Al_2O_3 was consistently higher than its elevated temperature strength.

Microhardness studies carried out on single-crystal MgO showed that the hardness was largest in the $\langle 110 \rangle$ direction and least in the $\langle 100 \rangle$ direction. Post-sintering diffusion of Fe_2O_3 increased the hardness of MgO; polishing, if continued beyond 2 min, effected an unusually large drop in the hardness measurements. The microhardness values of polycrystalline MgO were found to increase with rising concentrations of Cr_2O_3 , Fe_2O_3 and Al_2O_3 ; additions of ZrO_2 , TiO_2 and SrO lowered the microhardness values. Preliminary work was performed on sintering and recrystallization studies, and on the preparation of translucent high-density MgO.

TASK 8 - IMPURITY INFLUENCES

1. INTRODUCTION

The basic objective of this task is to investigate the effects that carefully controlled additions of selected impurities have on the mechanical properties of high-purity polycrystalline MgO and Al_2O_3 . Studies reported here represent a continuation phase of work done from September 1960 to October 1961, as has been reported previously (8-1). The researches made during the continuation phase of this program are discussed in the present report in the following order:

- (1) Improvements in the methods used for the preparation of high-purity MgO and Al_2O_3 powders and polycrystalline test specimens,
- (2) Effects of annealing and/or etching on the modulus of rupture of pressed and fired specimens of MgO,
- (3) Modulus of rupture of pressed and fired MgO as a function of temperature from liquid N_2 temperatures (ca. -196°C) to 1000°C ,
- (4) Influence of Fe_2O_3 , Al_2O_3 , ZrO_2 , TiO_2 , SrO , and Cr_2O_3 impurities on the modulus of rupture of pressed and air-fired MgO,
- (5) Influence of Fe_2O_3 , TiO_2 , Cr_2O_3 , Na_2O , and MgO impurities on the modulus of rupture of pressed and air-fired Al_2O_3 at room temperature.
- (6) Statistical treatment of data on the modulus of rupture,
- (7) Microhardness measurements,
- (8) Sintering and recrystallization studies, and
- (9) Preparation of translucent, high-density MgO.

In addition studies were originally also planned in connection with

- (1) The effect of Fe_2O_3 , ZrO_2 , Cr_2O_3 , MgO and MnO on the modulus of rupture of pressed and air-fired Al_2O_3 at high temperatures
- (2) The preparation of high-purity translucent Al_2O_3 ,
- (3) The preparation of ultrahigh-purity Al_2O_3 from zone-refined aluminum ingots, and
- (4) The effect of post-sintered doping with selected impurities on the modulus of rupture of polycrystalline MgO and Al_2O_3 . However, the pursuit of these research studies was frustrated by equipment failures and lack of time.

2. METHODS OF SAMPLE PREPARATION

Methods used for the preparation of high-purity MgO and Al_2O_3 powders were essentially the same as those previously reported⁽⁸⁻¹⁾. In the past, difficulty was encountered quite frequently at the stage of the MgO preparation where $\text{Mg}(\text{OH})_2$ is precipitated from an aqueous MgCl_2 solution by the addition of NH_4OH , which is subsequently separated from the chloride-containing solution by filtration and washing. The $\text{Mg}(\text{OH})_2$ would sometimes form a gelatinous cake of very small particle size that severely retarded the filtration and washing operation. As a result, the operation required too much time. There was often sufficient MgCl_2 left the cake to give a product that contained intolerable amounts of $\text{Mg}(\text{OH})\text{Cl}$ after calcination, and loss of $\text{Mg}(\text{OH})_2$ through the filter was sometimes excessive. An innovation was introduced into the previous preparation procedure that largely circumvented these problems. It was found that when the precipitation of the $\text{Mg}(\text{OH})_2$ was carried on at ca. 8°C and a pH of ca. 9.7, a more suitable precipitate was obtained. With the filtration and washing operation also

conducted at 8°C, a satisfactory cake was consistently obtained. It is suspected that loss of $\text{Mg}(\text{OH})_2$ through the filter, though reduced from that suffered previously, is still large. Efforts to improve further this aspect of the MgO preparation procedure may be worthwhile.

In an effort to eliminate any variation in the control sample, a large single batch of the MgO and one of the Al_2O_3 was prepared. All the specimens fired in air in the high-temperature electric kiln were made of material drawn from these two large batches. Spectrographic analyses of the small lots of MgO that were blended to make up the single large batch are given in Table 8-1. Those of the small lots of Al_2O_3 were not considered meaningful owing to the fact that a comparatively impure Al_2O_3 was mistakenly used as standard. However, the same careful technique was used as previously reported⁽⁸⁻¹⁾ and it is believed that the resulting materials are equally as pure. Lot 3 of the MgO was discarded because of the abnormally high Ag content. The Al_2O_3 specimens broken at 1050°C, and the powders used to prepare the translucent, high density, high purity MgO were taken from the lots made earlier.

The porosities of pressed and fired specimens prepared from the as-calcined Al_2O_3 powders were found to be higher than was considered desirable. This was attributed to clustering of Al_2O_3 particles in the powder. These clusters were not altogether broken down in the pressing process, leading to a resulting porosity in the fired pieces. It was found that the pressed and fired densities of the Al_2O_3 specimens (in this case, firing was in a gas-fired kiln) could be increased from 3.71-3.74 to 3.81 gram per cc by either of two modified pressing processes. The modified pressing processes were as follows:

Table 8-1
COMPARATIVE SPECTROGRAPHICAL ANALYSIS

	Al	Ca	Cu	Fe	Ni	Si	Ag	Na	V
Our MgO (1961)	tr	2	0	0	0	0	5	0	0
J. M. Standard MgO (1961)	tr	2	0	0	0	0	6	0	tr
J. M. Analysis of J. M. Mgo	0	1ppm	1ppm	0	2ppm	0	1ppm	2ppm	0
J. M. Standard MgO (1962)	2	1	2	3	0	2	2	0	0
ARF MgO (1962)									
1	1	1	1	1	1	1	2	0	0
2	2	1	3	2	0	1	3	0	0
3	2	1	2	5	0	1	1x	0	0
4	2	1	3	3	0	1	3	0	0
5	2	1	3	4	0	1	3	0	0
6	2	1	3	4	0	1	3	0	0
7	2	1	3	3	0	1	4	0	0
Batch No. 8	2	1	3	4	0	1	3	0	0
9	2	1	3	4	0	1	3	0	0
10	2	1	3	4	0	1	4	0	0
11	2	2	3	3	0	1	3	0	0
12	2	1	1	3	0	1	2	0	0
13	2	2	1	4	0	1	2	0	0
14	2	1	1	3	0	1	1	0	0
15	2	1	2	3	0	1	2	0	0
16	2	1	2	2	0	1	2	0	0
17	2	1	2	2	0	1	2	0	0

Key: Relative impurity levels identified by:

x > 1 > 2 > 3 > 4 > 5 > 6 > tr > 0

with x largest, and tr (trace) smallest

Process 1

- (1) Cold-press calcined Al_2O_3 powder into discs using a pressure of 20 t/in²,
- (2) Grind the pressed discs back to powder in a polyethylene container and mix,
- (3) Repress the powders into discs using a pressure of 20 t/in²,
- (4) Fire the resulting discs at 1735°C (\pm 20°C) for 8 hr.

Process 2

- (1) Cold press calcined Al_2O_3 powder into discs using a pressure of 20 t/in²,
- (2) Fire the discs to ca. 1500°C,
- (3) Tumble the fired discs in a polyethylene bottle until they are broken into a fine powder,
- (4) Repress the powders so obtained into discs at 20 t/in²,
- (5) Fire the resulting discs at 1735°C (\pm 20°C) for 8 hr.

Another approach used to overcome the high porosity which is due to clustering involved dry tumbling of the calcined Al_2O_3 powders in polyethylene bottles with clean chunks of high-purity aluminum metal. This procedure left metallic aluminum in the powder which was later converted to the chloride by the addition to reagent grade HCl. The AlCl_3 was subsequently washed from the Al_2O_3 powder with distilled and deionized water. This procedure lead to specimens with fired densities comparable to those obtained with the powders produced by Processes 1 and 2. However, it is important that care be taken during the leaching operation to avoid an intolerable degree of rehydration of the Al_2O_3 powders. Aluminum oxide that has been excessively rehydrated does not tend to sinter satisfactorily.

Another important improvement in the sample preparation procedure was in the final firing of the pressed discs. Previously, firing was in gas-fired kilns, and the nature of the firing atmosphere was not reproducible from one firing to another. This year, the majority of the firings used to prepare test specimens were in a high-temperature (1750°C) air atmosphere electric resistance furnace. It was also found that specimen damage during the sawing operation was reduced substantially by pre-firing the pressed discs to ca. 1450°C in a Globar kiln, sawing the test prisms from the prefired discs, and finally firing the cut prisms in the high-temperature electric furnace at ca. 1740°C.

3. STUDIES ON POLYCRYSTALLINE MAGNESIUM OXIDE

A. Effect of Annealing, Polishing and Temperature on Strength

Studies conducted during this phase of the program concerned first the effect of annealing on the strength of high-purity polycrystalline MgO. The annealing cycle consisted of soaking for 30 min at 1500°C, followed by various cooling schedules in different environments. In addition, some specimens were broken in liquid N₂ (~77°K) to eliminate the effect of adsorbed water on the strength and, further, preliminary studies were conducted to evaluate the effects of chemical polish on the fracture strength of the resulting pieces.

It was hypothesized⁽⁸⁻¹⁾ that the increase observed in the strength of the MgO specimens at temperatures up to 1000°C is due to adsorbed water vapor that reduced the strength near room temperature. It was assumed that as the temperature is increased, water is desorbed from the surface, thereby increasing the strength. Accordingly, it was decided to anneal some MgO specimens at 1500°C, then cool these to room temperature.

The specimens were annealed in an impervious tube with the closed end inside a gas-fired kiln. A dry atmosphere was achieved by applying a vacuum of about 1 torr to the specimens when they had cooled to ca. 1000°C by means of a mechanical backing pump connected to the encapsulating tube through a rubber stopper and vacuum hose. Some of the specimens were cooled in a vacuum to room temperature where they were put into mineral oil without being exposed to the air. Other specimens were quenched in mineral oil after they had cooled to 508°C; none of the specimens were exposed to air during the quenching process. The specimens were subsequently broken under oil at room temperature *.

The results, given in Table 8-II, show that the annealed specimens have lower average strengths than the untreated specimens. In fact, the manner of annealing and the suppression of air (moisture) contact with the specimen during quenching appears to have little influence on the resulting strength of the MgO specimens, with the exception that specimens quenched in oil from 500°C showed a decidedly lower strength than those used in the other series. If the re-adsorption of water vapor upon the surfaces of the annealed specimens were the only cause of the decreasing strength with decreasing temperature below 500°C, one would expect the strengths of the annealed and quenched specimens to be slightly higher than those of the control samples. It is evident that some factor (or factors) in addition to the re-adsorption of water vapor is operative. For example, it appears that thermal stresses set up during cooling may have introduced cracks to weaken the specimens. This would be particularly true in the case of the specimens quenched in mineral oil from 500°C.

* Specimens studied in these particular tests were cut from discs fired 2 hr at 1700°C in a gas-fired kiln.

Table 8-II
**THE EFFECT OF ANNEALING, POLISHING AND TEMPERATURE
ON STRENGTH OF HIGH-PURITY POLYCRYSTALLINE
MAGNESIUM OXIDE ***

Annealing and Quenching Treatment	No. of Specimens	Average Modulus of Rupture (10 ⁻³ psi)	Range (10 ⁻³ psi)	Standard Deviation (10 ⁻³ psi)
No treatment, broken fresh	15	22.6	18.4-26.5	2.25
No treatment, broken after 8 days in unfiltered air	15	22.8	14.4-26.0	3.20
Annealed at 1500°C for 30 min. Cooling rate, 2.7°C/min to 1000°C. Below 1000°C, air blown on specimens to cool faster. Broken in air at 25°C.	15	20.4	16.8-23.3	2.75
Annealed at 1500°C for 30 min. Cooling rate, 2.7°C/min to 500°C, then quenched in room temp. mineral oil until; broken under oil.	15	16.12	8.1-23.2	5.34
Annealed at 1500°C for 60 min. Cooling rate, 0.9°C/min to room temp. in air. Broken in air.	15	20.6	16.7-23.7	2.44
Annealed at 1500°C for 60 min. Cooled at 0.9°C/min to room temp. Vacuum was used below 1000°C. Specimens removed from vacuum into oil at room temp. Broken under oil.	15	20.9	16.8-25.1	2.20
Etched in boiling H ₃ PO ₄ , washed by hot and warm water, alcohol, ether.	15	24.4	12.3-31.9	5.69
Broken in air atmosphere of liquid N ₂ (-195°C)	12	25.7	20.3-29.7	2.92

* Fired 2 hr at 1700°C in gas-fired furnace.
Average density, 3.51 g/cc (98.00% of theoretical range: 97.42-98.59% of theoretical density)
Calcined 2 hr at 1100°C in gas-fired furnace.
Average grain size: 27.9 μ .

These investigations were augmented by further studies, in which the effect of annealing was examined on undoped high-purity MgO prepared by a different method, as well as on specimens doped with Fe_2O_3 additions. For the undoped specimens an electric furnace was used with the firing schedule noted on Table 8 - III. The doped specimens were fired in a gas-furnace, according to the schedule noted on Table 8 - II. All specimens were annealed at 1500°C , the undoped specimens being soaked for 10 min, the Fe_2O_3 -doped ones for 30 min. Cooling was carried out inside the gas-fired furnace with the gas and air lines closed.

The data resulting from these experiments are presented in Table 8-III; note, in particular, that grain size and density did not change greatly as a result of annealing. The results shown in Tables 8-II and 8-III, excluding the iron-doped MgO series, but including some elevated temperature test results obtained during the previous phase of the program (8-1), are summarized in Fig. 8-1.

The hypothesis that adsorption of water vapor on the specimen surface has a deleterious effect on the strength of polycrystalline MgO received some additional support from tests carried out in liquid N_2 ; in this environment the strength is substantially larger than those obtained at room temperature in ordinary air, as shown in Table 8-II and Fig. 8-1. This might be attributed to the elimination of adsorbed water at the low temperature of liquid N_2 which could enhance the strength of the specimen. However, it is much more likely that this strengthening effect is a reflection of the N_2 environment on the one hand, and that of the testing temperature on the other. In support of this observation, one may note that in Task 11 G. T. Murray reports a similar strength enhancement for MgO tested at elevated temperatures in a gaseous N_2 environment, while the work of N. J. Petch (Task 6) shows that the strength of both

Table 8-III
THE EFFECTS OF ANNEALING ON THE ROOM TEMPERATURE STRENGTH OF IRON-DOPED
HIGH-PURITY POLYCRYSTALLINE MAGNESIUM OXIDE *

Fe ₂ O ₃ Impurity Level (ppm)	Annealing and Quenching Treatment	No. of Specimens	Average Modulus of Rupture (10 ⁻³ psi)	Range (10 ⁻³ psi)	Std. Dev. (10 ⁻³ psi)	Average Density		Density Std. Deviation (%)	Average Grain Size (μ)
						(g/cc)	(Percent of Theo- retical)		
-	None	29	18.5	8.6-31.0	5.91	3.47	96.9	-	20.1
-	Annealed and Furnace Cooled	39	17.3	12.4-25.5	5.73	3.48	97.2	-	21.3
100	None	9	17.3	12.6-21.6	3.78	3.47	97.0	2.92	52.0
100	Annealed and Furnace Cooled	10	16.7	12.2-19.1	2.04	3.54	98.9	2.18	59.8
10,000	None	7	11.2	9.8-12.4	1.14	3.36	93.8	1.06	47.6
10,000	Annealed and Furnace Cooled	9	11.5	9.6-15.2	1.71	3.42	95.5	1.41	55.6

* Undoped MgO calcined for 2 hr at 1100°C in gas-fired furnace, then fired for 2 hr in air at 1650°C in electric furnace.
Iron doped specimens prepared as in Table 8-II, using gas-fired furnace.

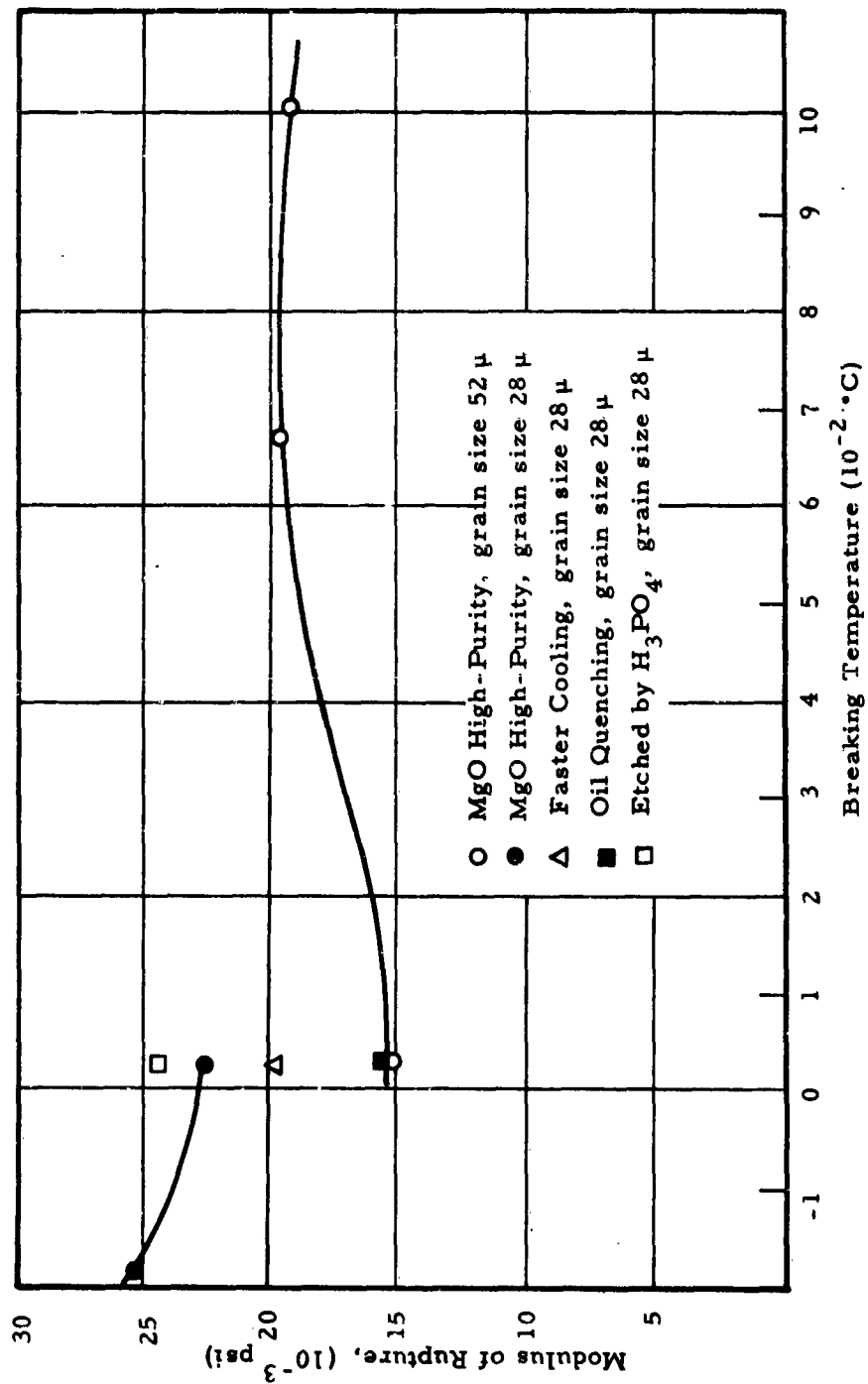


Fig. 8-1 STRENGTH OF MAGNESIUM OXIDE AT VARIOUS TEMPERATURES

Al_2O_3 and MgO was significantly raised when tested at liquid N_2 temperatures.

It will be noted from Fig. 8-1 that there are two different average strengths given for the room temperature values. This is because the specimens used for the room temperature and liquid N_2 test series were prepared by different firing methods than those used for the test series involving temperatures from room temperature to 1000°C , with the result that the grain size of the specimens used in the liquid N_2 tests was about 28μ , as compared to an average grain size of 52μ for the high temperature tests. As would be expected and in agreement with the findings of Task 4, and the specimen with the larger grain size proved to have a lower strength.

B. Effect of Impurities on Strength of Room Temperature

Iron oxide, Al_2O_3 , ZrO_2 , SrO , TiO_2 and Cr_2O_3 were added to high-purity MgO powders in controlled quantities of 0, 100, 1000, 10,000 and 20,000 ppm. Procedures for adding these impurities and obtaining the test prisms for breaking were essentially the same as those used in the previous phase of this project⁽⁸⁻¹⁾. An important difference is that in the present investigation the pressed discs were fired in air in an electric kiln. Furthermore, all the discs to which a given kind of impurity had been added were fired together. A few undoped discs, used as control samples, were included with each firing. The firing schedule is used in preparing these specimens is plotted in Fig. 8-2.

Experiments in this series were confined to room temperature tests. Results of these tests are given in Fig. 8-3, 8-4, 8-5, 8-6, 8-7 and 8-8. Table 8-IV presents the average grain sizes and densities for the specimens corresponding to each level of impurity.

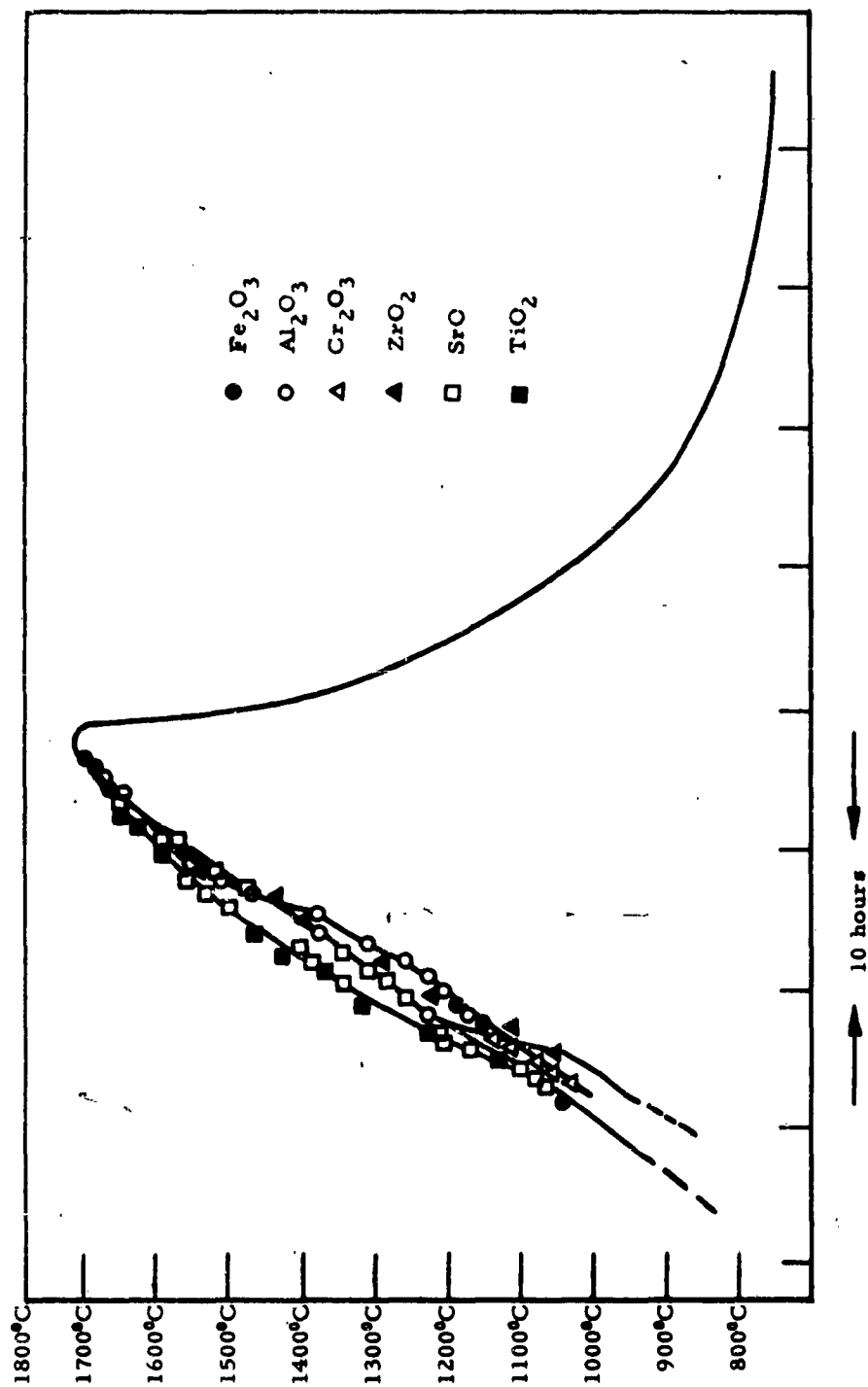


Fig. 8-2 FIRING SCHEDULE OF IMPURE MAGNESIUM OXIDE DISCS IN ELECTRICAL FURNACE, AVERAGE FIRING RATE, 27°C PER HR

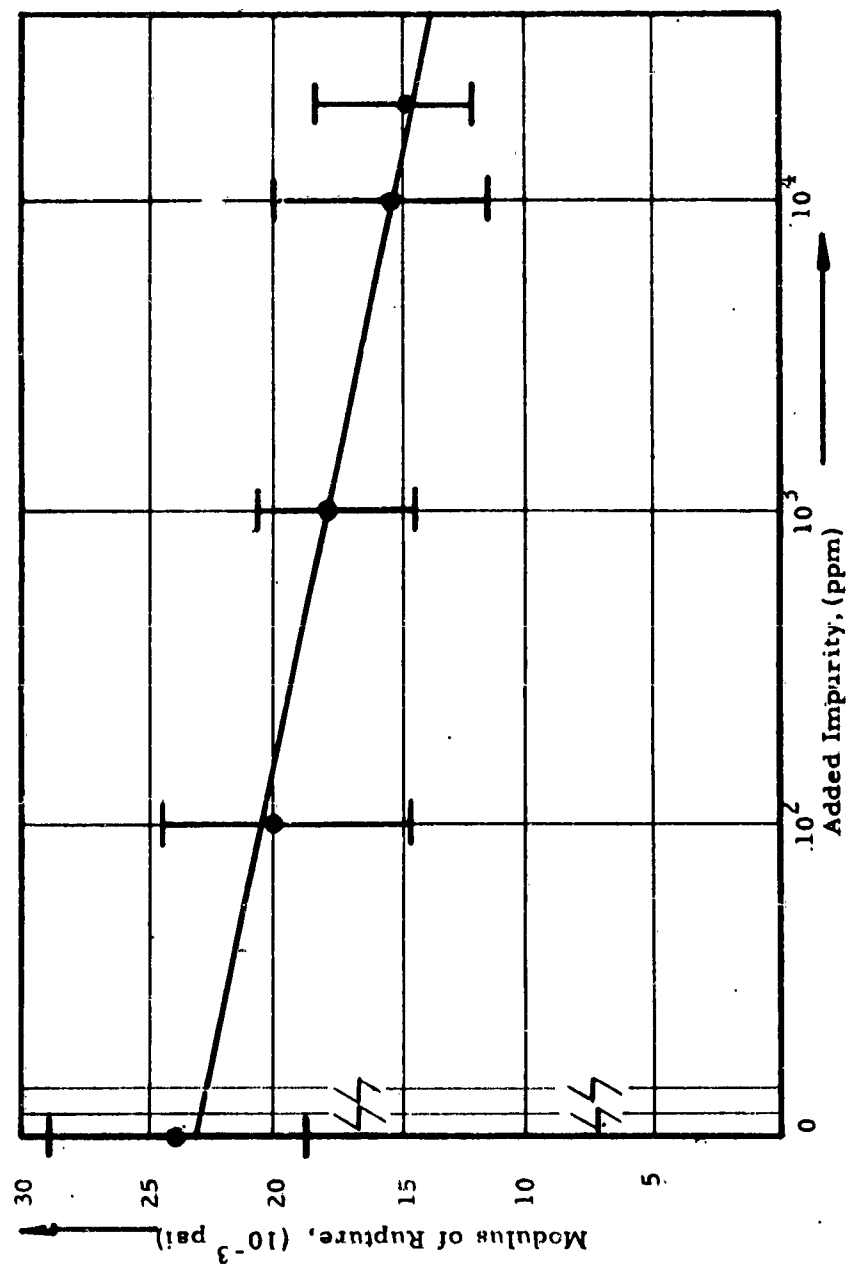


Fig. 8-3 ROOM TEMPERATURE STRENGTH OF MAGNESIUM OXIDE AS A FUNCTION OF FERRIC OXIDE IMPURITY LEVEL

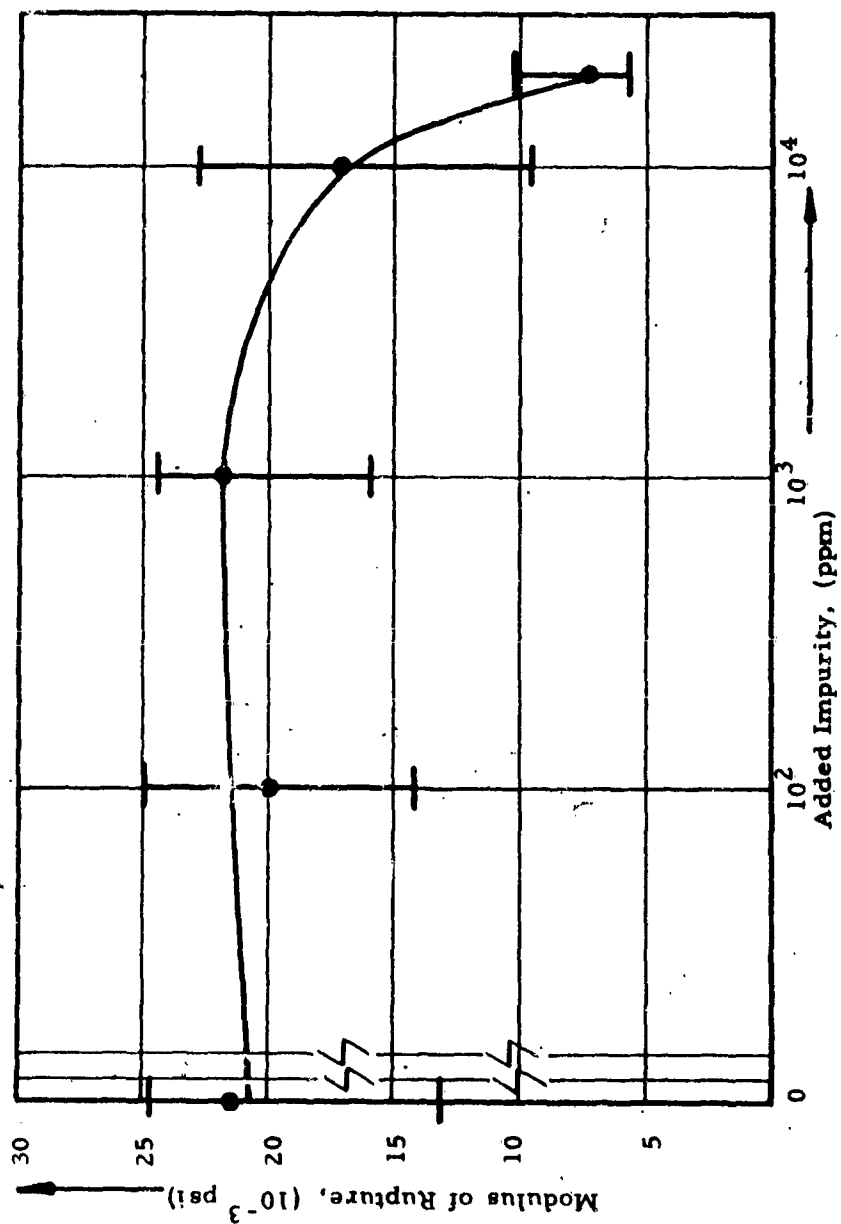


Fig. 8-4 ROOM TEMPERATURE STRENGTH OF MAGNESIUM OXIDE AS A FUNCTION OF ALUMINUM OXIDE IMPURITY LEVEL

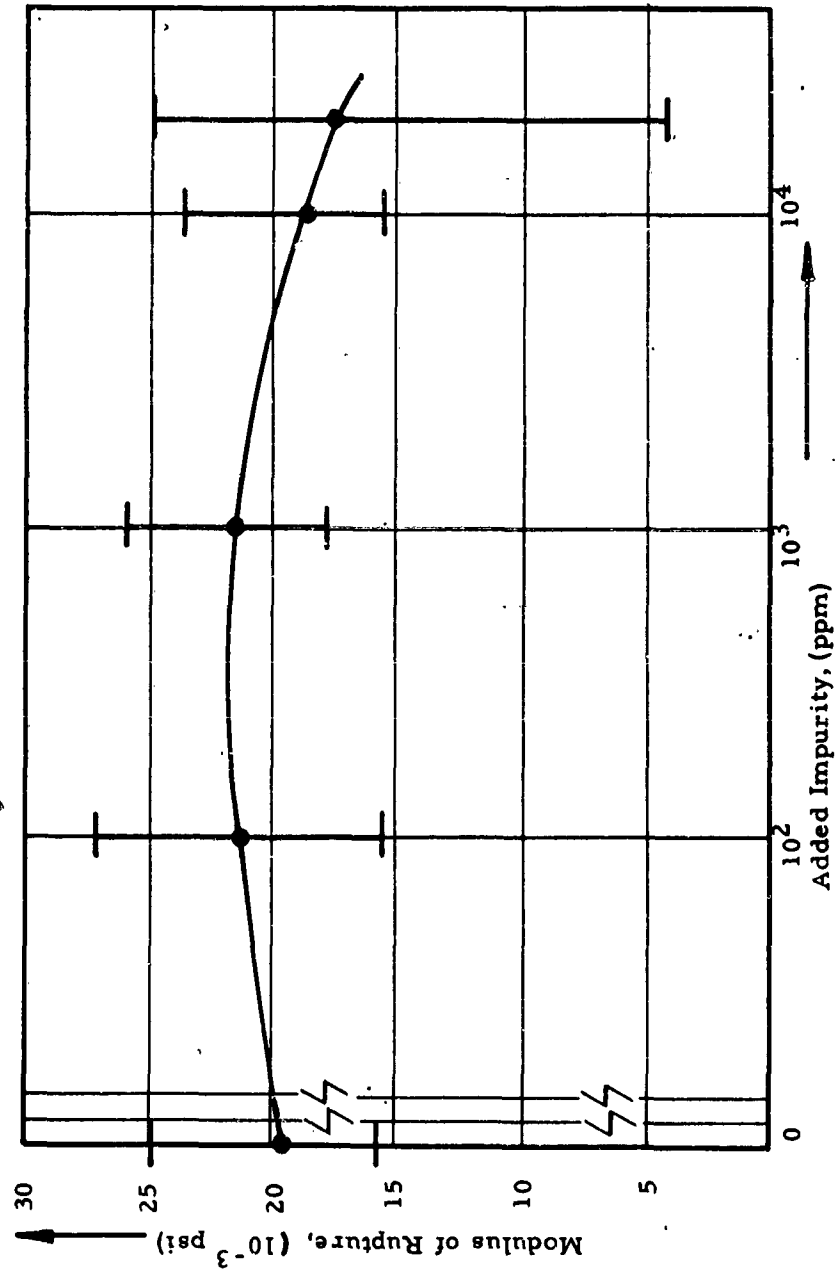


Fig. 8-5 ROOM TEMPERATURE STRENGTH OF MAGNESIUM OXIDE AS A FUNCTION OF ZIRCONIUM OXIDE WITH IMPURITY LEVEL

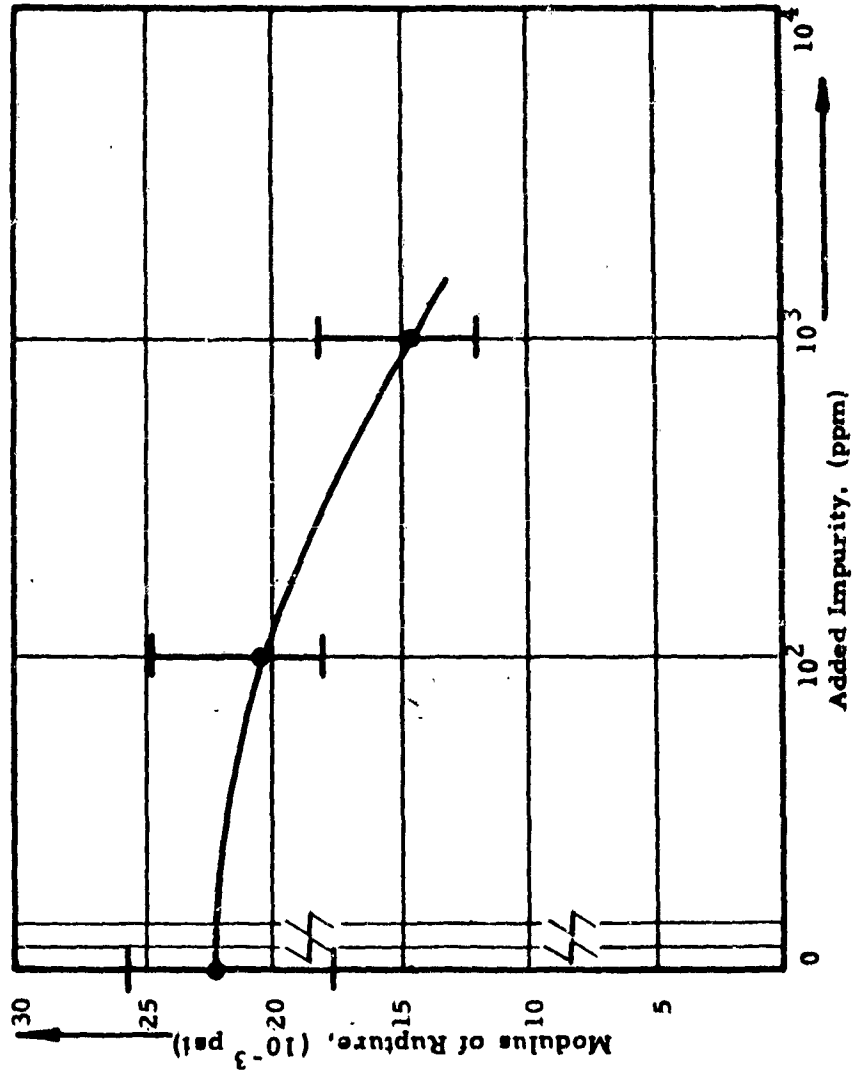


Fig. 8-6 ROOM TEMPERATURE STRENGTH OF MAGNESIUM OXIDE AS A FUNCTION OF CHROMIC OXIDE IMPURITY LEVEL

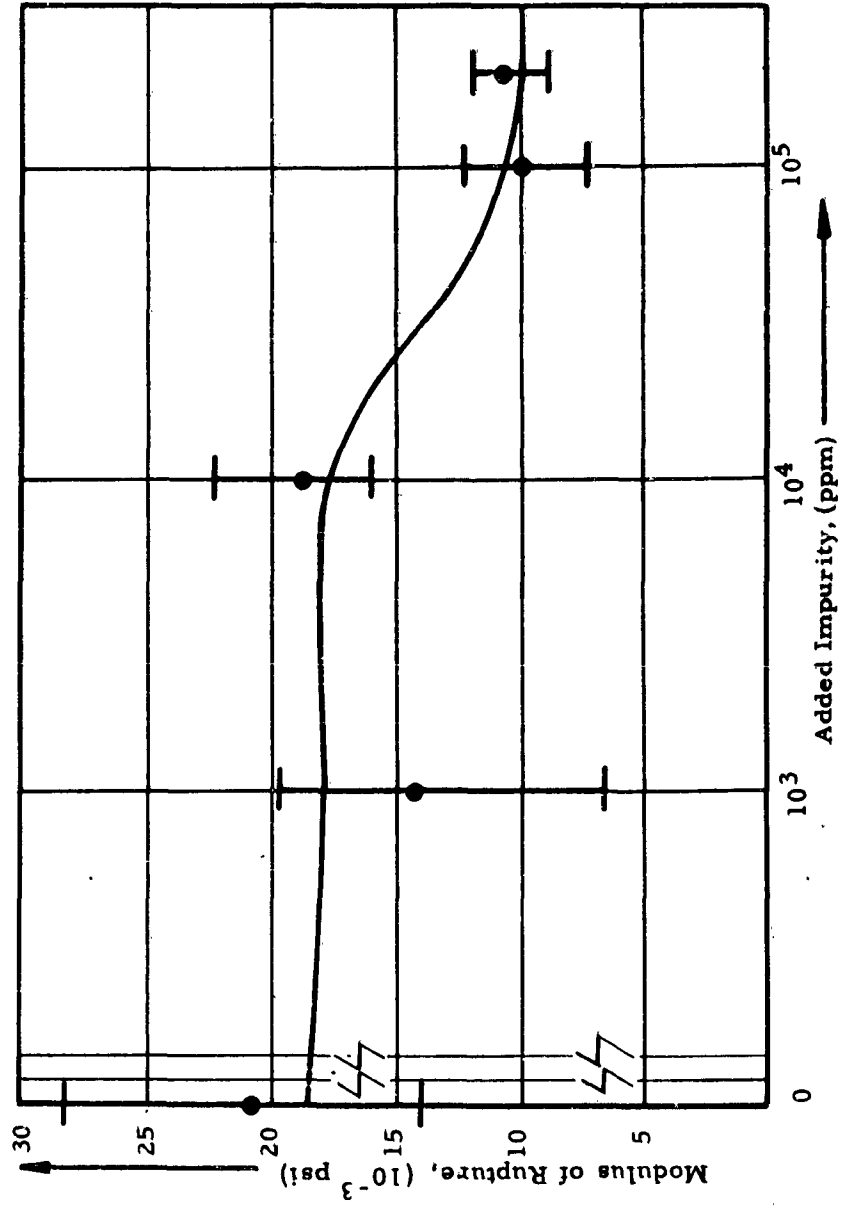


Fig. 8-7 ROOM TEMPERATURE STRENGTH OF MAGNESIUM OXIDE AS A FUNCTION OF TITANIUM OXIDE IMPURITY LEVEL

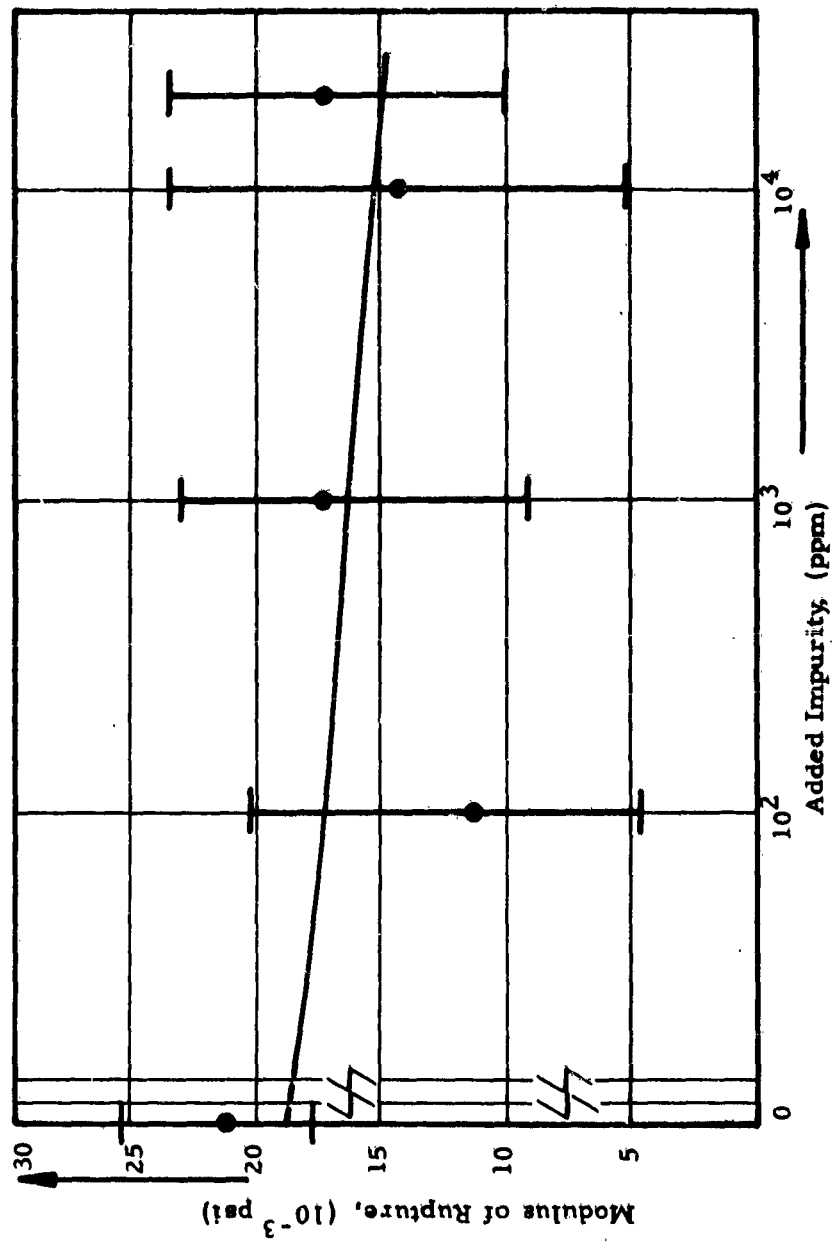


Fig. 8-8 ROOM TEMPERATURE STRENGTH OF MAGNESIUM OXIDE AS FUNCTION OF STRONTIUM OXIDE IMPURITY LEVEL

Table 8-IV

AVERAGE FIRED DENSITY AND GRAIN SIZE OF MAGNESIUM
OXIDE SPECIMENS DOPED WITH IMPURITIES BEFORE SINTERING

Nature of Impurity	Amount Added (ppm)	Density (g/cc)	Percent of Theoretical Density	Average Grain Size (μ)
Fe_2O_3	0	3.500	97.8	21
	10^2	3.516	98.2	23
	10^3	3.519	98.3	24
	1×10^4	3.525	98.5	31
	2×10^4	3.530	98.6	28
Al_2O_3	0	3.498	97.7	29
	10^2	3.521	98.4	29
	10^3	3.508	98.0	22
	1×10^4	3.500	97.8	31
	2×10^4	3.481	97.3	25
ZrO_2	0	3.488	97.5	23
	10^2	3.486	97.7	24
	10^3	3.489	97.5	37
	1×10^4	3.530	97.6	20
	2×10^4	3.490	97.5	30
SrO	0	3.496	97.7	23
	10^2	3.495	97.6	28
	10^3	3.490	97.5	17
	1×10^4	3.498	97.7	10
	2×10^4	3.514	98.2	9
TiO_2	0	3.497	97.7	22
	10^2	3.497	97.7	25
	10^3	3.477	97.2	30
	1×10^4	3.488	96.0	57
	2×10^4	3.484	97.4	48
Cr_2O_3	0	3.496	97.7	24
	10^2	3.524	98.5	25
	10^3	3.515	98.2	32
	1×10^4	3.516	98.2	16
	2×10^4	3.446	96.3	10

Theoretical density of pure MgO = 3.5789 g/cc

Linear regression analyses were made of the strength data obtained by breaking the doped and undoped MgO prisms. A Burroughs 1620 digital computer was used for these calculations. Modulus of rupture was considered the dependent variable. Added impurity concentration, grain size and density were taken as the independent variables. The results of statistical tests aimed at determining whether the undoped MgO control specimens that were fired with different doped lots came from the same or a different population than the average of all control specimens as given in Table 8-V, while the results of the regression analysis are summarized in Table 3-VI.

Studies made to determine the effects of chemical polishing on the strength of MgO were aimed at determining the effect of surface cracks and a number of other factors that give rise to spurious results. Phosphoric acid at room temperature gave a very rough surface and resulted in an insignificant change in the strength over that of unetched specimens. Sulfuric acid was also found unsatisfactory; it attacked the grain boundaries too extensively. Hot H_3PO_4 , an etchant used by numerous investigators in studying MgO, was found to provide visually smooth surfaces. Specimens were dye-checked for cracks, prior to the chemical polishing; and those with detectable cracks were discarded. The remaining specimens were boiled in H_3PO_4 , washed vigorously in boiling water, then in warm water (40°C), followed by alcohol and ether rinses. Modulus of rupture tests run an hour following the etching treatment gave an average room temperature strength of 24,400 psi with a standard deviation of 5,690 psi.

It was subsequently noted that the etched specimens had a thin coating, presumably redeposited $MgO^{(8-2)}$. Attempts were made to eliminate this coating by changing the etching procedure, by using clean acid with a low MgO content and

Table 8-V
STATISTICAL ANALYSES FOR POPULATION IDENTIFICATION
OF UNDOPED MAGNESIUM OXIDE SAMPLES FIRED
WITH DIFFERENT DOPED LOTS

Impurity With Which Pure MgO Discs Were Fired	$Z_c = \frac{ X_{avg} - X_1 }{\sqrt{\frac{\sigma_{avg}^2}{N_{total}} + \frac{\sigma_1^2}{N_1}}}$	Sample From Same Or Different Population *
Fe_2O_3	5.032	Different
Al_2O_3	0.151	Same
ZrO_2	3.409	Different
SrO	0.200	Same
TiO_2	0.476	Same
Cr_2O_3	1.252	Same

* $Z_c > 1.96$ for samples from population different from the average, and
 $Z_c < 1.96$ for those from the same population.

Table 8-VI
RESULTS OF LINEAR REGRESSION ANALYSES OF THE STRENGTHS
OF DOPED AND UNDOPED POLYCRYSTALLINE MAGNESIUM OXIDE

Added Impurity	Dependence		Coefficient	Standard Error	Correlation Coefficient
	Order of Importance	Kind			
Fe_2O_3	1	Density	-205,000.	43,060.	0.6632
	2	Grain Size	149.0	97.14	
	3	Impurity	0.04356	0.03976	
Al_2O_3	1	Impurity	- 0.7429	0.09654	0.7023
	2	Grain Size	184.2	156.5	
	3	Density	- 49,250.	62,080.	
ZrO_2	1	Density	3,284.	19,850.	0.1738
	2	Grain Size	103.2	52.66	
	3	Impurity	- 0.1751	0.03622	
SrO	1	Grain Size	- 619.78	109.505	0.5636
	2	Density	-369,900.	87,630.	
	3	Impurity	0.2194	0.1249	
TiO_2	1	Grain Size	- 204.2	108.6	0.02355
	2	Impurity	- 0.1663	0.1016	
Cr_2O_3	1	Grain Size	- 730.630	118.1	0.3722
	2	Density	- 18,940.	36,780.	

moving the specimen rapidly from the hot acid into the hot wash water⁽⁸⁻²⁾. In the present investigation, however, it was found that rapid introduction of specimens into the boiling wash water from the hot H_3PO_4 resulted in excessive thermal shock. Specimens were cracked and broken. The only successful method for removing the coating, once it was deposited turned out to be mechanical polishing; this, however, defeated the purpose of etching. Even though the chemically polished specimens displayed a superior strength, as can be seen from the data listed in Table 8-II, the remanent coating was believed to have almost as great an effect on the strength as normally existing surface cracks or impurities might have had. Further studies with chemical polishing techniques, therefore, were abandoned.

A brief statement regarding certain aspects of these results for polycrystalline MgO now seems to be in order. Note from Table 8-VI that the regression analyses indicate that in the lots doped with Fe_2O_3 , ZrO_2 , SrO , TiO_2 , and Cr_2O_3 , variables other than added impurity concentration are specified as having the most significant effect upon the modulus of rupture. Only in the case where the doping element was Al_2O_3 was the added impurity concentration indicated as being the most important independent variable. Yet the plots of modulus of rupture versus added impurity concentration show obvious dependencies for Fe_2O_3 , Cr_2O_3 , and TiO_2 impurities. Consider, for example, the lot in which Fe_2O_3 was added as the impurity. Regression analysis indicated density as the prime independent variable affecting strength. Inspection of Table 8-IV reveals that density increases in a regular fashion with the impurity added, but that this increase is only 0.8 percent. The change in strength seems too large to arise exclusively from such a small density change. Furthermore, one sees that while density increases

with added Fe_2O_3 , the modulus of rupture decreases. Modulus of rupture should increase with increasing density^(8-3, 8-4, 8-5). So while the regression analysis specifies density as the most important independent variable, the accuracy of this conclusion is doubted. The regression analysis does not take into account the fact that density (and grain size as well) is not independent of the impurity content. Furthermore, the concentration range of the added impurities is large (0 to 20,000 ppm) and one might expect considerable non-linearity. This could also contribute to spurious answers from the regression analyses.

C. Effect of Impurities on Strength at Elevated Temperatures

Measurements of the modulus of rupture of MgO specimens containing controlled levels of impurities were made at $660^\circ\text{C} \pm 10^\circ\text{C}$ and at 1000°C . The MgO used as a basis for these tests was some of the high-purity material produced during the previous year's work⁽⁸⁻¹⁾. Iron oxide Al_2O_3 , TiO_2 , and SiO_2 were the impurities added, sintering was accomplished in a gas-fired kiln. The results are summarized in Table 8-VII. Notice that with the exception of the two series with SiO_2 and Fe_2O_3 as the added impurity, the general trend of increased strength at increased temperature reported previously for MgO continues⁽⁸⁻¹⁾. The 1000°C strength values for MgO doped with Fe_2O_3 are less than the $660^\circ\text{C} \pm 10^\circ\text{C}$ values.

4. STUDIES ON POLYCRYSTALLINE ALUMINUM OXIDE

A. Effect of Impurities on Strength at Elevated Temperatures

The Instron testing machine, fitted with the high temperature furnace described previously⁽⁸⁻¹⁾, was used to determine modulus of rupture of Al_2O_3 at 1050°C as a function of added impurity concentration. The high-purity Al_2O_3 at 1050°C used

Table 8-VII
SUMMARY OF MODULUS OF RUPTURE EXPERIMENTS ON DOPED
MAGNESIUM OXIDE SPECIMENS TESTED AT 660°C ± 10°C
AND AT 1000°C IN AIR

Impurity	Amount Added (ppm)	Number Broken		Modulus of Rupture (10 ⁻³ psi)	
			Arithmetic Average	Range	Std. Dev.
Fe ₂ O ₃ *	10.	9	28.5	23.2 - 35.6	3.50
	1,000.	10	26.1	18.0 - 32.5	4.60
None*		4	23.0	21.3 - 23.9	1.28
Fe ₂ O ₃	10.	8	25.2	22.0 - 28.2	2.75
	1,000.	8	25.1	21.1 - 29.8	2.65
Al ₂ O ₃	10.	4	27.8	25.1 - 32.0	2.09
	100.	5	26.9	23.5 - 30.9	2.81
	1,000.	3	22.0	19.0 - 25.1	3.00
	10,000.	5	30.2	23.5 - 39.4	6.39
TiO ₂	10.	5	27.7	22.9 - 30.2	3.33
	100.	5	30.4	21.3 - 35.3	5.82
	1,000.	5	23.9	19.3 - 27.2	3.25
	10,000.	6	19.2	19.1 - 19.8	0.14
SiO ₂	10.	6	22.0	18.3 - 22.8	3.00
	100.	1	22.0	--	--
	1,000.	5	25.0	24.3 - 25.4	0.24
	10,000	2	33.9	29.1 - 38.7	6.78

* For the first added impurity of Fe₂O₃ a temperature of 660°C ± 10°C was used; for the remainder a temperature of 1000°C was used.

as a base material was same as that prepared last year, and sintering was done in a gas-fired kiln. The added impurities were Cr_2O_3 , MgO , Fe_2O_3 , TiO_2 and Na_2O ; the test results are summarized in Table 8-VIII. When comparing these results with data obtained on the same materials at lower temperatures⁽⁸⁻¹⁾, it is noted that with the exception of the case where TiO_2 was added as the impurity, the strength at 1050°C is consistently less than that measured at the lower temperatures. This behavior is in contrast with that observed for MgO . The density and grain size data for the specimens used in the current test series are also compiled in Table 8-VIII.

In addition to the impurities mentioned above, a special series of Fe_2O_3 -doped Al_2O_3 specimens was prepared, doped with an added amount of Na_2O sufficient to alter the grain growth strikingly, as shown in Table 8-VIII. The Fe_2O_3 was added to the high-purity Al_2O_3 in controlled amounts by the procedure previously described⁽⁸⁻¹⁾. The Na_2O , on the other hand, was introduced adventitiously during firing by placing the specimen on a bed of Na_2O contaminated Al_2O_3 setting sand. The ratio of Na to Fe in these specimens was not determined. The excessive grain growth that was characteristic of this series was not observed when setting sand essentially free of Na_2O was used. Table 8-VIII summarizes the results for this series.

B. Statistical Analysis of Data

In order to evaluate the significance of data obtained, statistical tests were made to determine the influence of two primary parametric groups. The first was an analysis to determine if specimens with the various impurity additions (i. e., TiO_2 , Fe_2O_3 , Cr_2O_3 , MgO and Na_2O) came from

Table 8-VIII
SUMMARY, MODULUS OF RUPTURE, DENSITY, AND GRAIN SIZE OF DOPED
ALUMINUM OXIDE TESTED IN AIR AT 1050°C

Impurity	Amount Added (ppm)	Arithmetic Average, (10 ⁻³ psi)	Number Broken	Modulus of Rupture, (10 ⁻³ psi)			Avg. Density, (g/cc)	Avg. Grain Size (μ)
				Range	Std. Dev.			
None		22.1	18	10.7 - 25.5	3.67			
Cr ₂ O ₃	10.	20.4	7	17.8 - 24.3	2.72	3.68		15.4
	100.	23.6	8	16.6 - 27.4	3.22	3.68		16.3
	1,000.	18.9	9	15.3 - 23.7	3.33	3.67		16.6
	10,000.	21.2	8	13.6 - 25.4	4.35	3.69		16.7
MgO	10.	23.4	9	14.6 - 30.1	6.35	3.82		14.2
	100.	14.0	9	10.5 - 15.7	1.54	3.84		16.2
	1,000.	15.4	8	14.3 - 16.3	0.83	3.82		11.8
	10,000.	15.2	8	12.8 - 17.9	1.84	3.82		13.0
Fe ₂ O ₃	10.	21.6	9	17.8 - 24.5	1.95	3.71		13.9
	100.	24.7	8	21.6 - 27.9	2.11	3.74		15.3
	1,000.	22.9	7	19.8 - 25.9	2.22	3.71		15.1
	10,000.	24.4	4	19.9 - 28.5	3.54	3.77		14.1
Fe ₂ O ₃ *	0	10.4	3	8.1 - 12.1	2.06	3.82		123.
	10	13.8	5	9.6 - 20.7	5.51	3.68		20.
	100	14.8	6	10.9 - 21.7	4.32	3.74		20.
	1,000	6.1	6	1.9 - 10.2	2.83	3.78		124.
	10,000	3.9	4	3.0 - 5.0	0.84	3.80		20,000.
TiO ₂	10.	24.7	9	14.5 - 28.2	5.80	3.68		16.3
	100.	22.1	5	20.0 - 25.6	2.35	3.67		13.8
	1,000.	18.0	4	16.1 - 19.2	1.34	3.71		18.5
	10,000.	10.9	3	9.4 - 13.0	1.60	3.77		45.1
Na ₂ O	10.	20.8	10	13.2 - 26.7	4.10	3.78		15.9
	100.	21.0	6	16.8 - 25.7	3.37	3.78		12.7
	1,000.	18.3	8	13.4 - 25.6	4.07	3.79		15.2
	10,000.	21.0	7	16.8 - 23.9	2.48	3.79		16.7

* This Fe₂O₃ series was adventitiously contaminated with Na₂O from setting sand.

different populations according to the particular kind of impurity added or if they were merely random samples from the same population. The second kind of test was a linear regression analysis to ascertain the extent to which the strength measurements correlated with impurity content, density and grain size. Regression analyses were run for each kind of impurity except Cr_2O_3 at three temperatures: viz., 25°, 500°, and 1050°C. For specimens doped with Cr_2O_3 , data for only two temperatures (25° and 500°C) were available for analysis. Many of the data used for these statistical tests were obtained previously⁽⁸⁻¹⁾.

The first test involved the same statistical formula used to obtain the data on the high-purity MgO (Table 8-V):

$$Z_c = \frac{|\bar{X}_{\text{pure}} - \bar{X}_i|}{\sigma_{\bar{X}_{\text{pure}} - \bar{X}_i}} = \frac{|\bar{X}_{\text{pure}} - \bar{X}_i|}{\sqrt{\frac{\sigma_{\text{pure}}^2}{N_{\text{pure}}} + \frac{\sigma_i^2}{N_i}}} \quad (8-1)$$

where Z_c is the index number, \bar{X}_{pure} is the arithmetic mean value of the modulus of rupture for all undoped specimens, \bar{X}_i is the arithmetic mean value of the modulus of rupture for specimens in the i^{th} group of doped specimens, $\sigma_{\bar{X}_{\text{pure}} - \bar{X}_i}$ is the standard deviation of the difference of the means \bar{X}_{pure} and \bar{X}_i , N_{pure} is the number of pure specimens broken, and N_i is the number of specimens of the i^{th} group broken. Results of these analyses are summarized in Table 8-IX.

A program employed in these statistical evaluations was devised by the Hercules Powder Co., Bacchus, Utah, using an IBM 7074 digital computer. The results are presented in Tables 8-X and 8-XI, which are based on a Cartesian and logarithmic treatment of the impurity content, respectively.

Table 8-IX
**STATISTICAL ANALYSES FOR POPULATION IDENTIFICATION
 COMPARING DOPED POLYCRYSTALLINE ALUMINUM
 OXIDE SAMPLES WITH UNDOPED LOTS**

Impurity	Amount	25°C	500°C	1050°C
TiO ₂	10	same	same	same
	100	different	different	same
	1,000	different	different	different
	10,000	different	different	different
Fe ₂ O ₃	10	same	same	same
	100	different	same	same
	1,000	different	same	same
	10,000	different	same	same
Cr ₂ O ₃	10	same	same	same
	100	different	same	same
	1,000	different	same	same
	10,000	different	same	same
MgO	10	same	same	same
	100	same	different	different
	1,000	same	same	different
	10,000	same	same	different
Na ₂ O	10	same	same	same
	100	same	same	same
	1,000	different	same	same
	10,000	same	same	same

Note: All specimens were sintered in a gas-fired kiln.

Table 8-X
RESULTS OF LINEAR REGRESSION ANALYSES FOR STRENGTH DATA ON
DOPED AND UNDOPED ALUMINUM OXIDE TESTED AT
VARIOUS TEMPERATURES
(Based on Cartesian Representation of Impurity Content)

Impurity	Breaking Temperature (°C)	Most Important Variable (X ₁)	2nd Variable (X ₂)	Regression Equation			Correlation Coefficient
				y-Intercept	Slope (X ₁)	Slope (X ₂)	
TiO ₂	25	impurity	density	107.5713	0.0024	37.9627	0.87636
	500	impurity	crystal size	19.9271	0.0013	0.0624	0.69144
	1050	impurity	density	169.5935	0.0013	51.3705	0.65115
Fe ₂ O ₃	25	crystal size	impurity	9.3049	1.4699	0.0	0.25140
	500	crystal size	density	44.1864	1.3517	0.0	0.27646
	1050	crystal size	density	22.6739	0.0	0.0	0.0
Cr ₂ O ₃	25	density	impurity	338.8036	99.4204	0.0	0.37972
	500	crystal size	density	46.1313	1.5621	0.0	0.16559
MgO	25	density	impurity	118.1666	22.3803	0.0	0.22538
	500	density	impurity	97.1161	32.2941	0.0	0.32897
	1050	density	impurity	1157.9341	36.4617	0.0004	0.50102
Na ₂ O	25	density	impurity	269.6878	68.1859	0.0	0.46874
	500	density	impurity	22.5795	0.0	0.0	0.00
	1050	density	crystal size	116.6750	25.4235	0.0	0.2207

All specimens were sintered in a gas-fired kiln.
The second variable is listed to show the order of importance of the second or third variables; however, a slope is not listed if the additional variable does not improve the fit of the regression equation.

Table 8-XI
RESULTS OF LINEAR REGRESSION ANALYSES OF STRENGTH DATA
ON DOPED AND UNDOPED ALUMINUM OXIDE TESTED AT
VARIOUS TEMPERATURES
(Based on Logarithmic Representation of Impurity Content)

Impurity	Breaking Temperature (°C)	Most Important Variable (X_1)	2nd Variable (X_2)	Regression Equation		Correlation Coefficient
				y Intercept	Slope (X_1) Slope (X_2)	
TiO ₂	25 500 1050	impurity impurity impurity	crystal size density	163.8964	4.1733	0.0787
				140.2740	2.3564	31.6837
				22.3621	2.3185	0.0
TiO ₂ *	25 500 1050	impurity impurity impurity	density	30.7521	-0.0018	0.0
				19.0952	0.0008	0.0
				127.9103	0.0014	40.4809
Fe ₂ O ₃	25 500 1050	impurity crystal size none	density	34.3645	2.3257	0.0
				44.1864	0.0	0.0
				0.0	0.0	0.0
Cr ₂ O ₃	25 500	density crystal size	density	338.8036	99.4204	0.0
				46.1313	1.5621	0.0
				118.1666	22.3803	0.0
MgO	25 500 1050	density density impurity	density	97.1161	32.2941	0.0
				22.4845	2.1218	0.0
				269.6878	63.1859	0.0
Na ₂ O	25 500 1050	density none density	density	0.0	0.0	0.0
				116.6750	25.4235	0.0
						0.22207

* Data obtained by ignoring results corresponding to pure samples.

All specimens were sintered in a gas-fired kiln.
(X_3) density 34.0740.

From these tests, it appears at first glance that, with the exception of the series with the TiO_2 additive, impurity content has little influence on the strength. However, one should exercise the same reservations regarding the conclusions indicated by the regression analyses as those already mentioned in the discussion of the air-fired MgO data. Neither density nor grain size are independent of the impurity content, and the concentration range is comparatively large. These factors could lead to spurious results from the regression analyses.

Titanium oxide was the only additive for which strength was found to be consistently correlated with impurity content (correlation coefficient > 0.7). For specimens doped with Fe_2O_3 , Cr_2O_3 , or MgO , the regression analyses would lead one to conclude that grain size and density have the most influence on the strength. Even for grain size and density, however, the correlation coefficients are very low. For this reason, no attempts were made to use the Knudsen⁽⁸⁻⁵⁾ or Petch⁽⁸⁻⁶⁾ equations to subtract the effects of grain size and density from the overall results.

These results should be regarded as preliminary in nature. Effects of additive content, grain size and density on the strength could easily have been masked by some uncontrolled and undetermined factor or factors. For example, the surface condition may strongly influence the strength. Also, tests made by Harbison-Walker Co.⁽⁸⁻⁷⁾ show that the impurity contents of some samples of high-purity Al_2O_3 used in this research were increased by factors of from two to ten by sintering in the gas-fired kilns at this laboratory. This was one reason for firing subsequent specimens in an electric resistance furnace rather than in gas-fired kilns. The specimens broken to obtain the data used for these regression analyses were not systematically

checked for any increase in the impurity content as a result of firing.

C. Effect of Titanium Oxide Additions on Strength of
Aluminum Oxide at Room Temperature

To eliminate the potentially deleterious influences introduced into the previous series by firing the specimens in the gas furnace, a new series of experiments was planned using multi-crystalline Al_2O_3 specimens sintered in an air atmosphere in an electric resistance heated kiln. The test specimens were cut from discs made from high-purity Al_2O_3 powders that had been treated to eliminate clustering of the powder particles. The procedure involved in this treatment was discussed earlier in this report. Discs were cold-pressed at 20 tons per sq in, then fired at ca. 1740°C for 8 hr in an air atmosphere electric resistance furnace. The heating and cooling portions of the firing schedule were essentially the same as for the MgO discs fired earlier in the same furnace (Fig. 8-3).

The results of bend tests made at room temperature on specimens of high-purity Al_2O_3 doped prior to sintering with 0, 100, 1000, 10,000 and 20,000 ppm TiO_2 are summarized in Fig. 8-9. As can be seen, the extremely strong dependence of strength upon TiO_2 impurity concentration, noted in the previously discussed experiments, has been reconfirmed in this series using the expectedly much less contaminated, electric-kiln sintered, specimens. Additional modulus of rupture measurements were also planned for air-fired Al_2O_3 doped with Fe_2O_3 , ZrO_2 , Cr_2O_3 , MgO and MnO. However, an untimely burn-out of the electric kiln, prevented the execution of these plans.

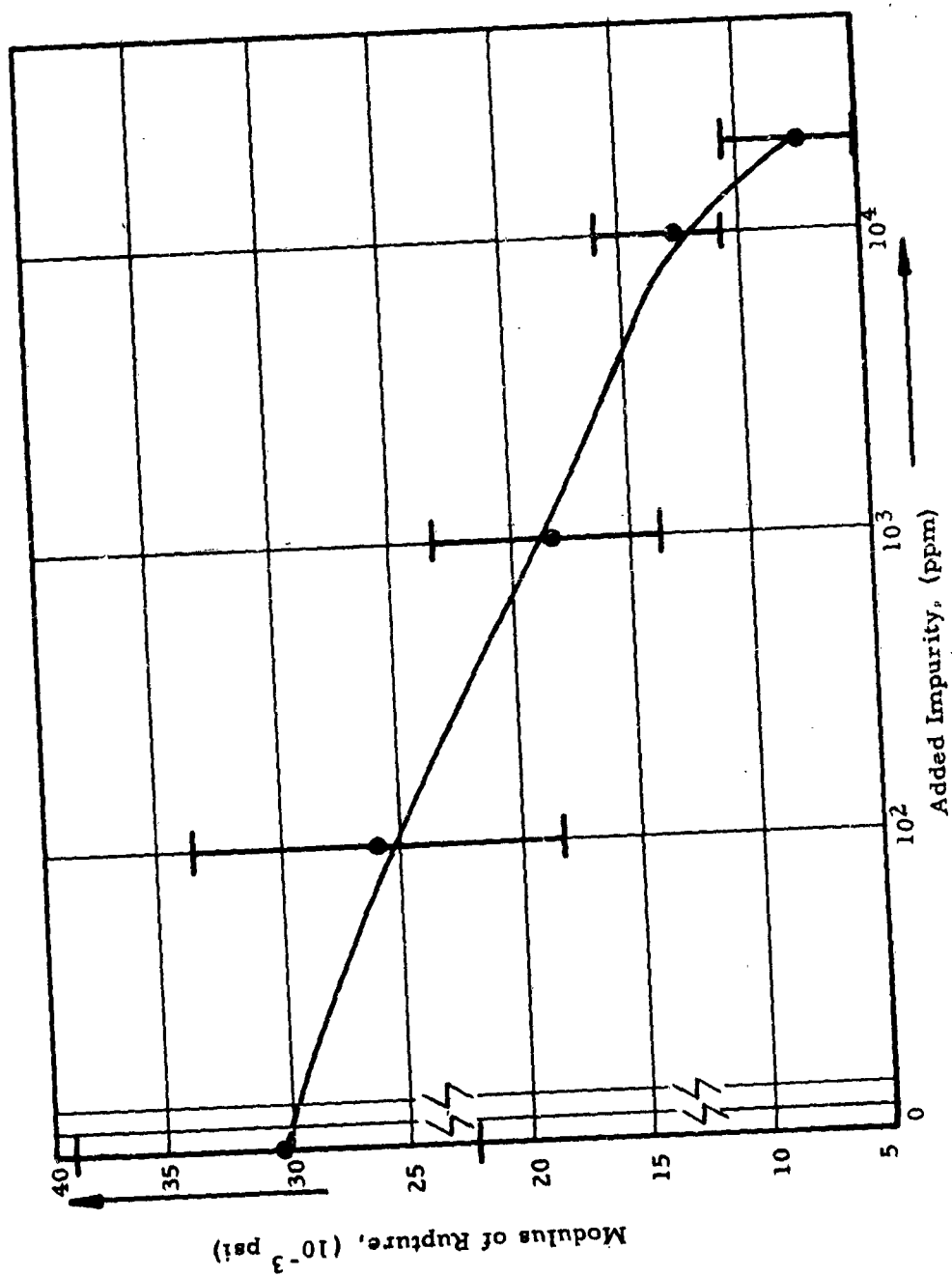


Fig. 8-9 ROOM TEMPERATURE STRENGTH OF ALUMINUM OXIDE AS A FUNCTION OF TITANIUM OXIDE IMPURITY LEVEL

D. Recrystallization Studies

The excessive grain growth experienced with certain Al_2O_3 specimens that had been doped with Fe_2O_3 was investigated. Oxides of Cs, V, Mo, Cd, Ti, Mn, Mg, Ce, B and Fe were added to high-purity Al_2O_3 . It was found that of these additives only the Fe_2O_3 gave the excessive grain growth, and that only in the presence of Na. When discs that had been doped with Fe_2O_3 were placed on Al_2O_3 setting sand that was contaminated with Na, excessive grain growth was found to occur. When these Fe_2O_3 -doped discs were packed in Na_2O , fluxing of the Al_2O_3 occurred, but the excess grain growth was observed only in regions of the Al_2O_3 disc that were not in direct contact with the Na_2O and were, therefore, not fluxed.

5. MICROHARDNESS STUDIES

All microhardness measurements reported here were made with a diamond indenter on a Tukon microhardness instrument. A magnification of 20 X was used for measurement of the indentation. The scale is Knoop hardness. Small fractures were observed to occur around the indentation marks in the majority of the early tests. As long as the measurement technique was not improved to the point where the formation of these fractures could be avoided, results were considered to be of questionable value. Some of these earlier results are interesting, however, and will be discussed here. Many variations in the measurement technique were tried before a satisfactory method was finally evolved. It was found that fracture-free indentations could be made consistently when the time involved in making the indentation was of the order of a minute. Fractures were almost always observed when indentation times of thirty seconds or less were used. When the shorter indentation times were used and fractures were prone to appear, the size of the weight used to drive the indenter into the material seemed inconsequential as far as eliminating the fractures was concerned.

Previous microhardness measurements on polished but unetched specimens of our pressed and sintered Al_2O_3 showed negligible variation of microhardness with the amount of impurity (8-1). Current results on polycrystalline Al_2O_3 and MgO , and on single crystal MgO indicate that the surface condition of the specimen has a profound influence on microhardness values. Thus, polished specimens that had been etched gave different results than specimens that had only been polished. Also, microhardness values obtained on the single crystal MgO were found to be dependent on the orientation of the diamond indenter with respect to the crystallographic directions of the MgO specimen, and on how well the crystal had been cleaved.

Several procedures that seemed attractive for the preparation of specimens for microhardness determination were investigated. One of the early procedures used for polycrystalline MgO consisted of the following steps.

- (1) Specimen was mounted in plastic.
- (2) Polishing was done sequentially with 600 mesh SiC , 1000 mesh SiC and 0.3μ Al_2O_3 powder (Linde A5175) until specimen surface was uniformly flat.
- (3) Surface dust from the polishing operation was removed from the specimen with a mild soap and water solution. The specimen was then wiped gently with soft paper.
- (4) The polished specimen was etched for four minutes in dilute H_2SO_4 solution (one part acid to nine parts water).

Later procedures for polycrystalline MgO were similar to those listed, except that ethanol was substituted for the soap and water solution in Step (3), the gentle wiping with soft paper in Step (3) was eliminated, and other etchants such as boiling H_3PO_4 and dilute HCl solution (one part acid to nine parts water) were used. The etchants H_3PO_4 , HCl , and H_2SO_4 all left undesirable surface precipitates on the MgO specimens that affected the

values of microhardness obtained. It was later decided, therefore, to omit the etching step in the procedure, and measure microhardness on the surfaces of the specimens that had been mounted in plastic, polished as in Step (2), and washed with ethanol. An early procedure for preparation of polycrystalline Al_2O_3 specimens for measurement of microhardness included Steps (1), (2), and (3), but Step (4) was replaced with a ten-minute etch in hot H_3PO_4 . Treatments that were used to prepare single crystal MgO specimens for measurement of microhardness will be discussed later along with the descriptions of the tests.

The microhardness and modulus of rupture values for doped and undoped polycrystalline Al_2O_3 sintered in a gas-fired kiln are summarized in Table 8-XII. Table 8-XIII presents similar data for both etched and unetched polished specimens of polycrystalline MgO taken from discs sintered in a gas-fired kiln. Note the differences in the values obtained for the etched and unetched specimens; the microhardness values in these particular tests do change considerably less with the amount of added impurity in the case of the polished but unetched specimens as they do for the etched specimens. The data reported in Tables 8-XII and 8-XIII were obtained prior to the time when the problem of the fractures around the indentation marks was solved and are, therefore, to be regarded with appropriate reservation.

The MgO single crystals used in these investigations were cleaved from stock purchased from the General Electric Co. These crystals contained ca. 2 percent Fe impurity. In experiments made early in the continuation phase of the program, a cut specimen was first mounted in plastic with the freshly cleaved face exposed. The cleaved surface appeared smooth. The microhardness of the cleaved surface was determined before polishing. These measurements were made with the indenter

Table 8-XII
ROOM TEMPERATURE KNOOP HARDNESS AND
MODULUS OF RUPTURE FOR DOPED AND
UNDOPED POLYCRYSTALLINE ALUMINUM OXIDE *

Impurity	Amount of Impurity Added (ppm)	Knoop Hardness	Modulus of Rupture, (10^{-3} psi)
MgO	0.	403.4**	35.1
	10.	456.0**	32.0
	100.	1970.8	32.7
	1,000.	2124.0	34.0
	10,000.	1796.6	30.8
Cr ₂ O ₃	0.	343.6**	35.1
	10.	351.4**	28.3
	100.	492.6**	25.6
	1,000.	302.0**	21.4
	10,000.	2068.0	30.6
TiO ₂	0.	306.2**	35.1
	10.	597.8	34.5
	100.	351.4**	30.5
	1,000.	480.0**	24.3
	10,000.	2208.0	13.3
Na ₂ O	0.	413.0**	35.1
	10.	367.4**	30.8
	100.	384.8**	32.3
	1,000.	907.4	27.8
	10,000.	208.4	31.6

* All specimens etched.

** Specimen fractured around indentation mark.

Note: The difference in microhardness values for each added impurity at zero ppm is due to the fact that all compositions in each impurity type were fired together.

Table 8-XIII
ROOM TEMPERATURE KNOOP HARDNESS AND
MODULUS OF RUPTURE FOR DOPED AND
UNDOPED POLYCRYSTALLINE MAGNESIUM OXIDE *

Impurity	Amount Added (ppm)	Knoop Hardness		Modulus of Rupture (10 ⁻³ psi)
		Etched	Unetched	
None		219.0	790.4	-
Fe ₂ O ₃	10	-	830.8	-
	100	-	790.4	-
	1,000	-	413.0**	-
	10,000	-	248.6**	-
Al ₂ O ₃	10	-	846.0	21.0
	100	-	760.0	21.8
	1,000	-	728.0	19.8
	10,000	-	253.0**	19.2
TiO ₂	10	740.4	907.4	18.3
	100	846.6	790.4	21.8
	1,000	780.4	804.0	18.7
	10,000	145.2	714.8	13.9
Cr ₂ O ₃	10	764.8	817.6	14.1
	100	776.2	764.0	13.1
	1,000	222.8	716.0	12.6
	10,000	126.4	650.0**	7.9
SiO ₂	10	-	840.0	20.6
	100	-	820.0	16.0
	1,000	-	790.0	18.4
	10,000	-	634.0**	14.8

* Etched and unetched polished specimens

** Fracture occurred around indentation

at various angles with respect to the $\langle 100 \rangle$ direction. The results, summarized in Table 8-XIV, show that the microhardness is minimum in the $\langle 100 \rangle$ direction and maximum in the $\langle 110 \rangle$ direction.

The effects of polishing and etching on the microhardness of single crystal MgO are presented in Table 8-XV. Polishing was done on a high speed wheel with 0.3μ Al_2O_3 powder. Etching was done for various times with dilute H_2SO_4 (one part acid to nine parts water). During polishing, a high and uniform density of dislocations was produced on the surface being polished. Proper etching would be expected to remove the work-hardened surface and reveal more truly the nature of the bulk crystal. This task would be more difficult with polycrystalline material than with a single crystal. The unusually large decrease in microhardness observed following a two-minute etch is interesting. No definite explanation of this phenomenon is offered, although it may be that the high value is due to the presence of some sort of surface precipitate.

In some microhardness experiments made with single crystal MgO during subsequent phases of the program, a freshly cleaved specimen was mounted in a disc-shaped metal holder with wax. Great care was taken to protect the cleaved surface from damage before, during and after mounting had been completed. The surface was not handled manually, and care was given to prevent dust particles from settling on the surface prior to testing. Results of the microhardness measurements on the freshly cleaved single crystals are presented in Table 8-XVI.

After the microhardness of a freshly cleaved MgO single crystal was determined, the specimen was mounted in a plastic briquette and polished on high-speed wheels successively with 600 mesh SiC, then with 1000 mesh SiC, and finally with

Table 8- XIV
MICROHARDNESS SINGLE CRYSTAL MAGNESIUM OXIDE
AS A FUNCTION OF ANGLE

Angle, θ , (deg)	Crystallographic Direction	Hardness	Fracture (see Fig. 8-10)
0, 90, 180, 270	$\langle 100 \rangle$ $\langle 001 \rangle$ $\langle 010 \rangle$	442. 4	large fracture to slip direction and fracture directions also
45, 135, 225	$\langle 110 \rangle$ $\langle 101 \rangle$ $\langle 011 \rangle$	876. 45	no fracture
225, 67. 5 112. 5, 157. 5 202. 5, 247. 5 292. 5, 337. 5	$\langle 210 \rangle$ $\langle 120 \rangle$ $\langle 201 \rangle$ $\langle 102 \rangle$	639. 7	a few fractures in the direction to $\langle 110 \rangle$ and $\langle 100 \rangle$ directions (slip) $\langle 010 \rangle$ (fracture) (or cleavage)

Table 8- XV
EFFECTS OF POLISHING AND ETCHING ON THE MICRO-
HARDNESS OF SINGLE CRYSTAL MAGNESIUM OXIDE *

Polishing Time, (min)	Etching Time, (min)	Knoop Hardness			
		Unetched		Etched	
		$\langle 110 \rangle$	$\langle 1\bar{1}0 \rangle$	$\langle 110 \rangle$	$\langle 1\bar{1}0 \rangle$
0 (as cleaved)	0	876. 5	442. 4	-	-
2	0	790. 4	370. 2**	-	-
5	0	244. 0**	103. 3**	-	-
7	0	273. 6**	124. 8**	-	-
9	0	207. 8**	103. 3**	-	-
9	2	-	-	1653. 2	634.
9	4	-	-	239. 6**	95. 1**
9	6	-	-	433. 8**	143. 1**
9	8	-	-	396. 0**	-

* Preliminary data only.

** Fracture occurred around indentation.

Table 8- XVI
MICROHARDNESS DATA ON MAGNESIUM OXIDE

Single Crystals			High Purity Polycrystals		
	Measured Direction	Average	Measured Direction	Average	Comments
Freshly cleaved	<100> <110>	115.46 (Fracture) 893.6 (Fracture)	<110>	276.8 (Fracture)	
Polished Successively With	600 Mesh SiC		<100>	1344.8 (No Fracture)	No clear indentation.
	1000 Mesh SiC		<100>	807.4 (No Fracture)	(No fracture)
	0.3 μ Al ₂ O ₃	139.2 (Fracture) 443.8 (Fracture)	<110>	1693.0 (No Fracture)	1950.2 (No Fracture)
Annealed	Rapid Cooling		<100>	1288.2 (No Fracture)	Rough surface.
	Slow Cooling		<100>	1235.2 (No Fracture)	Rough surface
			<110>	1234.4 (No Fracture)	Fracture depends on grains crystallographic orientation.
			<110>	332.4 (Fracture)	
			<110>	961.6 (Fracture)	
			<110>	1025.4 ϕ (Fracture)	
			<110>	790.4	
			<110>	901.8# (Fracture)	Fracture depends on grains crystallographic orientation.
			<110>	284.6# (Fracture)	
			<110>	1032.8 (Fracture)	
			<110>	1010.2	
			<110>	347.4* (Fractured)	
			<110>	301.6# (Fractured)	
			<110>	201.0* (Fractured)	

= spotty area * = clear area ϕ = plenty of 0.3 H₂O₃ powder used in polishing
 first column for single crystals annealed at 1450°-1475°C, second column at 1500-1520°C. Polycrystals annealed at 1540°C. Soaking time for all specimens: 30 minutes.

0.3 μ Al_2O_3 powder (Linde A5175). The final polishing step was done because the surface was too rough and dark for fully satisfactory observation of the indentation mark following the polishing with SiC. Surface dust was removed with ethanol before microhardness measurements were made. Surfaces were dried by evaporation without wiping. Microhardness determinations were made following each stage of the polishing operation. These results are also presented in Table 8-XVI. The polishing operation employed for the polycrystalline MgO specimens used to obtain the data in Table 8-XVI is identical to that described for single crystals.

Following the polishing operation and the subsequent microhardness measurement, both single crystal and polycrystalline specimens were carefully removed from the plastic briquette without touching the surface, and annealed 30 min at ca. 1500°C in a closed Mullite tube in a gas-fired kiln. Recrystallized alumina boats were used to contain the specimens during this firing. Specimens were either pulled quickly out of the hot zone of the furnace and quenched in the cold air, or allowed to remain in the furnace for slow cooling to room temperature after the furnace was shut down. The heat treated specimens were again mounted in the iron disc with wax, and tested for microhardness on the same surface as before. The results for this set of tests are again given in Table 8-XVI.

Wide variation in hardness was found from one location on a single crystal surface to another. This variation may arise from chemical heterogeneity in the specimens. The average Knoop hardness of freshly cleaved MgO was found to be 891.4 in the $\langle 110 \rangle$ direction.

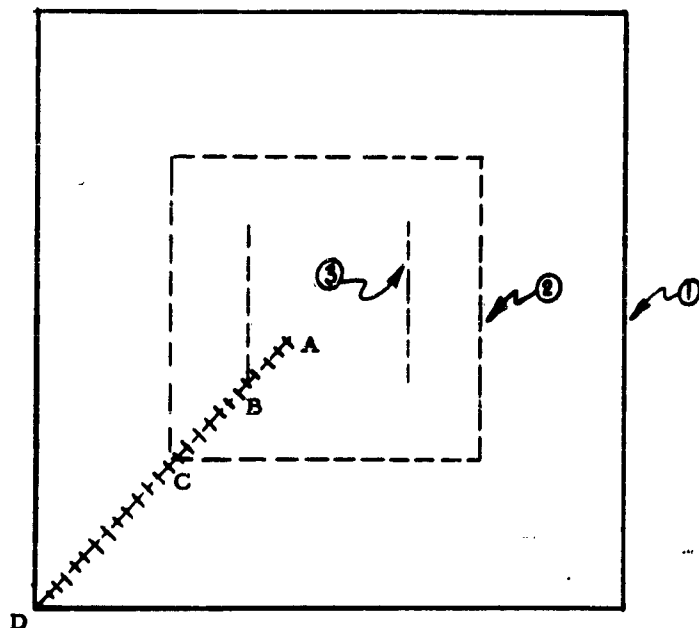
The same surface of the specimen was polished in the $\langle 100 \rangle$ direction with 600-mesh SiC. As has been pointed out, the condition of the specimen surface following polishing

with 600-mesh SiC was such that fully satisfactory measurements could not be made. However, it was interesting to note that essentially no fracture occurred for indentations made in the $\langle 100 \rangle$ or $\langle 110 \rangle$ directions, even when indentation times of the order of 30 sec. were used. Polishing of the surface with 1000-mesh SiC improved the surface condition over that obtained with the 600-mesh SiC, but not enough to give good measurements. Again, no fractures occurred around the indentations. The surface was next polished with 0.3- μ Al_2O_3 powder. It was found that the value measured for microhardness and the extent of fracture was dependent in a sensitive way on the polishing technique used. For example, careful polishing using plenty of the Al_2O_3 powder and water yielded higher values with less fracture than when less Al_2O_3 powder was used.

When the single crystal specimens were annealed at 1450°C to 1500°C for 30 min, they acquired a spotty appearance, which may be due to segregation of impurities. It was found that the quenched specimens had lower values of microhardness with less fracture than the specimens that were cooled slowly.

In the case of the high-purity polycrystalline MgO, it was observed that heat-treated specimens, quenched or slow-cooled, had large clear regions and small spotted areas. The clear areas had lower apparent microhardness than the spotted areas, and were more highly susceptible to fracture around the indentation.

Microhardness measurements were also made on a single crystal specimen of MgO into which FeO had been diffused. The measurements were taken at points on the specimen located as shown schematically in Fig. 8-10. The concentration of FeO at Boundary 2 in Fig. 8-10 is between 50 and 60 mole percent. At Boundary 3, the FeO concentration is only slightly greater than that originally existing in the MgO. Two sets of measurements in which the virgin MgO was cleaved from single crystal stock obtained



- Boundary 2:** External boundary of original MgO crystal. Diffusion of FeO was from the crystal periphery towards its interior.
- Region 1-2:** MgO-FeO polycrystalline region formed from a mixture of FeO and MgO powder that was packed around the MgO single crystal.
- Region 2-3:** MgO-FeO single crystal (i. e., single crystal MgO into which FeO has diffused from Region 1-2.
- Boundary 3:** Boundary between virgin MgO and the diffusion zone.
- Region 3:** Zone within MgO single crystal into which FeO has not yet diffused.
- Line A-D:** Line along which microhardness measurements were made. Long axis of indentation was in a direction normal to the line A-D.

Fig. 8-10

SCHEMATIC DIAGRAM SHOWING LOCATIONS AT WHICH MICROHARDNESS MEASUREMENTS WERE MADE ON SINGLE CRYSTAL MAGNESIUM OXIDE INTO WHICH FERROUS OXIDE HAD BEEN DIFFUSED.

from G. E. gave similar results. Indentations were made starting at A and moving along the line A-D toward D. Microhardness was found to be ca. 275-300 on the Knoop scale from position A until just before B was reached. In the vicinity of position B (Boundary 3) the microhardness seemed to rise to 325-350. We have not yet ascertained the meaning of this apparent rise in hardness at Boundary 3. It may be no more than scatter in the experimental points. However, other data taken in similar fashion on a Norton single crystal MgO that had been diffused with FeO showed the same trend of behavior at Boundary 3. The Knoop microhardness was found to increase from 850 to ca. 950. Moving from position B to position C, the microhardness falls off slowly but steadily. Beyond Boundary 2, the microhardness rises rather sharply from a little over 200 to ca. 600 on the Knoop scale.

Table 8-XVII and Fig. 8-11 present the summary of microhardness data obtained on doped and undoped polycrystalline MgO sintered in air atmosphere in an electric resistance furnace. Specimens were prepared for microhardness measurement by

- (1) Mounting in plastic.
- (2) Polishing successively with 600-mesh SiC, then 1000-mesh SiC, and finally with 0.3- μ Al_2O_3 .
- (3) Washing with ethanol.

In making these measurements, the time of indentation was extended to the order of one minute, and a weight of fifty grams was used to drive the indenter. Indentations were found to be fracture-free, and a plot of log (indentation length) versus log (load) gave a straight line. These are probably the most reliable microhardness data obtained to date in these investigations.

Table 8-XVII

**KNOOP MICROHARDNESS MEASUREMENTS AS FUNCTION OF
IMPURITY CONCENTRATION IN POLYCRYSTALLINE
MAGNESIUM OXIDE**

Impurity	Amount of Impurity Added (ppm)	Knoop Hardness	Indentation Length (μ)
Fe_2O_3	0	941	27.5
	10^2	1013	26.5
	10^3	1035	28.2
	1×10^4	1139	25.0
	2×10^4	1166	24.7
Al_2O_3	0	983	26.9
	10^2	1089	25.8
	10^3	1077	25.7
	1×10^4	991	26.8
	2×10^4	1121	25.2
ZrO_2	0	1029	26.3
	10^2	914	27.9
	10^3	908	28.0
	1×10^4	901	28.1
	2×10^4	852	28.9
SrO	0	955	27.3
	10^2	1086	25.6
	10^3	870	28.6
	1×10^4	852	28.9
	2×10^4	708	31.7
TiO_2	0	1013	26.5
	10^2	898	28.6
	10^3	914	27.9
	1×10^4	889	28.3
	2×10^4	807	29.7
	0	950	27.4
	10^2	969	27.1
	10^3	1013	28.5
	1×10^4	1150	24.9
	2×10^4	1176	26.6

(Test Load = 50 grams, Indentation time, ca. 1 min.)

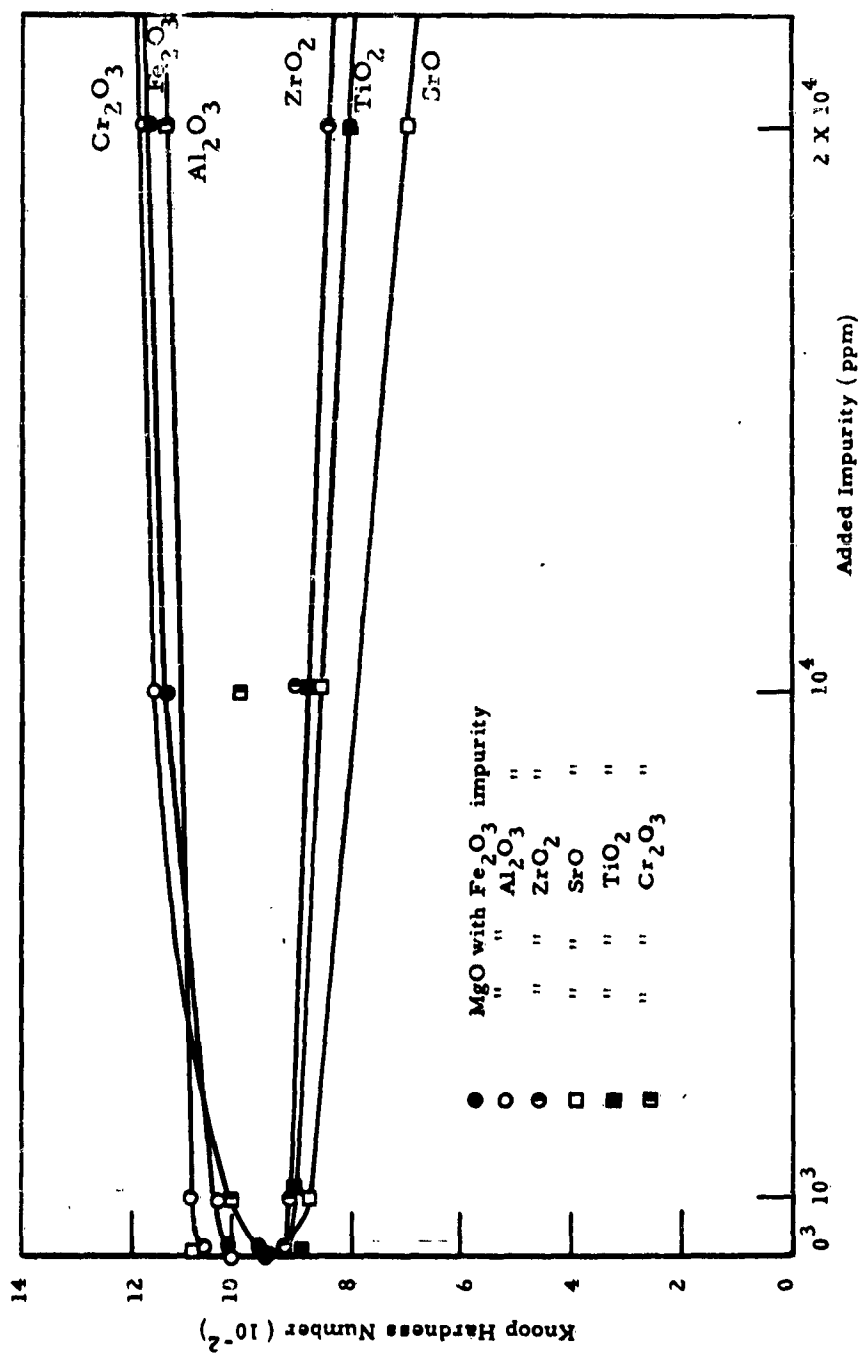


Fig. 8-11 MICROHARDNESS NUMBER OF POLYCRYSTALLINE MAGNESIUM OXIDE AS A FUNCTION OF IMPURITY

6. SINTERING AS A FUNCTION OF IMPURITY CONTENT

D. L. Johnson, a former graduate student of the University of Utah, recently extended existing sintering theories; his studies contribute significantly to the understanding of sintering phenomena⁽⁸⁻⁸⁾. These studies included the high-purity Al_2O_3 and high-purity Al_2O_3 doped with MgO . The theory developed and work done on the doped and undoped high-purity Al_2O_3 are briefly summarized along with some preliminary data on the effect of TiO_2 additions on the sintering of the high-purity Al_2O_3 .

Johnson re-evaluated diffusion models for sintering by first refining the geometrical approximations used by previous investigators. A graphical method was used to determine the quantities ρ/r , x/r and A/r^2 , which were related to $\Delta r/r$ for various diffusion paths and vacancy sinks for spheres and for shapes other than spheres. Table 8-XVIII⁽⁸⁻⁸⁾ shows the differences between these improved relationships and those obtained by previous workers.

For the case of bulk diffusion, the following assumptions were made.

- (1) The excess vacancy concentration at the concave surface of the neck is given by the Kelvin equation

$$\frac{C - C_0}{C_0} = \frac{\gamma a^3}{kT} \left(\frac{1}{\rho} - \frac{1}{x} \right) \approx \frac{\gamma a^3}{kT\rho} \quad (8-2)$$

where C is the concentration of vacancies at the concave surface of the neck, C_0 the equilibrium vacancy concentration under a flat surface, γ the surface free energy, a^3 the vacancy volume, k is the Boltzmann constant, T is the absolute temperature, and $X \gg \rho$.

Table 8-XVIII
GEOMETRY RELATIONSHIPS USED IN DIFFUSION SINTERING MODELS

Vacancy Sink	Diffusion Path	Initial Contact (Particle Geometry)	p	x	A	Reference
Grain boundary	Bulk	Spherical	$\frac{x^2}{4r}$		$\frac{2^3}{\pi x} - \frac{2}{r}$	8-9
"	"	"	$\frac{x^2}{4r}$ or $r \left(\frac{\Delta L}{L_0}\right)$	$2x \left(\frac{\Delta L}{L_0}\right)^{1/2}$	$2\pi x r$, or $\frac{3}{4\pi r^2} \left(\frac{\Delta L}{L_0}\right)$	8-10
"	"	"	$\frac{7}{8} \pi x \left(\frac{\Delta L}{L_0}\right)^{6/5}$	$\frac{5\pi}{9} x \left(\frac{\Delta L}{L_0}\right)^{0.46}$	$7\pi x^2 \left(\frac{\Delta L}{L_0}\right)^{3/2}$	8-8
Surface	"	"	$\frac{x^2}{2r}$		$\frac{2^3}{\pi} \frac{x}{r}$	8-9
"	"	"	$\frac{x^2}{2r}$		$\frac{2^3}{\pi} \frac{x}{r}$	8-10
"	"	"	$\frac{3\pi x}{5} \left(\frac{x}{r}\right)^{2.4}$		$\frac{2^3}{\pi} \frac{x}{r}$	8-8
Grain boundary	Grain boundary	"	$\frac{x^2}{4r}$ or $r \left(\frac{\Delta L}{L_0}\right)^{6/5}$	$2x \left(\frac{\Delta L}{L_0}\right)^{1/2}$	$2\pi r (5a)$	8-10
"	"	"	$\frac{7}{8} \pi x \left(\frac{\Delta L}{L_0}\right)^{0.18}$	$\frac{5\pi}{9} x \left(\frac{\Delta L}{L_0}\right)^{0.46}$	$2\pi r b$	8-8
"	Bulk	Paraboloid	$\frac{7}{8} \pi x \left(\frac{\Delta L}{L_0}\right)^{1.18}$	$\frac{7\pi}{12} x \left(\frac{\Delta L}{L_0}\right)^{0.51}$	$23x^2 \left(\frac{\Delta L}{L_0}\right)^{1.54}$	8-8
"	Grain boundary	"	$\frac{7}{8} \pi x \left(\frac{\Delta L}{L_0}\right)^{1.18}$	$\frac{7\pi}{12} x \left(\frac{\Delta L}{L_0}\right)^{0.51}$	$2\pi r b$	
"	Bulk	160° cone on a plane	$0.29x \left(\frac{\Delta L}{L_0}\right)^{1.94}$	$3\pi x \left(\frac{\Delta L}{L_0}\right)^{1.02}$	$20x^2 \left(\frac{\Delta L}{L_0}\right)^{2.08}$	8-8
"	"	140° cone on a plane	$0.35x \left(\frac{\Delta L}{L_0}\right)^{1.07}$	$4.45 \left(\frac{\Delta L}{L_0}\right)^{1.02}$	$11.6x^2 \left(\frac{\Delta L}{L_0}\right)^{2.08}$	8-8

- (2) The vacancy concentration at the center of the neck is equal C_0 .
- (3) The slow step is the diffusion of vacancies through the bulk.
- (4) The vacancies diffuse with cylindrical symmetry^(8-9, 8-10).
- (5) The vacancy annihilation rate is constant over the entire grain boundary.
- (6) Fick's first law can be applied. Diffusion is rapid compared with neck growth and appears to be steady state.
- (7) The concave neck surface is circular in cross section and tangent with both spherical particles.
- (8) The vacancy diffusion constant is independent of vacancy concentration.

The following assumptions were made for the case of grain boundary diffusion

- (1) The slow step is the diffusion of vacancies within the grain boundary that is formed between the particles.
- (2) The grain boundary vacancy diffusion constant is independent of vacancy concentration.
- (3) The assumptions designated (1), (2), (4), (5), (6), and (7) under the case for bulk diffusion.

Johnson then derived an equation of the form,

$$-\frac{\Delta L}{L_0} = \left(\frac{K \gamma a^3 D}{k T \rho} \right)^m t^m \quad (8-3)$$

where K , M and ρ are numerical constants, $-\frac{\Delta L}{L_0}$ is the shrinkage, and D is either the volume or grain boundary self-diffusion coefficient, depending on the model. Johnson found $m = 0.21$ for the grain boundary diffusion case. Table 8-XIX gives values of K , m and ρ for the various models proposed.

Table 8-XIX
VALUES OF THE PARAMETERS APPEARING IN EQUATION 8-3
FOR VARIOUS DIFFUSION MODELS

Diffusion Path	Initial Contact	K	m	p	Reference
Bulk	Spherical	$\frac{20}{2}$	0.40	3	8-9
Bulk	Spherical	2	0.50	3	8-10
Bulk	Spherical	$\frac{31}{\pi^2}$	0.46	3	8-8
Grain Boundary	Spherical	15a	0.33	4	8-10
Grain Boundary	Spherical	$\frac{51b}{7\pi}$	0.31	4	8-8
Bulk	Paraboloid	$\frac{20}{\pi}$	0.46	2	8-8
Bulk	160° Cone on a plane	$\frac{180 \tan^2 10^\circ}{\pi^2}$	0.33	3	8-8
Bulk	140° Cone on a Plane	$\frac{45 \tan^2 10^\circ}{\pi}$	0.33	3	8-8
Grain Boundary	Paraboloid	$\frac{102b}{7\pi}$	0.31	3	8-8
Grain Boundary	160° Cone on	$55(\tan^2 10^\circ)b$	0.25	4	8-8
Grain Boundary	140° Cone on a Plane	$46(\tan^2 20^\circ)$	0.25	4	8-8

Note: The neck surface is the vacancy source and the grain boundary is the sink.

It was found that after a specific amount of initial shrinkage had occurred, the shrinkage of non-ideal compacts of several different Al_2O_3 powders became ideal. This initial shrinkage was found to be dependent upon the type of Al_2O_3 starting powder and the pressure used in pressing the specimen, but was independent of temperature. The pressing pressure dependence was observed to be characteristic of Al_2O_3 in which the powder particles had agglomerated into comparatively loose clusters. When suitable corrections were made for this initial shrinkage, the shrinkage due to sintering was found to be proportional to $t^{0.31}$. This indicates that the mechanism that controls in the sintering of the powdered Al_2O_3 studied⁽⁸⁻¹⁾ is grain boundary diffusion. The activation energy for the process was found to be 151 kcal/mole for the high-purity Al_2O_3 . Previous investigators, using less refined models and somewhat different conditions, had concluded that the sintering of Al_2O_3 powders was a bulk diffusion process. Johnson's conclusion was supported by the work of other investigators on grain growth in Al_2O_3 and the diffusion of an oxygen isotope of at wt. 18 into Al_2O_3 .

Preliminary work on the effects of small amounts of MgO and TiO_2 in the high-purity Al_2O_3 gave interesting results. It was found that 100 ppm MgO retarded the sintering of Al_2O_3 without changing the activation energy or the rate controlling mechanism. The addition of TiO_2 (added as TiCl_4 then calcined at 500°C and cooled before pressing) to the high-purity Al_2O_3 increased the sintering rate. Figure 8-12 indicates the difference in sintering rate at 1488°C between an undoped sample and one doped with 10,000 ppm TiO_2 . The exponent m in Eq. (8-3) is ca. 0.31 for TiO_2 concentrations less than 1000 ppm and ca. 0.46 for 10,000 ppm. This would indicate that TiO_2 promotes sintering by creating cation vacancies in the Al_2O_3 which, in turn, causes bulk diffusion to predominate over grain boundary

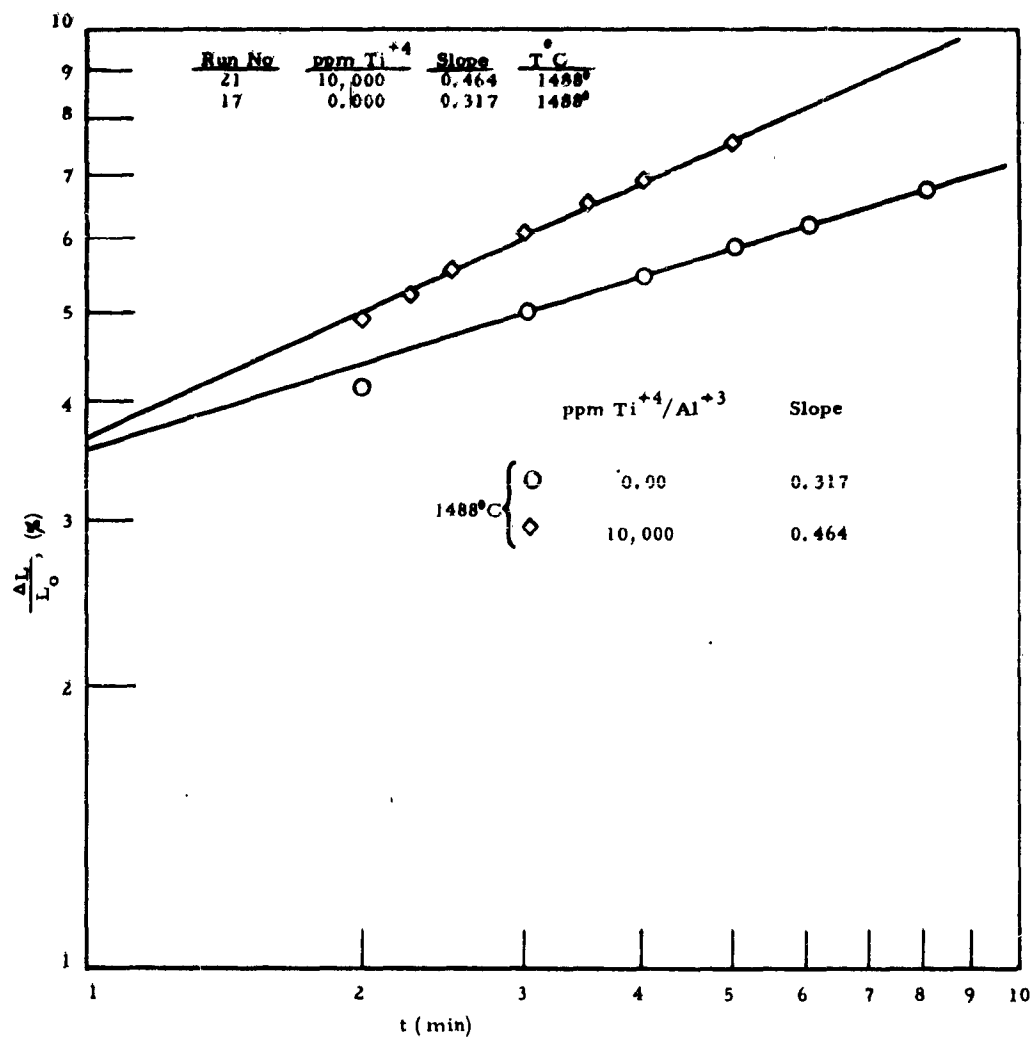


Fig. 8-12 EFFECT OF 10,000 ppm TITANIUM OXIDE ON SINTERING OF ALUMINUM OXIDE

diffusion with increasing TiO_2 content. Since a period of time is required for the Ti^{+4} to diffuse into the Al_2O_3 , the preceding results may have to be re-evaluated as more data are obtained. Samples of higher TiO_2 content are being prepared which will be calcined as a powder before pressing into discs so that the Ti^{+4} will be more homogeneously distributed in the Al_2O_3 lattice.

7. PRELIMINARY STUDIES FOR THE PREPARATION OF HIGH-PURITY, POLYCRYSTALLINE OXIDES

An effort was made to make translucent polycrystalline MgO of high-purity. It was also planned that work would be done to prepare dense, translucent, high-purity Al_2O_3 , but time did not permit execution of the plan.

Discs of the high-purity MgO were pressed at a pressure of 20 tons per sq in. Firing was done at ca. 1650°C inside a Mullite tube that had been mounted horizontally in a gas-fired kiln. Satisfactory connections were made with the tube, and oxygen gas was fed through the tube throughout the firing. The MgO specimens were put on alumina boats in the Mullite tube to circumvent fluxing with the Mullite. The first firing was of 84-hr duration, and specimens were removed at intervals of 12, 36, 60 and 84 hr. The second firing was of 108-hr duration with specimens being removed at intervals of 12, 36, 60, 84 and 108 hr. Table 8-XX shows the density as a function of firing time for the two firings. Also given are data on grain size for the first firing. Some of the fired specimens were quite translucent.

8. CONCLUSION

The purpose of this task is to investigate the numerous problems associated with the presence of impurities in ceramic oxides. To undertake a systematic study of this broad problem area, the investigation started out with developing methods for

Table 8-XX
**DENSITY AND GRAIN SIZE OF POLYCRYSTALLINE,
HIGH-PURITY MAGNESIUM OXIDE AS FUNCTIONS
OF FIRING TIME**

Firing Time, (hr)	Density, % of Theoretical		Grain Size (μ)
	Run 1	Run 2	
12	98.4	98.3	52.0
36	98.8	99.2	68.1
60	97.2	100.0	78.0
84	98.4	99.4	78.0
108	-	99.4	-

Firing done at ca. 1650°C in O₂ atmosphere
Run 1 only

producing MgO and Al₂O₃ bodies of the highest attainable purity, and adding carefully controlled amounts of impurities to them. Methods for this purpose, using the presintered doping methods were successfully developed, largely during the previous phase of the program. Refinements in specimen preparation during the current year consisted primarily of substituting an electric resistance heated furnace for the gas-fired furnace used previously for sintering of the polycrystalline bodies, to preserve specimen purity in the greatest possible degree. Some work was also carried forward on post-sintered doping methods, primarily in connection with single crystals used for hardness measurements.

The findings of research conducted during the current phase of the program can be summarized as follows.

(1) Annealing treatments carried out on high-purity MgO polycrystals had a consistently deleterious effect on strength.

(2) Prevention of moisture deposition on MgO polycrystals by means of vacuum-cooling following annealing, and breaking the specimens subsequently under oil, had no strengthening effect on the test pieces. These specimens, in fact, were found to be weaker than the control specimens broken fresh in an open air atmosphere, presumably because of the possible thermal shock damage suffered during quenching.

(3) Chemical polishing by a boiling H₃PO₄ etch significantly increased the strength of pure MgO bodies, on account of the removal of a surface layer containing severe flaws and scratches.

(4) Testing at liquid N₂ temperature also raised the strength of MgO appreciably. While this may be ascribed to a suppression of a moisture surface film formation at this temperature, it is much more likely that the observed strength enhancement is due to the N₂ environment on the one hand, and the cryogenic test temperature on the other, in keeping with the findings of research conducted on Tasks 6 and 11.

(5) Regarding the effect of impurities, added in concentrations varying from 0 to 2×10^4 ppm, to polycrystalline specimens, none were found that improved the room temperature strength of MgO. Ferric oxide and Cr_2O_3 had pronouncedly deleterious effects, the strength of MgO dropping nearly linearly with the logarithm of the impurity concentration; with Al_2O_3 and TiO_2 a significant drop in strength was noted only at concentrations in excess of 10^3 ppm, whereas ZrO_2 and SrO left the strength of MgO largely unaltered at concentrations up to 2×10^4 ppm.

(6) Statistical regression analysis carried out to segregate the effect of porosity, grain size and impurity levels upon the strength of multicrystalline MgO bodies appeared to show that only in the case of Al_2O_3 additions was the impurity concentration the primarily influential variable. Since, however, all three of these variables are intrinsically interrelated on the one hand and, on the other, considerable non-linearities are bound to be present at doping levels up to 2 per cent (as opposed to a linear model assumed in the (regression analyses), the results of these statistical studies must be treated at present with a substantial degree of reservation.

(7) The effect of added impurities, represented by Fe_2O_3 , Al_2O_3 , TiO_2 and SiO_2 , on the strength of MgO was explored at elevated temperatures, principally at 1000°C . It was found that a significant weakening resulted only for TiO_2 at concentrations in excess of 10^3 ppm; the other doping element left the strength largely unaltered. Silicon dioxide, in fact, had a distinct strengthening effect as its concentration rose from 10 to 10^4 ppm in MgO. Moreover, the strength of these bodies at comparable impurity concentrations was always higher at 1000°C than at room temperature.

(8) In regard to polycrystalline Al_2O_3 , tested at 1050°C , MgO additions had a distinctly weakening effect, while TiO_2 served to reduce the strength only at concentrations in excess of 100 ppm. Chromic oxide, Fe_2O_3 and Na_2O additions had no perceivable effect on the strength of Al_2O_3 over the concentration range of $10 - 10^4$ ppm.

(9) Statistical regression analyses confirmed the effect of the TiO_2 impurity as the primary factor influencing the strength of Al_2O_3 at 1050°C . However, for the other doping elements, including MgO, either porosity or grains was found to be the statistically most important variable. These regression analyses must be regarded with the same reservations as those mentioned for MgO under Point 6.

(10) The effect of TiO_2 additions on the strength of Al_2O_3 was repeatedly explored on specimens maintained free of possible contaminations by means of firing in an electric resistance heated kiln. Tests at room temperature confirmed the pronounced weakening effect of TiO_2 impurity additions. The strength of TiO_2 -doped Al_2O_3 , however, was consistently higher at room temperature than at 1050°C for comparable impurity concentrations.

(11) Extensive microhardness measurements carried out on single crystal MgO showed fracture-free indentations could be made only at indentation times larger than about 1 min. The surface condition and crystallographic orientation of specimens were found to have a profound influence on microhardness values. The microhardness was highest along the $\langle 110 \rangle$ directions (and its conjugates), and at least in the $\langle 100 \rangle$ directions and its conjugates. Polishing induces an unusually large decrease in microhardness if continued beyond 2 min probably because of a rapid multiplication of dislocation slip-hands due to thermal stress generated near the surface.

Chemical polishing invariably increases the microhardness values. On the other hand, polishing done successively with 600 mesh and 1060 mesh SiC powder, followed by 0.3- μ Al_2O_3 powder, results at first in an increase (600 mesh SiC powder) of hardness as compared to cleaved specimens, followed by a gradual diminution of Knoop hardness values. Rapid cooling following annealing is also more deleterious to residual hardness values than slow cooling.

(12) For single crystal MgO specimens, into which FeO was diffused from the external boundary, the hardness was found to be lowest at the central portion containing pure MgO, and increased gradually with rising impurity concentration of the FeO.

(13) Heat-treated high-purity polycrystalline MgO developed large clear regions and small spotted areas; the former displayed lower microhardness values than the latter, which probably represent areas to which impurities have diffused during the high-temperature soaking cycle.

(14) The microhardness of polycrystalline MgO increases with rising concentrations of Cr_2O_3 , Fe_2O_3 and Al_2O_3 , but declines with increasing amounts of ZrO_2 , TiO_2 and SrO added.

(15) Extensive theoretical studies were carried out by D. L. Johnson, in partial fulfillment of his Ph. D. requirements, on the subject of sintering. This work, closely allied with the investigation carried out on this task, is reported here as an adjunct of the investigation. The theory developed represents a substantial improvement over previously existing analyses, and its predictions were confirmed on sintering work conducted on Al_2O_3 powders whose activation energy, incidentally, was found to be 151 kcal per mole.

Sintering studies carried out on doped Al_2O_3 showed that small amounts (100 ppm) of MgO additions retarded the sintering, while TiO_2 additions had an accelerating effect on the sintering of Al_2O_3 .

Additional preliminary work was also carried out on recrystallization studies, and on attempts at producing high-density translucent Al_2O_3 and MgO . This work will be continued.

9. REFERENCES

- 8-1 Cutler, I. B., "The Influence of Impurities on the Brittle Fracture of Inorganic Non-Metallic Ceramics", pp. 326-369 in Studies of the Brittle Behavior of Ceramic Materials, N. A. Weil, ed., ASD-TR-61-628, April 1962.
- 8-2 Murray, G. T., "Surface Active Environment", op. cit. pp. 447-476.
- 8-3 Bal'shin, M. Yu., "Relation of Mechanical Properties of Powder Metals and their Porosity and the Ultimate Properties of Porous Metal-Ceramic Materials" Doklady Acad. Sci. USSR, 67 831-34 (1949).
- 8-4 Ryshkewitch, E., "Compression Strength of Porous Sintered Alumina and Zirconia - 9th Communication to Ceramography", J. Amer. Ceram. Soc., 36, 65-69 (1953).
- 8-5 Knudsen, F. P., "Dependence of Mechanical Strength of Brittle Polycrystalline Specimens on Porosity and Grain Size", J. Amer. Ceram. Soc. 42, 376-87 (1959).
- 8-6 Petch, N. J., Phil. Mag. 1, 866 (1956).
- 8-7 Private communication.
- 8-8 Johnson, D. L., "The Kinetics of Sintering of Alumina" PhD Thesis, University of Utah (1962).
- 8-9 Kingery, W. D., and Berg, M., "Studies of Initial Stages of Sintering Solids by Viscous Flow, Evaporation-Condensation, and Self-Diffusion," J. Appl. Phys., 26, 1205, (1955).
- 8-10 Coble, R. L., "Initial Sintering of Alumina and Hematite," J. Am. Ceram. Soc., 41 (2), 55-62 (1958).

TASK 9 - STATIC FATIGUE: DELAYED FRACTURE

Principal Investigator: Dr. R. J. Charles
General Electric Research

ABSTRACT

The corrosion processes which affect the long-term strength of single and polycrystalline Al_2O_3 were studied. It was found that single and polycrystalline Al_2O_3 is subject to static fatigue. The reaction responsible for fatigue near room temperature is probably one in which water vapor from the atmosphere combines with the Al_2O_3 to form one or more of the many possible hydrated states of Al_2O_3 . The reduction in strength of sapphire and polycrystalline Al_2O_3 specimens caused by corrosion fatigue can be as high as 80 percent of their intrinsic strengths. In mechanical tests, the fatigue process in Al_2O_3 manifests itself in the same fashion as is observed in glass.

The application of a fatigue theory to the low temperature fatigue data for sapphire and polycrystalline Al_2O_3 resulted in values for the activation volume (0.66 cu cm per mole), the surface energy between Al_2O_3 and its hydration product (less than one-hundred ergs per sq cm) and the activation energy for the hydration reaction (14 kcal per mole) which are reasonable for a stress corrosion reaction.

The observed bend strength of sapphire is quite sensitive to its prior thermal history. In this investigation, heat-treating as-received ground rods improved their low-temperature strength in all atmospheres by about 50 percent, up to about 500°C. The atmosphere present during heat-treatment at 1125°C has no noticeable effect on the low-temperature bend strength. With an essentially inert gas saturated with water vapor at room temperature, the fatigue reaction in both Lucalox and sapphire is sufficiently strong to give evidence of fatigue up to temperatures approaching 800°C. Superimposed on the atmosphere fatiguing process of sapphire, which operated up to about 800°C, appears to be a further weakening process of equal severity which may depend only on temperature and not on atmosphere. Strengthening of sapphire by plastic deformation is observable at temperatures as low as 900°C. Evidences for plastic deformation in Lucalox at temperatures below 1100°C were not obtained.

TASK 9 - STATIC FATIGUE: DELAYED FRACTURE

Principal Investigator: Dr. R. J. Charles
General Electric Research

I. INTRODUCTION

Task 9 consisted of a study of the corrosion process which affect the long-term strength of single-crystal and polycrystalline aggregates of Al_2O_3 . It was desired to obtain information on the identity of the corrosion reactions, their mechanisms, and their effect upon the rupture strength of these ceramics.

The most noticeable effect of delayed failure, or static fatigue, is the sharp dependence of observed strength on the test atmosphere. Another related effect is the decrease in resistance to failure with decrease in the rate of loading in certain atmospheres, i. e., the observed strength is lower the longer it takes to apply the breaking load. At zero rate of loading (dead-weight loading), the observed strength should be at a minimum, and time-to-failure under a given set of external conditions may be measured.

Much work along these lines has been done on inorganic glasses. Oxide glasses are nearly ideal materials for study of this kind because of their homogeneity, isotropy, and brittleness. Delayed failure has been found to depend heavily on strain rate, temperature, pressure, atmosphere, surface condition, composition, and prior thermal history.

Very little work has been done, however, on crystalline oxides. Among the first references to the delayed failure effect in crystalline oxides was that of Roberts and Watt,⁽⁹⁻¹⁾ who, in 1949, noted that sintered Al_2O_3 test specimens failed at 5 minutes and 120 minutes after loading in tension. Wachtman and Maxwell,⁽⁹⁻²⁾ working in air with single-crystal Al_2O_3 , found a delayed fracture effect in most of the dozen samples tested at room temperature. Williams,⁽⁹⁻³⁾ using a low-density (3.84 g per cu in.) sintered

Al_2O_3 body, found times-to-failure in air as long as 10^5 seconds, depending on the stress level applied. Pearson⁽⁹⁻⁴⁾ also working with rather low-density sintered Al_2O_3 , found that delayed fracture effects in ordinary atmospheric conditions could be largely eliminated by heating to about 350°C , cooling, and testing, all under a vacuum of less than 10^{-5} mm Hg. From this it was concluded that the effect was caused by an unspecified atmospheric attack on Griffith flaws in the stressed material.

All of these investigations were conducted at room temperature. At other temperatures, Brenner⁽⁹⁻⁵⁾ statically loaded sapphire whiskers at 1100°C and 1450°C in dry hydrogen and found no evidence of delayed failure: These results were inconclusive, however, since the load was only one-third to two-thirds of the dynamic failure stresses, and the times were relatively short. Later work in both hydrogen and oxygen atmospheres demonstrated fatigue in whiskers, the time-to-fracture being exponentially related to the applied stress. Charles⁽⁹⁻⁶⁾ reported work on oxides including fused silica, granite, albite, spodumene, hornblende, sapphire, quartz, and magnesium oxide. This work included both crossbend tests on sapphire and compression tests on the other oxides, done in atmospheres of nitrogen-water combinations over a temperature range of -200° to 240°C . It was shown that minimum strength values were obtained with a simultaneous application of stress and corrosive atmospheres. Atmospheres alone had little weakening effect on stress-free material, even MgO . Of great interest was the appearance of a definite strain-rate dependency of the failure stress.

In summary, it is clear that both polycrystalline and single crystal Al_2O_3 exhibit static fatigue in normal atmospheres. It is not clear, however, whether MgO , either in single or polycrystalline form, exhibits behavior which may be characterized correctly as static fatigue. It seems⁽⁹⁻⁶⁾ that MgO hydrates readily and that hydration with simultaneous plastic deformation can lead to low rupture strengths. Since it has been, however, the experience of the

present author, and others,⁽⁹⁻⁷⁾ that standard dead-load tests on single crystal MgO specimens under ordinary conditions do not give evidence of static fatigue, this material was not studied under Task 9.

2. METHOD OF APPROACH

To determine whether a delayed failure or fatigue effect exists in a given material, it is generally useful to obtain "base level" data, gathered in the absence of fatigue, against which comparisons of failure strengths under ordinary conditions may be made. The possibilities which exist for gathering base level data include;

- (1) using low temperatures to inhibit the temperature-dependent kinetic factors which govern reaction rates.
- (2) maintaining environmental conditions such that an atmospheric reaction cannot occur, i. e., vacuum or inert atmospheres.
- (3) using a very fast loading rate.

For a given group of specimens with equivalent severity of surface notches or microcracks, destructive tests may be made under various conditions of load, time, and environment and the failure strength values compared to a maximum strength obtained under one of the above base level conditions. In this manner the severity of the fatigue effect may be estimated.

A. Dynamic and Static Testing

Obviously, if fatigue does not occur, the strength of a sample is dependent only on stress level and not at all on time. Conversely, if fatigue occurs, the failure strength or observed strength will be a complex function of the time of load application and the load changes, if any during testing. Thus, in principle, fatigue data can be obtained from tests at constant load or constant strain rate.⁽⁹⁻⁶⁾ Both techniques were used in the experimental work described.

B. Atmospheres and Temperatures

It is apparent that water vapor is one of the most influential atmospheres which cause fatigue in oxides. The reaction is generally the formation of a hydrate. In the case of Al_2O_3 , the specific hydrate formed is a function of temperature and pressure, with water or (OH^-) groups being lost as temperature increases.

Thus, if the hydration reaction is important in the fatigue of Al_2O_3 , one would expect to emphasize the delayed failure effects by conducting tests at moderate or low temperatures wherein mono- or multi-layer absorptions of water vapor are readily obtainable (i. e., the vapor pressure of water should be at least 0.4 times the saturation water vapor pressure for the temperature considered). These considerations led to a selection of an experimental temperature range for static testing from -35°C to about 200°C wherein fatigue effects due to hydration could be studied.

It is conceivable that mechanisms dependent on the hydrogen reduction of Al_2O_3 to sub-oxides could result in static fatigue. Such a reduction reaction is known to result in the formation of Al_2O_3 whiskers at high temperatures and it is possible that similar mass transport processes may change microcrack geometries such that a stressed specimen may experience a time dependent failure. For these reasons it was considered necessary to perform further experiments with Al_2O_3 at temperatures in excess of 800°C in hydrogen atmospheres to determine whether or not a reduction reaction could lead to fatigue. Vacuum tests at these temperatures allowed estimates of the severity of the fatigue effect to be made.

3. MATERIALS

The specimens used in this investigation were both single-crystal and polycrystalline Al_2O_3 .

A. Sapphire

The sapphire single crystals used were obtained from the Linde Company, and consisted of random lengths of ground rod from which

specimens of appropriate size were prepared. The diameter of these specimens was 0.070 ± 0.0003 inches. To ensure that proper correlations between these specimens and the 0.125-in. specimens used throughout the other Tasks could be made, a number of these larger specimens were obtained and their bend strength values were compared with bend strength values of the 0.070-in. material. Correlations were exact within a few percent.

The use of such single crystals in a research program presents certain special problems. The material itself is made by the Verneuil process, and is rarely completely free of spherical gas bubbles trapped during the process. Careful selection of specimens must be made to exclude such faulty material. Internal strains are to be expected because of the discontinuous manner in which material is added to the growing boule. Annealing after manufacture (details unavailable) is done to help lessen the effect of these strains. And finally, the individualistic nature of each rod must be taken into account, for, during growth, each rod experiences somewhat different conditions such as temperature fluctuations and different seed stock. Because of all these inherent sources of non-uniformity, it was decided to use numerous individual rods in each test and take their average, rather than try to compare the properties of individual rods under a given range of conditions.

Sapphire presents further problems because of its anisotropy. In bending, the effect of specimen orientation with respect to the optic axis is especially important: It has been reported⁽⁹⁻⁸⁾ that loading parallel to the optic axis results in observed strengths nearly three times as high as loading perpendicular to the axis. It was decided to use one standard orientation throughout testing, with the load applied perpendicular to the line of intersection of the neutral surface with the basal plane, which intersection was in turn perpendicular to the specimen rod axis (Fig. 9-1). This position corresponds to a maximum extinction position in polarized light when the rod axis is parallel to the vibration direction of one of the crossed polarizing prisms.

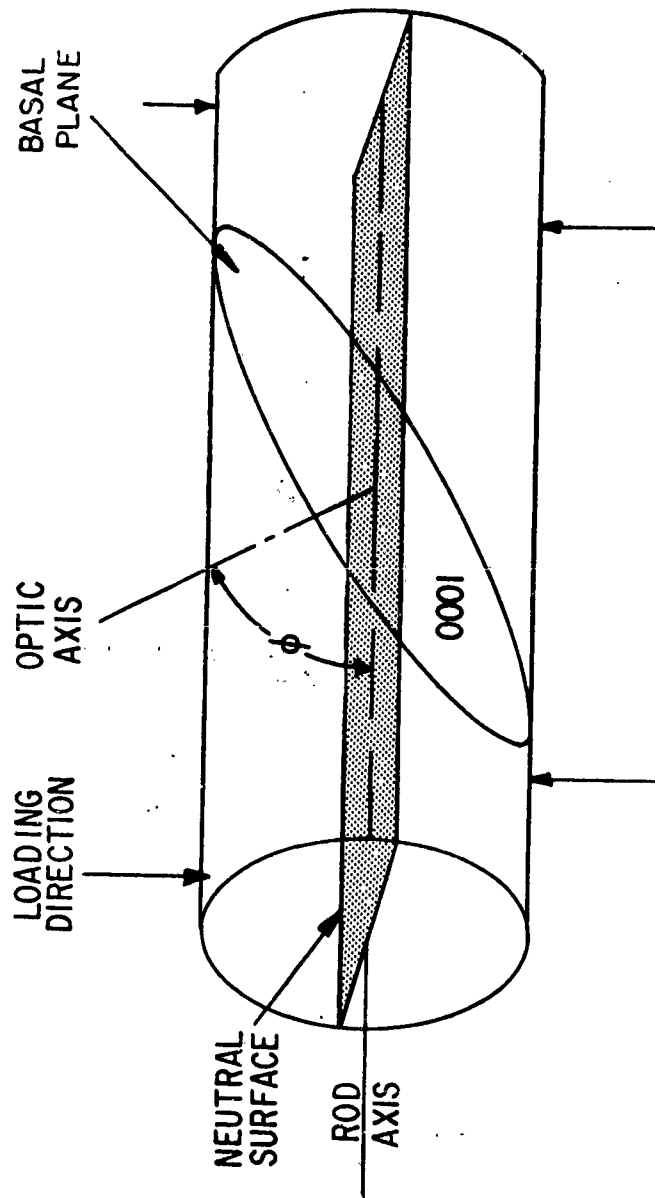


Fig. 9-1 LOAD GEOMETRY FOR SAPPHIRE

No account was taken of the test orientation with respect to the second-order prism axes a_1 , a_2 , and a_3 , i.e., the $3L_2$ axes. These axes correspond with the direction of basal slip in the material, which is important at higher temperatures in producing plastic flow and fracture. This investigation, however, was concerned only with brittle fracture at temperatures generally well below those required for plastic deformation at the strain rates employed. In addition, experimental work⁽⁹⁻⁸⁾ indicates that little or no effect of L_2 axis orientation on the observed low-temperature bend strength can be observed. Thus the angle ϕ , with the optic axis in the plane of bend, was taken as the only critical parameter.

Boules grown by the Verneuil process as a rule do not have optic axis parallel to the boule axis, and similarly the rods made from them have optic axes tipped at some angle from the rod axes. The effect of the growth angle on mechanical properties is quite large, as seen by modulus of rupture values reported by Seemann⁽⁹⁻⁹⁾ and the Linde Company (Table 9-1; test conditions unknown). The angle is usually measured as the one enclosed by the optic axis (normal to the basal plane 0001) and the longitudinal rod axis. This is designated by ϕ in Fig. 9-1. The preferred growth direction is near 60 deg according to the manufacturer. To check the orientations of incoming samples, a fixture was constructed to orient the samples by optical principles and to obtain values of ϕ . Some specimens were also oriented by x-ray techniques, partly as a check on the optical equipment. Figure 9-2 demonstrates the angular distribution of ϕ for some 360 samples checked during the investigation. This distribution is similar to that of Wachtman and Maxwell^(9-2, 9-10) whose "X" is the complement of ϕ . Only those samples falling in a range of 58 to 68 deg were used in this investigation. It is of interest that some 15 percent of the off-the-shelf samples received from the manufacturer were rejected in this manner; this percentage of nonstandard specimens could seriously effect the results of almost any testing program.

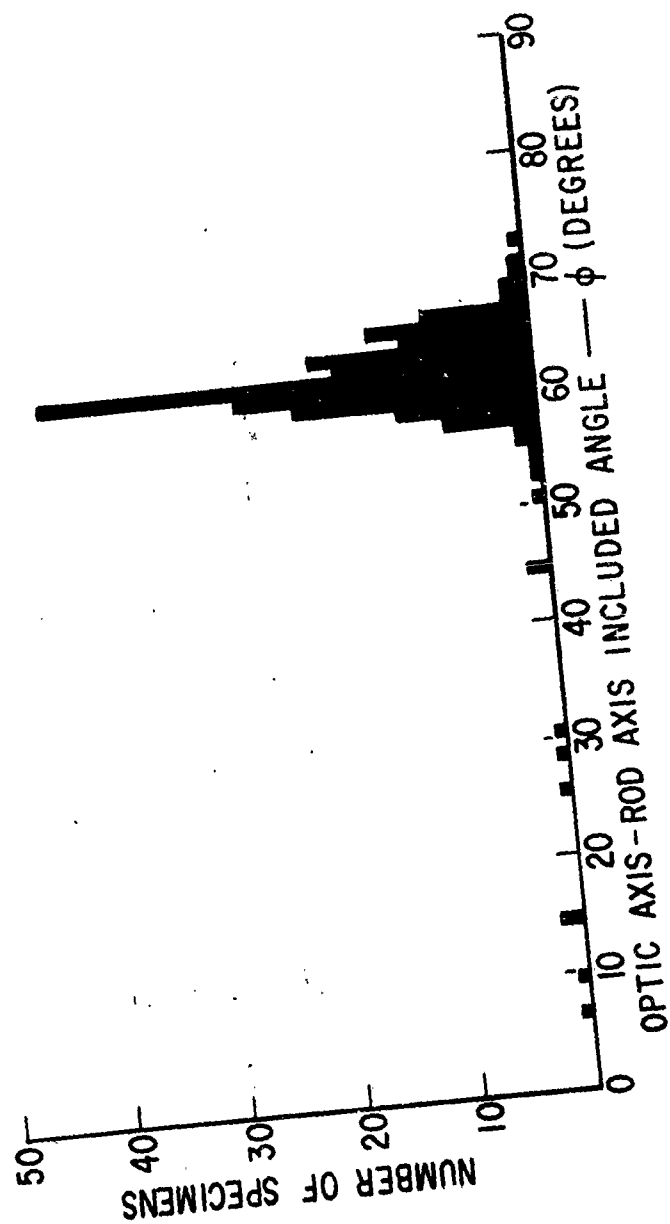


Fig. 9-2 OPTIC AXIS ORIENTATIONS FOR SAPPHIRE

All specimens were cleaned before testing to remove oil, dust, and other contaminants from the surface. The cleaning process was a series of baths of toluene and acetone, interspersed and concluded with distilled water rinses. Specimens were dried and stored in cardboard until ready for use.

Table 9-1
REPORTED ROOM TEMPERATURE BEND STRENGTH
DATA FOR SAPPHIRE (9-9)

Opic Axis - Rod Axis Included Angle, θ (deg)	Modulus of Rupture
30	100,000
45	78,000
60	65,000
75	94,000

B. Polycrystalline Aluminum Oxide

Lucalox* Al_2O_3 was used for the fatigue experiments. The type of testing done by this Task required a specimen size and shape different from the dogbone. Therefore, polycrystalline samples were extruded to order, prefired, and finally sintered to the requisite degree of density and strength. Pains were taken to ensure that the rod specimens used had the same surface grain size and strength characteristics as the specimens used in the other investigations. To do this, some preliminary work was done on the relationship between the density, grain size, and observed four-point bend strength of polycrystalline Al_2O_3 .

* Trade-mark of General Electric Company.

All polycrystalline material was tested in the as-fired condition. No particular preparation of the surface was made, other than the pretest cleaning by consecutive rinses in toluene, distilled water, acetone, and distilled water, as described for the sapphire specimens.

4. EXPERIMENTAL EQUIPMENT

The equipment and fixtures used in this investigation were designed to test the material in two ways, dynamic bending and static bending.

A. Dynamic Bending

Dynamic bending consisted of four-point bending with a constant strain rate applied to the gage section of the specimen. Four-point bending was selected because of the constant bend moment it provides across the inner span. Because of the brittle nature of the specimens and their small deflections prior to fracture, the usual expression for stressing load beams was used, i.e., $\sigma = \frac{Mc}{I}$, where

σ = failure stress at outer fiber,

M = bending moment,

c = distance from outer (tension) fiber to neutral axis, and

I = section moment of inertia.

An Instron testing machine was adapted for dynamic tests at temperatures up to 1150°C in various neutral or reducing atmospheres. This consisted of a molybdenum bend fixture which could be used in air or encased within a stainless steel jacket for other atmospheres. A triple-wound Kanthal furnace surrounding the jacket provided heat for the higher temperature tests using liquid nitrogen. Temperature in all cases was controlled by three chromel-alumel thermocouples within the bend fixture itself, and could be held to within $\pm 10^\circ\text{C}$ of the nominal temperature at all temperatures.

In view of the large number of tests required for the program, a molybdenum fixture permitting the sequential testing of up to twenty specimens per run was constructed. This fixture, adaptable to the temperature range mentioned previously, is shown in Fig. 9-3. Specimens are loaded at four points as the outer fixture moves past the inner one. Loading spans are 1.20 x 0.70, respectively. Various modifications have not changed the principle of the apparatus. During tests involving sapphire, orientation was assured by winding the specimens with three wraps of 0.010-in. nickel wire, and allowing the weight of the wire to keep the specimen oriented correctly. Effect of the wire on specimen strength was apparently negligible. Fracture seldom occurred at the point of wire contact.

Vacuum levels to 10^{-5} mm Hg pressure were provided by mechanical pumps and an oil diffusion pump, and were measured by a cold cathode gage. "Wet" hydrogen atmospheres and saturated air atmospheres were provided by bubbling these gases through several water bubblers and a detrainning flask. Dry hydrogen atmospheres were produced first by using commercial pure tank hydrogen; later dry hydrogen was produced by putting line hydrogen through oxygen, liquid nitrogen, and desiccant traps. The measured dew point was -46°C , corresponding to a water vapor concentration of 5×10^{-5} mols per liter.

B. Static Bending

Static bending consisted of four-point bending with a constant stress applied to the gage section following a nearly instantaneous loading. This was accomplished in the apparatus shown in Fig. 9-4. The heating jacket shown on the autoclave permitted the use of saturated steam atmosphere up to 200 psi. Ten specimens can be tested at a time in this fixture. A relay-contact system permits times-to-failure to be read directly from the series of clocks shown, to an accuracy of ± 5 seconds. A Styrofoam jacket permits testing in any atmosphere down to -150°C , using liquid nitrogen.

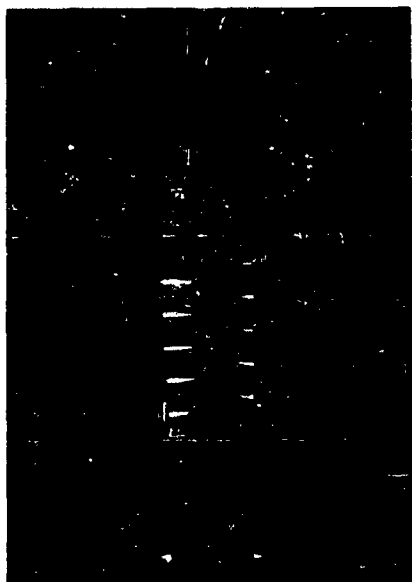


Fig. 9-3 MOLYBDENUM HIGH-TEMPERATURE TEST APPARATUS

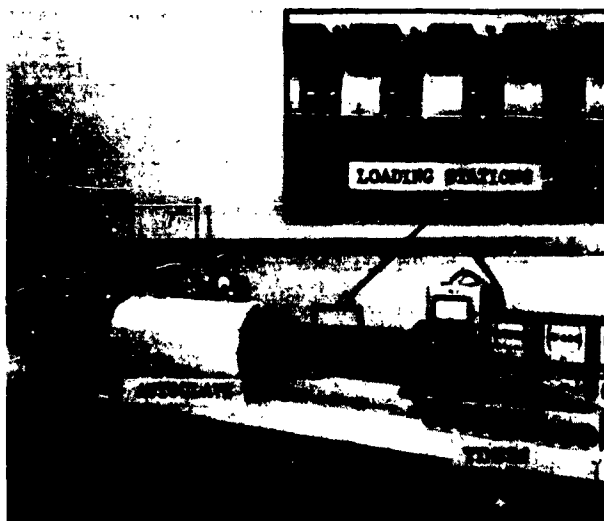


Fig. 9-4 LOW-TEMPERATURE AUTOCLAVE TEST APPARATUS

Weights may be adjusted to permit any stress level desired to be applied to the specimen. Outer and inner spans are 3.75 and 1.0 in., respectively.

5. EXPERIMENTAL RESULTS FOR SAPPHIRE

A. Condition of Specimens

The marked anisotropy of sapphire monocrystals required a certain standard orientation to make comparative results meaningful. Another effect of this anisotropy is the variable resistance to wear or abrasion which different crystallographic planes and directions exhibit. Steijn (9-11) has shown experimentally that resistance to wear of the basal plane can be nearly two orders of magnitude lower than that of the prismatic and rhombohedral planes. In particular, it is shown that the rate of wear of sapphire rods is some thirty times greater for "ninety-degree" material ($\theta = 90^\circ$) oriented for attack on the basal plane than for zero-degree material oriented on prismatic planes. This is indicated schematically in Fig. 9-5.

The standard material used in the present investigation is around 60 deg, so that its wear rate in the orientation illustrated is intermediate between the two extremes. This means that during the centerless grinding of sapphire rods the grinding rate will be increased when the rods come into this relative orientation with the grinding rolls. The result is that the rods will not be ground round in cross section.

This effect was quite noticeable in the present work. Under medium reflected light and at the proper viewing angle, "flats" or bright bands on the as-ground rods can be easily detected on opposite sides of the rod. This amounts to a diameter difference of 0.2 to 0.4 mils, which is usually within the specified tolerance of the rod as supplied. Thus the gross geometrical effect on the rod is negligible. However, the effect on a microscopic scale may be more serious, for the areas of greatest grinding attack are also the top (compression) and bottom (tension) surfaces of the specimens

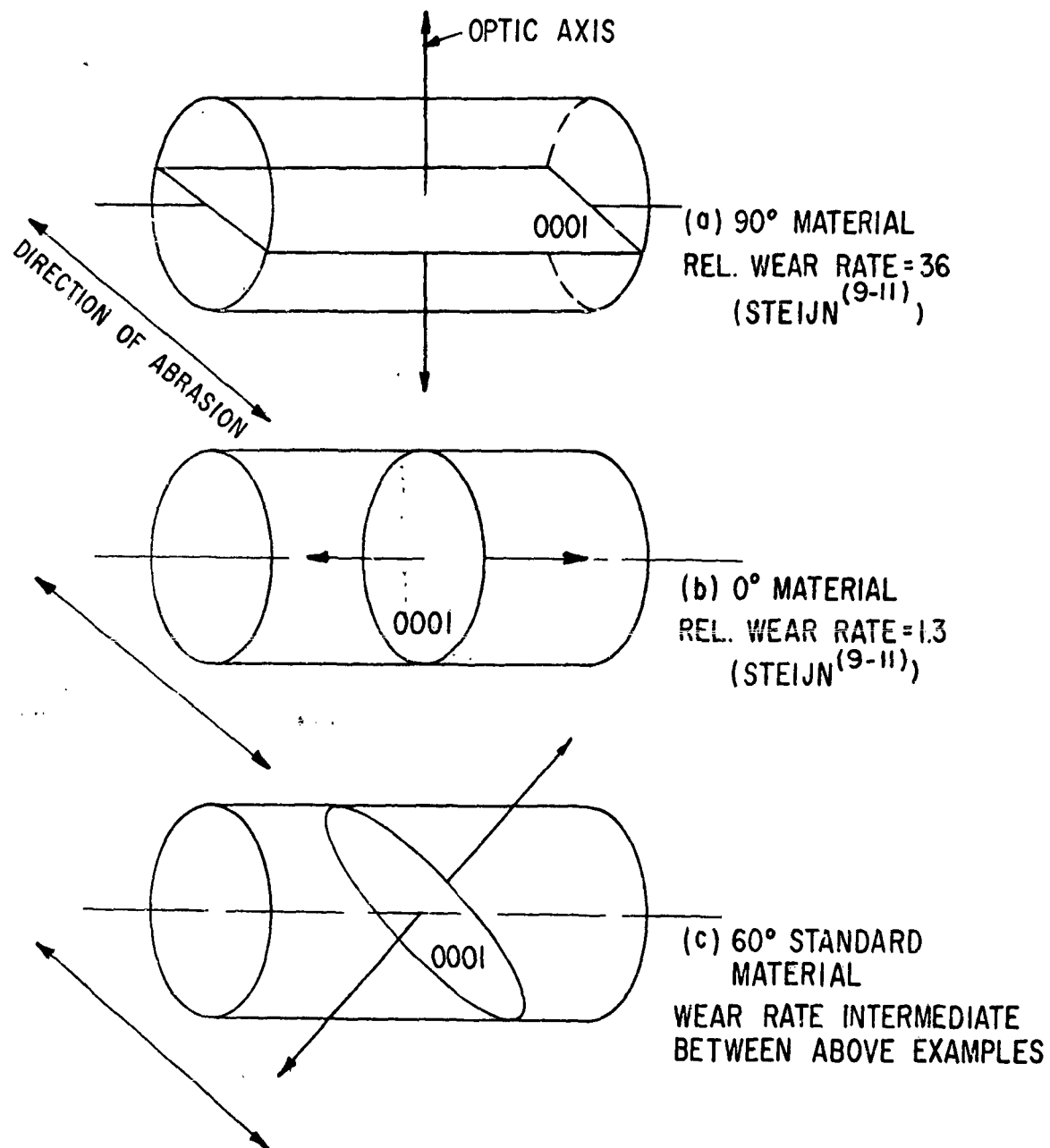


Fig. 9 5 RELATIVE WEAR RATES OF SAPPHIRE RODS OF VARIOUS ORIENTATIONS

when in the standard test orientation. No attempt was made in this investigation to find the real significance of this effect; all data are uncorrected for it.

B. Effect of Thermal History

Jackman and Roberts, (9-12) and Wachtman and Maxwell, (9-13) noted that the observed bend strength of sapphire at first declined with increasing temperature, and then rose again at temperatures near 1000°C. Also, Tomilovskii (9-14) found that heat treatments of sapphire prisms to temperatures of 1300°C produced a 30 to 40 percent increase in the observed bend strength, measured at room temperature. In both cases the effects were ascribed to high-temperature relief of internal stresses which had been introduced during manufacture.

Both of these observations were confirmed in the present test work, indicating that the observed strength of sapphire is very sensitive to its prior thermal history. Figure 9-6 shows the dependence of observed bend strength of as-received sapphire rods at room temperature on annealing time at 1200°C in air. It is seen that the "annealing" mechanism operates fairly quickly at this temperature, with the bend strength reaching its maximum value in a few hours. Longer heat treatments (up to 6 hours) produced less scatter. Results of various annealing tests are presented in Table 9-II. The atmosphere during the heat treatment apparently has little effect on the final mechanical properties, at least at the temperature studies.

C. Base Level Strength of Sapphire

Because of the sensitivity of sapphire to its prior thermal history, it was decided to conduct parallel tests on both "as-received" material and samples heat treated at 1200°C for 6 hours in air. These two sets of samples are referred to as "as-received" and "annealed", respectively, through this paper. Table 9-III lists the liquid nitrogen and room temperature bend strengths of sapphire

Table 9-II
EFFECT OF HEAT TREATMENT OF SAPPHIRE ON
BEND STRENGTH AT ROOM TEMPERATURE

Original Strength (psi)	Temperature (°C)	Time (hr)	Atmosphere	Final Strength (psi)	Increase (%)
65,000	1300	1-6	Air	87,600	35 (9-15)
59,000	1000	4	Vacuum	92,200	56*
54,000	1200	1-6	Air	69,000	28
71,000	1125	6	Air	100,000	
			Wet Hydrogen	100,000	
			Dry Hydrogen	100,000	40**
			Vacuum	100,000	
			Dry Nitrogen	100,000	

* -- all tests in vacuum
** -- all tests in liquid nitrogen

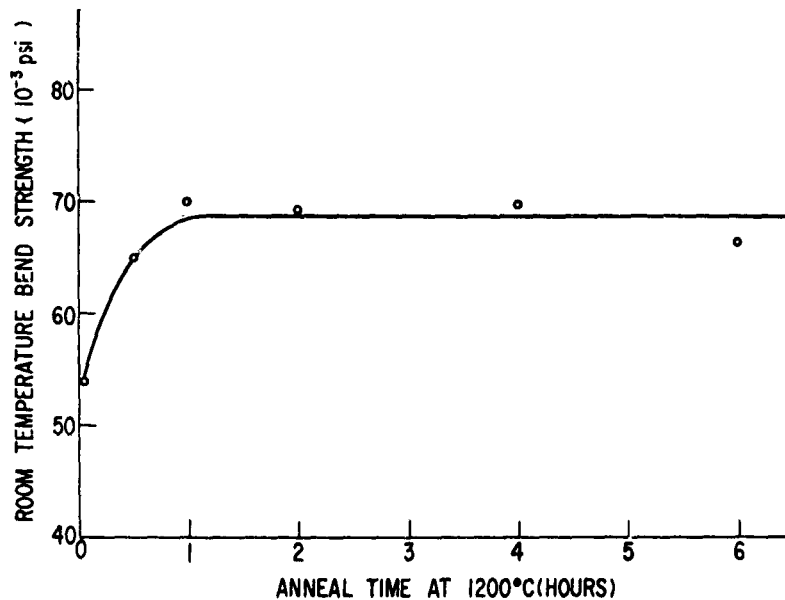


Fig. 9-6 EFFECT OF ANNEAL TIME AT 1200°C ON BEND STRENGTH OF SAPPHIRE

Table 9-III

**EFFECT OF TEMPERATURE AND BASAL PLANE
ORIENTATION ON OBSERVED BEND STRENGTH
OF SAPPHIRE**

	Orientation	No. Tests	Temperature (°C)	Test Atmosphere	Rupture Strength (psi)
<u>As-Received</u>	Zero-degree 0.070 in. diam	10	25	Air	102,000
	Zero-degree 0.070 in. diam	20	-196	Liquid Nitrogen	170,000
	60° 0.070 in. diam	9	25	Air	54,600
	60° 0.070 in. diam	35	-196	Liquid Nitrogen	71,000
	60° 0.125 in. diam	11	25	Air	59,800
	60° 0.125 in. diam	9	-196	Liquid Nitrogen	75,100
<u>Annealed</u>	Zero-degree 0.070 in. diam	3	-196	Liquid Nitrogen	175,000
	60° 0.070 in. diam	35	-196	Liquid Nitrogen	100,000
	60° 0.070 in. diam	35	25	Air	69,000

crystals in which the base planes exhibited two different orientations to the specimen axes.

It will be noted that the strength of the zero-degree rods is approximately twice that of the 60 deg specimens at both temperatures for the as-received material. This shows a very real effect on strength of variation of the angle θ , as discussed. The close agreement between the strengths of the two different specimen sizes, including a nearly two-fold variation of diameters, is also evident.

Annealed zero-degree material is still stronger than annealed 60 deg stock, but not as wide a margin as in the as-received specimens. In fact, there seems to be little or no change in the observed liquid nitrogen strength of zero-degree sapphire on annealing. This indicated that: (1) either the zero-degree material has had a full anneal before leaving the manufacturer, or (2) its unique crystallographic orientation masks any thermal effects.

For subsequent comparisons, the base-level strengths of sapphire were taken to be 71,000 psi and 100,000 psi for as-received and annealed 60 deg specimens, respectively, on basis of the test results presented in Table 9-III.

D. Constant Strain-Rate Tests on Sapphire

Figure 9-7 presents the variation in the strength of as-received sapphire rods as functions of environment and temperature. Each point represents the average of 10 to 20 samples, tested in four-point bending at an outer-fiber strain rate of 3×10^{-4} in. per in. per min. "Wet" hydrogen refers to hydrogen saturated at room temperature with water.

Several items are of immediate interest from these data. First, at temperatures up through 850°C the bend strength diminishes in the order of vacuum dry hydrogen, and wet hydrogen atmospheres. Thus strength decreases as the atmosphere becomes more reactive chemically, which is one of the main predictions of a stress-corrosion hypothesis. Secondly, strength minima occur at intermediate temperatures, confirming the findings of previous investigations (9-12, 9-13).

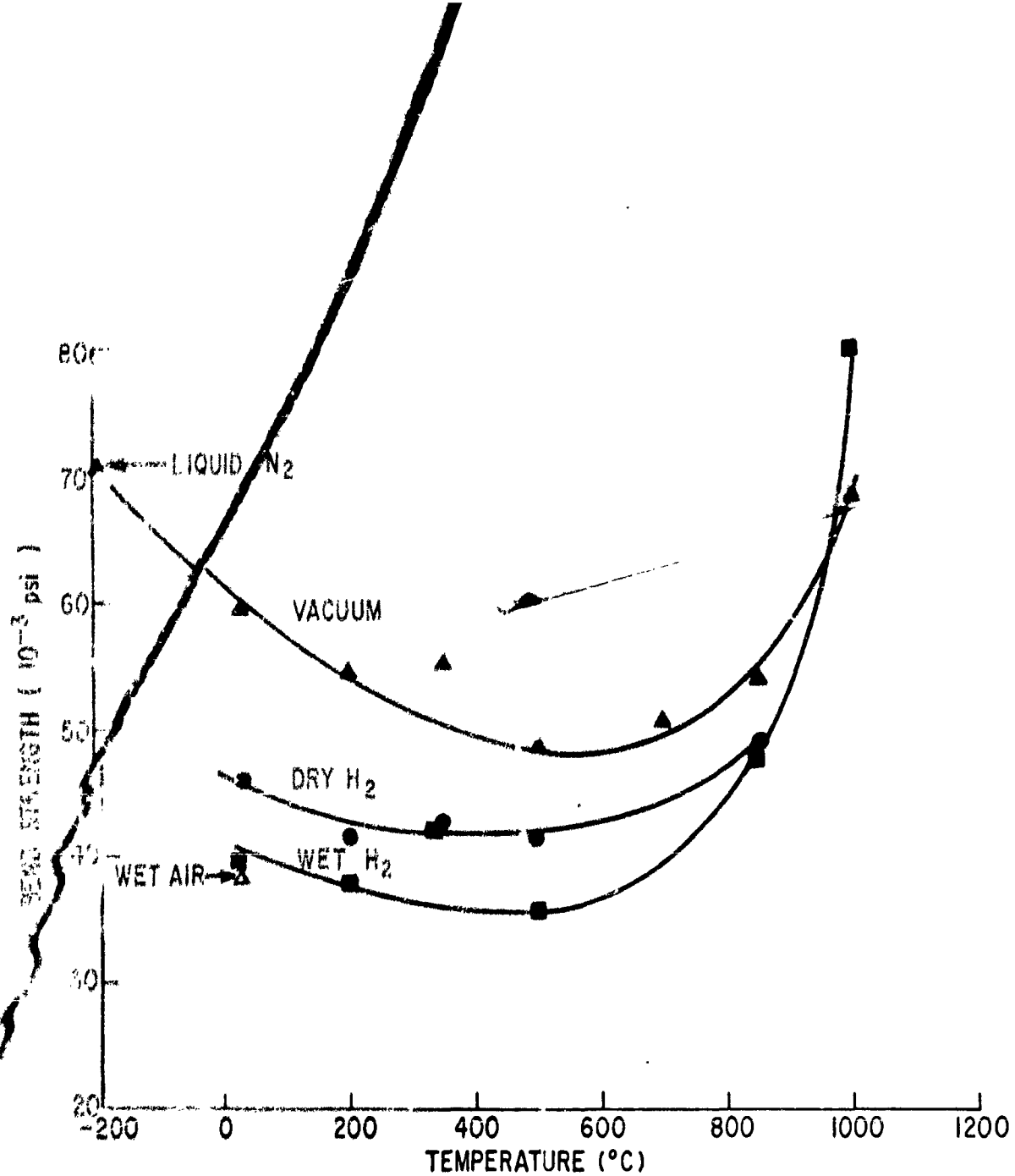


Fig. 9-7 TEMPERATURE-ATMOSPHERE EFFECTS ON THE BEND STRENGTH OF AS-RECEIVED SAPPHIRE

Third, the difference in observed strength in the various atmospheres decreases with increasing temperature, indicating that the surface effect is lessening. Above 900°C there is no apparent effect.

At 1000°C, plastic deformation of the samples was evidenced by curvature in the load-time plots; no equilibrium flow stress was reached before fracture. Extrapolated data from a recent paper by Kronberg⁽⁹⁻¹⁵⁾ on strain-rate effects in sapphire indicate that the maximum strain rate to observe an initial yield point in sapphire is about 5×10^{-6} in. per in. per min. at 1000°C, about two orders of magnitude less than the strain rate actually used. However, at 1150°C the maximum strain rate plotted from Kronberg's data is the same as the strain rate used here. Thus, it seems quite plausible that the extraordinarily high strength of as-received sapphire at 1000°C is occasioned by localized stress relief by plastic deformation.

Figure 9-8 presents the behavior of annealed sapphire rods; each point represents the average of 4 or 5 tests. It is seen that these curves are fundamentally different from those shown in Fig. 9-7 for the as-received material. No minima are evident in Fig. 9-8 up to 850°C, and the stress values are very much higher. The order of decreasing strength in the various atmospheres is preserved to about 850°C. No attempt was made to perform comprehensive tests at higher temperatures because of the observed plastic flow which defeats the study of brittle fracture.

Figure 9-9 combines, for comparison, the curves of Fig. 9-7, and 9-8 for both the "as-received" and "annealed" varieties of sapphire tested. Their behavior is that of two different materials up to a temperature of about 850°C, above which mechanisms of plastic flow take over at the strain rate.

Figure 9-10 presents normalized values of the vacuum strength and Young's Modulus of sapphire as a function of temperature up to

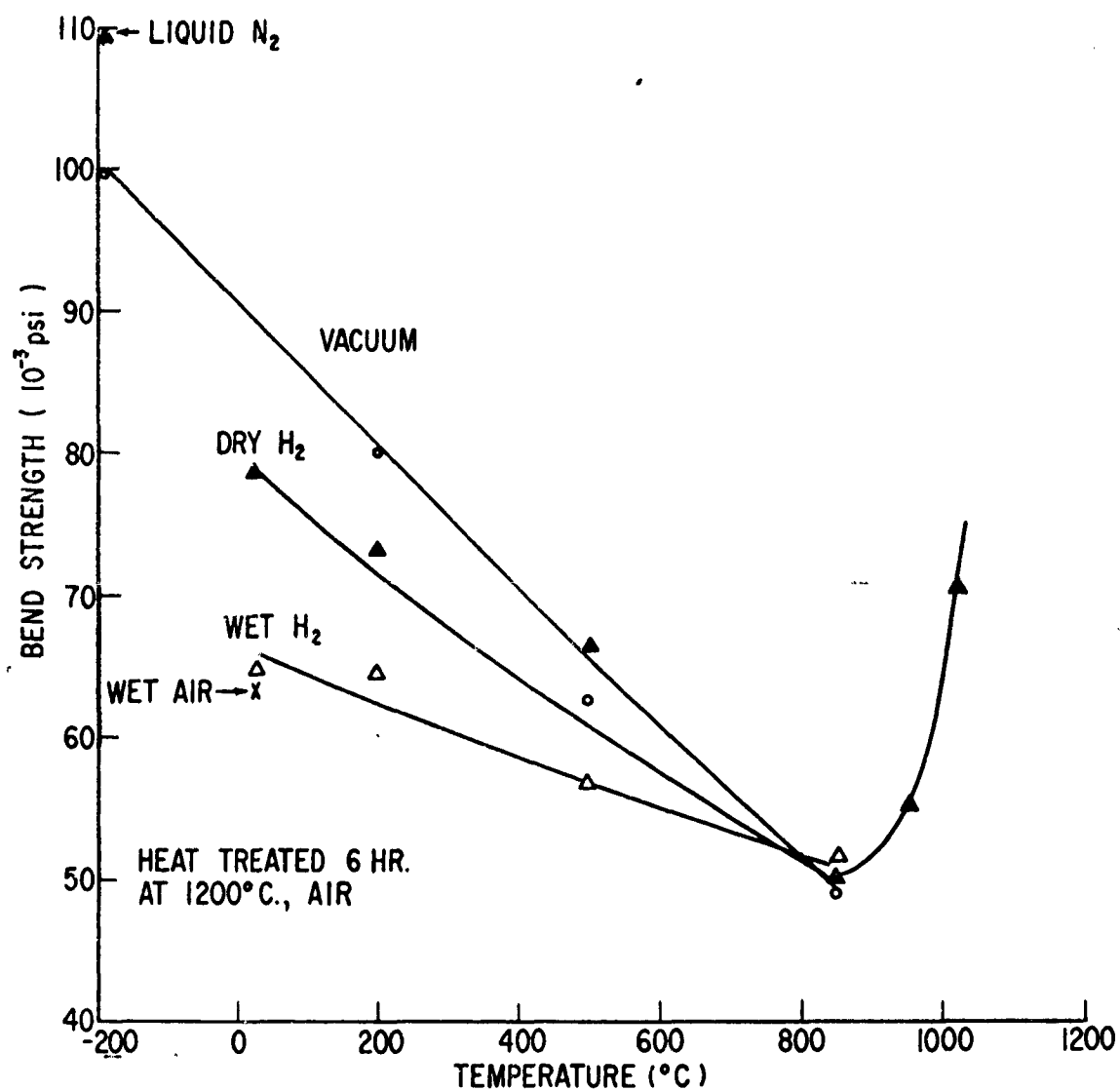


Fig. 9-8 TEMPERATURE-ATMOSPHERE EFFECTS ON THE BEND STRENGTH OF HEAT-TREATED SAPPHIRE

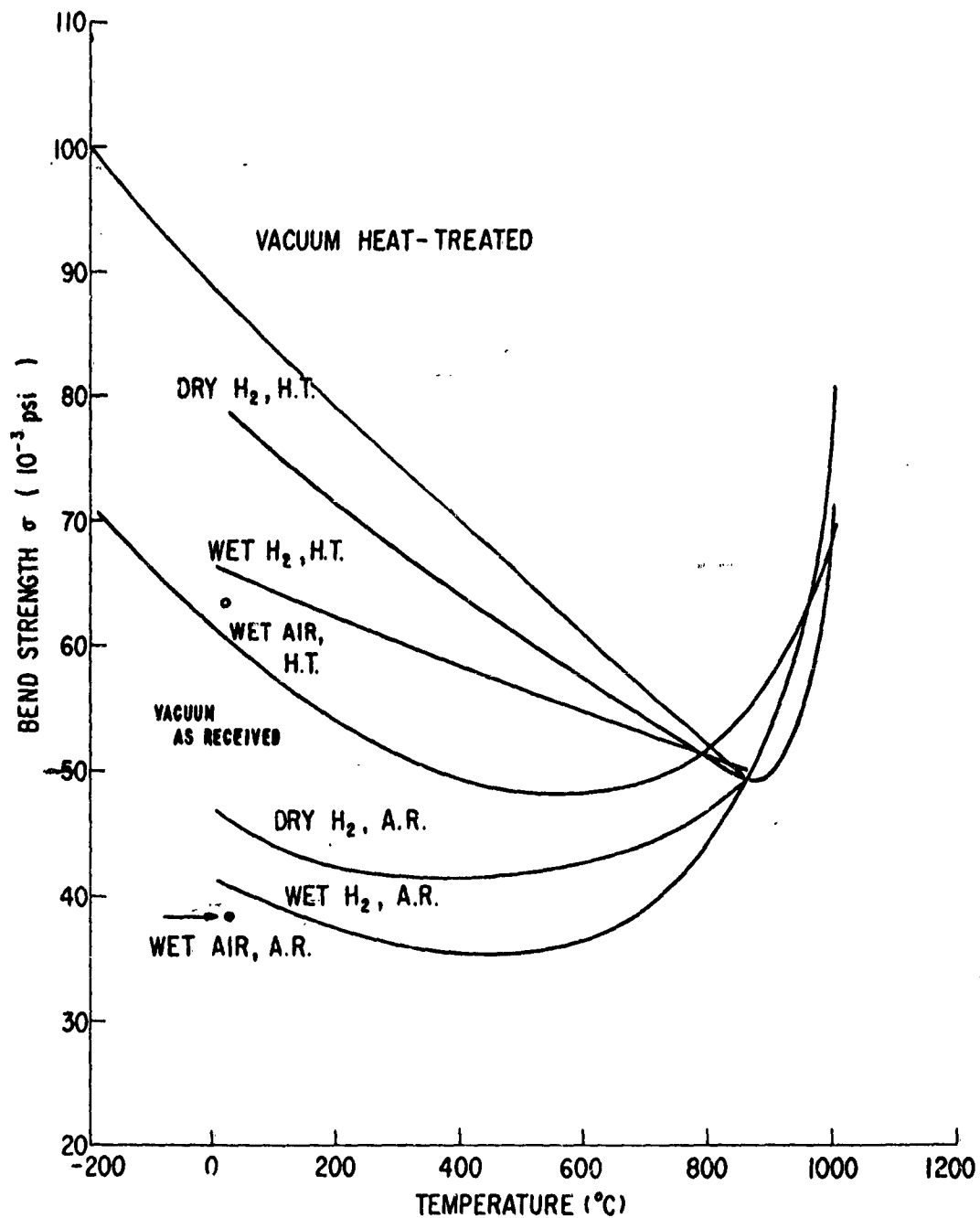


Fig. 9-9 COMPARISON OF BEND STRENGTHS OF AS-RECEIVED AND ANNEALED SAPPHIRE

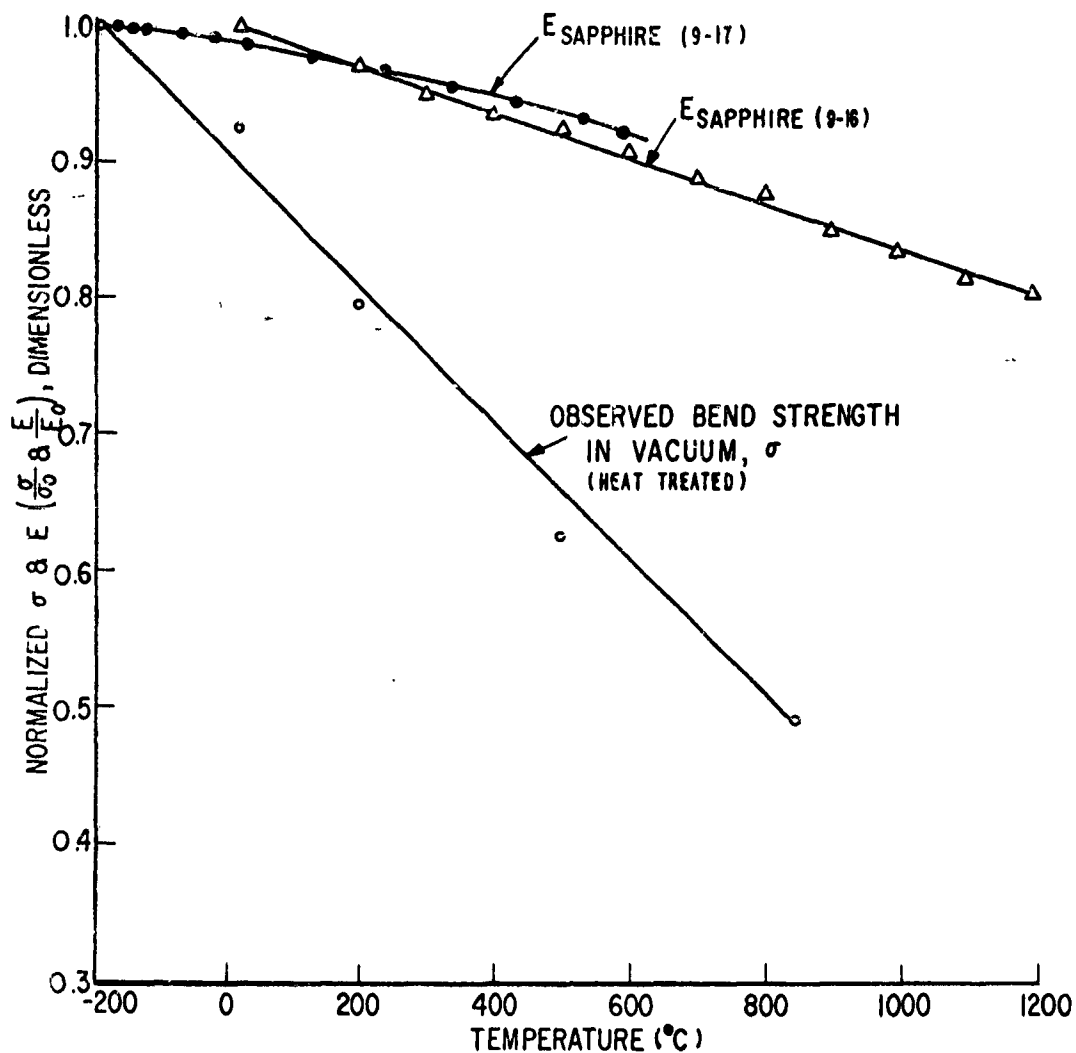


Fig. 9-10 BEND STRENGTH AND YOUNG'S MODULUS
VERSUS TEMPERATURE FOR ANNEALED SAPPHIRE

850°C. Both are approximately linearly dependent upon temperature, but it is seen that the observed strength for sapphire is much more strongly affected by temperature increases than is Young's Modulus.

E. Delayed Failure Tests on Sapphire

Table 9-IV lists times-to-failure data for various conditions for sapphire specimens under static load. Figure 9-11 is a plot of the observed breaking stress (normalized on the base level stress) versus time-to-failure. No complete curve for any one temperature could be obtained, because the median times-to-failure were either forbiddingly long at low stresses for the low-temperature segment, or impossibly short to measure at high stresses for the high-temperature segment. The temperature dependence of the apparent corrosion process is obviously quite strong.

F. Sapphire Fracture Surfaces

It might be expected that a stress-corrosion mechanism would affect the mode of fracture, which could be detected by examining the fracture surfaces.

Pigolina, et al, (9-18) and Winchell (9-19) investigated fracture modes of sapphire crystals. Their work shows that the first- and second-order prism planes, basal plane, and rhombohedral planes are the common parting planes. Of these, the basal and rhombohedral (10 $\bar{1}$ 2) faces have the highest degree of development possibly indicating that these planes are most susceptible to parting during fracture. Petch (9-20) suggests that "interrupted cleavage" may occur on basal, prismatic, and bipyramidal (11 $\bar{2}$ 2) planes.

Examination of the fracture surfaces produced during this program indicates that a considerable variation in fracture behavior can be induced by varying the test conditions. Failure under static load in a water vapor atmosphere at 200°C, for example, almost invariably produces a bright curved mirror surface, completely

Table 9-IV
STATIC FATIGUE DATA ON SAPPHIRE

Constant Stress, σ , (psi)	Conditions	No. Specimens Failing Within Indicated Time Decades (min)										Most Prob. Time-to-failure (min)
		10^{-2}	10^{-1}	10^0	10^1	10^2	10^3	10^4	10^4	10^4	10^4	
41,600	T = 198°C 200 psig steam	10										0
23,500	T = 198°C 200 psig steam	6										3
20,500	T = 198°C 200 psig steam											
18,400	T = 198°C 200 psig steam											
16,800	T = 198°C 200 psig steam											
34,400	T = -35°C Sat. water vapor											
39,000	T = -35°C Sat. water vapor											
46,100	T = -35°C Sat. water vapor											
53,400	T = -35°C Sat. water vapor											
34,400	Room Temp Sat. water vapor											

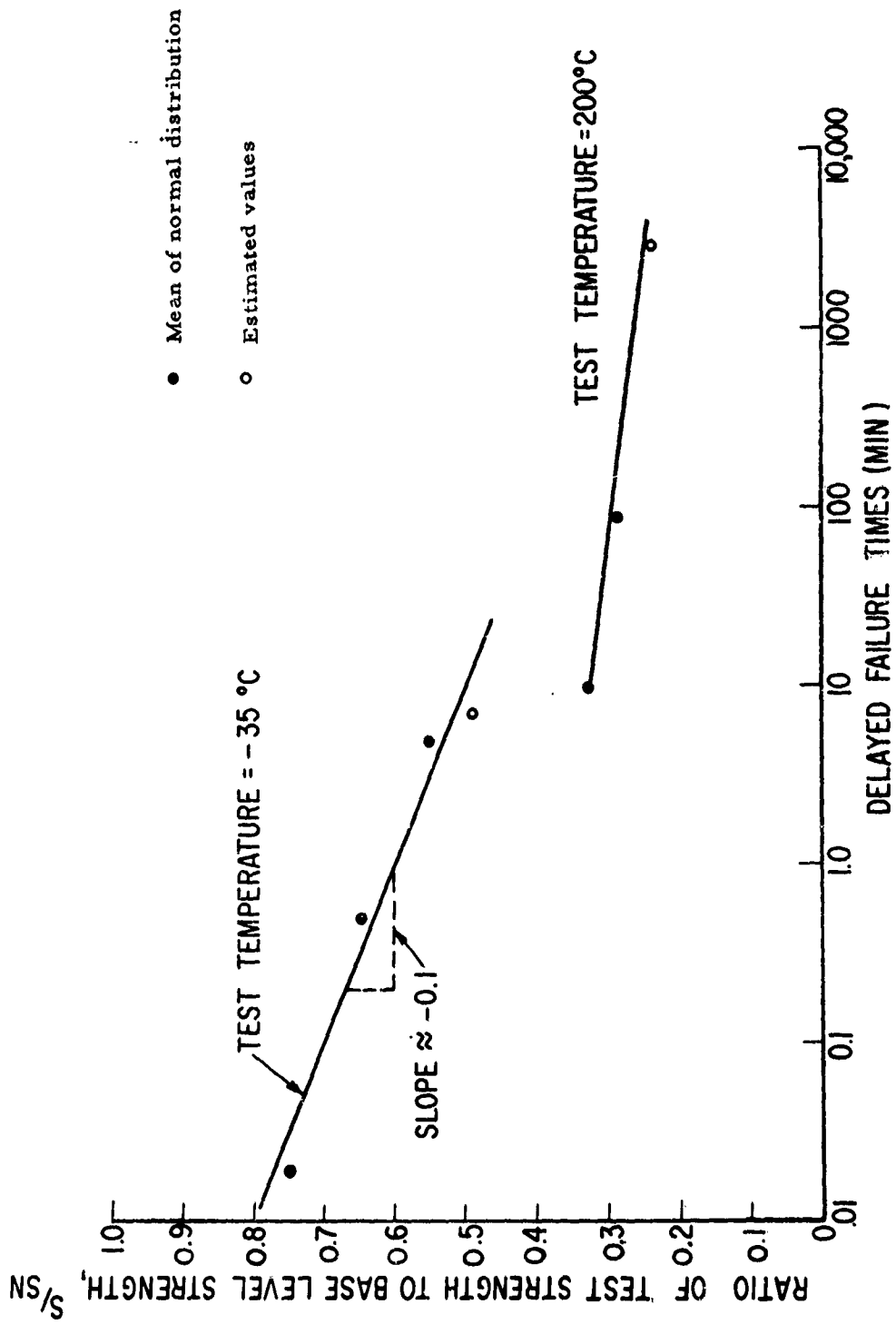


Fig. 9.11 STATIC FATIGUE CURVE FOR SAPPHIRE

free of markings. The identical test at -35°C produces almost no mirror surfaces, and conchoidal surfaces with a horde of checks, steps, rivulets, etc., predominate. At room temperature an intermediate appearance obtains. Occasionally minor cleavage or parting occurs along definite crystallographic planes; x-ray analysis determines these planes to be $(10\bar{1}2)$.

Failure under a dynamic load operates in a similar manner. Zero-degree material commonly fractures along $(10\bar{1}2)$ at room temperature in air, but in liquid nitrogen it is extremely rare to find a planar fracture. Standard material fracture surfaces showed the effect of both temperature and atmosphere: tests conducted in wet hydrogen at all temperatures generally produced more mirror surfaces than in dry hydrogen; dry hydrogen and vacuum testing produced generally rough, featureless fracture surfaces, with a few planar facets showing.

6. EXPERIMENTAL RESULTS FOR POLYCRYSTALLINE ALUMINUM OXIDE

A. Strength Versus Grain Size and Testing Rate

Figure 9-12 represents the results of the preliminary grain size-strength investigation mentioned earlier. Each point represents twenty to thirty individual tests, performed at a constant strain rate of 1.4×10^{-2} in. per in. per min. in air at room temperature on as-fired specimens. Support and loading span lengths varied from 1.25×0.25 to 1.50×0.68 in. to preserve the constant strain-rate feature of tests on the different diameters of the varying batches of material which averaged out at about 65 mils. Density was measured by standard displacement methods. The average grain size was determined from the relationship $\bar{D}_{ave} = \frac{3}{2}\bar{l}$, where \bar{l} is the mean traverse length⁽⁹⁻²¹⁾, as obtained from lineal measurements taken on photomicrographs of the surface layers of specimens.

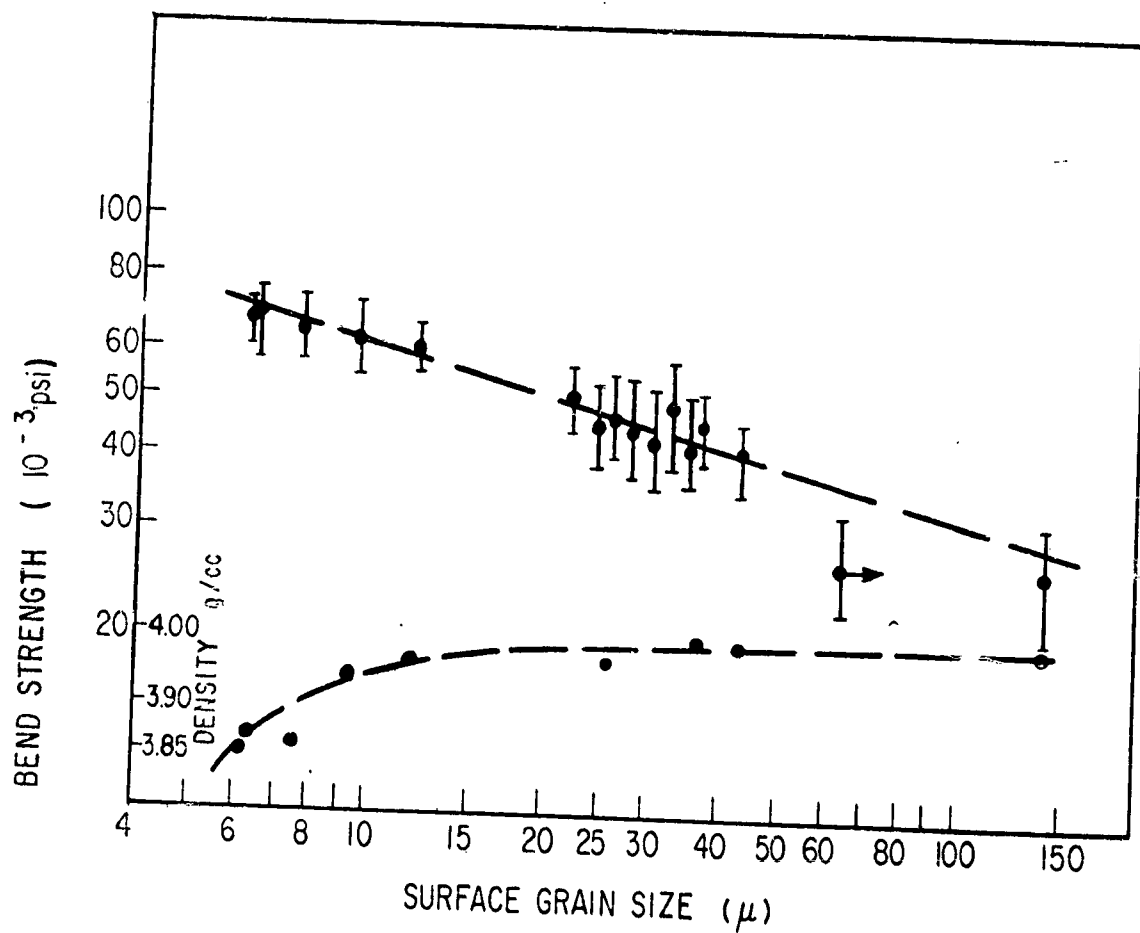


Fig. 9-12 BEND STRENGTH AND DENSITY AS A FUNCTION OF SURFACE GRAIN SIZE FOR LUCALOX EXTRUDED RODS

As Fig. 9-12 shows, essentially full density is achieved above 30-micron grain size. The lower density material may be likened to high-purity commercial Al_2O_3 , with the reservation that the grain size is more uniform in the Lucalox. An exception to this was the single point shown at a nominal grain size of 66 microns. This particular batch of material had experienced rather severe discontinuous grain growth during processing, and had a very broad grain-size distribution. Some surface grains were as large as 200 microns. To preserve consistency in the handling of data, the nominal grain size of this batch was computed from lineal analysis measurements as before, and was plotted accordingly. The standard material selected for use throughout the major portion of the fatigue work ranged 30-40 microns in grain size, with a corresponding bend strength of about 45,000 psi under the cited conditions. The microstructure of this standard Lucalox Al_2O_3 is presented in Fig. 9-13.

Figure 9-14 illustrates the effect of grain size and testing rate on the strength of the polycrystalline Al_2O_3 for this investigation was selected. This figure also includes the strength-grain size dependence for tests at liquid nitrogen temperature. Even with these results it is clear that a fatiguing effect operates for, in general, the strength of the specimens tested in air at a strain rate of 2.7×10^{-4} is approximately 20 percent less than that tested at a strain rate of 1.4×10^{-2} and 30 percent less than the base level strength determined at liquid nitrogen temperature. Within the limits of accuracy of the data it would appear that although grain size affects the base level strength, it does not alter the fatigue effects that are observed.

B. Constant Strain-Rate Tests on Lucalox

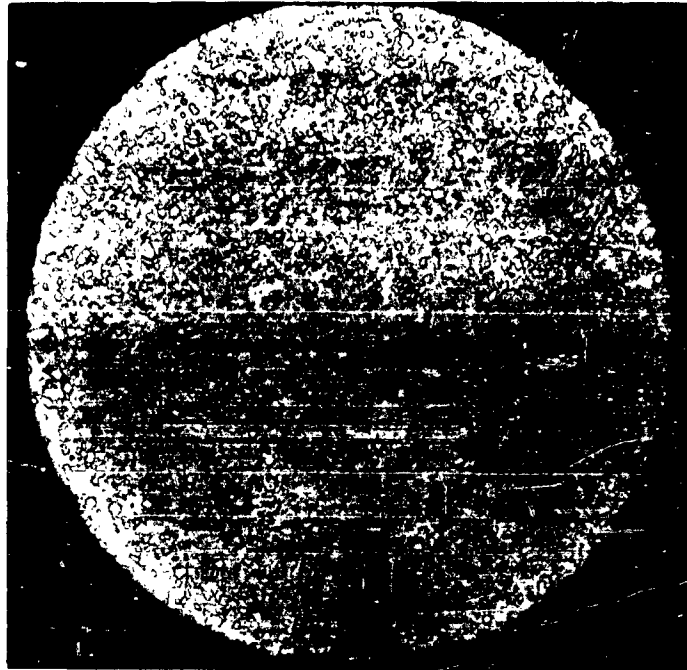
A calculated strain rate of 2.7×10^{-4} in. per in. per min. on the outer tensile fiber was selected for the bend tests. Figure 9-15 presents the bend strength behavior of this material in the same temperature-atmosphere conditions as for sapphire.

As Fig. 9-12 shows, essentially full density is achieved above 30-micron grain size. The lower density material may be likened to high-purity commercial Al_2O_3 , with the reservation that the grain size is more uniform in the Lucalox. An exception to this was the single point shown at a nominal grain size of 66 microns. This particular batch of material had experienced rather severe discontinuous grain growth during processing, and had a very broad grain-size distribution. Some surface grains were as large as 200 microns. To preserve consistency in the handling of data, the nominal grain size of this batch was computed from lineal analysis measurements as before, and was plotted accordingly. The standard material selected for use throughout the major portion of the fatigue work ranged 30-40 microns in grain size, with a corresponding bend strength of about 45,000 psi under the cited conditions. The microstructure of this standard Lucalox Al_2O_3 is presented in Fig. 9-13.

Figure 9-14 illustrates the effect of grain size and testing rate on the strength of the polycrystalline Al_2O_3 for this investigation was selected. This figure also includes the strength-grain size dependence for tests at liquid nitrogen temperature. Even with these results it is clear that a fatiguing effect operates for, in general, the strength of the specimens tested in air at a strain rate of 2.7×10^{-4} is approximately 20 percent less than that tested at a strain rate of 1.4×10^{-2} and 30 percent less than the base level strength determined at liquid nitrogen temperature. Within the limits of accuracy of the data it would appear that although grain size affects the base level strength, it does not alter the fatigue effects that are observed.

B. Constant Strain-Rate Tests on Lucalox

A calculated strain rate of 2.7×10^{-4} in. per in. per min. on the outer tensile fiber was selected for the bend tests. Figure 9-15 presents the bend strength behavior of this material in the same temperature-atmosphere conditions as for sapphire.



(a) Overetching of Grain Boundaries has Occurred



Fig. 9-13 MICROSTRUCTURE OF STANDARD LUCALOX
TEST MATERIAL (Average surface grain size:
30-40 Microns Etchant: H_3PO_4 10 min)

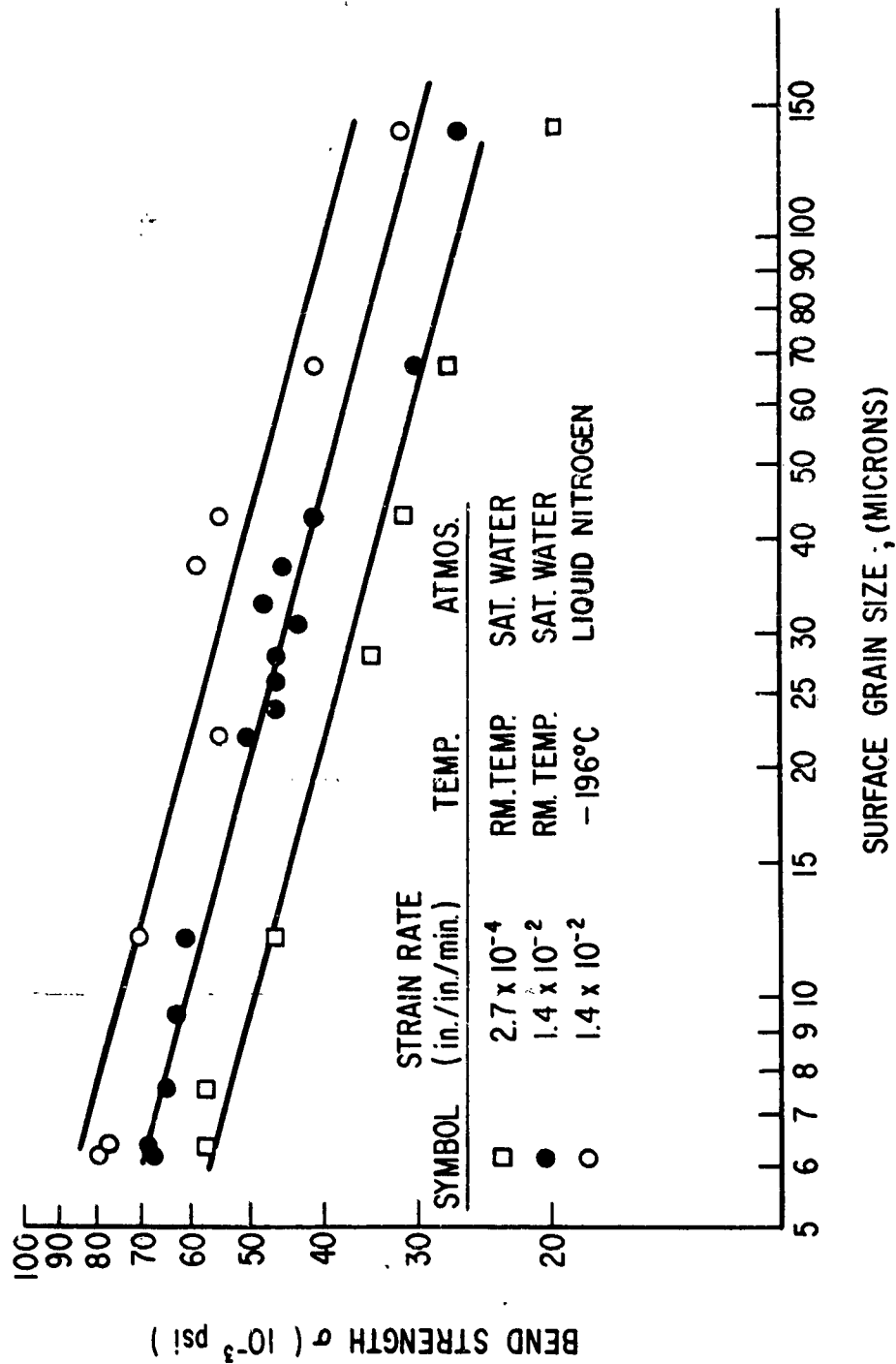


Fig. 9-14 EFFECT OF SURFACE GRAIN SIZE, LOADING RATE AND TEMPERATURE ON THE BEND STRENGTH OF LUCALOX

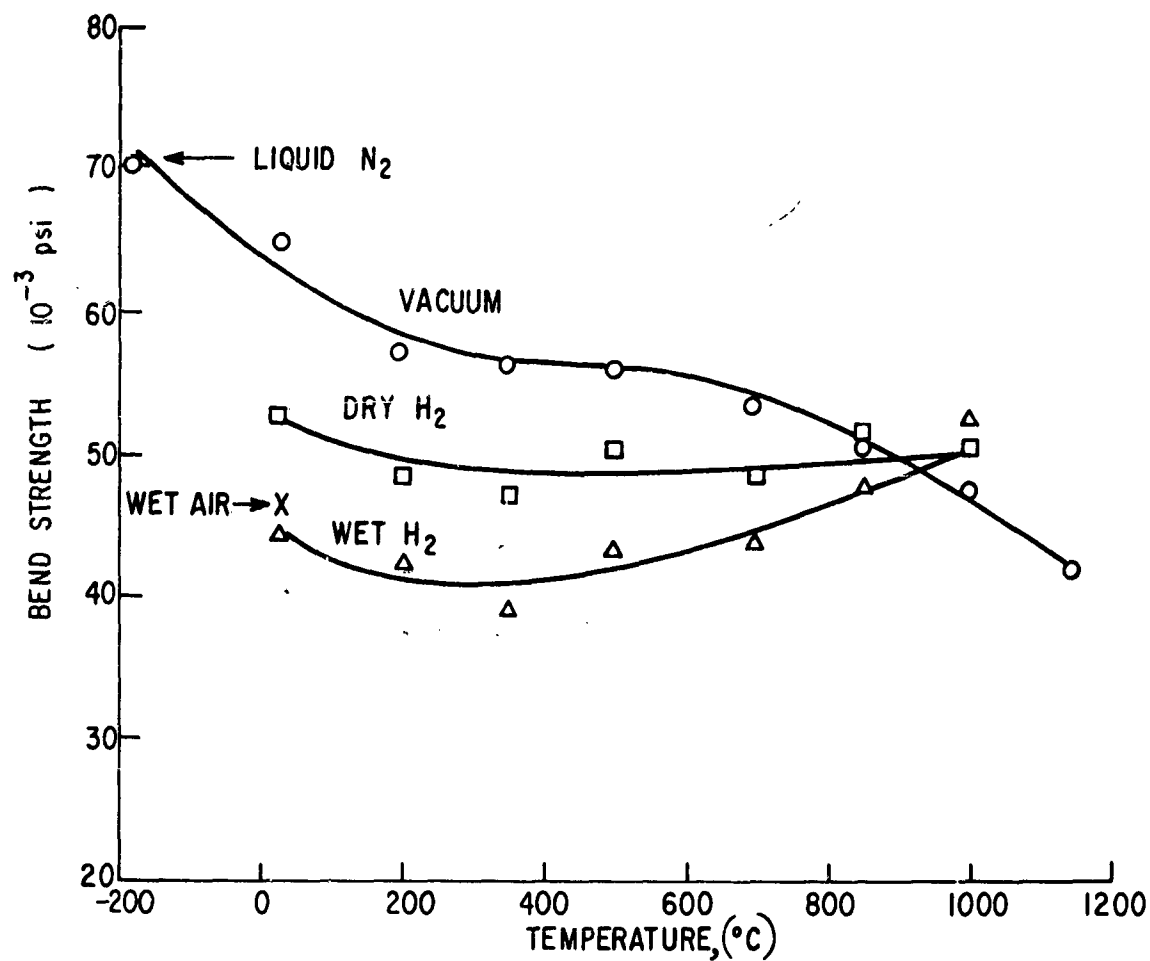


Fig. 9-15 TEMPERATURE-ATMOSPHERE EFFECTS ON THE BEND STRENGTH OF STANDARD LUCALOX

It can be seen that this behavior is somewhat similar to that of sapphire in that the bend strength decreases in the order vacuum, dry hydrogen, and wet hydrogen atmospheres. Again, the curves become indistinguishable around 850°C, showing that corrosion fatigue effects have largely disappeared.

Figure 9-16 illustrates the normalized vacuum strength of Lucalox as a function of temperature, compared with the normalized Young's Modulus of polycrystalline Al_2O_3 over the same temperature range. A similarity of the curves suggests that the fall off of strength of Al_2O_3 in vacuum with increased temperatures may possibly be attributed to the changes in theoretical strength as reflected by the changes in modulus with increased temperature.

A slight curvature in the load-time plots at the highest temperature used (1150°C) raised the question of whether or not plastic deformation of the polycrystalline samples was occurring. Plastic deformation may take place by grain boundary sliding or by the Nabarro-Herring stress-induced diffusion mechanism; for the latter, Folweiler (9-24) has calculated the oxygen diffusion coefficient over the temperature range 1400-1800°C. Extrapolation of these data yields a diffusion coefficient of about 10^{-15} sq cm per sec at 1150°C; however, the coefficient as calculated from the experimental data in this paper, assuming plastic flow occurs, yields a diffusion coefficient of about 10^{-11} , which is absurdly high. Therefore, the observed curvature is very probably only that associated with the metal parts of the fixture, and no plastic flow of the Al_2O_3 is occurring. The presence of the curvature, however, means that the strain rate is being changed, and no further tests were done at this temperature.

Both bend strength and Young's Modulus are seen to decay quite rapidly in this high temperature region. This is in marked contrast to the behavior of single-crystal sapphire, whose apparent bend strength increases rather than decreases at these temperatures, and whose modulus remains linear. The strength increase of sapphire

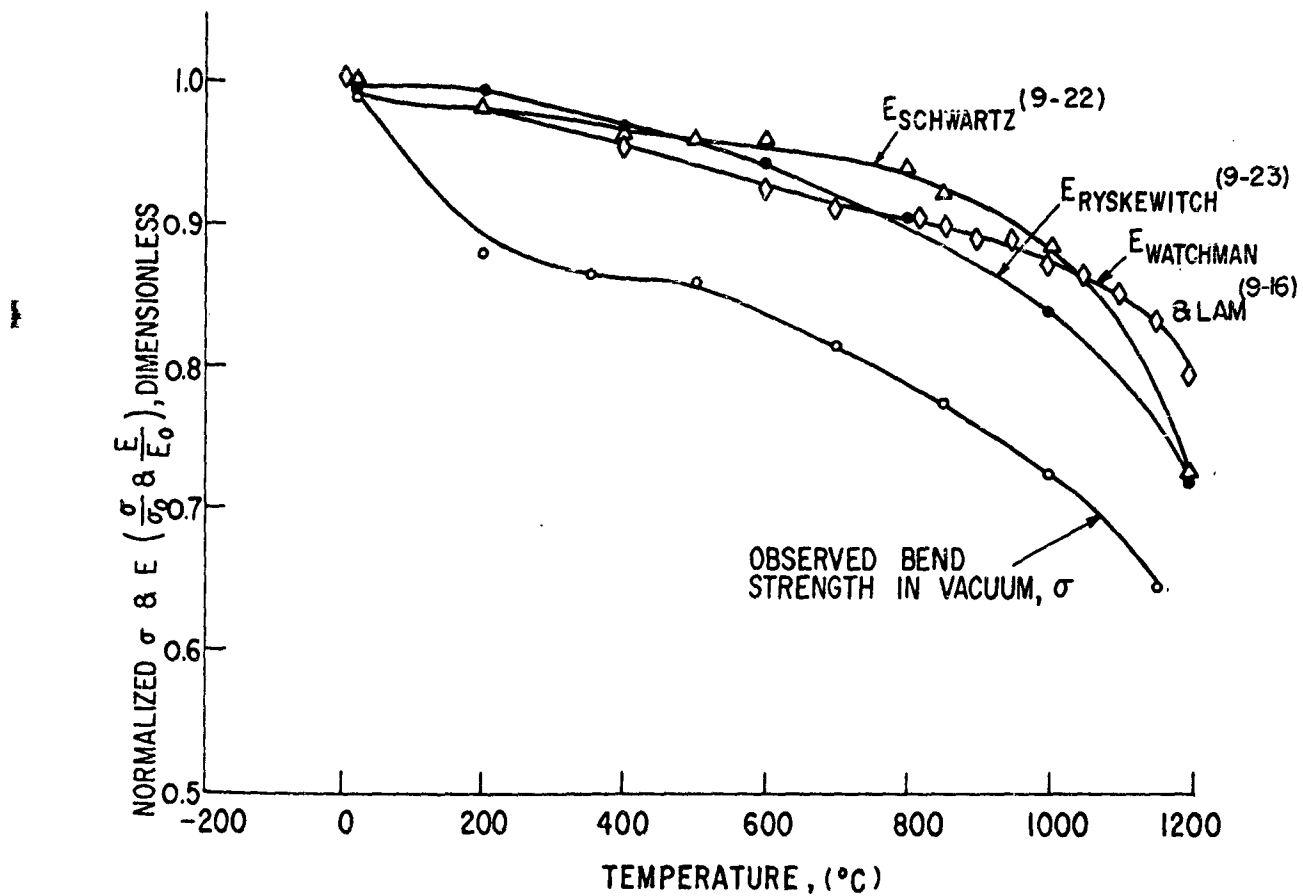


Fig. 9 16 VACUUM BEND STRENGTH AND YOUNG'S MODULUS
VERSUS TEMPERATURE FOR LUCALOX

can be explained qualitatively on the basis of local stress relief by basal slip, well known to operate at these temperatures and strain rates. Presumably, polycrystalline material shows increased viscous characteristics with increasing temperature, whose source must be sought in the enhanced tendency of grain boundary layers for viscous creep.

C. Delayed Failure Tests On Lucalox

Table 9-V presents time-to-failure data at several temperatures. It is seen that again the data, while not extensive, are analogous to those obtained for sapphire, with times-to-failure being strongly related to stress level and atmosphere at each temperature. This facet of the investigation, however, was not pursued in great detail, major emphasis of the delayed-failure investigation having been placed on experiments with standard single crystal specimens.

7. DISCUSSION OF EXPERIMENTAL RESULTS

A. Fatigue Failure Theory

Charles and Hillig⁽⁹⁻²⁵⁾ have presented a theory for static fatigue of isotropic brittle materials in which the material is considered an elastic continuum which chemically reacts with its environment. Failure of the material under load is attributed to the alteration, by a corrosion or dissolution reaction, of the geometries of pre-existing flaws or cracks on the surface.

The well known "Joffe effect" is concerned with the blunting or rounding out of surface flaws by etching or dissolution. By this process the effectiveness of surface flaws as stress concentrators is reduced, and the solid will withstand a larger than usual load before rupture. It is not generally recognized, however, that if the rate of etching or dissolution is sensitive to the stress state, as well as the chemical conditions existing around a flaw or crack, sharpening (rather than blunting) of the crack with time becomes a possible consequence under certain conditions, leading to catastrophic failure. The failure time depends on the magnitude of the

Table 9 V
STATIC FATIGUE DATA ON STANDARD LUCALOX

Constant Stress, σ , (psi)	Conditions	No. Specimens Failing Within Indicated Time Decades (min)										Most Prob. Time-to-failure (min)
		10^{-2}	10^{-1}	10^0	10^1	10^2	10^3	10^4	10^4	10^4	10^4	
55,100	Room Temp Rough Vacuum (10 mm Hg)	10	6	4	3	3	6	2	3			10^{-1}
48,100	Room Temp Rough Vacuum (10 mm Hg)						2	2	7			
44,100	Room Temp Rough Vacuum (10 mm Hg)							2	2			
48,500	Room Temp Air, 20% RH	2	1	2	1	1						
48,500	198°C 200 psig steam	10										0
41,600	198°C 200 psig steam	3	1	1	3	1						
29,600	198°C 200 psig steam						2		6			

applied stress, the duration of exposure to a reactive environment, and parameters characteristic of the material.

The model examined (9-25) consisted of an element of material under uniaxial stress and containing a semi-elliptical surface flaw. The material was considered to be immersed in a reactive environment such that, under zero stress, the thermally activated reaction rate of a plane surface would be given by an Arrhenius equation of the form:

$$v_2 = v_0 \exp (-A/RT) \quad (9-1)$$

where

v_2 is the rate of penetration of the solid-reaction product plane interface,

v_0 is the constant,

A is the activation energy,

R is the gas constant, and

T is the temperature, °K.

The reaction rate of a curved surface differs from that of a plane surface and since the curvatures associated with stress concentrating flaws are very large the effect must be considered. Thus, for a curved surface Eq. 9-1 took the form:

$$v_1 = v_0 \exp \left[- (A + \Gamma V_M / \rho) / RT \right] \quad (9-2)$$

where

v_1 is the rate of penetration of the solid-reaction product curved interface,

Γ is the surface free energy between the solid and the reaction product,

V_M is the molar volume of solid material, and

ρ is the radius of curvature of the interface.

Many kinetic processes in solids (diffusion, ionic conductivity) are affected by hydrostatic pressure in a manner that indicates that the activation energies for the processes are linearly related to the

applied pressure. The proportionality constant is termed an activation volume and has typical values of a few cu cm per mole of reacting species. The assumption is made that such a description of the effect of stress on the reaction rate model under discussion is adequate. Thus the local velocity, v , of corrosion or dissolution normal to the solid surface is expressed by:

$$v = v_0 \exp \left[- (A - V^* + \sigma V_M / \rho) / RT \right] \quad (9-3)$$

where V^* is the activation volume and σ the local stress.

Starting with a flaw of known geometry one can apply the Inglis⁽⁹⁻²⁶⁾ theory and determine the stress distribution around the contour of a flaw. Equation 9-3 may then be utilized to set up a differential equation expressing the change of the flaw contour with time. It is evident that a change in flaw contour leads to a change in stress distribution which, in turn, modifies the rate of change of flaw contour. Thus, depending on the relative values of the parameters involved, a number of possibilities exist for the progress of the flaw with time. Figure 9-17 illustrates these possibilities. If the applied stress is sufficiently high the change of stress concentration of the flaw with time ($\partial u / \partial \tau$) may be positive and the flaw will sharpen and lead to specimen failure (Fig. 9-17a); if the applied stress is low the change of stress concentration with time may be negative and the flaw will round out and the specimen may appear to strengthen (Fig. 9-17c). At some intermediate applied stress, the sharpening of the flaw by stress corrosion may just balance the rounding out effect and the stress concentration of the flaw may remain constant (Fig. 9-17b).

It is evident that a theory, as proposed, is of little value unless it is applicable to cracks or flaws which differ in initial configuration. In the testing of brittle solids, a measure of the initial severity of a flaw may be obtained by testing under conditions whereby no alteration, except elastic deformation, of the flaw occurs until spontaneous propagation takes place. It is felt that, experimentally, testing at liquid nitrogen temperatures satisfies these conditions

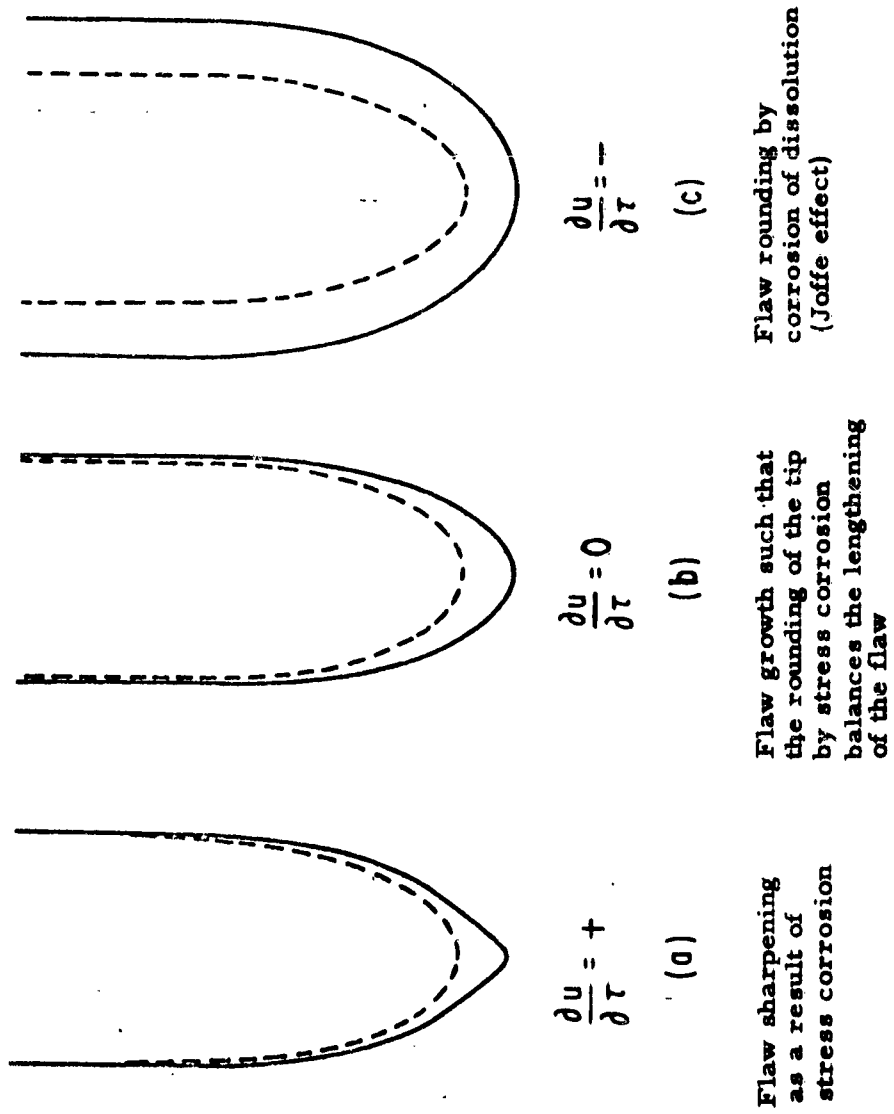


Fig. 9-17 HYPOTHETICAL CHANGES IN FLAW GEOMETRY DUE TO CORROSION OR DISSOLUTION (9-25)

for most materials. Further, the comparison of the initial configuration of a flaw with its configuration at a later time, just prior to spontaneous propagation, is of little practical interest. What is of practical interest, however, is the failure stress of a material when flaw growth is prevented as compared to the failure stress of the material when flaw growth, by stress corrosion and prior to spontaneous propagation, occurs. Because of the direct relationship between flaw configuration and failure stress, it is probably evident that a comparison of a failure stress, S , obtained under arbitrary conditions, with a failure stress, S_N , obtained under liquid nitrogen temperatures is nothing more than a comparison of final and initial configuration of a flaw subject to alteration by corrosion.

It is for this reason that the static fatigue equations for failure time as a function of stress, developed by the previously mentioned authors, do not require any further knowledge of the geometries of flaws than their initial depths.

The basic equations which are a result of the above theory are given as follows:

$$S_L = \left[\frac{3\sigma_{th} \sqrt{V_M}}{8V^* L} \right] \quad (9-4)$$

where S_L is the fatigue limit stress, or the applied stress below which no failure of the specimen can occur (condition (b) in Fig. 9-17), σ_{th} is the theoretical strength of the material and L the initial depth of the flaw. The other terms have previously been defined. From this result, the relationship governing static fatigue can be shown to have the following pseudo-normalized form:

$$\log(t/t_{0.5}) \approx - \frac{T}{RT} \sigma_{th} \left[\frac{S}{S_N} - 1/2 \right] - f(S/S_N), \quad (9-5)$$

where t is the time to failure, $t_{0.5}$ is the time to failure at one-half of the liquid nitrogen applied stress, $f(S/S_N)$ is a slowly varying function which relates the short time behavior of a fatigue

system to the time behavior of the system as it approaches the fatigue limit, and all logarithms are Napierian. Figure 9-18 illustrates the essential characteristics of Eq. 9-5.

An examination of Fig. 9-18 shows that to evaluate the parameters that control fatigue in a given system, it is necessary to make fatigue measurements in the range near the fatigue limit for an estimation of the ratio S_L/S_N as well as in the range $1 > S/S_N > 0.5$ to determine the slope $d(S/S_N)/d[\log(t/t_{0.5})]$. Substitution of reasonable values for the theoretical strength of the material, the molar volume and the initial lengths of cracks then allows calculations to be made for estimates of the surface energy, Γ , and the activation volume, V^* for the fatigue process in question.

As mentioned, the above theory was developed for an isotropic solid. Even though single crystal Al_2O_3 is anisotropic, it was felt that the application of the above theory to the material at hand might prove worthwhile if reasonable Γ and V^* values were obtained from experimental results.

8. APPLICATION OF THE FATIGUE THEORY TO LOW TEMPERATURE TESTS ON Al_2O_3

A. Sapphire

The data for low temperature fatigue of sapphire in saturated water atmosphere were plotted in Fig. 9-11, in accordance with the plotting procedure illustrated in Fig. 9-18.

The fatiguing characteristics of sapphire in a water-containing atmosphere are sufficiently extensive that a test temperature as low as $-35^\circ C$ was required for the material to withstand stresses of the order of 0.5 to 0.7 the liquid nitrogen failure stresses for measurable lengths of time (0.01 to 10 min). The slope of the line passing through the $-35^\circ C$ data in Fig. 9-11 is approximately -0.1. Thus $d \log t / d(S/S_N) \approx -V^* \sigma_{th} / RT \approx -10$. The modulus of elasticity, E , of sapphire at this temperature is approximately $3.6 \times 10^6 \text{ kg/cm}^2$ and thus one would estimate the theoretical

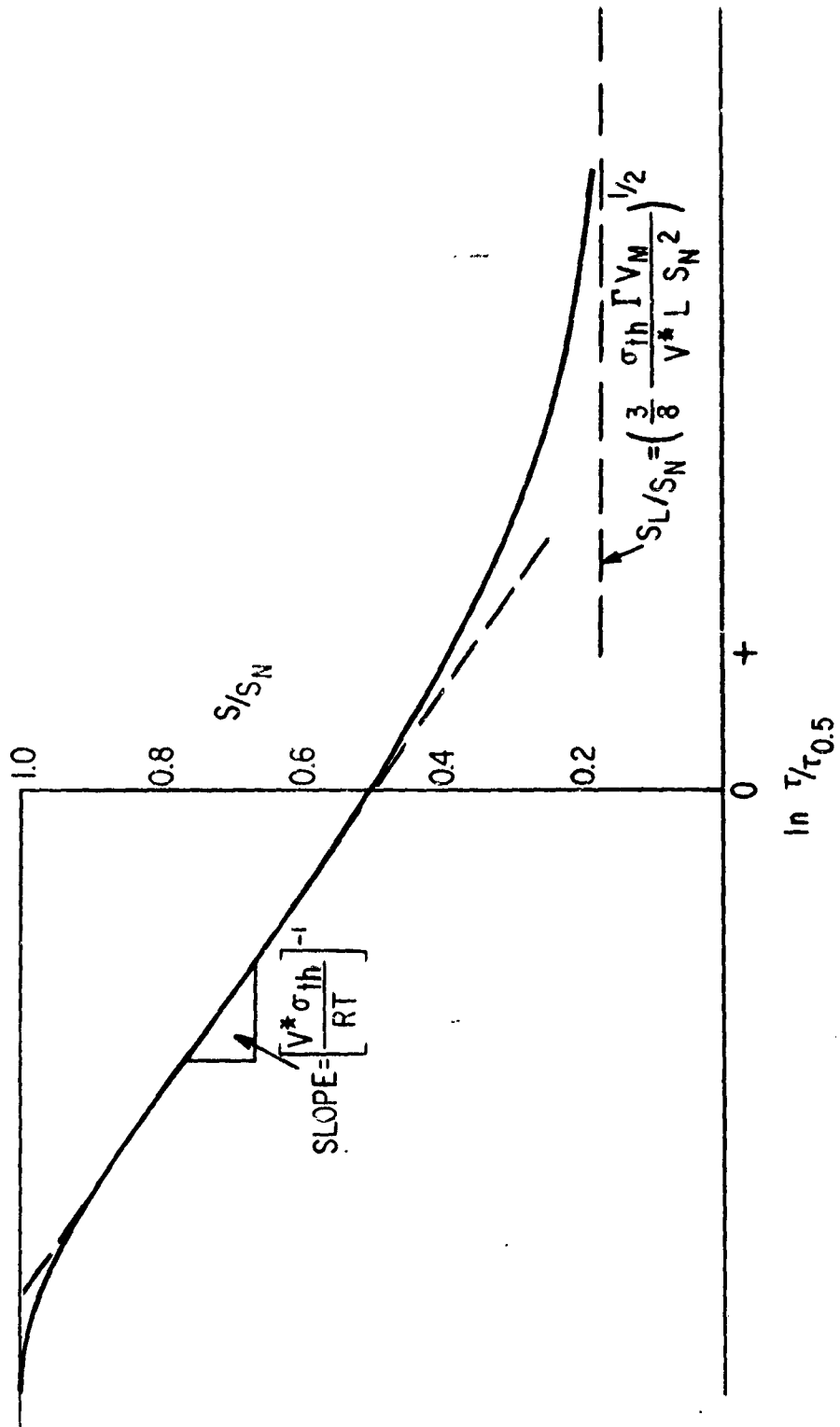


Fig. 9-18 SCHEMATIC FATIGUE CURVE⁽⁹⁻²⁵⁾ (Where τ is Time-to-failure and $\tau_{0.5}$ is the Time-to-failure for a stress, $S = S_N/2$)

strength, σ_{th} , of sapphire as about $E/5$ or 7×10^5 kg/cm². Using this value, the activation volume for the corrosion reaction resulting in fatigue of sapphire is about 0.66 cc/mole (referred to a uniaxial stress). This result compares with such typical values as about 0.5 cm³/mole for the activation volume for carbon in iron (referred to a hydrostatic stress) and about 4.0 cc/mole for activation volume of alkali metal ion diffusion in silicate glasses (referred to a hydrostatic stress).

Referring once more to Fig. 9-11, it is noted that the fatigue data, at a test temperature of 200°C, appear to approach a fatigue limit of about $S_L/S_N \approx 0.2$. This value is only slightly higher than that for typical glasses, *i.e.*, about 0.15⁽⁹⁻²⁵⁾. Using Eq. 9-4, a value of the molar volume of sapphire of about 25 cc in Eq. 9-4, along with the previously estimated values of σ_{th} and V^* the ratio Γ/L turns out to be approximately 10^5 . Thus, for a crack depth of 2 microns, Γ is about 20 ergs/cm². Since Γ is the surface energy between Al₂O₃ and its hydrated corrosion product, it would certainly be much lower than the surface energy between Al₂O₃ and vacuum, which is variously estimated to be between 1000 and 2000 ergs/cm². This value for Γ may be low but is perhaps correct to within an order of magnitude.

In Eq. 9-1 to 9-3 the factor A, is defined as the activation energy for the chemical reaction which results in the static fatigue of Al₂O₃. In Table 9-IV, it will be noted that sapphire rods underwent static fatigue tests in saturated water vapor at two different temperatures (-35°C to 25°C) at equal applied bending stresses of 34,400 psi. This applied bending stress corresponded to an S/S_N value of 0.48. The estimated failure time for the specimens at room temperature was one second, whereas, under the same load, the failure time at -35°C was estimated at 7 min. Utilizing these data an estimate of the quantity A may be made from any of Eqs. 9-1 to 9-3 in the form;

$$\log \frac{7(60)}{1} = \frac{A}{R} \left(\frac{1}{238} - \frac{1}{298} \right)$$

From the above, A calculates to be about 14 kcal per mole. This value is reasonable for the activation energy of a low-temperature hydration reaction of an oxide such as Al_2O_3 .

B. Polycrystalline Aluminum Oxide

Insufficient experimental results on the low-temperature static fatigue of Lucalox Al_2O_3 were obtained to draw definitive comparisons between its fatigue behavior and that of sapphire. It is noted, however, by reference to Table 9-V, that most of the failure times for applied stresses of 29,600 psi under saturated water vapor at 200°C were in excess of 10^4 min. The fatigue limit stress for Lucalox must therefore be approximately this value. Since the liquid nitrogen bend strength of these particular samples was about 90,000 psi, the fatigue limit ratio, S/S_N , would be about 0.33. It is of interest that this value is considerably higher than that obtained for sapphire under similar conditions, i. e., 0.2. From these data it is concluded that the low-temperature fatiguing behavior of polycrystalline Al_2O_3 is not as severe as that for sapphire. The presence of grain boundaries and the small MgO addition in Lucalox would, in all probability, lead to a difference in the corrosion behavior between Lucalox and sapphire. From this it would follow that the fatigue behaviors would also differ. Whether, under the above fatigue theory, one would attribute this difference to a change in the activation volume for the corrosion reaction or to a difference in the interfacial surface energy values cannot be resolved at this time. In all probability both factors are sensitive to the compositional and structural characteristics of the two materials.

That fatigue of Lucalox occurs under constant strain rate conditions is shown by the data in Fig. 9-14. Under constant environmental conditions, a lowering of the strain rate results in a lowering of the rupture stress and this effect is independent of grain size.

Further, at liquid nitrogen temperatures where corrosion cannot be a weakening factor, highest rupture strengths are obtained.

With reference to Fig. 9-14 one concludes that the fatigue mechanism in Lucalox is not affected by constitutional variables such as the grain size of the material. This conclusion follows from the fact that the relative reduction in strength from the base level value of the Lucalox to the level obtained at room temperature under a small strain rate is independent of the grain size. It is well to elaborate somewhat on this point for within the initial planning of that phase of the overall program assigned to Task 9, consideration was given to the manner in which the data obtained on the special samples required by Task 9 could be correlated with data on different samples used by other investigators in the program. The necessary correlation proves to be relatively simple and results from the following argument. The intrinsic strength of an actual brittle ceramic body is controlled by the factors that determine the theoretical strength of the material composing the body, along with the geometry of the particular surface flaw subjected to the most severe stress conditions. Failure occurs when the stress at the tip of this flaw reaches the theoretical strength of the material. Thus the intrinsic strength of the body is subject to constitutional variables such as grain size and distribution, surface treatment, and the area of sample under stress as well as the variables introduced by test arrangements. As has been shown in the previous data, the intrinsic strength of an Al_2O_3 specimen, of arbitrary preparation and shape, may be reduced if the environment permits a fatigue reaction. Prevention of this fatigue reaction by testing at reduced temperature, however, allows a measurement of the intrinsic or base-level strength of this specimen. Since the data already obtained (e.g. Fig. 9-11) indicate that the maximum reduction of the intrinsic strength of Al_2O_3 by corrosion fatigue is approximately 80 percent one can, in principle, obtain the approximate fatigue level stress of any specimen of Al_2O_3 , tested in a water-containing atmosphere, by first determining the intrinsic or base-level strength at low temperature.

9. THE HIGH TEMPERATURE FATIGUING CHARACTERISTICS OF Al_2O_3

A. Sapphire

Figure 9-9, which is a summary of all the constant strain rate bend tests performed on sapphire rods, indicates that the sapphire specimens were markedly strengthened by a prior anneal at high temperature. However, irrespective of the initial states of the specimens, testing in various atmospheres showed a fatiguing effect which, to a limit, became more severe with increasing temperature. As mentioned previously, other investigators have shown the trend to decreasing strengths as temperature is increased. In the present tests, however, it is seen that a wet atmosphere has the most pronounced fatiguing effect and vacuum (10^5 mm Hg) has the least. The dry hydrogen tests are somewhat inconclusive for it was found after the experiments that the quoted dew point of the hydrogen was not as low as initially expected (-60°C). In any event, for both the annealed and as-received specimens, the difference in failure behavior in different atmospheres must be interpreted as an atmosphere effect. This difference diminishes with increasing temperature until, at a temperature of about 800°C , an atmosphere effect on the failure strengths can no longer be observed. As mentioned previously, the upturn of the failure strength curves at temperatures in excess of 800°C is probably due to a plastic flow process.

The question remains as to whether or not the initial drop off in strength of the vacuum-tested specimens up to the 600 to 800°C range should be attributed to a residual atmosphere and therefore a corrosion effect. Such an explanation may be entirely reasonable for a vacuum of 10^{-5} mm Hg must be considered as still relatively reactive. Because of this ambiguity five annealed sapphire specimens were tested at the end of the program at a temperature of 500°C in a positive pressure atmosphere of nitrogen gas derived solely from gas evaporated from liquid nitrogen. As far as water vapor was concerned this atmosphere would be considered dry, yet, the failure stresses were no different than those previously obtained

under a vacuum of 10^{-5} mm Hg. This last experiment indicates that a water reaction cannot be responsible for the strength drop off with temperature of the vacuum tested specimens. This experiment also suggests that sapphire decreases in strength as temperature is raised to about 800°C and that this strength decrease is a consequence of temperature alone.

B. Polycrystalline Aluminum Oxide

Figure 9-15 shows the effect of atmosphere on the bend strength of Lucalox. Once again the vacuum-tested specimens are stronger than the wet-hydrogen tested specimens until a temperature of about 900°C is reached, and no atmosphere effect remains. Thus it must be concluded that evidences of corrosion fatigue due to water vapor may be obtained in the testing of Lucalox to relatively high temperature. As might reasonably be expected, Lucalox shows no evidence of strengthening by plastic flow at as low a temperature as observed for sapphire.

10. CONCLUSION

The results reported in previous sections confirm and extend previous investigator's findings that Al_2O_3 , both in single and polycrystalline form, is subject to static fatigue. From these results a number of general conclusions may be made.

(1) The reaction responsible for fatigue near room temperature is probably one in which water vapor from the atmosphere combines with the Al_2O_3 to form one or more of the many possible hydrated states of Al_2O_3 . The reduction in strength of sapphire and polycrystalline Al_2O_3 specimens due to corrosion fatigue can be as high as 70 to 80 percent of their intrinsic strengths.

(2) In mechanical tests, the fatigue process in Al_2O_3 manifests itself in the same fashion as is observed for other materials (e. g., glass). First, one observes delayed failure of Al_2O_3 specimens at constant load in which the most probable failure time is a very strong function of the applied stress, atmosphere, and temperature.

Second, the failure stress at a constant loading rate increases with the absolute value of the loading rate (Fig 9-14). Third, the coefficient of variation of failure stresses of samples subjected to similar mechanical testing procedures is considerably less when the fatigue process is permitted than when it is prevented. This situation is illustrated by the data in Table 9-VI in which the coefficient of variation for mechanical tests at liquid nitrogen temperature or in vacuum (fatigue process prevented) is considerably higher than that obtained in mechanical tests in wet hydrogen or air at moderate temperatures (fatigue process permitted). Fourth, the fracture behavior of single crystals at a given temperature depends on the atmosphere present during the test. Mirror fracture surfaces, characteristic of delayed failure fractures, appear only when humid conditions obtain. Under other conditions, interrupted cleavage or parting on definite crystallographic planes is the rule.

(3) The application of a fatigue theory to the low temperature fatigue data for sapphire and polycrystalline Al_2O_3 resulted in values for the activation volume (0.66 cu cm per mole), the surface energy between Al_2O_3 and its hydration product (less than one-hundred ergs per sq cm) and the activation energy for the hydration reaction (14 kcal per mole) which are reasonable for a stress corrosion reaction.

(4) The observed bend strength of sapphire is quite sensitive to its prior thermal history. In this investigation, heat-treating as-received ground rods improved their low-temperature strength in all atmospheres by about 50 percent, up to about 500°C. The atmosphere present during heat-treatment at 1125°C has no noticeable effect on the low-temperature bend strength.

The mechanism by which this strengthening occurs is not firmly known, but the fact that annealing has less of an effect on samples in which the base planes are at zero deg to the longitudinal axis of the rod specimens than on samples whose base planes are at 60 deg to the rod axis suggests that surface preparation (grinding) may introduce more surface flaws on the latter specimens and that these flaws heal under the annealing treatment.

Table 9-VI

LOW-TEMPERATURE BEND STRENGTHS AND COEFFICIENTS
OF VARIATIONS OF STANDARD LUCALOX SPECIMENS

$\dot{\epsilon} = 3 \times 10^{-4}$ in. per in. per min

N = number of tests

σ = average failure stress $\times 10^3$ psi

v = coefficient of variation

Temperature (°C)		Saturated Air	Dry Hydrogen	Wet Hydrogen	Vacuum	Liquid Nitrogen
-196°C	N					20
						66.5
	v					13.2%
Room	N	11	11	10	10	
		46.5	52.3	44.9	65	
	v	5%	5.9%	6.8%	9%	
200°C	N		11	9	34	
			48.4	42	57.2	
	v		7.8%	7.4%	12.8%	

(5) With an essentially inert gas (hydrogen) saturated with water vapor at room temperature, the fatigue reaction in both Lucalox and sapphire is sufficiently strong to give evidence of fatigue up to temperatures approaching 800°C.

(6) Superimposed on the atmosphere fatiguing process of sapphire, which operated up to about 800°C, appears to be a further weakening process of equal severity which may depend only on temperature and not on atmosphere. Whether or not such an effect truly exists can only be determined by very exacting experiments.

(7) Strengthening of sapphire by plastic deformation is observable at temperatures as low as 900°C. Evidences for plastic deformation in Lucalox at temperatures below 1100°C were not obtained.

11. REFERENCES

- 9-1 Roberts, J. P. and Watt, W., "Mechanical Properties of Sintered Alumina", p. 53, Ceramics and Glass Volume 10, (1952).
- 9-2 Wachtman, J. B., Jr. and Maxwell, L. H., "Plastic Deformation of Ceramic-Oxide Single Crystals", J. Am. Cer. Soc. 37 (7), 291-99 (1954).
- 9-3 William, L. S., "Stress-Endurance of Sintered Alumina", Tr. Brit. Cer. Soc. 35, 287-312 (1956).
- 9-4 Pearson, S., "Delayed Fracture of Sintered Alumina", Proc. Soc. (London) 69(B), 1293-96 (1956).
- 9-5 Brenner, S. S., "Mechanical Behavior of Sapphire Whiskers", J. Appl. Phys. 33-39 (1962).
- 9-6 Charles, R. J., "The Strength of Silicate Glasses and Some Crystalline Oxides", pp. 225-249 in Fracture, John Wiley and Sons, New York, (1959).
- 9-7 Clarke, F. P., private communication.
- 9-8 Klassen-Nekhlyudova, M. V., as reported in Oxide Ceramics, E. Ryshkewitch, Academic Press, New York, 1960, p. 155; see also "Dependence of the Strength of Corundum Crystals on Crystallographic Orientation During Testing in Bend and Tension", Physical Properties of Synthetic Corundum, A Symposium, Trudy Inst. Krist. Akad. Nauk U. S. S. R., No. 8, pp. 215-224 (1953).

- 9-9 Seemann, A. K., "Gens, Synthetic", Encyclopedia of Chemical Tech. 7, 1951, p. 162, "Alumina Properties", Technical Paper No. 10, Alcoa Research Labs, 1960.
- 9-10 Wachtman, J. B., Jr., and Maxwell, L. H., "Plastic Deformation of Ceramic Oxide Single Crystals III", J. Am. Cer. Soc. 40 (11), 377-85 (1957).
- 9-11 Steijn, R. P., "On the Wear of Sapphire", J. Appl. Phys. 32 (10) 1951-58 (1961).
- 9-12 Jackman, E. A., and Roberts, J. P., "On the Strength of Polycrystalline and Single Crystal Corundum", Tr. Brit. Cer. Soc. 54, 389-98 (1955).
- 9-13 Wachtman, J. B., Jr. and Maxwell, L. H. WADC-TR 53-265 and supplements, Nat. Bur. Stand., 1956, as presented by R. D. Olt, Linde Bulletin F-917-A, 1958.
- 9-14 Tomilovski, G. E., "Effects of Heat Treating Synthetic Corundum Crystals at 1300°C on Mechanical Properties", Phys. Prop. of Synth. Corun., A. Symposium, Trudy Inst. Krist. Akad. Nauk. U.S.S.R., No. 8, 341-54 (1953).
- 9-15 Kronberg, M. L., "Dynamical Flow Properties of Single Crystals of Sapphire, Part I", General Electric Research Laboratory Report 61-GC-197, December, 1961.
- 9-16 Wachtman, J. B. and Lam, D. G., Jr. "Young's Modulus of Various Refraction Materials as a Function of Temperature", J. Am. Cer. Soc. 42 (5) 254-50 (1959).
- 9-17 Wachtman, J. B., Jr., Tefft, W. E. and Lam, D. G., Jr., "Young's Modulus of Single Crystal Corundum from 77° 850°K", Ch. 15 pp. 221-223, in Mechanical Properties of Engineering Ceramics, Kriegel and Palmour, Editors, Interscience, New York, N. Y., 1961.
- 9-18 Pigolina, E. M., and Svyatuklin, V. V., "An Investigation of the Parting Planes of Synthetic Corundum by Optical and X-ray Methods", Phys. Prop. Syn. Corun., A. Symposium, Trud. Inst. Krist. Akad. Nauk. U.S.S.R., No. 8, 299-308 (1953).
- 9-19 Winchell, H., "Orientation of Synthetic Corundum for Jewel Bearings", Am. Mineralogist 29, 399-414 (1944).
- 9-20 Petch, N. J., "Effect of Surface Energy on Brittle Behavior", pp. 285-293, in "Studies of the Brittle Behavior of Ceramic Materials", ASD-TR-61-628, N. A. Weil, Editor, (1961).

- 9-21 Fullman, R. L., "Measurement of Particle Sizes in Opaque Bodies", J. Met. 5, 447 (1953).
- 9-22 Schwartz, B., "Thermal Stress Failure of Pure Refractory Oxides", J. Am. Cer. Soc. 35 (12) 325-333 (1952).
- 9-23 Ryshkewitch, E., Oxide Ceramics, P. 148, Academic Press, New York, N. Y., (1960).
- 9-24 Folweiler, R. C., "Creep Behavior of Pore-Free Polycrystalline Aluminum Oxide", J. Appl. Phys. 32 (5) 773-78 (1961).
- 9-25 Charles, R. J. and Hillig, W. B., "The Kinetics of Glass Failure by Stress Corrosion", Symposium sur la Resistance Mechanique du Verre et les Moyens de l'Ameliorer, Florence, Italy, September 1961.
- 9-26 Inglis, C. E., "Stresses in a plate Due to the Presence of Cracks and Sharp Corners", Proc. Inst. Naval Arch. 55, 219 (1913).

TASK 10 - EFFECT OF THERMAL-MECHANICAL HISTORY

Principal Investigator: R J Stokes
Minneapolis Honeywell Research Lab

ABSTRACT

The objectives of this study concern the determination of the effect of thermal or mechanical treatment on the stress strain behavior of ceramic oxides. The work carried out during the current period included three principal investigations: (1) the effect of heat treatment on the aging of fresh dislocations, (2) the effect of heat treatment on the microstructure MgO single crystals and the resistance of the lattice to the movement of fresh dislocations, and (3) the mobilization of grown-in dislocations by various means including heat treatment, fluctuating thermal stresses and stressing at high temperatures.

These studies were pursued by means of mechanical tests, etch pit studies and electron transmission microscopy. All work was done on MgO single crystals, most of which were preannealed at 2000°C.

It was found that the strength of crystals containing fresh dislocation was unchanged up to an annealing temperature of 600°C; their ductility fell and their strength rose as the annealing temperature exceeded 600°C. The rise in strength with anneal temperature above 600°C is approximately linear until a strength is reached at which the crystal simply crushed without any evidence of plastic flow. This phenomenon is actually equivalent to an aging treatment, the reasons for which are attributable to (1) an increased lattice resistance to dislocation motion by a precipitation hardening process, (2) migration of impurities to dislocation sites and the consequent locking of dislocations, (3) changes in dislocation configurations.

'Grown-in' dislocations in MgO show an amazing resistance to stress, and cannot be moved at all by the experimental approaches attempted. This is ascribed to a rigid impurity locking of grown-in dislocations in this material.

TASK 10 - EFFECT OF THERMAL-MECHANICAL HISTORY

1. INTRODUCTION

It has been shown in previous work on this project ⁽¹⁰⁻¹⁾ that the plastic deformation normally associated with magnesium oxide single crystals at room temperature is entirely dependent upon the presence of 'fresh' surface dislocation sources. Normally fresh surface dislocations can move when a shear stress of approximately 5,000 psi is applied to the ⁽¹⁰⁻²⁾ and single crystals show macroscopic plastic bending when the outer fiber stress resolved over (110) planes reaches a value of about 15,000 psi. Under these conditions the stress deflection curves are smooth and the plastic deformation before fracture is considerable. However, when great care is taken to eliminate fresh surface dislocations by a chemical polishing technique, the crystals become extremely strong and deform elastically up to stresses well in excess of 100,000 psi ⁽¹⁰⁻¹⁾. While chemical polishing removes the surface dislocations, it obviously does not remove the dislocations grown into the bulk at the melting temperature. Thus it is concluded that 'grown-in' dislocations in this material can withstand stresses at least 20 times (and probably much more) the stresses at which fresh dislocations have been shown to move.

It is important to understand the nature of the extremely strong dislocation locking mechanism responsible for immobilizing 'grown-in' dislocations in this material and most of our recent work on thermal-mechanical history effects has been directed to this end. The work falls into a number of categories. First, we have studied the effect of heat treatment on the aging of individual fresh dislocations using mechanical tests, etch pit and electron transmission techniques. Although part of this work was described in the previous final report ⁽¹⁰⁻¹⁾ it is included here for the purpose

of continuity. Second, we have studied the effect of heat treatment on the microstructure of MgO single crystals and the lattice resistance to the movement of fresh dislocations. Third, we have attempted to mobilize grown in dislocations by various heat treatments, by applying a fluctuating stress or by stressing at high temperatures.

2. EFFECT OF THERMAL HISTORY ON THE MOBILITY OF 'AGED' DISLOCATIONS AT ROOM TEMPERATURE

A. Experimental Procedure

All of the tests to be described in this section were conducted under bending. Single crystal beams were cleaved to the appropriate dimensions ($1/4$ in. \times $1/8$ in. \times 1 in) and were generally given a preliminary anneal in a carbon furnace (through which nitrogen was passed) at 2000°C for $1/2$ hour. The preliminary anneal served a number of purposes: first it standardized the starting condition by dissolving the impurity precipitate particles to produce optically clear specimens and second it provided a background which was clear for etching purposes. It will be indicated later that this preliminary anneal actually had a profound effect on the subsequent mechanical behavior.

The annealed beams were chemically polished to remove surface microcracks and then sprinkled with silicon carbide to introduce a moderate density of fresh surface dislocation loops. They were preloaded in the Instron machine at a deflection rate of 0.002 in./per min until the macroscopic yield point could just be detected. Preloading served two purposes: first it introduced 'fresh' slip band segments well beneath the tension surface of the beam and second it provided a measure of the room temperature flow stress of the individual crystals.

The pretrained crystals were next subjected to a variety of heat treatments and then retested at room temperature to establish the yield strength and deformation behavior of crystals in the 'aged'

condition. In addition the effects of heat treatment and restressing were assessed by double etching techniques. It is important to mention that during all annealing, etching and handling steps of the experimental procedure it was essential to support the beams carefully at their ends, otherwise mechanical contact within the gauge length led to the reintroduction of 'fresh' dislocations and thereby to erroneous conclusions regarding the behavior of 'aged' dislocations.

To supplement the mechanical and etch pit studies, changes in dislocation configuration during heat treatment were examined with the electron transmission technique. Thin films were prepared using the procedure developed by Washburn, et al (10-3) and described in the book by Thomas (10-4) in which a jet of boiling orthophosphoric acid was directed at the area to be thinned. It was found advantageous to add 2 percent of concentrated sulfuric acid to overcome the tendency for 'pyramids' to form on the surface in the vicinity of the thinned area.

B. Mechanical Tests

A typical sequence of mechanical tests is illustrated in Fig. 10-1 where the annealing time at the different temperatures was one hour. As can be seen in Fig. 10-1 all of the specimens increased in strength after annealing and most of the stress deflection curves became very jerky, both indications that 'aging' had taken place. Figure 10-2 contains a plot of the flow stress ratio σ_2/σ_1 (where σ_1 was the stress level at which preloading stopped and σ_2 was the maximum stress level supported by the beam after annealing) as a function of the temperature and time of anneal.

There are a number of interesting points to be made in connection with these curves and the corresponding mechanical behavior.

(1) Anneals at temperatures up to 500°C produced virtually no effect on the subsequent mechanical behavior.

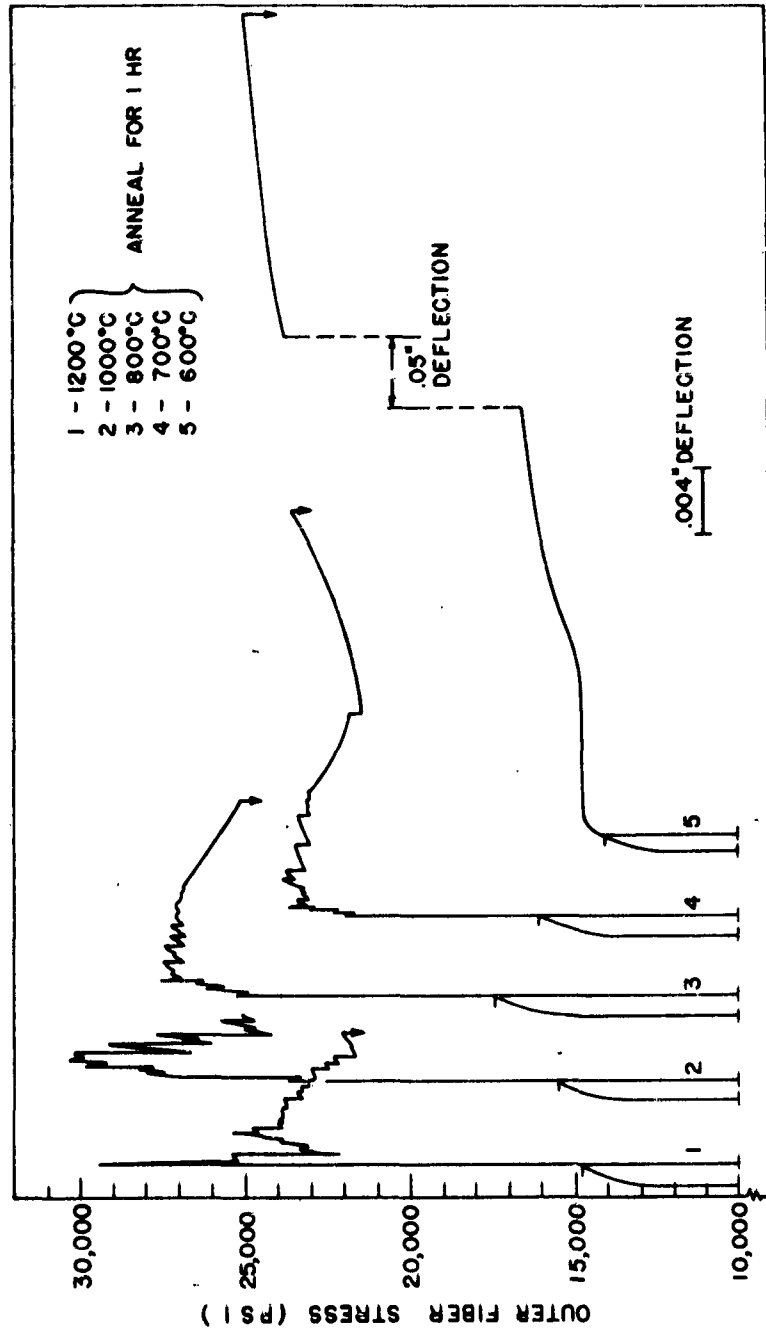


Fig. 10-1 EFFECT OF HEAT TREATMENT ON THE STRENGTH OF PRESTRAINED CRYSTALS. STRESS DEFLECTION CURVES BEFORE AND AFTER ONE HOUR ANNEALS.

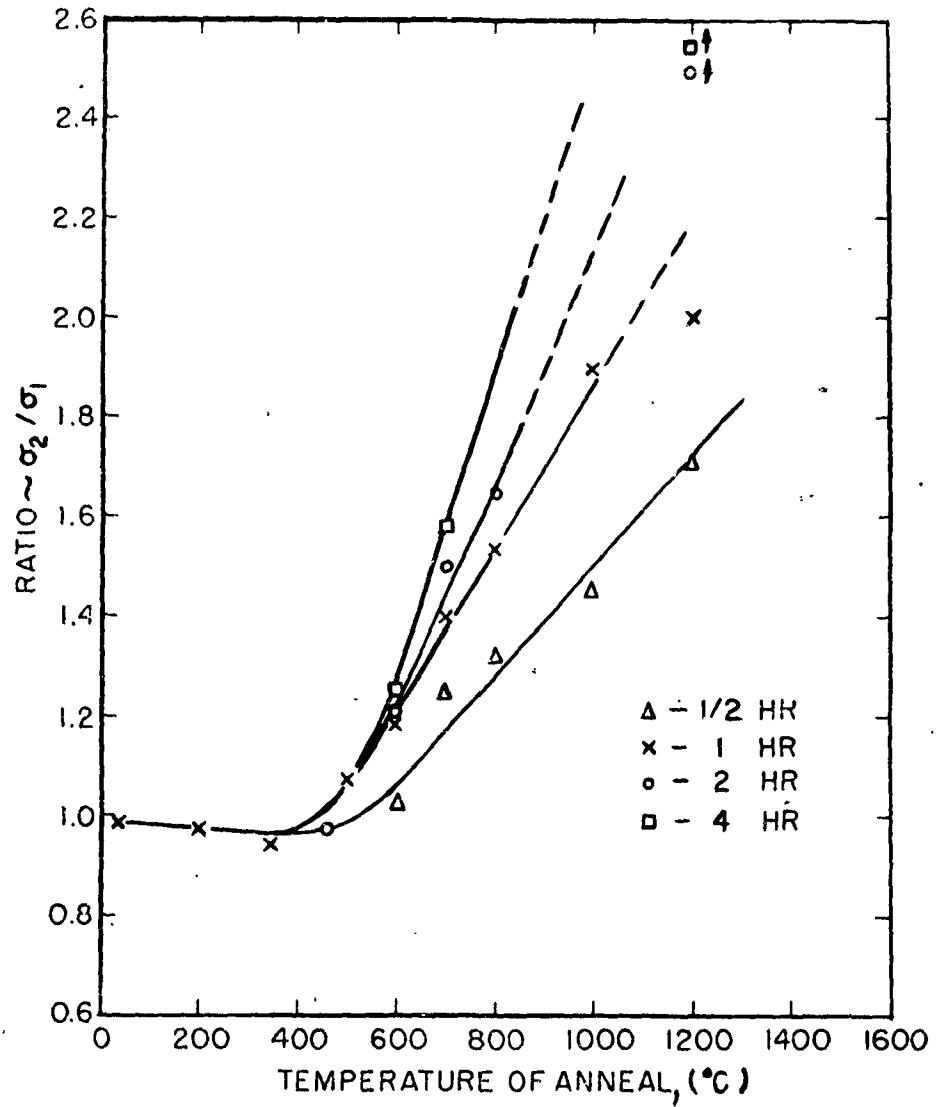


Fig. 10-2

EFFECT OF HEAT TREATMENT ON THE STRENGTH OF PRESTAINED CRYSTALS

Ratio of yield stress after (σ_2) to yield stress before (σ_1) aging, as a function of annealing temperature and time

(2) An anneal at 600°C resulted in a slight increase in strength, with the flow stress ratio increasing from 1.02 after 1/2 hr at temperature to 1.25 after 4 hr at temperature. However, the stress strain curves remained smooth and the plastic deflection before fracture was considerable as indicated in Fig. 10-1 for all periods of annealing at this temperature.

(3) When the annealing temperature was raised above 600°C the strength increased markedly, the stress-deflection curves became initially very jerky and the ductility anneal decreased. At modest temperature, such as after 1 hour at 700°C (see Fig. 10-1), the curve was initially jerky but became smoother, leveled out and finally exhibited some work hardening before fracture. It is important to note that the curve leveled out at a stress higher than that value normally required to promote deformation in the presence of fresh dislocations. This is an observation to which we shall return in a later section. After 1 hour at 800°C the curve likewise became smoother but never leveled out. At higher anneal temperatures, such as after 1 hour at 1000°C or 1200°C, the yield drops were very pronounced and the specimens quite brittle.

(4) Prolonged annealing at 1200°C or short time anneals at higher temperatures (1400°C and above) resulted in specimens which were so strong that they deformed by crushing at the upper loading beam before yielding commenced in the tension surface. This, naturally, placed a limit on the measurement of the flow stress ratio in bending. As indicated in Fig. 10-2 the limit occurred at a value of σ_2 / σ_1 above 2.0.

From these studies therefore it is obvious that 'fresh' dislocations which can move through the preannealed (2000°C) MgO crystals at a relatively low stress level (approx. 5,000 psi) experience a strong resistance to their motion following an aging treatment at a sufficiently high temperature. The question now arises as to the nature of the strengthening following heat treatment; is it due to impurity locking of the dislocations alone, is it a conse-

quence of precipitation increasing the lattice resistance to dislocation motion, or is it due to a combination of both of these two factors. Our present contention to be amplified in later sections is that the strengthening observed in their experiments is a combination of both.

C. Etch Pit Studies

The fact that individual dislocations are locked by impurities when annealed above 600°C has been demonstrated directly by etch pit techniques. The essential feature of the technique is to etch a prestrained crystal after its anneal so that the location of the aged dislocations is marked, and then to re-etch the crystal after restraining so that the particular dislocations which participated in the plastic deformation may be identified.

Figure 10-3 compares the appearance of two crystals annealed at 600°C and 800°C for one hour and subjected to this double etching procedure. For an anneal at 600°C there were many examples of short slip band segments on the tension surface of the bend specimen which had been reactivated upon restraining as shown in Fig. 10-3(a). From this observation, and the mechanical studies described earlier, it was obvious that dislocation locking by impurity at this temperature was not very great. By comparison, the specimen annealed at 800°C showed only a few examples of reactivated slip bands (one such is shown in the photomicrograph in Fig. 10-13(b)); in fact the number of reactivated bands corresponded exactly with the number of yield drops (see Fig. 10-1) observed upon restraining. This represented direct evidence for impurity locking of the dislocations in the slip band segment, and confirmed that the yield points represented their sudden release from the impurity atmospheres.

There was further evidence of dislocation interaction with impurities at temperatures of 700°C and above. This was the change in appearance of the etch pits. Etch pits on fresh dislo-



(a) at 600°C



(b) at 800°C
X 250

Fig. 10-3
EFFECT OF HEAT TREATMENT ON ETCH PIT
APPEARANCE FOLLOWING A ONE HOUR ANNEAL

cations and dislocations aged up to 600°C were sharper, larger, more regular in size and more unsymmetrical than dislocations aged at temperatures above 600°C as may be seen by comparing the larger etch pits in Fig. 10-3(a) and 10-3(b). Figures 10-4(a) and 10-4(b) also compare the appearance of a short slip band segment etched before and after an anneal at 1000°C for 1/2 hr. It was shown that the change in symmetry and size of the etch pits was not associated with a change in the plane in which the dislocations lay, but rather was due to a slowing of the etching rate along the dislocations lines. This was interpreted as being due to the fact that impurities had condensed on to the dislocation lines to lower their elastic core energy.

It was interesting to note that etch pits in Fig. 10-3(a) on dislocations aged at 600°C were still sharp after restraining. This indicated that the surface dislocations responsible for them had not moved upon restressing and they too were presumably locked temporarily by the anneal. By contrast, the application of a stress to dislocations annealed at 500°C for 2 hr resulted in many of the old etch pits becoming flat-bottomed indicating that their site of etching had been displaced and therefore that the dislocations were not locked.

Double-etching techniques were also used to study the change in dislocation density and distribution upon annealing. While these experiments showed that many of the dislocations were eliminated during the anneal, they were not nearly so revealing in detail as the thin film studies to be described in the next section.

In summary, the mechanical and etch pit studies compliment one another well, and show that fresh dislocations in preannealed (at 2000°C) MgO crystals can be locked temporarily by an anneal at 600°C. The locking becomes much stronger and more permanent once the annealing temperature exceeds 700°C. Thus at least part of the strengthening observed in Fig. 10-1 is due to impurity locking of the individual dislocations.



(a) before 1/2 hr
anneal at 1000°C



(b) after 1/2 hr
anneal at 1000°C
X 500

Fig. 10-4
EFFECT OF HALF-HOUR ANNEAL AT 1000°C
ON ETCH PIT APPEARANCE

D. Thin Film Studies

To gain a better appreciation of the changes in dislocation configuration occurring during annealing use was made of the electron transmission thin film technique for MgO. Transmission electron microscopy has already shown that slip bands produced in magnesium oxide at room temperature contain a high proportion of elongated prismatic edge dislocation loops ⁽¹⁰⁻³⁾ and the breakup of these loops upon annealing by diffusion has been considered in detail by Groves and Kelly ⁽¹⁰⁻⁵⁾. However, the exact temperature range where annealing effects may be resolved and their possible relation to the strengthening observed here have not been considered.

To study the room temperature dislocation configurations, fairly thin Norton single crystals were preannealed at 2000°C, chemically polished, sprinkled with silicon carbide and bent between the fingers to an approximate angle of 30 deg and restraightened. They were then thinned by the jet polishing technique. To study the effect of heat treatment on slip bands the deformed bulk crystals were annealed before thinning. Attempts to anneal thinned films resulted in a contamination on the surface and consequent loss of resolution.

In order to appreciate many of the features found in slip bands produced at room temperature it is useful first to examine the simple dislocation distributions produced when slip bands are injected into thin films. Besides providing an introduction, such studies can also provide fundamental information on dislocation behavior. Figure 10-5 is a particularly instructive example. The plane of the film is (100) so the (110) slip planes cut across it at 45 deg to leave traces in the surface parallel to $[001]$ as shown in Fig 10-5. Since the slip direction is $[110]$ pure edge dislocations project as straight lines parallel to this $[001]$ direction while pure screw dislocations project as straight lines perpendicular to it,



Fig. 10-5
ELECTRON TRANSMISSION MICROGRAPH OF A SIMPLE SLIP BAND
CONSISTING OF SCREW DISLOCATIONS INJECTED INTO A THIN FILM
OF MAGNESIUM OXIDE. NOTE DEBRIS BETWEEN DISLOCATIONS
AT C AND D.

i. e., - along $[010]$. The lines joining the points where pure screw dislocations emerge through the top and bottom surfaces of the film are separated by a distance (d in Fig. 10-5) equal to the thickness of the film. There are many examples such as X in Fig. 10-5 where a dislocation in the screw orientation is observed with a length less than d ; these represent cases where the screw dislocation has cross slipped out of the (110) plane, probably over the (001) plane normal to the film

As mentioned earlier, many of the features found in room temperature slip bands are in fact elongated prismatic edge dislocation loops. The mechanism by which these loops are formed has been the topic of a number of recent papers (10-3, 10-6, 10-7). The mechanism originally proposed by Johnston and Gilman (10-6) and Washburn, et al (10-7) suggests that an advancing screw dislocation (S_2S_2' in Fig. 10-6(a)) becomes held up at some point in the slip plane. In overcoming the obstacle the screw dislocation cross slips leaving the jog J in the Fig. 10-6(a) behind. The two edge components E and E' move toward one another resulting in the formation of an elongated positive and negative edge dislocation dipole. When the screw dislocation cross slips back again the dipole is pinched off and remains immobile as 'debris' in the slip plane. The spacing between the edge dislocations and thus their chance of being resolved in the electron microscope depends upon the size of the jog J . The spacing J along a given dipole may increase or decrease discontinuously due to further cross slip of the advancing screw dislocation. Tetelman (10-7) has criticized this mechanism on the grounds that obstacles to the advancing screw dislocation are never seen in the microscope. He has suggested another mechanism whereby dipoles are formed by the interaction of mixed edge and screw dislocations of opposite sign moving on adjacent planes.

While both of these mechanisms may operate in bulk material, the observations included in the slip band at ABCD in

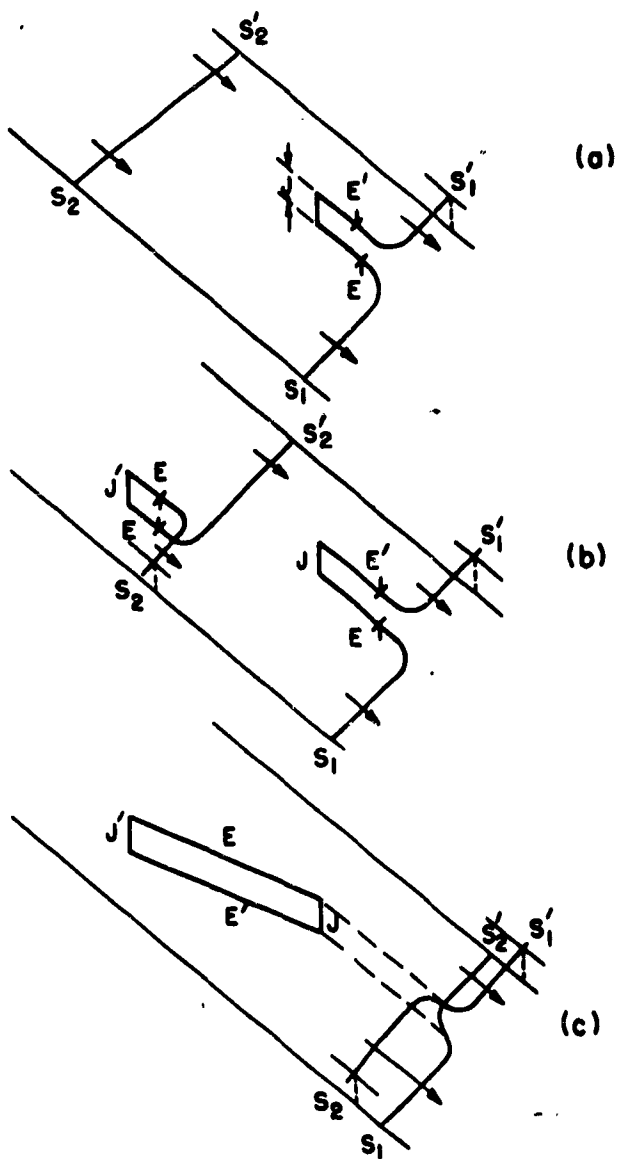


Fig. 10-6
MECHANISM FOR THE GENERATION OF DEBRIS CONSISTING OF
POSITIVE AND NEGATIVE DISLOCATION DIPOLES IN A SLIP PLANE

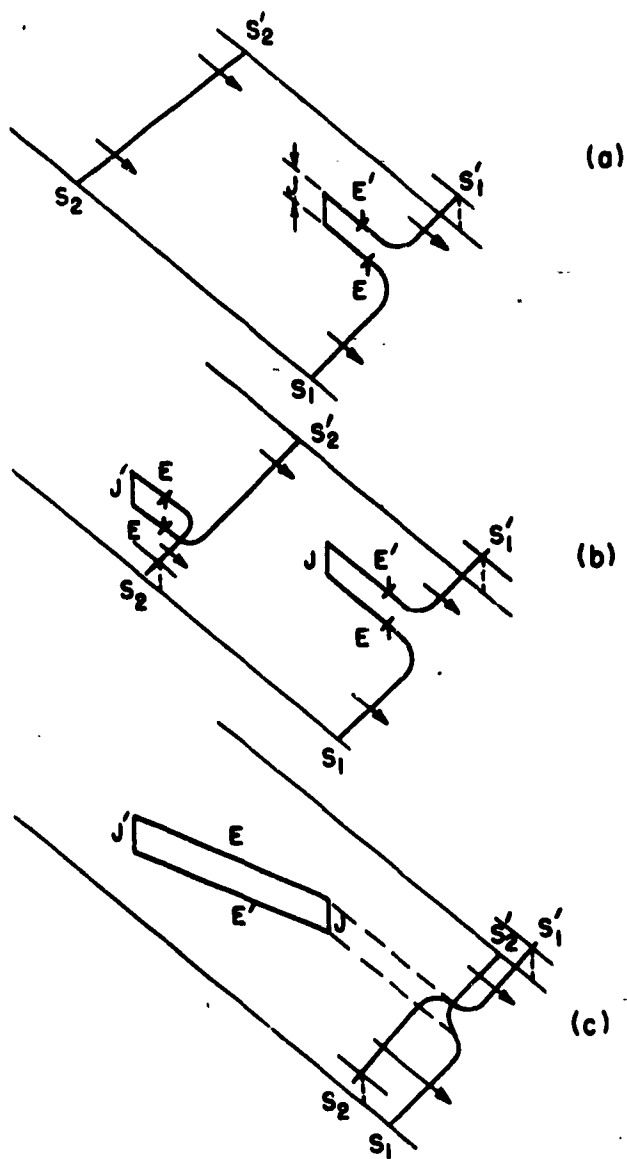


Fig. 10-6
MECHANISM FOR THE GENERATION OF DEBRIS CONSISTING OF
POSITIVE AND NEGATIVE DISLOCATION DIPOLES IN A SLIP PLANE

Fig. 10-5 cannot be accounted for satisfactorily by either of them. The dislocations in this slip band probably originated at the edge of the film to the right and were pushed into the crystal from right to left. Because they were formed in the thin film they were assumed all to have the same Burgers vector, the same sign and therefore to move in the same direction. In a bulk crystal, dislocation multiplication⁽¹⁰⁻⁶⁾ can result in dislocations of opposite sign moving in opposite directions on adjacent planes so that Tetelman's⁽¹⁰⁻⁷⁾ mechanism may operate. However it is not considered that a film is thick enough for the multiplication mechanism to operate. Thus we have the situation at A and B in Fig. 10-5 where apparently two screw dislocations of the same sign have either interacted or crossed over. The possibility of them lying on intersecting orthogonal (110) planes is ruled out since the intersection would then always take place at their midpoint ($d/2$) and it can be seen that this is not the case.

Figure 10-6 illustrates a mechanism whereby two screw dislocations of the same sign can become crossed. It is assumed that the two screw dislocations (S_1 and S_2) cross slip at the points J and J' by equal amounts but in the opposite direction. The two screw components S_1' and S_2 then find themselves on the same slip plane, as do S_1 and S_2' , and they cross link as shown in Fig. 10-6(c) to form a crossed screw dislocation pair. The component S_2 cannot overtake S_1 unless the spacing between them (equal to J) is large enough to avoid elastic interaction. As a result of this mechanism debris is left in the slip plane between J and J'.

Variations of this mechanism can be used to explain some of the features in Fig. 10-5. For example, if J and J' are coincident and equal in magnitude then no debris is produced, this may be the case at A and B in Fig. 10-5. If the two original screw dislocations S_1 and S_2 should become separated again, then a dipole must stretch between them. This may be the case

at C in Fig. 10-5 where a faint trace possibly corresponding to the dipole can be seen linking the two screw dislocations. The situation at D appears more complicated since two crossed dislocations are linked to a third by a dipole. At the moment this mechanism seems the most reasonable one to explain the observations in Fig. 10-5; however, further studies are obviously required to substantiate it or to suggest a modification.

Figure 10-7 illustrates the dislocation distribution and debris left in a slip band produced in the bulk material at room temperature. There are many examples of screw dislocations with dipoles dragging behind them as illustrated in Fig. 10-6(a), see for example at A. In addition much of the slip plane contains fine and coarse debris of varying length and direction, see for example at B. Unfortunately one sees no examples of crosslinked screw dislocations as illustrated in Fig. 10-6(c). This means either that this mechanism does not occur in the bulk or that it is modified by further dislocation reactions.

Figure 10-8 shows the effect of annealing for 2 hr at 650°C. While the general dislocation density has not decreased, there does appear to be a decrease in the debris, especially the short segments of fine debris. It seems reasonable to presume that this has dispersed by diffusion of the excess vacancies or interstitials to the nearby debris which grows coarser at its expense. After 2 hr at 850°C almost all of the fine debris has disappeared and there is a decrease in the screw dislocation density. There is no resolvable evidence for breakup of the coarse dipoles at this temperature.

The first evidence of breakup becomes apparent following anneals between 875°C and 900°C for 2 hr. Figure 10-9 shows the appearance of an annealed slip band after 2 hr at 920°C. The dislocation density has obviously decreased tremendously and most of the debris remaining in the slip bands is in the form of coarse partially broken up debris.



Fig. 10-7
ELECTRON TRANSMISSION MICROGRAPH SHOWING DISLOCATION
DISTRIBUTION IN A BULK MAGNESIUM OXIDE CRYSTAL DEFORMED
AT ROOM TEMPERATURE.



Fig. 10-8
ELECTRON TRANSMISSION MICROGRAPH SHOWING DISLOCATION
DISTRIBUTION IN A BULK CRYSTAL DEFORMED AT ROOM TEMP-
ERATURE AND ANNEALED AT 650 °C FOR TWO HOURS.



Fig. 10-9
ELECTRON TRANSMISSION MICROGRAPH SHOWING DISLOCATION
DISTRIBUTION IN A BULK CRYSTAL DEFORMED AT ROOM TEMP-
ERATURE AND ANNEALED AT 920°C FOR TWO HOURS. NOTE
SOME OF THE COARSE DIPOLES ARE BEGINNING TO BREAK UP.

Annealing at temperatures of 950°C and above for 2 hr results in a complete breakdown of the coarse dipoles into strings of circular prismatic loops as described by Groves and Kelly⁽¹⁰⁻⁵⁾ Figure 10-10 shows an example of this. There are instances as at A where the original cross slipped screw dislocations are still attached to their respective dipoles. At higher temperatures the circular loops get larger through bulk diffusion and by 1250°C each coarse dipole has become almost a single circular loop, and only a few dislocations remain. The appearance of a slip band after 2 hr at 1250°C is shown in Fig. 10-11.

To summarize the electron transmission studies, it has been found that the high density of dislocations and debris produced in a slip band at room temperature undergo the first discernible change as a result of annealing around 650-700°C. At this temperature the fine dislocation dipoles disappear and the coarse ones become more prominent. This transfer of material must involve bulk diffusion over short distances. As the temperature is raised, the dislocation density decreases while the dipoles become coarser and longer, the first evidence for their breakup into circular loops occurs at 900°C, the loops then become larger until they form single loops by 1250°C. The agreement between the temperature (650°C) where debris starts to disappear and where strengthening due to dislocation locking is observed may be coincidental or real. The coincidence may lie in the fact that short range bulk diffusion is necessary both to disperse the fine debris and transport impurities to the dislocations. On the other hand, dislocations locking may result from the diffusion of vacancies or interstitials constituting the fine debris to the dislocation lines which become jogged and thereby immobilized.



Fig. 10-10
ELECTRON TRANSMISSION MICROGRAPH SHOWING DISLOCATION
DISTRIBUTION IN A BULK CRYSTAL DEFORMED AT ROOM TEMP-
ERATURE AND ANNEALED AT 1050°C FOR TWO HOURS.

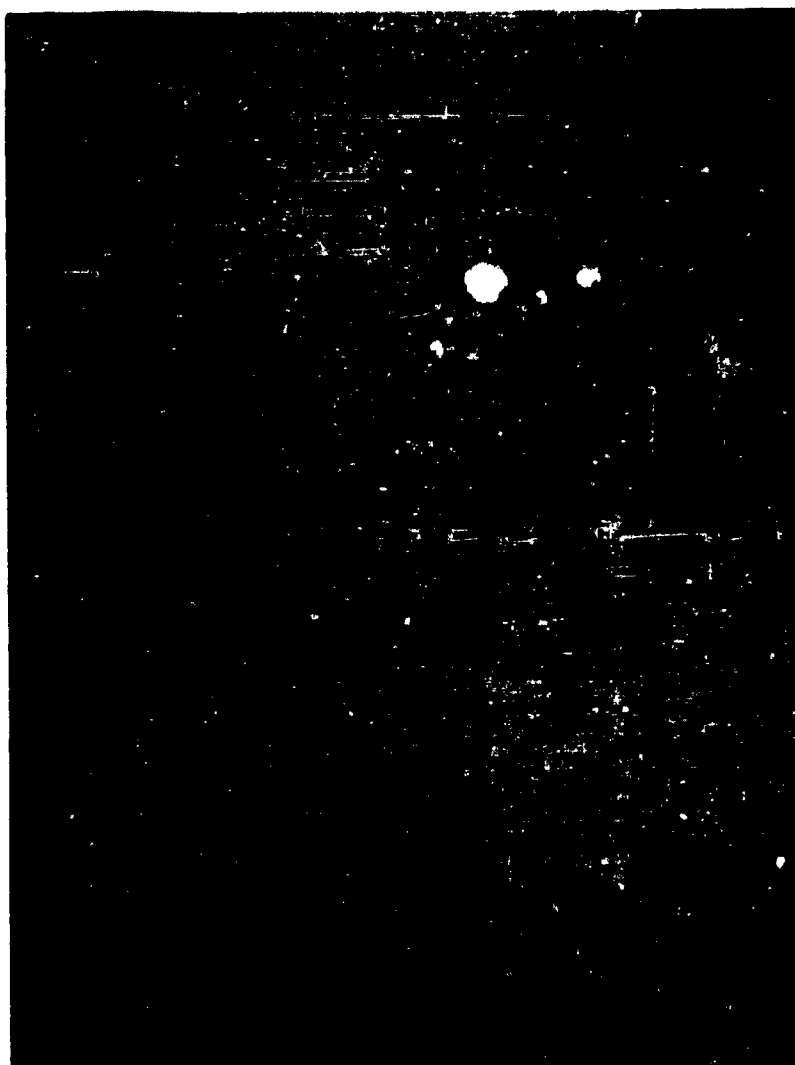


Fig. 10-11
ELECTRON TRANSMISSION MICROGRAPH SHOWING DISLOCATION
DISTRIBUTION IN A BULK CRYSTAL DEFORMED AT ROOM TEMP-
ERATURE AND ANNEALED AT 1250°C FOR TWO HOURS.

It is significant to note at this point that the electron micrographs do not provide direct evidence for either of these two possibilities. One sees neither jogged dislocations nor any resolvable precipitate on the dislocation lines.

3. EFFECT OF THERMAL HISTORY ON THE MOBILITY OF 'FRESH' DISLOCATIONS AT ROOM TEMPERATURE

The purpose of these experiments was to determine the variation in lattice resistance to the motion of 'fresh' dislocations following heat treatment so that its contribution to the strengthening observed in Fig. 10-1 could be assessed. A series of mechanical tests were performed on single crystals cleaved from the same parent block but having two different starting conditions, (1) as-received (i.e., after a slow cool from the melting temperature), (2) pre-annealed at 2000°C . The respective crystals were sprinkled and prestrained slightly to establish their initial room temperature strength and then annealed at a low temperature (600°C) for two hours. They were then resprinkled so that fresh dislocations were reintroduced and the room temperature yield strength redetermined. The procedure was repeated on the same specimen but with the two hour annealing period at successively higher temperatures. Since the resistance to dislocation motion was directly related to the macroscopic yield point, this parameter could be plotted as a function of the annealing temperature.

Figure 10-12 reproduces the preliminary results from such a test. It can be seen that in agreement with the observations of Gorum et al⁽¹⁰⁻⁸⁾ the material preannealed at 2000°C was initially much softer (by 50%) than the as-received material. The strength of the preannealed material showed an increase upon re-annealing above 600°C rising to a maximum at approximately 1200°C . It is interesting to note that the shape of this curve corresponds closely with yield stress dependence upon

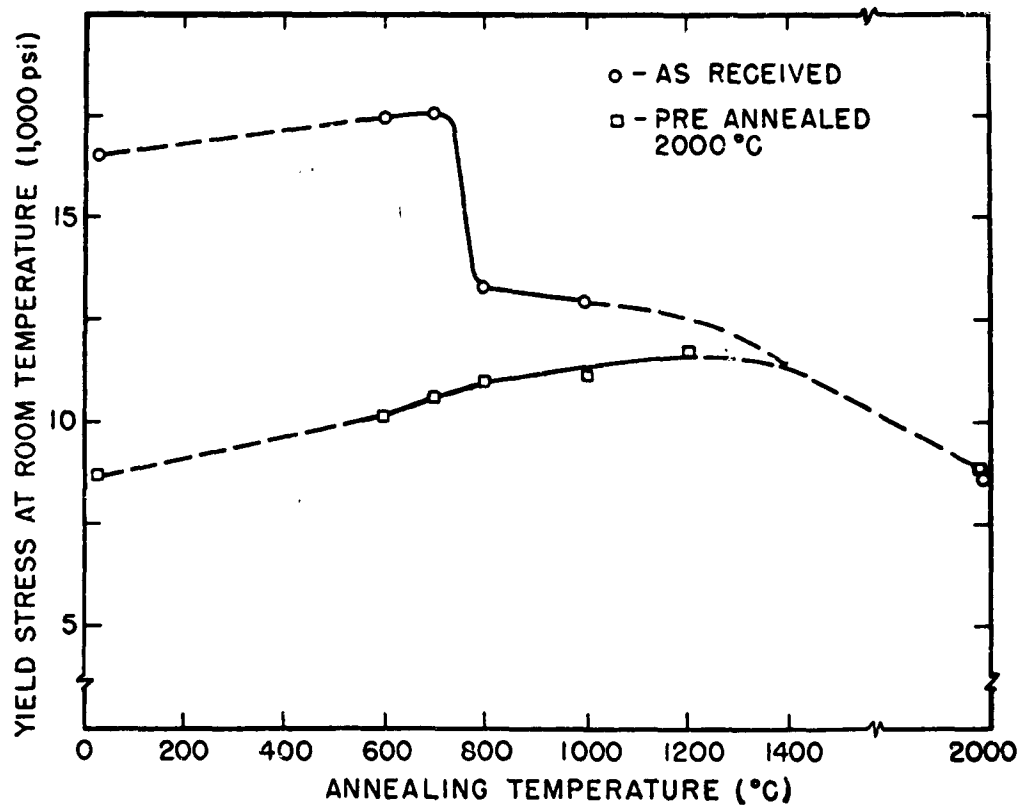


Fig. 10-12

EFFECT OF HEAT TREATMENT ON THE LATTICE RESISTANCE
TO THE MOTION OF FRESH DISLOCATION
Yield strength of sprinkled crystals as a function of annealing temperature for both as-received and preannealed crystals

temperature for pre-annealed crystals as described in the previous annual report⁽¹⁰⁻¹⁾ and by May and Kronberg⁽¹⁰⁻⁹⁾. By comparison the strength of the as-received material dropped sharply at 800°C and obviously must drop further by 2000°C to equal the value of the preannealed crystal.

To supplement these mechanical studies we examined the etch pit distribution produced on MgO crystals following different heat treatments. As described previously⁽¹⁰⁻¹⁾ as-received MgO showed a distribution of etch pits similar to that normally associated with the distribution of a precipitating phase in a two phase alloy. Upon annealing at 2000°C most of these etch pits disappeared indicating that the precipitating phase had been taken into solution. It was interesting to know whether the etch pit technique could detect any reprecipitation upon reannealing at lower temperatures around 1000°C for example. It was found that there was indeed an increase in the background density of pits upon reannealing as may be seen for example in the background of Fig. 10-4(b) compared with Fig. 10-4(a). However there were a number of variables which made a systematic study difficult, first the impurity level changed from crystal to crystal, second the impurity level within a given crystal changed from the surface to the interior of the grain and finally the grown-in dislocation density varied and impurities precipitated on to them preferentially. Variations in the mechanical strength appeared to provide a much more sensitive indication of the microstructure than could be revealed by etching. This aspect is still under investigation.

From the observations reported in this section it could be deduced that a change in microstructure brought about by annealing preannealed (2000°C) crystals above 600°C contributed partly to the increase in strength observed in Fig. 10-1. The fact that curve 4 in Fig. 10-1 did not drop all the way down to

the original stress level when the dislocations were unlocked was almost certainly a consequence of the change in microstructure.

4. SOME ATTEMPTS TO MOVE 'GROWN-IN' DISLOCATIONS IN MAGNESIUM OXIDE SINGLE CRYSTALS

Now that we have a fairly comprehensive understanding of the effects of heat treatment on the mobility of fresh and aged dislocations there remains the question of the mobility of 'grown in' dislocations. It is known from electron transmission^(10-10, 10-11) and ultramicroscopic⁽¹⁰⁻¹²⁾ studies that grown in dislocations have impurity particles strung along their length and these particles have in certain instances been identified as ZrO_2 ⁽¹⁰⁻¹³⁾. We have made a number of attempts to free the grown-in dislocations from their environments by various thermal and mechanical treatments.

A. By Heat Treatment

In the first series of experiments crystals were given different heat treatments prior to stressing at room temperature. Crystals from both Norton Company and Semi-Elements Inc. stock were tested following anneals for 1 hr. at 600°C, 1000°C, 1500°C and 2000°C respectively and double anneals consisting of a 2000°C preanneal followed by a reanneal at 600°C, 1000°C and 1500°C all with fast rates of cooling. After annealing the crystals were polished thoroughly so that no fresh or aged surface dislocations remained and then loaded in three point bending. Irrespective of the heat treatment all the crystals behaved essentially the same. They all deformed and fractured by the mechanism described elsewhere involving crushing at the upper compression loading point. Slip did not occur in the tension region even though stresses as high as 60-90,000 psi (based on the elastic beam formula) were reached there.

The conclusion was that heat treatment alone could produce no striking change in the locking of grown in dislocations at least not within the resolution of the present technique.

B. By the Application of a Tensile Stress at Room Temperature

The second series of experiments was designed to see if the grown in dislocations could be unlocked by the application of unidirectional or fluctuating tensile stress at room temperature.

The remainder of the mechanical tests to be described in this report were conducted under simple tension. Although the technique underwent many revisions the procedure was essentially to machine reduced gauge sections into single crystal slabs with an ultrasonic cutter, the large reduction in cross section being accomplished either in single or multiple steps. Such crystals were all preannealed at 2000°C , polished and carefully mounted into split tensile grips with an epoxy resin cement.

The room temperature tensile behavior has already been published elsewhere⁽¹⁰⁻¹⁾ but a number of additional tests have been performed and their interesting features will be included here. One specimen supported a tensile stress of 160,000 psi before fracturing in the gauge section. This specimen was etched before and after loading and etch pits on the grown in dislocations gave no indication that they had moved. The fracture stress was approximately $E/200$ (where E is Young's Modulus) of $1/20$ of the theoretical fracture strength. Presumably fracture originated at an internal flaw, although the fracture surface was too complicated to identify the source on this particular specimen. At this stress level a defect 0.5μ in length could propagate by the simple release of elastic energy according to the Griffith criterion. Defects in the form of included gas bubbles or precipitate particles of this dimension were almost certainly present.

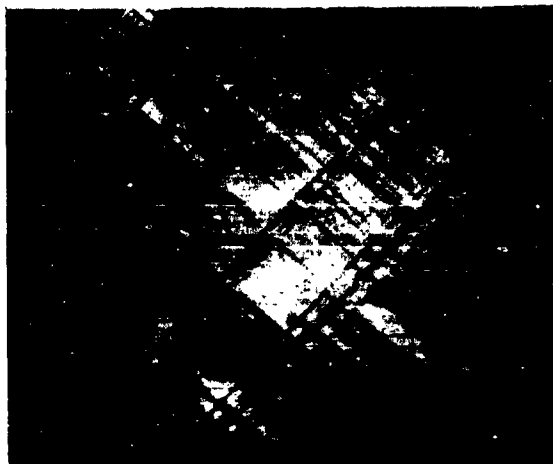
A second specimen supported a stress of 98,000 psi elastically before dropping suddenly down to 15,000 psi. This lower yield stress is the characteristic stress level at which fresh dislocations can move and multiply fast enough in MgO for the plastic elongation of the specimen to keep up with machine⁽¹⁰⁻²⁾. This specimen, like a number of others with less spectacular yield drops, started yielding by the propagation of fresh dislocations, unavoidably introduced at the grips, down into the reduced gauge length region. Slip propagated from the source by the expansion of a single slip band along the gauge length in the manner of a Lüders band. When the slip band reached the end of the gauge length (corresponding to about 5 percent elongation) it slowed down because the stress level dropped at the head of the slip band. As the load started to increase the sharp stress discontinuity at the edge of the band could be seen to build up under polarized illumination and then fracture occurred. Separation took place in all the specimens over the (110) plane defining the interface between the slipped and unslipped material. The cleavage lines pointed toward the surface as the source of fracture. It was interesting to note that the surface defect responsible for fracture had already supported a stress of 98,000 psi elastically and yet it propagated for failure at 20,000 psi in the presence of the slip band. This was considered as further evidence to support the current attitude that plastic flow assists the growth of subcritical Griffith cracks^(10-14, 10-15). The weakness of the (110) interface at the edge of the slip band was understandable since many atomic bands were already broken there. This represented another example of fracture resulting from heterogeneous slip in MgO, whereas in previous cases slip bands have been held up by microstructural discontinuities in this case the slip band was arrested by the change in specimen geometry.

C. By the Application of a Fluctuating Stress at Room Temperature

The purpose of these experiments was to determine whether fluctuating stresses would promote yielding from grown in dislocations at room temperature. Fatigue type tests were conducted in the Instron using both tension-compression (referred to as full cycle) and tension-release (half-cycle) methods of loading.

A few specimens were fatigued under elastic stress conditions at levels up to 23,000 psi for a few hundred cycles in both full and half-cycle loading. Unfortunately difficulties in alignment and the operation of dislocation sources introduced at the grips prevented cyclic loading to higher stresses. There was no evidence for the movement of grown in dislocations or the operation of grown-in sources in those specimens which were fatigued successfully.

More interesting were the observations made concerning the contrast in slip distribution between specimens containing fresh surface dislocations subjected to half cycle and full cycle loading. Under half-cycle loading fairly uniform broadening of slip bands between orthogonal intersections of the type developed in conventional tensile tests at room temperature were developed as shown in Fig. 10-13. Under full-cycle loading on the other hand the slip bands showed most unusual intersections as illustrated in Fig. 10-14. It was considered that they developed by the non-uniform expansion of a slip band along different segments of its length during any cycle, the segments being defined by intersections with other slip bands particularly those intersections at 60 deg. or 120 deg. Attempts were made to determine whether these two slip band distributions would result in different tensile properties subsequently, however, the observations were not conclusive.



X 150

Fig. 10-13
SLIP BAND INTERSECTIONS PRODUCED IN
CRYSTALS SUBJECTED TO HALF CYCLE
(TENSION-UNLOAD) MECHANICAL STRESSING.



X 250

Fig. 10-14
SLIP BAND INTERSECTIONS PRODUCED IN
CRYSTALS SUBJECTED TO FULL CYCLE
(TENSION-COMPRESSION) MECHANICAL
STRESSING.

D. By the Application of a Tensile Stress at High Temperatures

The tensile behavior of preannealed (2000°C) and chemically polished MgO single crystals was investigated at elevated temperatures. The purpose here was to determine whether the grown in dislocations could be moved at a temperature where impurities were known to be mobile. The initial tests were performed in an argon atmosphere at 850°C , and are reproduced in Fig. 10-15.

The most interesting features of Fig. 10-15 were the large yield drops and the considerable amount of plastic deformation (~ 20 percent) which generally preceded fracture. Furthermore the curves were jerky and all showed non-linear work hardening immediately after the yield drop. By contrast the stress-strain curves at room temperature⁽¹⁰⁻¹⁾ showed little or no work hardening after yielding while the Lüders band spread along the gauge length.

Etching the specimens deformed at 850°C after any amount of plastic deformation, including specimen 1 which apparently underwent no plastic deformation before fracture, showed that the gage length was always densely filled with slip dislocations. The implication both from this observation and from the non-linear rate of work hardening was either that slip was nucleated homogeneously throughout the gauge length at the yield point or that the rate of slip band widening by cross slip was faster at this temperature than at room temperature. Whether the homogeneous nucleation of slip corresponds to the release of grown in dislocations remains to be determined by more careful etch pit studies. At the moment indications are that it does not, although this study is continuing.

In summary, there was no evidence that 'grown-in' dislocations in MgO could be moved under tensile stresses as high as 160,000 psi at room temperature. The application of a fluctuating stress at room temperature and the use of different heat treatments had no effect on this result.

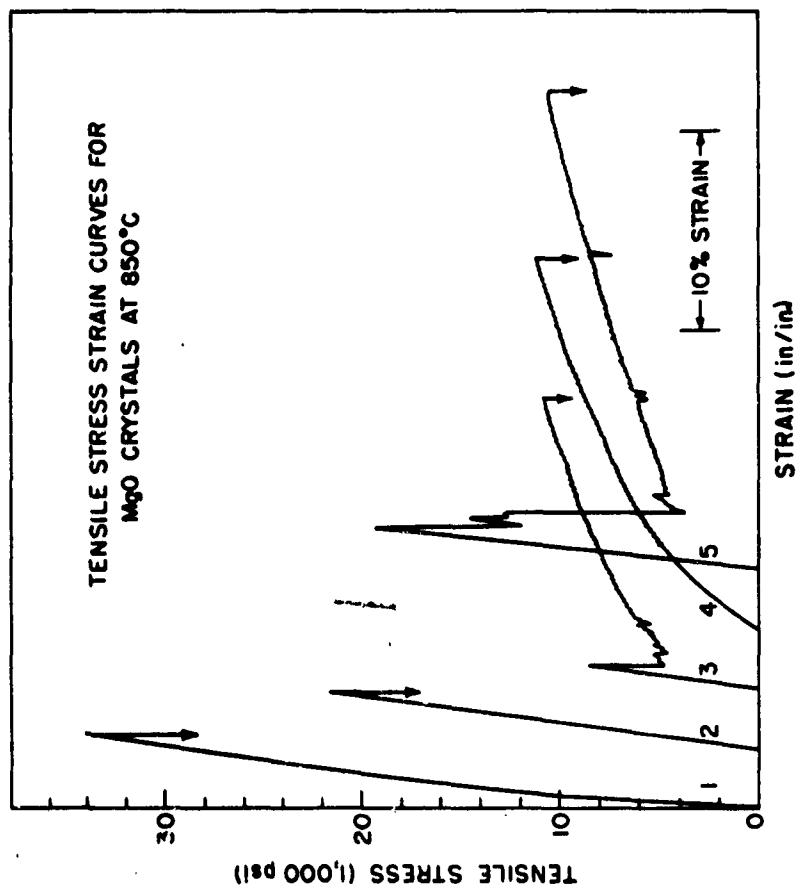


Fig. 10-15 TENSILE STRESS STRAIN CURVES FOR CHEMICALLY POLISHED MAGNESIUM OXIDE CRYSTALS DEFORMED AT 850°C.

5. CONCLUSION

We have studied the effect of heat treatment on the mobility of fresh, aged and grown in dislocations in MgO single crystals. Most of the tests have been performed on crystals which were preannealed at 2000°C and the results are summarized in Fig. 10-16. The strength of crystals containing fresh dislocations is unchanged until the annealing temperature exceeds 600°C whereupon the strength rises to a maximum following a re-anneal at 1200°C . Crystals containing aged dislocations show an increase in strength when the annealing temperature exceeds 600°C which rises approximately linearly with temperature until the strength is so high that the crystal cannot be tested in bending. Crystals containing grown-in dislocations only are always too strong to be tested in bending irrespective of the heat treatment. The increase in strength of crystals containing aged dislocations with the annealing temperature must be attributed to the combination of a number of factors:

- (1) the increase in lattice resistance force to the motion of dislocations by a precipitation hardening process
- (2) dislocation locking by impurities
- (3) the change in dislocation configuration

A similar study of the behavior of fresh and aged dislocations in as-received crystals is currently being made.

Numerous attempts have been made to move 'grown in' dislocations in MgO, all apparently without success. The amazing resistance of grown in dislocations to movement under stress must be attributed to the presence of impurity particles strung along their length.

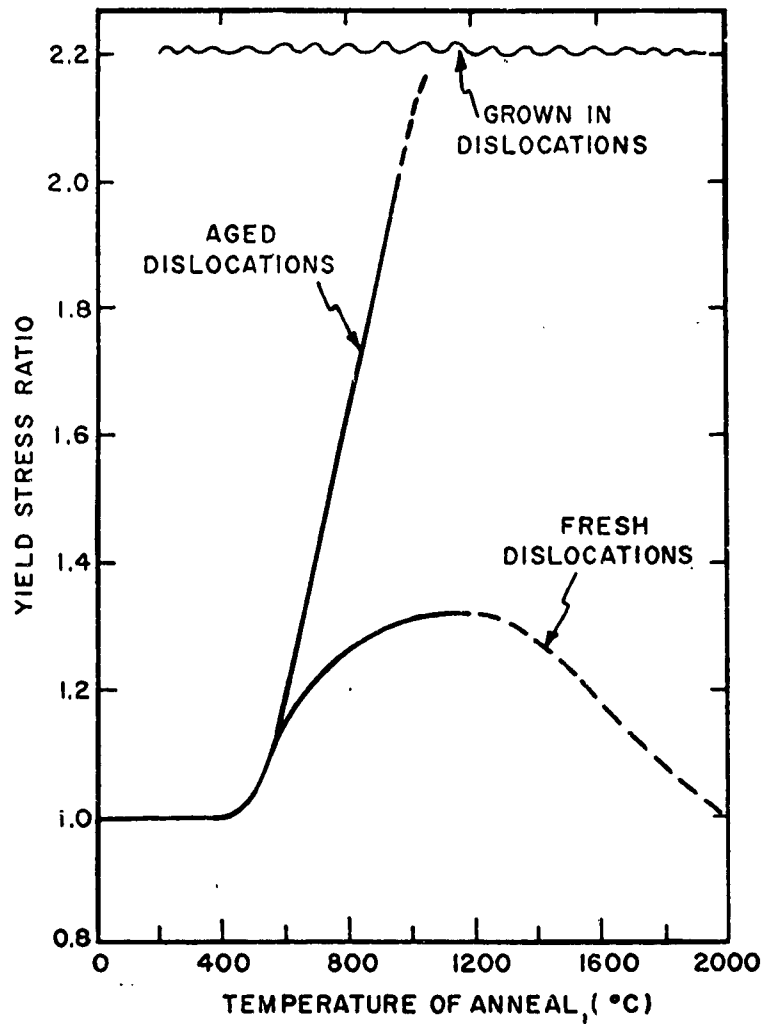


Fig. 10-16

**EFFECT OF HEAT TREATMENT ON YIELD STRESS
OF CRYSTALS PREANNEALED AT 2000°C**
Yield stress ratio after anneal to before anneal plotted
as a function of annealing temperature for crystals
containing fresh, aged and grown-in dislocations

6. REFERENCES

- 10-1 Stokes, R. J., in "Studies of the Brittle Behavior of Ceramic Materials", (N. A. Weil, Ed.) ASD-TR-61-628, April 1962.
- 10-2 Stokes, R. J., Johnston T. L. and Li, C. H., Transactions A.I.M.E., 215, 437 (1959).
- 10-3 Washburn, J., Groves, G. W., Kelly, A. and Williamson, G. K., Philosophical Magazine, 5, 991 (1960).
- 10-4 Thomas, G., Transmission Electron Microscopy of Metals, 168, John Wiley and Sons, (1962).
- 10-5 Groves, G. W. and Kelly, A., J. Appl. Phys. 33, 456, (1962).
- 10-6 Johnston, W. G. and Gilman, J. J., J. Appl. Phys. 31, 632, (1960).
- 10-7 Tetelman, A. S. Acta Metallurgica 10, 813 (1962).
- 10-8 Gorum, A. E., Luhman, W. J. and Pask, J. A., Amer. Ceram. Soc., 43, 241, (1960).
- 10-9 May, J. E. and Kronberg, M. L., J. Amer. Ceram. Soc. 43, 525, (1960).
- 10-10 Groves, G. W. and Kelly, A., Private Communication.
- 10-11 Venables, J. D., Phys. Rev. 122, 1388 (1961).
- 10-12 Miles, D. G., Private Communication.
- 10-13 Venables, J. D., Bulletin Am. Phys. Soc. II, 7, 436 (1962).
- 10-14 Clarke, F. J. P., Sambell, R. A. J. and Tattersall, H. G., Philosophical Magazine, 7, 393 (1962).
- 10-15 Stokes, R. J. and Li, C. H. Paper presented at A.I.M.E. Conference on Fracture, Seattle (1962).

TASK 11 - SURFACE ACTIVE ENVIRONMENTS

Principal Investigator: G. T. Murray
Materials Research Corporation
Orangeburg, New York

ABSTRACT

The objective of this task was to explore the embrittling effect of different environments at various temperatures on the mechanical properties of single- and multicrystalline forms of MgO and Al_2O_3 .

Lengthy exposures (160 hr) at 600 °C embrittled MgO single crystals in an environment of oxygen or air, with a lesser degree of embrittlement noted for exposure to nitrogen or argon. To determine whether a similar embrittlement would occur at grain boundaries, bicrystals of MgO were exposed first to the common constituents of the atmosphere (N_2 , O_2 , CO_2 , and H_2O) at 800 °C for 160-200 hr, and subsequently tested at room temperature, 900 °C or 1400 °C. Although the mode of failure varied with the temperature of testing, none of these environments induced any significant amount of embrittlement in MgO bicrystals.

Exposure of sapphire crystals to moisture resulted in serious embrittlement through the formation of hydrates, confirming the findings of previous investigators. This effect, however, proved reversible; the hydration products could be removed by heating in dry argon which led to a full restoration of the initial strength of the specimens.

Exposure of sapphire to hydrogen or nitrogen at 800-1000 °C for 200 hr caused no embrittlement, nor did a 52 hr steam exposure at 180 °C impair the strength of multi-crystalline Al_2O_3 . Although this contradicts the results of previous investigators, the current exposure tests were conducted with the specimen in an unstressed condition, where the chemical attack mechanism may be substantially different from that corresponding to the conventional delayed fracture test.

TASK 11 - SURFACE ACTIVE ENVIRONMENTS

1. INTRODUCTION

The mechanical properties of certain non-metallic crystals are strongly dependent on surface condition and environment. In the case of NaCl, which has been extensively investigated, embrittlement has been attributed to surface flaws, residues, compound formation, and dissolved solutes.⁽¹¹⁻¹⁾⁽¹¹⁻²⁾⁽¹¹⁻³⁾ For NaCl crystals free of surface flaws and residues it has been shown⁽¹¹⁻¹⁾ that the embrittlement incurred by short exposures to the ambient atmosphere is a result of the formation of a thin coherent NaClO₃ surface layer. In a study* of the effect of various environments on MgO single crystals, it was shown that the common constituents of the ambient atmosphere (O₂, N₂, H₂O, and CO₂) did not embrittle carefully polished MgO crystals at temperatures below 250 °C, even after prolonged exposures. The only embrittlement of real practical significance found was that of air-aging at 600 °C. This was thought to be due to the diffusion of gaseous atoms into the surface layers and the locking of dislocation sources.

The present work was undertaken to investigate the effects of various gaseous atmospheres on the fracture strength of by-crystals of MgO and the single as well as the polycrystalline forms of Al₂O₃. In the case of Al₂O₃, the effect of moisture on the fracture strength was of particular interest in view of the fact that moisture embrittlement in the presence of a stress has been reported⁽¹¹⁻⁵⁾⁽¹¹⁻⁶⁾⁽¹¹⁻⁷⁾⁽¹¹⁻⁸⁾⁽¹¹⁻⁹⁾ for sapphire crystals and polycrystalline Al₂O₃. Some "clean-up"-type work was also conducted on MgO single crystals to complete the previous year's study.

*Reference 11-4, Task 11.

2. EXPERIMENTAL PROCEDURES

A. Materials

Magnesium Oxide Single Crystals and Bicrystals were obtained from two sources: Semi-Elements, Inc. and the Norton Company. The specimens obtained from Norton have been coded N and those from Semi-Elements, S; and the impurity content was quoted by the supplier as follows:

Impurity	Semi- Elements Material	Norton Co. Material *
	(ppm)	
BeO	50	
Fe ₂ O ₃	700	1500
SiO ₂	500	2000
CaO	800	2000
K	100	
Al ₂ O ₃		3500
B		15

Magnesium oxide bicrystals were cut from large lumps containing several grains. The dimensions of prepared specimens were approximately 3/16 in. x 1/8 in. x 5/16 in., with the grain boundary at a 45 deg angle to the longest specimen dimension as shown in Fig. 11-1.

All specimens were carefully polished in hot phosphoric acid, followed by a hot water rinse, an alcohol rinse, and thoroughly dried. Magnesium oxide single crystal specimens were cleaved from Semi-Elements blocks and prepared by chemical polishing as described previously. (11-4)

Sapphire single crystals were obtained from the Linde Company in the form of rectangular blocks from which specimens of dimensions 1 in. x 0.08 in. x 0.08 in. were cut using diamond wheels.

* Optical Grade Magnorite

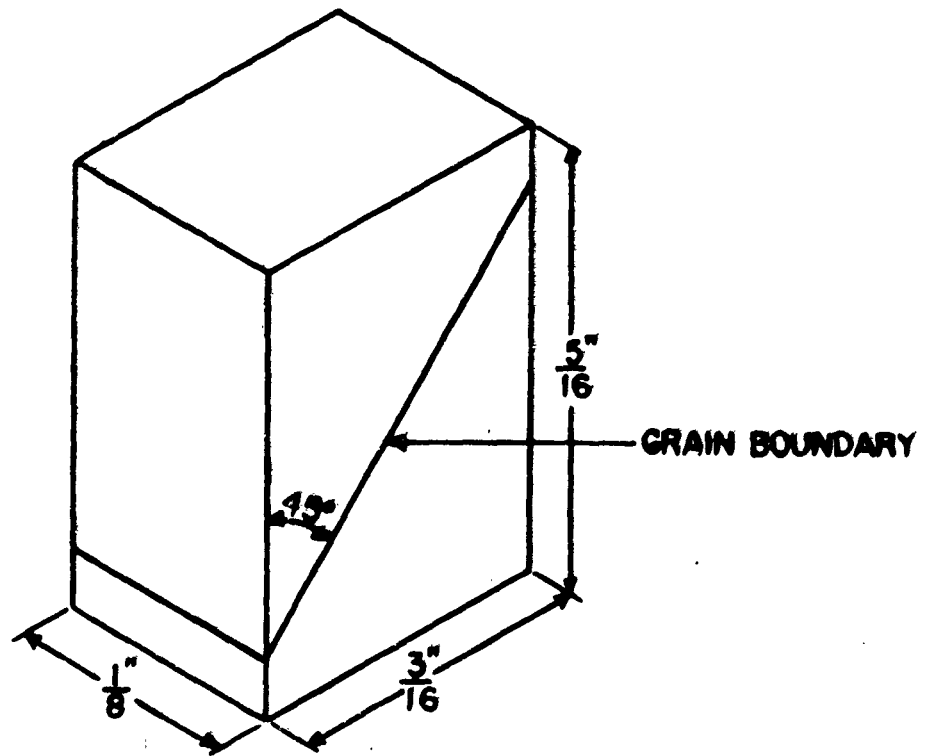


**Fig. 11-1 FORM OF MAGNESIUM OXIDE BICRYSTALS
USED IN THE TESTS**

Because of its anisotropy, the mechanical properties of sapphire are strongly dependent on specimen orientation. It has been reported⁽¹¹⁻¹⁰⁾ that in bend tests, loading parallel to the optic axis gave a strength nearly three times the value obtained from loading perpendicular to the axis. Because of this marked effect of specimen orientation, all specimens were x-rayed using the L  ue back-reflection technique. Standard information obtained for all specimens included: the angle between the optic axis and the longitudinal rod axis (ϕ), the angle between the optic axis and the loading direction (θ), and the angle between the rod axis and the nearest $[12\bar{0}0]$ direction (α). These crystallographic orientations relative to the specimen faces are shown in Fig. 11-2. In the tests performed two standard orientations were used which have the following crystallographic characteristics:

(1)	(2)
$\phi = 60^\circ$	$\phi = 75^\circ$
$\theta = 30^\circ$	$\theta = 60^\circ$
$\alpha = 30^\circ$	$\alpha = 30^\circ$

These two types of oriented specimens have different fracture strengths and have been analyzed separately.

Sapphire also presents an additional problem by way of internal faults and inhomogeneities that may have been introduced during its growth from the Verneuil process. The specimens may contain large internal strains as well as trapped air bubbles. Therefore, great care was taken to examine microscopically all specimens and the tests were conducted on selected specimens only.

All specimens were polished in phosphoric acid at 375°C. The procedure used was as follows: the specimens were suspended by means of thin platinum wire (outside the gauge length of the bend apparatus) in a pyrex beaker containing orthophosphoric acid at room temperature. The temperature of the acid was raised

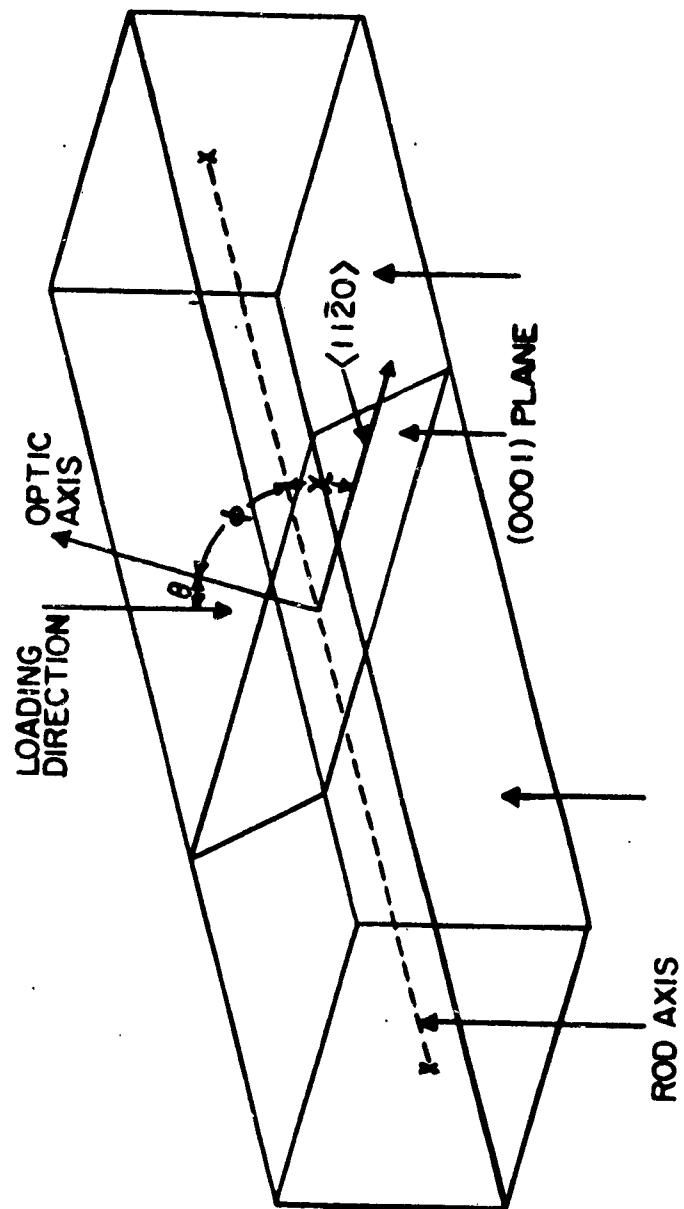


Fig. 11-2 CRYSTALLOGRAPHIC ORIENTATION FOR SAPPHIRE SPECIMENS

above boiling at which point it converts into a complex mixture of metaphosphoric acids. (11-11) At 375°C the mixture begins to turn cloudy when the temperature is held constant for about 25 min. At this point, polishing was discontinued by removing the burner and allowing the mixture, with the specimen, to cool. The specimens were removed between 100°-130°C, cleaned in boiling water, then rinsed in hot water followed by alcohol, and thoroughly dried. Polycrystalline Aluminum Oxide rods having a uniform grain size were obtained from Morganite. From these specimens having 1/8 in. diameter and 1 in. length were cut. The specimens were cleaned in benzene and acetone with distilled water rinses then thoroughly dried and stored in a desiccator.

B. Specimen Exposure

In all cases a number of freshly polished specimens were tested as controls, without any prior exposure to a gaseous environment. Others were exposed to various gaseous media and then tested.

For exposure to N_2 and H_2 , the MgO bicrystal specimens were encapsulated in 0.5 atmosphere of the gas and held for about 200 hr at 800°C for H_2 exposures and 1000°C for N_2 exposures. These specimens were then carefully repolished to remove any possible surface effects prior to testing.

A humidifier was used for lengthy exposures of sapphire crystals to moisture at room temperature. Specimens were also exposed to steam by placing them near the orifice of a boiling water container. A higher temperature exposure was accomplished by heating the specimens with a radiant energy lamp during the steam exposure. Single crystal MgO specimens were encapsulated in Ar, N_2 and O_2 , and heated for long periods at 600°C. Other specimens containing intentional surface flaws were heated in air and AR at 240°C for long periods.

C. Testing Procedure

The single crystal Al_2O_3 and MgO specimens were tested, after the exposure to various gaseous media, in three-point bending at room temperature employing a constant deflection rate of 0.0024 in. per min. The average outer fiber strength was computed from MC/I .

For bicrystal specimens the fracture strength in compression was determined at various temperatures. The specimens were loaded between a fixed alumina pedestal attached to a rigid base plate and an alumina plunger. The load was transmitted to the plunger by a lever arm attached to a shaft operated by a 1/50-hp constant-speed motor with reduction gears. The bicrystal grain boundary was oriented at a 45 deg angle to the stress direction so as to be subjected to a maximum shear stress. This apparatus is shown schematically in Fig. 11-3. During operations the specimens were heated with a molybdenum-wound tube furnace: The whole apparatus was enclosed by a water-cooled metal bell jar inside which an Ar atmosphere was maintained.

3. RESULTS

A Magnesium Oxide Bicrystal Studies

The various gaseous environments that were studied for MgO bicrystals consisted of H_2 , N_2 , air and water vapor. An Ar atmosphere was employed on control specimens.

It had been previously determined⁽¹¹⁻¹²⁾⁽¹¹⁻¹³⁾ that MgO bicrystal specimens usually fractured transgranularly at temperatures below 1200 °C, whereas above this temperature failure most often occurred along the grain boundary (the exact behavior is also dependent upon the misorientation of the two crystals). It was thought that if grain boundary embrittlement resulted from the gaseous exposure, fracture along the boundary should be evident at temperatures much below the 1200 °C "transition" temperature.

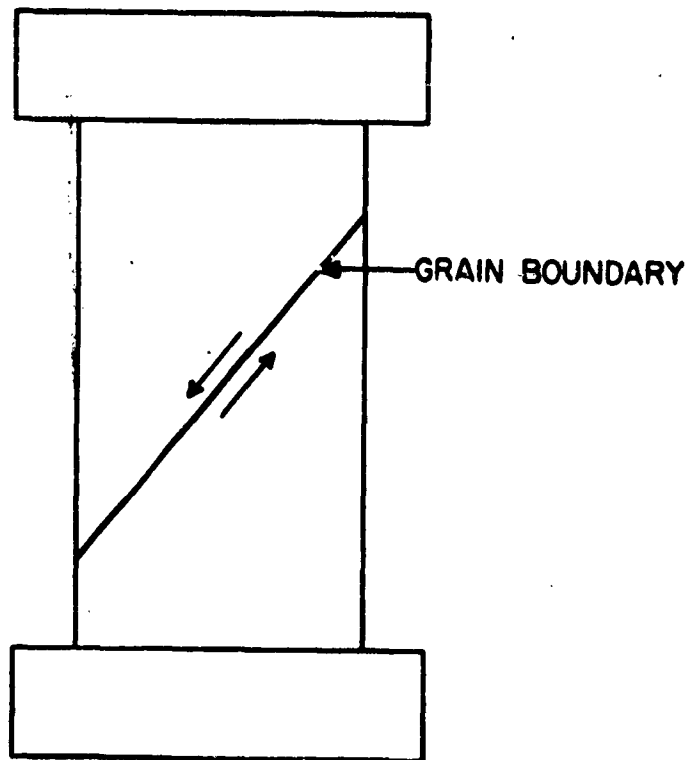


Fig. 11-3 SCHEMATIC ARRANGEMENT OF BICRYSTAL IN TESTING JIG

Consequently, the earlier experiments were designed to determine if grain boundary embrittlement could be detected in room temperature tests after gaseous exposures at elevated temperatures. The results obtained on specimens cut from the same high-angle boundary are listed in Table 11-I. All of these specimens fractured in the body of the crystals rather than along the grain boundary. No grain boundary embrittlement was obtained. The apparent strengthening effect of N_2 is, in all probability, a volume effect and has nothing to do with the grain boundary.

Table 11-I

**MAGNESIUM OXIDE BICRYSTAL* COMPRESSION TESTS
AT ROOM TEMPERATURE**

Atmosphere	Exposure Time (hr at 800 °C)	Fracture Stress (g/mm ²)	Max Shear Stress (g/mm ²) along Boundary	Type of Fracture
Ar	160	5060	2530	Transgranular
H ₂	160	4700	2355	Transgranular
N ₂	160	8460	4230	Transgranular
Water Vapor	120	4000	2000	Transgranular

* Bicrystal with high angle boundary misorientation.

In a second series of experiments, similar bicrystal specimens of different misorientations, were exposed to N_2 and H_2 for long period at 800 °C, but were subsequently tested at 900 ° and 1400 °C. Here, the object was to work on both sides of the temperature (~1200 °C) at which grain boundary sliding occurs in order to determine if the gases either weakened (i.e., embrittled) or strengthened the boundary with respect to the boundary shear strength. The results are listed in Tables 11-II and 11-III.

At 900 °C all specimens fractured by shattering indicating that the fracture was initiated within the grain. For N_2 -exposed

Table 11-II
MAGNESIUM OXIDE BICRYSTAL COMPRESSIVE
TESTS AT 900 °C

Spec. * No.	Misorientation		Atmosphere (exposed at 800 °C for 200 hr)	Fracture Stress (g/mm ²)
	Twist (deg)	Tilt (deg)		
NA-1	14	24	Ar	11,620
NA-2	14	24	N ₂	6,550
SA-1	28	19	Ar	15,550
SA-2	28	19	N ₂	16,040
NB-1	24	43	Ar	7,870
NB-2	24	43	N ₂	9,200
SB-1	41	44	Ar	19,170
SB-2	41	44	N ₂	16,070
NC-1	17	32	Ar	11,250
NC-2	17	32	H ₂	9,320

*N series obtained from Norton Co., S series from Semi-Elements

Table 11-III
MAGNESIUM OXIDE BICRYSTAL COMPRESSIVE
TESTS AT 900 °C

Spec. * No.	Misorientation		Atmosphere (exposed at 800 °C for 200 hr)	Shear Stress on Boundary at Fracture (g/mm ²)
	Twist (deg)	Tilt (deg)		
NA-3	14	24	Ar	314
NA-4	14	24	N ₂	199
SA-3	28	19	Ar	2,441
SA-4	28	19	N ₂	2,681
NC-3	17	32	Ar	1,368
NC-4	17	32	H ₂	46
NB-3	24	43	Ar	6,200
NB-4	24	43	H ₂	6,380
SB-3	41	44	Ar	6,400
SB-4	41	44	H ₂	8,670
SB-5	3	19	Ar (600 °C for 168 hr)	
SB-6	3	19	Air (600 °C for 168 hr)	

*N series obtained from Norton Co., S series from Semi-Elements

specimens, in only one case was there a significant change in the fracture stress and here the fracture was still transgranular. It is highly probable that some undetected specimen defect could be responsible for this low fracture stress. For the H_2 -exposed specimens the fracture stress was about 80 percent of the control specimen, which cannot be considered a significant difference.

At the 1400° test temperature, no grain boundary embrittlement or strengthening was observed for N_2 exposures. In the case of H_2 , three groups of bicrystal specimens with different crystal misorientations were tested. In the first group (Table 11-III, specimens NC) there was a difference in the grain boundary fracture stress of the control and the H_2 -exposed specimens. However, both the control and the exposed specimens had some grain boundary voids. The remaining two groups of bicrystal specimens (Table 11-III, specimens NB and SB) had a good defect-free grain boundary. With these specimens no grain boundary embrittlement was obtained. All specimens fractured intergranularly.

The effect of O_2 was studied by exposing a bicrystal specimen (Table 11-III, specimen SB-6) to air for 168 hr at $600^\circ C$. Again no significant change was observed in a subsequent test at $1400^\circ C$.

The results obtained indicate that H_2 , N_2 , O_2 and water vapor do not have any significant effects on the shear fracture strength of the grain boundary in MgO bicrystals, at room or at elevated temperatures.

B. Magnesium Oxide Single Crystal Studies

In the earlier work⁽¹¹⁻⁴⁾ it was shown that cleaved and carborundum-sprinkled specimens became embrittled when exposed to air at $240^\circ C$, whereas carefully polished specimens remained ductile. The carborundum sprinkle is capable of introducing surface microcracks.⁽¹¹⁻¹⁴⁾ It was suggested⁽¹¹⁻⁴⁾ that the ingredients of the atmosphere reacted preferentially at these

microcracks thereby causing the observed embrittlement. To ensure that the heating effect alone was not involved, similar specimens were heated in Ar for identical periods. The results are summarized in Table 11-IV. The embrittlement obtained in air-aging is evident.

Table 11-IV

**OUTER FIBER STRAIN AT FRACTURE
ON MAGNESIUM OXIDE CRYSTALS CLEAVES AND SPRINKLED
WITH 250-MESH CARBORUNDUM POWDER**

Aging Treatment	No. Specimens Tested	Strain at Fracture (%)	Standard Deviation
None	8	1.2	0.2
40 hr in Ar at 250 °C	8	1.3	0.8
40 hr in Air at 250 °C	8	0.5	0.4

It was thought that the embrittlement observed in these tests resulted from enhanced compound formation or crack growth at the surface defects. Consequently, small surface cracks were intentionally introduced into carefully polished crystal surfaces by sliding the specimens through a glass tube. These specimens were then aged in air at 240 °C and the crack appearance observed microscopically as a function of time. No significant change could be detected even after a 112 hr aging period. It is conceivable that some reaction does occur on the crack's fracture surface that does not appear when viewing the crack slit microscopically.

Other experiments were conducted on MgO single crystals to determine if the 600 °C air-aging embrittlement reported previously⁽¹¹⁻⁴⁾ was due to either O₂ or N₂. Specimens prepared as before were encapsulated separately in these media and heated at 600 °C for 160 hr. Specimens were also heated in Ar for a comparison of the effect of the heating itself on the subsequent ductility. The results obtained are listed in Table 11-V. For

Table 11-V
ELEVATED TEMPERATURE AGING OF MAGNESIUM OXIDE CRYSTALS,
BEND TESTS CONDUCTED AT ROOM TEMPERATURE

Treatment	No. of Specimens	Average Yield Stress (mm ²)	Average Fracture Stress (mm ²)	Outer Fiber Strain	Standard Deviation (%)
Aged in N ₂ 160 hr 600 °C	4	22, 300	27, 650	1.9	1.4
Aged in O ₂ 160 hr 600 °C	4	21, 100	25, 650	0.5	0.1
Aged in Air 160 hr 600 °C	8	18, 100	20, 740	0.9	0.8
Aged in Ar 160 hr 600 °C	6	17, 100	20, 600	1.9	1.0
Controls - no heating	12	14, 900	19, 200	2.8	1.2

comparison, the earlier results⁽¹¹⁻⁴⁾ on control specimens and the effect of air-aging at 600°C are also included. It is apparent that O₂ is a more severe embrittling agent than N₂. The N₂-exposed specimens showed a higher strength level and about the same average strain at fracture as was found for the Ar-exposed specimens. It is not clear whether the slight embrittlement observed in these two groups of specimens is a result of the N₂ per se or traces of O₂ that could be present in both capsules. The release of gas from the quartz capsule during encapsulation or the original reagent grade gases employed could account for the O₂ content. Internal impurities could also cause an embrittlement, such as that found by Stokes.⁽¹¹⁻⁴⁾

C. Aluminum Oxide Single Crystal Studies

The control specimens consisted of freshly polished crystals subjected to no gaseous environment and free of microscopic defects. Several specimens were employed to obtain the average result reported (outer fiber strength) in Tables 11-VI and 11-VII for control specimens of the two different orientations used in this investigation. For specimens in which 0~75 deg, the average outer fiber strength obtained in three-point bend tests at room temperature was 96,742 psi. For specimens with 0~60 deg the average outer fiber strength was 141,000 psi.

Table 11-VI

EFFECT OF HYDROGEN AND NITROGEN ON THE ROOM-TEMPERATURE BEND STRENGTH OF ALUMINUM OXIDE SINGLE CRYSTALS

Specimen Orientation, ϕ (deg)	Treatment	No. of Specimens Tested	Average Fracture Stress* (psi)
75	Control	5	96,742
75	H ₂ (800°C, 200 hr)	2	(std. dev. 6,580) 98,250
75	N ₂ (1000°C, 200 hr)	2	101,200

*Computed from MG/I

Table 11-VII

**EFFECT OF MOISTURE ON OBSERVED BEND STRENGTH
OF ALUMINUM OXIDE SINGLE CRYSTALS
AT ROOM TEMPERATURE**

Specimen Orientation, ϕ (deg)	Treatment	No. of Specimens Tested	Average Frac- ture Stress* (psi)
75	Control (as polished)	5	96,742
75	Humidifier (r.t. 400 hr)	2	107,800
75	Steam spray ($\sim 100^\circ\text{C}$ 4 hr)	2	101,200
75	Steam spray (spec. held at 160°C , 50 hr)	3	83,132
75	Steam spray (spec. held at 180°C , 50 hr)	4	69,350
75	Steam spray (as above, 180°C followed by heat- ing in Ar for 60 hr at 400°C)	4	110,980
75	Control (heated in Ar for 60 hr at 400°C)	2	109,000
60	Control (as polished)	4	141,000
60	Steam spray (spec. held at 180°C , 50 hr)	5	109,140
60	Steam spray (as above followed by heating in Ar for 60 hr at 400°C)	4	144,333
60	Control (heated in Ar for 60 hr at 400°C)	2	139,300

* Computed from MC/1

2

The results obtained on specimens exposed for lengthy periods to H_2 and N_2 gases at elevated temperatures and then tested at room temperature are compared to control specimen data in Table 11-VI. All the specimens used in these tests had a similar orientations of $0 \sim 75$ deg. No effect of the gaseous exposure on strength could be detected in either case. Microscopic examination of the surface did not reveal any precipitate formation.

The deteriorating effect of atmospheric water vapor on the mechanical properties of a number of oxides and silicates has been reported. Watchman and Maxwell⁽¹¹⁻⁵⁾ and Charles⁽¹¹⁻⁶⁾ have shown that sapphire crystals are susceptible to delayed fatigue in the presence of moisture. It was of particular interest in the present work to examine the effect of water vapor in the absence of stress. Moisture reportedly reacts with Al_2O_3 to form hydrates. The exact nature of the hydrate probably depends upon the temperature and the vapor pressure. A series of experiments were carried out by exposing unstrained sapphire specimens to moisture under different ambient conditions. The results of subsequent room temperature bend tests listed in Table 11-VII were used. In each case appropriate standard control specimen results are listed for comparison.

Exposure to moisture at room temperature in a humidifier for about 400 hr did not alter the strength of the crystals. Likewise, specimens exposed for 4 hr to steam ($\sim 100^\circ C$) by placing them near the orifice of a boiling water container showed no effect of the gaseous exposure on the subsequent room temperature strength. Microscopic examination revealed only a very few scattered precipitate spots.

As the room temperature moisture exposure and $100^\circ C$ steam exposure did not show any significant surface precipitate formation it was decided to increase the exposure temperature. This was accomplished by heating the specimen with a radiant

energy lamp during the steam exposure. When specimens were heated to 180°C during steam exposure a definite precipitate formation (along with some surface dissolution) occurred (Fig. 11-4). The strengths of these crystals were markedly reduced, for both types of orientations, as shown in Table 11-VII. A similar set of specimens was also subjected to a steam spray but heated only to 160°C. The amount of precipitate formation was less than that observed on specimens steam sprayed at 180°C. The specimens were embrittled but the reduction in strength was less in comparison with those embrittled at the higher exposure temperatures.

These experiments indicate that the strength impairment is related to a surface compound formation, presumably an Al_2O_3 hydrate of some type. Although several modifications of this hydrate exist, $\text{Al}_2\text{O}_3 \cdot \text{H}_2\text{O}$ decomposes at about 360°C. To check for compound formation effects, similar steam exposed specimens (i. e. steam-sprayed at 180°C) were encapsulated under dry Ar and heated for 60 hr at 400°C. Control specimens were heated under the same conditions. On subsequent testing the steam-exposed specimens were found to have strengths comparable to those of the control specimens. Thus, a recovery effect is evident and is presumably due to the hydrate decomposition. The recovery specimens on subsequent microscopic examination revealed precipitate spots. However, it is not possible to predict the nature of the precipitate and its degree of coherency or incoherency on the specimen surface after heating to 400°C.

To determine the nature of the surface precipitate and the temperature conditions under which a hydrate is formed, and to correlate the embrittlement effect with compound formation, experiments were carried out in an attempt to identify the surface compound by x-ray techniques. To obtain sufficient compound volume for x-ray diffraction large surface areas are needed. Consequently thin layers of $\alpha\text{-Al}_2\text{O}_3$ powder were spread out on aluminum foil and placed in alumina boats in a temperature gradient



X 600

Fig. 11-4
ALUMINUM OXIDE CRYSTAL SURFACES
EXPOSED TO STEAM SPRAY FOR 48 HR,
SPECIMEN HELD AT 180°C.

furnace. Steam was passed for about 60 hr through a perforated tube over the powder held at different temperatures. The upper layers of the sprayed powders were analyzed by x-ray diffraction to determine the nature of the compound or compounds formed. Four different exposure temperatures used were, namely, 100, 140, 180 and 300 °C. A portion of the powder exposed at 180 °C was reheated for 60 hr at 400 °C to duplicate the conditions under which strength "recovery" occurred in the sapphire single crystal specimens. The results obtained from the x-ray analysis are compared in Table 11-VIII. These results indicate that at 100 °C no compound formation was detected. At 140 °C, diffraction lines corresponding to $\text{Al}_2\text{O}_3 \cdot \text{H}_2\text{O}$ and $\text{Al}_2\text{O}_3 \cdot 3\text{H}_2\text{O}$ were obtained along with Al_2O_3 lines. In addition, an unidentified diffraction line of medium intensity corresponding to a d-spacing of 1.96 a. u. diffraction line is more intense. At 300 °C a few weak hydrate lines are present but the 1.96 a. u. diffraction line is very weak in intensity. The powder reheated to 400 °C for possible "recovery" does not have the prominent 1.96 a. u. line, although some weak hydrate lines are still present.

Table 11-VIII

X - R A Y A N A L Y S I S
O F S T E A M - S P R A Y E D A L P H A - A L U M I N U M O X I D E P O W D E R

Test Temperature (exposed for 60 hr)	Compound Identification (excluding Al_2O_3)		
	$\text{Al}_2\text{O}_3 \cdot \text{H}_2\text{O}$	$\text{Al}_2\text{O}_3 \cdot 3\text{H}_2\text{O}$	Unknown Phase (d = 1.96 a. u.)
100 °C	absent	absent	absent
140 °C	medium	medium	medium
180 °C	medium	weak	strong
300 °C	very weak	absent	very weak
Steam Spray at 180 °C - Reheated in Air to 400 °C	weak	absent	absent

D. Polycrystalline Aluminum Oxide Studies

In the preceding section it was shown that Al_2O_3 single crystals were not embrittled by exposure to H_2 or N_2 , but there was a definite embrittlement effect on exposure to steam in the temperature range $160^\circ\text{--}190^\circ\text{C}$. It was, therefore, decided to determine the effect of moisture alone on the fracture strength of polycrystalline Al_2O_3 .

The exposure to steam was carried out at 180°C . This was accomplished, as with sapphire, by heating the specimens with a radiant energy heat lamp. The specimens were subsequently tested in three-point bending at room temperature. The results obtained, shown in Table 11-IX, do not reveal a strength impairment as a result of the moisture exposure.

Table 11-IX

**EFFECT OF MOISTURE ON OBSERVED BEND STRENGTH
OF POLYCRYSTALLINE ALUMINUM OXIDE (MORGANITE)
AT ROOM TEMPERATURE**

Treatment	Average Frac- ture Stress* (psi)	No. of Specimens
Control	34,083	3
Steam Spray at 180°C for 52 hr	35,160	3
Steam Spray at 180°C for 52 hr Followed by 17 hr at 400°C in Vac.	39,183	3

* Computed from MC/1

4. DISCUSSION

A. Magnesium Oxide

2 The results obtained on MgO bicrystal tests show that there is little cause for concern about grain boundary embrittlement from the common atmosphere constituents. The single crystal tests show that, despite profuse surface compound formation on exposure to moisture, one need not be alarmed about atmospheric exposures at temperatures below about 250°C. However, elevated temperature air exposure does cause impairment of ductility as measured in subsequent room temperature bend tests. Stokes⁽¹¹⁻⁴⁾ has also reported marked increases in strength and loss of ductility on heating above 800°C. Whether these two phenomena are related is not clear at the moment. Nevertheless, the results are similar and must be considered when elevated temperature applications are in question.

These results must now be extrapolated to polycrystalline MgO behavior. (Unfortunately, suitable polycrystalline test specimens were not available.) It has been recently demonstrated⁽¹¹⁻¹²⁾⁽¹¹⁻¹³⁾ that above about 1200°C, MgO fails by grain boundary sliding and fracture. Thus, for operation in this vicinity, surface condition and environment is of little consequence. In the vicinity of room temperature, Stokes has shown⁽¹¹⁻¹⁵⁾ that polycrystalline MgO is inherently brittle because of dislocation pile-up and crack nucleation at grain boundaries. Thus, at this temperature surface condition and environment would play a secondary role at most with respect to ductility. In the intermediate temperature range (e.g. 400-1200°C) polycrystalline MgO would be expected to become more plastic as a result of the relative ease for cross slip.⁽¹¹⁻¹⁵⁾ If environment or surface condition plays a role in polycrystalline MgO properties it would do so within this temperature range. Again, the grain boundary behavior may be the controlling factor but an exact answer to this question must await experiments on

polycrystalline material subjected to atmospheres and stress within this temperature range.

B. Aluminum Oxide

The results reported in this investigation on the effect of moisture on the strength impairment of sapphire crystals are in accord with those obtained by previous investigators. However, most of the previously reported results were for specimens exposed to moisture in the presence of a stress field, while the effects reported herein are in the absence of stress. Both Watchman and Maxwell⁽¹¹⁻⁵⁾ and Charles⁽¹¹⁻⁶⁾ in reporting a delayed fracture effect in sapphire concluded that the reaction responsible for static fatigue was probably one in which water vapor from the atmosphere combined with Al_2O_3 to form a hydrate. The experimental results obtained in this investigation show rather conclusively that the effect of moisture on sapphire is due to the formation of a hydration product on the surface and the removal or change in this surface compound causes a "recovery" whereby no strength impairment is obtained.

Although the reaction has been determined, it is not yet possible to define the exact mechanism involved. It is conceivable that a coherent layer of a hydrate is formed on sapphire specimens and that such a layer blocks the egress of dislocations from the crystal, thereby causing dislocation pile-up and crack-up nucleation. A similar embrittlement effect has been observed⁽¹¹⁻¹⁾ with NaCl because of the formation of a coherent $NaClO_3$ coating.

Strength impairment of polycrystalline Al_2O_3 resulting from moisture in the presence of a stress has been reported by several investigators.⁽¹¹⁻⁶⁾⁽¹¹⁻⁷⁾⁽¹¹⁻⁸⁾⁽¹¹⁻⁹⁾ In the present work, exposure of polycrystalline specimens in the absence of a stress did not disclose any strength impairment. It is possible that porosity in the specimens employed in the present work

controls the strength and thus masks any surface effect. On the other hand, the observations of static fatigue (delayed fracture) in the presence of moisture could operate by an entirely different mechanism than that currently observed on "before and after" tests conducted on sapphire.

5. REFERENCES

- 11-1 Class, W. H., Machlin, E. S., and Murray, G. T., Trans. AIME, 221, 769 (1961).
- 11-2 Stokes, R. J., Johnston, T. L., and Li, C. H., Trans. AIME, 218, 655 (1960).
- 11-3 Aerts, E., and Dekeyser, D., Acta Met., 4, 577 (1956).
- 11-4 Weil, N. A., Ed., Studies of the Brittle Behavior of Ceramic Materials, ASD-TR-61-628, April (1962).
- 11-5 Wachtman, J. B., and Maxwell, L. H., J. Am. Ceram. Soc., 7, 291 (1954).
- 11-6 Charles, R. J., "Task 9 - Static Fatigue Delayed Fracture", Studies of the Brittle Behavior of Ceramic Materials, edited by N. A. Weil, E., ASD-TR-61-682, April (1962).
- 11-7 Robert, J. P., and Watt, W., "Mechanical Properties of Sintered Alumina", Ceramics and Glass, 10, 53 (1952).
- 11-8 Williams, L. S., "Stress-Endurance of Sintered Alumina", Trans. Brit. Ceram. Soc., 35, 287-312 (1956).
- 11-9 Pearson, S., "Delayed Fracture of Sintered Alumina", Proc. Phys. Soc. (London), 69B, 1983-96 (1956).
- 11-10 Klassen-Nekhlyudova, M. V., as reported in Oxide Ceramics Ryshkewitch, E., Academic Press, New York, p. 155 (1960).
- 11-11 Yost, D. M., and Russel, Jr., H., Systematic Inorganic Chemistry of Fifth and Sixth Group Nonmetallic Elements, Prentice-Hall, Inc., New York, Ch. 6, p. 209-10 (1944).

- 11-12 Mountvala, A. J., Silgailis, J., and Murray, G. T., "The Role of the Grain Boundary in the Deformation of Ceramic Materials", Contract No. AF 33(616)-7961, Final Report, January, 1962.
- 11-13 Adams, M. A., and Murray, G. T., "Direct Observations of Grain-Boundary Sliding in Bi-Crystals of Sodium Chloride and Magnesia", J. Appl. Phys. 33, 2126-2131 (1962).
- 11-14 Stokes, R. J., private communication.
- 11-15 Stokes, R. J., and Li, C.H., 15th Technical Report, Contract NONR 2456(00), March, 1962.

TASK 12 - DISLOCATION STUDIES

Principal Investigator: A. E. Gorum
Stanford Research Institute

ABSTRACT

The purpose of this task is to study the existence of plastic flow in polycrystalline samples of non-metallic ceramics. Two methods of approach were followed: thin fiber electron transmission microscopic and plastic flow studies in bulk specimens.

Electron transmission microscopy studies have been confined to thin fibers of Al_2O_3 , deposited in the amorphous condition and crystallized by heat treatment. To date it has not been possible to study the mobility of dislocations in the samples, because of extensive wrinkling of the fibers in the thermal field of the microscope.

Bulk specimens of MgO were studied for evidence of plastic flow by means of careful determination of stress-strain curves and by post-fracture etch-pit studies and clear evidences of plastic deformation were found in an MgO specimen of 70μ grain size having dimensions of 12 units thickness and 300 units width. Etch-pit studies on the fracture facets confirmed the existence of up to three operative slip systems in some of the grains.

TASK 12 - DISLOCATION STUDIES

1. INTRODUCTION

With the increased demand for high temperature structural materials, more and more emphasis is being placed on the inherently attractive temperature and environmental resistance of ceramics.

Normal ceramics, of course, exhibit sufficient plastic deformation at high temperatures, but thermal shock sensitivity and a supposedly characteristic brittleness at low temperatures make them unusable in most any type of dynamic structure.

In the last few years, it has become apparent that many materials, at least those with relatively simple structures, exhibit a certain amount of ductility at room temperature. The problem remains then to take advantage of this inherent ductility to improve the shock resistance of an engineering ceramic.

The research on plastic properties has been primarily concerned with single crystals, and the most-investigated high temperature material has been MgO. Out of these studies has come a fair understanding of the basic flow and fracture phenomena which must be evaluated for a concrete approach to a shock-resistant polycrystalline material. It appears that slip must take place to a small extent on many planes for a polycrystalline sample to exhibit sufficient deformation to be observed in a mechanical test. If a few planes are involved, then very high stresses build up at the boundaries, and fracture in the boundaries probably prohibits observation of any ductility in a mechanical test.

The purpose of the work reported here was to ascertain if there is any appreciable plastic flow in polycrystalline materials at moderate temperatures and to study the optimum structure for the urban cement ductility at these temperatures. The work was

concerned with two materials; Al_2O_3 and MgO . Two methods of investigation were followed; thin-film electron microscopy and mechanical studies on bulk polycrystalline samples. The thin film work was confined Al_2O_3 and the bulk sample work MgO .

2. EXPERIMENTAL PROCEDURES AND OBSERVATIONS

A. Electron Microscope Studies

As stated in ASD-TR-61-628⁽¹²⁻¹⁾, the Al_2O_3 specimens are prepared by evaporation on electron microscope grids in an amorphous condition, and crystallized by heat treatment. The specimens are then subjected to a high thermal gradient in the microscope, causing a recrystallization front to move through the material, which results in a final grain size of about one micron. Early heat treatments were at 600°C and the final structure of the Al_2O_3 was the delta phase. Subsequent heat treatments have been at 900°C , which has resulted in a final structure of $\alpha\text{-Al}_2\text{O}_3$. The reason for this change in structure is not readily apparent; the structure after heat treatment is the same (gamma). What happens on the final step as a result of the thermal gradient is not clear at all, and considerable thought is being given to this phenomenon; hopefully, some mechanism can eventually be defined.

The bulk of the work has been done on films in the order of \AA thick, and some structure effects have been observed, but, because of wrinkling in the films, a large number of interference effects tend to mask the observation of dislocations. Attempts to use films in the order of 1000 \AA thick have been unsuccessful. It has not been possible to bring about the final recrystallization step in the thicker films. Further work should explore various thicknesses up to 1000 \AA and also techniques for producing polycrystalline films of other materials. It is very unlikely that the films really represent the bulk material, but it does seem likely that dislocation interactions observed in the films, particu-

larly at the boundary, should be representative of polycrystalline material, and, consequently, this method of investigation is worth a considerable effort.

B. Plastic Flow Studies in Bulk Samples of Polycrystalline Magnesium Oxide

Magnesium oxide specimens prepared as indicated previously by hot-pressing MgO containing 2 percent LiF, followed by subsequent heat treating to produce a larger grain size. Mechanical testing thus far has been in three-point bending on a micro testing machine. The tests are not designed to determine the mechanical properties, but to try to observe plastic deformation during the test followed by subsequent indirect studies on dislocation mobility through etch pit techniques. Figure 12-1 shows typical test results. Except in one case, the specimens did not indicate plastic deformation. The specimen that indicated plasticity was of a different geometry: 12 mils thick by 300 mils wide, whereas the others were approximately 25 mils thick by 100 mils wide. The grain sizes were approximately the same: about 50-75 microns. If this indicated plasticity was real, it should certainly have been apparent in the grains, and this was indeed found to be the case, as is shown in Fig. 12-2. Three slip systems are seen to have been active in one of the grains photographed. These grains are quite difficult to photograph because of the prior treatment of the specimen. It was observed earlier that mechanical damage during polishing would obscure any subsequent observations of slip, so it was reasoned that if the specimen were polished before the grain growth step, the subsequent heat treatment would remove the bulk of the damage. This indeed was the case, but unfortunately the grains do not retain the flat surface exactly; instead they tend to distort during growth, and, while observation of dislocations structures is possible, high magnification photography is difficult. No crack nucleation has, as yet, been observed, but

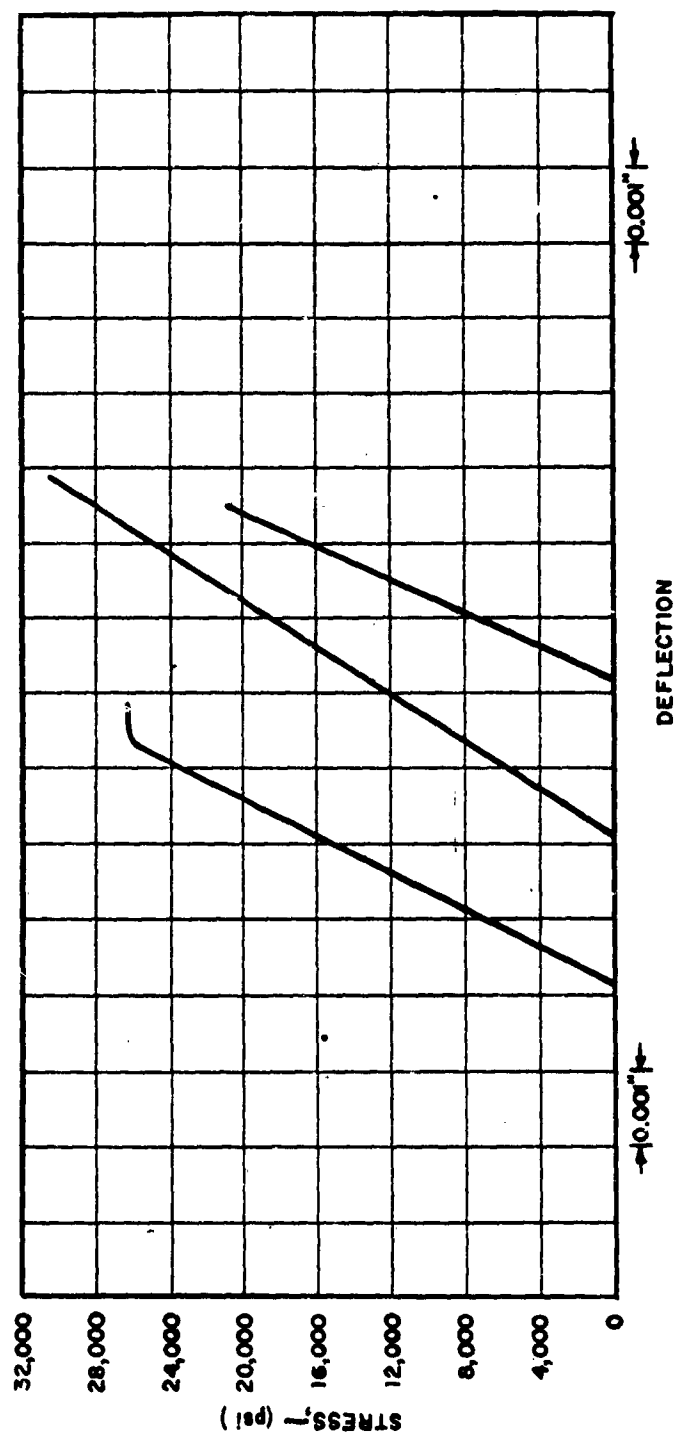


Fig. 12-1 BEND CHARACTERISTICS OF 97 PERCENT DENSE
POLYCRYSTALLINE MAGNESIUM OXIDE



X 350

Fig. 12-2
TENSION SURFACE OF POLYCRYSTALLINE
MAGNESIUM OXIDE BEND SPECIMEN

future work with thinner specimens (so that effective use of transmitted polarized light is possible) should lead to interesting observations. It has at least been shown that deformation can take place in a polycrystal, and future observations will hopefully lead to some criterion for geometry, grain size, etc. It should be borne in mind that no great attention has, as yet, been paid to purity, and this, of course, may be quite significant.

3. CONCLUSION

Studies for the direct observation of dislocation mobility and corresponding plastic flow in multicrystalline ceramic oxides have been begun using two techniques: electron transmission microscopy and etch-pit studies.

Electron transmission microscopy is being pursued with thin fibers of Al_2O_3 , deposited in 300 Å to 1000 Å thickness in the amorphous condition on a substrate, and crystallized by subsequent heat treatment to a final grain size of about 1 micron. The bulk of the work was carried out with fibers 300 Å thick crystallized by a 900°C heat treatment to $\alpha\text{-Al}_2\text{O}_3$. However, these fibers were found to wrinkle and distort in the thermal field of the electron microscope, masking the direct observation of dislocation movement in the samples. Attempts to recrystallize fibers of 1000 Å thickness, whose greater stiffness might prevent the deleterious distortion observed, did not yet prove to be successful.

Etch-pit studies for dislocation mobility were confined to bulk specimens of MgO , using multicrystalline samples of 50-75 micron grain size. Successful plastic deformation was accomplished in one sample 12 mils thick by 300 mils wide; subsequent etching of the fracture facet of this sample disclosed the existence of three actively operative dislocation slip systems. This method requires extremely careful control of the polishing and etching techniques employed, since improper polishing may preclude any

observation of subsequent slip, while excessive etching may result in developing only grain-to-grain textural variations by means of excessive attack at the grain boundaries.

Work on both of these methods will continue during the extension period of this program. In addition to studies already in progress, crack nucleation studies in thin samples of bulk multigrystals will be begun using polarized transmitted light techniques, and an investigation will be made of the effect of the nature and amount of impurities upon dislocation slip system formation in polycrystalline oxides.

4. REFERENCES

- 12-1 Wei' N.A., Ed., Studies of the Brittle Behavior of Ceramic Materials, ASD-TR-61-628, April 1962

TASK 13 - CRACK PROPAGATION

Principal Investigators: Part One: W. F. Riley
Armour Research Foundation
Part Two: E. L. McDowell
Armour Research Foundation

ABSTRACT

The purpose of this task is to study conditions surrounding the propagation of cracks in brittle materials, in order to define conditions required for the catastrophic propagation of such cracks, and methods that may be available for their arrest. The investigation is pursued in two parallel parts, dealing with experimental and theoretical studies respectively.

Experimental work centered about developing techniques for the determination of stress fields about cracks. A Schardin-type multiple spark camera unit was built with Foundation support, capable of 20 exposures spaced at 5 to 50 μ sec intervals. The method was successfully adapted to the determination of stress fields about moving cracks in birefringent brittle plastics; however, an attempt to adapt the method to opaque brittle materials provided with photoelastic coatings has failed for lack of an available light source having the requisite flux strength. Further work will be concentrated on birefringent brittle oxides, as represented by MgO single crystals.

Analytical studies have been limited to a searching review of existing steady-state and dynamic solutions for stress fields surrounding cracks in semi-infinite plates. Some common features of existing solutions have been defined, and preliminary work has been initiated on the solution of the transient dynamic problem.

TASK 13 - CRACK PROPAGATION

Part One - Experimental Work
Principal Investigator: W. F. Riley
Armour Research Foundation

1. INTRODUCTION

In recent years a number of investigators have been concerned with the problem of determining the stress distributions associated with both stationary and moving cracks and crack propagation velocities in various types of ceramic materials. The failure of glass under impact has been studied, among others, by Barstow and Edgerton⁽¹³⁻¹⁾ in this country, and by Schardin and Struth⁽¹³⁻²⁾ in Germany. In these investigations high-speed cameras of various types were employed to determine the crack propagation velocities. Similar measurements of crack propagation velocity were made electronically by Dimmick and McCormick⁽¹³⁻³⁾ and by Lundborg and Johansson⁽¹³⁻⁴⁾. In these investigations the time required for the crack to propagate the distance between thin metal lines deposited on the surface of the specimen was accurately measured.

Experimental investigations concerned with the determination of stress fields in the vicinity of stationary or moving cracks have been conducted using either electrical resistance strain gauges or photoelasticity methods. Since the strain gauge approach can provide information only at isolated points near the crack, the photoelastic method which provides full field coverage has been used more extensively. Recent stationary crack studies using conventional two-dimensional techniques include the work of Post⁽¹³⁻⁵⁾, Dixon⁽¹³⁻⁶⁾, and Guernsey and Gilman⁽¹³⁻⁷⁾. More recently Gerberich⁽¹³⁻⁸⁾ has conducted a study about a slowly growing crack using the photoelastic coating method. Dynamic crack propagation studies to date have essentially been limited to the work of Schardin⁽¹³⁻⁹⁾ and Wells and Post⁽¹³⁻¹⁰⁾.

Over the past eight years a considerable amount of research effort in the ARF Experimental Stress Analysis Section was devoted toward developing dynamic photoelasticity and moire methods for determining transient stress distributions. The objective of the research conducted in this phase of the current program was to investigate the feasibility of applying these same methods to a study of crack propagation in opaque ceramic materials by using photoelastic coatings.

2. EXPERIMENTAL STUDIES

At the time the current program was initiated it was decided that existing equipment would be used if possible in all of the early phases of the work. The equipment which was available included a 14-in polariscope suitable for dynamic studies, a single spark type light source (microflash) together with associated electronic timing units, several Fastax cameras, and a number of falling weight and explosive loading devices. All of this equipment had been used successfully in studies with low modulus model materials but had not been used for studies with the conventional rigid model materials.

The model material selected for the current study was Columbia Resin CR-39. This material is one of the commonly used photoelastic materials with a modulus of elasticity of approximately 250,000 psi. The specimen shape selected for the study was a rectangular bar 12 in x 1 in x 1/4 in. The bar was supported as a simple beam and subjected to a central transverse impact. The impact was provided by a 2.0-lb weight falling from a height of 30 in. This particular type of loading was used in the early studies since it is easy to apply and is very reproducible. A number of photographic records of the fracture of the beams were recorded using an 8mm Fastax camera operating at 15000 frames per second. From these records it was possible to conclude that fracture of the beam occurred approximately 1200 μ sec after impact

of the striker, if a 0.05-in. deep cut was introduced into the bottom surface of the beam to serve as a crack initiator. The photographic records obtained using the Fastax camera were not suitable for analysis, since the time required for the crack to propagate across the beam was less than the approximate 60μ sec time interval between frames. Photographs suitable for analysis had to be obtained using a very short duration spark-type light source (microflash) and a 5 in x 7 in studio camera. Since the duration of the flash from one of these units is only 0.5μ sec, the fringe movement is effectively stopped and the fringe patterns appear sharp and clear. Typical examples of the fringe patterns obtained at the instant the crack has moved 15 percent and 85 percent of the distance across the depth of the beam are shown in Fig. 13-1. These two photographs were obtained by fracturing two different beams. The patterns were obtained using transmitted light in a polariscope whose optical elements were arranged as shown in Fig. 13-2.

The results of the transmitted light studies with CR-39 beams indicated that the crack propagation phenomena are not reproducible from specimen to specimen. Therefore, all data required for a stress analysis must be obtained during a single loading. The technique of using repeated loadings to obtain fringe patterns at different times after loading or to obtain additional information required for separating stresses, which was successfully used for wave propagation studies, will be difficult to apply in crack propagation work.

For this reason the Foundation decided to support the crack propagation program by supplying internal funds to construct a multiple spark-type camera. The camera being built is patterned after the one originally designed by Cranz and Schardin⁽¹³⁻²⁾. When completed, the camera will have the capability of recording 20 photographs at equal time periods which can be varied

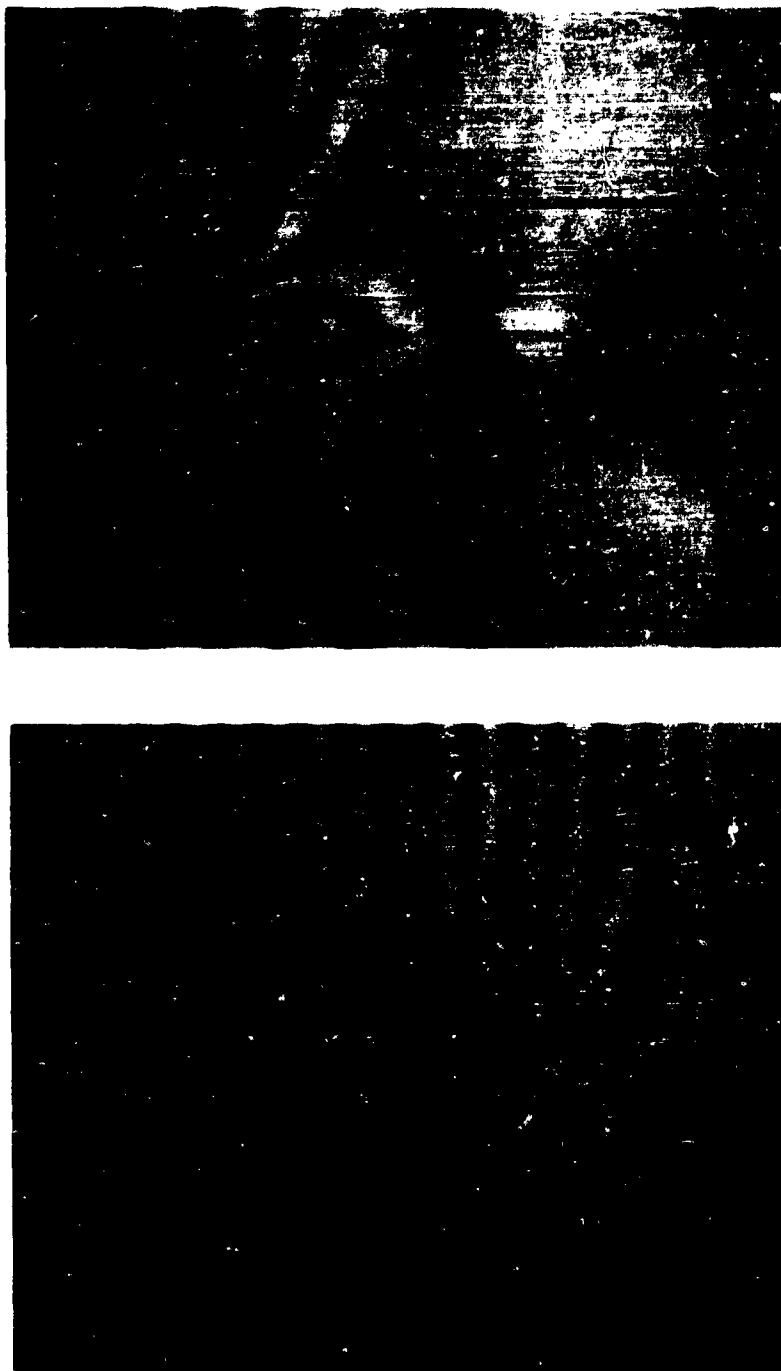


**Fig. 13-1 PHOTOELASTIC FRINGE PATTERNS ASSOCIATED WITH
A RUNNING CRACK IN A CR-39 BEAM**

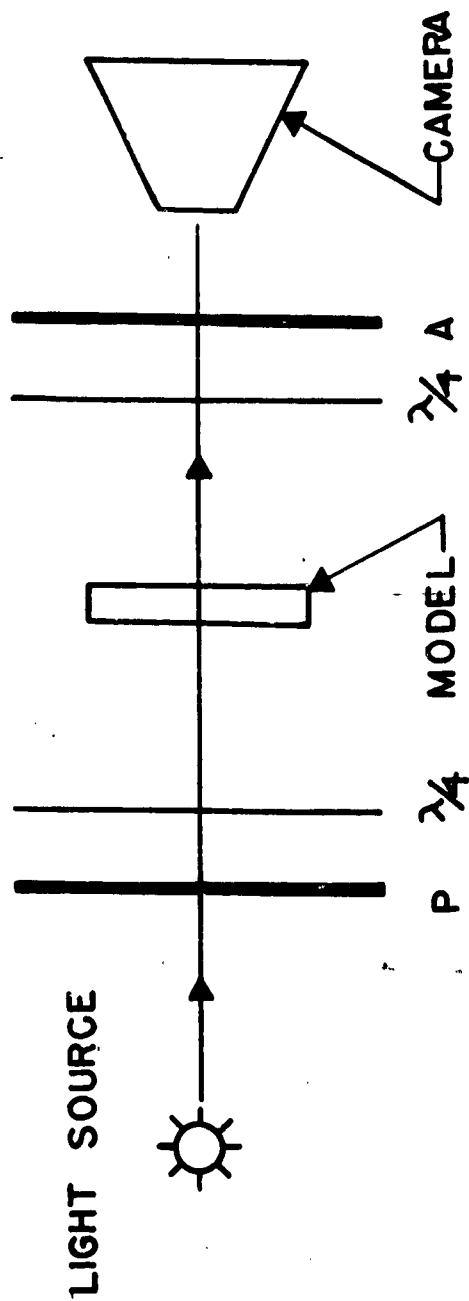


Fig. 13-2 ARRANGEMENT OF THE OPTICAL ELEMENTS IN THE POLARISCOPE
FOR THE STUDIES WITH TRANSMITTED LIGHT

over the range from 5 to 50 sec. The exposure time for each photograph will be approximately $0.5\mu\text{sec}$.

After the techniques were developed for obtaining single photographs of a crack as it propagates, some beam specimens were prepared with photoelastic coatings on one face. Since reproducible loadings could not be used to obtain fringe patterns with the coatings to compare with those obtained using CR-39 beams and transmitted light, the optical elements of the polariscope were rearranged so that patterns from the coating and beam could be simultaneously recorded and compared.

A schematic drawing of the system is shown in Fig. 13-3. In future studies this same type of arrangement can be used to record simultaneously the two types of data required to separate stresses.

Thus far in the program the results from the coating evaluation study have been completely negative. The amount of light available from the microflash unit has been found to be insufficient to produce usable fringe patterns. In fact, it is estimated that the intensity of light required to produce useful fringe patterns with this method would require an intensification of currently available light flux by several orders of magnitude. Since a flash duration of one microsecond or less is required for sharp clear patterns, little can be done to compensate for the lack of intensity by increasing the exposure.

3. RECOMMENDATIONS FOR FUTURE WORK

During the last few weeks several samples of transparent MgO were obtained and cut into specimens suitable for photoelastic analysis. A preliminary examination of these specimens indicates that the material is birefringent and sufficiently sensitive to receive serious consideration for photoelastic studies. As a result of the preliminary study conducted under the current program, the photoelastic coating approach should be temporarily abandoned, and future

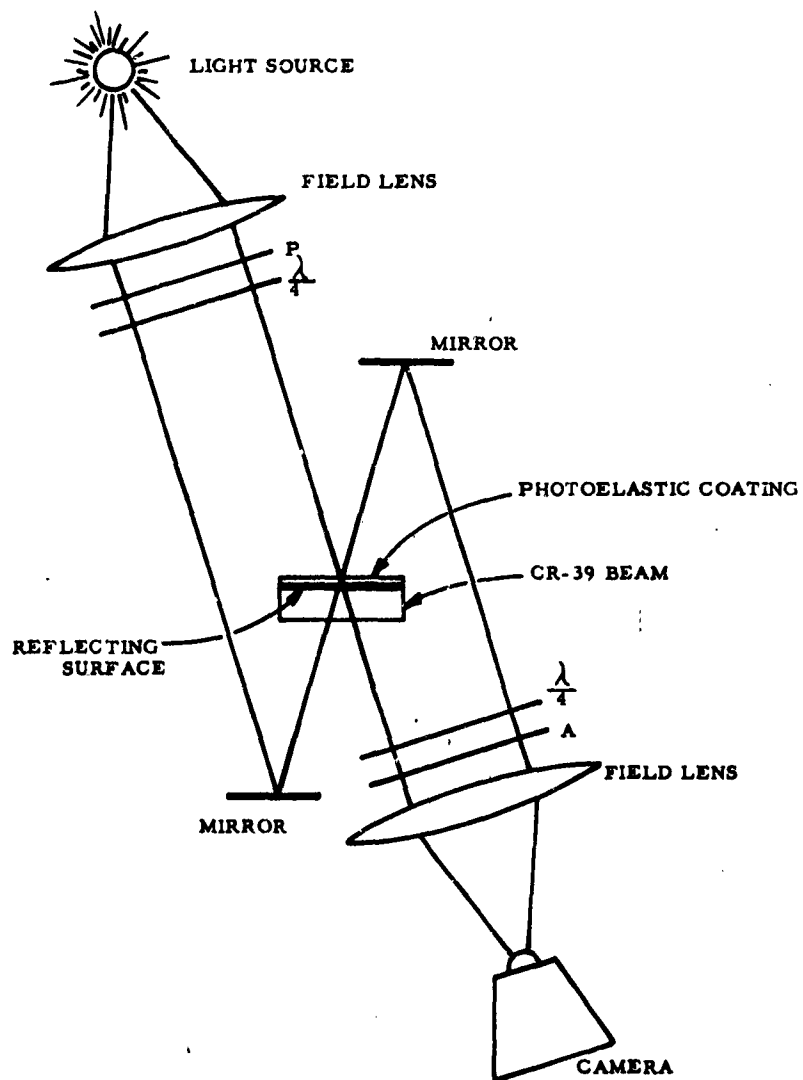


Fig. 13-3
SCHEMATIC ARRANGEMENT OF THE ELEMENTS OF THE POLARISCOPE WHICH PERMIT SIMULTANEOUS RECORDING OF PATTERNS FROM THE BEAM AND COATING

research effort should be devoted to a study in which transparent MgO is used as the model material.

Part Two - Theoretical Work
Principal Investigator: E. L. McDowell
Armour Research Foundation

Problems in linear elasticity which are pertinent to crack propagation studies can be roughly classified as being static, steady-state dynamic or transient dynamic. Of these three categories, the largest proportion of available solutions are devoted to the static problem. The present study has been limited to a review of the existing literature and an attempt to consolidate certain existing solutions (including static and steady-state dynamics) in common terms. In addition, some preliminary efforts regarding the transient dynamic problems have been initiated.

4. STATIC AND STEADY DYNAMIC CRACK SOLUTIONS

The presently available solutions examined thus far have been the static solution of Westergaard⁽¹³⁻¹¹⁾ the steady state solutions of Craggs⁽¹³⁻¹²⁾ and Yoffe⁽¹³⁻¹³⁾ and the general Sneddon-Radok⁽¹³⁻¹⁴⁾ solution of the plane dynamical equations. These solutions are as follows.

Westergaard⁽¹³⁻¹¹⁾ has shown that in an important group of cases the normal and shearing stress in a plane strain problem can be written in the form

$$\begin{aligned}\sigma_c &= \operatorname{Re} Z - y \operatorname{Im} Z' \\ \sigma_y &= \operatorname{Re} Z + y \operatorname{Im} Z' \\ \tau_{xy} &= -y \operatorname{Re} Z'\end{aligned}\tag{13-1}$$

where Z is an analytic function of the complex variable $z = x + iy$. This solution has the property that on the line $y = 0$,

$$\tau_{xy} = 0 \quad \text{and} \quad \sigma_x = \sigma_y$$

Two readily available solutions in this form are for the internal crack and the crack opened by a wedge (the cases shown in Fig. 13-4) which have the stress functions:

Internal crack

$$Z = P / \sqrt{1 - (a/z)^2} \quad (13-2)$$

crack opened by wedge

$$Z = \frac{P}{\pi(a+z)} \sqrt{\frac{a}{z}} \quad (13-3)$$

where P, p, and a are as defined in Fig. 13-4

Craggs ⁽¹³⁻¹²⁾ has provided a solution for the propagation at constant velocity of a semi-infinite crack in an infinite plate under the action of wedging stresses on the surface of the crack (Fig. 13-5). The solution is made up of two complex functions of the form

$$\mu \pi D W_j(Z_j) = -2 \left\{ \left[1 - (V/C_2)^2 \right]^{1/2} S - i (2 - V/C_2)^2 P \right\} \quad (13-4)$$

$$\left\{ \text{Log} \frac{A^{1/2} - i Z_j^{1/2}}{A^{1/2} + i Z_j^{1/2}} + i \pi - \frac{2 i A^{1/2}}{Z_j^{1/2}} \right\}$$

where μ is the shear modulus

V is the crack velocity

C_1, C_2 are dilatation and-distortion wave velocities

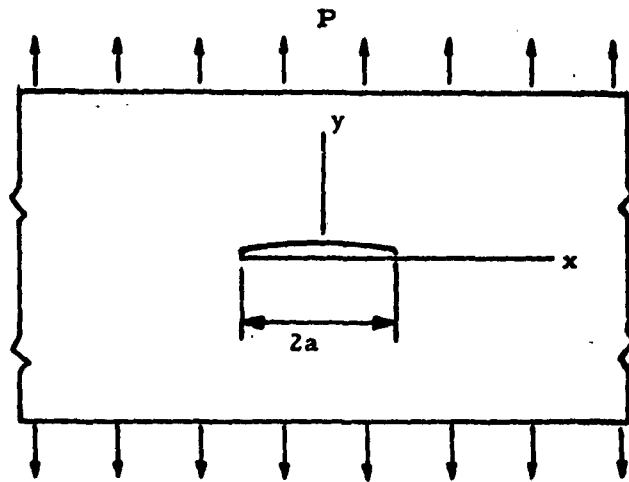
P, S wedge stresses of Figure 2

a loaded length of crack

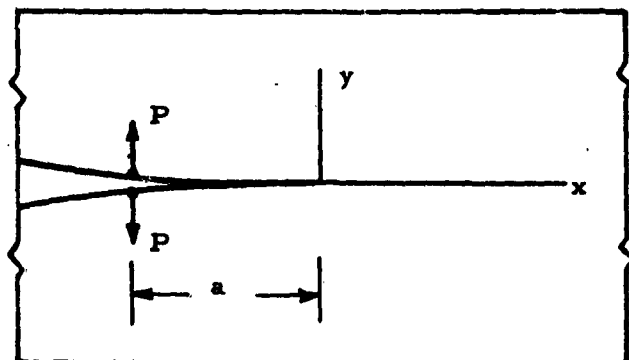
$$Z_j = \bar{X} + i (1 - V^2/C_j^2)^{1/2} y$$

$$X = x - V t$$

and j takes the values 1 and 2.



(a) INTERNAL CRACK



(b) CRACK OPENED BY WEDGE

Fig. 13-4 WESTERGAARD CRACK PROBLEMS

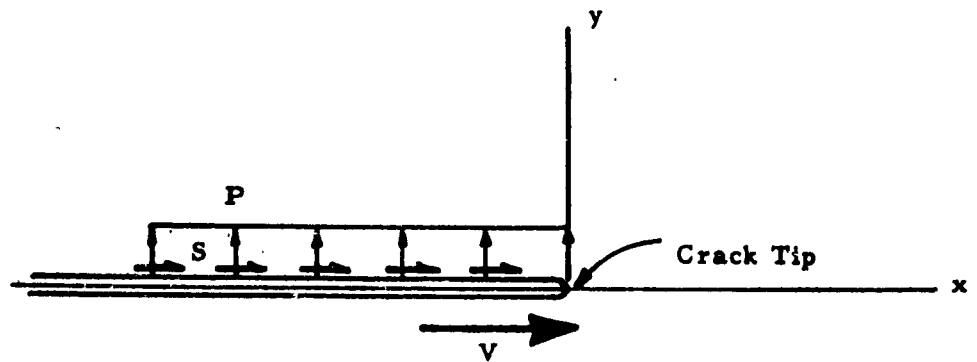


Fig. 13-5 PROPAGATING SEMI-INFINITE CRACK

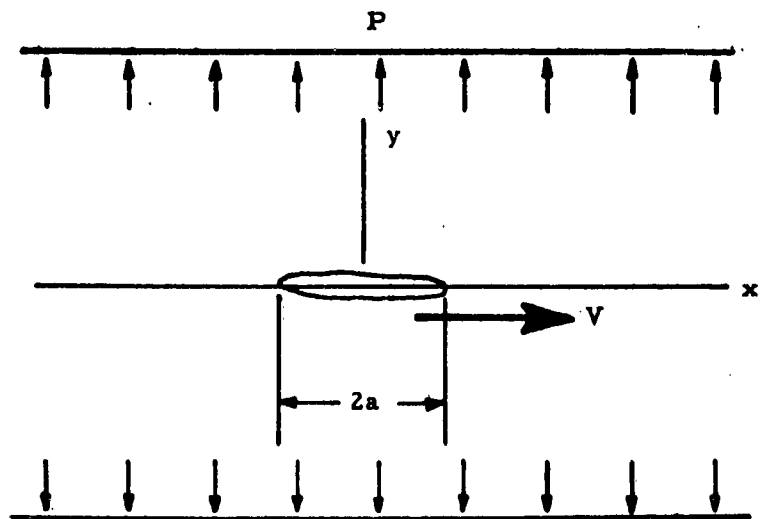


Fig. 13-6 PROPAGATING INTERNAL CRACK

Yoffe (13-13) provided another steady state solution for the internal crack of constant length propagating with constant velocity in an infinite plate (Fig. 13-6). This solution is derived formally from an integration of all possible Rayleigh type waves along the line $y = 0$ ahead of the crack. However, the solution indicates a relation between the Westergaard static solution of the internal crack with the steady dynamic solution. In order to avoid dealing with mixed boundary values along $y = 0$, Yoffe indicates that the static form of solution can be used to transform the line $y = 0$ to either a purely stress or purely displacement dependent boundary. In fact her solution, in final form, is seen to be a linear combination of Westergaard's static solution with combinations of elastic and dynamic constants as coefficients.

The Sneddon-Radok (13-14) in general form, applies to disturbing influences moving with constant velocity parallel to the axis. According to this solution two analytic functions $F_1(Z_1)$, and $F_2(Z_2)$ give rise to displacement components satisfying the steady dynamic equations of elasticity. From these functions the stresses are derived by

$$\begin{aligned}\sigma_y &= (1 + \beta_2^2) \left[F_1''(Z_1) + F_2''(Z_2) \right] \\ \sigma_x + \sigma_y &= -2(\beta_1^2 - \beta_2^2) \operatorname{Re} \left[F_1''(Z_1) \right] \\ \tau_{xy} &= 2 \operatorname{Im} \left[\beta_1 F_1''(Z_1) + \frac{(1 + \beta_2^2)}{4\beta_2} F_2''(Z_2) \right]\end{aligned}\quad (13-5)$$

where

$$\beta_1^2 = 1 - (V/C_1)^2$$

$$\beta_2^2 = 1 - (V/C_2)^2$$

$$X = x - V t$$

$$Z_1 = X + i\beta_1 y$$

$$Z_2 = X + i\beta_2 y$$

5. STEADY STATE SOLUTIONS FROM STATIC SOLUTION

Sneddon has also shown how the solution for the moving internal crack (Yoffe) can be derived from the static internal crack solution of Westergaard, by applying the Sneddon-Radok form of solution. Thus if the functions F_1 , F_2 are taken as defined by:

$$\begin{aligned} F_1''(Z_1) &= A_1 + B_1 / \sqrt{1 - (A/Z_1)^2} \\ F_2''(Z_2) &= A_2 + B_2 / \sqrt{1 - (A/Z_2)^2} \end{aligned} \quad (13-6)$$

where A , B , H , B are constants (possibly imaginary) which are evaluated to satisfy stress boundary conditions. The constants are readily evaluated as

$$A_1 = -A_2 = \frac{P}{[4\beta_1\beta_2 - (1+\beta_2^2)^2]} \left\{ \left[1 + \frac{(1+\beta_2^2)}{\beta_1^2 - \beta_2^2} \right] (1 + \beta_2^2) - 4\beta_1\beta_2 \right\} \quad (13-7)$$

$$B_1 = - \frac{(1 + \beta_2^2) P}{[4\beta_1\beta_2 - (1 + \beta_2^2)^2]} \quad B_2 = \frac{P}{1 + \beta_2^2} \left[1 - \frac{(1 + \beta_2^2)^2}{4\beta_1\beta_2} \right]$$

which is Yoffe's solution.

What seems to have been generally overlooked, however, is that Cragg's solution can also be obtained using the Westergaard static solution with the Sneddon-Radok dynamic equations. In fact, there appears to be a close relation between the Westergaard form and the steady state, at least for some range of problems.

To obtain the steady-dynamic solution for the semi-infinite crack we must first obtain a modification for the Westergaard

crack opened by a wedge. Instead of the solution for a concentrated force, P , previously cited, we replace P by a distributed load over a small length of crack, da , and sum up such loads for all $b \leq a \leq 0$, as shown in Fig. 13-7. After integrating and manipulating, a new solution is obtained for the semi-infinite crack loaded by uniform compressive stress, w , for a distance, b , behind the crack tip. (The solution for shear stresses behind the crack has not been obtained but should be similar in view of Cragg's solution to the result given here.) These considerations lead to

$$Z = \frac{-2W}{4i\pi} \left[\text{Log} \frac{b^{1/2} - iZ^{1/2}}{a^{1/2} + iZ^{1/2}} + i\pi - \frac{2ib^{1/2}}{Z^{1/2}} \right] \quad (13-8)$$

For this solution, which applies to the static case, the term in brackets is exactly that obtained by Craggs in the dynamic solution. The exact form of Craggs' solution follows by assuming the functions F_1, F_2 in the Sneddon-Radok solution to be defined by

$$F_1''(Z_1) = A \left[\text{Log} \frac{b^{1/2} - iZ_1^{1/2}}{b^{1/2} + iZ_1^{1/2}} + i\pi - \frac{2ib^{1/2}}{Z_1^{1/2}} \right] \quad (13-9)$$

$$F_2''(Z_2) = B \left[\text{Log} \frac{b^{1/2} - Z_2^{1/2}}{b^{1/2} + iZ_2^{1/2}} + i\pi - \frac{2ib^{1/2}}{Z_2^{1/2}} \right]$$

where A and B may be complex. To satisfy stress boundary conditions (including shear stress on the crack) the constants must have the values

$$\text{Re } A = \text{Re } B = \frac{-2\beta_2 S}{\pi \left[(1 + \beta_2)^2 - 4\beta_1\beta_2 \right]} \quad (13-10)$$

$$\frac{\text{Im } A}{(1 + \beta_2)^2} = -\frac{\text{Im } B}{4\beta_1\beta_2} = \frac{-P}{\pi(1 + \beta_2^2) \left[(1 + \beta_2^2)^2 - 4\beta_1\beta_2 \right]}$$

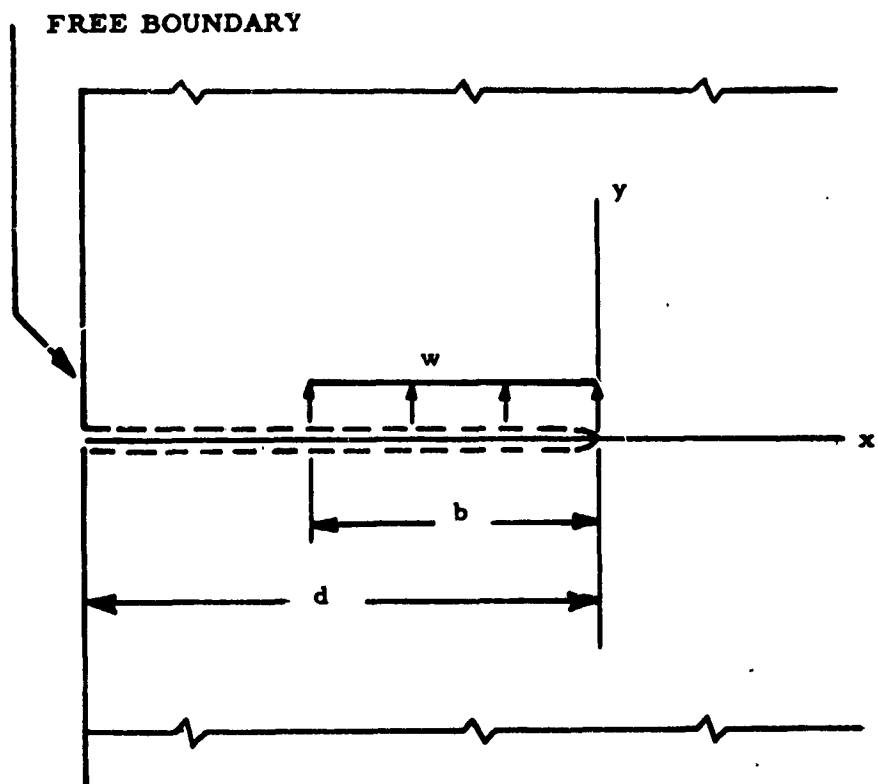


Fig. 13-7 CRACK AT FREE BOUNDARY

where P and S now refer to normal and shear stress on the crack boundary $-b \leq -X \leq 0$. With appropriate change in notation this is exactly Craggs' solution.

In passing we also note that by a transformation

$$\eta = Z^2 - d$$

we can arrive at a static solution of the case shown in Fig. 13-7. We cannot employ the Sneddon-Radok solution in this case, however, since the appearance of a boundary makes the problem inherently non-steady. In other words, d , in this case would depend on time.

6. TRANSIENT DYNAMIC CRACK PROPAGATION

The transient-dynamic solution available to date is by Baker⁽¹³⁻¹⁵⁾ for a problem similar to Craggs' semi-infinite crack. For the transient-dynamic solution the semi-infinite crack suddenly appears in a stretched sheet and then propagates with constant velocity. An apparent difficulty with this solution, however, is that in the limiting case of zero propagation velocity after the crack appears we have the case of the semi-infinite length of crack loaded along its entire length. Contrary to the steady-dynamic problems, this situation does not have a static counterpart.

7. CONCLUSION

We have shown how the two available steady-dynamic crack propagation solutions are related to the analogous static solutions. It appears at least plausible, also, that additional steady-dynamic problems can be derived in this manner.

The investigation of the transient dynamic problem has, as yet, not progressed to a stage where definitive conclusion can be

reached. The study will continue in the direction of determining the strain energy distribution in the vicinity of the tip of the crack as well as the establishment of transient dynamic solutions for bounded regions.

8. REFERENCES

- 13-1 Barstow, F. E., and Edgerton, H. E., J. Am. Ceram. Soc. 22, 302-307 (1939).
Edgerton, H. E. and Barstow, F. E., J. Am. Ceram. Soc. 24 131-137 (1941).
- 13-2 Schardin, H. and Struth, W., Glastechn Ber. 16, 219-231 (1938).
- 13-3 Dimmick, H. M. and McCormick, J. M., J. Am. Ceram. Soc., 34, 240-241 (1951)
- 13-4 Lundborg, N. and Johansson, C. H., Arkiv Fysik, 4, 55-58 (1952)
- 13-5 Post, D., Proc. SESA, 12, No. 1, 99-116 (1954)
- 13-6 Dixon, J. R., Royal Aeronautical Society, 64, 141-145 (1960).
- 13-7 Guernsey, R. and Gilman, J., Proc. SESA, 18, No. 2, 50-54 (1961).
- 13-8 Gerberich, W., to be published in Experimental Mechanics.
- 13-9 Schardin H., Kunststoff, 44, No. 2, 48 (1954).
- 13-10 Wells, A. A. and Post, D., Proc. SESA, 16 No. 1 69-92 (1948).
- 13-11 Westergaard, H. M., "Bearing Pressures and Cracks", J. Appl. Mech. June (1939)
- 13-12 Craggs, J. W., "On the Propagation of a Crack in an Elastic-Brittle Material", J. Mech. Phys. Solids, 8 (1960).
- 13-13 Yoffe, E. G., "The Moving Griffith Crack", Phil. Mag. 42 (1951)

- 13-14 Sneddon, I. N., "Crack Problems in the Mathematical Theory of Elasticity" No. Carolina State College, ERD-1261, May, 1961.
- 13-15 Baker, B. R., "Dynamic Stresses Created by a Moving Crack", J. Appl. Mech., Paper 61-APMW-28

TASK 14 - RHEOTROPIC BEHAVIOR

Principal Investigator: P. R. V. Evans

A B S T R A C T

The initial purpose of this task was to explore the possibility of introducing small but measurable amount of room temperature ductility into multicrystalline oxides by means of rheotropic effects ascribable to elevated temperature deformation. Magnesium oxide was selected as the candidate material, and extrusion as the process for achieving high temperature deformation. Back extrusion using a 3:1 reduction ratio yielded promising results. However, the perfection of extrusion studies appeared to require a major effort, disproportionate to the size of the current study.

Emphasis, therefore, was diverted to a study of the sintering characteristics of submicron MgO powders produced by the Vitro Laboratories; studies were carried out for hot pressing, and for cold pressing and sintering methods.

The Vitro material and Fisher powder were subjected to hot pressing at 2350° F and 3000-psi pressure, with or without 1/2 w/o LiF. The LiF addition proved beneficial for the Fisher powder, but had no effect on the Vitro material. Highest densities were obtained for the Fisher MgO powder with 1/2 w/o LiF; under identical conditions the final grain size of the Vitro material was about 50 percent larger than that of the Fisher powder.

TASK 14 - RHEOTROPIC BEHAVIOR

Part One - Sintering Studies of Submicron Magnesium Oxide Powders

1. INTRODUCTION

The objective of this task is to examine whether the rheotropic effects observed in body-centered cubic metals which result in significant improvements in low-temperature ductility following high temperature deformation, exist also in polycrystalline metallic oxides. Two approaches recommend themselves in this regard:

- (1) Using small amounts of prestrain up to 10 percent, so that "grown-in" dislocations are unlocked from their impurity atmospheres. This prestrain has to be carried out at temperatures where the impurities are essentially immobile.
- (2) Introducing considerable prestrain between 40-60 percent, to cause extensive glide and dislocation slip band formation throughout the body of the material. The slip lines generated will tend to cause twinning, thereby reducing the effective grain size, and increasing the density of screw dislocations which are thought to act as considerable barriers to the propagation of brittle type fractures.

2. DISCUSSION

Work commenced with MgO, since this material appeared to be more promising with regard to achieving some ductility than Lucalox. Results from Task 4 suggest that uniaxial compression testing is not a satisfactory method of achieving plastic deformation in polycrystalline MgO. Therefore, attention has been devoted

to studying extrusion as a method of prestraining. Two different extrusion techniques, illustrated in Fig. 14-1, were investigated in the temperature range of 1200°C-1600°C. Briefly, the results indicate that back extrusion, Fig. 14-1(b), is a considerably more promising method of extruding MgO than direct extrusion, Fig. 14-1(a). Even the experiments on back extrusion, however, have not, so far, yielded satisfactory specimens for testing. Extrusion ratios up to 3:1 have been investigated. It appears at this time that the achievement of satisfactory extrusion techniques for ceramics oxides is, in itself, a major development area.

In view of the fact that the development of successful extrusion techniques is a prerequisite to the intended nature of this task, further work on a study of the rheotropic behavior of multicrystalline oxides is suspended. Remaining effort was then re-oriented towards a study of the sintering characteristics of submicron MgO powder.

Part Two - Sintering Characteristics of Submicron Magnesium Oxide Powder

3. INTRODUCTION

The objective of this study was to examine the sintering characteristics of submicron MgO powder supplied by the Vitro Laboratories, West Orange, New Jersey and compare them with the behavior of some commercially available powders produced by more conventional techniques. It was thought that the extreme fineness of the Vitro product and thus its enhanced activity might possess certain advantages such as increased sintering rates. Of particular interest was the possibility of producing a high density magnesia ceramic at lower than normal fire temperatures. The Vitro powder is produced by an erosion process of the anode of a plasma arc apparatus.

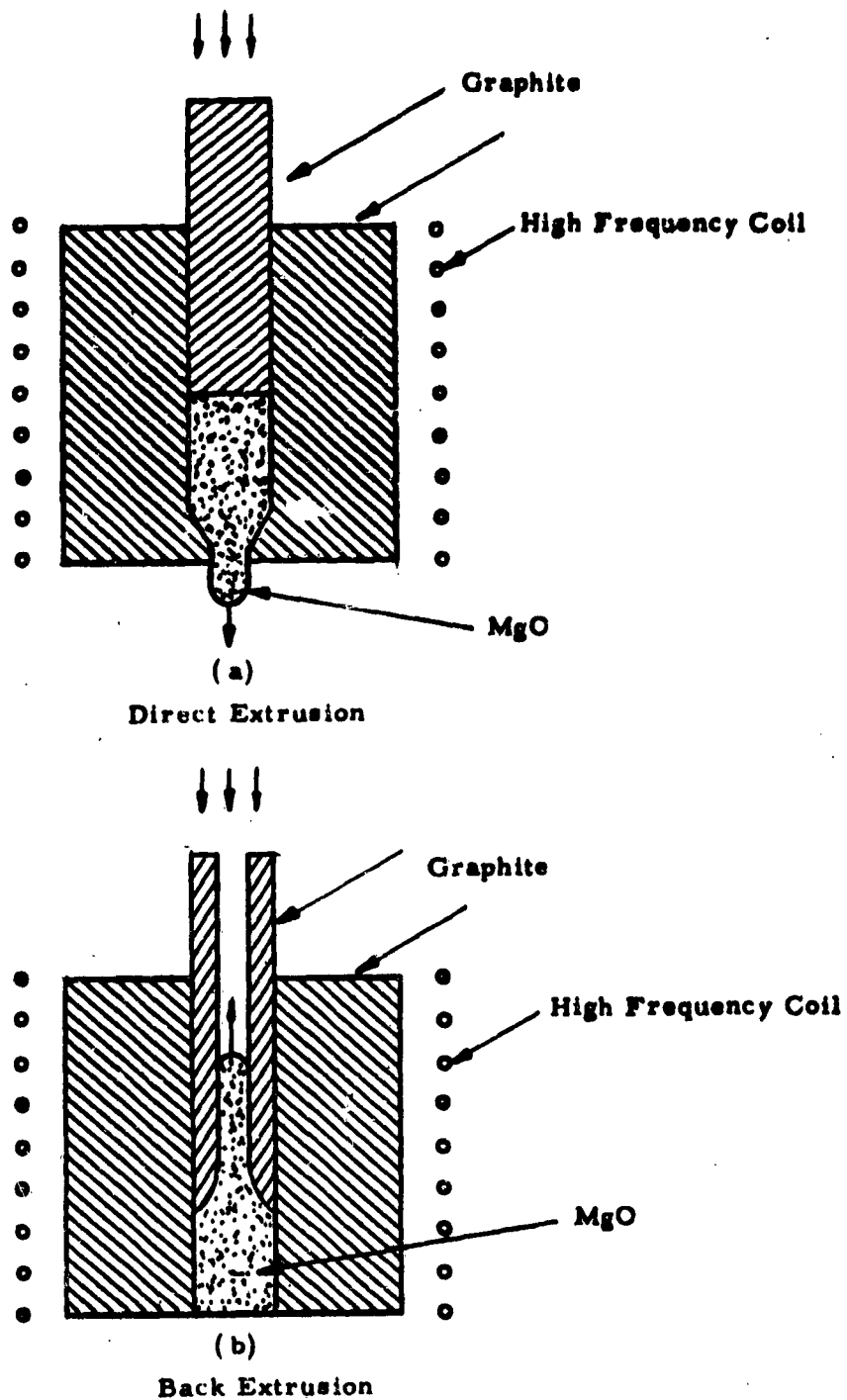


**Fig. 14-1 SCHEMATIC OUTLINE OF EXTRUSION TECHNIQUES
STUDIED FOR MAGNESIUM OXIDE**

Most of the experimental work involved a detailed study of the sintering of cold pressed bodies of known but varying green density. Green density may then be related to fired density and an analysis of such data provides comparable and accurate measurements of sinterability. This approach has been used before (14-1, 14-2, 14-3,) and takes into account the influence of initial powder particle size on cold-pressing characteristics which, in turn, effects subsequent sintering behavior. This consideration is important in the present study since the initial powder particle sizes varied considerably.

A limited number of hot pressing experiments was also performed.

4. MATERIALS

Three powders were studied.

Vitro Submicron Magnesium Oxide, Lot MgO-9-10 (C); produced by:

Vitro Laboratories, Inc.
200 Pleasant Valley Way
West Orange, New Jersey

Mallinckrodt AR-Grade Magnesium Oxide, Cat. No. 6015, Lot 9012L1; produced by:

Mallinckrodt Chemical Works
Second & Mallinckrodt Streets
St. Louis, Missouri

Fisher Magnesium Oxide, USP Light Calcined Magnesia, Cat. No. M-49, Lot 71064; produced by:

Fisher Scientific Company
Fairlawn, New Jersey

The Vitro powder was not commercially available and was obtained through the courtesy of Dr. J. D. Holmgren of Vitro. The Mallinckrodt and Fisher powders were obtained through commercial channels.

The Mallinckrodt and Fisher powders were chosen for study because they had been used to produce specimens for this program. The Mallinckrodt powder is used to produce the standard ARF cold-pressed and sintered MgO. It was selected three years ago after a survey and trial of thirteen commercial and experimental magnesium oxide powders on the basis of its high purity, excellent pressing behavior, uniformity, availability, and low cost. At the time of the survey, the Mallinckrodt powder was one of the few powders which could be relied upon to produce hot pressed MgO specimens for Task 4. Only the Vitro and Fisher powders were used in the hot-pressing experiments.

The chemical and physical properties of the three powders are tabulated in Tables 14-1 and 14-2. Electron micrographs are shown in Fig. 14-2, 14-3, and 14-4. The Vitro powder is produced by an erosion process of the anode of a plasma arc apparatus which produces a powder of high surface area, small average particle size, and presumably, quite different absorbed surface layers and surface stresses than powders produced at lower temperatures. The Mallinckrodt and Fisher powders are produced by the conventional method of precipitating MgO from solution as the basic carbonate and calcining the precipitate at low temperature, 1400°F for the Mallinckrodt powder, to produce the oxide. This method has been found to produce MgO with high sinterability and calcination of other magnesium salts, the chloride and sulfate for example, has been found to produce MgO of lower sinterability.

Table 14-I.

CHEMICAL ANALYSIS OF MAGNESIUM OXIDE POWDERS

Impurity	Vitro		Percent Impurity		Fisher	
	Powder*	Ceramic	Powder*	Ceramic** (Cold Pressed and Sintered)	Powder*	Ceramic** (Hot Pressed)
Al	0.002			0.05		0.03
As					<0.001***	
As B	0.002					
Ba			<0.005			
C	0.27					0.018
Ca	0.05		0.03	0.04	<1.5	0.5
Cr	0.002			0.003		0.0006
Cu	0.001			0.0002		0.0003
Fe	0.03		0.005	0.005	<0.05	0.03
K	0.1		0.003			
Mn	0.007		<0.0005			
Mo	0.003					
Na	0.02		0.1			
Ni	0.002					
Pb			<0.003		<0.004	
Si	0.1		<0.04	0.03		0.02
Sr			<0.001			
Ti	0.001					0.004

*Supplier's Typical Analysis

**Semi-Quantitative Spectrochemical by Chicago Spectro-Service Laboratory, Inc.

*** As Oxide

Reference to the tables and figures mentioned above shows that its unconventional method of production does indeed give the Vitro a higher surface area and smaller particle size altho not as high as that of some experimental calcined magnesium hydroxide which range to 200 sq meters/gram. The electron-micrograph of the Fisher powder (Fig. 14-4) shows a relic structure of the basic carbonate indicating that this powder may have been calcined at a higher temperature than the Mallinckrodt powder; the exact temperature is considered proprietary by Fisher. This structure gives the Fisher powder a much larger particle size than the other two powders.

Table 14-II

PROPERTY DATA

Property	Powder		
	Vitro	Mallinckrodt	Fisher
Surface Area* (sq. meter/gram)	68.5	12.9	13.2
Bulk Density** (lb/cu ft)	4-6	8-12	10.14

* Surface area determined by BET nitrogen absorption method by Particle Data Labs, Bronxville, New York.

** Bulk density varies with method of determination and cannot be determined precisely.

5. EXPERIMENTAL PROCEDURE AND RESULTS

A. Hot Pressing Experiments

The hot pressing experiments were confined to the conditions previously used at ARF to produce ultra-high density MgO for Task 4 with the exception that LiF additives were not made in some instances. The procedures used were described in detail previously ⁽¹⁴⁻⁴⁾. Briefly, cylinders 1/2 in. diam by 1 in. long were pressed in graphite dies at 2350°F and 3000 psi pressure. This was followed by a dicarburization treatment involving heating air at 1200°C for 168 hours to oxidize the carbon picked up during pressing. Density and grain size measurements were then performed.

The density results are given in Table 14-III and representative microstructures are illustrated in Fig. 14-5 through 14-7.



Fig. 14-2
ELECTRON MICROGRAPH,
VITRO MAGNESIUM OXIDE
POWDER



Fig. 14-3
ELECTRON MICROGRAPH,
MALLINCKRODT MAGNESIUM
OXIDE POWDER

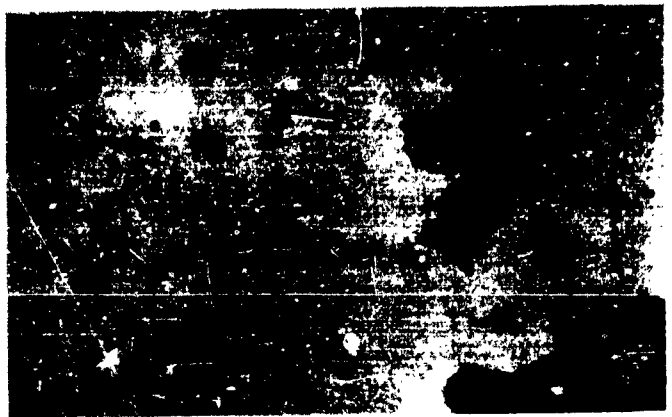


Fig. 14-4
ELECTRON MICROGRAPH,
FISHER MAGNESIUM OXIDE
POWDER

Table 14-III
DENSITY DATA FOR MAGNESIUM OXIDE COMPACTS

	Vitro	Mallinckrodt	Fisher
Compacting Pressure Range (psi)	150 - 60,000	300 - 60,000	200 - 50,000
Height of Compacts Range (in)	1.46 - 0.45	1.18 - 0.49	1.24 - .51
Green Density Range (g/cc)	0.72 - 2.16	0.93 - 2.29	0.56 - 1.29
as % of Theoretical Density	23 - 60	27 - 61	16 - 36
Fired Density Range, 1300°C, g/cc	1.83 - 2.87	1.20 - 2.81	0.96 - 1.67
as % of Theoretical Density	51 - 80	34 - 79	27 - 47
Fired Density Range, 1700°C, g/cc	2.65 - 3.48	2.91 - 3.46	3.08 - 3.39
as % of Theoretical Density	71 - 97	81 - 97	86 - 95

The following conclusions are based on their data:

- (1) The highest density hot pressed bodies prepared in this investigation were obtained using Fisher powder with LiF addition.
- (2) Lithium fluoride additions made little difference to the fired density or grain size of the Vitro powder. However, LiF greatly influenced the densities obtainable with the Fisher powder.
- (3) The grain sizes of the Vitro specimens were about 50 per cent larger than the Fisher material. Also, the Fisher powder gave a significantly smaller grain size than is normally associated with the hot pressing conditions used here. This observation remains unexplained.

The varying grain sizes might be explained by the average particle size and size distribution of the starting powders. Size data is currently being collected for these powders and will be included in the final report on the cold-pressing and sintering experiments described below.

Grain sizes were determined using equation described in Task 4.



X 250

Fig. 14-5

FISHER MAGNESIUM OXIDE POWDER + $\frac{1}{2}$ w/o LITHIUM FLOURIDE
HOT-PRESSED AT 2350 °F. Grain Size = 0.012 mm Density = 3.57 g/cc



X 250

Fig. 14-6

VITRO SUBMISION MAGNESIUM OXIDE POWDER + $\frac{1}{2}$ w/o LITHIUM
FLOURIDE HOT-PRESSED AT 2350 °F. Grain Size = 0.019 mm
Density = 3.49 g/cc Etchant = 50 % conc H_2SO_4 + 50% Sat. Sol. NH_4Cl

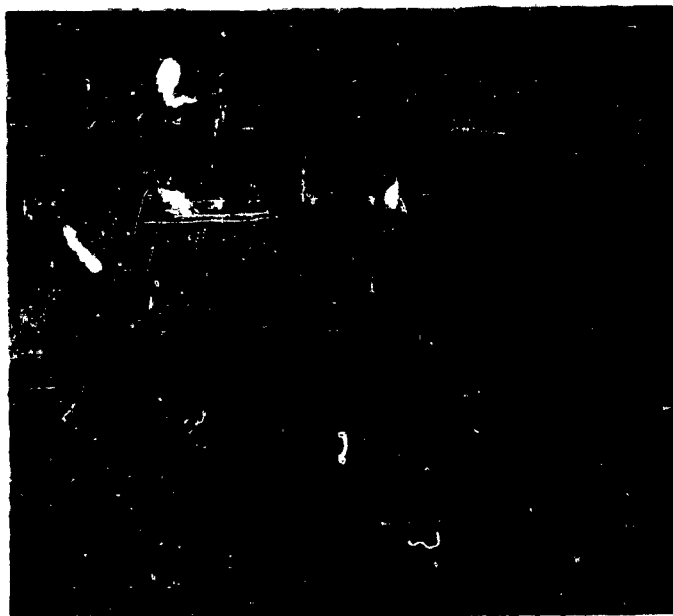


Fig. 14-7
VITRO SUBMICRON MAGNESIUM OXIDE POWDER HOT-PRESSED AT
2350 °F WITHOUT ANY ADDITIVES. Grain Size = 0.018 mm
Density = 3.48 g/cc Etchant = 50 % conc H_2SO_4 + 50% Sat. Sol. NH_4Cl

The lower densities exhibited by the Vitro powder may be attributed, in part at least, to the trapping of gas pockets between the very fine particles during compacting which remain trapped during subsequent sintering. Low densities have also been noted in the sintering of submicron metal powders (14-15) and it is thought that this is also due to a gas trapping mechanism. The larger grain sizes noted in the Vitro compacts could be due to the slightly higher purity of this material, according to Table 14-I, this material has lower purity than Fisher or Mallinckrodt together with its finer initial particle size.

The above results indicate that from the standpoint of producing ultra-high density fine grain ceramics, Fisher powder is a superior starting material at least for the hot-pressing conditions used here.

B. Cold Pressing and Sintering Experiments

In this phase all three MgO powders were used. The powders were treated with the binder for light fluffy powders developed at ARF and described previously (14-4). The binder is composed of stearic acid and polymethylmethacrylate dissolved in solvent, it is mixed with the powder to form a slurry and evaporated to dryness. The treated powders were compacted at varying pressures from both sides in a 1-in. diam. die to form compacts with as wide a range of free densities as possible. The lower limit of the green density range was determined by the need to produce a compact with sufficient integrity for handling; the upper limit was determined by the onset of laminations for the Vitro and Mallinckrodt powders and by reaching a terminal green density for the Fisher powder. The green density was varied by changing the compacting pressure; the variation of

green density with compacting pressure for each powder is shown in Fig. 14-8; the Mallinckrodt was the easiest to press while the Fisher was the most difficult. The green density was determined from the weight and dimensions of the compacts, allowing for the weight of binder.

The compacts were dried for 48 hr at 110°C., divided into two random groups, and placed in random order into two kilns. The low temperature firing was made in an air atmosphere in a Glo-bar kiln in which the temperature was increased at the rate of 20°C/hr to 1300°C., held one hour, and allowed to cool to room temperature before the specimens were removed. The high temperature firing was made in the combustion gas atmosphere of an air/gas kiln in which the temperature was increased at the rate of 200°C/hr to 1700°C., held for three hours, and allowed to cool to room temperature before removing the specimens. The high temperature firing is the standard firing schedule for ARF MgO. It was observed that all the Vitro compacts in the low temperature firing with green densities greater than 35 per cent of theoretical density had completely disintegrated to the extent that their fired density could not be determined. Compacts of the other powders were not affected nor were any of the compacts in the high temperature firing affected. The reason for this phenomena is not apparent.

The lower firing temperature was selected as 1300°C. since that is approximately the Tammann temperature for MgO, the temperature at which the effects of bulk diffusion starts to become active in sintering. The upper firing temperature is the standard firing temperature for ARF MgO.

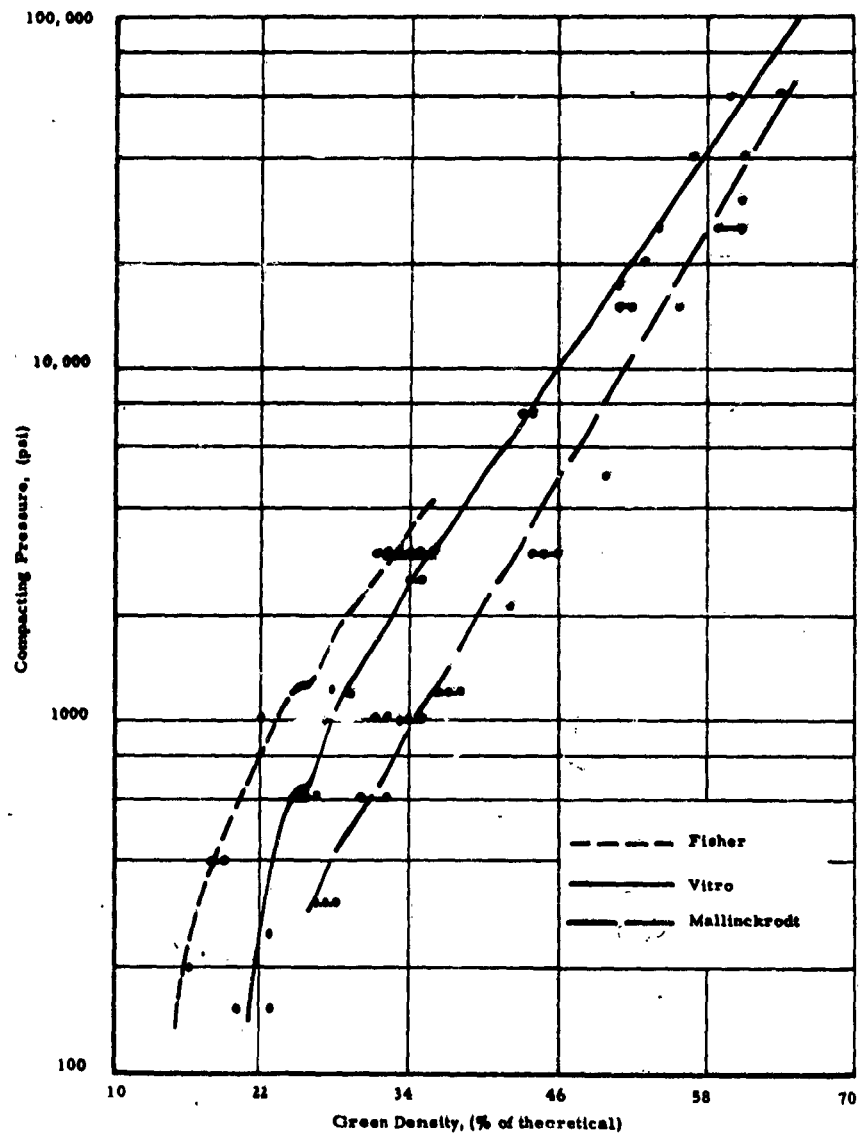


Fig. 14-8 COMPACTING PRESSURE VERSUS GREEN DENSITY,
ALL THREE MAGNESIUM OXIDE POWDERS

The bulk density of the specimens from the low temperature firing were determined by immersion in Meriam Red manometer oil, specific gravity 0.827; to avoid possible hydration that of the specimens from the high temperature firing by immersion in water, a less messy fluid. A few of the most dense specimens from the low temperature firing were also measured in water and their densities were found to be the same as those determined in oil. A bubble-free single crystal of MgO was used as a standard, its density was found to be between 3.57 g/cc and 3.58 g/cc in both oil and water which is the theoretical density for MgO.

The results of the firings are tabulated in Table 14-III. The plot of the green density as a percentage of theoretical density versus fired density as a percentage of theoretical density for the three powders at two firing temperatures is shown on Fig. 14-9, 14-10, 14-11. The lines were determined by regression analysis least squares method and have a correlation coefficient of 99.5 per cent or greater. The inflection points in the lines for the Vitro and Mallinckrodt powders at the upper firing temperature were determined visually. The regression of the points on either side of the inflection was found to be linear. Only the regression lines for the two firing temperatures and three powders are shown on Fig. 14-12 and 14-13. The slope, limits, and formula for these lines are given in Table 14-IV.

Considering Fig. 14-12 with the results of the low temperature firing, it will be seen that the Vitro powder sinters to a higher density than either of the other two powders. If the slope of the Vitro line is continued to the maximum green density obtainable in compacts of this powder, it will be observed

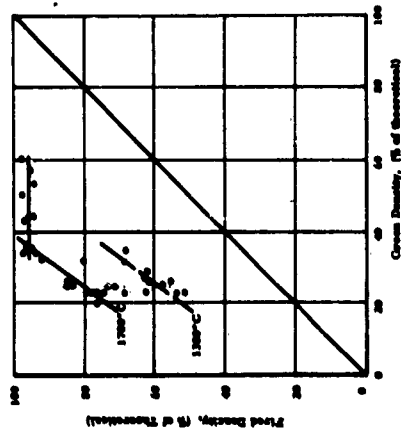


Fig. 14-9

FIRE DENSITY VERSUS
GREEN DENSITY, VITRO
MAGNESIUM OXIDE

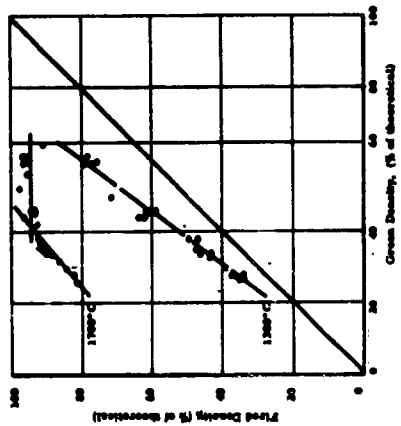


Fig. 14-10

FIRE DENSITY VERSUS
GREEN DENSITY, MALLINCKRODT
MAGNESIUM OXIDE

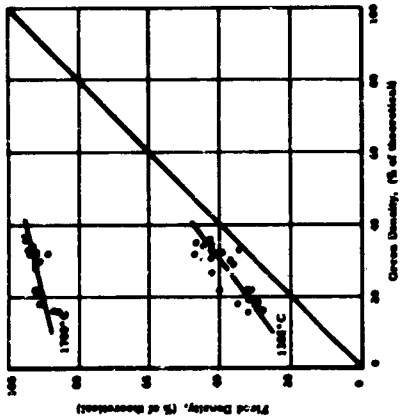


Fig. 14-11

FIRE DENSITY VERSUS
GREEN DENSITY, FISHER
MAGNESIUM OXIDE

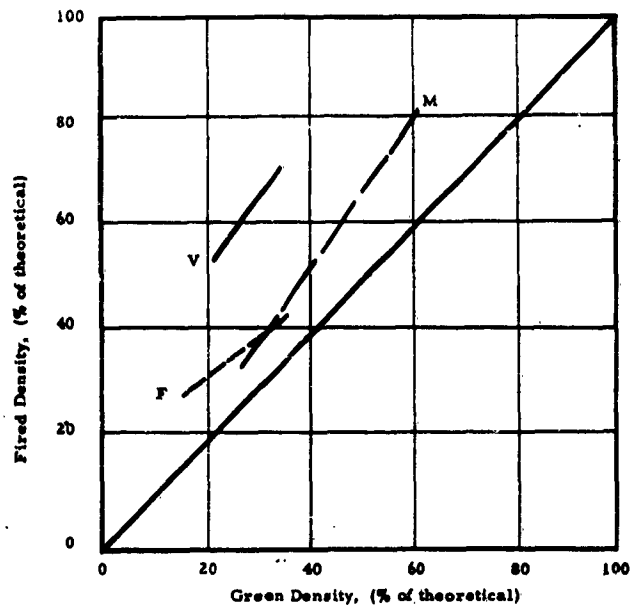


Fig. 14-12 FIRED DENSITY VERSUS GREEN DENSITY, 1300°C FIRING

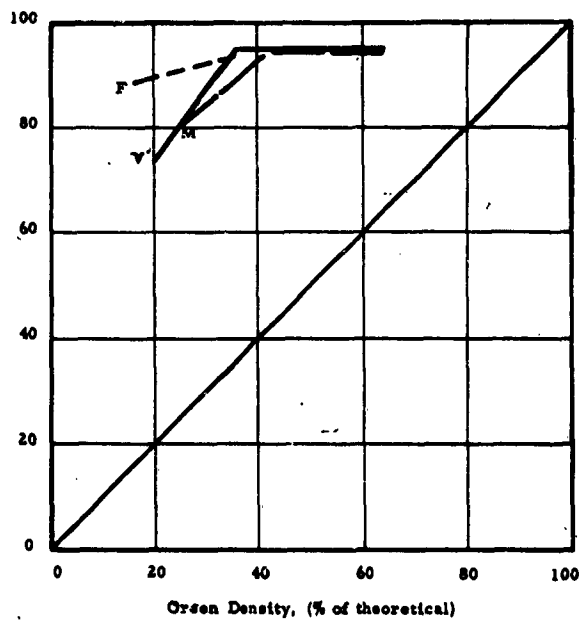


Fig. 14-13 FIRED DENSITY VERSUS GREEN DENSITY, 1700°C FIRING

Table 14-IV

REGRESSION ANALYSIS

Powder	Temperature (°C)	No. Specimens	Density Range (%)		Equation	Correlation Coefficient
			Green	Fired		
Vitro	1300	13	23-35	51-80	$y = 24.2 + 1.4 x$	0.69 (99.5% = .67)
	1700	20	20-35	71-97	$y = 46.5 + 1.4 x$	0.82 (99.5% = .56)
		13	35-60	93-97	$y = 95.4 + .003 x$	
Mallinckrodt	1300	25	27-61	34-79	$y = -1.9 + 1.4 x$	0.99 (99.5% = .5)
	1700	18	26-44	81-96	$y = 59.6 + .83 x$	0.97 (99.5% = .59)
		13	45-64	90-96	$y = 94.7 + .0006 x$	
Fisher	1300	33	16-36	27-47	$y = 16.8 + .75 x$	0.89 (99.5% = .44)
	1700	25	16-36	36-95	$y = 84.6 + .25 x$	0.77 (99.5% = .5)

that fired ceramics of very high density might have been obtained at this low temperature without the addition of LiF or other fluxing agent.

From Fig. 14-13, the results of the high temperature firing, it will be observed that the compacts of Vitro powder reach the terminal density sooner than those of Fisher or Mallinckrodt powder and that for low green density compacts, the Fisher powder produces much higher fired densities. Perhaps this is due to the fluxing action of its impurities. The difference between the terminal density reached by both Vitro and Mallinckrodt compacts with a green density greater than 42 per cent is not significant and the average of the two groups, 95 per cent of theoretical density can be considered the terminal density for both powders fired in this manner. In the course of preparing more than a thousand specimens of ARF MgO, the density of several hundred of them was measured; the green density ranged between 55 and 60 per cent while the fired density ranged between 95 and 97 per cent with monotonous regularity.

Photomicrographs of polished sections of ceramic specimens made from the three powders are shown in Fig. 14-14, 14-15, 14-16. These specimens were fired at 1700°C. and have a density of 95 per cent of theoretical. Grain counts were made from photomicrographs of two typical areas on three specimens made from each of the three powders. The data on the specimens and the results of the grain counts are given in Table 14-V. It will be noted that the variation of grain counts for the two areas on each specimen are smaller than the variation among the variation among the three specimens made from the same powder. The latter variation in the grain count does not seem to be dependent on either green density or fired density of the specimens. The difference in grain counts for the Fisher and Mallinckrodt specimens is not significant but there is a significant

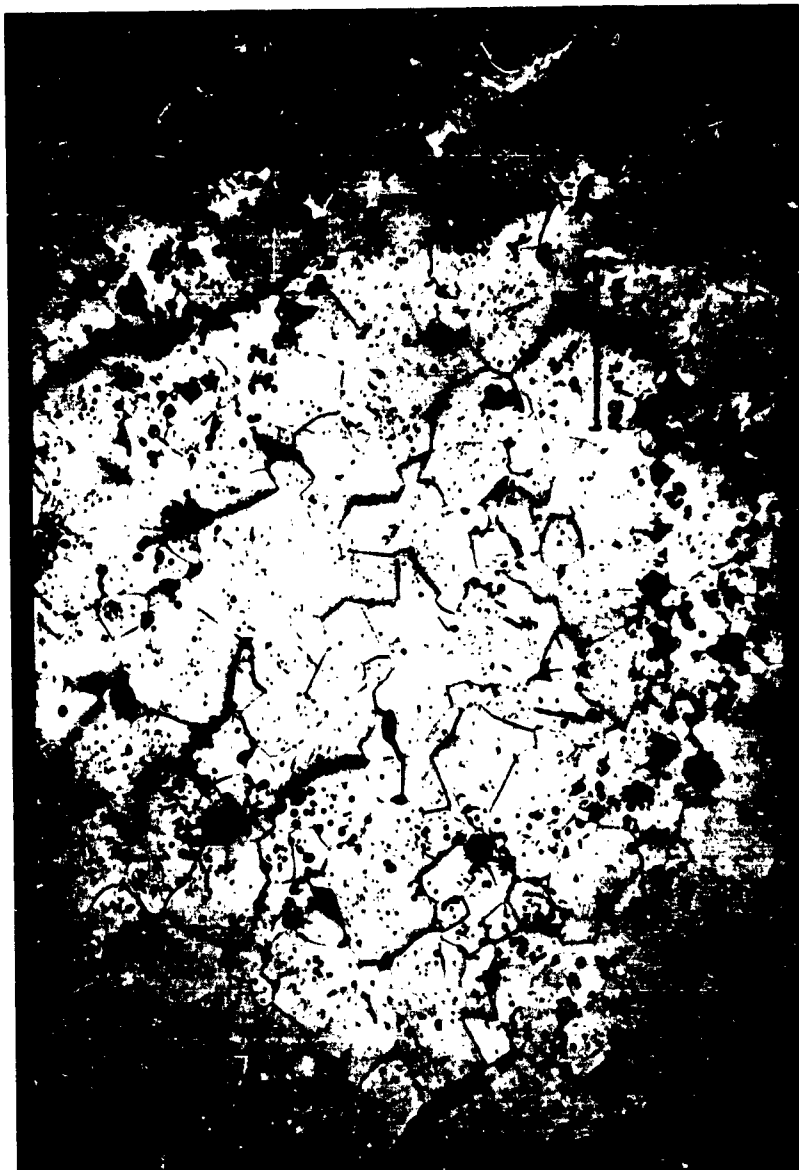


Fig. 14-14 PHOTOMICROGRAPH OF TYPICAL AREA ON VITRO MAGNESIUM
OXIDE SPECIMEN NO. 28



Fig. 14-15 PHOTOMICROGRAPHY OF TYPICAL AREA ON MALLINCKRODT
MAGNESIUM OXIDE SPECIMEN NO. 109

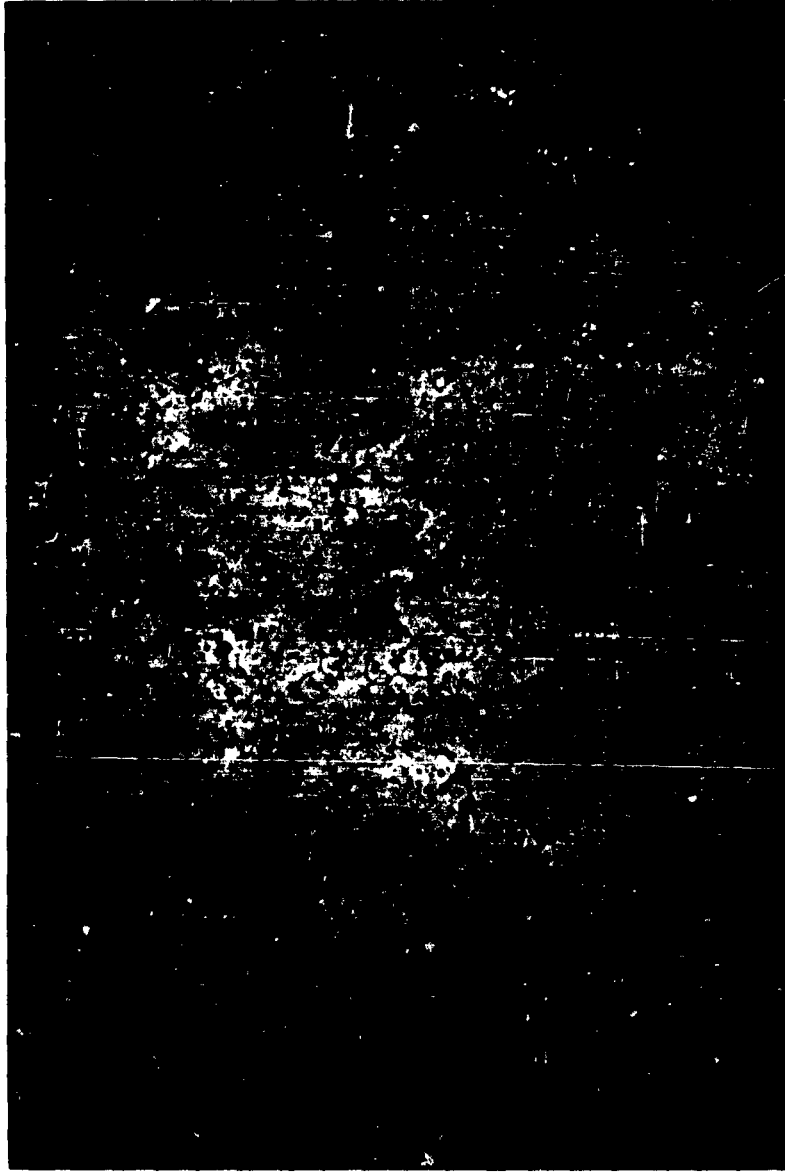


Fig. 14-16 PHOTOMICROGRAPH OF TYPICAL AREA ON FISHER MAGNESIUM
OXIDE SPECIMEN NO. 150

difference between these two and the Vitro specimens. It is interesting to note that both the Fisher and Mallinckrodt powders have the same average surface area and there may be an inverse dependence of fired grain size to surface area of the unfired powder.

Table 14-V
GRAIN COUNT DATA FOR SPECIMENS FIRED AT 1700°C

Powder	Specimen No.	Density (%)		Grains/ sq mm	Variation Coeff. (%)	Variation of Variation	
		Green	Fixed			Three Specimens	Coeff. (%)
Vitro	28	35	95	570	16	504	
	37	44	95	565	--	grains per	23
	53	57	95	377	--	sq mm	
Mallinckrodt	92	44	96	1100	3	778	
	101	56	95	510	--	grains per	44
	109	61	95	790	11	sq mm	
Fisher	131	36	95	1300	8	754	
	150	32	94	585	--	grains per	51
	158	33	94	615	--	sq mm	

It may be concluded from the foregoing, that the Vitro powder may be fired into high density MgO ceramics at much lower temperature than the Mallinckrodt or Fisher powders without the need of adding LiF or other sintering aids; for higher temperatures normally used to fire MgO, the Vitro and Mallinckrodt powders yield equivalent densities and the Mallinckrodt would be preferable on the basis of its higher purity and smaller grain size.

6. REFERENCES

- 14-1 Allison, A.G. et al, "Sintering of High Purity Magnesia", J. Amer. Ceram Soc. 39 No. (151-154) (1956)
- 14-2 Layden, G.K. and McQuarrie, M.C. "Effect of Minor Additions on Sintering of MgO", J. Amer. Ceram Soc. 42 No. 2 89-92, (1959)
- 14-3 Viola, Nazzareno and McQuarrie, M.C. "Note on Relation Between Unfired and Fired Densities of Aluminum Oxide Compacts", J. Amer. Ceram Soc. 42 No. 5 (261-262) (1959)
- 14-4 Weil, N. A., Ed., "Studies of the Brittle Behavior of Ceramic Materials", Report ASD-TR-61-628 April 1962
- 14-5 Holmgren, J. D., Vitro Laboratories, Private Communication

TASK 15 - EFFECT OF POROSITY

Principal Investigators: Part One: L. M. Atlas
Armour Research Foundation
Part Two: N. A. Weil
Armour Research Foundation

ABSTRACT

A two-part program was carried out on this Task to study the effect of porosity on the strength and elastic properties of ceramic oxides.

On Part One, the experimental phase of this work, groups of Al_2O_3 bars varying in porosity, grain size and conditions of fabrication have been prepared at temperatures between 1650° and $1845^{\circ}C$ by normal sintering, and by hot pressing at pressures ranging between 500 psi and 3000 psi. The porosity of the products varied from 0.5 to about 25 per cent; grain size measurements have not yet been completed. These bars as well as specimens of Lucalox, Wesgo AL995, and two grades of Alundum were subjected to measurements of Young's modulus, internal friction, and flexural strength in four-point loading. Relations between S and d , p , Q^{-1} , and E will be examined by multiple regression methods. A plot of $\log E$ vs P is presented; the slope of the resulting straight line is approximately 3.3.

Part Two deals with theoretical studies of the effect of porosity on elastic properties. Following a detailed literature review, Hashin's analysis on the effect of elastic inclusion is extended to yield closed-form solutions for Young's modulus. These results are then simplified for the particular case of porosity (empty inclusions), yielding definitive and simple expressions of uniform format for the effect of porosity on all of the elastic constants. The Hasselman-Shaffer equation is shown to be a singular case of the more general Hashin equations, and a semi-rational form of the strength-porosity relationship is suggested.

TASK 15 - EFFECT OF POROSITY

Part One: Experimental Work

Principal Investigator: L. M. Atlas
Armour Research Foundation

1. INTRODUCTION

As interest in ceramics for structural purposes has risen, increasing attention has been devoted to establishing theoretical and empirical relations between strength (and elastic constants) and such textural parameters as porosity and grain size. In the last few years, encouraging progress has been made in relating these two groups of variables -- provided that the ceramics have been fired at one temperature and prepared by the same general method. This is a serious restriction in cases where the previous history of a ceramic is unknown, or where new fabrication techniques have been used for their production. Therefore, the main objective of this program is to modify existing empirical equations so that the strength of a ceramic may be predicted from nondestructively measurable properties without knowledge of its history.

Because of the large scope of the problem, an attempt has been made to hold some of the undoubtedly important variables reasonably constant (i. e., specimen size and surface condition). Emphasis is being placed on parameters analogous to, or in addition to, porosity and grain size, but which in some way may also account for the more subtle changes of texture and bond strength that result from different firing temperatures or modes of preparation. Within the group of variables being studied, no attempt has been made to isolate one at a time. Instead, all parameters are being varied concomitantly, and multiple regression methods will be applied to the final experimental results. Knudsen⁽¹⁵⁻¹⁾

used this procedure to evaluate the constants for thoria in his empirical strength equation:

$$S = k d^{-a} e^{-b_p p} \quad (15-1)$$

where

S is the strength of a porous brittle polycrystalline body

d is mean grain diameter

p is volume fraction of pores

k, b_p, a = constants

Since regression analysis is more conveniently used with linear relationships, Eq. (15-1) was converted to the logarithmic form:

$$\ln S = \ln k - a \ln d - b_p p \quad (15-2)$$

In cases where Eq. (15-1) (and analogs for the elastic and shear moduli suggested by Spriggs⁽¹⁵⁻²⁾ and Spriggs and Brissette⁽¹⁵⁻³⁾) does not fully describe the data, the discrepancy has been assigned to a variability of the constant b (rather than that of a or k). This assumption not only gives the best agreement between calculated and measured strengths, but is also consistent with the following physical interpretation of Knudsen. The porosity affects strength through its indirect geometrical influence on the area of the minimum load bearing surface whose general trend is normal to the loading force⁽¹⁵⁻⁴⁾. Knudsen's interpretation suggests that this geometrical relationship (expressed through the term e^{-b_p}) may change with temperature because of differences in the relative importance of necking and shrinkage. On this basis, applicability of the strength equation might be widened if the minimum load bearing area could be directly measured or at least indirectly described by a parameter (other than the porosity) which has a more constant relationship to it. The ambitious task of measuring the minimum load bearing area has been undertaken by Knudsen.

In the present program, consideration is being given the replacement of porosity by a ratio containing the area of grain contact divided by the total area of grain surface (the shared surface + one-half of the unshared surface) in the same volume of material. This ratio appears to be sensitive to changes of contact area produced by necking processes that cause little shrinkage; therefore it may have a more constant relationship than porosity to the load bearing area. Unfortunately, pore boundaries are not clearly delineated in many of the polished and flash-etched sections prepared during this program; consequently, any gain derived from the use of the more refined area ratio would probably be offset by lack of precision of the measurements.

Another parameter that might be considered as a replacement for the porosity term is the elastic modulus, E . This substitution rests on the premise that after correction by the grain size term, the maximum stress in the ceramic (which governs the failure point) is approximately $K \times$ the average stress (which determines the overall deformation). If this is true, b_S in Eq. (15-1) equals $K b_E$ in the analog for the elastic modulus. Some corroboration for this relationship may perhaps be seen in Sprigg's⁽¹⁵⁻²⁾ observation that b_E , like b_S , varies with the fabrication conditions.

The special value of E in an empirical strength equation arises from the fact that in addition to providing a measure of the load bearing area, it should also be sensitive to variations of grain contact strength and deformability. Any weakening of the contacts caused by lowering the firing temperature or raising the impurity content should act both to increase the contribution of grain boundary slip to the total deformation and to reduce the stress level needed to initiate cracking in the contact zones. The question is, however, just how important these

effects are at room temperature, compared to the strength and deformation of the intragranular material.

The occurrence of extensive grain boundary slip in dense polycrystalline MgO at room temperature is confirmed by the internal friction measurements of Hanna and Crandall⁽¹⁵⁻⁵⁾ who found that Q^{-1} rises with increasing total grain surface area. Furthermore, their values of Q^{-1} are more than an order of magnitude higher than is generally found in MgO single crystals. Still, the close agreement between dynamic and static values of E for unheated dense ceramics strongly suggests that the sum effect of anelastic movements is relatively small compared to the total elastic deformation of the grains themselves. However, as the porosity rises, intergranular slip may make an increasing relative contribution both to the total deformation and to the initiation of cracks. This contribution may be much accentuated for those series of specimens in which low firing temperatures and high impurity concentrations limit the development of the highest possible grain contact strengths. The net effect of this variation should be to cause errors in Eq. (15-1) similar to those presently attributed to the variability of b_s and b_E .

If for theoretical reasons it is desired to separate the effects of load bearing area and contact strength, it may be necessary to incorporate an independent function of the latter into Eq. (15-1) to widen the range of its applicability. A function of the internal friction, Q^{-1} , may serve this purpose. This choice is based on two assumptions: (1) that friction losses in polycrystalline oxides are largely caused by grain boundary controlled slip -- even at room temperature, and (2) that an increase of these losses is inversely related to the contact strength. The first point is supported by the much higher losses that occur in polycrystalline ceramics than in single crystals of the same substance, and by

the grain size dependence found by Hanna and Crandall. The second point is not true for raw Q^{-1} measurements; these must first be normalized with respect to their dependence on grain size and possibly porosity (remembering that the variation of Q^{-1} with porosity may partly reflect a concomitant change of contact strength). The normalization might be carried out by using multiple regression methods to establish the proportion of the total variance of Q^{-1} might be assigned to variations of grain contact strength. This procedure will be applied to the Q^{-1} data measured during this program; however the poor precision of the internal friction measurements makes the value of this project somewhat doubtful for all but very large differences of intergranular strength.

To summarize, the primary objective of this program is to extend the applicability of an empirical strength equation based on nondestructively measured parameters. At the present time, the following specific approaches appear most promising:

(1) Wherever metallographic sections permit, porosity will be replaced by a ratio of grain contact area per unit volume of material, S_c , divided by one-half of the total grain surface area, S_t , in the same volume. The porosity term might then appear as:

$$ke^{-b(1 - 2S_c/S_t)} \quad (15-3)$$

or, following the Balshin form:

$$K \frac{2S_c}{S_t}^m \quad (15-4)$$

where b and m are hopefully constant. The areas in question may be statistically determined by the method of Smith and Guttman⁽¹⁵⁻⁶⁾ i.e.;

$$S_c = 2 N_c / L \quad (15-5a)$$

and

$$S_t = 2 N_s L \quad (15-5b)$$

where N_c and N_s are the number of intersections in a metallographic section between a traverse line of known length, L , and grain contacts, N_c , or grain surface, N_s .

(2) The porosity term will be replaced by a function of the elastic modulus -- probably a term of the form KE . This is based on the following premises:

$$S = e^{-b_S P} \quad (\text{grain size, etc. being constant}) \quad (15-6a)$$

$$E = e^{-b_E P} \quad (15-6b)$$

$$b_S = k b_E \quad (15-6c)$$

(Both b_S and b_E are considered as variables in (15-6a) and (15-6b) varying for example, with the impurity concentration or mode of fabrication).

(3) Attempts will be made to refine the grain size term d^{-2} by adding a range parameter. This might be the standard deviation of a randomly chosen population of grains from its mean diameter. This term might serve to compensate for the opposed effects of cracks tending to nucleate within or adjacent to the largest grains, and for smaller grains tending to act as barriers to the propagation of these cracks.

A secondary objective of the program is to provide additional information on the variation of E and Q^{-1} with p and d for Al_2O_3 ceramics prepared by different methods. Refinements such as the substitution of $1 - 2S_c/S_t$ for p , or the

incorporation of an internal friction term to account for changes of grain contact strength will be used wherever possible.

2. EXPERIMENTAL PROCEDURES

A. Preparation of Aluminum Oxide Specimens

Aluminum Oxide ceramics having an Al_2O_3 content above 99 per cent, a range of grain sizes of at least two orders of magnitude, and porosities varying from less than 0.5 percent to 25 percent, have been prepared by the methods outlined in Table 15-I. Each group number represents eight or more specimens except for 12686-9 which consisted of six. Specimens were in the form of bars measuring approximately 1.5 to 1.6 in. long, 0.2 in. wide, and 0.1 to 0.13 in. thick. All were ground flat and parallel to ± 0.001 in. with the same grinding wheel. After grinding, the bars were washed in organic solvents and distilled water, and dried at about 500 °C.

B. Strength Measurements

Bending strength was measured with a four point loading fixture mounted on a swivel head. The span between the outer loading points (all loading points were 3/16 in. diam. hardened steel rods) was 1.312 in. and between the inner points, 0.436 in. Cushioning the specimens from the inner rods with a sheet of 1/32 in. polyethylene reduced the coefficient of variation and raised the incidence of failure between, rather than at the bearing points. Load was applied at a constant rate of about 1-1/2 lb-sec; since the elastic moduli of the specimens differed, this constant loading rate resulted in a variable strain rate. However, the variation was probably less than ten fold and according to Task 2, the strength of Al_2O_3 appears to be invariant over a much larger range.

Table 15-I
PROCEDURES FOR PREPARING ALUMINUM OXIDE CERAMICS

Group No.	Materials	Procedure	Max. Firing Temperature (°C)	Time at Max. T	Atmosphere	Density (g/cc)
11950-12	Alucer Mix*	c. p. and sintered	1820	1 3/4 hr	O ₂	3.97
11950-16	Alucer Mix	c. p. and sintered	1810-1845	3/4 hr	air	3.92
12346-15-0 -8 -10	Alucer Mix + various amts. of Therman***	c. p. and sintered	1700	4 hr	gas combust prod.	3.70 3.51 3.69
12346-22	Alucer Mix	h. p. at 3000 psi	1555	5 min	Ar carb. gases	3.93
12686-4	Alucer Mix	h. p. at 600 psi	1550	5 min	Ar carb. gases	3.99
12686-7	Alucer Mix	h. p. at 500 psi	1655	5 min	Ar carb. gases	3.93
12686-9	Alucer Mix	h. p. at 3000 psi	1650	8 min	Ar carb. gases	3.97
12686-10	Alucer Mix	h. p. at 3000 psi	1655	5 min	Ar carb. gases	3.98
12686-12	Norton ++ 38-900	h. p. at 1000 psi	1655	5 min	Ar carb. gases	3.37
12686-13	Alcoa A 14 ^x	h. p. at 1000 psi	1660	5 min	Ar carb. gases	3.18
12686-11-12	54% Alucer MC 26% Alucer MA 20% Norton 38-900	c. p. and sintered	1700	15 min	gas combust prod.	3.04
12686-11-13	35% Alucer MC 17% Alucer MA 50% Norton 38-900	c. p. and sintered	1700	15 min	gas combust prod.	3.06
12686-11-14	17% Alucer MC 9% Alucer MA 50% Norton 38-900	c. p. and sintered	1700	15 min	gas combust prod.	3.02
12686-11-15	Norton 38-900	c. p. and sintered	1700	15 min	gas combust prod.	3.13
12686-11-16	Alcoa A 14	c. p. and sintered	1700	15 min	gas combust prod.	2.97

* Alucer Mix consists of 1/3 Cullen's Alucer MA; 2/3 Alucer MC + 0.25% MgO (added as the basic carbonate) to inhibit grain growth.

** c. p. cold pressed; h. p. = hot pressed in a graphite die.

*** Therman is a very finely divided carbon black.

+ Combustion products of natural gas in a hemmery kiln-probably slightly reducing.

++ Carbonaceous gases from the graphite hot pressing die being heated in an Ar atmosphere.

+++ Norton 38-900 aluminum, electronic grade.

x Alcoa A-14, -325 mesh, acid washed.

C. Elastic Modulus

Elastic modulus, E, was measured sonically in flatwise bending vibration. One end of a specimen bar was supported by a very fine wire located at or near the vibration node, while the other end rested on a 1-mm diameter sapphire rod connected to a ceramic phonograph pickup cartridge. The specimen was air driven at its center by a conventional P. A. system driver collimated to some extent through a 1/4-in. aperture in a 1/4-in. thick plate of sponge rubber. Reasonance was determined both by observing the Lissajou figure with an oscilloscope and noting the maximum deflection of a milliammeter. Elastic modulus was calculated from the resonant frequency with the aid of Hasselman's tables.⁽¹⁵⁻⁷⁾ Approximate values of Poisson's ratio (which varies with the porosity) were taken from the curve presented by Spriggs and Brissette.⁽¹⁵⁻³⁾

D. Bulk Specific Gravity, Porosity

The specific gravity of the specimen bars was measured by the liquid displacement method, using Merriam (gage) oil. After being weighed in air, the bars were vacuum-impregnated with the oil to avoid drifting values during subsequent immersed weighings. This necessitated a correction for the decrease in buoyancy caused by oil filling some or all of the specimen pores. The correction factor was determined by weighing the oil-filled bars after their surfaces were wiped clean with a slightly oily cloth. The specific gravity, G, is then given by:

$$G = \frac{Wd}{W_o - W_s} \quad (15-7)$$

where W is the weight in air of the dry specimens

d is the specific gravity of the oil at the measuring temperature (25°C) relative to water at 4°C

W_o is the final weight of the specimens in air after having absorbed oil, and

W_s is the weight of specimens while suspended in oil.

Oil was used in place of water because the specimen must be suspended in the liquid by some sort of wire hanger. The relatively high surface tension of water causes the apparent weight of the hanger to vary -- a difficulty which is much reduced with oil. Using this method, a specific gravity of 3.990 ± 0.005 was obtained for a block of sapphire. This value was the basis for calculating the total porosities from the measured bulk specific gravities.

E. Internal Friction

Internal friction, Q^{-1} , was measured with essentially the same apparatus and specimen mounting system used for the determination of E. However, the amplified signal from the pick-up cartridge was diverted to a Bruell and Kjaer high speed level recorder which logarithmically plotted the damping of the specimen vibration after the driver was shut off. The slope of the damping curve -- which ideally is a straight line -- is read as a reverberation time, RT, with a special protractor. Reverberation time may then be converted to Q^{-1} with the relation:

$$Q^{-1} = \frac{4.40}{RT \times f} \quad (15-8)$$

where f is the resonant frequency of the specimen at which the damping measurement was carried out.

In actual practice the damping curve was not always a straight line, possibly because of interference by a background damping effects (from the mounting system, etc.) at higher

vibration amplitudes. In such cases, an average slope was used for the calculation of RT.

F. Grain Size, Surface Area, and Grain Contact Area

Polished sections have been prepared for representatives of each of the specimen groups described in Table 15-I and in addition, for Lucalox, Wesgo AL-995, and for two grades of Norton Alundum. Flash etching⁽¹⁵⁻⁸⁾ was used to make the grain boundaries visible. This is a very rapid and effective procedure based on the selective evaporation of Al_2O_3 exposed to the slightly reducing flame of an oxy-acetylene torch for from five to ten seconds. The temperature is fairly critical, being just below the melting point of the oxide. As yet no grain size measurements have been made from the polished and etched specimens which, however, have been nearly all photographed.

3. EXPERIMENTAL RESULTS

Since grain size data are not yet available, the variation of S and Q^{-1} cannot be interpreted in this report. However, Table 15-II presents a summary of the properties measured thus far for the specimens fabricated at ARF and for a few commercial ceramic bodies. Each listed strength is the average of eight or more individual values (except for six in the case of 12686-9 and four in the case of Lucalox). The tabulated porosities, elastic moduli, and internal frictions are in the main the average of two or three representative specimens of each group. The coefficients of variation of the porosity and elastic modulus are generally considerably lower than those of the strength and internal friction. The high variance of S in some groups is probably not related to the loading technique since there is consistently low variance in groups made by other methods. In the

Table 15-II
PROPERTIES OF ALUMINUM OXIDE CERAMICS PREPARED BY DIFFERENT METHODS

Group No.	Avg. Sp. Gr.	Avg. Porosity (%)	Avg. Bend Strength (psi)	Max. Bend Strength (psi)	Avg. E (10^6 psi)	Avg. Q $\times 10^4$
11950-12	3.97 \pm 0.5%*	0.5	20,900 \pm 11%**	24,500	55.7 --*	2.4 --*
11950-16	3.92 \pm <0.2%	1.8	34,800 \pm 13%	40,800	54.7 \pm 0.2%	3.4 \pm 18%
12346-15-0	3.70 \pm 1.6%	7.5	29,700 \pm 5%	32,400	46.6 \pm 1.7%	4.0 \pm 13%
-8	3.51 \pm 0.6%	12.0	26,400 \pm 6%	28,100	39.2 \pm 1.6%	3.4 \pm 21%
-10	3.69 \pm 0.5%	7.5	37,400 \pm 12%	45,600	45.5 \pm 3.9%	3.6 \pm 14%
12346-22	3.93 \pm 0.3%	1.5	41,600 \pm 20%	53,200	53.2 \pm 0.5%	5.6 \pm 4%
12686-4	3.59 \pm 0.8%	10.0	32,900 \pm 12%	39,400	40.4 \pm 3.1%	3.9 \pm 8%
12686-7	3.93 \pm 0.8%	1.5	35,800 \pm 17%	48,300	53.7 \pm 0.1%	3.6 \pm 17%
12686-9	3.97 \pm 0.3%	0.5	31,800 \pm 19%	40,600	55.1 \pm <0.1%	5.5 \pm 9%
12686-10	3.98 \pm 0.5%	0.3	34,200 \pm 6%	36,400	55.3 \pm 0.4%	4.0 \pm 2%
12686-12	3.37 \pm 1.2%	15.5	22,100 \pm 6%	23,600	34.3 \pm 2.7%	8.0 \pm 13%
12686-13	3.18 \pm 1.6%	20.3	21,400 \pm 11%	24,300	31.8 \pm 5.8%	8.1 \pm 5%
12686-11-12	3.04 \pm 8.5%	23.8	25,200 \pm 17%	31,200	31.6 \pm 5.1%	7.3 \pm 3%
-13	3.06 \pm 3.3%	23.3	24,900 \pm 26%	37,000	27.3 \pm 6.4%	5.7 \pm 5%
-14	3.02 \pm 0.7%	24.3	23,100 \pm 19%	31,700	26.5 \pm 0.4%	7.0 \pm 9%
-15	3.13 \pm 0.6%	21.6	14,200 \pm 16%	18,000	24.6 \pm 5.4%	7.0 \pm 26%
-16	2.97 \pm 1.7%	25.6	12,900 \pm 11%	15,900	20.9 \pm 3.2%	6.2 \pm 37%
Lucalox	3.97 --	0.5	31,300 \pm 10%	35,400	56.8 \pm 1.9%	3.8 \pm 3%
Wesgo AL-995	3.84 --	3.8	32,700 \pm 7%	36,200	51.5 \pm 1.2%	4.2 \pm 17%
Alundum (medium)	2.07 --	48.0	2,050 \pm 10%	2,280	3.5 \pm 0.8%	16.0 \pm 25%
Alundum (coarse)	1.91 --	52.0	610 \pm 11%	840	1.6 \pm 16.4%	54.0 \pm 20%

* Percent max. relative variation = max deviation \times 100/average density, elastic modulus, or Q.⁻¹

** Coefficient of variation = standard deviation \times 100/average strength.

case of the internal friction, it is more likely that the measuring technique itself introduces the variance of Q^{-1} . Since the specimens made contact with both a thin supporting wire and a sapphire pickup rod, background damping might well be an important and variable factor.

Detailed analysis of the data of Table 15-II has not yet begun and is being deferred until grain size measurements have been completed. However, a preliminary plot of E vs p is shown in Fig. 15-1; the line being drawn (for the present) on purely a visual basis. Nevertheless, considering the variety of preparation methods, there is a surprising constancy of b (= approximately 3.3) for all but the Alundum specimens. The scatter of points near 25 percent porosity occurs largely within a single group of specimens, which also show considerable variability of p and E .

The measured values of E for the Alundum specimens (3.5 and 1.6×10^6 psi) definitely do not fall on the line of Fig. 15-1. Letting $b = 3.3$ and $E_0 =$ approximately 58×10^6 psi, E values calculated for these specimens are approximately 12 and 10×10^6 psi. The source of the anomaly may lie in a significant difference of intergranular bond strength; Alundum consists of dense Al_2O_3 grains bonded by a glassy phase, whereas little if any glassy cement occurs in any of the other ceramics. On this basis, substitution of KE for e^{-bp} in the strength equation might permit a fairly close prediction of the strength of Alundum with constants obtained from measurements on the other, very different types of alumina ceramics. Even the addition of a normalized internal friction term into the equation for E , appears to have some promise for making up at least part of the discrepancy. If one or more of the refinements described in this report turns out to be effective in enabling a single set of constants to

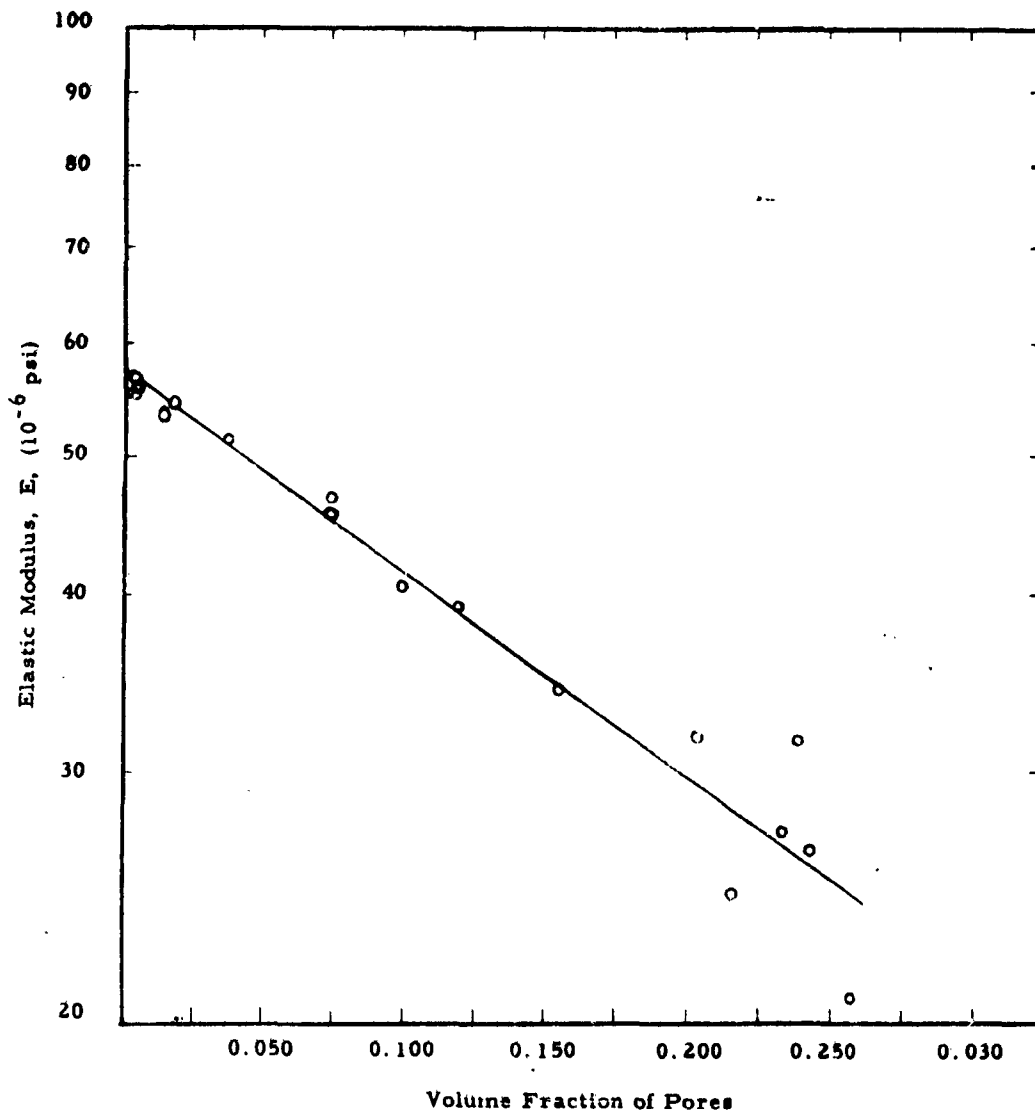


Fig. 15-1 POROSITY DEPENDENCE OF ELASTIC MODULUS OF ALUMINUM OXIDE CERAMICS

predict the strengths of materials as widely divergent in mode of manufacture and composition as Lucalox and Alundum, the main objective of this program will have been fulfilled.

Part Two: Theoretical Studies
Principal Investigator: N. A. Weil
Armour Research Foundation

4. INTRODUCTION

A substantial amount of effort, past and present, has been expended on the subject of the behavior of two-phased materials consisting of a matrix containing discrete and dispersed inclusions of a second material having different properties from those of the matrix. The degree of interest evidenced in the subject is quite understandable, in view of the fact that cermets, some binary alloys, of the intermetallic substances and some of the ceramics, as well, are composed precisely in the fashion described above. Furthermore, almost all of the single-phase ceramics contain a certain degree of porosity; the successful development of a theory applicable to two-phase materials would also allow for the treatment of a porous material (containing only closed pores) by the simple expedient of setting the rigidity of the included phase equal to zero.

Despite the importance of the subject, the specific appreciation of the current state of understanding of theoretical treatments, or their specific applicability, is inadequately understood. Part Two of Task 15, therefore, was initiated to collect all of the evidence available on theoretical predictions regarding the effect of porosity on elastic properties, to extend the theories where such appeared warranted, to define the extent to which analytical studies are capable of predicting the actual performance of materials.

Several points are worthy of note at the very outset. The first is that the primary purpose of this study is to define theoretically the anticipated behavior of porous oxide ceramics.

Thus, although porosity is recognized to be but a special case of the more general problem of the elastic inclusions contained in a matrix of different properties, the latter problem will be treated here only insofar as it assists with shedding light on the problem of the effect of porosity.

Secondly, attention will be concentrated solely upon the effects of porosity. While it is recognized that numerous other effects are also operative in determining the strength of elastic substances, it will be assumed that such effects, if occurring covariantly with porosity changes, can be suitably evaluated by existing theoretical or empirical formulations (e. g., the effect of grain size being accounted for by the semi-empirical Petch equation or the empirical Knudsen formulation).

Lastly, and most importantly, the limitations and applicability of analytical studies should be recognized. In this regard it is quite a different matter whether one deals with elastic properties or the strength of the material. The elastic properties, represented by Young's modulus E , the shear modulus G , the bulk modulus K , and Poisson's ratio ν , reflect the bulk properties of the material. Phrased in another way, these properties measure the average response of a large sample of the material to elastic loads; therefore, idealizations of material properties and porosity texture, necessarily made in analytical attacks on the problem, are fully applicable to the treatment of the effect of porosity upon the resulting elastic constants of the material.

Such, however, is not at all the case when it comes to the consideration of the effect of porosity upon strength. Strength in this sense is synonymous with fracture, and fracture depends intrinsically upon the texture and nature of pores. In fact, two separate elements come into play now: one is the bulk weakening effect associated with the volumetric removal of the material by the presence of the pores, the other one is the stress concentrations associated with the shape, size and orientation of pores.

It is primarily the latter that causes extreme problems, and prevents the rigorous analytical treatment of the effect of porosity upon strength. The case can be illustrated readily by considering the extremes of a fully dense ceramic plate with a single, infinitely sharp notch, and another one containing many uniformly dispersed perfectly spherical cavities. Even though the former will have a density near theoretical values, it will fail far sooner than the latter which contains a substantial amount of pores. This comparison, while somewhat forced, demonstrates the extreme importance of the shape and texture of pores upon the resulting fracture strength of the substance. Furthermore, this comparison also explains why rigorous theories cannot be expected to solve the porosity-strength relationship; rather, one must adopt an empirical expression based either upon semi-rational analytic principles or upon experimentally observed behavior.

Because of the divergent effect of pores on elastic constants on the one hand, and strength on the other, these two topics will be treated separately below. Where appropriate, the assumptions and limitations involved in analytical derivations will be fully defined.

5. EFFECT OF POROSITY ON ELASTIC CONSTANTS

A. The State-of-the-Art

All theoretical analysis dealing with the effect of porosity upon the elastic properties assume that two-phased or porous materials can be described by an elastic, homogeneous and isotropic matrix, containing a uniform volumetric concentration of another elastic, homogeneous and isotropic matrix generally in the form of equi-distant discrete spheres placed according to a predetermined packing arrangement. Thus, the problem reduces to that of a material which can be regarded as being quasi-homogeneous and quasi-isotropic.

The first attempt to solve the problem consisted of a study of the bulk compressibility of liquids containing uniformly

suspended rigid spherical particles⁽¹⁵⁻⁹⁾ where volume concentration was assumed small enough to prevent particle interaction. The case of small concentrations, assuming always spherically shaped inclusions, has been solved for a variety of conditions: empty holes in an elastic solid⁽¹⁵⁻¹⁰⁾, rigid inclusions in an elastic solid⁽¹⁵⁻¹¹⁾, and elastic inclusions in another elastic material^(15-12, 15-13). Recently, even the problem of the early plastic behavior of polyphased materials containing a small concentration of inclusions has been attacked⁽¹⁵⁻¹⁴⁾ with some success.

The consideration of finite (large) concentrations poses far more difficult problems. Most of this effort has been to extend Einstein's work⁽¹⁵⁻⁹⁾ to higher concentrations in a semi-empirical fashion; results have been differing formulas, at times leading to direct contradictions. A review of these semi-empirical attempts is found in two excellent summary papers^(15-15, 15-16).

The effort which, instead of attempting closed-form solutions, concentrates on defining the upper and lower bounds for the elastic moduli has been most fruitful. If these bounds are close enough, then an empirical relationship remaining within these bounds can be accepted as a reasonably valid description of overall behavior. The first solution employing bounds on elastic moduli was presented by Paul⁽¹⁵⁻¹⁷⁾, who obtained bounds for Young's modulus under a simple tension deformation for an admissible displacement field, using variational theorems of the theory of elasticity. While such bounds are exact, they are generally too far apart to give good estimates of the effective true solution. A more successful derivation of this nature was carried out by Hashin⁽¹⁵⁻¹⁸⁾; because of the importance of this work to the present analysis, its basic assumptions and results will be reviewed later.

Because of their application to earlier work relating to porosity effects, it is worthwhile to identify the results of Mackenzie's derivations, and to review briefly some of the empirical formulas proposed. Mackenzie⁽¹⁵⁻¹⁰⁾ considered the

problem of a spherical cavity surrounded by a thick shell of the solid; the bulk of the porous material lying outside of this shell is represented by an "equivalent homogeneous" material forming a continuum. The elastic constants K and G are then determined by applying a hydrostatic pressure and homogeneous shear, respectively, to the outer sphere. The effective constants resulting from these assumptions are given by

$$\frac{1}{K^*} = \frac{1}{1-p} + \frac{3 K_0}{4 G_0} \frac{p}{1-p} + A p^2$$

$$\gamma = 1 - \frac{5 (3 K_0 + 4 G_0)}{9 K_0 + 8 G_0} p + B p^2 \quad (15-2)$$

where

$K = K/K_0$ is the normalized bulk modulus

$\gamma = G/G_0$ is the normalized shear modulus

p is the absolute porosity (volume fraction pores)

A, B are constants

and the subscript zero refers to the dense (matrix) material, the asterisk to the properties of the porous substance. The analysis does not yield the value of the coefficients A and B . Actually, the constant B can be evaluated from the boundary condition that $\gamma^* = 0$ at $p = 1$; then, if it is assumed that $K_0/G_0 = 2.16$ (which corresponds to $\nu = 0.3$), $B = -0.91$ results. No such simple expedient can be found to determine the constant of A , the numerical value of which must be derived experimentally. The remaining two elastic constants can be found from the basic relationships

$$\nu = \frac{3K - 2G}{2(3K + G)} ; E = \frac{9KG}{3K + G} \quad (15-3)$$

which are valid for the dense as well as the porous substance.

The empirical expression most frequently employed is that of Spriggs⁽¹⁵⁻²⁾ and Spriggs and Vasilos⁽¹⁵⁻¹⁹⁾;

$$\eta^* = e^{-bp} \quad (15-4)$$

where $y = E/E_0$, b is a constant and e is the Naperian logarithm base. While Spriggs and Vasilos did not so specify, presumably similar expressions are assumed to hold either for K or ν .

Numerous experimental studies were carried out to determine the observed effects of porosity, and to confirm the validity of proposed analytical or empirical relationships. Of these, the work of Coble and Kingery⁽¹⁵⁻²⁰⁾ which provided some support for the predictions of Mackenzie; the work of Spriggs and Vasilos already quoted; and Knudsen's⁽¹⁵⁻²¹⁾ brief summary note which appeared to confirm the formulation of Eq. 15-4, are worthy of note even though rather wide variation in experimental results exist. Interestingly, the value of b was found to equal 4.5 for both hot-pressed Al_2O_3 and MgO by Spriggs and Vasilos⁽¹⁵⁻¹⁹⁾; their reinterpretation of the Coble and Kingery results, in turn, yielded a value of $b = 2.6 - 2.8$ for slip cast and sintered Al_2O_3 ; a similar reinterpretation of Lang's data provided a value of $b = 3.0$ for cold-pressed and sintered MgO . Knudsen⁽¹⁵⁻²¹⁾, in turn, derived a general value of $b = 3.95$ from a collection of all previous experimental work on porous polycrystalline Al_2O_3 .

While the empirical expression Eq. 15-4 provides a reasonably acceptable fit to observed behavior, it has three shortcomings. First, as all empiricisms, it relies on arbitrarily chosen constants, in this case b , the values of which must be determined experimentally. As noted, various experimenters have found the value of b to vary from 2.6 to 4.5. While variation may be assumed modest, its effects, in fact, are enormously magnified in that b appears in the exponent of Eq. 15-4. Secondly the proposed relationship neither satisfies the basic interrelations existing between elastic constants, as defined by Eq. 15-3, nor accounts for the effect of other factors, such as K or ν , which

necessarily must enter this relationship. Thirdly, and most importantly, the proposed form of Eq. 15-4 does not satisfy the boundary condition of $y^* = 0$ when $p = 1$. Instead, the formula yields $y^* = e^{-b}$ at $p = 1$ which, at an assumed value of $b = 4$, provides $y^* = 0.0182$. Because this is patently impossible, Eq. 15-4 must deviate in an increasing fashion as $p \rightarrow 0$.

The work of Hashin⁽¹⁵⁻¹⁸⁾, being based on rational analytical assumptions, suffers from none of the shortcomings. In fact, the rational aspects and correctness of predictions of the Hashin theory are so promising that a further development of this work appeared to be amply warranted. It is worth briefly mentioning here that Hasselman and Sheffer⁽¹⁵⁻²²⁾ came to identical conclusions regarding the shortcomings of the Spriggs equation and the promise inherent in the Hashin development; their interpretation of the latter theory, and the results of their experimental work will be reviewed later.

B. Analytical Studies

The Hashin solution⁽¹⁵⁻¹⁸⁾, the basis of this analytical work, is based on the assumptions that the inclusions are spherical, uniformly spaced, and the action of the heterogeneous material onto a single inclusion is transmitted through a spherical shell lying wholly in the matrix. Beyond these assumptions, however, the treatment is quite general, and is not confined to small concentrations of the included substance. The bounds on the elastic moduli are obtained by selecting a unit volume representing a quasi-homogeneous and quasi-isotropic material, and analyzing it under conditions of (1) a space-wise homogeneous stress system which supplies the lower bounds for the solutions, and (2) a linear surface displacement associated with a uniform strain tensor which supplies the upper bounds. The solutions, obtained by a minimization of strain energy, show that for the bulk modulus the bounds merge into a single expression

$$k^* = 1 + \frac{3(1-\nu_0)(k-1)c}{2(1-2\nu_0) + (1+\nu_0)[k - (k-1)c]} \quad (15-5)$$

where c is the volumetric concentration of elastic inclusions, the subscripts and superscripts are as previously defined, and unsubscripted quantities stand for the properties of the inclusions (e. g., $k = K/K_0$; $k^* = K^*/K_0$).

Expressions for the shear modulus yielded two distinct bounds, given by

$$\gamma_1^* = \frac{1}{1 + \sum_{i=1}^k (1-\gamma_i) \gamma_{1i}^{\sigma} c_i} \quad (15-6)$$

$$\gamma_2^* = \left[1 + \sum_{i=1}^k (\gamma_i - 1) \gamma_{1i}^{\epsilon} c_i \right]$$

where $\gamma_1^* < \gamma^* < \gamma_2^*$ and the notation is analogous to that used before, the expressions for γ being given by

$$\gamma_1^{\sigma} \left\{ \frac{2(1-\gamma)}{5(1-\gamma_0)} (p^7 - p^5) \right\} + \left\{ \gamma_2^{\sigma} \left[-7 - 10\nu - (7 - 10\nu_0) \theta \right] 4p^7 - (7 + 5\nu_0) \theta \right\} = 0 \quad (15-7)$$

$$\gamma_1^{\sigma} \left[\gamma + \frac{7-5\nu_0}{15(1-\nu_0)} (1-\gamma) (1-p^3) \right] + \gamma_2^{\sigma} 21\theta \left(\frac{1}{p^2} - 1 \right) = 1$$

$$\gamma_1^{\epsilon} \frac{2(1-\gamma)}{5(1-\nu_0)} (p^7 - p^5) + \gamma_2^{\epsilon} \left\{ \left[7 - 10\nu - (7 - 10\nu_0) \theta \right] 4p^7 + 4(7 - 10\nu_0) \theta \right\} = 0 \quad (15-8)$$

$$\gamma_1^{\epsilon} \left[\gamma + \frac{7-5\nu_0}{15(1-\nu_0)} (1-\gamma) + \frac{2(4-5\nu_0)}{15(1-\nu_0)} (1-\gamma) p^3 \right] + \gamma_2^{\epsilon} 21\theta \left(\frac{1}{p^2} - 1 \right) = 1$$

with

$$0 = \frac{4(7 - 10\nu) + \gamma(7 + \dots)}{35(1 - \nu_0)} ; p^3 = c$$

It will be noted that Eq. 15-6 are written for the general case of i inclusions of different elastic properties. For the case of a single inclusion, the subscript i and summation signs would simply vanish from these expressions.

It was found, following numerical evaluation, that the bounds on shear modulus represented by Eq. 15-6 are very close together, and that a simple formula, analogous in form to that of Eq. 15-5, provided results which were always within the defined bounds. This expression is given by:

$$\gamma^* = 1 + \frac{15(1 - \nu_0)(\gamma - 1)c}{7 - 5\nu_0 + 2(4 - 5\nu_0)[\gamma - (\gamma - 1)c]} \quad (15-9)$$

With Eq. 15-3, 15-5 and 15-9, it is now possible to define the third major item of interest, notably the value of Young's modulus for the heterogeneous substance. Specifically, Eq. 15-5 and 15-9 can be put into the form

$$\begin{aligned} K^* &= \frac{b_1 K + a_1 [1 + (K - 1)c]}{a_1 + b_1 [K - (K - 1)c]} \\ \gamma^* &= \frac{b_2 \gamma + a_2 [1 + (\gamma - 1)c]}{a_2 + b_2 [\gamma - (\gamma - 1)c]} \end{aligned} \quad (15-10)$$

where

$$\begin{aligned} a_1 &= 2(1 - 2\nu_0) ; & b_1 &= 1 + \nu_0 \\ a_2 &= 7 - 5\nu_0 ; & b_2 &= 2(4 - 5\nu_0) \end{aligned} \quad (15-11)$$

It can be shown now that the second of Eq. 15-3 can be put into the form:

$$\frac{E^*}{E_o} = \frac{9 K^* G^*}{3 K^* + G^*} \frac{3 K_o + G_o}{9 K_o G_o} = \frac{3 \frac{K_o}{G_o} + 1}{3 \frac{K_o}{G_o} \frac{G_o}{G^*} + \frac{K_o}{K^*}} \quad (15-12)$$

But, from Eq. 15-3,

$$\frac{K}{G} = \frac{2(1+\nu)}{3(1-2\nu)}$$

and, when the notation of Eq. 15-11 is used,

$$K_o/G_o = 4 b_1/3 a_1 \quad (15-13)$$

With this result, Eq. 15-12 can be rewritten in the dimensionless form adopted here:

$$\eta^* = \frac{4 \frac{b_1}{a_1} + 1}{4 \frac{b_1}{a_1} \frac{1}{\gamma} + \frac{1}{K^*}} \quad (15-14)$$

when Eq. 15-10 are inserted into Eq. 15-14

$$\eta^* = f_1/f_2$$

where

$$f_1 = (a_1 + 4b_1) \left\{ \frac{b_1}{a_1} K + \left[1 + (K-1)c \right] \right\} \left\{ b_2 \gamma + a_2 \left[(1+(\gamma-1)c) \right] \right\}$$

$$f_2 = (a_1 + 4b_1) \left(1 + \frac{b_1}{a_1} K \right) (a_2 + b_2 \gamma) +$$

$$\left[- (a_1 a_2 + 3a_2 b_1 - 4b_1 b_2) + 2b_1 \left(\frac{2b_1 b_2}{a_1} + a_2 \right) K \right. \\ \left. + (a_1 a_2 - 7b_1 b_2) \gamma - b_1 \left(\frac{4b_1 b_2}{a_1} - a_2 - 3b_2 \right) K \gamma \right] c - \\ b_1 (a_2 + 4b_2) (1-K) (1-\gamma) c^2 \quad (15-15)$$

or, when Eq. 15-11 are resubstituted into this result,

$$\begin{aligned}
 f_1 &= 2 \left\{ \frac{1 + \nu_0}{2(1 - 2\nu_0)} K + \left[1 + (K - 1)c \right] \right\} \left\{ 2(4 - 5\nu_0)\gamma + (7 - 5\nu_0) \left[1 + (\gamma - 1)c \right] \right\} \\
 f_2 &= 2 \left(1 + \frac{1 + \nu_0}{2(1 - 2\nu_0)} K \right) \left[(7 - 5\nu_0) + 2(4 - 5\nu_0)\gamma \right] + \\
 &\quad \left[-(1 - 3\nu_0)(1 - 5\nu_0) + \frac{2(1 + \nu_0)(5 - 7\nu_0)}{1 - 2\nu_0} K - \right. \\
 &\quad \left. 2(7 + 4\nu_0 - 15\nu_0^2)\gamma + \frac{(1 + \nu_0)(1 - 5\nu_0)(5 - 6\nu_0)}{1 - 2\nu_0} K \gamma \right] c - \\
 &\quad (1 + \nu_0)(13 - 15\nu_0)(1 - K)(1 - \gamma)c^2
 \end{aligned} \tag{15-16}$$

To this extent the derivation concerns a heterogeneous material containing an elastic dispersed phase within a matrix of different elastic properties. Focusing attention on the porous material, the problem simplifies considerably; the elastic properties of the inclusions can now be represented by vanishing values, while the symbol c is replaced by p . Thus,

for a porous material $K = \gamma = 0$; $c = p$

so that Eq. 15-10 and 15-15 reduce to

$$\begin{aligned}
 K^* &= \frac{a_1(1 - p)}{a_1 + b_1 p} \\
 \gamma^* &= \frac{a_2(1 - p)}{a_2 + b_2 p} \\
 \eta^* &= \frac{a_2(a_1 + 4b_1)(1 - p)}{a_2(a_1 + 4b_1) + b_1(a_2 + 4b_2)p}
 \end{aligned} \tag{15-17}$$

Reinserting Eq. 15-11 into these results and rearranging the expressions to a uniform representation, one arrives at the extremely simple results

$$\begin{aligned}K^* &= \frac{1-p}{1+k_1 p} \\ \gamma^* &= \frac{1-p}{1+k_2 p} \\ \eta^* &= \frac{1-p}{1+k_3 p}\end{aligned}\tag{15-18}$$

where

$$\begin{aligned}k_1 &= \frac{1+\nu_o}{2(1-2\nu_o)} \\ k_2 &= \frac{2(4-5\nu_o)}{7-5\nu_o} \\ k_3 &= \frac{(1+\nu_o)(13-15\nu_o)}{2(7-5\nu_o)}\end{aligned}\tag{15-19}$$

As can be seen at a glance, Eq. 15-18 satisfy both boundary conditions that

$$\begin{aligned}K^* = \gamma^* = \eta^* &= -1 \text{ at } p = 0 \\ K^* = \gamma^* = \eta^* &= 0 \text{ at } p = 1\end{aligned}$$

Thus, the use of these expressions is not limited to small values of the porosity, but is valid over the entire range of $0 \leq p \leq 1$, subject only to the limitations of the assumptions stated above.

C. Evaluation and Discussion

It is now possible to compare these results with those of Hasselman and Shaffer⁽¹⁵⁻²²⁾ who conducted an extremely well documented study on the effect of graphite inclusions and porosity

on the elastic and strength properties of ZrB_2 . They proposed a general expression, valid for all elastic constants, and covering the general case of elastic inclusions in an elastic matrix, rather than its special variant of the simpler case of porosity, of the form

$$\frac{E^*}{E_0} = 1 + \frac{A \left(1 - \frac{E}{E_0}\right) c}{1 - (A + 1) \left[\frac{E}{E_0} + \left(1 - \frac{E}{E_0}\right) c \right]}$$

or, in terms of the notation used here

$$\eta^* = 1 + \frac{A (1 - \eta) c}{1 - (A + 1) \left[\eta + (1 - \eta) c \right]} \quad (15-20)$$

where A is a constant to be determined experimentally, and the form of the equation is assumed to be equally valid for κ^* and γ^* .

To evaluate the validity of this formulation, recourse must be made to Eq. 15-5, which can be brought to the form

$$\kappa^* = 1 + \frac{-3(1 - \nu_0)(1 - \kappa) c}{2(1 - 2\nu_0) - \left[2(1 - 2\nu_0) - 3(1 - \nu_0) \right] \left[\kappa + (1 - \kappa) c \right]}$$

or

$$\kappa^* = 1 + \frac{A_1(1 - \kappa) c}{a_1 - (A_1 + a_1) \left[\kappa + (1 - \kappa) c \right]}$$

where

(15-21)

$$A_1 = -3(1 - \nu_0)$$

$$a_1 = 2(1 - 2\nu_0)$$

Likewise, it can be shown that by a similar manipulation, Eq. 15-9 can be brought to the form

$$\gamma^* = 1 + \frac{A_2 (1 - \gamma) c}{a_2 - (A_2 + a_2) [\gamma + (1 - \gamma) c]}$$

where

(15-22)

$$A_2 = -15 (1 - \nu_0)$$

$$a_2 = 7 - 5 \nu_0$$

Lastly, Eq. 15-15 dealing with η^* , cannot be brought to the form shown above.

The following conclusions become evident from a comparison of Hasselman and Shaffer's form of Eq. 15-20 with that derived from the Hashin solution, as shown in Eq. 15-21 and 15-22.

(1) Equation 15-20 is merely a simplification of the correct form of the expressions, valid only for the special case of $a_1 = a_2 = 1$. To satisfy this condition, however, it is necessary for $\nu_0 = 0.25$ to satisfy $a_1 = 1$ and, alternately, for $\nu_0 = 1.20$ to satisfy $a_2 = 1$. Apart from the contradictions involved in requiring different values of ν_0 for the same material to satisfy the Hasselman-Shaffer form of the equation, the second requirement for ν_0 is patently impossible.

(2) While Hasselman and Shaffer leave the value of A open, to be determined experimentally for each material and each elastic constant, such does not appear necessary in view of the fact that theory predicts specifically the value of A to be expected for each elastic constant.

(3) The expression for $\eta^* = E^*/E$, at this stage of theoretical development, cannot be brought to the form suggested by Hasselman-Shaffer, for the case of elastic inclusions in an elastic matrix. Such simplifications for η^* become possible only for the simpler case of porosity (inclusions with vanishingly small elastic constants).

In conclusion, the Hasselman-Shaffer suggestion, while correct format-wise is an oversimplification of the actual solution. This oversimplification, first, leads to physically impossible stipulations and, secondly, is unnecessary in view of the satisfactory stage of correct theoretical development.

In the simpler case of porosity represented by Eq. 15-18 and 15-19, it is interesting to evaluate the numerical values of the constants appearing in these expressions. This has been carried out, with the appropriate numerical values presented in Tables 15-III and 15-IV. The results compiled in Table 15-IV are, in turn, graphically presented in Fig. 15-2 to 15-4. The following comments are apparent from inspection of these results.

Table 15-III

VALUES OF CONSTANTS FOR ELASTIC MODULI

Poisson's Ratio for Matrix, ν_o	Numerical Values of Constants, from Eq. 15-19		
	k_1	k_2	k_3
0	0.5	1.14285	0.92857
0.1	0.6875	1.07692	0.96923
0.2	1.0	1.0	1.0
0.3	1.625	0.90909	1.00455
0.4	3.5	0.8	0.980
0.5	∞	0.66667	0.91667

(1) The value of the bulk modulus, $\kappa^* = K^*/K$ shows the largest sensitivity to the value of ν_o , the Poisson's ratio for the dense material. The equations correctly anticipate total compressibility of the material, represented by $\kappa^* = 0$, when $\nu_o = 0.5$, regardless of the porosity level. Naturally, this case corresponds to volume constancy in the matrix material, so that total compressibility at $\nu_o = 0.5$ must be interpreted as a

Table 15-IVa

VALUES OF NORMALIZED BULK MODULUS, $K^* = K^*/K_0$, AS A
FUNCTION OF POROSITY AND POISSON'S RATIO OF MATRIX

Absolute Porosity, p	Poisson's Ratio of Dense Substance, ν_0					
	0	0.1	0.2	0.3	0.4	0.5
0	1.0	1.0	1.0	1.0	1.0	0.0
0.1	0.95714	0.84360	0.81818	0.77419	0.66667	0.0
0.2	0.72727	0.70330	0.66667	0.60377	0.47059	0.0
0.3	0.60870	0.58031	0.53846	0.47059	0.34146	0.0
0.4	0.5	0.47059	0.42857	0.36364	0.25	0.0
0.5	0.4	0.37209	0.33333	0.27586	0.18182	0.0
0.6	0.30769	0.28319	0.25	0.20253	0.12903	0.0
0.7	0.22222	0.20253	0.17647	0.14035	0.08696	0.0
0.8	0.14444	0.12903	0.11111	0.08696	0.5263	0.0
0.9	0.06667	0.06178	0.05556	0.04061	0.02410	0.0
1.0	0.0	0.0	0.0	0.0	0.0	0.0

Tabulated values based on first of equations (15-18).

Table 15-IVb

VALUES OF NORMALIZED SHEAR MODULUS, $\gamma^* = G^*/G_0$, AS A
FUNCTION OF POROSITY AND POISSON'S RATIO OF MATRIX

Absolute Porosity, p	Poisson's Ratio of Dense Substance, ν_0					
	0	0.1	0.2	0.3	0.4	0.5
0	1.0	1.0	1.0	1.0	1.0	1.0
0.1	0.80769	0.81250	0.81818	0.725	0.83333	0.84375
0.2	0.65116	0.65823	0.66667	0.67692	0.68966	0.70588
0.3	0.52128	0.52907	0.53846	0.55	0.56452	0.58333
0.4	0.41177	0.41936	0.42857	0.44	0.45455	0.47368
0.5	0.31818	0.32500	0.33333	0.34375	0.35714	0.375
0.6	0.23729	0.24299	0.25	0.25882	0.27027	0.28571
0.7	0.16667	0.17105	0.17647	0.18333	0.19231	0.20455
0.8	0.10448	0.10744	0.11111	0.11579	0.12195	0.13043
0.9	0.04930	0.05096	0.05556	0.055	0.05814	0.0625
1.0	0.0	0.0	0.0	0.0	0.0	0.0

Tabulated values based on second of equations (15-18).

Table 15-IVc

VALUES OF NORMALIZED YOUNG'S MODULUS, $\eta^* = E^*/E_0$, AS
A FUNCTION OF POROSITY AND POISSON'S RATIO OF MATRIX

Absolute Porosity, p	Poisson's Ratio of Dense Substance, ν_0					
	0	0.1	0.2	0.3	0.4	0.5
0	1.0	1.0	1.0	1.0	1.0	1.0
0.1	0.82353	0.82048	0.81818	0.81784	0.81967	0.82443
0.2	0.67470	0.67010	0.66667	0.66616	0.66890	0.67606
0.3	0.54749	0.54231	0.53846	0.53790	0.54096	0.54902
0.4	0.43750	0.43237	0.42857	0.42802	0.43103	0.43902
0.5	0.34146	0.33679	0.33333	0.33283	0.33557	0.34286
0.6	0.25688	0.25292	0.25	0.24957	0.25189	0.25806
0.7	0.18405	0.17874	0.17647	0.17614	0.17794	0.18274
0.8	0.11475	0.11265	0.11111	0.11089	0.11211	0.11538
0.9	0.05447	0.05341	0.05556	0.05252	0.05313	0.05479
1.0	0.0	0.0	0.0	0.0	0.0	0.0

Tabulated values based on third of equations (15-18).

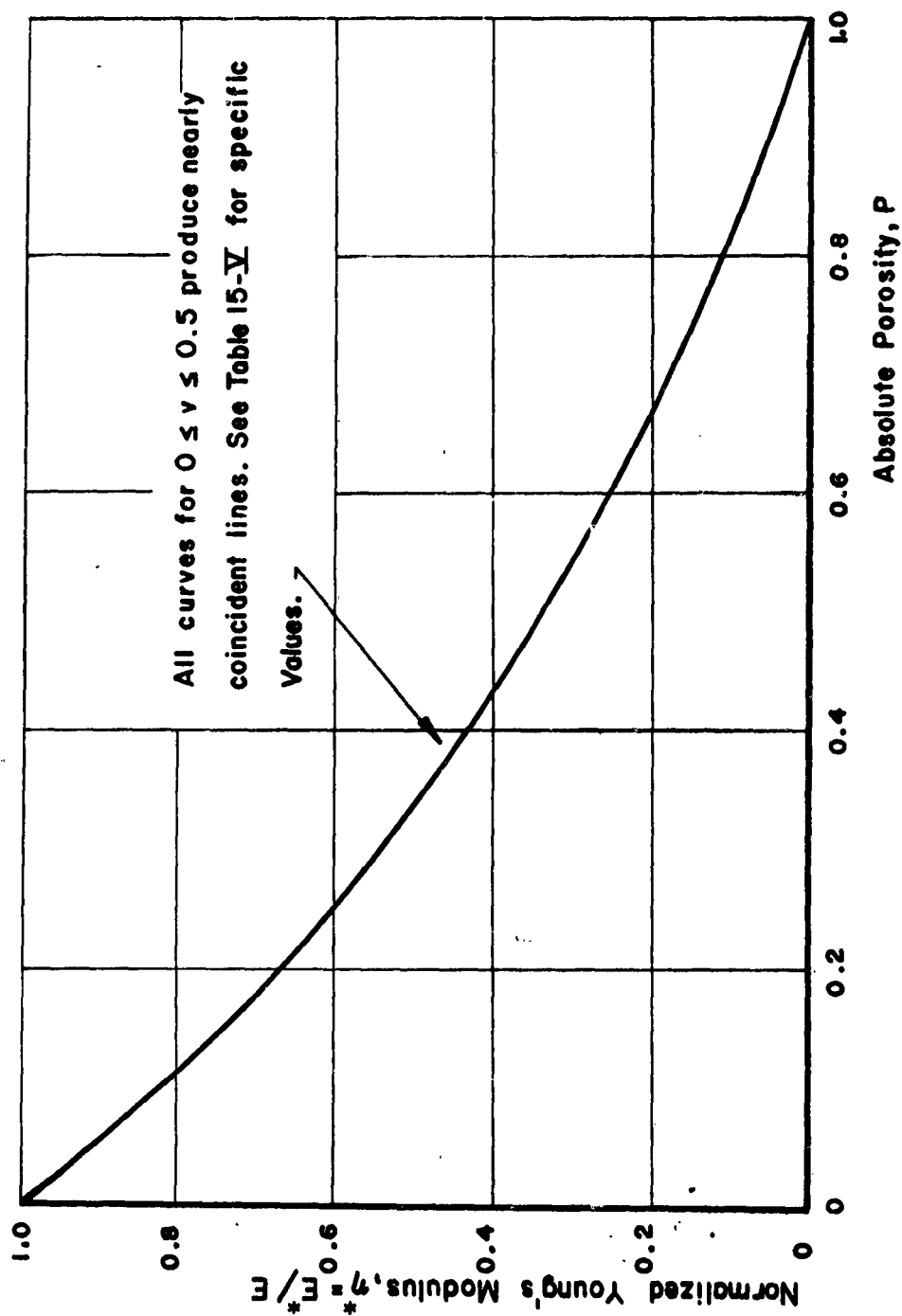


Fig. 15-2 ANALYTICAL PREDICTION FOR EFFECT OF POROSITY AND POISSON'S RATIO UPON YOUNG'S MODULUS

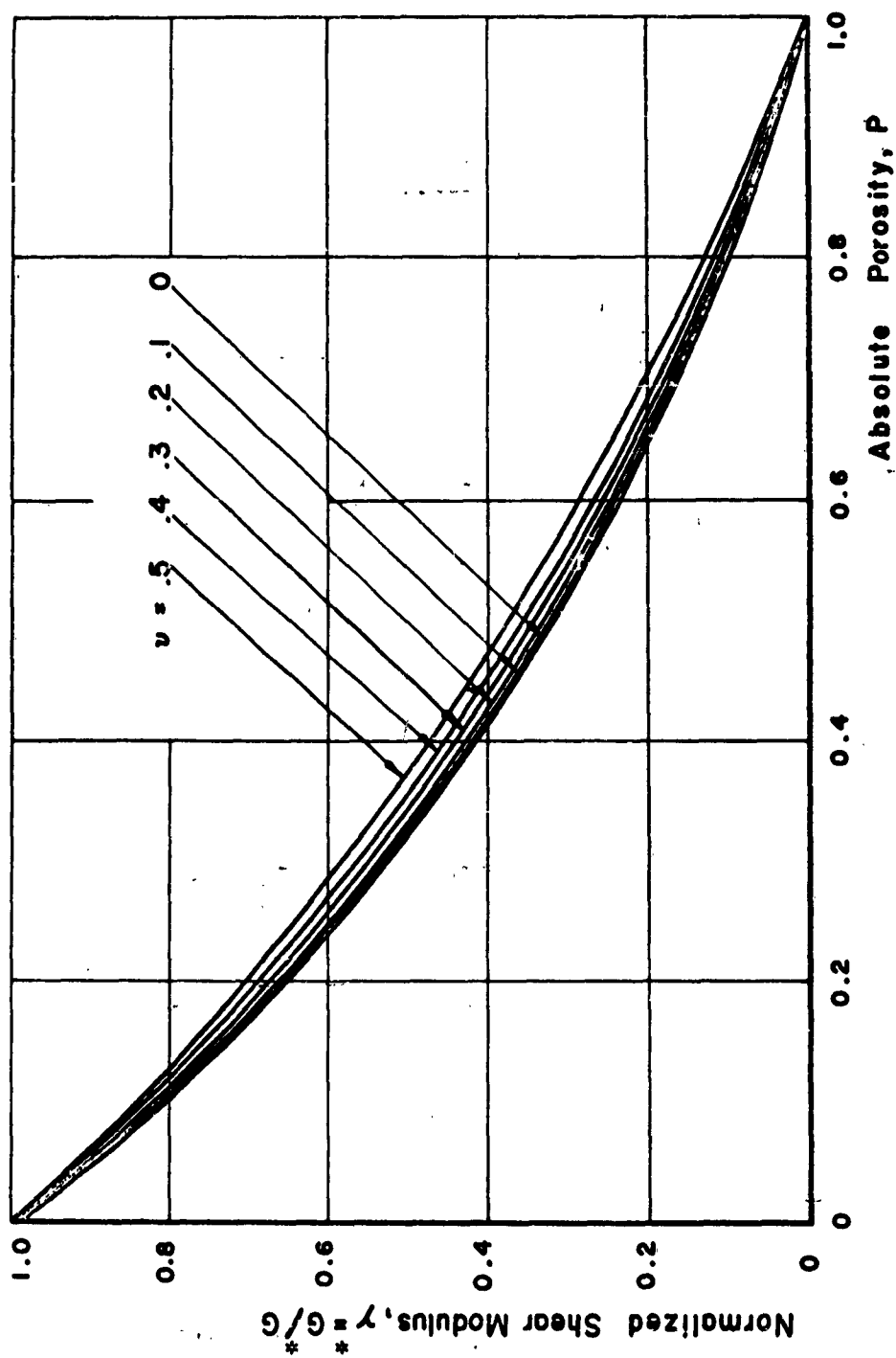


Fig. 15-3 ANALYTICAL PREDICTION FOR EFFECT OF POROSITY AND POISSON'S RATIO UPON SHEAR MODULUS

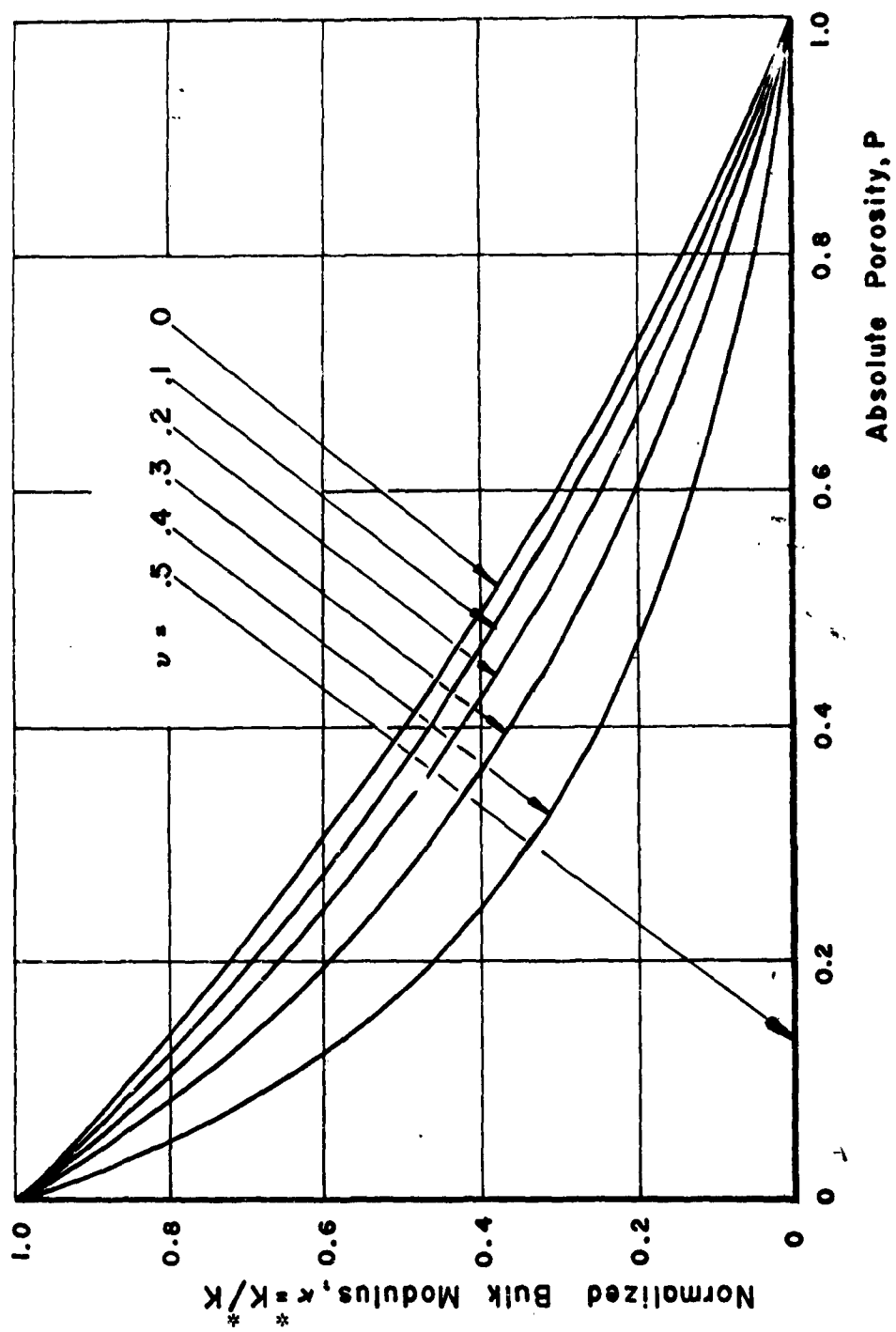


Fig. 15-4 ANALYTICAL PREDICTION FOR EFFECT OF POROSITY AND POISSON'S RATIO UPON BULK MODULUS

diminution of volume of the material under hydrostatic compression at the sole expense of the shrinkage of pores. This state of affairs, naturally, must terminate when all the pores have been completely filled.

(2) The effect of Poisson's ratio on the shear modulus is comparatively modest, as shown by Fig. 15-3.

(3) The effect of Poisson's ratio on Young's modulus is virtually non-existent. This conclusion, in fact, can be anticipated from the results shown in Table 15-III, where k_3 is seen to vary over the narrow range of only 0.917-1.005. Because of this, it appears completely admissible to set $k_3 = 1$, which then leads to the exceedingly simple expression

$$\eta^* = (1 - \rho)/(1 + \rho) \quad (15-23)$$

(4) The values of all three normalized elastic moduli are identical at $\nu_0 = 0.2$, for all levels of porosity, as can be seen from Tables 15-IV.

(5) The analytical expressions satisfy the boundary conditions in that all of the normalized elastic constants have a value of 1.0 at zero porosity; that is the elastic constants of the heterogeneous material are equal to those of the dense material in the absence of pores. Conversely, all elastic constants vanish when the material consists entirely of pores ($p = 1.0$).

Because of their factual nature and simple closed form, the analytical expressions derived here offer substantial promise for determining the effect of porosity upon the elastic behavior of substances. An extensive effort will be made to confirm the correctness of the predictions rendered by this theory during the continuation phase of this program by carefully planned experimental studies. In this regard, it is reiterated that the derivations presented here do not consider effects extraneous to that of porosity; if, therefore, grain size or surface texture are also allowed to vary in the experiments, such considerations must be

taken into account by suitable analytical or empirical formulations additive to those concerning the effect of porosity. Also, the derivations assume purely elastic behavior. Therefore, elastic effects, as manifested by such phenomena as dissipative damping, must again be allowed for by additive factors modifying the basic formulations presented here.

The discussion to this point has concerned only the variation of elastic constants in porous materials; the effect of porosity upon the strength of elastic substances will next be examined.

6. EFFECT OF POROSITY ON STRENGTH OF ELASTIC SUBSTANCES

As discussed, the effect of porosity on the short-time strength of sintered bodies cannot be predicted on purely analytical grounds, because the shape, size and orientation of the pores (determining the effective stress concentration factors associated with them) have significant bearing upon the resulting strength, in addition to the gross volumetric effects ascribable to the removal of solid volume by the presence of pores. Thus the subject has been treated primarily by proposing empirical expressions which were found to fit experimental results to a satisfactory degree. These will be reviewed briefly below.

The first empirical relationship of this nature, and the one in broadest use at present, was suggested by Duckworth⁽¹⁵⁻²³⁾ in a discussion to a paper by Ryshkewitch⁽¹⁵⁻²⁴⁾. The expression is of the simple exponential form

$$S = S_0 e^{-bp} \quad (15-24)$$

where

S is the strength of porous substance
 S_0 is the strength of dense substance
 b is a constant

This expression will be recognized as identical in form to the elastic modulus versus porosity relationship of Eq. 15-4 subsequently proposed by Spriggs and Vasilos⁽¹⁵⁻¹⁹⁾ and, in fact, has served as the model for the latter proposal. The objections to this equation are, therefore, identical to those already voiced in connection with Eq. 15-4 before, the principal amongst these being that this expression does not satisfy the boundary conditions: at $p = 1$ Eq. 15-24 still predicts a finite value of S , instead of the correct value of $S = 0$.

We shall return later to the evaluation of Eq. 15-24 on the basis of experimental work; in the meanwhile, we shall continue the review of other empirical formulations suggested on the strength-porosity relationship. Coble and Kingery⁽¹⁵⁻²⁰⁾ have proposed in their paper, almost parenthetically, a relationship of the form

$$0.6p = \exp \left[- \frac{S}{8000(1-p)} \right] \quad (15-25)$$

This function has the apparent advantage of not containing any arbitrary constants. On the other hand, its form is very unwieldy, and it would be much more easily applied if transformed to the expression

$$S = -8000(1-p) \log(0.6p) \quad (15-26)$$

The more serious objections to this empirical equation, as already noted by Coble and Kingery, are that the functional form is indeterminate at $p = 1$, although it approaches zero at the limit. However, at $p = 0$ (i. e., theoretical density), it predicts an infinite strength which is patently impossible. Lastly, the constants of 8000 and 0.6 have no rational basis, and were selected only to fit the limited data of Coble and Kingery. Thus, it would appear far more logical to replace these numbers by arbitrary constants determined from experiments; in this event, however, the expression,

apart from being less factual, would also become more cumbersome than the simple Duckworth-Ryshkewitch form.

Another form of the porosity-strength relationship is the one suggested by Balshin⁽¹⁵⁻⁴⁾ which has the simple power function nature of

$$S = S_0 (1 - p)^m \quad (15-27)$$

A comparison of this form with empirical data showed that m , an arbitrary material constant, varied between 3 and 6 for different materials. It is also of passing interest to note that the differences between this form, and that of Eq. 15-24, for the case of $b = 1.33m$, amount to only 9 per cent for $b = 3$ and 18 per cent for $b = 6$, over the porosity range of $0 < p < 0.6$.

The objection to the form of the Balshin suggestion is only that it is purely empirical, requiring a reviewed determination of m for each material considered. However, unlike the Duckworth-Ryshkewitch proposal, Eq. 15-27 correctly anticipates the boundary conditions, in that $S = S_0$ when $p = 0$ and $S = 0$ when $p = 1$. In this regard, at least, it is preferential to the much more commonly employed Duckworth-Ryshkewitch form.

There is one more form of the strength-porosity relationship attributed to Hasselman and Shaffer, which merits attention. However, because of its intimate bearing on the semi-rational strength-porosity expression to be proposed here, this subject will be treated later in the text.

Let us return now for an appraisal of the adequacy of the Duckworth-Ryshkewitch expression embodied in Eq. 15-24. Recognizing that in practical cases porosity can be seldom made to vary without a concurrent variation of grain size, Knudsen⁽¹⁵⁻¹⁾ proposed the general equation (shown as Eq. 15-1)

$$S = k d^{-a} e^{-bp} \quad (15-1, \text{bis})$$

The portion dealing with the porosity dependence in Eq. 15-1 will be recognized as identical to that of Eq. 15-24, excepting that the

apart from being less factual, would also become more cumbersome than the simple Duckworth-Ryshkewitch form.

Another form of the porosity-strength relationship is the one suggested by Balshin⁽¹⁵⁻⁴⁾ which has the simple power function nature of

$$S = S_0 (1 - p)^m \quad (15-27)$$

A comparison of this form with empirical data showed that m , an arbitrary material constant, varied between 3 and 6 for different materials. It is also of passing interest to note that the differences between this form, and that of Eq. 15-24, for the case of $b = 1.33m$, amount to only 9 per cent for $b = 3$ and 18 per cent for $b = 6$, over the porosity range of $0 < p < 0.6$.

The objection to the form of the Balshin suggestion is only that it is purely empirical, requiring a reviewed determination of m for each material considered. However, unlike the Duckworth-Ryshkewitch proposal, Eq. 15-27 correctly anticipates the boundary conditions, in that $S = S_0$ when $p = 0$ and $S = 0$ when $p = 1$. In this regard, at least, it is preferential to the much more commonly employed Duckworth-Ryshkewitch form.

There is one more form of the strength-porosity relationship attributed to Hasselman and Shaffer, which merits attention. However, because of its intimate bearing on the semi-rational strength-porosity expression to be proposed here, this subject will be treated later in the text.

Let us return now for an appraisal of the adequacy of the Duckworth-Ryshkewitch expression embodied in Eq. 15-24. Recognizing that in practical cases porosity can be seldom made to vary without a concurrent variation of grain size, Knudsen⁽¹⁵⁻¹⁾ proposed the general equation (shown as Eq. 15-1)

$$S = k d^{-a} e^{-bp} \quad (15-1, bis)$$

The portion dealing with the porosity dependence in Eq. 15-1 will be recognized as identical to that of Eq. 15-24, excepting that the

symbol b replaces S_0 because of the added factors entering the equation.

This expression, accounting for grain size dependence as well, bring additional objections into the picture. Thus, the strength is predicted as approaching an infinitely high value as the grain size tends toward zero, and to fall to vanishingly small values as the grain size becomes very large (i. e., for large single crystals). Both predictions are obviously objectionable; while not pertaining closely to the subject, Weil⁽¹⁵⁻²⁵⁾ proposed a relationship based on the Petch-type grain size dependence, which would eliminate these objections, in the form

$$S = (S_0 + k d^{-1/2}) e^{-bp} \quad (15-28)$$

The most extensive evaluation of Eq. 15-1 was carried out by Knudsen himself⁽¹⁵⁻¹⁾, who conducted original work on ThO_2 and re-evaluated the previous work of Hamjian and Lindman on hot-pressed chromium carbide. These results are compiled in Table 15-V. Also shown in this table is the reinterpretation of results on Lucalox by Knudsen⁽¹⁵⁻²⁵⁾, and the results of Spriggs and Vasilos⁽¹⁵⁻¹⁹⁾ derived from tests conducted on porous Al_2O_3 and MgO . For completeness, Table 15-V includes values of the grain size exponent, in addition to those pertaining to porosity.

A review of the compilation presented in Table 15-V yields the following observations:

The value of a , the grain size exponent, fluctuates very near to a value of $1/2$, the exponent postulated by Petch. In fact, it is quite plausible that a value of $a = 0.50$ would have been derived, had the friction stress appearing in the Petch relationship, as exemplified in Eq. 15-28, been taken into account. Such a data review was not carried out here, primarily because neither is this question the focal point of the current study, nor are the forms of Eq. 15-1 or 15-28 adjudged suitable for the relationship sought.

The porosity exponent, b , is seen to vary over wide ranges (3.7 to 7.3) in Table 15-V; even for the same material, such as ThO_2 , b displays a large sensitivity to the firing temperature. This is quite disconcerting in view of the fact that it negates the hope of fixing the value of b for a given material, and expecting it to vary only from substance to substance. Such a variation with firing temperatures, naturally, stands to reason, since the viscosity and self-diffusion coefficients of the material are highly influenced by the sintering temperature. Therefore, the higher the sintering (or hot-pressing) temperature, the more rounded will be the pores, and the lower should be the stress concentration factors associated with them. Thus one should expect a lesser sensitivity to porosity as the sintering temperature is increased.

This is substantiated by the data assembled in Table 15-V, where the value of b is seen to undergo a general drop with increased sintering (hot-pressing) temperatures, both for the ThO_2 of Knudsen, and for the chromium carbide of Hainjian and Lindman. This finding also means that, if the Knudsen functional relationship of Eq. 15-1 is accepted as valid, a revised determination of all the constants appearing in the relationship for each variation in pressing and firing technique would be required for the same materials.

As an added attempt to provide some rational assessment for his relationship, Knudsen⁽¹⁵⁻¹⁾ assembled a set of values for the constant b , using averages reasonably representative of each material. This set of data, expanded by adding the averages of results shown in Table 15-V, is assembled in Table 15-VI. There is no rational assessment that can be appended to this compilation; the values of b are seen to vary over the broad range of 4 to 9 for materials as widely divergent as sintered powder metal objects and hot-pressed oxides. In fact, the pressing technique is seen to be far more important than the material considered: the listing of values is bracketed by the same material, Al_2O_3 , prepared by different techniques.

Table 15-V

COMPILATION OF CONSTANTS IN KNUDSEN'S POROSITY-GRAIN SIZE-STRENGTH RELATIONSHIPS

$S = k d^{-a} d^{-bp}$; d = grain size; p = absolute porosity

Investigator	Material and Preparation Technique	Firing or Hot-Pressing Temperature, °C	Test Temperature, °C	Values of Constants in Knudsen Relationship		
				k (10^{-3} psi)	a	b
Knudsen (15-1)	Cold-pressed and sintered ThO_2	1800	20	78.6	0.40	4.2
		1800	1000	113.5	0.46	6.6
		1800	20	1666.0	0.50	6.6
		1650	20	69.7	0.39	5.5
		1725	20	69.7	0.39	4.7
Hamjian and Lindman, as re-interpreted by Knudsen (15-1)	Hot-pressed Chromium Carbide	1800	20	69.7	0.39	3.8
		1850	20	69.7	0.39	3.7
		1371	20	228.0	0.56	6.5
		1426	20	228.0	0.56	5.8
Spriggs and Vasilos (15-19)	Al_2O_3 , hot-pressed at 4000 psi	1482	20	228.0	0.56	4.6
		1537	20	228.0	0.56	5.5
Knudsen (15-25)	Lucalox Al_2O_3	1425	20	150.0	0.35	4.0
		1525	20	86.0	0.33	6.0
Knudsen (15-25)	-	-	20	150.0	0.35	4.0

Table 15-VI

COMPILATION OF VALUES FOR POROSITY EXPONENT,
FOR KNUDSEN STRENGTH RELATIONSHIP

Investigator	Material	Value of Porosity Exponent, b
Ryshkewitch (15-24)	Al_2O_3 (sintered) ZrO_2	9.0*
		8.0**
		7.0
Spriggs and Vasilos (15-19)	Al_2O_3 (hot-pressed)	6.6
Duwez and Martens (15-26)	Powder-metal steel	7.0
	Powder-metal iron	5.0
Knudsen (15-1)	ThO_2 (sintered)	5.5
Hamjian and Lindman (15-1)	Chromium carbide (hot-pressed)	5.5
Squire (15-27)	Powder-metal iron	5.0
Coble and Kingery (15-20)	Al_2O_3 (sintered)	4.0
Knudsen (15-25)	Lucalox Al_2O_3	4.0

* Loaded normal to sintering direction.

** Loaded parallel to sintering direction.

As this discussion shows, the Knudsen relationship can be accepted, at best, for what it is: i. e., an empirical expression which fits experimental data reasonably well, particularly in the range of low porosities. However, the constants appearing in it require an experimental redetermination not only for each material, but for each change in preparation technique. Because of its complex form, such determinations generally require multiple regression techniques which, in turn, demand a great number of tests for a reliable determination of the constants. Therefore, it seemed extremely desirable to develop a relationship which would place the porosity dependence of strength on a firmer ground, and require fewer tests for the determination of the correct form of the equation.

Such a relationship was recently proposed by Hasselman and Shaffer⁽¹⁵⁻²²⁾. Proceeding in the reverse (and correct) sense from the analogy of Spriggs and Vasilos, they argued that the general form of their equation (15-20), found to provide an excellent correlation for the effect of porosity upon the elastic constants, could also be extended to cover the effect of porosity on strength. Thus, they proposed the relationship

$$S = S_0 \left[1 - \frac{A c}{1 + B c} \right] \quad (15-29)$$

where A and B are constants related to the mechanical properties of the matrix and the inclusion, respectively; they are related to one another by means of a postulated relationship of the form $B = -\alpha + BA$.

Working with ZrB_2 , containing both a pre-determined amount of graphite (added to the starting powder in carefully controlled amounts) and porosity (the by-product of the sintering technique employed), they found the relationship proposed in Eq. 15-29 to provide an excellent fit to the observed data. The specific values obtained were:

Strength normal to the pressing direction

$$S_o = 30,000$$

$$B = -1.756 + 1.418 A; A = 9.34$$

and

$$S = 30,000 \left[1 - \frac{9.34c}{1 + 11.46c} \right]$$

whereas, for strength parallel to the pressing direction

$$S_o = 30,000$$

$$B = -1.756 + 1.281A; A = 8.03$$

and

$$S = 30,000 \left[1 - \frac{8.03c}{1 + 8.53c} \right]$$

However, a closer examination of equation (15-29) yields the following results. It is clear that this expression, with the explanatory notes appended to it, can be brought to the forms

$$\left. \begin{aligned} S &= S_o \frac{1 + (B - A)c}{1 + Bc} \\ \text{or} \quad S &= S_o \frac{1 - [\alpha + (1 - \beta) A] c}{1 + (\beta A - \alpha) c} \end{aligned} \right\} \quad (15-30)$$

and, in simpler notation

$$S = S_o \frac{1 + B_1 c}{1 + B_2 c} \quad (15-31)$$

where

$$\begin{aligned} B_1 &= \begin{cases} B - A \\ (\beta - 1) A - \alpha \end{cases} \\ B_2 &= \begin{cases} B \\ \beta A - \alpha \end{cases} \end{aligned} \quad (15-32)$$

By extension of these concepts to the case of porosity, the same expressions would remain valid, except that one would have to replace the symbol c by p , so that equation (15-31) would modify to

$$S = S_0 \frac{1 + B_1 p}{1 + B_2 p} \quad (15-33)$$

the meaning of the constants being given by equation (15-32), as before.

An examination of these expressions, which are perhaps the most realistic ones yet proposed, yields the following observations. First, as the form of equation (15-29) or (15-33) shows the Hasselman-Shaffer suggestion is a "two-parameter" equation, which is more complicated than the single parameter forms proposed by Balshin and Duckworth-Ryshkewitch. The use of such an equation will invariably demand the application of statistical regression techniques, as were indeed employed by Hasselman-Shaffer to find appropriate values of the constants.

Secondly, and most importantly, the Hasselman-Shaffer proposal satisfies only one of the two boundary conditions, i. e., that at $p = 0$, $S = S_0$. However, at the other extreme of $p = 1$ (material consisting only of porosity), the proposed form does not satisfy $S = 0$. Instead, it tends to a value of $S = S_0 (1 + B_1)/(1 + B_2)$.

Because of the complexities involved in the use of the Hasselman-Shaffer form, and since it does not satisfy the prescribed boundary conditions, it is appropriate to suggest a simpler format for the effect of porosity upon the strength of porous substances. Such a relationship suggests itself almost automatically, in the light of derivations completed in the previous section for the effect of porosity on elastic constants. Thus, following the form of equations (15-18), the suggested porosity dependence of strength would be written as

$$S = S_0 \frac{1 - p}{1 + Ap} \quad (15-34)$$

where A is a constant to be determined experimentally. The proposed form of equation (15-34) is seen to be a single parameter equation, which satisfies both boundary conditions that $S = S_0$ at $p = 0$ and $S = 0$ at $p = 1$.

The predictive power and adequacy of the proposed form of this strength-porosity relationship has not been evaluated as yet; such work, comparing the predictions of the proposed form of equation (15-34) with past experimental data, and test results to be secured on this program, will be carried out on this task by the work during the forthcoming year.

7. CONCLUSION

A detailed review on the effect of porosity on the mechanical properties of sintered ceramics was carried out. Because of the realization that vigorous analytical techniques are inapplicable to the prediction of the effect of porosity on the strength of the resulting body, the discussion was divided up into two parts: that dealing with the elastic constants of the material, and a second part concerning strength considerations.

The effect of porosity on elastic properties is determinable from the bulk properties of the material; since failure consideration is not involved (only purely elastic behavior is considered), the direct effect of the pore shape and its associated stress concentration factors do not enter the problem. It therefore becomes admissible to adopt idealization of identical spherical pores uniformly dispersed through the volume, and to study the volumetric or distortional changes of a unit volume containing a single pore, when subjected to hydrostatic pressures or shear tractions. Naturally, the actual pores will be neither spherical, nor uniform in size, nor are they uniformly dispersed in the matrix material. Nonetheless, the theoretical idealizations are valid, provided one accepts the analytically assumed pore shape as representative of an "equivalent spherical pore", quite identical to the "equivalent particle size" characterization involved in the Stokes-law particle size determinations of the spectral distribution of powders.

Prior to the development of rigorous theoretical formulations, only empirical relationships existed on this subject.

Among these, a brief review is made of the empirical relationship of Spriggs and Vasilos, and the semi-rational form proposed by Mackenzie. The analytical work is then reviewed, beginning with the work of Einstein and culminating in the recent contributions of Hashin. The latter's analytical derivations, valid for finite (large) values of the absolute porosity, are presented, and the derivation is extended to obtain closed-form solutions for the variation of the elastic modulus as a function of porosity, in addition to comparable expressions for the bulk and shear modulus, derived previously by Hashin.

These expressions refer to the completely general case of an elastic inclusion contained in an elastic matrix; in addition to the assumption of equidistant uniform spherical inclusions, the only other postulate made is that the inclusions be sufficiently spaced so as not to be in physical contact with one another (no open porosity). It is then shown that the recent Hasselman-Shaffer equation represents but a special case of the general Hashin form for the bulk and shear modulus; it is inapplicable to the Hashin formulation of the general case for Young's modulus.

When simplifying the case to the replacement of elastic inclusions by empty pores, the derived equations take on a uniformly simple, identical, format. These expressions contain a single constant, different for each elastic constant, dependent only upon the Poisson's ratio, ν_0 , for the dense (matrix) substance. These expressions are evaluated as parametric variables of ν_0 and p , and presented in graphical form. The results for Young's modulus are found to be particularly simple, and virtually independent of the value of ν_0 .

In regard to the effect of porosity on strength, it is shown that only empirical or semi-rational relationships can be postulated, since the stress-concentration factors corresponding to the particular shape of the "worst" pore initiating fracture have an intrinsic effect upon strength considerations, in addition to the otherwise analyzable volumetric effects associated with the

presence of pores. Among the empirical relationships proposed, a review is made of the Duckworth-Ryshkewitch, Coble and Kingery, Bal'shin and Knudsen suggestions. Of these forms, the Bal'shin relationship is found to be the only one satisfying the imposed boundary conditions. However, this expression has received comparatively little attention in the literature. The most popular expression, the exponential form proposed by Duckworth-Ryshkewitch, and extended by Knudsen, is then received. While this form is capable of fitting experimental observations, at least within comparatively small ranges of the porosity, it requires extensive experimentation on account of the multiple-regression techniques required by it for the determination of the constants entering the expression. Furthermore, the porosity exponent is shown to be more sensitive to the method of material preparation and fabrication than to the material itself, necessitating a redetermination of the functional values of the constants for each change in the preparation technique employed.

Lastly, the recent Hasselman-Shaffer semi-rational form, derived from an analogy with the influence of porosity on elastic constants, is reviewed. The relationship, shown to have provided an excellent fit to experiments conducted on ZrB_2 sintered with predetermined additions of graphite and containing arbitrary levels of porosity, is analyzed in the light of theoretical derivations, and a more universal, simplified, form of the strength/porosity relationship is proposed which fits the prescribed boundary conditions.

The continuation phase of this program will be concerned with the following extensions of the current work:

- (1) An evaluation of the adequacy of agreement between the factually predictive closed-form expressions for the porosity effect on elastic moduli, and the experimental results obtained by previous investigators.

- (2) A comparable evaluation of the adequacy of the strength-porosity relationship proposed here, in the light of previous test work.

presence of pores. Among the empirical relationships proposed, a review is made of the Duckworth-Ryshkewitch, Coble and Kingery, Bal'shin and Knudsen suggestions. Of these forms, the Bal'shin relationship is found to be the only one satisfying the imposed boundary conditions. However, this expression has received comparatively little attention in the literature. The most popular expression, the exponential form proposed by Duckworth-Ryshkewitch, and extended by Knudsen, is then received. While this form is capable of fitting experimental observations, at least within comparatively small ranges of the porosity, it requires extensive experimentation on account of the multiple-regression techniques required by it for the determination of the constants entering the expression. Furthermore, the porosity exponent is shown to be more sensitive to the method of material preparation and fabrication than to the material itself, necessitating a redetermination of the functional values of the constants for each change in the preparation technique employed.

Lastly, the recent Hasselman-Shaffer semi-rational form, derived from an analogy with the influence of porosity on elastic constants, is reviewed. The relationship, shown to have provided an excellent fit to experiments conducted on ZrB_2 sintered with predetermined additions of graphite and containing arbitrary levels of porosity, is analyzed in the light of theoretical derivations, and a more universal, simplified, form of the strength/porosity relationship is proposed which fits the prescribed boundary conditions.

The continuation phase of this program will be concerned with the following extensions of the current work:

- (1) An evaluation of the adequacy of agreement between the factually predictive closed-form expressions for the porosity effect on elastic moduli, and the experimental results obtained by previous investigators.

- (2) A comparable evaluation of the adequacy of the strength-porosity relationship proposed here, in the light of previous test work.

(3) An extension of the porosity relationship derived here to include the effect of grain size, textural effects, statistical strength variations and anelastic properties, either in the form suggested in Part One of this task, or in some other suitable form.

(4) Experimental work on Al_2O_3 and MgO specimens prepared with carefully controlled levels of porosities, to assess the validity of the proposed analytical and semi-rational relationships advanced here. The experimental work will consist first of non-destructive experiments aimed at the determination of elastic constants and internal damping on specimens subjected to a careful determination of the relative ratio of open to closed pores, grain size and surface finish. This will be followed by destructive tests aimed at strength determinations, and subsequent fractographic examinations inquiring into the nature and location of fracture nucleation, the size and distribution of pores, and the apparent relationships between grain texture, sintering practices and resulting porosity.

8. REFERENCES

- 15-1 Knudsen, F. P., "Dependence of Mechanical Strength of Brittle Polycrystalline Specimens on Porosity and Grain Size," J. Am. Ceram. Soc., 42, No. 8, 376-87 (1959)
- 15-2 Spriggs, R. M., "Expression for Effect of Porosity on Elastic Modulus of Polycrystalline Refractory Materials, Particularly Aluminum Oxide," J. Am. Ceram. Soc., 44, No. 12, 628-9 (1961)
- 15-3 Spriggs, R. M. and Brissette, L. A., "Expressions for Shear Modulus and Poisson's Ratio of Porous Refractory Oxides," J. Am. Ceram. Soc., 45, No. 4, 198-9 (1962)
- 15-4 Bal'shin, N. Y., "Relation of Mechanical Properties of Powder Metals and Their Porosity, and the Ultimate Properties of Porous Metal-Ceramic Materials," Doklady Akad. Sci. USSR 67, No. 5, 831-34 (1949)
- 15-5 Hanna, R. and Crandall, W. B., "Dissipation of Energy by the Grain Boundaries," ASTIA Doc. No. 274956 (1962)

- 15-6 Smith, C. S. and Guttman, L. , "Measurement of Internal Boundaries in Three-Dimensional Structures by Random Sectioning," Trans. AIME 197, 81-87 (1953)
- 15-7 Hasselman, D. P. H. , "Tables for the Computation of the Shear Modulus and Young's Modulus for Elasticity from the Resonant Frequencies of Rectangular Prisms," Appi. Res. Branch, Carborundum Co. , Niagara Falls, N. Y. (1961)
- 15-8 Beauchamp, E. K. , "Flash Etching of Al_2O_3 Grain Boundaries," J. A. Ceram. Soc. , 43, No. 10, 552 (1960)
- 15-9 Einstein, A. , "Eine Neue Bestimmung der Molekül-dimensionen," Annalen der Physik, 19, 289-306 (1906) also Ann. der Phys. , 34, 591-592(1911)
- 15-10 Mackenzie, J. E. , "The Elastic Constants of a Solid Containing Spherical Holes," Proc. Phys. Soc. Ser. B, 63, 2-11, (1950)
- 15-11 Hashin, Z. , "The Moduli of an Elastic Solid Reinforced by Rigid Particles," Bull. Rés. Council of Israel, 5C, 46-59 (1955)
- 15-12 Eshelby, J. D. , "The Determination of the Elastic Field of an Ellipsoidal Inclusion and Related Problems," Proc. Roy. Soc. (London), Ser. A, 241, 376-396 (1957)
- 15-13 Hashin, Z. , "The Moduli of an Elastic Solid, Containing Spherical Particles of Another Elastic Material," Proc. IVTAM Symp. , Warsaw, Poland, No. 17 (1958)
- 15-14 Budiansky, B. , Hashin, Z. and Sanders, J. L. , "The Stress Field of a Slipped Crystal and the Early Plastic Behavior of Polycrystalline Materials," Proc. 2nd Symp. on Naval Structural Mechanics, Pergamon Press, N. Y. , 239-258 (1960)
- 15-15 Frisch, H. L. and Simka, R. , "The Viscosity of Colloidal Suspensions and Macro-Molecular solutions," Chap. 14 in "Rheology," Vol. 1, Academic Press, N. Y. (1956)
- 15-16 Reiner, M. , "Rheology," in Encyclopedia of Physics, S. Flugge, ed. , Vol. 6, J. Springer, Berlin, 304-313 (1956)
- 15-17 Paul, B. , "Prediction of Elastic Constants of Multiphase Materials," Trans. AIME, 218, 36-41 (1960)
- 15-18 Hashin, Z. , "The Elastic Moduli of Heterogeneous Materials," Paper No. 61-WA-39, pres. at Ann. Mtg. ASME, New York, (Nov. 1961)

- 15-19 Spriggs, R. M. and Vasilos, T., "Effect of Grain Size and Porosity on Transverse Bend Strength and Elastic Modulus of Hot-Pressed Alumina and Magnesia," 63rd Ann. Mtg., Am. Cer. Soc., Toronto, Canada, April 1960
- 15-20 Coble, R. L. and Kingery, W. D., "Effect of Porosity on Physical Properties of Sintered Alumina," J. Am. Cer. Soc., 39, 377-85 (1956)
- 15-21 Knudsen, F. P., "Effect of Porosity on Young's Modulus of Alumina," J. Am. Cer. Soc., 45, 2, 94-95 (1962)
- 15-22 Hasselman, D. P. H. and Shaffer, P. T. B., "Factors Affecting the Thermal Shock Resistance of Polyphase Ceramic Bodies," WADD-TR-60-749, (April 1960)
- 15-23 Duckworth, W., "Discussion of Ryshkewitch' Paper," J. Am. Cer. Soc., 36, 2, 68 (1953)
- 15-24 Ryshkewitch, E., "Compression Strength of Porous Sintered Alumina and Zirconia - 9th Communication to Ceramography," J. Am. Cer. Soc., 36, 2, 65-68 (1953)
- 15-25 Weibull, N. A., Ed., Studies of the Brittle Behavior of Ceramic Materials, "ASD-TR-61-628, pp. 21-28, April 1962
- 15-26 Duwez, P. and Martens, H. E., "Powder Metallurgy of Porous Metals and Alloys Having a Controlled Porosity," Trans. AIME, 175, (12), 848-74 (1948)
- 15-27 Squire, A., "Density Relationships in Iron Powder Compacts," Trans. AIME, 171, (9), 485-563 (1947)

Aeronautical Systems Division, Dir./Materials and Processes, Metals and Ceramics Lab, Wright-Patterson AFB, Ohio
 Rpt No ASD-TR-61-628, Part II. STUDIES OF THE BRITTLE BEHAVIOR OF CERAMIC MATERIALS. Final report, Dec. 62, 676 p. Incl illus., tables, refs.
 Unclassified Report

The fundamental behavior of brittle non-metallic ceramics was probed. Materials studied included poly and single crystals of MgO, BeO and two grades of Al₂O₃. The statistical fracture was found to be characterized by the Weibull theory. The effect of strain rates from 10⁻¹ to 10⁴ sec⁻¹ at from 75° to 1000°F on the fracture stress in bending was determined experimentally. The

(over)

effects of non-uniform stress fields, of microstructure and of surface energy were investigated. Internal friction was measured to determine the effect of anneal time and temperature, stress amplitude and dislocation density on dislocation damping. Fracture mechanisms and the variation of strength with impurity level were studied. The corrosion processes which affect long-term strength were investigated and fatigue theory applied. The effect of thermal mechanical history on the mechanical properties of MgO was investigated. Surface active environments, crack propagation and rheotropic behavior were explored. Dislocation studies of the existence of plastic flow were conducted. The effect of porosity and grain size on strength and elastic modulus was studied analytically and experimentally.

Aeronautical Systems Division, Dir./Materials and Processes, Metals and Ceramics Lab, Wright-Patterson AFB, Ohio
 Rpt No ASD-TR-61-628, Part II. STUDIES OF THE BRITTLE BEHAVIOR OF CERAMIC MATERIALS. Final report, Dec. 62, 676 p. Incl illus., tables, refs.
 Unclassified Report

The fundamental behavior of brittle non-metallic ceramics was probed. Materials studied included poly and single crystals of MgO, BeO and two grades of Al₂O₃. The statistical fracture was found to be characterized by the Weibull theory. The effect of strain rates from 10⁻¹ to 10⁴ sec⁻¹ at from 75° to 1000°F on the fracture stress in bending was determined experimentally. The

(over)

effects of non-uniform stress fields, of microstructure and of surface energy were investigated. Internal friction was measured to determine the effect of anneal time and temperature, stress amplitude and dislocation density on dislocation damping. Fracture mechanisms and the variation of strength with impurity level were studied. The corrosion processes which affect long-term strength were investigated and fatigue theory applied. The effect of thermal mechanical history on the mechanical properties of MgO was investigated. Surface active environments, crack propagation and rheotropic behavior were explored. Dislocation studies of the existence of plastic flow were conducted. The effect of porosity and grain size on strength and elastic modulus was studied analytically and experimentally.

1. Ceramic Materials
 L. AFSC Project 7350,
 Task 735001
 II. Contract AF 33
 (416)-7465
 III. Armour Research
 Foundation,
 Chicago 16, Ill.
 IV. N. A. Weil
 V. ARF Project No.
 8203
 VI. Avail fr OTS
 VII. In ASTIA collection

1. Ceramic Materials
 L. AFSC Project 7350,
 Task 735001
 II. Contract AF 33
 (416)-7465
 III. Armour Research
 Foundation,
 Chicago 16, Ill.
 IV. N. A. Weil
 V. ARF Project No.
 8203
 VI. Avail fr OTS
 VII. In ASTIA collection